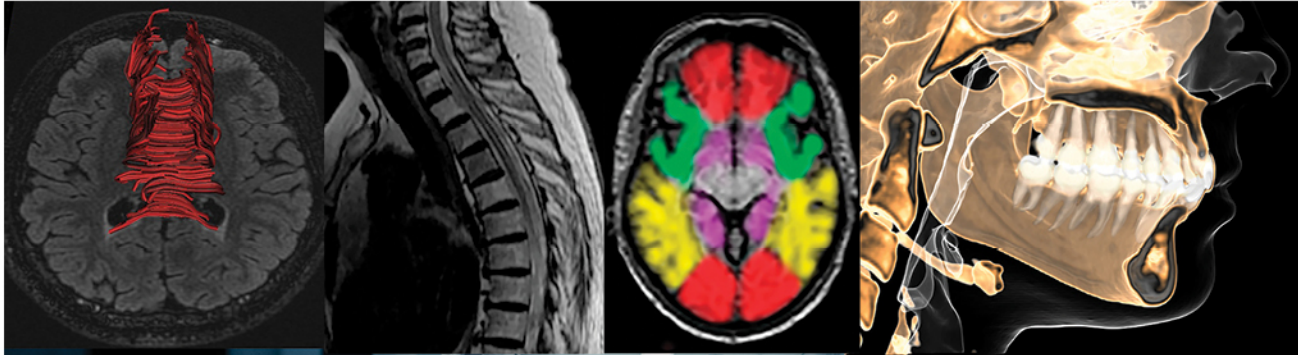
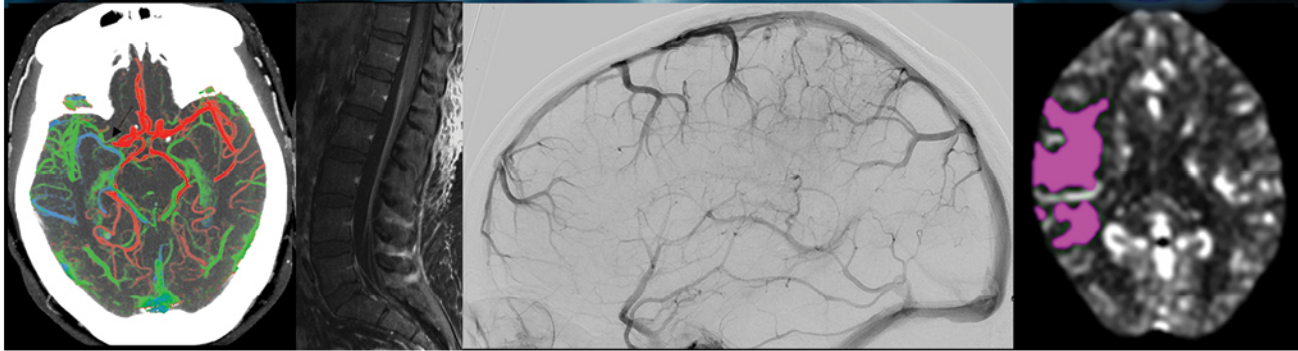


RadioGraphics

The journal of continuing medical education in radiology



Emergency Neuroradiology



October Special Issue 2019

Volume 39 • Number 6

radiographics.rsna.org

RSNA®
Radiological Society
of North America



The 2019 *RadioGraphics* Monograph Issue: Emergency Neuroradiology

Christopher T. Whitlow, MD, PhD, MHA • Michael H. Lev, MD • Achala S. Vagal, MD, MS

Editor's Note.—Initiated in 1999 by William W. Olmsted, MD, Editor Emeritus of *RadioGraphics*, the annual monograph issue has consistently been one of the most valued components for the journal's readers. These focused issues have covered a spectrum of topics across the radiologic subspecialties, including practice management, pediatric imaging, musculoskeletal imaging, quality and safety, cardiothoracic imaging, women's imaging, abdominal imaging, genitourinary imaging, vascular and interventional radiology, breast imaging, featured material from the Armed Forces Institute of Pathology (now known as the American Institute for Radiologic Pathology), and highlights of the education exhibits from the RSNA Annual Meeting. The guest editors of these monographs have typically served as *RadioGraphics* editorial board members; they have engaged experts in their subspecialty areas and solicited educational material from the annual meeting to provide original material for this series. This year, the guest editors are Achala S. Vagal, MD, MS, and Christopher T. Whitlow, MD, PhD, MHA, editorial board members for neurologic/head and neck imaging; and Michael H. Lev, MD. They have coordinated the present compilation, the 21st in the series, of up-to-date reviews of the state of the art in the important subject area of neuroradiologic emergencies. I am grateful for the effort that Drs Vagal, Whitlow, and Lev have devoted to this project and to the numerous authors who volunteered their time and expertise to provide *RadioGraphics* readers with the articles that fill this volume.—JEFFREY S KLEIN, MD

* * *

The *RadioGraphics* monograph for 2019 focuses on emergency neuroradiology and was strategically curated to include topics related to the brain, head and neck, and spine, ranging from common emergent entities such as ischemic stroke and traumatic brain injury to focused conditions affecting the soft-tissue neck and

spinal cord. The topic of emergency neuroradiology is timely and important. Medical imaging continues to advance, facilitating the ability of radiologists to add value to acute patient care and contribute substantially to complex medical management decisions that affect the lives of our patients. Keeping abreast of the latest advances in emergency neuroradiology is an important part of serving our patients and referring colleagues. In this regard, we hope that this special issue will be a valuable source of continuing medical education and will become a well-thumbed reference for our radiology readership on the front lines of diagnostic imaging and emergency neuroradiology, as well as our colleagues in related fields of medicine. We especially hope that the information in the exceptional articles in this monograph issue will be useful to our trainees (medical students, residents, and fellows) in fostering their rapidly expanding knowledge base and inspiring them to advance our field of medicine into the future.

Brain Imaging

Treatment for acute ischemic stroke has evolved significantly in recent years and has changed how we image and treat patients with acute stroke. Given this paradigm shift, several articles in this monograph focus on stroke imaging. Nael and colleagues review imaging strategies related to recently updated American Heart Association/American Stroke Association guidelines regarding endovascular treatment for acute ischemic stroke. Potter et al review CT-based workup of ischemic stroke for making treatment decisions involving intravenous tissue plasminogen activator and endovascular thrombectomy, focusing on practical skills, interpretation challenges, mimics, and pitfalls. The etiology and outcomes associated with ischemic stroke can differ most drastically between young and older adults. McCarty and colleagues provide an image-rich review of the epidemiology, workup, and etiology of ischemic infarction in young adults. Cerebral venous thrombosis (CVT) can

RadioGraphics 2019; 39:1569–1570
<https://doi.org/10.1148/rg.2019194010>

From the Department of Radiology, Wake Forest University School of Medicine, Winston-Salem, NC (C.T.W.); Division of Emergency Radiology, Department of Radiology, Massachusetts General Hospital, Boston, Mass (M.H.L.); and Department of Radiology, University of Cincinnati Medical Center, 234 Goodman St, Cincinnati, OH 45267-0525 (A.S.V.). Address correspondence to the authors (e-mail: cwhitlow@wakehealth.edu, mlev@partners.org, vagala@ucmail.uc.edu).

result in high morbidity and mortality, including ischemic stroke and intracranial hemorrhage, but it is reversible if quickly and accurately diagnosed and appropriately treated. Canedo-Antelo et al review different subtypes of CVT and describe typical findings and pitfalls for CVT across various imaging techniques.

Like ischemic stroke, traumatic brain injury (TBI) is a major public health problem, with an estimated yearly global incidence of 69 million. Schweitzer et al review appropriate imaging utilization and classification of TBI, as well as key diagnostic imaging findings that impact patient management and prognosis. Brain herniation from trauma and other causes can lead to devastating brain injury, compression of vessels resulting in hemorrhage or ischemia, and/or obstruction of cerebrospinal fluid producing hydrocephalus. Riveros Gilardi et al review the spectrum of imaging features of cerebral herniation syndromes and provide a systematic approach to analyze imaging data for prompt and accurate diagnosis. Oliveira et al review toxic and metabolic disorders affecting the brain and propose a systematic approach for the diagnosis of these disorders on the basis of the most common imaging patterns. Guryildirim and colleagues review common and less common causes of acute headache in the emergency setting by incorporating clinical history and multimodality imaging techniques.

Head and Neck Imaging

Go and colleagues focus on blunt and penetrating traumatic injuries to the skull base and the soft tissues of the neck. They review the pertinent anatomy and classification schemes for traumatic emergencies involving the neck and skull base and describe key findings that require time-sensitive surgical or endovascular treatment in the acute setting. Kamalian et al focus on nontraumatic head and neck emergencies, with a review of common conditions that bring patients to the emergency department. Cunqueiro et al provide a systemic approach to interpreting CT images of the neck for identifying salient findings; formulating the correct diagnosis; and reporting in a complete, clear, logical manner. Loureiro and colleagues review dental emergencies and provide imaging protocols, as well as descriptions of relevant anatomy and key imaging findings of common dental emergencies ranging from infection and trauma to those with iatrogenic causes.

Spine Imaging

Over the past 2 decades, the number of annual spine surgeries has been steadily increasing, and therefore it is important to be familiar with the postoperative spine. Many times, spine imaging studies are ordered as emergent examinations in the immediate postoperative period. Ghodasara and colleagues describe normal postoperative findings, signs of successful surgery, and a broad spectrum of postoperative complications, all of which will aid radiologists in the generation of reports that facilitate optimal patient management. Two articles are dedicated to reviewing issues related to spinal cord imaging in the emergency setting. Lee and colleagues focus on signal abnormalities and introduce an algorithmic diagnostic approach to evaluate T2 signal hyperintensity within the spinal cord that may help radiologists narrow the differential diagnosis in patients with myelopathy. Laur and colleagues focus on acute myelopathy in the nontrauma setting and describe a compartmental approach applied to spine MRI to refine the diagnosis and determine appropriate management. Infectious diseases with neurologic manifestations have been reemerging owing to many factors, including human population growth, increased international travel, and greater contact with wild animal reservoirs. Carmo et al review the epidemiologic aspects of these diseases that affect the brain and spine.

Organizing this monograph issue was a great honor and absolute delight. Each author invested substantially to incorporate content of exceptional quality that is also visually impactful, as is the hallmark of *RadioGraphics*. Our dedicated reviewers contributed insights and comments to the individual manuscripts that were firmly grounded in their content domain expertise, which augments the value of this issue. The *RadioGraphics* editorial team was instrumental in guiding the efforts of all involved in producing this monograph, endeavoring tirelessly to organize the workflow and maintain the close connectivity between the monograph authors, reviewers, and guest editors. Of course, the leadership and vision of Editor Jeffrey S. Klein, MD, resonates from each page and brilliant image contained in this issue, as has been the case for every *RadioGraphics* article published during his lauded tenure. We feel especially privileged and grateful to have worked with Dr Klein, one of the great editors and educators in the radiologic sciences, whose incredible insight and guidance has resulted in the outstanding monograph issue that you are reading today.



Traumatic Brain Injury: Imaging Patterns and Complications

*Andrew D. Schweitzer, MD
Sumit N. Niogi, MD, PhD
Christopher J. Whitlow, MD, PhD,
MHA
A. John Tsioris, MD*

Abbreviations: ACR = American College of Radiology, CSF = cerebrospinal fluid, DAI = diffuse axonal injury, DTI = diffusion-tensor imaging, EDH = epidural hematoma, FLAIR = fluid-attenuated inversion recovery, GCS = Glasgow Coma Scale, SAH = subarachnoid hemorrhage, SDH = subdural hematoma, TAI = traumatic axonal injury, TBI = traumatic brain injury, 3D = three dimensional

RadioGraphics 2019; 39:1571–1595

<https://doi.org/10.1148/rg.2019190076>

Content Codes: **CT** **ER** **HN** **MR** **NR**

From the Department of Radiology, Weill Cornell Medicine/New York-Presbyterian Hospital, 525 E 68th St, Starr 630C, New York, NY 10075 (A.D.S., S.N.N., A.J.T.); and Department of Radiology, Wake Forest School of Medicine, Winston-Salem, N.C. (C.T.W.) Received March 22, 2019; revision requested May 31 and received June 15; accepted June 19. For this journal-based SA-CME activity, the authors S.N.N. and A.J.T. have provided disclosures (see end of article); all other authors, the editor, and the reviewers have disclosed no relevant relationships.

Address correspondence to A.J.T. (e-mail: apt9001@med.cornell.edu).

See discussion on this article by Mathur and Nicolaou (pp 1595–1597).

©RSNA, 2019

SA-CME LEARNING OBJECTIVES

After completing this journal-based SA-CME activity, participants will be able to:

- Understand the benefits and limitations of CT, MRI, and angiographic techniques in TBI.
- Describe the primary injury patterns of TBI on the basis of the mechanism of injury.
- Recognize secondary injuries that can occur as complications of mass effect and herniation.

See rsna.org/learning-center-rg.

While the diagnosis of traumatic brain injury (TBI) is a clinical decision, neuroimaging remains vital for guiding management on the basis of identification of intracranial pathologic conditions. CT is the mainstay of imaging of acute TBI for both initial triage and follow-up, as it is fast and accurate in detecting both primary and secondary injuries that require neurosurgical intervention. MRI is more sensitive for the detection of certain intracranial injuries (eg, axonal injuries) and blood products 24–48 hours after injury, but it has limitations (eg, speed, accessibility, sensitivity to motion, and cost). The evidence primarily supports the use of MRI when CT findings are normal and there are persistent unexplained neurologic findings or at subacute and chronic periods. Radiologists should understand the role and optimal imaging modality to use, in addition to patterns of primary brain injury and their influence on the risk of developing secondary brain injuries related to herniation.

©RSNA, 2019 • radiographics.rsna.org

Introduction

Traumatic brain injury (TBI) is a major public health problem, with an estimated yearly global incidence of 69 million and with an increasing prevalence over the past 25 years (1,2). In the United States in 2013, there were nearly 2.8 million TBI diagnoses, 282 000 TBI-related hospitalizations, and 56 000 TBI-related deaths (3). Imaging—CT and, to an increasing extent, MRI—plays a critical role in TBI management and prognostication (4). This article reviews the classifications of TBI, summarizes the utility of each imaging modality, and presents TBI imaging findings categorized by anatomic location. Illustrative cases highlight important injury patterns and their mechanisms, and findings that influence management and prognosis are emphasized.

Classification of TBI

Glasgow Coma Scale

TBI is a clinical diagnosis traditionally classified using the Glasgow Coma Scale (GCS). GCS scores 13–15 are mild brain injuries, 9–12 are moderate, and 3–8 are severe. There is a strong correlation between GCS score and morbidity and/or mortality at the severe end of the spectrum but limited correlation at the mild end of the spectrum.

The GCS has been a long-standing clinical tool used to quickly categorize TBI as mild, moderate, or severe solely on the basis of physical examination findings without the need to use specialized tools. GCS score is determined by summing the scores from three categories: best eye response (score 1–4), best verbal response (score 1–5), and best motor response (score 1–6), yielding scores of 3–8 (severe), 9–12 (moderate), and 13–15 (mild) (5). The value of this method has been

TEACHING POINTS

- TBI is a clinical diagnosis traditionally classified using the GCS. GCS scores 13–15 are mild brain injuries, 9–12 are moderate, and 3–8 are severe. There is a strong correlation between GCS score and morbidity and/or mortality at the severe end of the spectrum but limited correlation at the mild end of the spectrum.
- Nonenhanced head CT is critical for triage, imaging of intracranial pathologic conditions, and follow-up of patients with intracranial findings given its speed, accessibility, and sensitivity for depicting brain injuries that require neurosurgical intervention, such as large-volume hemorrhage, herniation, and infarction
- MRI has substantially higher sensitivity than CT for the detection of EDH, SDH, nonhemorrhagic cortical contusions, brain-stem injuries, and white matter axonal injuries (supported by level Ib evidence).
- It is important to note that mixed-attenuation SDHs are not necessarily acute or chronic. The hypoattenuating portions may represent hyperacute and/or unclotted chronic blood products, particularly in patients with coagulopathy.
- DAI can be hemorrhagic and/or nonhemorrhagic, and both hemorrhagic and nonhemorrhagic lesions are more sensitively detected at MRI. Acute DAI lesions may restrict diffusion. Characteristic locations for TAI lesions include the gray-white matter junction (especially in the frontal lobes because the axis of rotation of the head is posterior, allowing greater differences in momentum anteriorly), corpus callosum (especially the splenium), internal capsules, and dorsal midbrain and/or pons.

its ease of use combined with the strong correlation to morbidity and mortality at the severe end of the TBI spectrum.

The GCS still remains a primary tool both clinically and in research for the classification of TBI. Unfortunately, correlation with morbidity on the mild end of the spectrum is poor. A perfect score of 15 does not signify absence of a TBI, nor does it exclude the possible development of postconcussive syndrome. Despite the gross limitations for patients with mild TBI, a recent review of 811 143 patients from the National Trauma Data Bank showed that a GCS score less than or equal to 13 can discriminate the need for trauma center care (6). GCS scores have been used to discriminate in-hospital mortality, receipt of neurosurgical interventions, severe brain injury, and emergency intubation (7). For mild TBI, duration of loss of consciousness and posttraumatic amnesia have a much stronger correlation with outcome and worse Glasgow Outcome Scale scores at 6–12 months (8).

American Academy of Neurology Concussion Guidelines

The terms *TBI* and *concussion* historically have often been used interchangeably. In recent years, concussion has been more closely linked to mild

TBI. Moreover, recent efforts have focused on further refinement of these definitions. Concussion has been suggested to reflect a transient condition avoiding the potential stigma associated with brain injury (9).

Along these efforts, in 2013 the American Academy of Neurology revised the prior 1997 concussion guidelines (10). These new guidelines report that concussion is a clinical diagnosis and that CT “should not be used to diagnose sports-related concussion but might be obtained to rule out more serious TBI such as an intracranial hemorrhage in athletes with a suspected concussion who have LOC [loss of consciousness], posttraumatic amnesia, persistently altered mental status ([GCS] <15), focal neurologic deficit, evidence of skull fracture on examination, or signs of clinical deterioration (Level C evidence)” (10).

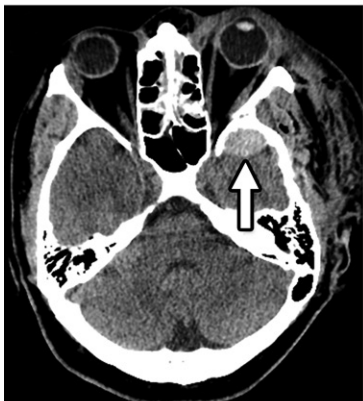
Imaging Utilization

Nonenhanced head CT is critical for triage, imaging of intracranial pathologic conditions, and follow-up of patients with intracranial findings given its speed, accessibility, and sensitivity for depicting brain injuries that require neurosurgical intervention, such as large-volume hemorrhage, herniation, and infarction. Other specific benefits of CT over MRI include a much higher sensitivity for the detection of a fracture (associated with epidural hematoma [EDH], vascular injury, and cerebrospinal fluid [CSF] leak) and no need to screen for safety, which is especially important in penetrating or blast injuries (Figs 1–5). The New Orleans Criteria, the Canadian Head CT Rule, and the National Emergency X-Radiography Utilization Study II (NEXUS-II) criteria are the most widely used clinical decision-making tools that help determine whether nonenhanced head CT is clinically warranted in cases of mild TBI (11). These criteria are used to inform the American College of Radiology (ACR) Appropriateness Criteria for head trauma (12–14). Nonenhanced head CT is a class I recommendation for patients with moderate to severe TBI (4).

For the nonenhanced CT protocol for adults, we recommend using multidetector CT, axial views, head tilt or angled gantry to reduce lens radiation exposure, 120 kVp, 240 mAs, 22-cm field of view, and 5-mm section thickness. The following reconstructions should be obtained: (a) axial images at 2.5-mm sections in standard algorithm, (b) axial images at 5-mm sections in standard algorithm, (c) axial images at 2.5-mm sections in bone algorithm, (d) coronal images at 2 × 2-mm sections, (e) sagittal images at 2 × 2-mm sections, and (f) axial images at 0.625-mm sections that can be used to make 3D reconstructions of



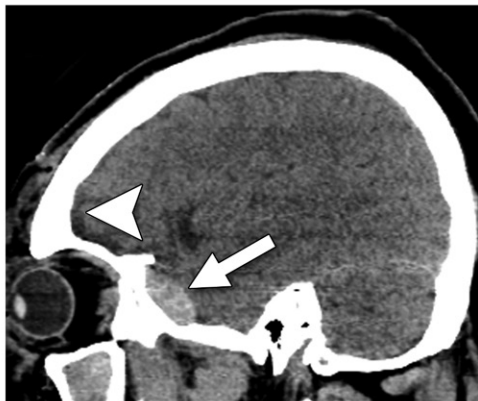
a.



b.



c.



d.

Figure 1. Blunt head injury with depressed skull fracture, complex maxillofacial fractures, venous and arterial EDH, subdural hematoma (SDH), and hemorrhagic contusions in a 19-year-old man who was assaulted with a baseball bat following a road rage incident. His GCS score at presentation was 15. (a) Axial nonenhanced CT image shows multiple comminuted left-sided maxillofacial fractures (arrowhead) and a depressed fracture (arrow) of the squamosal segment of the left temporal bone. A left frontal bone fracture was also present (not shown). (b-d) Axial (b, c) and sagittal (d) nonenhanced CT images show a venous EDH anteriorly within the middle cranial fossa adjacent to the sphenoid bone fracture (arrow in b and d), a small arterial EDH associated with the depressed temporal bone fracture (straight arrow in c), and a shallow SDH (arrowheads in c and d) along the left frontal convexity. There were multifocal small hemorrhagic contusions (curved arrow in c) underlying the depressed temporal bone fracture.

the calvarium and skull base when necessary. The use of reformatted coronal and sagittal images maximizes diagnostic sensitivity for the detection of intracranial hemorrhage, extra-axial collections, and herniation (15).

MRI has substantially higher sensitivity than CT for the detection of EDH, SDH, nonhemorrhagic cortical contusions, brainstem injuries, and white matter axonal injuries (supported by level Ib evidence) (4,16–22). MRI is also more sensitive for the detection of hemorrhagic parenchymal contusions (level Ib–II evidence), all stages of SAH (level II evidence), and subacute SAH (level Ib–II evidence) (16–18,20–27).

A class I recommendation exists for MRI when nonenhanced CT is normal and there are persistent unexplained neurologic findings (4,28). However, in other clinical scenarios, the optimal role of MRI in TBI remains unclear, especially in light of safety concerns (eg, metallic foreign bodies), limited availability, longer imaging time, sensitivity to patient motion, and higher cost.

For adults, our nonenhanced brain MRI protocol includes performing diffusion-weighted and susceptibility-weighted imaging and fat-suppressed two-dimensional (2D) or 3D T2-weighted fluid-attenuated inversion-recovery (FLAIR), T2-weighted, and 2D or 3D T1-weighted sequences. The 3D sequences are acquired in the sagittal plane at 1-mm isotropic res-

olution and reformatted in the axial and coronal planes. Numerous studies have shown the higher sensitivity of susceptibility-weighted imaging over that of gradient-recalled-echo sequences for the detection of intracranial hemorrhage (29–33). Diffusion-weighted imaging is particularly important for the detection of nonhemorrhagic axonal injuries (34–37).

Imaging performed after the administration of contrast material (postcontrast) is not routinely performed in the trauma setting. However, early studies have shown that meningeal enhancement, a finding suggestive of meningeal injury, can be more sensitively detected with postcontrast T2-weighted FLAIR sequences (37–39).

Performing CT or MR angiography is recommended when a fracture traverses the carotid canal, in cases of penetrating injury, when there is concern for posttraumatic vasospasm, and when the intracranial hemorrhage pattern is atypical for trauma (11,40,41). Hemorrhage patterns that are atypical for trauma include isolated SAH in the basilar cisterns, isolated large-volume SAH in the sylvian fissure, and isolated SAH in the anterior interhemispheric fissure. Angiography should be considered in these cases to evaluate for a ruptured aneurysm (42). Additionally, a large hematoma with associated calcifications or prominent veins should raise suspicion for vascular malformation and

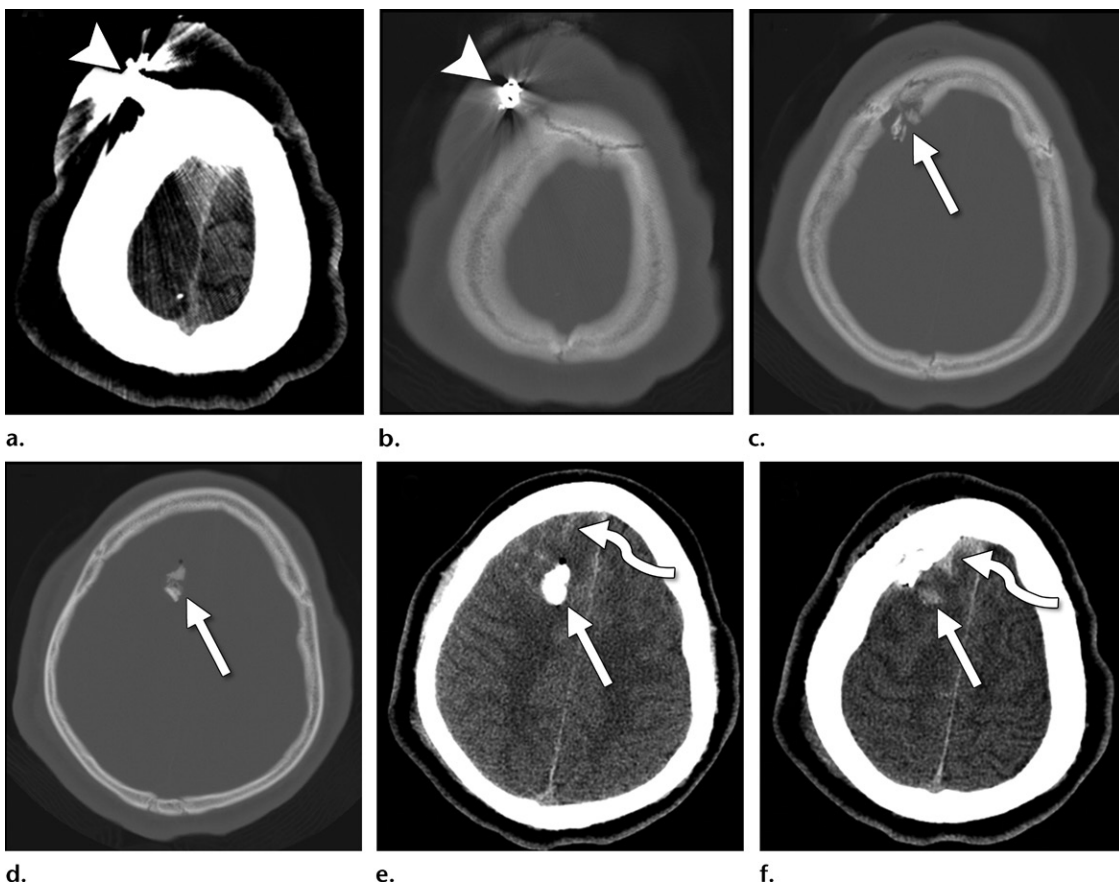


Figure 2. Penetrating trauma in a man shot with a .22-caliber bullet. (a, b) Axial nonenhanced brain window (a) and bone window (b) CT images show a bullet (arrowhead) that did not penetrate the skull. (c–e) Axial nonenhanced bone window (c, d) and brain window (e) CT images show a focal comminuted depressed right frontal bone fracture (arrow in c), with multiple bone fragments projecting into the right frontal lobe (straight arrow in d, e). (f) Axial nonenhanced CT image (brain window) shows a small associated right frontal lobe hemorrhagic contusion (straight arrow) and subarachnoid hemorrhage (SAH) (curved arrow in e, f).

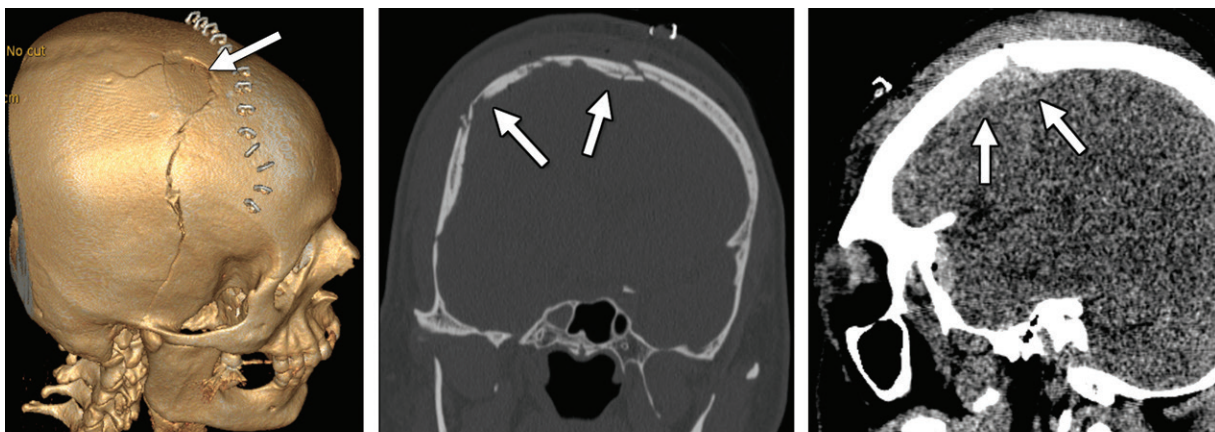


Figure 3. Focal depressed skull fracture in a young man who was hit on the head by a falling brick. Three-dimensional (3D) reconstructed (left) and coronal (middle) nonenhanced CT images show a focally depressed comminuted skull fracture (arrows). Sagittal CT image (right) shows an associated underlying small lentiform EDH (arrows). There was no hemorrhagic contusion or SAH.

should prompt angiography (42). CT or MR venography is helpful in cases where a fracture traverses a dural venous sinus, as these fractures are associated with venous EDHs and dural venous sinus thrombosis (43–47).

The ACR Appropriateness Criteria are evidence-based guidelines that describe the level of appropriateness in performing imaging studies for various clinical scenarios. Within the head trauma subsection of the neurologic

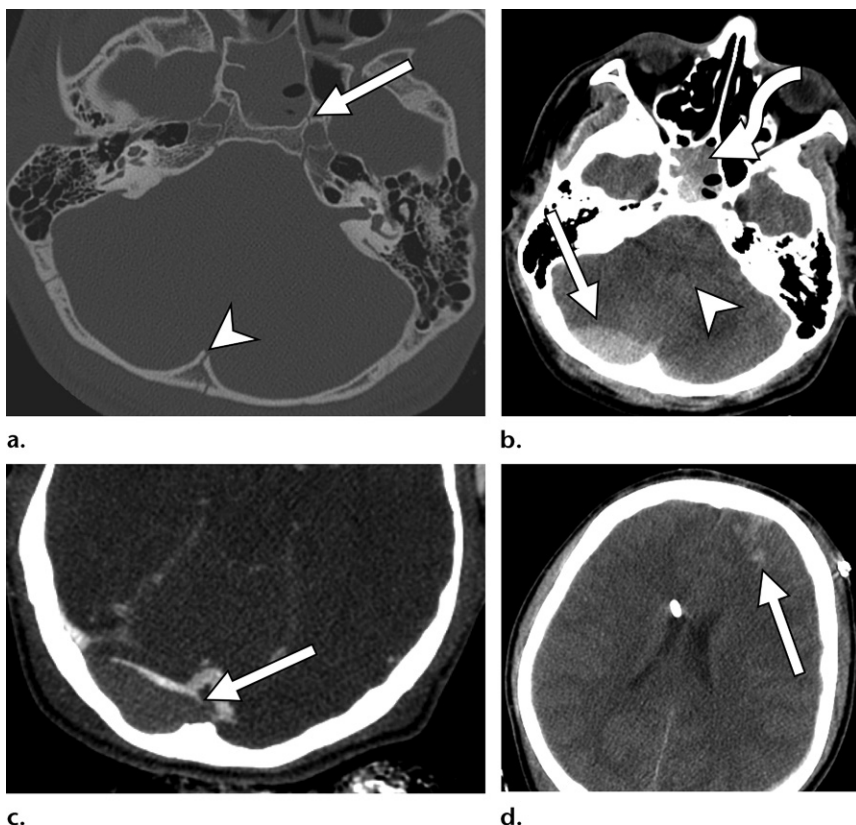


Figure 4. Posterior fossa occipital and skull base fracture with venous EDH in a 34-year-old man who was struck in the back of the head with a tire iron. His GCS score was 7. (a) Axial nonenhanced CT image shows a nondisplaced midline occipital bone fracture (arrowhead) extending through the left occipital condyle into the left petrous carotid canal and sphenoid sinus (arrow). (b) Axial nonenhanced CT image shows a lentiform venous EDH (straight arrow) causing regional mass effect, with compression of the fourth ventricle (arrowhead). Note the hemorrhage (curved arrow) within the sphenoid sinus related to the sphenoid fracture. (c) Axial nonenhanced CT venogram shows elevation and compression of the right transverse sinus and a probable venous laceration (arrow). (d) Axial nonenhanced CT image shows a focal contrecoup hemorrhagic contusion (arrow) in the left frontal lobe. A right frontal approach ventricular shunt catheter was emergently placed to treat the noncommunicating hydrocephalus and to decrease intracranial pressure.

criteria section, there are currently nine variant clinical scenarios (<https://acsearch.acr.org/list/GetAppendix?TopicId=139&PanelName=Neurologic>) with listings of the appropriateness of each applicable imaging modality (11). The criteria are frequently updated by expert panels on the basis of the peer-reviewed literature.

Diffusion-Tensor Imaging and Other Advanced Imaging Techniques

Growing awareness of the incidence and morbidity of TBI has led to extensive research in recent years to develop better diagnostic and prognostic imaging techniques. At the forefront, diffusion-tensor imaging (DTI) has been shown to be sensitive to the microstructural axonal injuries associated with mild TBI (48).

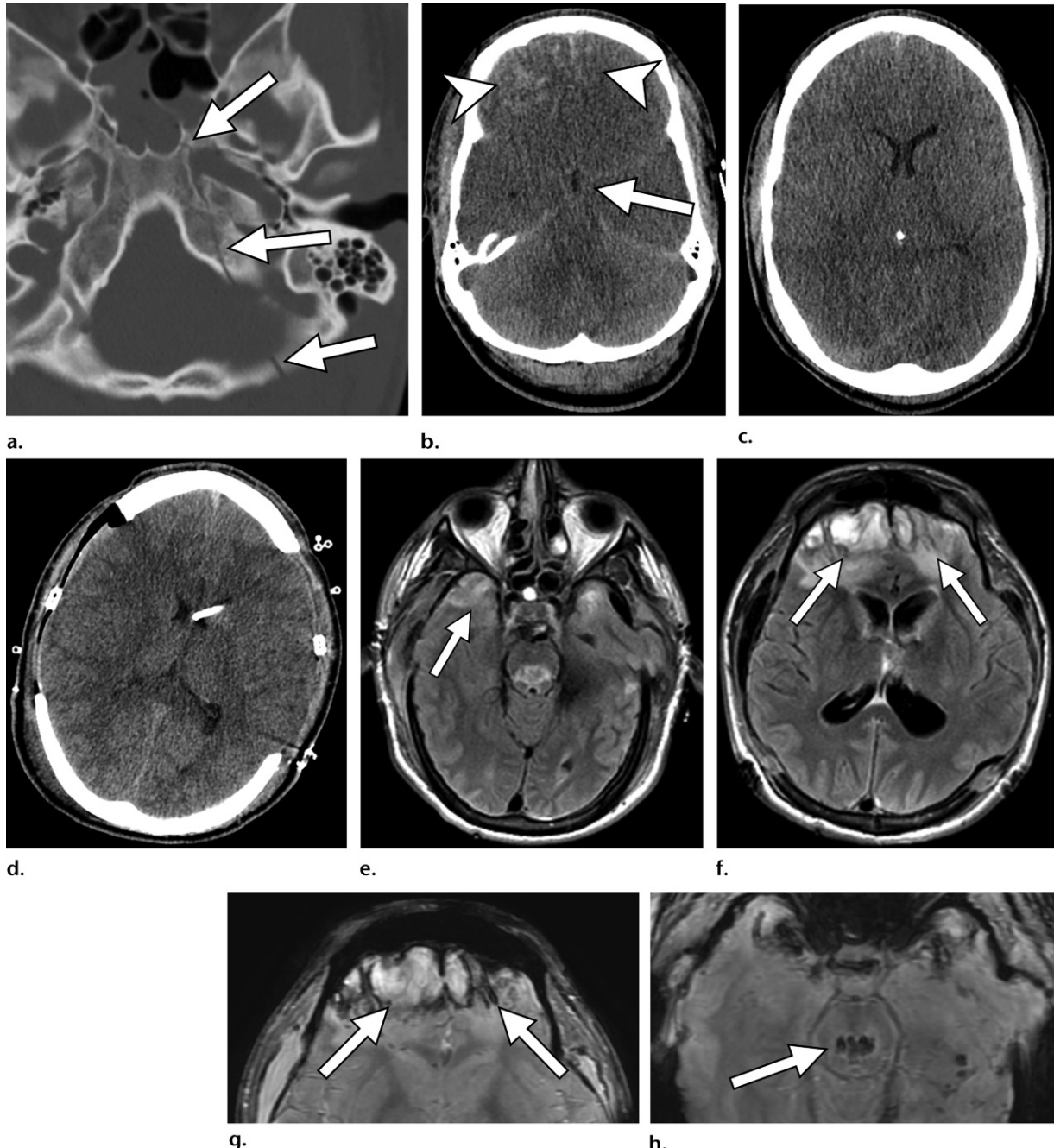
While DTI is currently valuable for group-based comparisons in the research arena, there are many barriers preventing the application of DTI in patients. While DTI is very sensitive to microstructural changes, there is a complete lack of specificity to relate findings to a specific cause. In the absence of premorbid imaging, diffusion-tensor images must be compared with images from normal controls for quantitative assessment. Increases in mean diffusivity and/or decreases in fractional anisotropy typically are interpreted to reflect decreased microstructural integrity of white matter in TBI studies. However, these same types

of changes can be visualized in any number of comorbidities (49–51) or even demographic variation (52–56). As a result, accurate and meaningful interpretation of individual DTI examinations is not feasible.

Although outside the scope of this article, there are numerous additional barriers to the application of DTI in patients, which include (a) a lack of understanding of the normal range of variability in the population for DTI metrics; (b) the absence of an accepted robust analysis methodology suitable for individual use; (c) marked variability in DTI measurement owing to sequence parameter and hardware selection; (d) a paucity of multi-center trials establishing criteria for normal and abnormal findings; and (e) a lack of standardized methods for image acquisition, assessment, and interpretation. Each of these factors (ie, MR scanner type, sequence type, and analysis technique) cause variability in the mean diffusivity and fractional anisotropy measurements.

Newer forms of quantitative diffusion imaging are being continuously developed, which have been shown to provide a more detailed understanding of the diffusion properties in the brain. Some newer and more advanced techniques include diffusion-kurtosis (also called multishell DTI) (57), diffusion-spectrum (58), and restriction-spectrum (59) imaging and the application of biophysical models such as neurite orientation distribution and density

Figure 5. Skull base fracture, large anterior frontal hemorrhagic contusions, diffuse brain edema, herniation, and Duret hemorrhages in a 40-year-old woman who was hit by a car. Her GCS score was 3. (a) Axial nonenhanced head CT image shows a nondisplaced left occipital bone and skull base fracture (arrows) extending through the left carotid canal into the sphenoid sinus. No carotid injury was depicted at CT angiography (not shown). (b) Initial axial nonenhanced head CT image shows multifocal large hemorrhagic frontal lobe contusions (arrowheads) that increased at follow-up imaging. Temporal lobe contusions were also noted (not shown). Central downward herniation results in effacement of the suprasellar cistern and brainstem compression (arrow). (c) Axial nonenhanced head CT image shows global brain edema with diffuse loss of the cerebral sulci. (d) Axial nonenhanced CT image shows a left frontal approach ventriculostomy catheter, which was placed emergently. Decompressive bilateral craniectomies were immediately performed. Short-term interval follow-up MRI was performed because the patient remained in a persistent vegetative state. (e–g) Axial T2-weighted (e, f) and susceptibility-weighted (g) MR images show the expected involutional changes within the frontal and temporal lobes from the hemorrhagic contusions (arrows) and developing hydrocephalus from the SAH (f). (h) Axial susceptibility-weighted MR image shows large Duret hemorrhages (arrow) within the mid- and dorsal pons, a sequela of herniation.



imaging (60). These techniques may yield better sensitivity and specificity in the future.

National efforts are underway to tackle existing barriers to clinical use, such as variation owing to

hardware and understanding of normal population variability. There is great promise that a form of quantitative diffusion imaging will be a suitable biomarker for mild TBI in the future, but it cur-

rently remains investigational and not applicable for the assessment of patients.

Prognostic Utility

Obtaining initial head CT images has prognostic implications. The Rotterdam, Marshall, Stockholm, and Helsinki CT scores are among the tools that have been used to predict mortality at 6 months (61,62). More recently, the NeuroImaging Radiological Interpretation System has been used to grade the severity of acute TBI (63). Among patients with a GCS score of 15, 6.9% had acute findings at head CT in a seminal article (12). A recent meta-analysis of patients with complicated mild TBI (GCS scores of 13–15) found that acute traumatic findings on head CT images are important for both management and prognosis, as there are low but clinically important rates of clinical deterioration (11.7%), neurosurgical intervention (3.5%), and death (1.4%) in this subpopulation of patients with mild TBI (64). Quantitative CT may further improve prognostication over qualitative CT interpretation in cases of acute TBI (65). Quantitative CT refers to the use of computer-aided image analysis to quantify the volume of hemorrhage in different compartments, volume of the basilar cisterns, and degree of midline shift (65). Yuh et al (65) found that use of quantitative CT on admission head CT studies resulted in improved ability to predict the 6-month Extended Glasgow Outcome Scale (GOS-E) score in patients with TBI (65).

The prognostic value of MRI in addition to that of CT is an area of active investigation, but early findings from the prospective Traumatic Research and Clinical Knowledge in TBI (TRACK-TBI) study suggest added prognostic value (66). Specifically, cases of one or more contusions at MRI or at least four foci of hemorrhagic axonal injury were associated with worse clinical outcome at 3 months on the GOS-E even when controlling for CT findings and demographic, socioeconomic, and clinical factors (66). A separate study evaluating patients with severe TBI found that the addition of MRI features improved prognostication for outcome after 1 year in patients with severe TBI (67). A recent systematic review and meta-analysis of early MRI in cases of moderate and severe TBI suggested added prognostic value with lesions detected at MRI, but most studies included were at high risk of bias (68).

Standardized Reporting and Data Collection for TBI

The TBI Reporting and Data System (TBI-RADS) (69), an initiative of the ACR Head Injury Institute (70), is part of a greater national effort led by the ACR to standardize reporting and data collection for TBI and create an evidence-based management scheme for patient disposition. This system

will undergo continuous revision as newer data and additional evidence are collected and analyzed. At present, TBI-RADS incorporates three features: (a) acute head CT findings, (b) demographic information, and (c) focused medical history and/or physical examination findings.

The most immediate potential implication for this system is to stratify the disposition of patients with acute TBI. The goal is to use current evidence to determine which patients can be safely discharged with close follow-up, those who should be admitted to a non-intensive care unit (ICU) floor as a precaution, those who need close monitoring in the ICU, and those who require immediate surgery. Standardizing reporting and management have multiple benefits, including allowing data to be pooled easily from multiple institutions and care centers. By stratifying the disposition of patients with acute TBI, there is a potential for considerable nationwide health care savings in terms of both money and resources.

Additional benefits include creating a template for education across disciplines and a standardized system to create use cases for the development of artificial intelligence and deep learning algorithms. It is the goal of TBI-RADS to reduce interpretation variability and errors, enhance communication with ordering clinicians, facilitate quality improvement and research, and ultimately improve outcomes of patients with TBI (71).

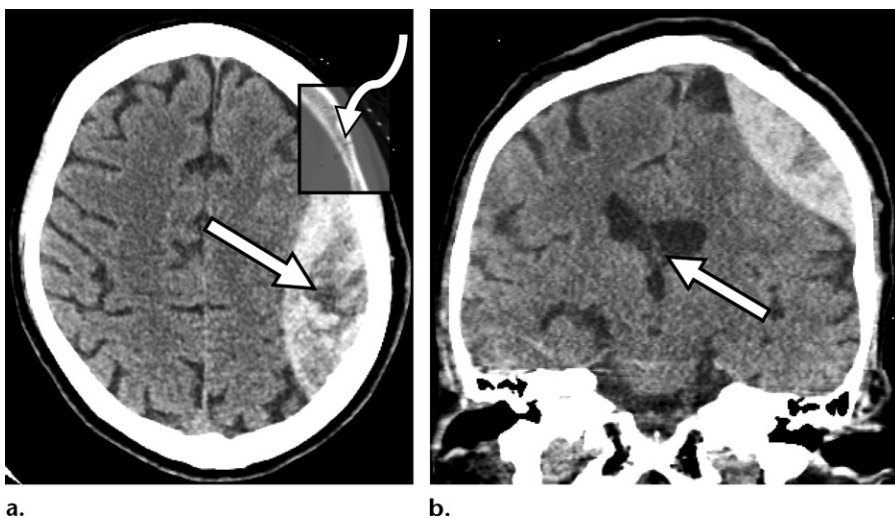
Injury Types and Imaging Findings in TBI

Skull Fracture

Skull fractures can be caused by blunt (Fig 1) or penetrating (Fig 2) injury and frequently tear the underlying meninges if depressed (Fig 3). Anterior cranial fossa fractures are frequently associated with a CSF leak, especially when comminuted or oblique (72). Fractures that traverse a dural venous sinus (Fig 4) or the jugular bulb are associated with injury to the underlying vein in two-thirds of cases (43). This is commonly due to extrinsic compression caused by extra-axial hematoma (in particular a venous EDH as seen in Fig 4) and/or thrombosis (which occurs in 23%–41% of cases) (43–47). Fractures extending to a suture can be associated with diastasis, especially in children. Skull base fractures (Fig 5) are beyond the scope of this article, but imaging of temporal bone trauma in the emergency setting has been previously reviewed (73).

Epidural Hematoma

EDHs occur between the inner table of the skull and the superficial layer of the dura and are often



a.

b.

Figure 6. Hyperacute EDH with swirl sign in a middle-aged woman who fell and struck her head while walking down stairs. Her GCS score was 15. (a) Axial nonenhanced head CT image shows a large lentiform left frontoparietal convexity EDH that does not cross the coronal or lambdoid sutures. A subtle fracture is best visualized on the bone window image inset (curved arrow in inset). Mixed low-attenuation internal blood products are findings compatible with hyperacute nonclotted hemorrhage, otherwise known as the swirl sign (straight arrow). (b) Coronal nonenhanced head CT image shows regional mass effect on the left parietal lobe with compression of the left lateral ventricle and mild rightward subfalcine shift (arrow), which are best appreciated on the coronal reformatted image.

lenticular in shape (Fig 6). EDHs typically do not cross suture lines as the superficial dural layer is attached to the calvarium tightly along the sutures (74). In the rare case in which the fracture involves the suture (more common in children), one may visualize the EDH crossing the suture line (Fig 7).

EDHs can accumulate owing to arterial or venous hemorrhage. In the pterional region, arterial EDHs classically arise from the middle meningeal artery. If there is an internal hypodense component (swirl sign), this suggests active bleeding (Fig 6) (75). Venous EDHs can occur when the fracture crosses a dural venous sinus (Fig 4) and can cross the falx cerebri and tentorium cerebelli. The source of a vertex venous EDH is typically the superior sagittal sinus. The source of an anterior temporal EDH is the sphenoparietal sinus (Fig 8). These have a more benign course and do not require surgery as they are limited by the sphenotemporal suture and the orbital fissure (76). EDHs can be treated with surgical evacuation or middle meningeal artery embolization for stabilization of nonsurgical small- to medium-sized EDHs (77).

Subdural Hematoma

SDHs occur between the dura and arachnoid mater, are most commonly caused by a tear in a bridging cortical vein as it crosses the dura, and can cross suture lines but not the falx or tentorium, as these are dural reflections (74). The general progression of SDHs from acute

to chronic is the appearance progressing from hyper- to hypoattenuating. However, there are a number of potential pitfalls to assigning an SDH an age based only on attenuation. It is important to note that mixed-attenuation SDHs are not necessarily acute on chronic. The hypoattenuating portions may represent hyperacute and/or unclotted chronic blood products, particularly in patients with coagulopathy. Furthermore, SDHs that are isoattenuating relative to the brain parenchyma can be acute, for example, in a profoundly anemic patient or in a patient with an arachnoid tear and a mixture of hemorrhage and CSF.

A large meta-analysis showed substantial overlap in the CT and MRI appearances of SDHs of different ages, with hyperattenuating and mixed-attenuating SDHs reported after a median interval of 1–2 days, isoattenuating SDHs reported after a median interval of 11 days, and hypoattenuating SDHs reported after a median interval of 14 days (78).

In the subacute stage, membranes composed of granulation tissue can form within the hematoma (Fig 9). These types of membranes can enhance. In subacute-to-chronic SDHs, the membranes are friable and can result in recurrent hemorrhage, resulting in an acute-on-chronic SDH. This will often show hematocrit levels (Fig 9). Chronically, calcifications can form. SDHs can be treated with burr hole drainage, craniotomy for evacuation, subdural evacuation port system (Fig 10) placement, and/or middle meningeal artery embolization (79,80).

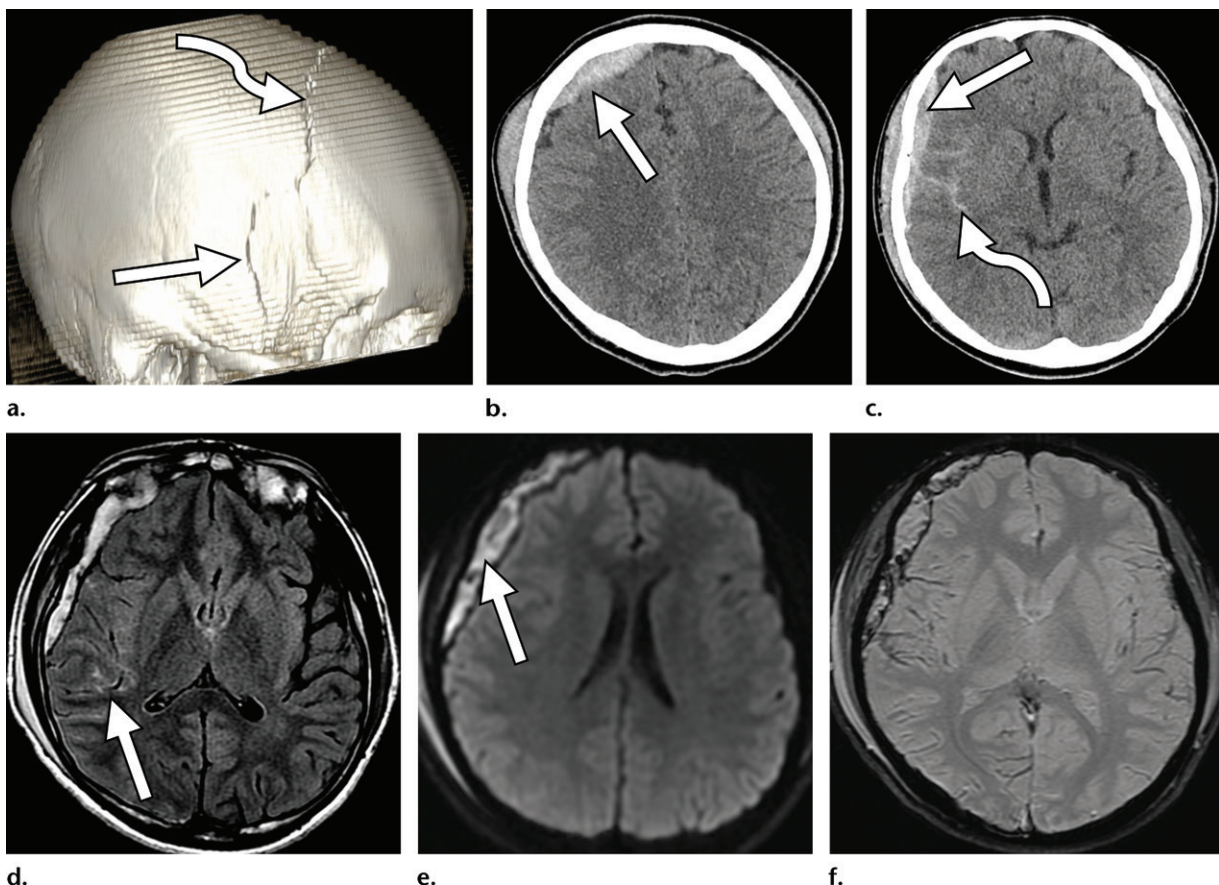
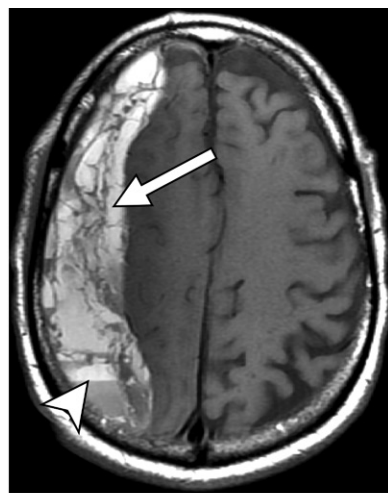


Figure 7. Mixed hyperacute and acute EDH associated with calvarial fracture and coronal suture diastasis in a 24-year-old man with a large right temporoparietal scalp hematoma following assault. His GCS score was 15. (a) 3D volume-rendered nonenhanced reconstructed head CT image shows a nondisplaced right parietotemporal fracture (straight arrow) extending into the coronal suture, which was diastatic (curved arrow). (b, c) Axial nonenhanced CT images show a bilobular lentiform hyperacute and acute EDH (straight arrow) along the right frontal and temporal convexities. Mixed low- and high-attenuating blood products within the temporal component of the EDH are suggestive of active bleeding and/or unclotted hemorrhage. Note the SAH (curved arrow in c) within the right sylvian fissure. (d) Axial T2-weighted FLAIR MR image obtained at follow-up shows residual SAH (arrow). (e) Axial diffusion-weighted image shows evolving subacute blood products (arrow), with restricted diffusion within the EDH. Mass effect is mildly decreased, with less compression of the right lateral ventricle. (f) Axial susceptibility-weighted image does not show any associated contusions or traumatic axonal injury (TAI).

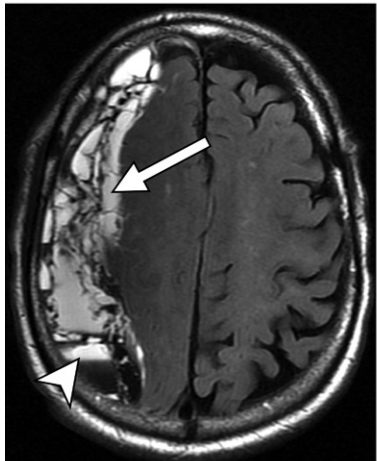


Figure 8. Zygomaticosphenoid fracture with sphenoparietal venous EDH and intraorbital subperiosteal hematoma in a 78-year-old woman who fell on the right side of her face. Her GCS score was 15. (a) Axial maxillofacial CT image (bone window) shows comminuted right zygomatic and sphenoid bone fractures (arrows) with air in the temporalis fossa, a right cheek hematoma, and right exophthalmos. (b) Axial maxillofacial CT image (soft-tissue window) shows a small venous EDH (straight arrow) along the anterior middle cranial fossa related to traumatic laceration of the sphenoparietal sinus. Note the extraconal intraorbital subperiosteal hematoma (curved arrow).

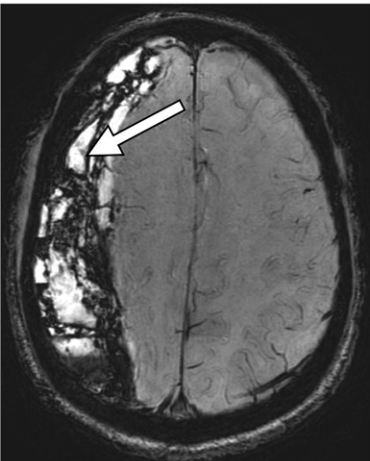
Figure 9. Posttraumatic mixed-signal-intensity SDH resulting in cerebral herniation in an elderly man undergoing anticoagulation therapy who fell at home 2 weeks earlier and presented with progressive right-sided headache. (a–c) Axial MR images show a large complex mixed-signal-intensity crescentic right hemispheric SDH. Predominately T1-hyperintense (arrow in a) and T2-hyperintense (arrow in b) late subacute internal blood products are depicted, with hemosiderin-stained internal septa on the susceptibility-weighted image (arrow in c), a finding suggestive of recurrent internal hemorrhage. There is a layering hematocrit level (arrowheads in a, b) posteriorly, compatible with poor coagulation. (d) Coronal postcontrast T1-weighted MR image shows significant mass effect on the right cerebrum with mild leftward subfalcine herniation (straight arrow) and early right uncal herniation (curved arrow). Note the secondary dural inflammation and intrasulcal linear enhancement (arrowheads), representing venous congestion. Postcontrast imaging is not routinely performed in the trauma setting, but these findings should not be mistaken for other pathologic conditions such as infection.



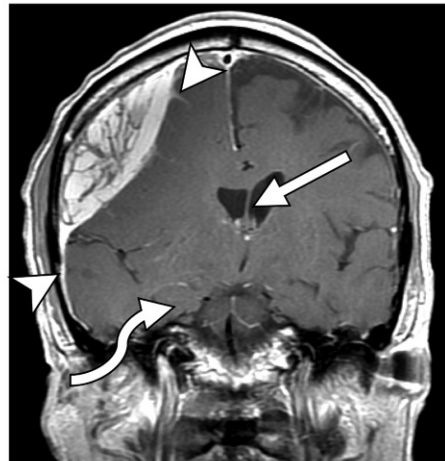
a.



b.



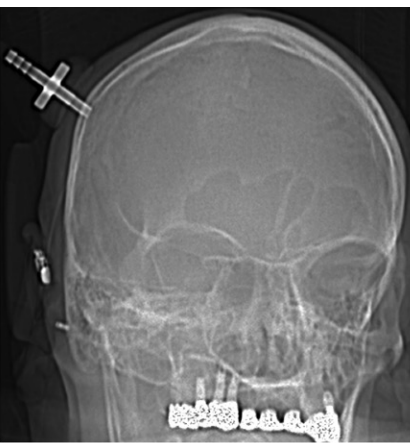
c.



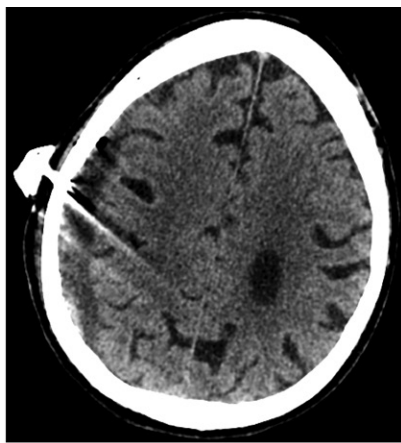
d.



a.



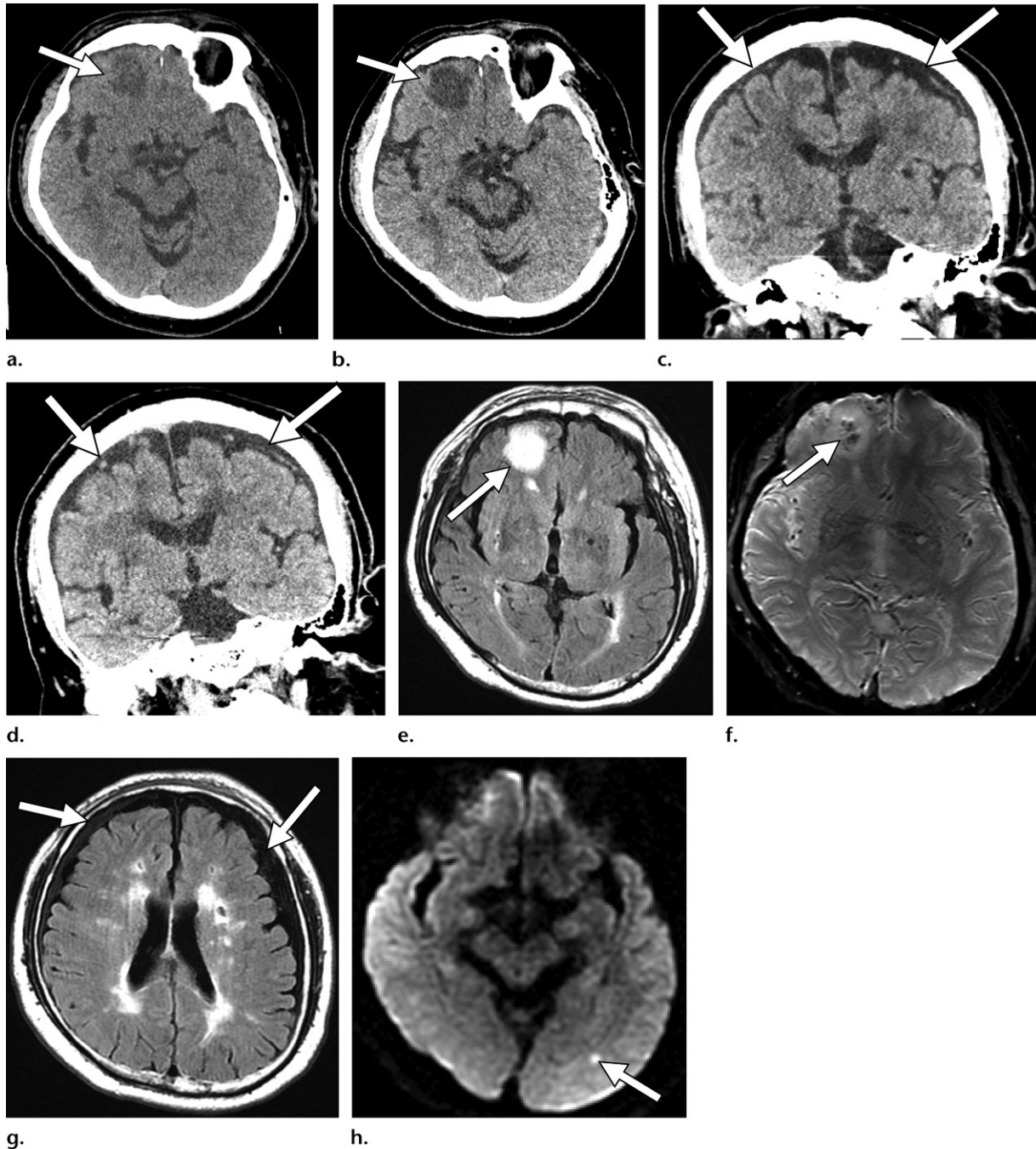
b.



c.

Figure 10. Subdural evacuating port system (SEPS) in an 82-year-old woman with a GCS score of 14 following a fall in the bathtub. (a) Axial nonenhanced head CT image shows a large acute-on-chronic SDH (arrow) containing mixed internal hemorrhage of varying densities and internal septa. Note the moderate mass effect on the right cerebral hemisphere. (b) CT scout image obtained following SEPS placement shows the device. (c) Axial nonenhanced head CT image shows a resultant decrease in the size of the SDH and cerebral compression.

Figure 11. Enlarging frontal lobe contusion and subdural hygromas in an elderly woman who fell down stairs and was diagnosed with a right frontal scalp contusion. Her GCS score was 13. (a, b) Initial axial nonenhanced head CT image (a) shows a small nonhemorrhagic anterior right frontal contusion (arrow) that increased in size and conspicuity on the follow-up nonenhanced head CT image (b) obtained 12 hours later. (c, d) Coronal nonenhanced head CT image (c) shows trace right and small left hemispheric subdural hygromas (arrows), which increased on the follow-up coronal nonenhanced head CT image (d). (e, f) Axial T2-weighted FLAIR (e) and susceptibility-weighted (f) MR images obtained the next day show the anterior right frontal contusion (arrow in e) with internal microhemorrhage (arrow in f). The internal microhemorrhages were not appreciable on the nonenhanced CT images. (g) Axial T2-weighted FLAIR MR (g) and diffusion-weighted (h) images show bilateral enlarging small subdural hygromas (arrows in g) and focal restricted diffusion (arrow in h) within the left occipital white matter. The focus of restricted diffusion in the left occipital white matter suggests a contre-coup TAI.



Subdural Hygroma

Subdural hygromas are caused by traumatic tears in the arachnoid membrane with resulting CSF accumulation in the subdural space and can coexist with other findings of intracranial injury (Fig 11) (81). As depicted in all subdural collec-

tions, hygromas displace vessels in the subarachnoid space from the inner table of the calvarium, but this finding is particularly important for the diagnosis of a subdural hygroma, as the fluid will be isoattenuating and isointense relative to CSF on CT and MR images, respectively. One

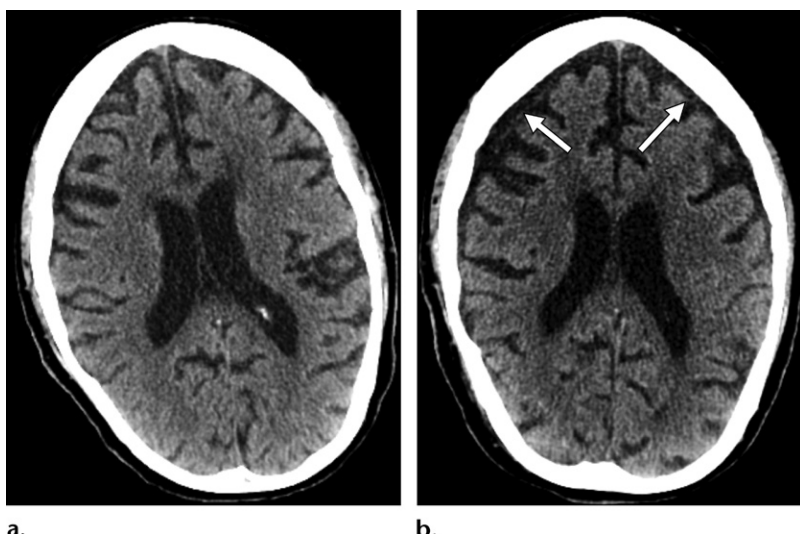


Figure 12. Delayed subdural hygromas. (a) Axial nonenhanced head CT image in an elderly patient following a mild TBI was interpreted as normal. The patient presented 6 days after discharge with persistent headache. (b) Axial nonenhanced head CT image obtained at follow-up shows new small posttraumatic subdural hygromas (arrows), causing minimal mass effect on the cerebral hemispheres. There is no herniation owing to the preexisting global brain atrophy.

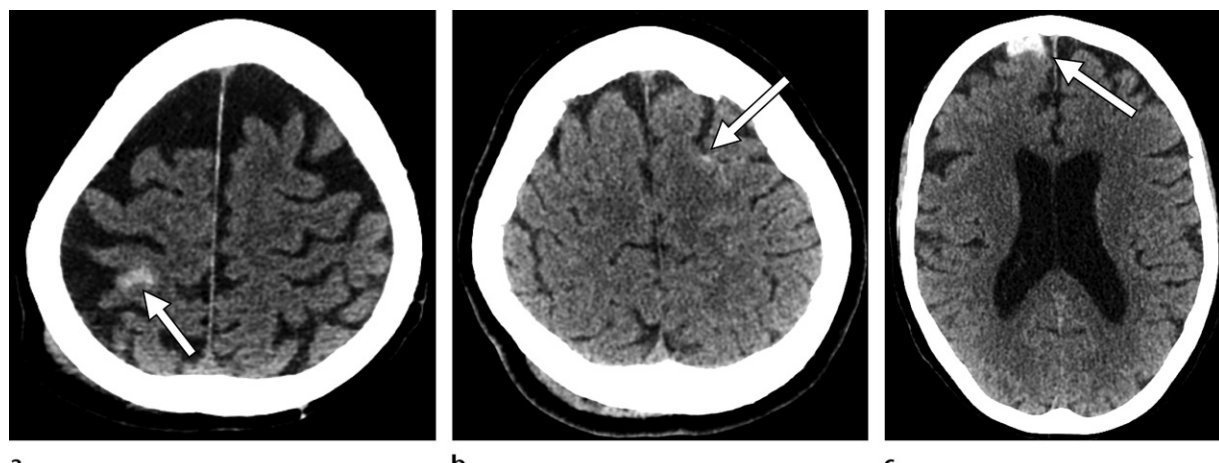


Figure 13. Posttraumatic SAH in three patients with minor head injuries whose GCS score was 15. Axial nonenhanced CT images show small amounts of SAH in coup (arrow in a) and contrecoup (arrow in b, c) patterns.

exception has been demonstrated in polytrauma patients who received intravenous contrast material during initial evaluation. Subsequent head CT images depicted subdural collections that were hyperattenuating relative to CSF on 120-kVp images but isoattenuating relative to CSF on virtual monoenergetic 190-keV images. This confirmed that not hemorrhage but iodine was the source of hyperattenuation on 120-kVp images (82).

Subdural hygromas can occur in the first day, but the mean time to appearance is 9 days after injury (Fig 12) (81). A pure subdural hygroma will not have internal membranes as can subacute SDHs (81). However, subdural CSF accumulation can occur with hemorrhage, particularly in children, resulting in a hematohygrama (83,84). Of note, subdural effusions are secondary to reactive fluid accumulation in the subdural space (eg, owing to meningitis) and should not be confused with subdural hygromas.

Traumatic SAH

Traumatic SAH occurs between the arachnoid and pia mater and is a usually small-volume sulcal SAH (Fig 13) that commonly occurs at the site of impact (coup) or opposite the site of impact (contrecoup). Patients with isolated traumatic SAH are less likely to clinically deteriorate than those with other types of traumatic intracranial hemorrhage (85). However, evidence shows impaired functional outcomes in patients with traumatic SAH. In the European Brain Injury Consortium survey (86), 41% of patients without traumatic SAH achieved good recovery, whereas 15% of patients with traumatic SAH achieved good recovery. Midline traumatic SAH (in the interhemispheric fissure or perimesencephalic cisterns) on initial head CT images (Fig 14) is a marker of diffuse axonal injury (DAI) at subsequent MRI, with a 61% sensitivity and 82% specificity for severe DAI in one study (87).



Figure 14. Interpeduncular hemorrhage, intraventricular hemorrhage, and temporal lobe hemorrhagic contusion in a 24-year-old woman who was struck by a car and presented with loss of consciousness. Her GCS score was 8. Initial axial nonenhanced head CT image shows multicompartimental hemorrhages. Interpeduncular SAH (white arrow), intraventricular hemorrhage (red arrow), and a small focal hemorrhagic contusion (arrowhead) in the anterior right temporal lobe are depicted. Note the small left temporal convexity subdural hygroma (curved arrow).



Figure 15. Traumatic septum pellucidum hemorrhage in an elderly woman following a fall from standing. Her GCS score was 13. (a, b) Axial (a) and coronal (b) nonenhanced head CT images show a focal hemorrhage (arrow) along the septum pellucidum, most likely related to a lacerated septal vein. (c) Axial nonenhanced CT image shows a small amount of associated intraventricular hemorrhage (arrow).

Isolated SAH in the basilar cisterns should prompt consideration of aneurysmal SAH, even in the setting of trauma. Traumatic SAH in the interpeduncular or perimesencephalic cisterns should raise suspicion for brainstem injury (88). Rarely, traumatic SAH can cause delayed vasospasm, although much less frequently than aneurysmal SAH. The risk of posttraumatic vasospasm is highest in severe TBI, where it occurs in up to 30%–40% of patients (41).

Intraventricular Hemorrhage

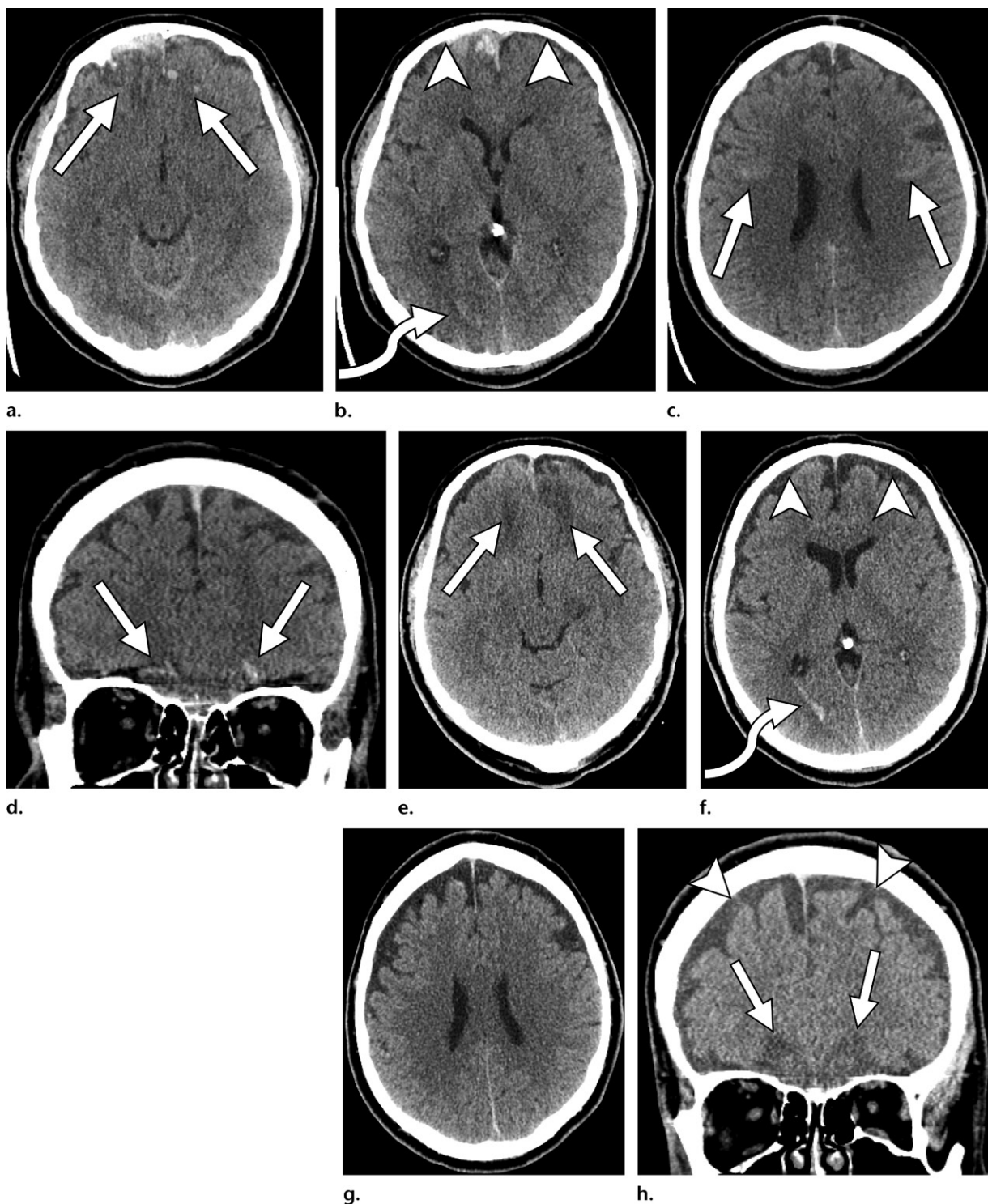
Intraventricular hemorrhage in the setting of trauma (Fig 14) can originate from a ruptured subependymal vein (Fig 15), extension from an intraparenchymal hematoma, or retrograde redistribution from the subarachnoid space. Intraventricular hemorrhage on initial head CT images is correlated with DAI on subsequent MR images, with univariate and multivariate odds ratios of 3.7 and 4.2, respectively, shown in one study (89).

Brain Contusion

Brain contusions are bruises of the brain parenchyma owing to impact. They characteristically occur at coup and contrecoup sites, most commonly in the inferior frontal lobes and anterior-inferior temporal lobes, thought to be due to the ridged morphology of the inner table, with a predilection for the crests of the involved gyri (Fig 16). Temporal lobe contusions on CT images are associated with worse functional outcome at 6 months than that of frontal lobe contusions, other intra-axial injuries, or extra-axial injuries (90). MRI is more sensitive than CT for the detection of contusions, especially small or nonhemorrhagic contusions (20,91). Contusions can increase in size (*ie*, “blossom” or “bloom”) over the first 48 hours after injury (Fig 17) (92). Significant progression of contusions (new contusion or doubling in contusion volume) is associated with worse clinical outcome (93).

Contusions are followed with serial imaging, and in cases where hemorrhagic progression leads to increasing mass effect and herniation, craniectomy

Figure 16. Classic evolving bifrontal hemorrhagic contusions, frontal SDHs, diffuse brain swelling, SAH, and intraventricular hemorrhage in a 58-year-old patient who was struck by a car while cycling. The patient's GCS score was 13. (a-d) Axial (a-c) and coronal (d) nonenhanced CT images show bifrontal hemorrhagic contusions (arrows in a, d), small bifrontal SDHs (arrowheads in b), right occipital intraventricular hemorrhage (curved arrow in b), and multifocal SAH (arrows in c). (e-g) Axial nonenhanced CT images obtained a few days later show the expected interval evolution of the bifrontal hemorrhagic contusions, with decreased internal hemorrhage but persistent edema (arrows in e). Note the decrease in internal hemorrhage but an increase in the size of the bifrontal SDHs (arrowheads in f). Intraventricular hemorrhage increased (curved arrow in f) and SAH resolved (g) owing to redistribution. The lateral ventricles increased in size over time, which was thought to be related to interval decrease in diffuse brain swelling. (h) Coronal nonenhanced CT image also shows increased edema and decreased hemorrhage within the bifrontal hemorrhagic contusions (arrows) and a slight increase in the size of the bifrontal SDHs (arrowheads).



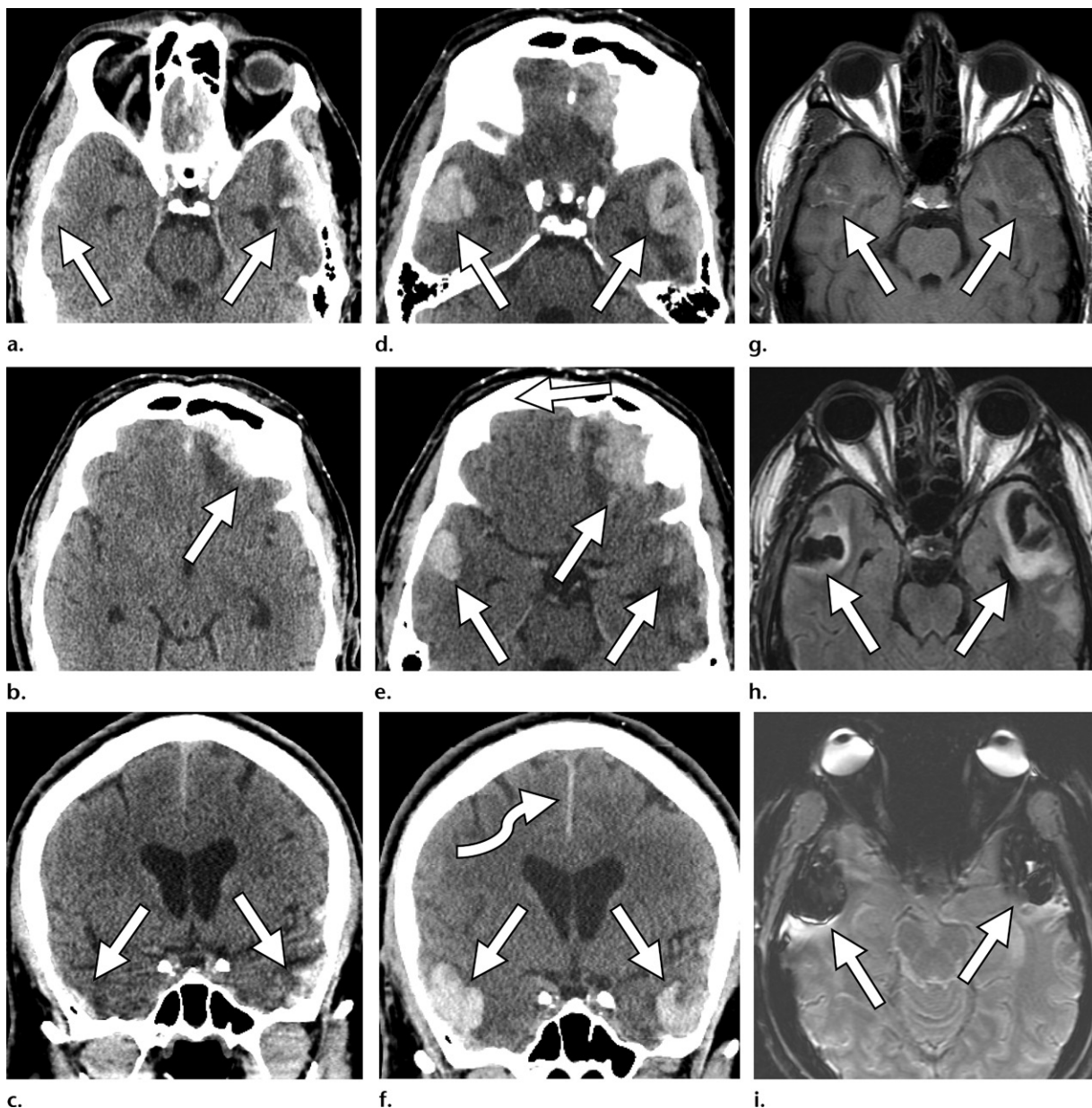


Figure 17. Enlarging hemorrhagic bilateral frontal and temporal lobe contusions in a 62-year-old woman who was thrown from a horse. Her GCS score was 6. (a–c) Initial axial (a, b) and coronal (c) nonenhanced head CT images show multifocal relatively small superficial hemorrhagic contusions (arrows) of the anterior temporal lobes and anteroinferior left frontal lobe, a pattern highly typical for moderate to severe TBI. (d–f) Axial (d, e) and coronal (f) nonenhanced head CT images obtained 24 hours later show a marked interval increase in the size of the hemorrhagic contusions (straight arrows) and the resultant mass effect without herniation. Note a small anterior parafalcine SDH (curved arrow in f) that has slightly increased in size. (g–i) Axial MR images obtained at short-term interval follow-up do not show evidence of TAI, but evolving acute to early subacute blood products (arrows) are depicted on the T1-weighted MR image (g) (with iso- to hyperintense signal), T2-weighted FLAIR image (h) (with predominately hypointense signal), and susceptibility-weighted image (i) (with hypointense signal).

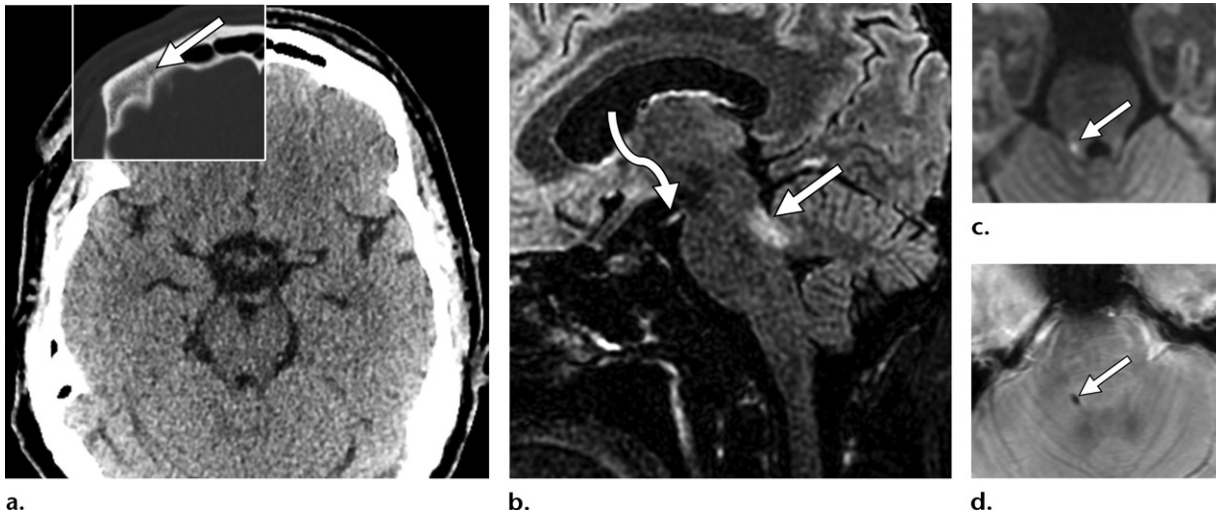
may be performed to prevent the secondary effects of herniation described later in this article. Severe acceleration and/or deceleration or rotational injury can result in brainstem contusions (eg, when the midbrain or superior cerebellar peduncle impacts the tentorial incisura) (Fig 18) (94).

Axonal Injury

Axonal injuries result from axonal stretch and/or shear stress and predominantly affect highly

organized white matter tracts and interfaces between brain tissues of different densities (ie, gray-white junction). There has been variable use of two related terms, *TAI* and *DAI*, and they are often used interchangeably. *DAI* is historically used to describe widespread multifocal white matter injury as a result of shearing forces from rotational and translational acceleration-deceleration injuries confirmed by pathologic studies demonstrating axonal

Figure 18. Frontal bone fracture in a 48-year-old man who tripped, fell, and hit a concrete ledge. He was diagnosed with persistent right pupillary mydriasis. His GCS score was 15. (a) Axial nonenhanced head CT image and bone-window image (inset) show a non-displaced right frontal bone fracture (arrow in inset), which is best depicted on the bone-window image. No intracranial hemorrhage or contusion is depicted. (b-d) Sagittal T2-weighted FLAIR MR image (b) obtained at follow-up shows a focal hemorrhagic contusion (straight arrow in b) of the right superior cerebellar peduncle, with focal restricted diffusion (arrow in c) on the axial diffusion-weighted image (c) and microhemorrhage (arrow in d) on the axial susceptibility-weighted image (d). Note the mild increased signal intensity in the right oculomotor nerve (curved arrow in b), a finding compatible with a traumatic cranial nerve injury, which explains the manifestation of mydriasis.



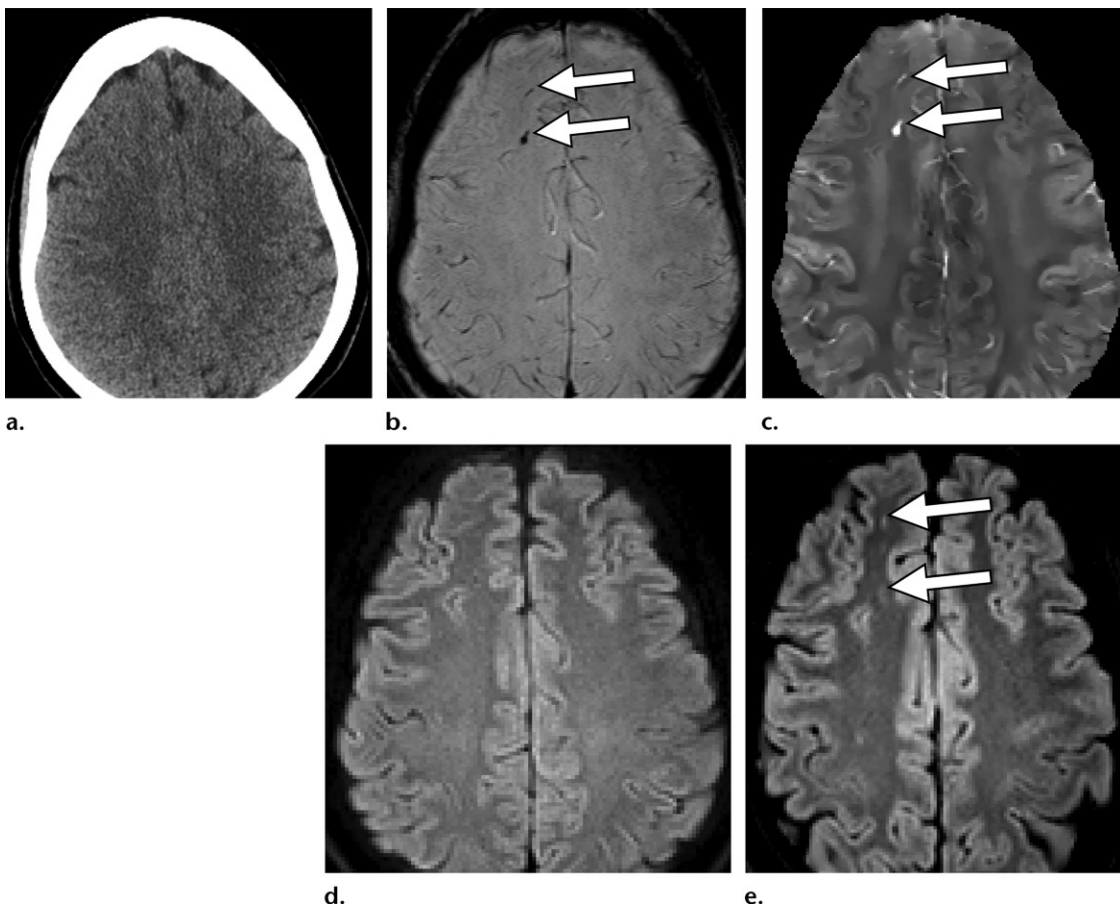
a.

b.

c.

d.

Figure 19. Focal mild acute axonal injury in a 34-year-old woman who was an unrestrained passenger in the backseat during a motor vehicle collision. She presented with severe headache and confusion. Her GCS score was 14. (a) Axial nonenhanced head CT image shows no abnormal findings. Short-term MRI was performed owing to persistent confusion. (b) Axial susceptibility-weighted MR image shows two foci (arrows) within the anterior right frontal white matter. (c) Axial postprocessed quantitative susceptibility map shows positive phase shifts (arrows) corresponding to the presence of internal ferromagnetic iron. (d) Axial diffusion-weighted image shows no associated abnormality. (e) Axial T2-weighted FLAIR image shows focal T2-hyperintense lesions (arrows), findings compatible with gliosis, that correspond to microhemorrhages.



a.

b.

c.

d.

e.

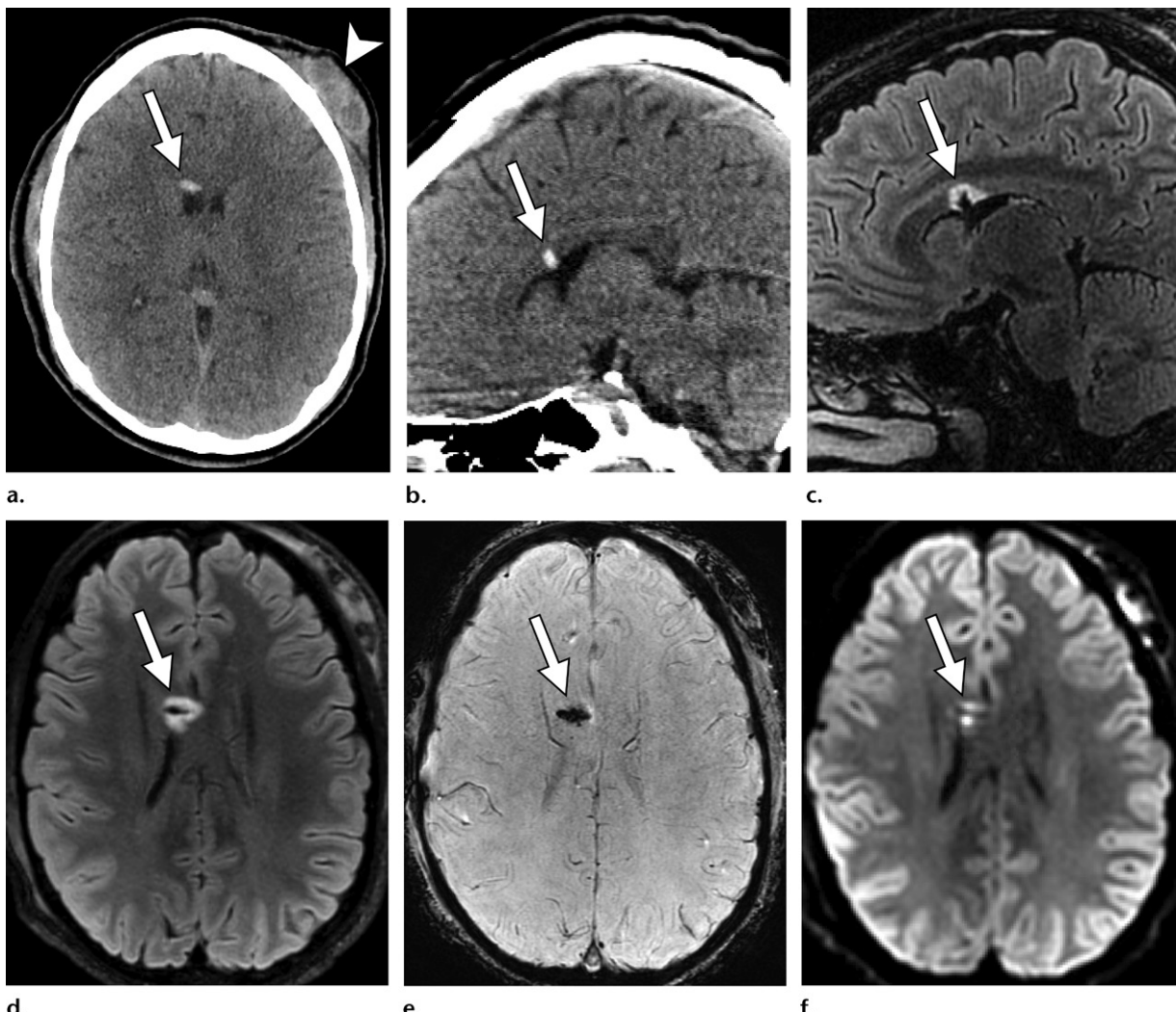


Figure 20. Isolated callosal hemorrhagic axonal injury in a 24-year-old-woman who was struck by a bicyclist while jogging and fell forward onto her left forehead. Her GCS score was 14. (a, b) Axial (a) and sagittal (b) nonenhanced head CT images show a large left frontal scalp hematoma (arrowhead in a), without an associated skull fracture, and a focal linear hemorrhage (arrow) along the right margin of the anterior body of the corpus callosum. (c–f) Sagittal (c) and axial (d) T2-weighted FLAIR, axial susceptibility-weighted (e), and axial diffusion-weighted (f) MR images show surrounding edema (arrows in c, d), linear hemorrhage (arrow in e), and marginal restricted diffusion (arrow in f) within the corpus callosum. All are findings compatible with a focal acute TAI. No additional intracranial injuries were noted.

degeneration. As MRI hardware and techniques advanced, it was recognized that shear injuries can occur with milder TBI injuries and to a lesser extent. As a result, the term TAI was used to reflect isolated unifocal or mild multifocal shear injuries (ie, three or fewer foci based on the TBI Common Data Elements) (20,66). DAI will be used in this article as it has the broadest historical definition, although the TBI Common Data Elements define DAI as having four or greater foci.

DAI can be hemorrhagic and/or nonhemorrhagic, and both hemorrhagic and nonhemorrhagic lesions are more sensitively detected at MRI (20,66). Acute DAI lesions may restrict diffusion. Characteristic locations for TAI lesions include the gray-white matter junction

(especially in the frontal lobes because the axis of rotation of the head is posterior, allowing greater differences in momentum anteriorly), corpus callosum (especially the splenium), internal capsules, and dorsal midbrain and/or pons. DAI is graded in order of increasing severity. Grade 1 involves the subcortical white matter (Fig 19), grade 2 involves the corpus callosum (Fig 20), and grade 3 involves the brainstem (Fig 21) (95). Thalamic lesions, while not part of the grading system, are associated with poor outcome when present (96).

DAI findings depicted on CT images (and even on MR images) are the tip of the iceberg in that they indicate substantial underlying axonal injury. Clinical findings are usually out of proportion to (ie, more severe than) imaging

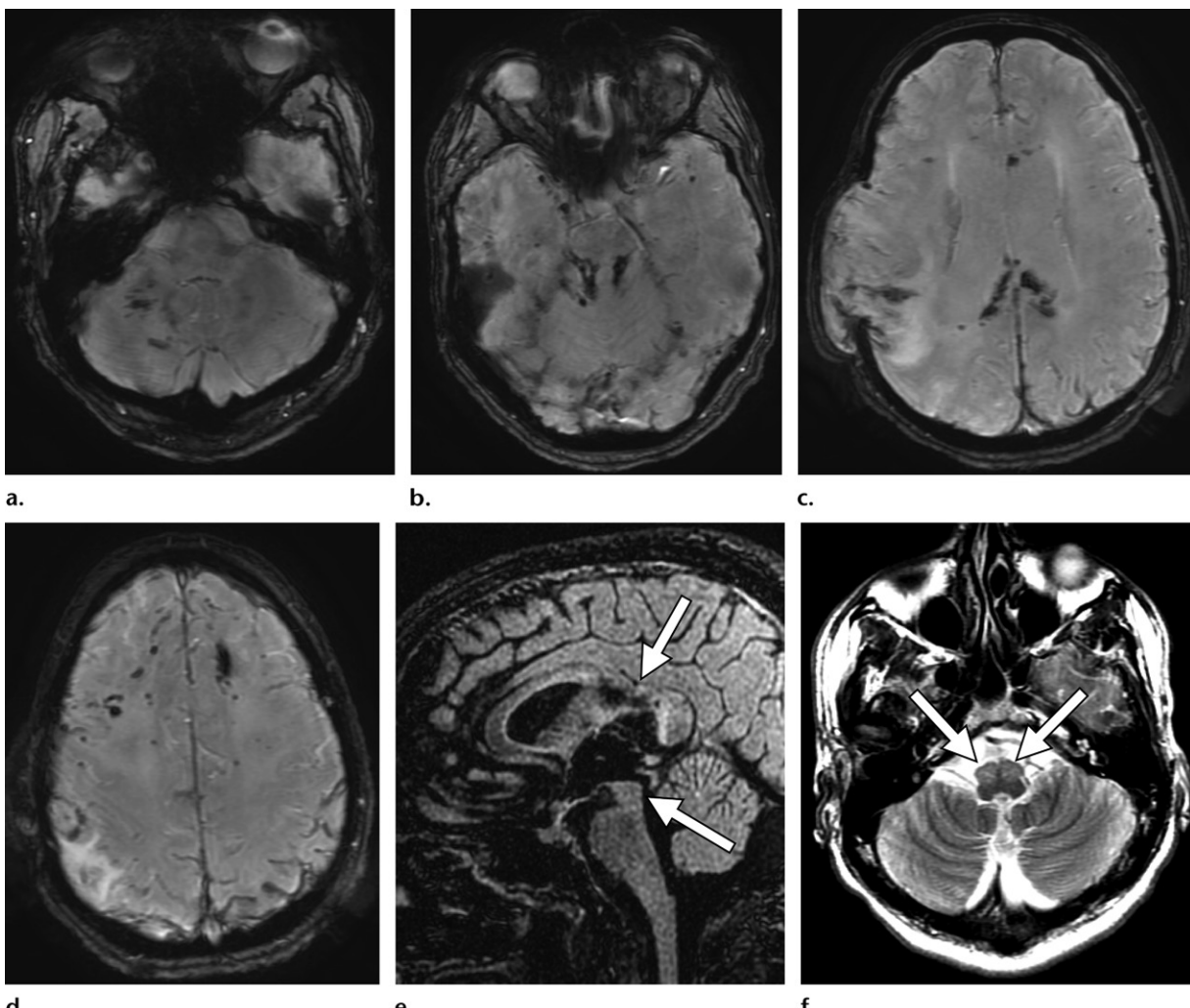


Figure 21. Severe diffuse TAI in a 25-year-old man following an ATV accident that occurred months earlier. His GCS score was 3. At the time of the accident, the patient underwent an emergent right hemispheric decompressive craniectomy. (a-d) Axial susceptibility-weighted MR images show innumerable chronic microhemorrhages throughout the right cerebellar white matter (a), dorsal pons and superior cerebellar peduncles (b), corpus callosum (c), and frontal white matter (d). (e) Sagittal T2-weighted FLAIR MR image shows pronounced focal atrophy of the posterior body of the corpus callosum and midbrain (arrows). (f) Axial T2-weighted MR image shows bilateral hypertrophic olivary degeneration (arrows), which developed secondary to the severe brainstem TAI.

findings. DAI usually causes much higher morbidity and mortality than extra-axial injuries and hemorrhagic contusions and is treated with close management of intracranial pressure and craniectomy if necessary to prevent herniation.

Axonal injuries can result in focal T2-hyperintense white matter lesions. However, these lesions are nonspecific and can occur from numerous nontraumatic causes that include ischemic or inflammatory demyelination, chronic migraine headaches, vasculopathies, and other conditions.

A recent prospective multicenter study found that while 27% of young patients (mean age, 23 years) with recent mild TBI had white matter lesions, fewer than 2% were attributable to the acute trauma, and 28% of matched controls also had white matter lesions (97). For patients who underwent imaging with MRI in the

acute stage after TBI, unless there is associated diffusion restriction or acute microhemorrhage, white matter T2-hyperintense lesions should be considered nonspecific in cause.

Diffuse Cerebral Edema and Vascular Injuries

Diffuse cerebral edema can result from head injury, possibly due to dysfunctional cerebral autoregulation and blood-brain barrier disruption (98–100). The onset of cerebral edema is variable but is thought to be related to the release of various mediators that can increase blood-brain barrier permeability and result in vasogenic and cytotoxic edema (98,101).

Vascular injuries include arterial dissection (Fig 22) (especially when a fracture traverses the skull base), pseudoaneurysm (most commonly involv-

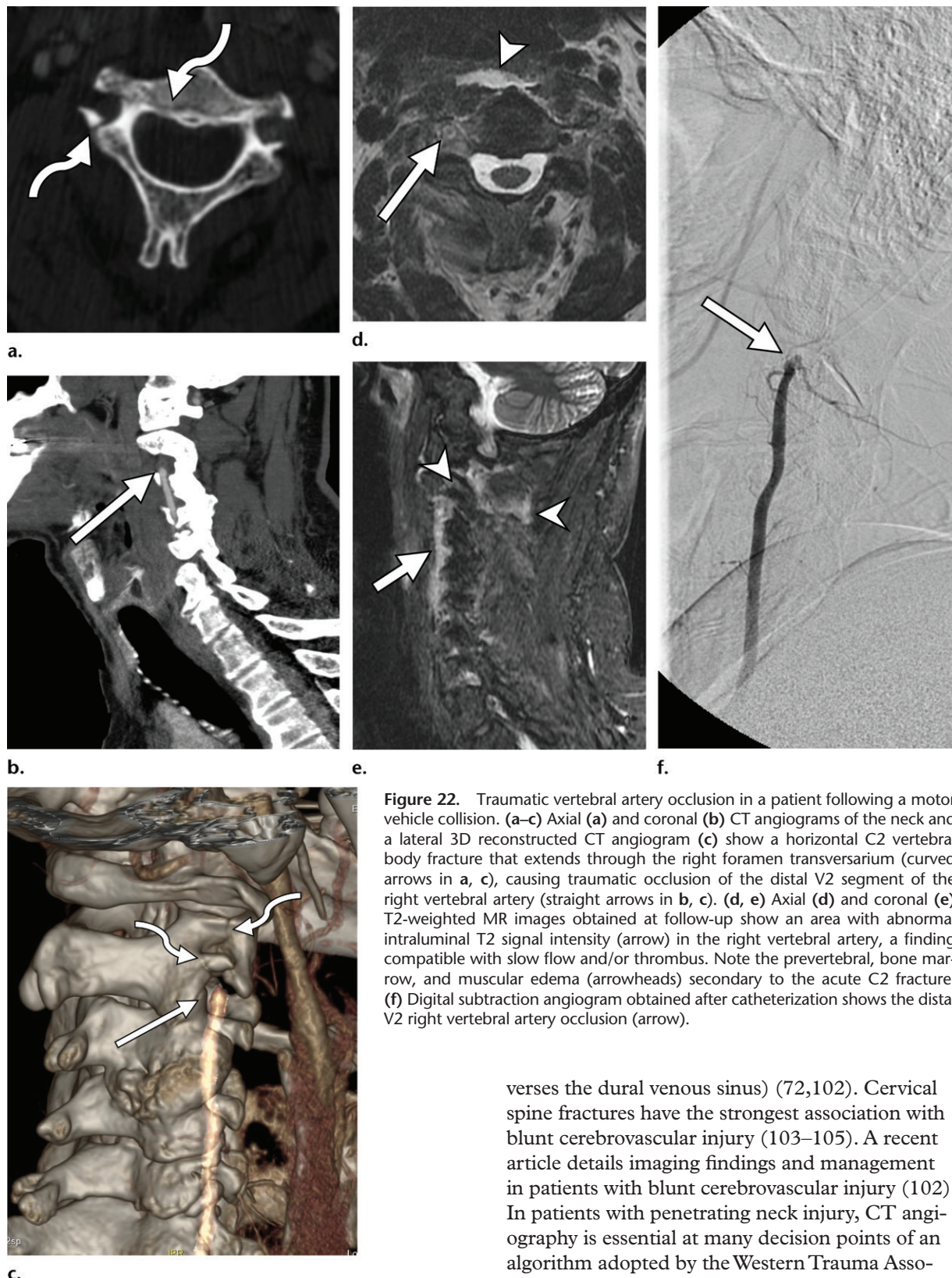


Figure 22. Traumatic vertebral artery occlusion in a patient following a motor vehicle collision. (a–c) Axial (a) and coronal (b) CT angiograms of the neck and a lateral 3D reconstructed CT angiogram (c) show a horizontal C2 vertebral body fracture that extends through the right foramen transversarium (curved arrows in a, c), causing traumatic occlusion of the distal V2 segment of the right vertebral artery (straight arrows in b, c). (d, e) Axial (d) and coronal (e) T2-weighted MR images obtained at follow-up show an area with abnormal intraluminal T2 signal intensity (arrow) in the right vertebral artery, a finding compatible with slow flow and/or thrombus. Note the prevertebral, bone marrow, and muscular edema (arrowheads) secondary to the acute C2 fracture. (f) Digital subtraction angiogram obtained after catheterization shows the distal V2 right vertebral artery occlusion (arrow).

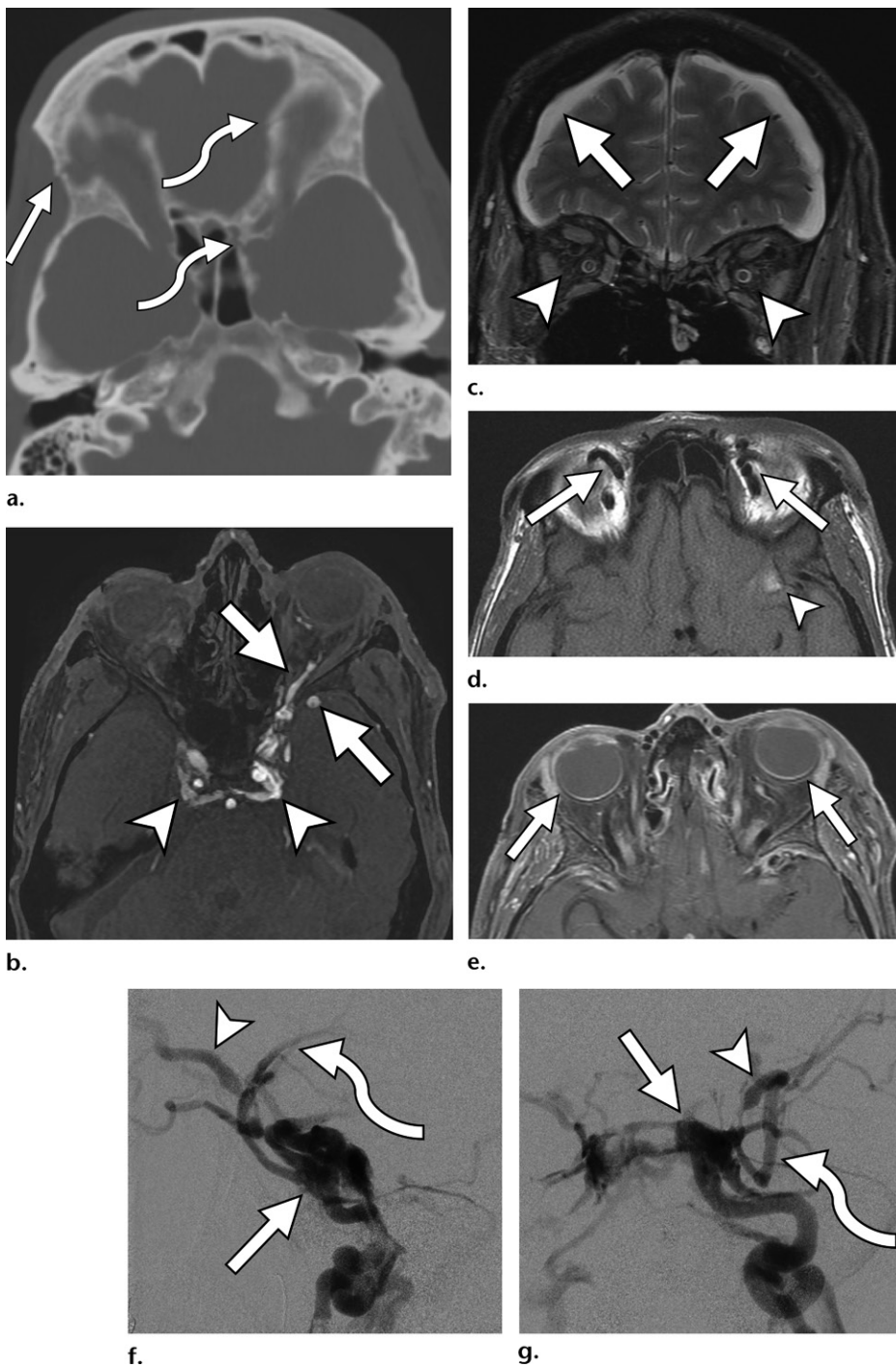
verses the dural venous sinus) (72,102). Cervical spine fractures have the strongest association with blunt cerebrovascular injury (103–105). A recent article details imaging findings and management in patients with blunt cerebrovascular injury (102). In patients with penetrating neck injury, CT angiography is essential at many decision points of an algorithm adopted by the Western Trauma Association, particularly for zone III injuries (superior to the angle of the mandible) (106).

Secondary Brain Injuries and Herniation

Secondary brain injuries are caused by mass effect resulting in herniation, which can lead to infarctions, hydrocephalus, and hemorrhages (107).

ing the vertebral artery, followed by the anterior cerebral artery), active extravasation, vascular occlusion, traumatic carotid-cavernous fistula (Fig 23), traumatic dural arteriovenous fistula, and venous thrombosis (especially when a fracture tra-

Figure 23. Traumatic direct carotid-cavernous fistula in a 50-year-old man with alcoholism who was found unconscious on the sidewalk. (a) Coronal nonenhanced CT image shows multiple maxillofacial fractures, including the right orbit (straight arrow) and left orbital roof and sphenoid bone (curved arrows). (b) Follow-up axial MR angiogram shows pronounced arterialized flow-related enhancement in the cavernous sinuses (arrowheads), left ophthalmic vein, and sphenoparietal sinus (arrows). (c) Coronal T2-weighted MR image shows diffuse intraorbital edema (arrowheads) and small bilateral subdural hygromas (arrows). (d) Axial T1-weighted MR image shows the ophthalmic veins (arrows) markedly dilated and a small subacute hemorrhagic contusion (arrowhead). (e) Axial gadolinium-enhanced T1-weighted MR image shows asymmetric left ocular proptosis (arrows). These findings are compatible with occult high-flow direct carotid-cavernous fistula. (f, g) Digital subtraction angiograms obtained after catheterization show direct arterial flow from the left cavernous carotid artery into the left cavernous sinus (straight arrow), also filling the contralateral right cavernous sinus through intersellar communications. Note the arterialized flow within the left ophthalmic vein (arrowhead) and left sphenoparietal sinus (curved arrow).



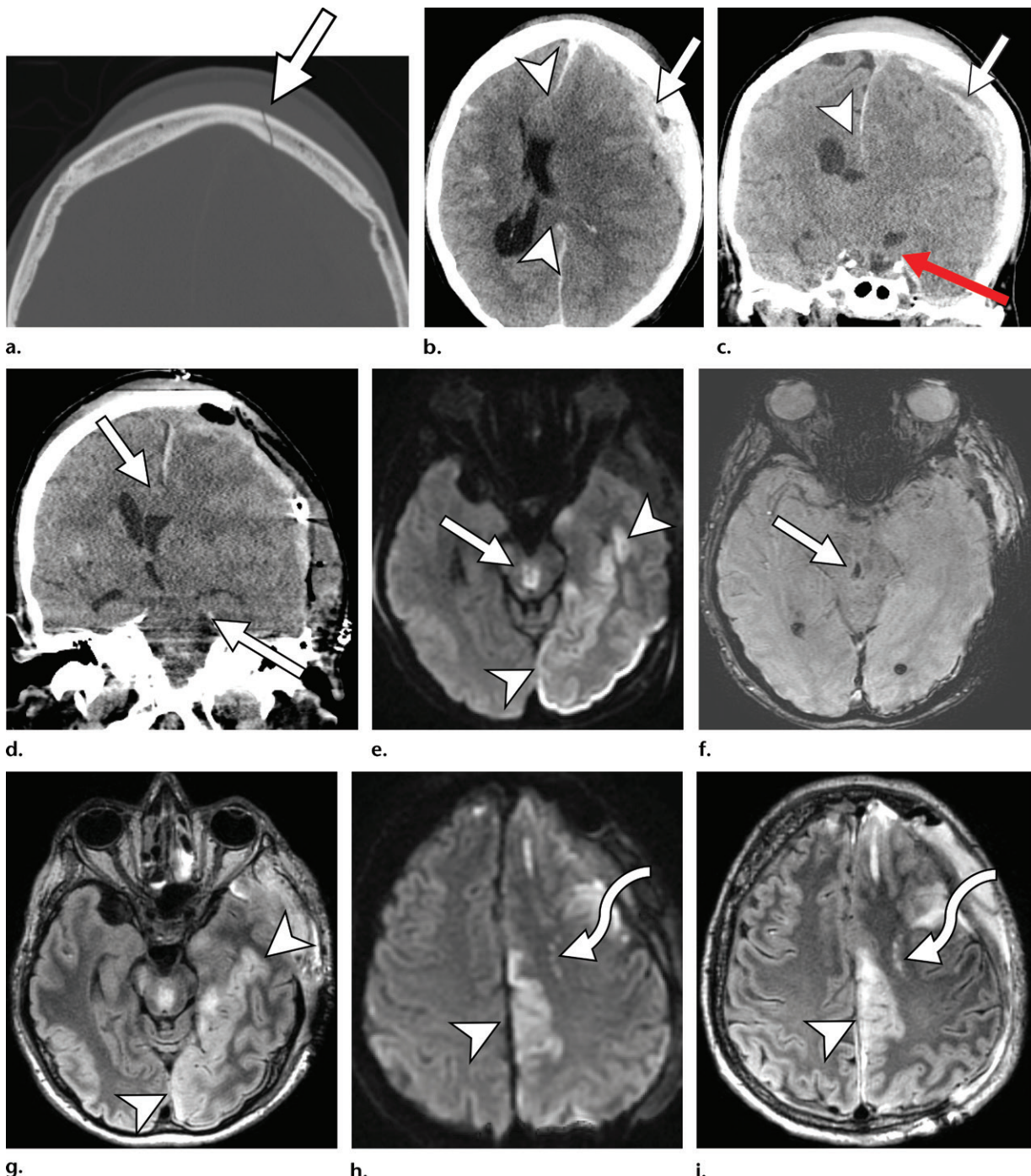


Figure 24. Secondary cerebral infarctions in a 34-year-old man who fell from scaffolding and was unconscious. His GCS score was 4. (a) Axial nonenhanced CT image shows a nondisplaced left frontal calvarial fracture (arrow). (b, c) Axial (b) and coronal (c) nonenhanced CT images show a large mixed-attenuating hyperacute and acute left cerebral convexity hematoma (white arrow) causing mass effect, rightward subfalcine herniation (arrowheads), and central downward herniation with effacement of the suprasellar cistern with brainstem compression (red arrow in c). (d) Coronal nonenhanced CT image shows improved right subfalcine and central downward herniation (arrows) after emergency decompressive craniectomy. (e, f) Axial diffusion-weighted image (e) shows central midbrain infarction (arrow in e), with associated hemorrhage (arrow in f) on the axial susceptibility-weighted image (f). (g) Axial T2-weighted FLAIR MR image shows a large left anterior cerebral artery infarct (arrowheads in e, g). (h, i) Axial diffusion-weighted (h) and T2-weighted FLAIR (i) MR images show a distal left anterior cerebral artery (arrowheads) related to vascular compression from herniation and multifocal T2-hyperintense restricted foci (curved arrow), compatible with TAs. Diffuse SAH, intraventricular hemorrhage, and multifocal frontal contusions were also noted.

Downward transtentorial herniation can result in third nerve palsy with pupillary involvement ("blown" mydriatic pupil). Various types of herniation can also result in secondary cerebral infarctions

(108,109) (Fig 24): (a) subfalcine herniation can cause anterior cerebral artery infarction on the side of the mass effect owing to compression of the anterior cerebral artery against the falx; (b) unilateral or

Potential Complications Due to Herniation in the Setting of TBI

| Type of Herniation | Ischemic Complications | Ventricular Entrapment and Other Findings |
|------------------------------------------------------------------|--------------------------------------------------------------------------------------------------------------|--------------------------------------------------------------------------------------------------------------------------|
| Subfalcine herniation (midline shift) | Anterior cerebral artery infarction on the side of the mass effect | Lateral ventriculomegaly on the side that the midline is shifting toward |
| Unilateral or asymmetric downward ward transtentorial herniation | Ipsilateral posterior cerebral artery infarction | Ipsilateral cranial nerve III palsy with pupillary involvement; ipsilateral hemiparesis (Kernohan phenomenon, if severe) |
| Severe or bilateral downward transtentorial herniation | Circle of Willis perforator occlusion; Midbrain Duret hemorrhages hypothalamic and basal ganglia infarctions | |
| Ascending transtentorial herniation | Superior cerebellar artery infarction (if severe) | Noncommunicating hydrocephalus at the level of the cerebral aqueduct |
| Cerebellar tonsillar herniation | Posterior inferior cerebellar artery infarction (if severe) | Noncommunicating hydrocephalus at the fourth ventricular outlet |

asymmetric downward transtentorial herniation can result in ipsilateral posterior cerebral artery infarction; (c) severe bilateral downward transtentorial herniation can compress perforating arteries arising from the circle of Willis, resulting in hypothalamic and basal ganglia infarctions; and (d) severe cerebellar tonsillar herniation can result in posterior inferior cerebellar artery infarction.

Various herniation patterns can also result in ventricular entrapment (Fig 24): (a) subfalcine herniation can occlude the foramen of Monro and result in lateral ventriculomegaly; (b) ascending transtentorial herniation effaces the quadrigeminal plate cistern, compresses the midbrain, and can result in noncommunicating hydrocephalus at the level of the cerebral aqueduct; and (c) cerebellar tonsillar herniation can cause fourth ventricular outlet obstruction and resulting hydrocephalus. Secondary midbrain (Duret) hemorrhages (Figs 5, 24) occur in severe downward transtentorial herniation. These complications are summarized in the Table.

Conclusion

Radiologists play a critical role in the diagnosis of complications of TBI and should understand injury patterns based on mechanism of injury, as well as secondary injuries that can occur owing to mass effect and herniation. CT is most important in acute TBI given its speed, accessibility, and high sensitivity for detecting lesions requiring neurosurgical intervention. MRI has higher sensitivity for the detection of intracranial injuries; while its optimal use in TBI is an area of active investigation, MRI is currently indicated when CT is normal and there are persistent unexplained neurologic findings. DTI remains investigational for assessment of TBI in patients.

Disclosures of Conflicts of Interest.—S.N.N. Activities related to the present article: grant from the ACR to develop TBI-RADS. Activities not related to the present article: disclosed no relevant relationships. Other activities: disclosed no relevant relationships. A.J.T. Activities related to the present article: disclosed no relevant relationships. Activities not related to the present article: blinded structured expert readings for clinical trials for BioClinica, Parexel, and ICON; expert medicolegal testimony for medical negligence and personal injury litigation, primarily for TBI that involves DTI. Other activities: disclosed no relevant relationships.

References

- Dewan MC, Rattani A, Gupta S, et al. Estimating the global incidence of traumatic brain injury. *J Neurosurg* 2018;118:1–18 [Epub ahead of print] <https://doi.org/10.3171/2017.10.JNS17352>.
- GBD 2016 Traumatic Brain Injury and Spinal Cord Injury Collaborators. Global, regional, and national burden of traumatic brain injury and spinal cord injury, 1990–2016: a systematic analysis for the Global Burden of Disease Study 2016. *Lancet Neurol* 2019;18(1):56–87.
- Taylor CA, Bell JM, Breiding MJ, Xu L. Traumatic Brain Injury-Related Emergency Department Visits, Hospitalizations, and Deaths - United States, 2007 and 2013. *MMWR Surveill Summ* 2017;66(9):1–16.
- Wintermark M, Sanelli PC, Anzai Y, et al. Imaging evidence and recommendations for traumatic brain injury: conventional neuroimaging techniques. *J Am Coll Radiol* 2015;12(2):e1–e14.
- Teasdale G, Maas A, Lecky F, Manley G, Stocchetti N, Murray G. The Glasgow Coma Scale at 40 years: standing the test of time. *Lancet Neurol* 2014;13(8):844–854.
- Brown JB, Forsythe RM, Stassen NA, et al. Evidence-based improvement of the National Trauma Triage Protocol: The Glasgow Coma Scale versus Glasgow Coma Scale motor subscale. *J Trauma Acute Care Surg* 2014;77(1):95–102; discussion 101–102.
- Chou R, Totten AM, Pappas M, et al. Glasgow Coma Scale for Field Triage of Trauma: A Systematic Review. Rockville, Md: Agency for Healthcare Research and Quality, 2017.
- Sussman ES, Pendharkar AV, Ho AL, Ghajar J. Mild traumatic brain injury and concussion: terminology and classification. *Handb Clin Neurol* 2018;158:21–24.
- Management of Concussion/mTBI Working Group. VA/DoD Clinical Practice Guideline for Management of Concussion/Mild Traumatic Brain Injury. *J Rehabil Res Dev* 2009;46(6):CP1–CP68.
- Giza CC, Kutcher JS, Ashwal S, et al. Summary of evidence-based guideline update: evaluation and management of concussion in sports—report of the Guideline Development

- Subcommittee of the American Academy of Neurology. *Neurology* 2013;80(24):2250–2257.
11. Shetty VS, Reis MN, Aulino JM, et al. ACR Appropriateness Criteria Head Trauma. *J Am Coll Radiol*. 2016 Jun;13(6):668–79.
 12. Haydel MJ, Preston CA, Mills TJ, Luber S, Blaudeau E, DeBlieux PM. Indications for computed tomography in patients with minor head injury. *N Engl J Med* 2000;343(2):100–105.
 13. Stiell IG, Wells GA, Vandemheen K, et al. The Canadian CT Head Rule for patients with minor head injury. *Lancet* 2001;357(9266):1391–1396.
 14. Mower WR, Hoffman JR, Herbert M, et al. Developing a decision instrument to guide computed tomographic imaging of blunt head injury patients. *J Trauma* 2005;59(4):954–959.
 15. Wei SC, Ulmer S, Lev MH, Pomerantz SR, González RG, Henson JW. Value of coronal reformations in the CT evaluation of acute head trauma. *AJR Am J Neuroradiol* 2010;31(2):334–339.
 16. Añón J, Remonda L, Spreng A, et al. Traumatic extra-axial hemorrhage: correlation of postmortem MSCT, MRI, and forensic-pathological findings. *J Magn Reson Imaging* 2008;28(4):823–836.
 17. Gentry LR, Godersky JC, Thompson B, Dunn VD. Prospective comparative study of intermediate-field MR and CT in the evaluation of closed head trauma. *AJR Am J Roentgenol* 1988;150(3):673–682.
 18. Han JS, Kaufman B, Alfidi RJ, et al. Head trauma evaluated by magnetic resonance and computed tomography: a comparison. *Radiology* 1984;150(1):71–77.
 19. Kelly AB, Zimmerman RD, Snow RB, Gandy SE, Heier LA, Deck MD. Head trauma: comparison of MR and CT—experience in 100 patients. *AJR Am J Neuroradiol* 1988;9(4):699–708.
 20. Paterakis K, Karantanas AH, Komnos A, Volikas Z. Outcome of patients with diffuse axonal injury: the significance and prognostic value of MRI in the acute phase. *J Trauma* 2000;49(6):1071–1075.
 21. Snow RB, Zimmerman RD, Gandy SE, Deck MD. Comparison of magnetic resonance imaging and computed tomography in the evaluation of head injury. *Neurosurgery* 1986;18(1):45–52.
 22. Zimmerman RA, Bilaniuk LT, Hackney DB, Goldberg HI, Grossman RI. Head injury: early results of comparing CT and high-field MR. *AJR Am J Roentgenol* 1986;147(6):1215–1222.
 23. Mitchell P, Wilkinson ID, Hoggard N, et al. Detection of subarachnoid hemorrhage with magnetic resonance imaging. *J Neurol Neurosurg Psychiatry* 2001;70(2):205–211.
 24. Hesselink JR, Dowd CF, Healy ME, Hajek P, Baker LL, Luerssen TG. MR imaging of brain contusions: a comparative study with CT. *AJR Am J Roentgenol* 1988;150(5):1133–1142.
 25. Noguchi K, Seto H, Kamisaki Y, Tomizawa G, Toyoshima S, Watanabe N. Comparison of fluid-attenuated inversion-recovery MR imaging with CT in a simulated model of acute subarachnoid hemorrhage. *AJR Am J Neuroradiol* 2000;21(5):923–927.
 26. Noguchi K, Ogawa T, Seto H, et al. Subacute and chronic subarachnoid hemorrhage: diagnosis with fluid-attenuated inversion-recovery MR imaging. *Radiology* 1997;203(1):257–262.
 27. Woodcock RJ Jr, Short J, Do HM, Jensen ME, Kallmes DF. Imaging of acute subarachnoid hemorrhage with a fluid-attenuated inversion recovery sequence in an animal model: comparison with non-contrast-enhanced CT. *AJR Am J Neuroradiol* 2001;22(9):1698–1703.
 28. Kara A, Celik SE, Dalbayrak S, Yilmaz M, Akansel G, Tireli G. Magnetic resonance imaging finding in severe head injury patients with normal computerized tomography. *Turk Neurosurg* 2008;18(1):1–9.
 29. Greenberg SM, Vernooy MW, Cordonnier C, et al. Cerebral microbleeds: a guide to detection and interpretation. *Lancet Neurol* 2009;8(2):165–174.
 30. Beauchamp MH, Ditchfield M, Babl FE, et al. Detecting traumatic brain lesions in children: CT versus MRI versus susceptibility weighted imaging (SWI). *J Neurotrauma* 2011;28(6):915–927.
 31. Geurts BHJ, Andriessen TMJC, Goraj BM, Vos PE. The reliability of magnetic resonance imaging in traumatic brain injury lesion detection. *Brain Inj* 2012;26(12):1439–1450.
 32. Huang YL, Kuo YS, Tseng YC, Chen DYT, Chiu WT, Chen CJ. Susceptibility-weighted MRI in mild traumatic brain injury. *Neurology* 2015;84(6):580–585.
 33. Trifan G, Gattu R, Haacke EM, Kou Z, Benson RR. MR imaging findings in mild traumatic brain injury with persistent neurological impairment. *Magn Reson Imaging* 2017;37:243–251.
 34. Liu AY, Maldjian JA, Bagley LJ, Sinson GP, Grossman RI. Traumatic brain injury: diffusion-weighted MR imaging findings. *AJR Am J Neuroradiol* 1999;20(9):1636–1641.
 35. Hergan K, Schaefer PW, Sorensen AG, Gonzalez RG, Huisman TA. Diffusion-weighted MRI in diffuse axonal injury of the brain. *Eur Radiol* 2002;12(10):2536–2541.
 36. Ezaki Y, Tsutsumi K, Morikawa M, Nagata I. Role of diffusion-weighted magnetic resonance imaging in diffuse axonal injury. *Acta Radiol* 2006;47(7):733–740.
 37. Roth TL, Nayak D, Atanasijevic T, Koretsky AP, Latour LL, McGavern DB. Transcranial amelioration of inflammation and cell death after brain injury. *Nature* 2014;505(7482):223–228.
 38. Kim SC, Park SW, Ryoo I, et al. Contrast-enhanced FLAIR (fluid-attenuated inversion recovery) for evaluating mild traumatic brain injury. *PLoS One* 2014;9(7):e102229.
 39. Chiara Ricciardi M, Bokkers RPH, Butman JA, et al. Trauma-Specific Brain Abnormalities in Suspected Mild Traumatic Brain Injury Patients Identified in the First 48 Hours after Injury: A Blinded Magnetic Resonance Imaging Comparative Study Including Suspected Acute Minor Stroke Patients. *J Neurotrauma* 2017;34(1):23–30.
 40. Bodanapally UK, Saksobhavivat N, Shanmuganathan K, Aarabi B, Roy AK. Arterial injuries after penetrating brain injury in civilians: risk factors on admission head computed tomography. *J Neurosurg* 2015;122(1):219–226.
 41. Perrein A, Petry L, Reis A, Baumann A, Mertes P, Audibert G. Cerebral vasospasm after traumatic brain injury: an update. *Minerva Anestesiol* 2015;81(11):1219–1228.
 42. Expert Panel on Neurologic Imaging, Salmela MB, Mortazavi S, et al. ACR Appropriateness Criteria® Cerebrovascular Disease. *J Am Coll Radiol* 2017;14(5S):S34–S61.
 43. Rischall MA, Boegel KH, Palmer CS, Knoll B, McKinney AM. MDCT Venographic Patterns of Dural Venous Sinus Compromise After Acute Skull Fracture. *AJR Am J Roentgenol* 2016;207(4):852–858.
 44. Fujii Y, Tasaki O, Yoshiya K, et al. Evaluation of posttraumatic venous sinus occlusion with CT venography. *J Trauma* 2009;66(4):1002–1006; discussion 1006–1007.
 45. Delgado Almandoz JE, Kelly HR, Schaefer PW, Lev MH, Gonzalez RG, Romero JM. Prevalence of traumatic dural venous sinus thrombosis in high-risk acute blunt head trauma patients evaluated with multidetector CT venography. *Radiology* 2010;255(2):570–577.
 46. Rivkin MA, Saraiya PV, Woodrow SI. Sinovenous thrombosis associated with skull fracture in the setting of blunt head trauma. *Acta Neurochir (Wien)* 2014;156(5):999–1007; discussion 1007.
 47. Slasky SE, Rivaud Y, Suberlak M, et al. Venous Sinus Thrombosis in Blunt Trauma: Incidence and Risk Factors. *J Comput Assist Tomogr* 2017;41(6):891–897.
 48. Niogi SN, Mukherjee P. Diffusion tensor imaging of mild traumatic brain injury. *J Head Trauma Rehabil* 2010;25(4):241–255.
 49. Xiong Y, Zhou XJ, Nisi RA, et al. Brain white matter changes in CPAP-treated obstructive sleep apnea patients with residual sleepiness. *J Magn Reson Imaging* 2017;45(5):1371–1378.
 50. Xie Y, Zhang Y, Qin W, Lu S, Ni C, Zhang Q. White Matter Microstructural Abnormalities in Type 2 Diabetes Mellitus: A Diffusional Kurtosis Imaging Analysis. *AJR Am J Neuroradiol* 2017;38(3):617–625.
 51. Li X, Ma C, Sun X, et al. Disrupted white matter structure underlies cognitive deficit in hypertensive patients. *Eur Radiol* 2016;26(9):2899–2907.
 52. Abe O, Aoki S, Hayashi N, et al. Normal aging in the central nervous system: quantitative MR diffusion-tensor analysis. *Neurobiol Aging* 2002;23(3):433–441.

53. Bender AR, Völkle MC, Raz N. Differential aging of cerebral white matter in middle-aged and older adults: A seven-year follow-up. *Neuroimage* 2016;125:74–83.
54. Ohtani T, Nestor PG, Bouix S, et al. Exploring the neural substrates of attentional control and human intelligence: Diffusion tensor imaging of prefrontal white matter tractography in healthy cognition. *Neuroscience* 2017;341:52–60.
55. Niogi S, Mukherjee P, Ghajar J, McCandless BD. Individual Differences in Distinct Components of Attention are Linked to Anatomical Variations in Distinct White Matter Tracts. *Front Neuroanat* 2010;4:2.
56. Johnson NF, Kim C, Gold BT. Socioeconomic status is positively correlated with frontal white matter integrity in aging. *Age (Dordr)* 2013;35(6):2045–2056.
57. Stokum JA, Sours C, Zhuo J, Kane R, Shanmuganathan K, Gullapalli RP. A longitudinal evaluation of diffusion kurtosis imaging in patients with mild traumatic brain injury. *Brain Inj* 2015;29(1):47–57.
58. Lemkadem A, Daducci A, Vulliemoz S, et al. A multi-center study: intra-scan and inter-scan variability of diffusion spectrum imaging. *Neuroimage* 2012;62(1):87–94.
59. White NS, Leergaard TB, D'Arceuil H, Bjaalie JG, Dale AM. Probing tissue microstructure with restriction spectrum imaging: Histological and theoretical validation. *Hum Brain Mapp* 2013;34(2):327–346.
60. Zhang H, Schneider T, Wheeler-Kingshott CA, Alexander DC. NODDI: practical in vivo neurite orientation dispersion and density imaging of the human brain. *Neuroimage* 2012;61(4):1000–1016.
61. Maas AIR, Hukkelhoven CWPM, Marshall LF, Steyerberg EW. Prediction of outcome in traumatic brain injury with computed tomographic characteristics: a comparison between the computed tomographic classification and combinations of computed tomographic predictors. *Neurosurgery* 2005;57(6):1173–1182; discussion 1173–1182.
62. Mata-Mbemba D, Mugikura S, Nakagawa A, et al. Early CT findings to predict early death in patients with traumatic brain injury: Marshall and Rotterdam CT scoring systems compared in the major academic tertiary care hospital in northeastern Japan. *Acad Radiol* 2014;21(5):605–611.
63. Wintermark M, Li Y, Ding VY, et al. Neuroimaging Radiological Interpretation System for Acute Traumatic Brain Injury. *J Neurotrauma* 2018;35(22):2665–2672.
64. Marinowitz C, Lecky FE, Townend W, Borakati A, Fabbri A, Sheldon TA. The Risk of Deterioration in GCS13–15 Patients with Traumatic Brain Injury Identified by Computed Tomography Imaging: A Systematic Review and Meta-Analysis. *J Neurotrauma* 2018;35(5):703–718.
65. Yuh EL, Cooper SR, Ferguson AR, Manley GT. Quantitative CT improves outcome prediction in acute traumatic brain injury. *J Neurotrauma* 2012;29(5):735–746.
66. Yuh EL, Mukherjee P, Lingsma HF, et al. Magnetic resonance imaging improves 3-month outcome prediction in mild traumatic brain injury. *Ann Neurol* 2013;73(2):224–235.
67. Cicuendez M, Castaño-León A, Ramos A, Hilario A, Gómez PA, Lagares A. The added prognostic value of magnetic resonance imaging in traumatic brain injury: The importance of traumatic axonal injury when performing ordinal logistic regression. *J Neuroradiol* 2018 Sep 1 [Epub ahead of print].
68. Haghbayan H, Boutin A, Laflamme M, et al. The Prognostic Value of MRI in Moderate and Severe Traumatic Brain Injury: A Systematic Review and Meta-Analysis. *Crit Care Med* 2017;45(12):e1280–e1288.
69. ACR Head Injury Institute. TBI-RADS. <http://www.head-injuryinstitute.org/tools/hi-rads/>. Accessed March 22, 2019.
70. Cramer JA, Eisenmenger LB, Pierson NS, Dhatt HS, Heilbrun ME. Structured and templated reporting: An overview. *Appl Radiol* 2014. <https://applie radiology.com/articles/structured-and-templated-reporting-an-overview>. Accessed March 22, 2019.
71. Allen B, Chatfield M, Burleson J, Thorwarth WT. Improving diagnosis in health care: perspectives from the American College of Radiology. *Diagnosis (Berl)* 2017;4(3):113–124.
72. Baugnon KL, Hudgins PA. Skull base fractures and their complications. *Neuroimaging Clin N Am* 2014;24(3):439–465, vii–viii.
73. Zayas JO, Feliciano YZ, Hadley CR, Gomez AA, Vidal JA. Temporal bone trauma and the role of multidetector CT in the emergency department. *RadioGraphics* 2011;31(6):1741–1755.
74. Ellis H. Anatomy of head injury. *Surgery* 2012;30(3):99–101.
75. Al-Nakshabandi NA. The swirl sign. *Radiology* 2001;218(2):433.
76. Gean AD, Fischbein NJ, Purcell DD, Aiken AH, Manley GT, Stiver SI. Benign anterior temporal epidural hematoma: indolent lesion with a characteristic CT imaging appearance after blunt head trauma. *Radiology* 2010;257(1):212–218.
77. Peres CMA, Caldas JGMP, Puglia P, et al. Endovascular management of acute epidural hematomas: clinical experience with 80 cases. *J Neurosurg* 2018;128(4):1044–1050.
78. Sieswerda-Hoogendoorn T, Postema FAM, Verbaan D, Majoe CB, van Rijn RR. Age determination of subdural hematomas with CT and MRI: a systematic review. *Eur J Radiol* 2014;83(7):1257–1268.
79. Ban SP, Hwang G, Byoun HS, et al. Middle Meningeal Artery Embolization for Chronic Subdural Hematoma. *Radiology* 2018;286(3):992–999.
80. Link TW, Boddu S, Paine SM, Kamel H, Knopman J. Middle Meningeal Artery Embolization for Chronic Subdural Hematoma: A Series of 60 Cases. *Neurosurgery* 2018 Nov 9 [Epub ahead of print] <https://doi.org/10.1093/neuro/nny521>.
81. Zanini MA, de Lima Resende LA, de Souza Faleiros AT, Gabarra RC. Traumatic subdural hygromas: proposed pathogenesis based classification. *J Trauma* 2008;64(3):705–713.
82. Bodanapally UK, Dreizin D, Issa G, Archer-Arroyo KL, Sudini K, Fleiter TR. Dual-Energy CT in Enhancing Subdural Effusions that Masquerade as Subdural Hematomas: Diagnosis with Virtual High-Monochromatic (190-keV) Images. *AJNR Am J Neuroradiol* 2017;38(10):1946–1952.
83. Zourou A, Bhargava R, Hoskinson M, Aronyk KE. Further characterization of traumatic subdural collections of infancy. Report of five cases. *J Neurosurg* 2004;100(5 Suppl Pediatrics):512–518.
84. Vezina G. Assessment of the nature and age of subdural collections in nonaccidental head injury with CT and MRI. *Pediatr Radiol* 2009;39(6):586–590.
85. Borczuk P, Penn J, Peak D, Chang Y. Patients with traumatic subarachnoid hemorrhage are at low risk for deterioration or neurosurgical intervention. *J Trauma Acute Care Surg* 2013;74(6):1504–1509.
86. Servadei F, Murray GD, Teasdale GM, et al. Traumatic subarachnoid hemorrhage: demographic and clinical study of 750 patients from the European brain injury consortium survey of head injuries. *Neurosurgery* 2002;50(2):261–267; discussion 267–269.
87. Mata-Mbemba D, Mugikura S, Nakagawa A, et al. Traumatic midline subarachnoid hemorrhage on initial computed tomography as a marker of severe diffuse axonal injury. *J Neurosurg* 2018;129(5):1317–1324.
88. Takenaka N, Mine T, Suga S, et al. Interpeduncular high-density spot in severe shearing injury. *Surg Neurol* 1990;34(1):30–38.
89. Mata-Mbemba D, Mugikura S, Nakagawa A, et al. Intraventricular hemorrhage on initial computed tomography as marker of diffuse axonal injury after traumatic brain injury. *J Neurotrauma* 2015;32(5):359–365.
90. Yue JK, Winkler EA, Puffer RC, et al. Temporal lobe contusions on computed tomography are associated with impaired 6-month functional recovery after mild traumatic brain injury: a TRACK-TBI study. *Neurol Res* 2018;40(11):972–981.
91. Scheid R, Ott DV, Roth H, Schroeter ML, von Cramon DY. Comparative magnetic resonance imaging at 1.5 and 3 Tesla for the evaluation of traumatic microbleeds. *J Neurotrauma* 2007;24(12):1811–1816.
92. Alahmadi H, Vachhrajani S, Cusimano MD. The natural history of brain contusion: an analysis of radiological and clinical progression. *J Neurosurg* 2010;112(5):1139–1145.
93. Chieregato A, Fainardi E, Morselli-Labate AM, et al. Factors associated with neurological outcome and lesion progression in traumatic subarachnoid hemorrhage patients. *Neurosurgery* 2005;56(4):671–680; discussion 671–680.

94. Saeki N, Yamaura A, Sunami K. Brain stem contusion due to tentorial coup injury: case report and pathomechanical analysis from normal cadavers. *Br J Neurosurg* 1998;12(2):151–155.
95. Adams JH, Doyle D, Ford I, Gennarelli TA, Graham DI, McLellan DR. Diffuse axonal injury in head injury: definition, diagnosis and grading. *Histopathology* 1989;15(1):49–59.
96. Moen KG, Brezova V, Skandsen T, Häberg AK, Folvik M, Vik A. Traumatic axonal injury: the prognostic value of lesion load in corpus callosum, brain stem, and thalamus in different magnetic resonance imaging sequences. *J Neuropauma* 2014;31(17):1486–1496.
97. Shetty T, Nguyen JT, Cogsil T, et al. Clinical Findings in a Multicenter MRI Study of Mild TBI. *Front Neurol* 2018;9:836.
98. Unterberg AW, Stover J, Kress B, Kiening KL. Edema and brain trauma. *Neuroscience* 2004;129(4):1021–1029.
99. Golding EM. Sequelae following traumatic brain injury. The cerebrovascular perspective. *Brain Res Brain Res Rev* 2002;38(3):377–388.
100. Werner C, Engelhard K. Pathophysiology of traumatic brain injury. *Br J Anaesth* 2007;99(1):4–9.
101. Marmarou A, Signoretti S, Fatouros PP, Portella G, Aygok GA, Bullock MR. Predominance of cellular edema in traumatic brain swelling in patients with severe head injuries. *J Neurosurg* 2006;104(5):720–730.
102. Rutman AM, Vranic JE, Mossa-Basha M. Imaging and Management of Blunt Cerebrovascular Injury. *RadioGraphics* 2018;38(2):542–563.
103. Biffl WL, Moore EE, Offner PJ, et al. Optimizing screening for blunt cerebrovascular injuries. *Am J Surg* 1999;178(6):517–522.
104. Franz RW, Willette PA, Wood MJ, Wright ML, Hartman JF. A systematic review and meta-analysis of diagnostic screening criteria for blunt cerebrovascular injuries. *J Am Coll Surg* 2012;214(3):313–327.
105. Cothren CC, Moore EE, Biffl WL, et al. Cervical spine fracture patterns predictive of blunt vertebral artery injury. *J Trauma* 2003;55(5):811–813.
106. Sperry JL, Moore EE, Coimbra R, et al. Western Trauma Association critical decisions in trauma: penetrating neck trauma. *J Trauma Acute Care Surg* 2013;75(6):936–940.
107. Johnson PL, Eckard DA, Chason DP, Brecheisen MA, Batnitzky S. Imaging of acquired cerebral herniations. *Neuroimaging Clin N Am* 2002;12(2):217–228.
108. Tawil I, Stein DM, Mirvis SE, Scalea TM. Posttraumatic cerebral infarction: incidence, outcome, and risk factors. *J Trauma* 2008;64(4):849–853.
109. Bae DH, Choi KS, Yi HJ, Chun HJ, Ko Y, Bak KH. Cerebral Infarction after Traumatic Brain Injury: Incidence and Risk Factors. *Korean J Neurotrauma* 2014;10(2):35–40.

This journal-based SA-CME activity has been approved for **AMA PRA Category 1 Credit™**. See rsna.org/learning-center-rg.

Invited Commentary on “Traumatic Brain Injury: Imaging Patterns and Complications”

From:

Shobhit Mathur, MD

Department of Radiology, Vancouver General Hospital, University of British Columbia, Vancouver, British Columbia, Canada

Department of Medical Imaging, St Michael’s Hospital, University of Toronto, Toronto, Canada

Savvas Nicolaou, MD

Department of Radiology, Vancouver General Hospital, University of British Columbia, Vancouver, British Columbia, Canada

TBI is one of the leading causes of disability with a significant socioeconomic burden. In 2010, the lifetime economic cost of TBI was estimated to be approximately \$76.5 billion, including direct and indirect medical costs (1). Imaging plays an important role in triage and prognostication in TBI. As in several disease processes, the role of radiologists in the care of patients with TBI has expanded over time from mere interpreters to consultants. This growing role is born of our ever-increasing appreciation for the pathophysiology of TBI, the strengths of various imaging modalities used in different disease stages, and the nuances of prognostication and predicting functional outcomes. Finally, radiologists play a vital role in advising clinicians on which imaging modality to perform that will best answer their clinical questions while mitigating radiation risk, especially among pediatric populations and in the developing fetus.

Schweitzer et al (2) outline an excellent approach for selecting which imaging modality to use in the various stages and types of TBI. As highlighted in the article, in acute mild, moderate, or severe TBI, CT is often the imaging modality of choice. Despite the higher sensitivity of MRI in acute TBI, its routine use is not recommended and is limited to special circumstances in which there are persistent unexplained neurologic findings and a negative CT study (3). In mild TBI, although negative imaging studies do not accurately identify patients who would have persistent postconcussive symptoms, positive imaging studies have been shown to be associated with worse functional outcomes compared with those of negative imaging studies (4).

In cases of subacute to chronic TBI with neurologic symptoms, MRI is the preferred imaging modality owing to its high sensitivity. Cerebral atrophy after TBI has been shown to correlate with

the severity of injury and functional outcomes (5). The pattern of post-TBI cognitive dysfunction could be related to specific sites of brain injury (6). Limited evidence exists regarding the correlation of MRI findings in subacute to chronic mild TBI with long-term neurobehavioral outcomes. Future research should be directed toward better understanding in this area.

Choosing which modality to use for follow-up imaging is an important clinical and radiologic question in routine practice and is dependent on the clinical scenario and the severity and chronicity of injury. Follow-up imaging with nonenhanced head CT is indicated only in certain cases of mild TBI (7). Patients with mild TBI with a convexity SAH, small convexity contusion, small intraparenchymal hemorrhage (≤ 10 mL), and/or small SDH may not require repeat CT if there is no neurologic decline (8). Follow-up nonenhanced head CT is indicated if there is worsening neurologic status, moderate to severe TBI, or an abnormal initial CT study in a patient undergoing anticoagulation therapy. Follow-up MRI for acute TBI is indicated if the initial head CT is negative and there are ongoing unexplained neurologic findings (9).

There is increasing evidence that repetitive TBI can result in progressive and additive brain injury. Chronic traumatic encephalopathy (CTE) describes neurodegenerative tauopathy associated with repetitive head injury. This is commonly diagnosed in patients who are in the military or who are athletes who play contact sports. Distinguishing CTE from other neurodegenerative conditions such as Alzheimer disease, frontotemporal dementia, and Lewy body dementia is challenging owing to overlap in clinical features. Hyperphosphorylated tau in neurons and astroglia around small blood vessels at the depths of cortical sulci in an irregular pattern are the pathologic hallmarks of CTE. As the pattern of tau aggregation in CTE is unique, it is hypothesized that CTE could be distinguished from other clinically similar neurodegenerative diseases at imaging (10).

Early *in vivo* detection of CTE is desirable and an area of active research. Several imaging techniques such as radionuclide PET, diffusion-weighted MRI, magnetic resonance spectroscopy, functional MRI, susceptibility-weighted imaging, SPECT, diffusion-tensor imaging, and arterial spin-labeled MRI have been investigated for the evaluation of CTE. Arguably, the most promising imaging technique is fluorine 18-FDDNP ($2-(1-\{6-[2-[^{18}\text{F}]\text{fluoroethyl})(\text{methyl})\text{amino}-2-\text{naphthyl}\} \text{ethylenedimaleononitrile}$) PET, as it uses a tau-binding radionuclide (11). With the rapidly growing body of evidence for imaging CTE, we anticipate that the next few years could

bring great changes in the way we image and understand this condition.

Special attention should be paid to imaging the developing brain. Pediatric imaging interpretation applies some of the same general principles of imaging in adults, with a few caveats. Children are at greater risk for harmful effects of ionizing radiation compared to adults, and pediatric imaging with ionizing radiation demands robust dose-reduction strategies. For mild TBI in children, increasing clinical observation in the emergency department could avoid unnecessary radiation exposure (12).

Several clinical decision rules have been investigated in the pediatric TBI population where nonenhanced head CT could be avoided, such as the Pediatric Emergency Care Applied Research Network (PECARN) rule, the Children's Head Injury Algorithm for the Prediction of Important Clinical Events (CHALICE) rule, and the Canadian Assessment of Tomography for Childhood Head Injury (CATCH) rule. Of these, the PECARN rule is the best validated (13). Although CT has the advantages of availability and speed and should not be delayed in the presence of TBI symptoms, MRI avoids ionizing radiation and offers more sensitivity in the detection of TBI. MRI is especially useful in nonaccidental injury where it is valuable for the detection of multiple injuries of varying ages and hypoxic-ischemic injury.

Intracranial injury is a significant nonobstetric cause of maternal mortality during pregnancy. The approach for interpreting imaging studies in trauma patients who are pregnant is similar to that for any other trauma patient. CT is also the modality of choice for evaluating suspected acute TBI in this population. One commonly raised concern is fetal radiation dose. Radiologists can play an important role in advising referring clinicians and patients about this and alleviating unnecessary anxiety and delays. As with the care of any patient, adherence to the “as low as reasonably achievable,” or ALARA, principle for radiation dose is essential. The benefit of performing an imaging examination using radiation in a patient who is pregnant or potentially pregnant must always outweigh the risk of not performing it, and this may sometimes require a discussion between the radiologist and referring clinician.

Undergoing a single diagnostic procedure involving ionizing radiation does not result in radiation exposure adequate to threaten the well-being of the pre-embryo, embryo, or fetus. The vast majority of medical imaging studies have a fetal radiation dose of less than 50 mGy with no known risk of impairment of mental or physical development, malformation, or fetal death. Multiple CT studies would need to be performed

before an appreciable increase in risk is observed (14). There are a few case reports in the literature about fetal head injury secondary to maternal trauma during pregnancy. In imaging studies of these neonates, skull fractures, intracranial hemorrhage, and hypoxic-ischemic encephalopathy were common findings (15).

Imaging of TBI is a rapidly evolving field for both radiologists and clinicians. Many radiologists may find themselves in an increasingly prominent role of being a consultant to the referring physician. Specifically, exciting clinical and research frontiers for radiologists in TBI include the selection of optimal imaging modalities to allow for accurate prognostication of functional outcomes, monitoring of TBI at all stages, early identification of CTE, and steps to reduce radiation exposure among vulnerable populations. We would like to congratulate the authors on a highly informative and well-illustrated review of imaging of TBI and hope this commentary complements an already extensive review of this exciting topic.

Disclosures of Conflicts of Interest.—**S.M.** Activities related to the present article: disclosed no relevant activities. Activities not related to the present article: one-time honorarium from Bayer for meeting attendance; institution has a master research agreement with Siemens Healthcare. Other activities: disclosed no relevant activities. **S.N.** Activities related to the present article: disclosed no relevant activities. Activities not related to the present article: institution has a master research agreement with Siemens Healthcare. Other activities: disclosed no relevant activities.

References:

1. Centers for Disease Control and Prevention. Severe TBI. <https://www.cdc.gov/traumaticbraininjury/severe.html>. Reviewed April 2, 2019. Accessed August 1, 2019.
2. Schweitzer AD, Niogi SN, Whitlow CJ, Tsioris AJ. Traumatic Brain Injury: Imaging Patterns and Complications. RadioGraphics 2019;39(6):1571-1595.
3. Amyot F, Arciniegas DB, Brazaitis MP, et al. A Review of the Effectiveness of Neuroimaging Modalities for the Detection of Traumatic Brain Injury. J Neurotrauma 2015;32(22):1693-1721.
4. Iverson GL, Lange RT, Wäljas M, et al. Outcome from Complicated versus Uncomplicated Mild Traumatic Brain Injury. Rehabil Res Pract 2012;2012:415740.
5. Sidaros A, Skimmeinge A, Liptrot MG, et al. Long-term global and regional brain volume changes following severe traumatic brain injury: a longitudinal study with clinical correlates. Neuroimage 2009;44(1):1-8.
6. Di Paola M, Phillips O, Costa A, et al. Selective Cognitive Dysfunction Is Related to a Specific Pattern of Cerebral Damage in Persons With Severe Traumatic Brain Injury. J Head Trauma Rehabil 30(6):402-410.
7. Reljc T, Mahony H, Djulbegovic B, et al. Value of repeat head computed tomography after traumatic brain injury: systematic review and meta-analysis. J Neurotrauma 2014;31(1):78-98.
8. Washington CW, Grubb RL. Are routine repeat imaging and intensive care unit admission necessary in mild traumatic brain injury? J Neurosurg 2012;116(3):549-557.
9. Wintermark M, Sanelli PC, Anzai Y, Tsioris AJ, Whitlow CT. Imaging Evidence and Recommendations for Traumatic Brain Injury: Conventional Neuroimaging Techniques. JACR 2015;12:e1-e14.
10. McKee AC, Cairns NJ, Dickson DW, et al. The first NINDS/NIBIB consensus meeting to define neuropathological criteria for the diagnosis of chronic traumatic encephalopathy. Acta Neuropathol 2016;131(1):75-86.
11. Dallmeier JD, Meysami S, Merrill DA, Raji CA. Emerging advances of in vivo detection of chronic traumatic encephalopathy and traumatic brain injury. Br J Radiol 2019;20180925.
12. Schonfeld D, Fitz BM, Nigrovic LE. Effect of the duration of emergency department observation on computed tomography use in children with minor blunt head trauma. Ann Emerg Med 2013;62(6):597-603.
13. Lytle MD, Crowe L, Oakley E, Dunning J, Babl FE. Comparing CATCH, CHALICE and PECARN clinical decision rules for paediatric head injuries. Emerg Med J 2012;29(10):785-794.
14. Tirada N, Dreizin D, Khati NJ, Akin EA, Zeman RK. Imaging Pregnant and Lactating Patients. Radiographics 2015;35(6):1751-1765.
15. Breysem L, Cossey V, Mussen E, Demaerel P, Van de Voorde W, Smet M. Fetal trauma: brain imaging in four neonates. Eur Radiol 2004;14(9):1609-1614.

Types of Cerebral Herniation and Their Imaging Features

Berta Riveros Gilardi, MD

José Ignacio Muñoz López, MD

Antonio Carlos Hernández Villegas, MD

Juan Alberto Garay Mora, MD

Oralia Cristina Rico Rodríguez, MD

Roberto Chávez Appendini, MD

Marianne De la Mora Malváez, MD

Jesús Antonio Higuera Calleja, MD

Abbreviations: CSF = cerebrospinal fluid, DTH = descending transtentorial hernia, ICP = intracranial pressure

RadioGraphics 2019; 39:1598–1610

<https://doi.org/10.1148/rg.2019190018>

Content Codes: **CT** **ER** **HN** **MR** **NR**

From the Department of Radiology, Instituto Nacional de Ciencias Médicas y Nutrición Salvador Zubirán, Vasco de Quiroga 15, Mexico City, Mexico 14080 (B.R.G., A.C.H.V., J.A.G.M., O.C.R.R., R.C.A., M.D.L.M.M., J.A.H.C.); and Department of Neuroradiology, Instituto Nacional de Neurología y Neurocirugía Manuel Velasco Suárez, Mexico City, Mexico (J.I.M.L.). Presented as an education exhibit at the 2018 RSNA Annual Meeting. Received February 15, 2019; revision requested March 28 and received May 23; accepted May 31. For this journal-based SA-CME activity, the authors, editor, and reviewers have disclosed no relevant relationships. **Address correspondence to** B.R.G (e-mail: dra.bertarg@gmail.com).

©RSNA, 2019

SA-CME LEARNING OBJECTIVES

After completing this journal-based SA-CME activity, participants will be able to:

- Identify the basic intracranial anatomy necessary for understanding the clinical and radiologic features of brain herniation syndromes.
- Discuss use of a systematic approach to cases of cerebral herniation to make an accurate diagnosis.
- Recognize the main imaging findings in cerebral herniation and integrate them with the clinical manifestations.

See rsna.org/learning-center-rg.

Cerebral herniation, defined as a shift of cerebral tissue from its normal location into an adjacent space, is a life-threatening condition that requires prompt diagnosis. The imaging spectrum can range from subtle changes to clear displacement of brain structures. For radiologists, it is fundamental to be familiar with the different imaging findings of the various subtypes of brain herniation. Brain herniation syndromes are commonly classified on the basis of their location as intracranial and extracranial hernias. Intracranial hernias can be further divided into three types: (a) subfalcine hernia; (b) transtentorial hernia, which can be ascending or descending (lateral and central); and (c) tonsillar hernia. Brain herniation may produce brain damage, compress cranial nerves and vessels causing hemorrhage or ischemia, or obstruct the normal circulation of cerebrospinal fluid, producing hydrocephalus. Owing to its location, each type of hernia may be associated with a specific neurologic syndrome. Knowledge of the clinical manifestations ensures a focused imaging analysis. To make an accurate diagnosis, the authors suggest a six-key-point approach: comprehensive analysis of a detailed history of the patient and results of clinical examination, knowledge of anatomic landmarks, direction of mass effect, recognition of displaced structures, presence of indirect radiologic findings, and possible complications. CT and MRI are the imaging modalities of choice used for establishing a correct diagnosis and guiding therapeutic decisions. They also have important prognostic implications. The preferred imaging modality is CT: the acquisition time is shorter and it is less expensive and more widely available. Patients with brain herniation are generally in critical clinical condition. Making a prompt diagnosis is fundamental for the patient's safety.

©RSNA, 2019 • radiographics.rsna.org

Introduction

Cerebral herniation is a potentially life-threatening condition that needs to be diagnosed promptly. The imaging spectrum can range from subtle changes to clear displacement of brain structures. The radiologist should be able to identify the main imaging features of the brain herniation subtypes.

The skull is a rigid vault-shaped structure containing three main components: brain, cerebrospinal fluid (CSF), and blood. It is compartmentalized by bony landmarks and inelastic dural reflections (1). Given the inflexible nature of the skull, the intracranial volume

TEACHING POINTS

- Cerebral herniation is a potentially life-threatening condition that needs to be diagnosed promptly. The imaging spectrum can range from subtle changes to clear displacement of brain structures.
- Brain edema, tumors, or hemorrhage are causes of cerebral herniation secondary to an increase in volume and intracranial pressure (ICP). A decrease in ICP can also produce herniation, as in paradoxical herniation.
- Brain herniation may cause brain pressure necrosis, compress cranial nerves and vessels causing hemorrhage or ischemia, and obstruct the normal circulation of CSF, producing hydrocephalus. Therefore, each type of hernia may be associated with a specific neurologic syndrome.
- The basal cisterns are spaces filled with CSF and located in the subarachnoid space. They contain the proximal portions of some cranial nerves and basal cerebral arteries. They are in close contact with the main intracranial structures. Basal cisterns are involved in almost any hernia type, making them a key anatomic landmark.
- In subfalcine hernias, the degree of midline shift correlates with the prognosis; less than 5-mm deviation has a good prognosis, whereas a shift of more than 15 mm is related to a poor outcome.

is fixed and there is little room for expansion. As the Monro-Kellie hypothesis states, the sum of volumes of the brain, CSF, and intracranial blood is constant. An increase in the volume of one component will result in a decrease in the volume of one or both of the other components (2).

When there is a change in the intracranial volume that exceeds these compensation mechanisms, brain tissue will be displaced from one compartment into another. It can be through anatomic or acquired spaces. Brain edema, tumors, or hemorrhage are causes of cerebral herniation secondary to an increase in volume and intracranial pressure (ICP). A decrease in ICP can also produce herniation, as in paradoxical herniation (1,3).

Brain herniation can be classified into two broad categories: intracranial and extracranial. Furthermore, intracranial hernias can be subdivided into three basic types: (*a*) subfalcine hernia; (*b*) transtentorial hernia, which can be ascending or descending (lateral and central); and (*c*) tonsillar hernia (Table, Fig 1) (4,5).

Brain herniation may cause brain pressure necrosis, compress cranial nerves and vessels causing hemorrhage or ischemia, and obstruct the normal circulation of CSF, producing hydrocephalus. Therefore, each type of hernia may be associated with a specific neurologic syndrome. Knowledge of the clinical manifestations ensures a focused imaging analysis.

The most useful imaging modalities are CT and MRI. In the emergency setting, CT is regu-

larly performed to readily identify a condition that may require surgical intervention (6). MRI findings are analogous to those on CT scans but with better tissue characterization, especially in posterior fossa disease. Anatomic MRI sequences (T1-weighted, T2-weighted, and contrast-enhanced T1-weighted) are the best for evaluation; coronal and sagittal acquisitions are encouraged (7). Historically, angiography was an important diagnostic tool, but this technique is now obsolete (8).

Approach to Diagnosing Brain Herniation Syndromes

We suggest a six-key-point approach to analyze all the clinical and imaging information to make a prompt and accurate diagnosis (Fig 2).

Clinical Information

Clinical information is useful for guiding a detailed analysis of the potentially involved anatomic structures. The patient's history, current clinical scenario, and specific neurologic syndromes should be considered when available.

Anatomic Landmarks

Anatomic landmarks are boundaries used as a reference for the different brain compartments that help determine if a specific brain structure is displaced.

Direction of Mass Effect

If there is any disease that causes mass effect, it is important to establish its location and determine the direction of the vector force it creates. This will point out the brain structures that may be displaced or involved.

Displaced Structure

Identifying the displaced structure is necessary to classify the type of hernia. Knowledge and adequate evaluation of specific anatomic regions that can herniate are fundamental.

Indirect Signs

Sometimes the herniation can be subtle and difficult to identify at first glance. Aside from looking at the specific brain structure that might be displaced, evaluating other potentially involved structures can provide valuable information by showing indirect signs of the herniation.

Herniation-related Complications

Brain herniation may cause different complications secondary to compression of vessels, nerves, and the ventricular system. Stroke of the anterior cerebral artery, posterior cerebral artery, or posterior inferior cerebellar artery occurs owing to vascular compression. Hydrocephalus manifests when

General Features of Main Intracranial Hernias

| Type of Hernia | Clinical Information and Neurologic Syndromes | Anatomic Landmarks | Direction of Mass Effect | Displaced Structure(s) | Indirect Signs |
|---------------------------|------------------------------------------------------------------------------------------------------------------------------------------------------------------------|---------------------------------------------------------------|----------------------------------------------------------------------|-----------------------------------------------------------------------------------------------------------------------------------------------------------------|------------------------------------------------------------------------------------------------------------------------------------------------------------------------|
| Subfalcine | Anterior cerebral artery syndrome | Midline, falx cerebri, cingulate gyrus, CC, and Monro foramen | Medial and anterior, beneath falx | Cingulate gyrus and CC | Dilatation of contralateral ventricle due to compression of contralateral foramen of Monro |
| Transtentorial descending | Paralysis of third nerve, compression of PCA and choroidal arteries (occipital and medial temporal infarction) | Tentorium, perimesencephalic cisterns | Downward from supratentorial compartment, through tentorial incisura | Anterior: uncus Posterior: parahippocampal gyrus, isthmus of fornical gyrus, and anterior portion of lingual gyrus Central: diencephalon, midbrain, and pons | Displacement, rotation, and elongation of brainstem Anterior or posterior: widening of contralateral ventricular atrium and temporal horn Central: hydrocephalus |
| Transtentorial ascending | Manifestations of increased ICP, brainstem and cerebellar compression PCA and SCA compression (occipital cerebral and superior cerebellar infarction) | Tentorium, superior cerebellar and quadrigeminal cisterns | Upward from posterior fossa through tentorial incisura | Superior cerebellar hemispheres and vermis, superior and inferior colliculi, midbrain | Obliteration of ipsilateral perimesencephalic and contralateral crural cisterns Anterior displacement of brainstem, hydrocephalus |
| Tonsillar | Manifestations of brainstem and cerebellar compression PICA compression (posterior inferior cerebellum, inferior cerebellar vermis, and lateral medulla infarction) | Foramen magnum (McRae line) Cerebellar tonsil | Downward through foramen magnum | Cerebellar tonsils Pons Medulla | Effacement of perimedullary CSF through foramen magnum Obliteration of cisterna magna and fourth ventricle Vertical orientation of folia of tonsil |

Note.—CC = corpus callosum, PCA = posterior cerebral artery, PICA = posterior inferior cerebellar artery, SCA = superior cerebellar artery.

there is involvement of the foramen of Monro or aqueduct of Sylvius. Cranial nerves may be affected when there is involvement of the brainstem and basal cisterns.

Relevant Anatomy

The cranial cavity is divided by bony landmarks and reflections of the dura mater. The main dural reflections are the falx cerebri and tentorium cerebelli, which divide the cranial cavity into right and left cerebral hemispheres and the posterior fossa, thus defining the supra- and infratentorial compartments (Fig 3) (7,9).

The falx cerebri has an anteroposterior orientation and is attached superiorly to the inside of

the skull. Anteriorly, it is fixed to the crista galli; posteriorly, it widens and adheres to the tentorium. Immediately inferior to the free edge of the falx is the corpus callosum and cingulate gyrus. The pericallosal artery runs through the pericallosal sulcus (Fig 4a) (7,10).

The tentorium cerebelli extends inferiorly and laterally from its confluence with the falx (10). It has a U-shaped opening called the tentorial incisura, which provides communication between the supratentorial space and the posterior fossa, a potential herniation site. The midbrain and cerebral peduncles pass through the incisura. The uncus and hippocampus are located just superior to the medial edges of the incisura.

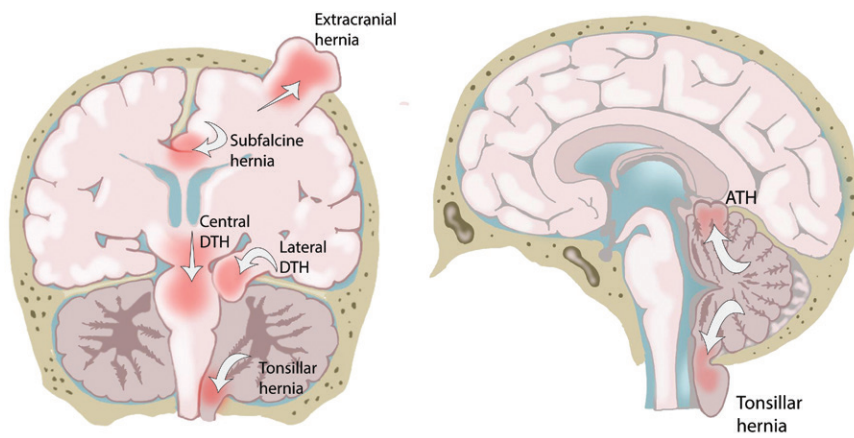
**a.****b.**

Figure 1. Drawings depict different kinds of brain herniation. *ATH* = ascending transtentorial hernia, *DTH* = descending transtentorial hernia.

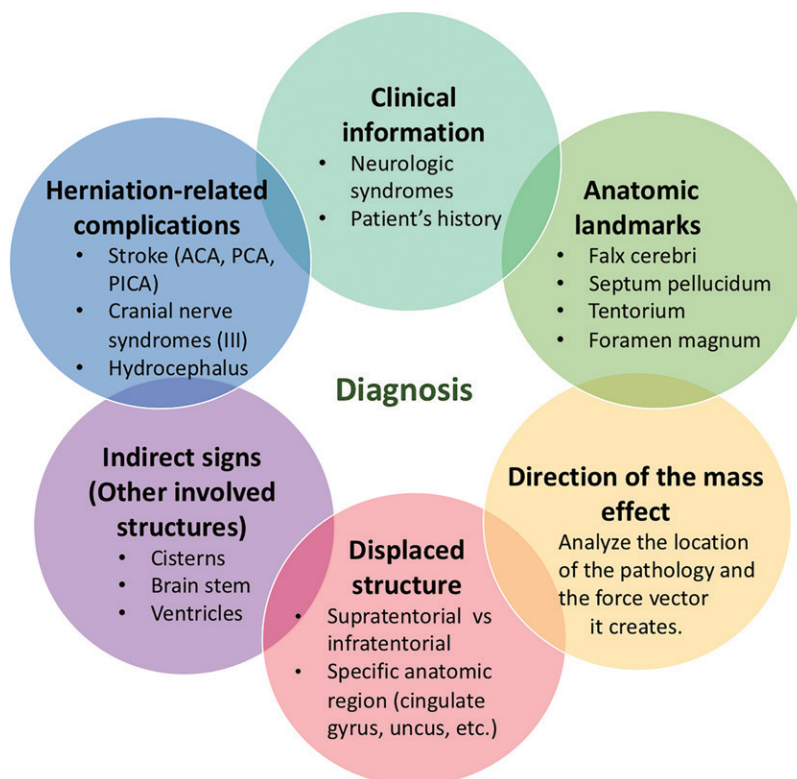


Figure 2. Approach to diagnosing brain herniation syndromes. Diagram shows the six-point guideline for analysis of cerebral herniation cases. *ACA* = anterior cerebral artery, *PCA* = posterior cerebral artery, *PICA* = posterior inferior cerebellar artery.

The basal cisterns are spaces filled with CSF and located in the subarachnoid space. They contain the proximal portions of some cranial nerves and basal cerebral arteries. They are in close contact with the main intracranial structures (Fig 4b, 4c) (11). Basal cisterns are involved in almost any hernia type, making them a key anatomic landmark.

The posterior cerebral arteries, anterior choroidal arteries, and basal veins of Rosenthal pass around the midbrain through the perimes-

encephalic cistern, close to the free edge of the tentorium. The oculomotor nerve exits the midbrain anteriorly and courses medially to the uncus on its way to the cavernous sinus. These structures are at risk of compression by the herniated tissue.

Finally, the ventricular system is a set of cavities that produce and circulate CSF through the central nervous system. It consists of two lateral ventricles divided by the septum pellucidum. They communicate with the third ventricle via

the foramen of Monro (interventricular foramen). The third ventricle is in communication with the fourth ventricle through the cerebral aqueduct, then empties into the subarachnoid space through the foramen of Luschka (side opening) and foramen of Magendie (median opening) (6).

Intracranial Hernias

Subfalcine Hernia

Subfalcine hernia, also known as midline shift or cingulate hernia, is the most common type of cerebral hernia. It is generally caused by unilateral frontal, parietal, or temporal lobe disease that creates a mass effect with medial direction, pushing the ipsilateral cingulate gyrus down and under the falk cerebri.

The anterior falk, although rigid, is displaced secondary to the mass effect. On the other hand, the posterior falk, wider and more rigid, will resist the displacement. This explains why subfalcine hernias occur anteriorly.

The septum pellucidum deviates at the level of the foramen of Monro, which serves as a landmark for quantification of the degree of midline shift (12). This shift can be measured on axial images by drawing a central line at the level of the foramen of Monro and measuring the distance between this line and the displaced septum pellucidum (Fig 5). In subfalcine hernias, the degree of midline shift correlates with the prognosis; less than 5-mm deviation has a good prognosis, whereas a shift of more than 15 mm is related to a poor outcome (13).

In more severe hernias, the displaced tissue may compress the corpus callosum and contralateral cingulate gyrus, as well as the ipsilateral ventricle and both foramina of Monro, causing dilatation of the contralateral ventricle (Fig 6). There may also be focal necrosis of the cingulate gyrus due to direct compression against the falk cerebri (7,12). Compromise of these structures manifests clinically as hypobulia, apathy, and indifference (14). Subfalcine hernias are best demonstrated at coronal MRI (Fig 7). Another potential complication is compression of the anterior cerebral artery, specifically the pericallosal artery, with consequent infarction of the corresponding vascular territory (4,7) (Fig 8). The most common clinical manifestation of anterior cerebral artery–territory infarction is contralateral leg weakness (14).

Descending Transtentorial Hernia

Descending transtentorial hernia (DTH) is the second most common type of cerebral hernia. It occurs when brain tissue is displaced downward through the tentorial notch (9).

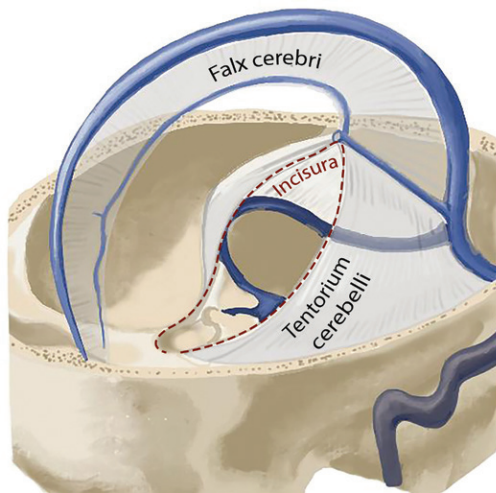


Figure 3. Drawing shows the main dural reflections.

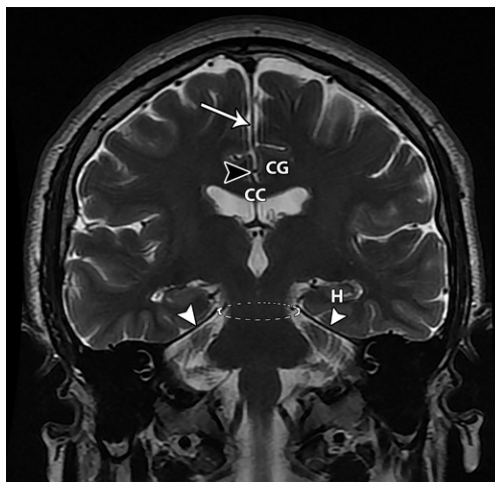
DTH may be divided into two types: lateral (anterior and posterior) and central hernias. Lateral hernias involve the medial temporal lobe. In the anterior subtype, the uncus is herniated downward into the ipsilateral crural cistern. In the posterior subtype, the parahippocampal gyrus is displaced downward into the posterolateral part of the tentorial incisura (9). Finally, in central hernias, there is descent of the diencephalon, midbrain, and pons (12). This classification can be understood as a continuum representing the progression of DTH.

In this type of hernia, the pressure caused by the crowding of tissue within the incisura compromises the third cranial nerve, posterior cerebral artery, and midbrain. Hydrocephalus develops because of the compression of the cerebral aqueduct. In cases with severe and abrupt downward displacement of the brainstem, stretching and shearing of perforating branches of the basilar artery occur, resulting in ischemia and hemorrhage in the brainstem. Usually, these findings are located near the pontomesencephalic junction. However, the effect can be multiple or even extend into the cerebellar peduncles. This is called Duret hemorrhage; it is a late finding and portends a poor prognosis, usually death (12).

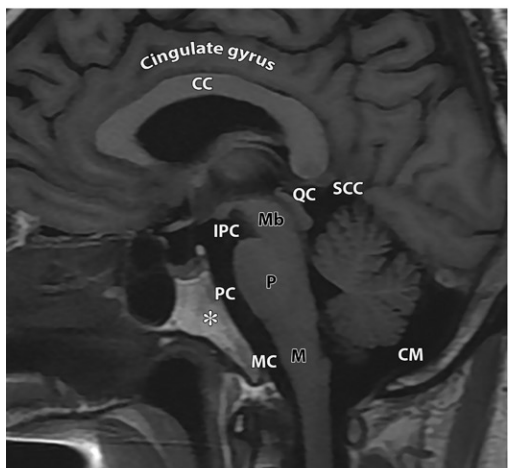
It is important to note that different types of cerebral hernias can be present at the same time. In DTH, if there is further descent of brain tissue, a tonsillar hernia might occur. Also, a subfalcine hernia may be present, depending on the location of the disease.

Lateral Hernia

Lateral hernias occur when the medial temporal lobe is displaced downward through the tentorium incisura. They can be divided into anterior and posterior hernias, depending on the portion that is displaced.



a.



b.



c.

Figure 4. Relevant radiologic anatomy in cerebral hernias. (a) Coronal T2-weighted MR image shows the cerebellar falx in the interhemispheric fissure (arrow), tentorium (white arrowheads), tentorial incisura (dashed oval), corpus callosum (CC), cingulate gyrus (CG), hippocampus (H), and pericallosal sulcus with the pericallosal artery (black arrowhead). (b) Sagittal T1-weighted MR image at the midline of the cranial cavity depicts the cisterna magna (CM), interpeduncular cistern (IPC), medullary cistern (MC), pontine cistern (PC), quadrigeminal cistern (QC), and supracerebellar cistern (SCC). The corpus callosum (CC), cingulate gyrus, and clivus (*) are also noted. The brainstem divisions are as follows: medulla (M), midbrain (Mb), and pons (P). (c) Axial T2-weighted MR image shows the aqueduct (arrowhead), posterior cerebral artery (arrow), crural cistern (CrC), hippocampal gyrus (HG), interpeduncular cistern (IPC), perimesencephalic cistern (PMC), quadrigeminal cistern (QC), and uncus (U).

Anterior Hernia.—Anterior (or uncal) hernia is the better understood subtype of DTH (12). Usually, a unilateral supratentorial lesion (particularly in the middle cranial fossa) causes an inferior and medial mass effect that pushes the uncus over the free edge of the tentorium (7). It is the first event in most cases of DTH, usually followed by herniation of more posteriorly located brain tissue. However, the distribution and sequence of the DTH will also depend on certain factors, such as the location of the disease and the size and configuration of the incisura (9).

The initial displacement of the uncus results in effacement of the suprasellar cistern, the earliest finding in this type of hernia. Often, that is all it effaces. As the herniation progresses, there

is widening of the ipsilateral perimesencephalic cistern, with displacement and rotation of the brainstem (Figs 9, 10). With more advanced herniation, the midbrain and opposite cerebral peduncle are compressed against the tentorial edge (Fig 9b) (7,12). Descending corticospinal and corticobulbar tracts may be affected above the medullary decussation, resulting in motor weakness on the same side as the lesion, known as the Kernohan notch phenomenon (false localizing sign) (15).

Compression of the posterior cerebral artery, third cranial nerve, and aqueduct of Sylvius may result in medial temporal and occipital lobe infarcts, blown pupil, hemiparesis, and hydrocephalus (Fig 11) (1).



Figure 5. Subfalcine hernia. Axial nonenhanced CT image shows a right subdural hematoma with mixed attenuation that represents different blood stages (*). The hematoma displaces the septum pellucidum to the left (arrow) relative to the midline (dashed line). The right lateral ventricle is compressed, but the left lateral ventricle is dilated.



Figure 6. Subfalcine hernia in a 33-year-old man with a cerebral metastasis from a germinal tumor. Coronal contrast-enhanced CT image shows herniation of the cingulate gyrus beneath the free edge of the falx cerebri from left to right (arrow) and associated inferior and lateral displacement of the ipsilateral corpus callosum (*). Note the compression of the ipsilateral ventricle and dilatation of the contralateral ventricle (arrowheads).

Posterior Hernia.—In patients with occipital and posterior temporal disease, the herniation of the medial temporal lobe occurs more posteriorly (12). The parahippocampal gyrus, behind the uncus, is displaced downward into the posterolateral part of the tentorial incisura. Larger posterior hernias may also include the isthmus of the fornical gyrus and the anterior part of the lingual gyrus. This brain tissue will impinge on the lateral part of the quadrigeminal plate cistern and cause displacement, rotation, and compression of the brainstem (Fig 12) (9). It may involve the tectum at the level of the superior colliculus, resulting in Parinaud syndrome, which is commonly present in this type of DTH. There is relatively less compression of the oculomotor nerve and posterior cerebral artery than in other types of DTH (12).

Central Hernia

In central hernia, there is descent of the diencephalon, midbrain, and pons. It usually manifests along with other types of DTH. Bilateral supratentorial disease causing mass effect, midline masses, severe brain edema, or supratentorial hydrocephalus may cause this type of hernia.

Effacement of the perimesencephalic cisterns is the most useful and consistent finding. Caudal displacement of the basilar artery and pineal gland, flattening of the pons against the clivus, and inferior and posterior displacement of the quadrigeminal plate are other use-

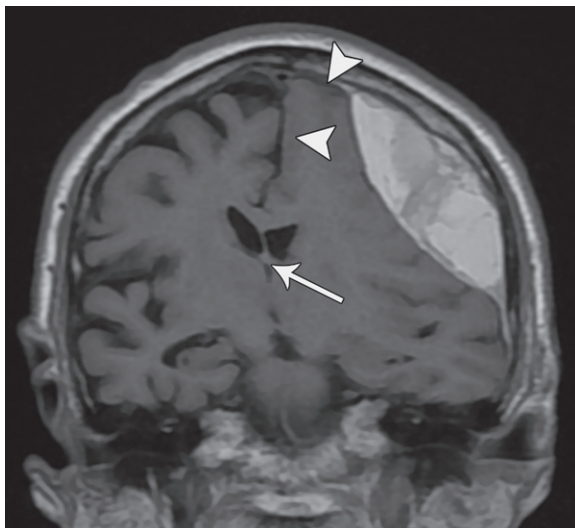


Figure 7. Coronal T1-weighted MR image shows a loculated subdural hematoma and subfalcine herniation. There is effacement of the subarachnoid space and compression of the left frontal lobe against the hard falx (arrowheads). Also note the mild displacement of the foramen of Monro to the right (arrow).

ful indicators of this type of hernia (Fig 12). Hydrocephalus and infarction of the posterior cerebral artery territory are common complications (12). Progressive central herniation can lead to oculomotor palsy, progressive alteration of consciousness, decerebrate posturing, coma, and eventually death (12).

Ascending Transtentorial Hernia

Ascending transtentorial hernia occurs when a mass effect, coming from the posterior cranial

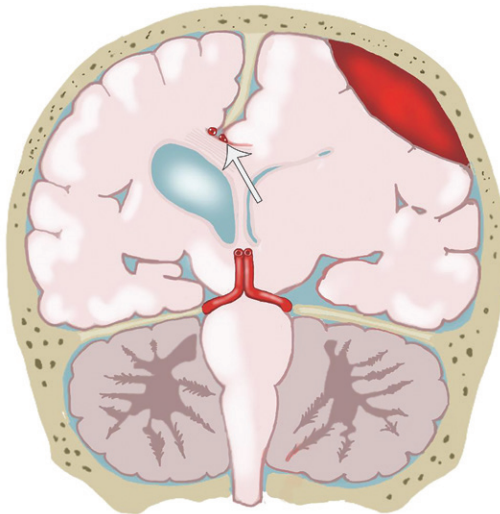
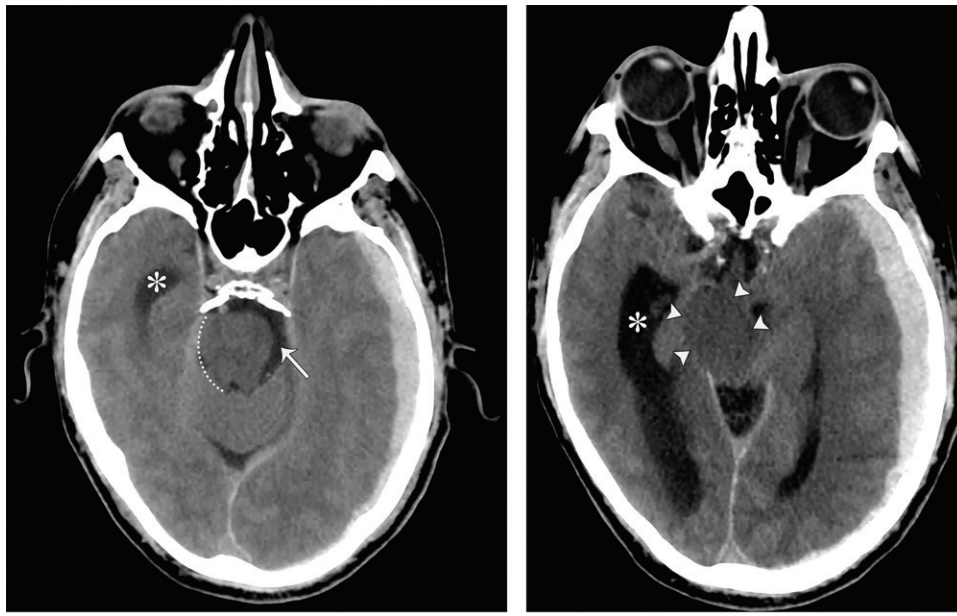


Figure 8. Drawing shows compression of the pericallosal artery (arrow) against the falx cerebri due to a subfalcine hernia.



a.

b.

Figure 9. DTH in a 38-year-old man with an acute head injury and left subdural hematoma. There is right shift and mild rotation of the brainstem. (a) Axial nonenhanced CT image shows widening of the left basal cistern (arrow) and effacement of the right basal cistern (dashed line), as well as dilatation of the temporal horn of the right lateral ventricle (*). (b) CT image shows compression and rotation of the midbrain, which appears elongated (arrowheads). There is complete obliteration of the perimesencephalic cisterns. Note the widening of the opposite ventricular atrium and temporal horn (*).

fossa with an upward direction, displaces the cerebellar vermis and hemispheres superiorly through the tentorial incisura. It is more likely to occur when the mass originates near the incisura, like in the cerebellar vermis (10). Another possible cause is sudden relief of supratentorial intracranial hypertension (7).

The tentorial incisura size is variable and influences whether ascending transtentorial hernia or tonsillar hernia occurs. In the context of increased intracranial pressure, brain tissue is displaced toward the site that offers less resistance. When the tentorial incisura is small, cerebellar

tissue will slide through the foramen magnum, causing tonsillar herniation. On the other hand, when the tentorial opening is large, upward herniation of the superior cerebellar vermis will occur before tonsillar herniation (10).

As there is upward herniation of the cerebellar vermis, anterior displacement of the midbrain and cerebral aqueduct takes place. The normal concave configuration of the quadrigeminal plate cistern is distorted, taking on a flat or convex morphology. If the posterolateral aspect of the midbrain is compressed bilaterally, the classic “spinning top” configuration will appear (16).



Figure 10. Subdural hematoma after a hemodialysis session in a 26-year-old man with a history of end-stage kidney disease. The right pupil was dilated and unresponsive to light. Axial CT image shows the uncus displaced downward across the tentorial incisura (curved arrow). The ipsilateral perimesencephalic cistern (double-headed arrow) is widened, and the contralateral cistern is compressed. Note the contralateral dilatation of the temporal horn of the lateral ventricle (*).

Hydrocephaly may be present due to compression of the aqueduct. The most relevant imaging findings are illustrated in Figure 13.

Hemispheric branches of the superior cerebellar arteries, as well as posterior cerebral arteries, may be compressed. This causes ischemic infarction of the superior portion of the cerebellar hemispheres and occipital cerebral lobe (10).

Clinically, signs of cerebellar and brainstem compression, as well as increased ICP, may be present (6,17).

Tonsillar Hernia

Tonsillar hernia is inferior displacement of the cerebellar tonsils through the foramen magnum into the cervical spinal canal. It may be congenital (Chiari spectrum) or acquired.

Normal tonsillar position relative to the foramen magnum varies with age. Mikulis et al (18) described the normal position of tonsils below the foramen magnum for different age groups. In the 1st decade of life, the presence of cerebellar tonsils more than 6 mm below the foramen magnum is considered abnormal. In the next 2 decades, the reference value is 5 mm; for the 4th to 8th decades, the threshold is greater than 4 mm; and at age 80 years or older, 3 mm is the limit (18,19).

The McRae line is used as a reference for this measurement. It is obtained by drawing a line from the basion to the opisthion. The degree of

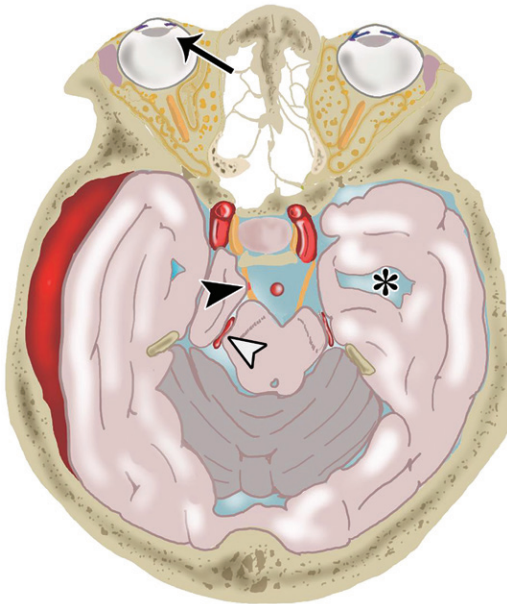


Figure 11. Drawing shows a lateral DTH with compression of the posterior cerebral artery (white arrowhead) and third cranial nerve (black arrowhead). Note the ipsilateral blown pupil (arrow) and contralateral temporal horn dilatation (*).

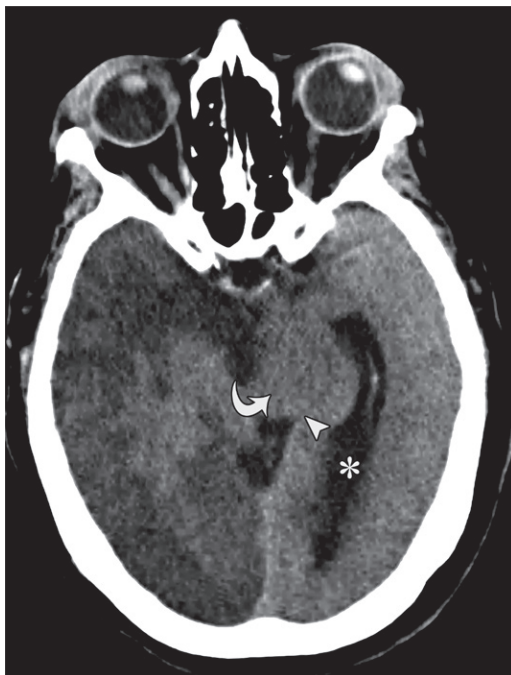
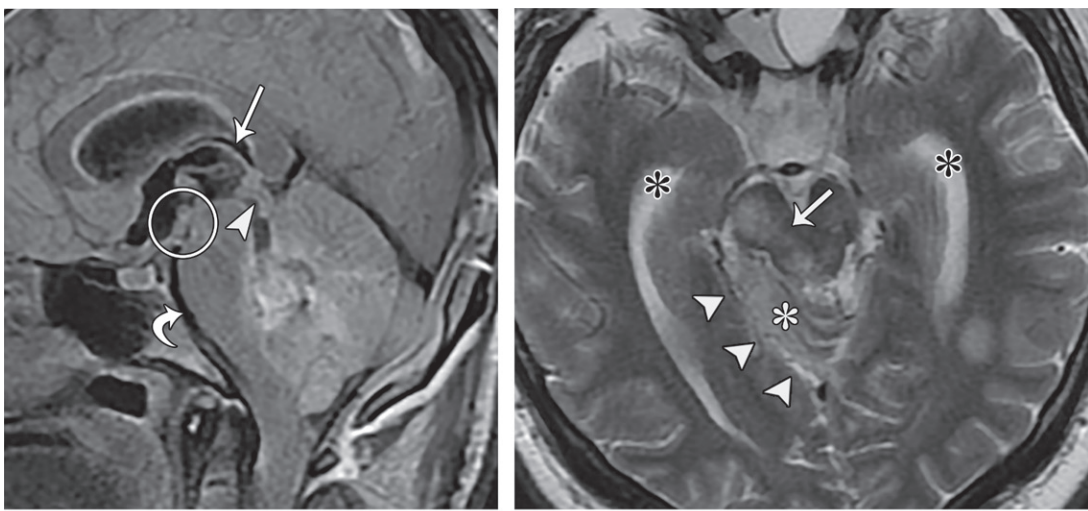


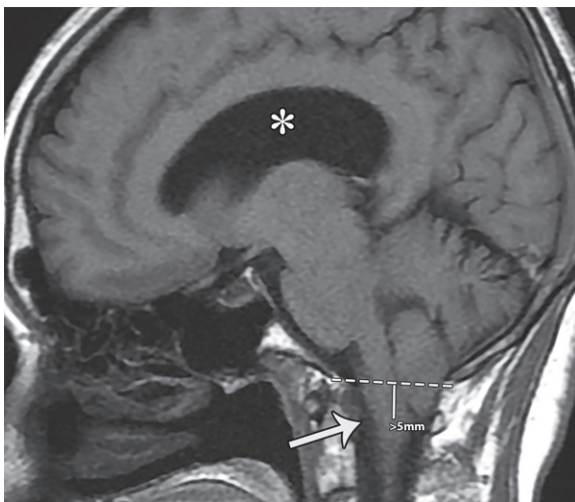
Figure 12. DTH in a 64-year-old man with a history of ischemic heart disease who presented with symptoms of sudden neurologic deterioration due to a stroke. DTH occurred secondary to brain edema. Axial nonenhanced CT image at the level of the midbrain shows left displacement and rotation of the mesencephalon (curved arrow), left displacement of the quadrigeminal plate (arrowhead), and obliteration of the perimesencephalic cisterns. In addition, dilatation of the atrium and temporal horn of the left lateral ventricle is present (*).



a.

b.

Figure 13. (a) Ascending transtentorial hernia in a 26-year-old man after resection of a medulloblastoma. Sagittal gadolinium-enhanced T1-weighted MR image shows obliteration of the quadrigeminal, superior cerebellar, and interpeduncular cisterns. There is associated folding of the inferior colliculi (arrowhead) under the superior colliculi, and both structures have shifted upward. Anterior displacement of the brainstem reduces the space of the pontine and medullary cisterns (curved arrow). Note the superior displacement of the third ventricle roof (straight arrow) and the anterior displacement of the mamillary bodies and tuber cinereum (circle), which are in close contact with the midbrain. (b) Ascending transtentorial hernia in a 33-year-old man suspected of having intracranial lesions. Axial T2-weighted MR image shows the cerebellum (white *) ascending through the right side of the incisura (arrowheads), causing obliteration of the right perimesencephalic and left crural cisterns, diminished space of the quadrigeminal cistern, enlargement of the temporal horns of the lateral ventricles (black *), and edema in the tectum and right cerebral peduncle (arrow).



tonsillar herniation is the perpendicular length from the McRae line to the tip of the displaced tonsil (Fig 14) (20).

The most common cause is an infratentorial mass creating a downward mass effect. It may also be secondary to a supratentorial mass, in which case it is usually associated with a DTH. It can cause severe neurologic damage followed by sudden respiratory arrest (12,19).

Visualization of tonsils extending below the foramen magnum, anterior brainstem displacement, and loss of CSF surrounding it are common features (Figs 15, 16). The fourth ventricle

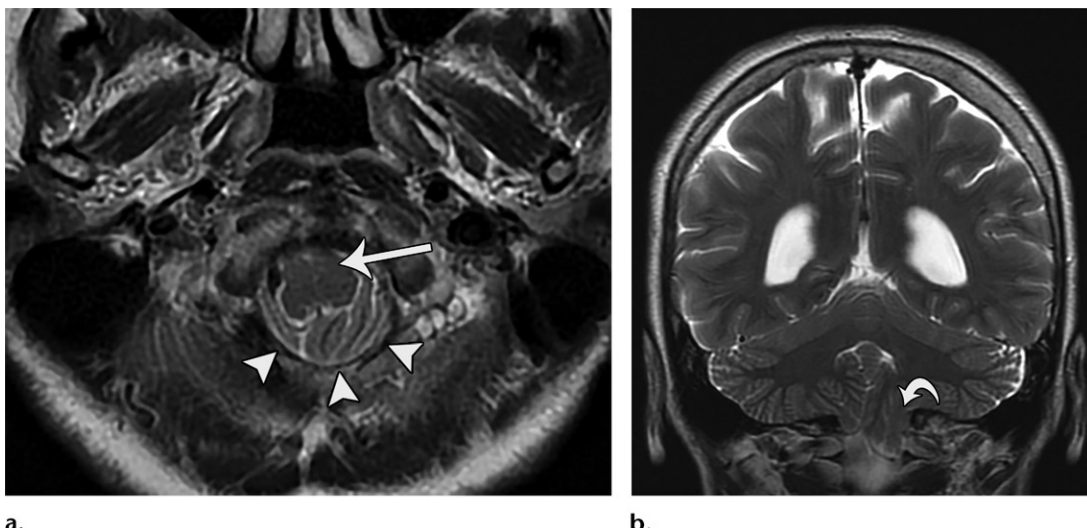
Figure 14. Sagittal T1-weighted MR image shows downward displacement of the cerebellar tonsils (>5 mm) relative to the McRae line (dashed line). Note the obliteration of the cisterna magna, anterior displacement of the medulla (arrow), and hydrocephalus (*).

may be compressed, producing obstructive supratentorial hydrocephalus (4,12). Compression of the posterior inferior cerebellar artery by the herniated tonsils can lead to cerebellar infarcts (7).

Transalar Hernia

Transalar hernia is an uncommon and less described type of hernia. It is usually associated with subfalcine and transtentorial hernias (21). It can be divided into descending and ascending transalar hernias. In the descending type, the frontal lobe is displaced posteriorly and inferiorly over the sphenoid wing. It manifests secondary to frontal lobe disease. It can cause compression of the middle cerebral artery against the sphenoid ridge with a middle cerebral artery infarction.

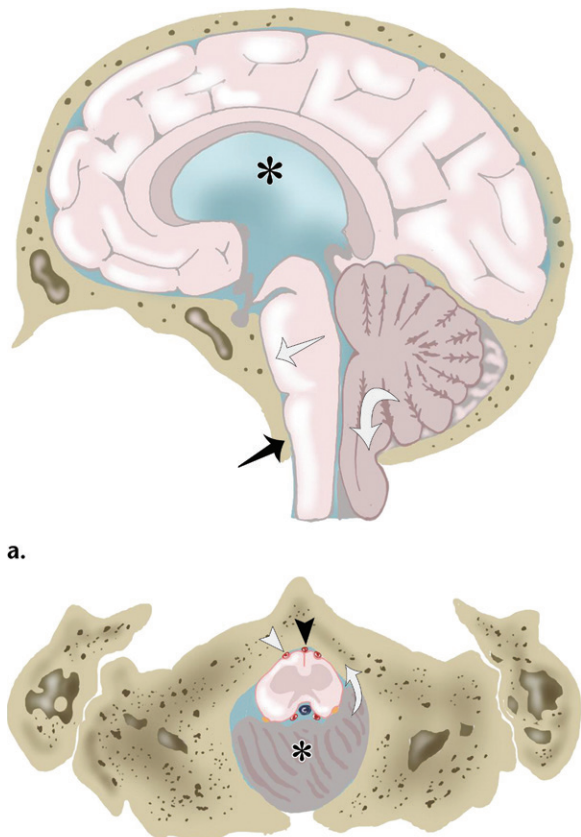
With ascending transalar hernia, the temporal lobe is displaced superiorly and anteriorly across the sphenoid ridge owing to a middle cranial fossa mass effect. This displacement can compress the supraclinoid internal carotid artery against the anterior clinoid process with infarction of the anterior cerebral artery and middle cerebral artery.



a.

b.

Figure 15. Chiari I malformation. Axial (a) and coronal (b) T2-weighted MR images show tonsillar descent (arrow in b) with anterior brainstem displacement (arrow in a) and effacement of the CSF in the foramen magnum (arrowheads in a).



b.

Figure 16. Drawings show tonsillar hernia. (a) Sagittal view demonstrates tonsils extending below the foramen magnum (curved arrow), brainstem compression against the clivus (straight white arrow), obliteration of the medullary cistern (black arrow), and obstructive hydrocephalus (*). (b) Axial view at the level of the foramen magnum. The displaced tonsils (*) cause obliteration of the surrounding CSF, anterior displacement of the medulla (arrow), and compression of the spinal (black arrowhead) and vertebral (white arrowhead) arteries.

territories (7). Identifying anterior or posterior displacement of the middle cerebral artery is useful for suspecting this type of hernia (21).

Extracranial Hernia

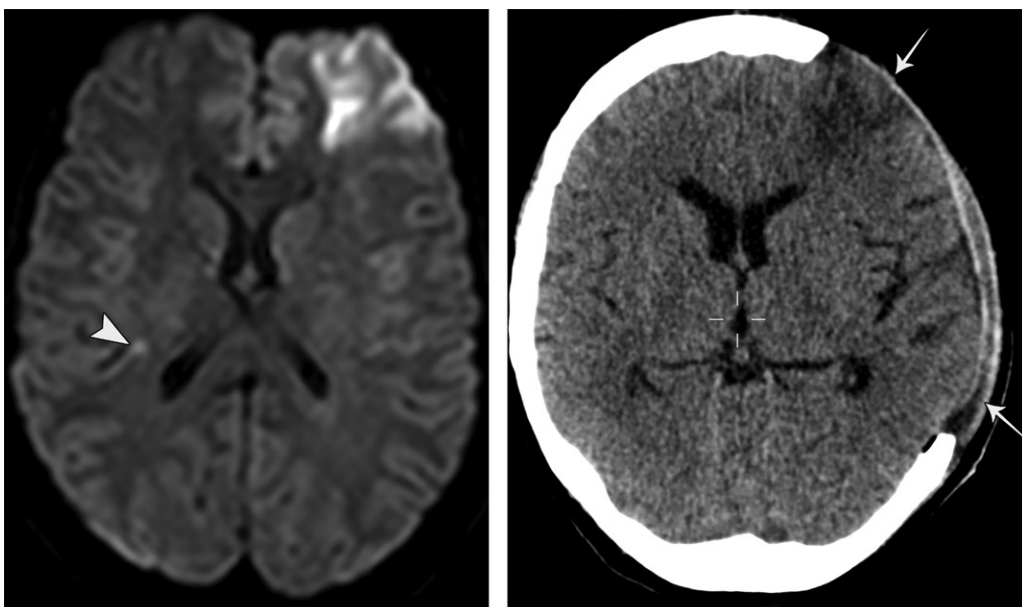
External hernias are less common than other types of hernias. They are most frequently caused by postsurgical and posttraumatic cranial defects that allow brain tissue to pass through.

Craniectomy may be performed to decompress intracranial contents in patients with intracranial hypertension after medical management fails (22). Brain edema is common in the 1st week after decompressive craniectomy. It may correspond to hyperperfusion and loss of resistance in brain tissue, causing a higher hydrostatic pressure gradient that favors transcapillary leakage of fluid (23).

A large craniectomy defect allows the brain to expand without constriction. If the defect is too small, swollen brain may herniate with a “mushroom cap” appearance. This can result in compression of cortical veins and lead to venous infarction and contusion of the brain at the craniectomy margins. Both CT and MRI are effective in depicting this hernia (3,12) (Fig 17).

Paradoxical hernia is a rare and potentially fatal complication of decompressive craniectomy. It is a neurosurgical emergency. Atmospheric pressure exceeding ICP at the site of the craniectomy causes a pressure imbalance and consequent subfalcine and/or transtentorial hernia. The brain tissue is displaced from the craniectomy defect (Fig 18). It is often triggered by an acute imbalance of ICP secondary to CSF drainage or lumbar puncture (3).

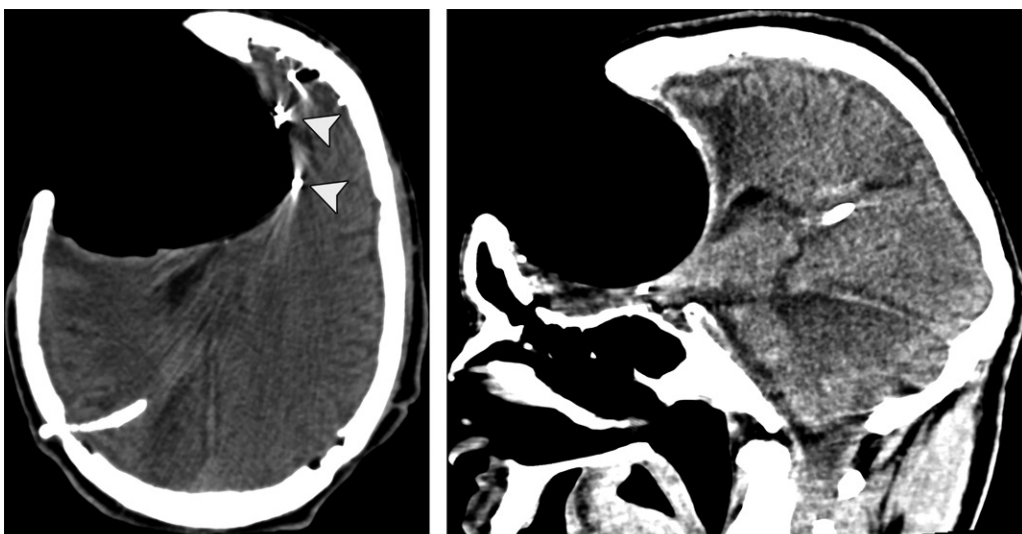
Symptoms include a depressed level of consciousness, autonomic instability, signs of brainstem release, and focal neurologic deficits (3).



a.

b.

Figure 17. Extracranial hernia. (a) Axial diffusion-weighted image shows an acute infarction in the left frontal lobe. Also note the small focus on the right (arrowhead). A few days later, the patient developed vasogenic brain edema, and decompressive craniectomy was performed. (b) Axial CT image after craniectomy shows brain parenchyma herniating through the defect of the frontal and temporal lobes (arrows). The sylvian fissure is enlarged, and the frontal and occipital horns of the left lateral ventricle are retracted.



a.

b.

Figure 18. Paradoxical hernia in a 32-year-old man who was shot in the head three times. He underwent decompressive craniectomy and developed sinking flap syndrome. (a) Axial nonenhanced CT image shows left midline displacement and right ventricle compression with associated edema. There is metal artifact in the left frontal lobe from remnants of the bullet (arrowheads). (b) Sagittal CT image demonstrates the frontal and temporal lobe displacement.

Intracranial Hypotension

Intracranial hypotension is another cause of cerebral herniation that should be considered. It must be suspected in patients without an intracranial mass or edema or when the degree of herniation is out of proportion to the degree of mass effect (12). It is caused by iatrogenic or spontaneous CSF leak. The loss of CSF volume results in

downward descent of the brain secondary to a negative pressure gradient between the cranial and spinal compartments. DTH and tonsillar hernia may manifest (23). Also, blood volume will increase to maintain the intracranial volume. This results in pachymeningeal hyperemia and edema, which can be identified at MRI as diffuse pachymeningeal enhancement (12).

Communicating Critical Results

Effective communication between interpreting physicians and ordering health care providers is a critical component of diagnostic imaging. Those responsible for making treatment decisions should be notified of imaging results in a timely fashion. In 2014, the American College of Radiology published the “ACR Practice Parameter for Communication of Diagnostic Imaging Findings” as an educational tool designed to assist practitioners in providing appropriate radiologic care for patients (24). In this guideline, different methods of communication are mentioned depending on the clinical scenario.

The guideline discusses the imaging final report, the preliminary report, and nonroutine communications. Nonroutine communications are used in emergent clinical situations. Many institutions have established policies and guidelines for communicating critical results. Specifically, in neuroradiology, there are multiple time-sensitive pathologic conditions that need urgent treatment once diagnosed. A list of critical findings for which immediate notification is required should be established (25), as well as the policy for communication and proper documentation.

Conclusion

Cerebral herniation syndromes represent a common life-threatening neurologic emergency. They manifest as complications of multiple different pathologic conditions. The patient history and clinical scenario are key for making an accurate diagnosis. Having a thorough understanding of cerebral herniation syndromes and their imaging spectrum is essential. The radiologist should keep in mind that many of these patterns of herniation may overlap and that common complications include compression of cranial nerves, CSF spaces, and blood vessels. Misdiagnosis can lead to increased patient morbidity and even death. CT and MRI are the imaging modalities of choice for establishing the diagnosis, guiding the therapeutic decisions, and determining the prognosis.

Acknowledgments.—The authors thank Carlos Casian Ruiz Velasco, MD, for the illustrations.

References

- Choi HH, Kelahan LC, Jay AK, Loevner LA. Brain imaging: anatomy, trauma, and tumors. In: Torigian DA, Ramchandani P, eds. *Radiology secrets plus*. 4th ed. Philadelphia, Pa: Elsevier; 2019; 443–452.
- Mokri B. The Monro-Kellie hypothesis: applications in CSF volume depletion. *Neurology* 2001;56(12):1746–1748.
- Sinclair AG, Scoffings DJ. Imaging of the post-operative cranium. *RadioGraphics* 2010;30(2):461–482.
- Nadgir R, Yousem DM. Head trauma. In: Thrall JH, ed. *Neuroradiology: the requisites*. 4th ed. Philadelphia, Pa: Elsevier; 2017; 150–173.
- Asso Escario J, Martínez Quiñones JV, Martín Gallego Á, Arregui Calvo R, Suarez Mier MP. Brain herniations: classification, neuropathology and medico-legal problems [in Spanish]. *Rev Esp Med Leg* 2015;41(3):91–102.
- Stevens RD, Shoykhet M, Cadena R. Emergency neurological life support: intracranial hypertension and herniation. *Neurocrit Care* 2015;23(suppl 2):S76–S82.
- Laine FJ, Shedd AI, Dunn MM, Ghatak NR. Acquired intracranial herniations: MR imaging findings. *AJR Am J Roentgenol* 1995;165(4):967–973.
- Osborn AG, Salzman KL, Jhaveri MD. Diagnostic imaging: brain. 3rd ed. Philadelphia, Pa: Elsevier, 2016.
- Stovring J. Descending tentorial herniation: findings on computed tomography. *Neuroradiology* 1977;14(3):101–105.
- Cuneo RA, Caronna JJ, Pitts L, Townsend J, Winestock DP. Upward transtentorial herniation: seven cases and a literature review. *Arch Neurol* 1979;36(10):618–623.
- Schuenke M, Schulte E, Schumacher U. *Atlas of anatomy: head and neuroanatomy*. Stuttgart, Germany: Thieme, 2010.
- Johnson PL, Eckard DA, Chason DP, Brecheisen MA, Batnitzky S. Imaging of acquired cerebral herniations. *Neuroimaging Clin N Am* 2002;12(2):217–228.
- Ross DA, Olsen WL, Ross AM, Andrews BT, Pitts LH. Brain shift, level of consciousness, and restoration of consciousness in patients with acute intracranial hematoma. *J Neurosurg* 1989;71(4):498–502.
- Kang SY, Kim JS. Anterior cerebral artery infarction: stroke mechanism and clinical-imaging study in 100 patients. *Neurology* 2008;70(24 Pt 2):2386–2393.
- Zhang CH, DeSouza RM, Kho JS, Vundavalli S, Critchley G. Kernohan-Woltman notch phenomenon: a review article. *Br J Neurosurg* 2017;31(2):159–166.
- Dähnert W. *Radiology review manual*. 8th ed. Philadelphia, Pa: Wolters Kluwer, 2017.
- Young GB. Impaired consciousness and herniation syndromes. *Neurol Clin* 2011;29(4):765–772.
- Mikulis DJ, Diaz O, Eggin TK, Sanchez R. Variance of the position of the cerebellar tonsils with age: preliminary report. *Radiology* 1992;183(3):725–728.
- Ishikawa M, Kikuchi H, Fujisawa I, Yonekawa Y. Tonsillar herniation on magnetic resonance imaging. *Neurosurgery* 1988;22(1 Pt 1):77–81.
- Vurdem ÜE, Acer N, Ertekin T, Savranlar A, Inci MF. Analysis of the volumes of the posterior cranial fossa, cerebellum, and herniated tonsils using the stereological methods in patients with Chiari type I malformation. *ScientificWorldJournal* 2012;2012:616934.
- Soto JA, Lucey BC. *Emergency radiology: the requisites*. Philadelphia, Pa: Mosby, 2009.
- Haddad SH, Arabi YM. Critical care management of severe traumatic brain injury in adults. *Scand J Trauma Resusc Emerg Med* 2012;20:12.
- Striver S. Complications of decompressive craniectomy for traumatic brain injury. *Neurosurg Focus* 2009;26(6):E7.
- Sherry CS, Adams MJ, Berlin L, Hartford A, Haseman D, Katzen JB. ACR practice parameter for communication of diagnostic imaging findings. <https://www.acr.org/-/media/ACR/Files/Practice-Parameters/communicationdiag.pdf>. Revised 2014. Accessed May 15, 2019.
- Viertel VG, Trotter SA, Babiarz LS, Nagy PG, Lewin JS, Yousem DM. Reporting of critical findings in neuroradiology. *AJR Am J Roentgenol* 2013;200(5):1132–1137.



Radiologic Clues to Cerebral Venous Thrombosis

*Maria Canedo-Antelo, MD
Sandra Baleato-González, MD, PhD
Antonio J. Mosqueira, MD, PhD
Jésica Casas-Martínez, MD
Laura Oleaga, MD, PhD
Joan C. Vilanova, MD, PhD
Antonio Luna-Alcalá, MD, PhD
Roberto García-Figueiras, MD, PhD*

Abbreviations: ADC = apparent diffusion coefficient, CVT = cerebral venous thrombosis, DCVT = deep CVT, DST = dural sinus CVT, FLAIR = fluid-attenuated inversion-recovery, 3D = three-dimensional, 2D = two-dimensional

RadioGraphics 2019; 39:1611–1628

<https://doi.org/10.1148/rg.2019190015>

Content Codes: **CT** **ER** **MR** **NR** **VA**

From the Department of Radiology, Complexo Hospitalario Universitario de Santiago de Compostela, Choupana s/n, 15701 Santiago de Compostela, A Coruña, Spain (M.C.A., S.B.G., A.J.M., J.C.M., R.G.F.); Department of Radiology, Hospital Clínic de Barcelona, Barcelona, Spain (L.O.); Department of Radiology, Institut Català de la Salut (IDI), Girona, Spain (J.C.V.); Clínica Girona, Girona, Spain (J.C.V.); Clínica Las Nieves, Health Time, Jaén, Spain (A.L.A.); and Department of Radiology, University Hospitals of Cleveland, Case Western Reserve University, Cleveland, Ohio (A.L.A.). Presented as an education exhibit at the 2018 RSNA Annual Meeting. Received February 19, 2019; revision requested March 28 and received April 24; accepted April 29. For this journal-based SA-CME activity, the author A.L.A. has provided disclosures (see end of article); all other authors, the editor, and the reviewers have disclosed no relevant relationships. **Address correspondence to** M.C.A. (e-mail: maria.canedo2020@hotmail.com).

©RSNA, 2019

SA-CME LEARNING OBJECTIVES

After completing this journal-based SA-CME activity, participants will be able to:

- Discuss the anatomy of the cerebral venous system and the predisposing factors and most common clinical manifestations of CVT.
- Describe imaging findings of the different subtypes of CVT.
- Recognize potential imaging pitfalls that may hinder correct diagnosis.

See rsna.org/learning-center-rg.

Cerebral venous thrombosis (CVT) is uncommon, representing approximately 0.5% of all cases of cerebrovascular disease worldwide. Many factors, alone or combined, can cause CVT. Although CVT can occur at any age, it most commonly affects neonates and young adults. CVT is difficult to diagnose clinically because patients can present with a wide spectrum of nonspecific manifestations, the most common of which are headache in 89%–91%, focal deficits in 52%–68%, and seizures in 39%–44% of patients. Consequently, imaging is fundamental to its diagnosis. MRI is the most sensitive and specific technique for diagnosis of CVT. The different MRI sequences, with and without the use of contrast material, have variable strengths. Contrast material–enhanced MR venography has the highest accuracy compared with sequences without contrast enhancement.

Online supplemental material is available for this article.

©RSNA, 2019 • radiographics.rsna.org

Introduction

Cerebral venous thrombosis (CVT) is an uncommon condition that is potentially reversible if it is diagnosed and treated appropriately and promptly. The annual incidence, as presented in the most recently published studies (1–3), is three or four to 13 cases per 1 million individuals. The differences in incidence in the studies are likely due to differences in diagnostic techniques. CVT can occur at any age, although it is more common in neonates and young adults (20–40 years old); it is also more common in women, because pregnancy, postpartum status, and the use of oral contraceptives increase the risk of CVT (1,4,5). Diagnosis is difficult because the clinical manifestations of CVT are nonspecific, such as headache, seizures, decreased level of consciousness, and focal neurologic deficits. For this reason, imaging is crucial to diagnosis, and radiologists must be able to identify the findings that raise suspicion of CVT so that appropriate treatment (anticoagulation therapy) can be started early to avoid complications and even death. CVT is one of the few causes of cerebral hemorrhage that call for anticoagulation therapy. Since anticoagulation is contraindicated in most cases of cerebral bleeding, diagnostic certainty is important, making the radiologist's task more difficult.

TEACHING POINTS

- Although most patients with CVT have more than one risk factor, up to 20% of cases are idiopathic, so the absence of risk factors does not rule out the diagnosis.
- The *empty delta sign* consists of a triangular area of contrast enhancement that surrounds a hypoattenuating area and represents the thrombus; although this sign classically is found in the superior sagittal sinus, a similar sign can be seen on sagittal and coronal images of the transverse sinus.
- The most commonly observed findings in the parenchyma are vasogenic and cytotoxic edema, which occasionally are found together, and intraparenchymal hemorrhage.
- At nonenhanced MRI, the characteristic finding for DCVT is bilateral thalamic edema, which is present in approximately 86% of patients. This edema may extend to the basal ganglia (in one-third of cases) and to the adjacent deep white matter.
- When edema or cortical or subcortical focal hemorrhage is detected, it is important to evaluate the attenuation and/or signal intensity of the adjacent cortical veins, especially when these lesions are not in an arterial distribution.

The objectives of this article are to (*a*) review the pathophysiology of CVT; (*b*) illustrate the anatomy of the cerebral venous system; (*c*) describe the different subtypes of CVT, including dural sinus CVT (DST), deep CVT (DCVT), and isolated cortical vein CVT; (*d*) review the accuracy of various imaging techniques for CVT diagnosis; and (*e*) show the main findings and pitfalls for these subtypes with different imaging techniques.

Pathophysiology

Venous occlusion has different effects on the brain parenchyma than does arterial occlusion, resulting in different imaging findings. In venous occlusion, changes in the brain parenchyma can develop secondary to vasogenic edema, cytotoxic edema, or intracranial hemorrhage, giving rise to two possible scenarios: CVT with local effects and CVT of the venous sinuses with increased intracranial pressure (1). CVT leads to the formation of an area of focal cerebral edema because of increased retrograde pressure, which is characterized by dilated veins, petechial hemorrhages that can converge and give rise to larger hematomas, and ischemic neuronal damage. Thus, two types of edema can develop: vasogenic and cytotoxic. DST obstructs venous drainage, leading to increased blood pressure due to delayed venous emptying and decreased absorption of cerebrospinal fluid. First, there is an increase in retrograde venous pressure, with venous congestion and drainage through the collateral vessels. If the collateral vessel circulation is good, the only symptoms are those related to intracranial hypertension. However, if the collateral vessel circulation is inadequate or the CVT extends to the cortical veins, intracranial pressure continues to

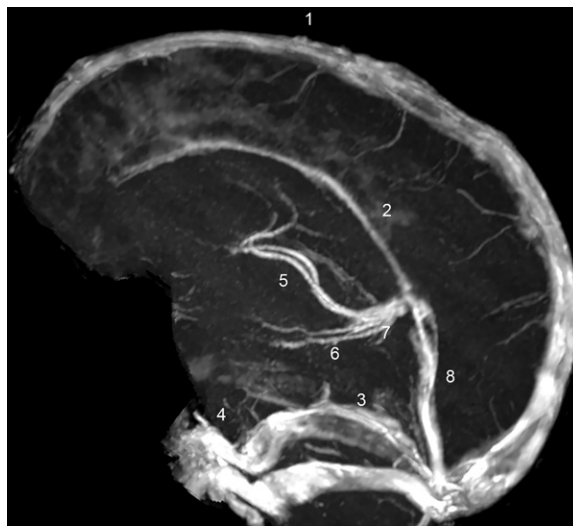


Figure 1. Sagittal contrast material-enhanced maximum intensity projection MR venogram shows the dural sinuses and the deep venous system. It includes the superior sagittal sinus (1), inferior sagittal sinus (2), transverse sinuses (3), sigmoid sinuses (4), internal cerebral veins (5), Rosenthal veins (6), vein of Galen (7), and straight sinus (8).

increase to the point at which the cerebral perfusion pressure decreases, which could give rise to ischemic damage and cytotoxic edema (6–9).

Subtypes of CVT

The imaging manifestations of CVT depend on the type of venous involvement.

Dural Sinus CVT

Anatomy.—The dural sinuses are divided into two groups: the superior and the inferior dural sinuses. The superior dural sinuses comprise the superior sagittal sinus, the inferior sagittal sinus, and the straight sinus (which converge at the confluence of sinuses, or the torcular herophili), and the transverse and sigmoid sinuses (Fig 1). The inferior dural sinuses comprise the cavernous sinuses, which are connected through the anterior and posterior intercavernous sinuses, and the superior and inferior petrosal sinuses, which drain toward the sigmoid sinus and then toward the jugular bulb (10). In addition to venous drainage, another important function of the dural sinuses is to absorb cerebrospinal fluid.

In most patients with CVT, multiple venous sinuses are involved. The superior sagittal sinus, transverse sinus, and sigmoid sinus are the most frequently involved (11,12).

Predisposing Factors and Clinical Manifestations.

DST is associated with a wide variety of clinical manifestations and with multiple risk factors and predisposing conditions (Tables 1, 2), including local causes (eg, head trauma, because

Table 1: Predisposing Factors for CVT

| Local factors |
|--------------------------------------------------------------|
| Trauma |
| Brain tumors |
| Infections (otitis, mastoiditis, sinusitis, meningitis) |
| Systemic factors |
| Hormonal (eg, pregnancy, puerperium, oral contraceptive use) |
| Surgery |
| Hematologic disorders |
| Dehydration |
| Malignancy |

Note.—CVT is idiopathic in 15%–20% of cases.

Table 2: Clinical Features of CVT

| |
|--------------------------------------------------------------------------------------------------------|
| Headache* |
| Focal neurologic deficit |
| Seizures |
| Nausea, vomiting |
| Altered states of consciousness† |
| Neurologic-ophthalmologic symptoms (eg, papilledema, loss of vision, constriction of the visual field) |
| Cranial nerve palsies |
| Psychological symptoms† |

*The most common manifestation.

†More common in patients with DCVT.

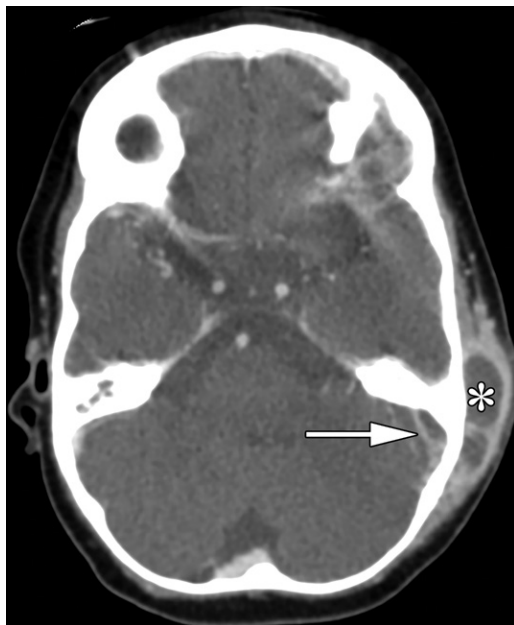


Figure 2. Sigmoid sinus CVT in a 15-month-old girl with mastoiditis. Axial contrast-enhanced CT image shows a filling defect in the left sigmoid sinus (arrow) and a postauricular collection of fluid that is consistent with an abscess (*).

CVT usually is associated with skull fractures that extend to the dural sinus or the jugular bulb; brain tumors; and local infections (Fig 2) and systemic causes (eg, hormonal imbalance, surgery, hematologic disease, systemic infections, and dehydration). In general, the most common predisposing factor is hypercoagulability in the context of a prothrombotic condition (eg, pregnancy, postpartum status, cancer, or use of oral contraceptives) (11,13). Nevertheless, although most patients with CVT have more than one risk factor, up to 20% of cases are idiopathic, so the absence of risk factors does not rule out the diagnosis (14–18).

The time to the appearance of symptoms of CVT varies widely; subacute presentation

(2–30 days) is the most common (50% of cases), followed by acute (<2 days) and chronic (>30 days) manifestation, occurring in 30% and 10% of cases, respectively (11,19). The symptoms most commonly associated with CVT are headache in 89%–91% of patients, motor deficits in 52%–68% of patients, and seizures in 39%–44% of patients (11,20). The clinical manifestations of DST also are associated with the time elapsed from the development of CVT; in the acute phases, focal neurologic deficits are common, whereas in the chronic phases, the symptoms are related to increased intracranial pressure (19,21). Patients with superior sagittal sinus CVT often have headaches, seizures, and motor and sensory symptoms. Patients with transverse sinus CVT present with headaches, aphasia, memory impairment, and seizures. Other less-common manifestations include papilledema, nausea, vomiting, altered states of consciousness, or in patients with CVT of the sigmoid and transverse sinuses, occipital and/or cervical pain (22).

CVT of the cavernous sinus is rare, accounting for only 1.3% of cases of CVT, but it has characteristic findings (11). Among the causes of cavernous sinus CVT, the most common are infectious processes of the paranasal sinuses (especially of the sphenoid sinus and ethmoid air cells), orbit, or face (23). Other possible causes of cavernous sinus syndrome include vasculitis, tumors, trauma, and Tolosa-Hunt syndrome (Fig 3) (24). Clinical manifestations of cavernous sinus CVT include headache, fever, periorbital edema, chemosis, proptosis, and ophthalmoplegia due to involvement of cranial nerve pairs III, IV, and VI (23–25).

Imaging Findings.—In general, nonenhanced CT of the head is the first-line imaging examination in patients who present at the emergency department with neurologic symptoms. However, the direct visualization of CVT as hyperattenuation

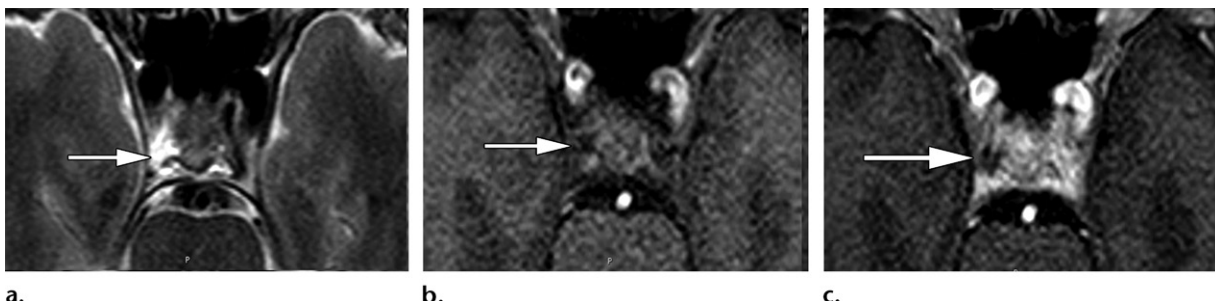


Figure 3. Cavernous sinus CVT in a 71-year-old man with horizontal monocular diplopia, paralysis of cranial pairs III and IV, right palpebral ptosis, and suspicion of Tolosa-Hunt syndrome. (a) Axial T2-weighted MR image shows hyperintensity of the right cavernous sinus (arrow). (b) Axial T1-weighted MR image shows hypointensity in the corresponding area (arrow). These findings are consistent with those of CVT. (c) Axial contrast-enhanced MR image shows the filling defect (arrow).

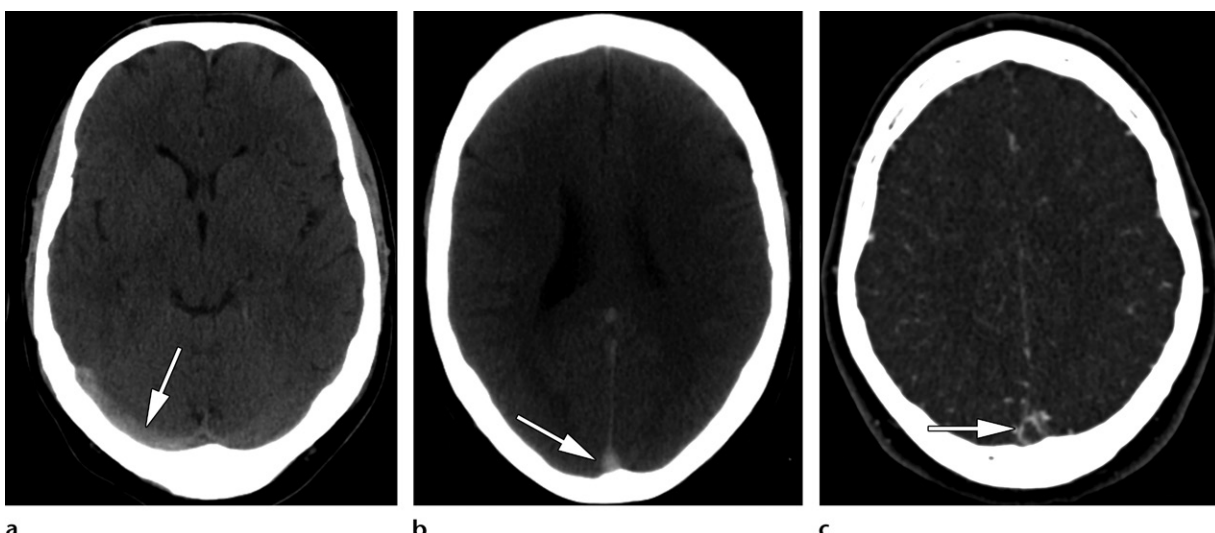


Figure 4. Superior sagittal sinus and right transverse sinus CVT in a 27-year-old man with a headache and a history of cocaine abuse. (a, b) Axial nonenhanced CT images show areas of abnormal hyperattenuation that are consistent with CVT (arrow) in the right transverse sinus (a) and superior sagittal sinus (b). (c) Axial contrast-enhanced CT image shows the empty delta sign (arrow).

in the occluded sinus (cord sign) (Fig 4) is not very sensitive and is present in only 25%–56% of cases (26–28). This increased attenuation coefficient in the sinus (50–80 HU) is caused by a decrease in the amount of serum and an increase in the amount of fibrinogen and proteins in the thrombus. This finding is seen only in acute and subacute cases, because the thrombus becomes isoattenuating after 2 weeks (26).

Administering contrast media to study the venous system (CT venography) makes it possible to identify a filling defect in the occluded dural sinus. To perform CT venography, we image the area from the calvarial vertex to the C1 vertebra to visualize the origin of the jugular internal veins, and we administer 90 mL of a nonionic contrast medium at a rate of 3 mL/sec, with a 45–50-second preimaging delay. For better visualization of the sinuses located immediately next to the bone, we advise varying the setting of the window (width, approximately 260 HU; level, 130 HU). Multiplanar and three-dimensional

(3D) reconstructions and maximum intensity projection imaging help in the diagnosis of CVT (29). The *empty delta sign* consists of a triangular area of contrast enhancement that surrounds a hypoattenuating area and represents the thrombus (Fig 4); although this sign classically is found in the superior sagittal sinus, a similar sign can be seen on sagittal and coronal images of the transverse sinus. The empty delta sign is seen in 29%–35% of cases and may be absent in the acute phases of the process, in which the thrombus is hyperattenuating (mimicking opacification of the sinus), and in the chronic phases, in which the thrombus can contain recanalization channels (27,30). Other imaging findings that can develop secondary to increased retrograde pressure and should raise suspicion of CVT include venous ectasia, prominent medullary veins, and enhancement of the falx cerebri and of tentorium.

Nonenhanced MRI is more sensitive than nonenhanced CT for detecting CVT in the venous sinuses (31). Blood flow in the dural

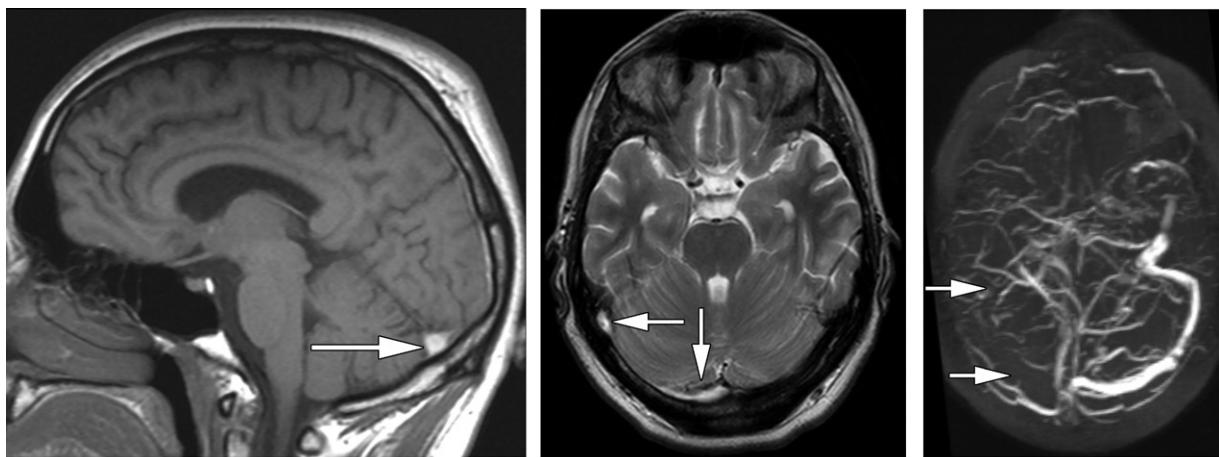


Figure 5. Subacute CVT in a 27-year-old woman with a severe headache for 7 days. (a, b) Sagittal T1-weighted MR image (a) and axial T2-weighted MR image (b) show an area of abnormally increased signal intensity in the right transverse sinus (arrow in a, arrows in b). (c) Axial maximum intensity projection time-of-flight MR venogram shows a lack of flow in the right transverse sinus and the sigmoid sinus (arrows).

sinuses is seen as a flow void, especially with T2-weighted and T2-weighted fluid-attenuated inversion-recovery (FLAIR) sequences. For this reason, when there is an absence of flow void or altered signal intensity in the dural sinuses, the possibility of CVT must be investigated (32), although slow or turbulent flow can mimic CVT. One of the main difficulties in evaluating CVT with MRI is the variation in the signal intensity of the thrombus depending on its age; this phenomenon is due to the paramagnetic effects of hemoglobin degradation products (32,33). Usually, acute CVT (1–5 days) is isointense on T1-weighted MR images and hypointense on T2-weighted MR images (deoxyhemoglobin); subacute CVT (6–15 days) is hyperintense on both T1- and T2-weighted MR images (methemoglobin) (Fig 5), and chronic CVT (>15 days) is isointense on T1-weighted images and isointense or hyperintense in T2-weighted MR images (Fig 6). However, the use of T2*-weighted gradient-recalled-echo and susceptibility-weighted MRI sequences (the latter being more sensitive than the former) improves the detection of acute-phase CVT because the magnetic susceptibility of deoxyhemoglobin makes dural sinus CVT hypointense (13,34,35). Idbaih et al (35) found that the sensitivity for diagnosis of CVT was 90% for T2*-weighted sequences, but only 70% for T1-weighted sequences. Diffusion-weighted sequences with high b values also can be useful for diagnosis of CVT. Sinuses with CVT have lower apparent diffusion coefficients (ADCs) (31,34–38), but the sensitivity of these sequences is low, because these findings are present in only 10%–40% of cases. Nevertheless, Favrole et al (36) found that restricted diffusion

in the sinus was associated with a lower probability of complete recanalization and a longer recovery period.

Two-dimensional (2D) time-of-flight and 3D phase-contrast MR venography are nonenhanced venography techniques that show the absence of normal signal intensity in sinus CVT. These are key methods when contrast agents are contraindicated, such as during pregnancy or in patients with severe renal failure (17). The 2D time-of-flight sequence is based on the inflow effect, and it is performed with sections that are perpendicular to the direction of the blood flow. This sequence is highly susceptible to flow artifacts and is dependent on the acquisition plane. A sinus parallel to the acquisition plane may have an artifactual signal intensity loss that mimics CVT. Furthermore, stationary tissue with short T1 (eg, fat or methemoglobin) may be mistaken for flowing blood. Another disadvantage of this technique is its reduced sensitivity for small vessels with slow flow (17,31,39–41). On the other hand, 3D phase-contrast MR venography is based on the dephasing of moving spins submitted to a bipolar gradient in gradient-echo acquisitions. 3D phase-contrast venography has better sensitivity to slow flow than does 2D time-of-flight MRI and is insensitive to short T1 tissue; however, with this technique, long acquisition times are required and aliasing artifacts can occur (40).

The use of contrast media is essential for assessment of the venous sinuses. Both contrast-enhanced MR venography and 3D contrast-enhanced gradient-recalled-echo T1-weighted MRI are excellent methods for the diagnosis of CVT (42). Lettau et al (43) found that contrast-enhanced MR venography is superior to 3D

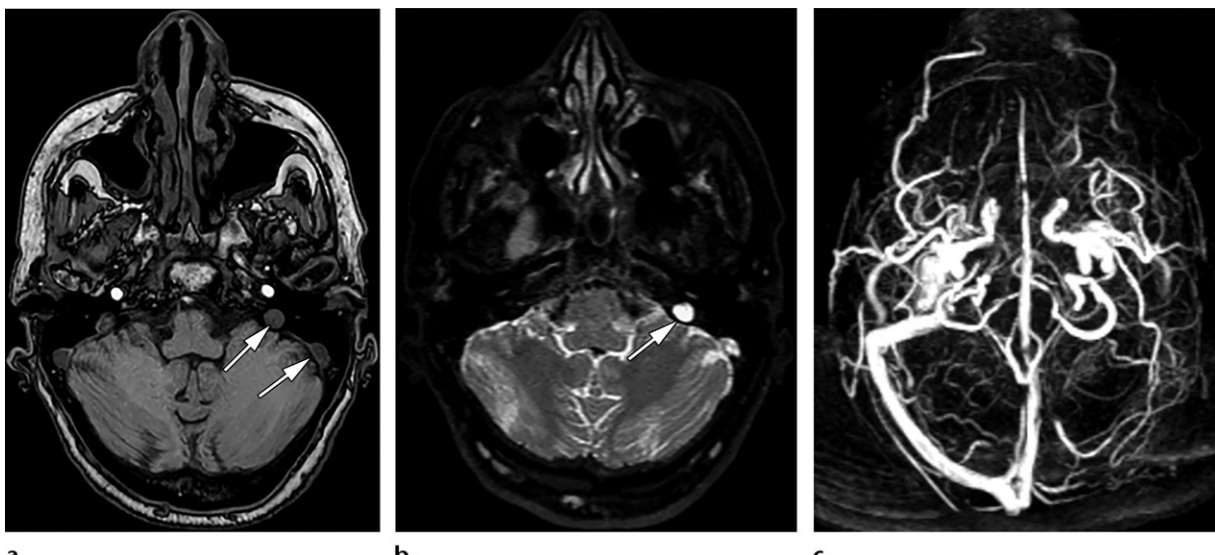
**a.****b.****c.**

Figure 6. Chronic CVT of the left transverse and sigmoid sinuses in a 62-year-old woman with seizures. **(a)** Axial T1-weighted MR image shows an isointense to hypointense thrombus (arrows). **(b)** Axial T2-weighted MR image shows a hyperintense thrombus (arrow). **(c)** Axial maximum intensity projection time-of-flight MR venogram shows a lack of flow in the left transverse sinus and the sigmoid sinus due to CVT.

contrast-enhanced gradient-recalled-echo T1-weighted MRI for visualizing CVT. Contrast-enhanced MR venography and CT venography are the best techniques for detecting CVT, and MR venography is the technique of choice for assessing recanalization after treatment (44–46). Complete recanalization is achieved more often in patients in whom CVT affects the superior sagittal sinus or the straight sinus than in those in whom it affects the transverse sinus or sigmoid sinus, although complete recanalization is not necessary for clinical recovery (47,48). When recanalization is incomplete, the appearance of the sinus at MR venography is irregular, with residual defects in the lumen of the venous sinus, channels in the sinus, and collateral dural vessels (Fig 7) (31).

The different MRI sequences, with and without contrast enhancement, that are used for CVT diagnosis have variable strengths. Contrast-enhanced MR venography has the highest accuracy, compared with nonenhanced MR venography (49). To study the CVT, the following MRI sequences should be included: T1- and T2-weighted, T2-weighted FLAIR, diffusion-weighted, susceptibility-weighted, and 3D contrast-enhanced (0.2 mmol/kg of body weight) gradient-recalled-echo T1-weighted MRI and MR venography (2D time-of-flight, 3D phase-contrast, and 3D contrast-enhanced MR venography).

Associated abnormalities in the brain parenchyma are present in 40%–60% of cases of CVT (12,31,50) and are located in subcortical territories that are not in the typical arterial vascular distribution. Changes in the parenchyma may be located near the drainage of the involved sinus

(Fig 8) (51,52). However, in some cases, parenchymal changes do not correlate with the site of venous occlusion (6,53). Bilateral parasagittal hemispheric lesions suggest CVT of the superior sagittal sinus; temporo-occipital lesions and lesions of the ipsilateral cerebellar lobe can be seen in patients with transverse sinus CVT (6). MRI can help to identify parenchymal lesions before they are visible at CT. This is important because, unlike arterial ischemic lesions, many parenchymal abnormalities in patients with CVT are reversible (54–57). The most commonly observed findings in the parenchyma are vasogenic and cytotoxic edema, which occasionally are found together, and intraparenchymal hemorrhage. Vasogenic edema develops secondary to elevated retrograde venous pressure; therefore, it is seen on diffusion-weighted MR images as hyperintense areas with high ADCs (Fig 9). In comparison, areas of cytotoxic edema appear as lesions with low ADCs. As we stated previously, vasogenic and cytotoxic edema may coexist, so a heterogeneous pattern at diffusion-weighted MRI and heterogeneous ADCs commonly are found.

Parenchymal hemorrhage is observed in 30%–35% of cases, typically in the cortex and extending subcortically (18,29,31). Hemorrhages in the frontal and parietal lobes are characteristic of superior sagittal sinus CVT (Fig 10), whereas those in the temporal and occipital lobes are more characteristic of transverse sinus CVT (Fig 11) (58).

Other less-frequent findings include gyral edema (Fig 12); diffuse edema with sulcal effacement; decreased size of the cisterns and ventricles; gyral enhancement, which may extend

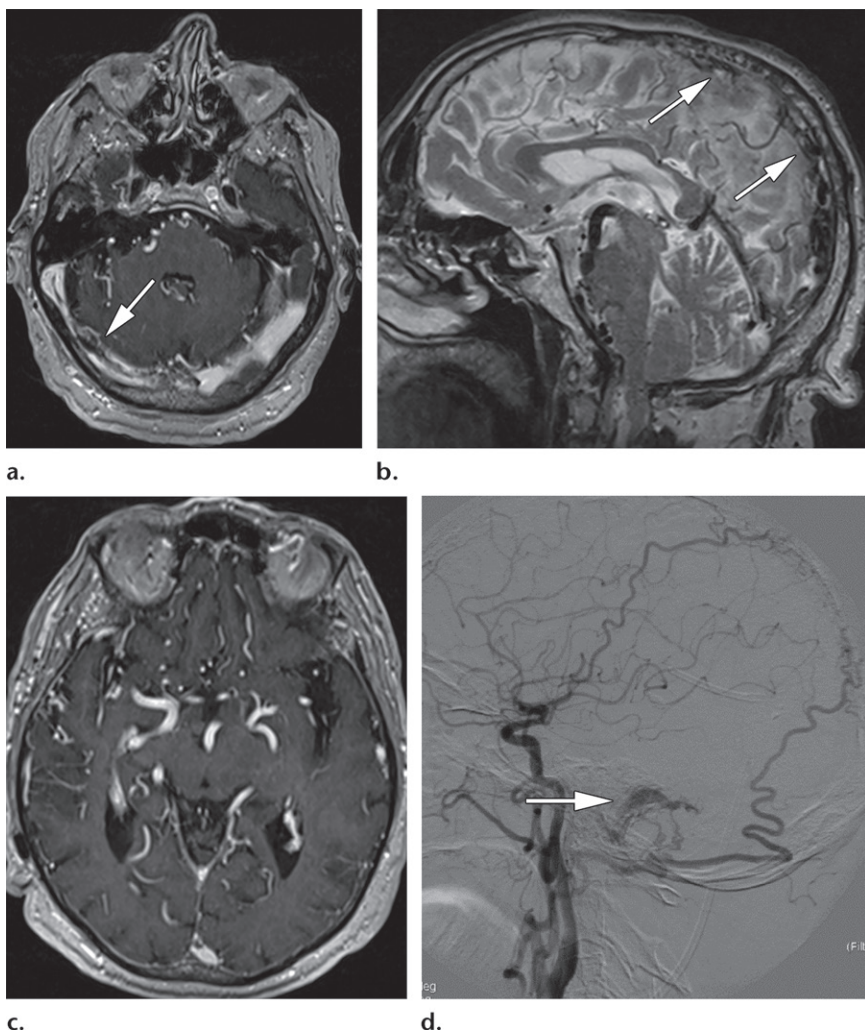


Figure 7. Incomplete recanalization in a 68-year-old man with a history of CVT for several years. (a) Axial contrast-enhanced MR venogram shows a residual intrasinus defect in the right transverse sinus (arrow). (b) Sagittal T2-weighted MR image shows the irregular appearance of the superior sagittal sinus (arrows). (c) Axial contrast-enhanced MR venogram shows severe diffuse areas of cerebral venous engorgement. (d) Lateral digital subtraction angiogram shows a dural arteriovenous fistula (arrow). Note the early drainage to the left transverse sinus and sigmoid sinus with afferent branches of the left carotid artery.

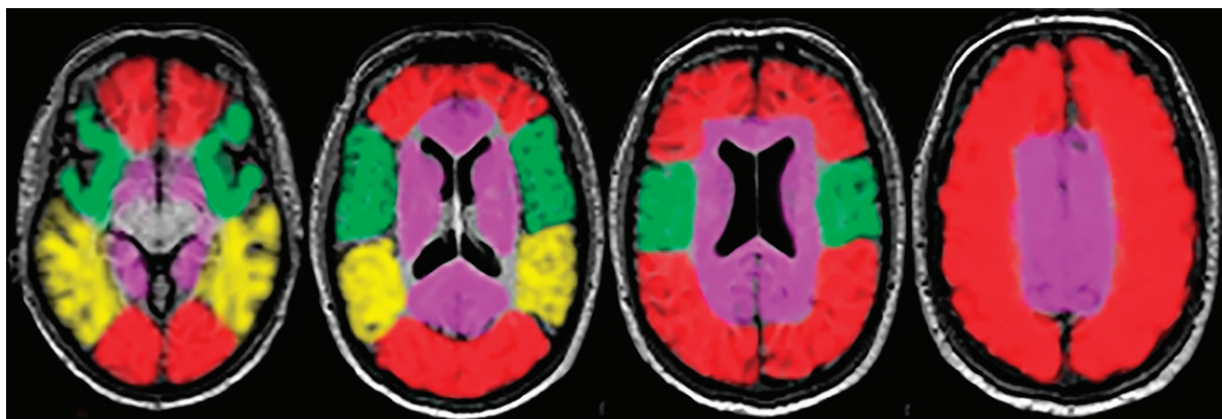


Figure 8. Series of axial MR images with a color overlay represents the venous drainage territories. The cortical veins and superior sagittal sinus (red), middle cerebral veins and cavernous sinus (green), transverse sinus and Labbé vein (yellow), and deep cerebral veins (lilac) are shown. Hemorrhage or edema in these territories may be indicative of CVT of the corresponding dural sinus or vein.

to the white matter; tentorial and leptomeningeal enhancement; and subdural hematomas or subarachnoid hemorrhage (18).

In cavernous sinus CVT, routine T2-weighted, FLAIR, and nonenhanced T1-weighted MRI of the entire brain should be performed. Thin-section

(3 mm) small-field-of-view, nonenhanced, and contrast-enhanced T1-weighted MRI should be performed in the axial and coronal planes, with at least one plane imaged with a fat-saturation technique. Thin-section contrast-enhanced axial images may be acquired with 3D gradient-spoiled

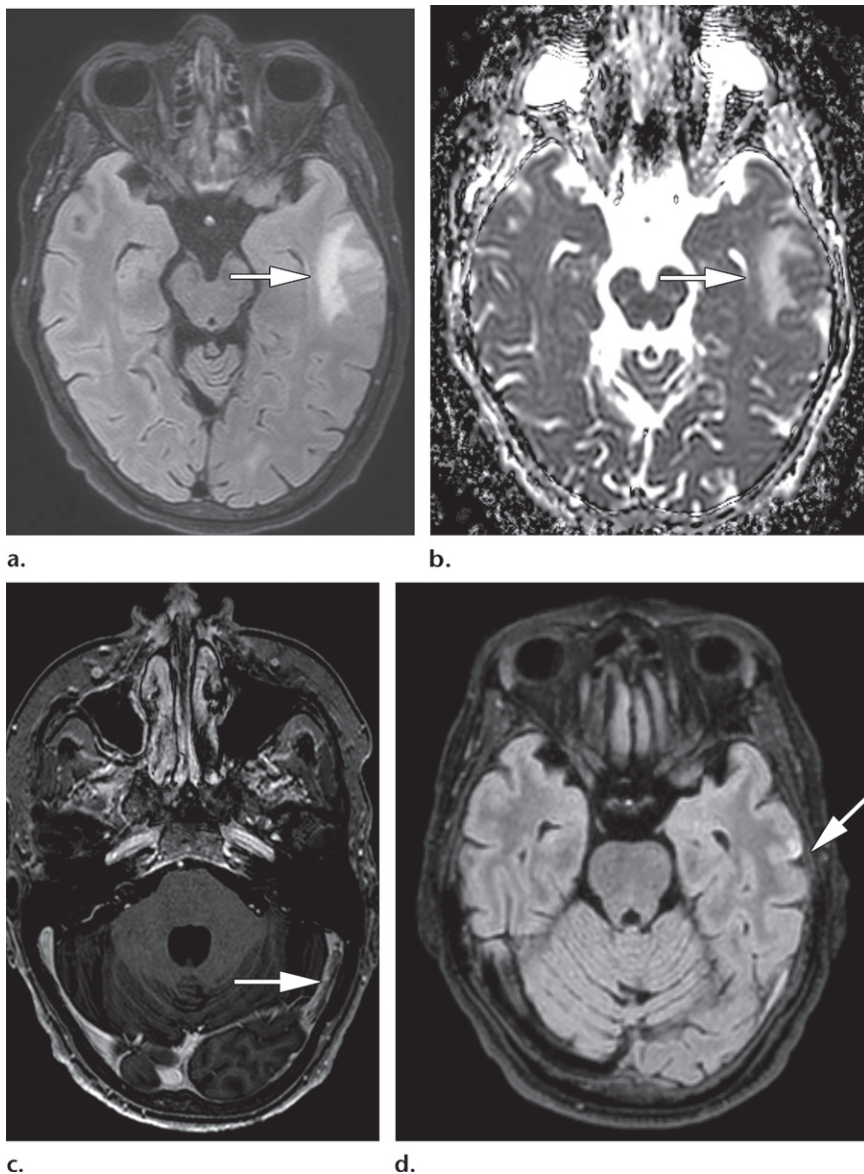
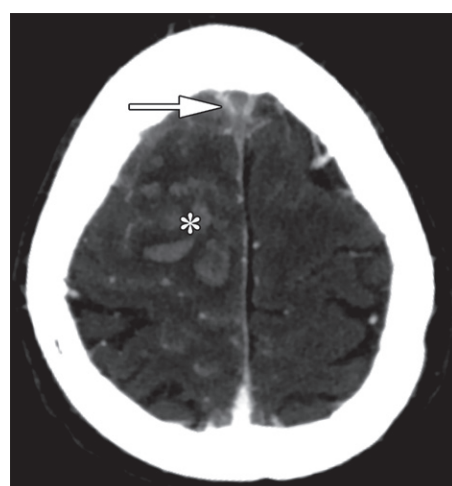
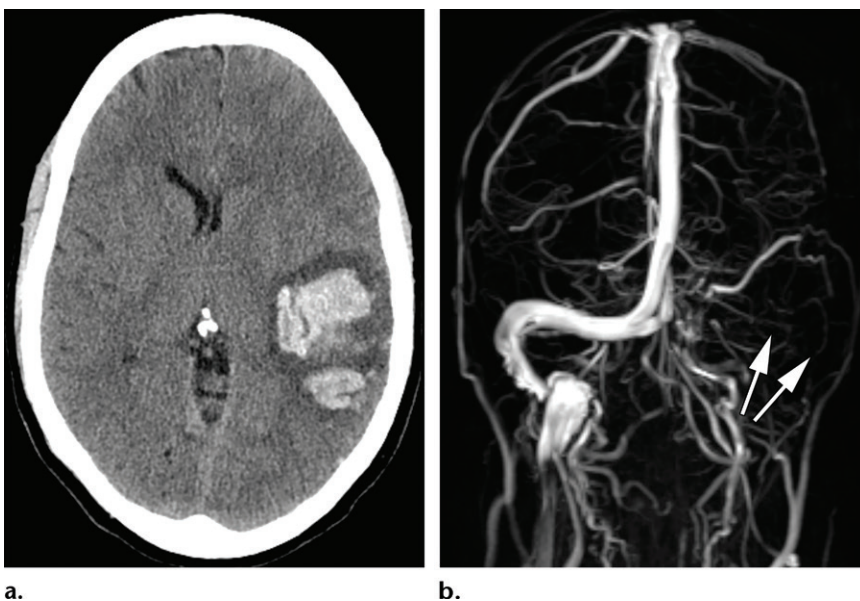


Figure 9. Vasogenic edema in a 62-year-old woman with seizures and stage IV stomach cancer. (a, b) Axial FLAIR MR image (a) shows subcortical temporal edema (arrow), and ADC map (b) shows increased ADCs (arrow). (c) Axial contrast-enhanced MR venogram shows a filling defect in the left transverse sinus (arrow). (d) Axial FLAIR MR image acquired 4 months later shows nearly complete resolution of the vasogenic edema (arrow).

Figure 10. Empty delta sign in an 85-year-old man with seizures and colon cancer. Axial contrast-enhanced CT image shows a hemorrhage in the frontal lobe (*) and the superior sagittal sinus CVT with the empty delta sign (arrow).

techniques. Generally images are acquired from the orbital apex through the prepontine cistern. For CT venography, images are acquired in the axial or coronal plane with section thickness of 1 mm and should be released and reformatted in other planes (24). Imaging features of cavernous sinus CVT include changes in signal intensity and/or in the size of the sinus and a filling defect after administration of contrast media. Indirect signs of cavernous sinus CVT are dilatation of the superior and inferior ophthalmic veins, fat stranding due to venous congestion, exophthalmos, and increased dural enhancement along the lateral border of the

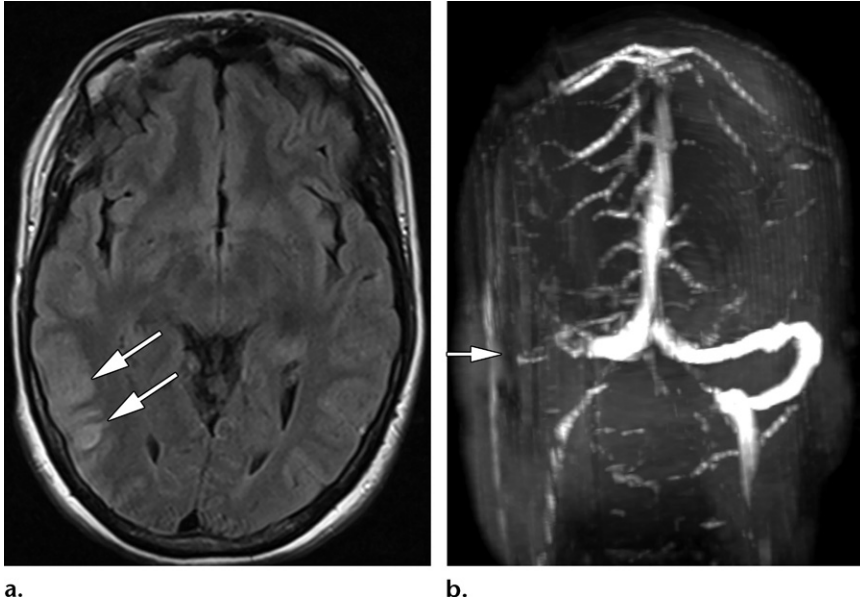




a.

b.

Figure 11. Parenchymal hemorrhage in a 37-year-old woman with a headache for 10 days and oral contraceptive use. (a) Axial nonenhanced CT image shows a left subcortical temporoparietal hematoma. (b) Coronal maximum intensity projection time-of-flight MR venogram shows lack of flow in the left transverse sinus, the sigmoid sinus, and the internal jugular vein due to CVT (arrows).



a.

b.

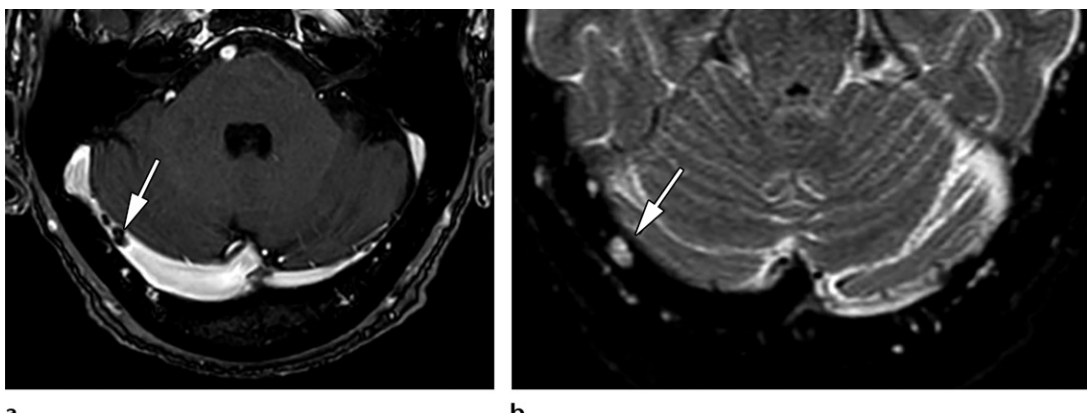
Figure 12. Cortical swelling in a 41-year-old woman with headache and seizures. (a) Axial FLAIR image shows cortical swelling in the right occipital and temporal lobes (arrows). (b) Coronal contrast-enhanced maximum intensity projection MR venogram shows a lack of flow in the right transverse and sigmoid sinuses that is consistent with CVT (arrow).

cavernous sinus and the ipsilateral tentorium. It is important to look for the underlying cause (eg, sinusitis) (23–25).

Advances in CT and MRI have drastically reduced the role of digital subtraction angiography in the diagnosis of CVT. Nevertheless, it can be useful for treatment of patients who do not respond to conventional treatment. The digital subtraction angiographic findings in patients with CVT include absence of the occluded sinus, venous congestion with dilatation of the cortical veins and/or the veins that drain the scalp and/or face, prominent collateral veins, and retrograde venous flow (17).

Pitfalls.—Imaging is fundamental in the diagnosis of CVT, but various conditions, normal

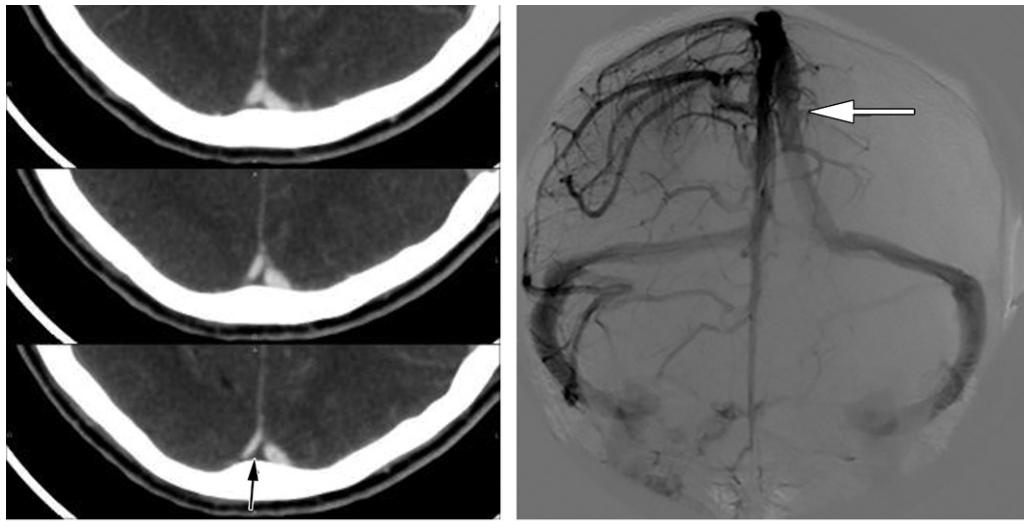
structures, and variants can mimic CVT (Tables E1–E3). For instance, at nonenhanced CT, increased attenuation of the dural sinuses can be seen in the absence of CVT in patients who are dehydrated, have high hematocrit values, or have subarachnoid or subdural hemorrhages. To differentiate between a physiologic increase in attenuation and attenuation caused by CVT, it is important to compare the attenuation of the venous sinuses and that of the arteries in both sides, because in cases of physiologic increase, the arteries also are hyperattenuating (59). On the other hand, a subdural hematoma can be mistaken for transverse sinus CVT, but the location of increased attenuation caused by a subdural hematoma is more medial than would be expected in a patient with transverse sinus CVT (29).



a.

b.

Figure 13. Normal appearance of arachnoid granulations. (a) Axial contrast-enhanced MR venogram shows well-defined filling defects with a rounded shape in the right transverse sinus (arrow). (b) Axial T2-weighted MR image shows the arachnoid granulation with signal intensity similar to that of cerebrospinal fluid (arrow).



a.

b.

Figure 14. High bifurcation of the superior sagittal sinus. (a) Consecutive axial contrast-enhanced CT images show a pseudo empty delta sign (arrow). (b) Frontal digital subtraction angiogram demonstrates high bifurcation of the superior sagittal sinus (arrow).

Normal structures and normal variants can give rise to findings similar to those reported in CVT. The transverse sinuses are asymmetric in 85% of cases. Hypoplasia and/or atresia of the transverse sinuses occur frequently and may mimic a lack of flow in the sinus at nonenhanced MR venography. The right transverse sinus is larger in 60% of cases (60), causing a false cord sign. Contrast-enhanced MR venography, contrast-enhanced 3D gradient-recalled-echo T1-weighted MRI, or CT venography help to solve these pitfalls. The arachnoid granulations are normal structures that protrude into the lumina of the venous sinuses, which can therefore be mistaken for filling defects; however, their typical location in the transverse sinuses (particularly within the middle and lateral portions of the sinus) and their characteristic rounded shape and signal intensity or attenuation similar to that of

cerebrospinal fluid at MRI help to avoid confusion (Fig 13) (61,62). Finally, a high or asymmetric bifurcation of the superior sagittal sinus (a normal variant) can give rise to a false empty delta sign (Fig 14) (60,63).

Our diagnostic capacity also can be limited by different aspects related to the imaging techniques employed. For example, because time-of-flight MR venography depends on blood flow velocity, flow gaps are common due to slow intravascular blood flow and/or a plane of imaging that is not perpendicular to blood flow in the sinus (Fig 15). These artifacts are more common in the transverse sinus (41). On the other hand, subacute CVT, which is hyperintense on T1-weighted images, can simulate normal flow at 2D time-of-flight MR venography (29). In these situations, the use of contrast-enhanced MR venography is of great help in avoiding an erroneous diagnosis.

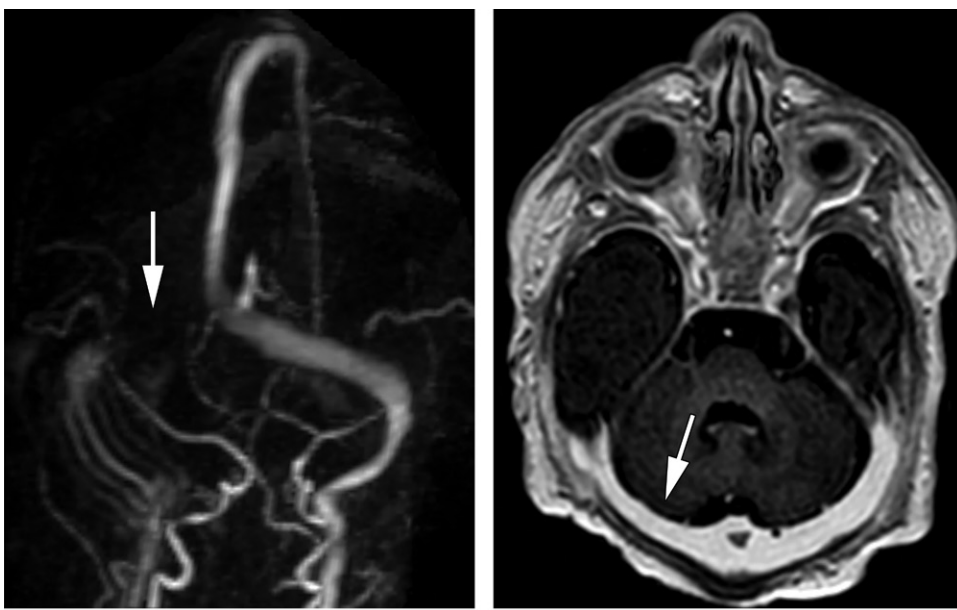
**a.****b.**

Figure 15. Transverse sinus flow gap. (a) Coronal time-of-flight MR venogram shows an apparent interruption of flow in the right transverse sinus (arrow). (b) Axial contrast-enhanced MR venogram shows normal flow in the right transverse sinus (arrow).

Occasionally, a gyriform enhancement associated with edema and hemorrhage can be interpreted as a tumor. In these cases, it is important to analyze carefully the venous structures in the search for CVT.

Sometimes, CVT diagnosis may be questionable, becoming a challenge for clinicians and radiologists. When the patient's clinical appearance is suggestive of CVT but the radiologic findings are inconclusive, anticoagulant therapy may be started anyway. On the other hand, if the clinical picture is nonspecific, repeating the MRI study is the best approach. The latter is a very common circumstance when CVT is found incidentally. Contrast-enhanced MR venography is the most specific sequence to ensure correct diagnosis of CVT (Fig 16).

Deep CVT

Anatomy.—The deep venous system includes the internal cerebral veins, which course through the roof of the third ventricle, joining the basal veins of Rosenthal to form the vein of Galen, which, in turn, joins the inferior sagittal sinus to form the straight sinus (64) (Fig 1). The deep system drains the thalamus; septum pellucidum; basal ganglia; upper brainstem; and deep white matter of the parietal, temporal, and frontal lobes (17).

Predisposing Factors and Clinical Manifestations.—The predisposing factors and clinical manifestations of DCVT are practically identical to those of DST (Table 2), although 61.5% of

patients with DCVT show a depressed level of consciousness (65). Less common clinical manifestations include focal neurologic deficits or psychiatric symptoms such as delirium, amnesia, apathy, or mutism (1,65,66).

Imaging Findings.—As in DST, nonenhanced CT is the first-line imaging study. In acute DCVT, the cerebral veins and/or the straight sinus may be hyperattenuating (Fig 17). This finding should raise suspicion of DCVT, but contrast-enhanced studies are necessary to confirm filling defects.

At nonenhanced MRI, the characteristic finding for DCVT is bilateral thalamic edema, which is present in approximately 86% of patients (67). This edema may extend to the basal ganglia (in one-third of cases) and to the adjacent deep white matter. FLAIR and diffusion-weighted MRI sequences are sensitive for detection of edema, which, as in DST, can be vasogenic (with high ADCs) or cytotoxic (with low ADCs); sometimes, both types are present (37) (Fig 18). Moreover, bilateral thalamic edema can compress the foramina of Monro or the third ventricle and cause hydrocephalus (67). Unilateral involvement is rare (68,69). Hemorrhagic transformation, typically in the thalamus, is seen in 19% of patients (67) (Figs 17, 18).

MR venography and susceptibility-weighted MRI sequences should be used to confirm the diagnosis whenever bilateral thalamic edema is observed.

Although there are no guidelines for the imaging follow-up of DCVT, some authors have

Figure 16. Absence of flow void in a 27-year-old woman with a headache. (a, b) Axial FLAIR (a) and T2-weighted (b) images show an absence of flow void in the left transverse sinus (arrow). (c) Coronal 3D phase-contrast MR venogram shows an absence of flow in the left transverse sinus (arrow). Although the findings in a–c were suspected to be artifacts, given that this is a young woman with headache, a contrast-enhanced study was performed. (d) Axial contrast-enhanced 3D gradient-recalled-echo T1-weighted MR image shows normal flow in the left transverse sinus (arrow).



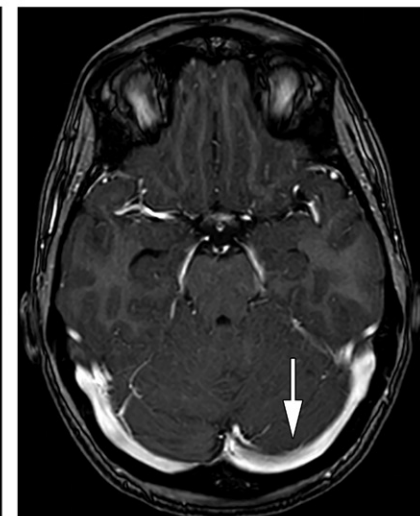
a.



b.



c.



d.

reported decreases in the affected area of the thalamus or even complete resolution of the edema at follow-up MRI (37,67).

In neonates with brain damage, the engorgement and CVT of deep medullary veins has been described as part of the pathologic chain of events in preterm and full-term neonatal encephalopathy, even without associated sinus CVT. Radial linear lesions in the white matter territory with deep medullary vein distribution appears as hyperintensity on T1-weighted MR images and hypointensity on T2-weighted MR images. These imaging findings are suggestive of engorgement and/or CVT of deep medullary veins (Fig 19). Deep medullary vein CVT may be isolated or associated with other lesions (edema, hemorrhage, infarction) (70,71).

Pitfalls.—The differential diagnosis of bilateral thalamic lesions and DCVT includes evaluation

for vascular lesions, infections, toxic or metabolic disorders, and tumors (Tables E2, E3) (72,73).

The thalamus receives its blood supply from the anterior circulation (anteroinferior thalamus) and from the posterior circulation (medial thalamus). An occlusion of the distal top of the basilar artery (top of the basilar syndrome) could give rise to bilateral thalamic infarction from occlusion of the paramedian perforating branches. Likewise, an occlusion of the artery of Percheron (a rare variant in which a single arterial trunk originates in the proximal segment of one of the posterior cerebral arteries) also could explain abnormalities in both thalamci. Therefore, in these cases, the arterial system must be evaluated to confirm the occlusion. Since arterial infarction normally occurs in the paramedian areas of the thalamus and has homogeneous restricted diffusion and little

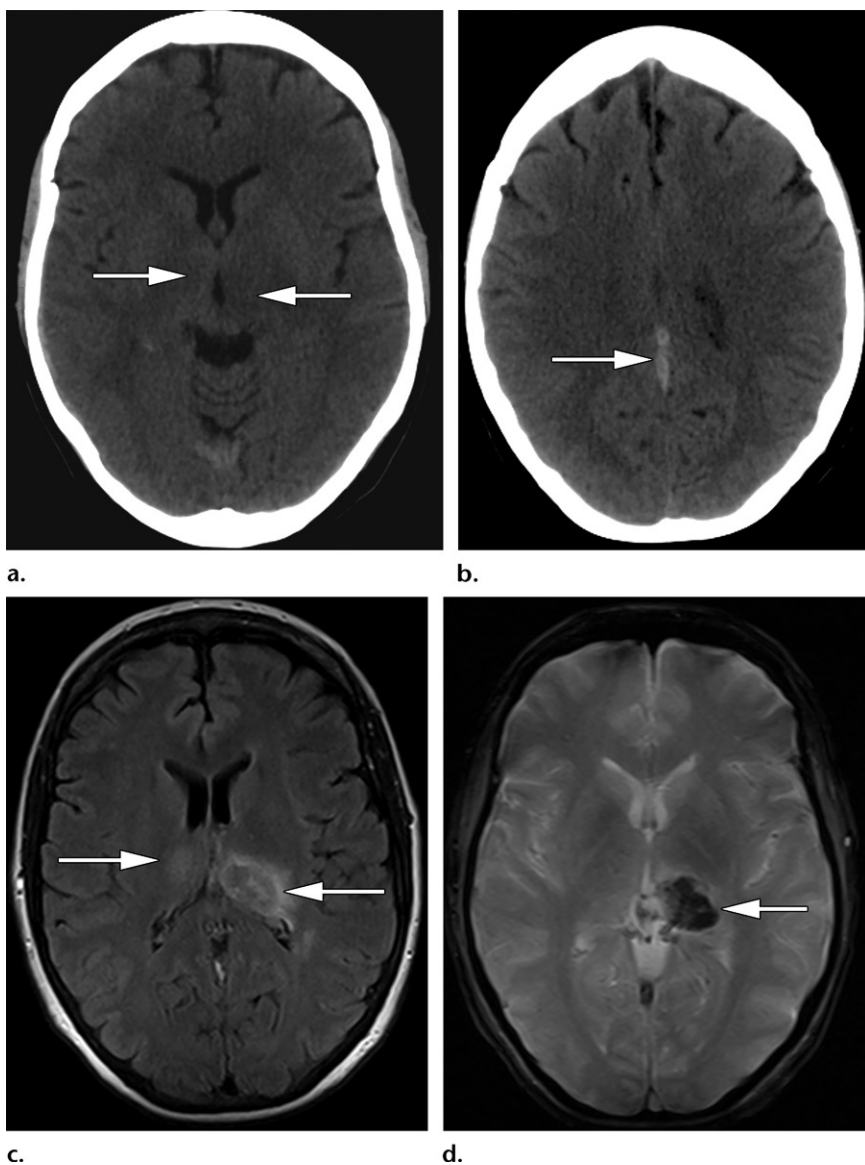


Figure 17. DCVT in a 50-year-old woman with bradypsychia. **(a)** Axial nonenhanced CT image shows hypoattenuation in both thalami (arrows) that is suggestive of edema. **(b)** Axial nonenhanced CT image shows the hyperattenuation of internal cerebral veins (arrow), which is suggestive of CVT. **(c)** Axial FLAIR MR image shows the bilateral thalamic edema (arrows). **(d)** Axial T2*-weighted gradient-echo MR image shows a hemorrhagic lesion in the left thalamus (arrow).

swelling; these findings also are important for differentiating among vascular conditions. In addition, in DCVT, when hemorrhagic transformation is present, it tends to extend from the center toward the periphery, whereas in arterial infarction, it tends to extend from the periphery to the center (64).

Posterior reversible encephalopathy syndrome, which is caused by a failure of self-regulation of the posterior circulation when changes in blood pressure occur, is seen at CT and MRI as bilateral areas of vasogenic edema. In patients with this syndrome, the edema generally involves the parieto-occipital regions; however, there is a variant involving the central brainstem and basal ganglia that lacks the cortical and subcortical swelling (central-variant posterior reversible encephalopathy syndrome). The distribution of the edema helps in the differential diagnosis because the brainstem is involved (74).

Many types of infection can appear at imaging with findings similar to those of DCVT. Thalamic involvement can be seen in the different types of viral encephalitis (WNV encephalitis, JEV encephalitis, eastern equine encephalitis, and Murray Valley encephalitis) (73). Toxoplasmosis, an opportunistic infection caused by the parasite *Toxoplasma gondii*, is seen as multiple focal lesions in the basal ganglia, the thalami, and the white matter–gray matter junction; however, unlike in DCVT, lesions in patients with toxoplasmosis manifest with a mass effect and nodular or ring enhancement.

Various metabolic disorders also must be considered in the differential diagnosis. Wernicke encephalopathy, which is caused by a thiamine deficiency, gives rise to characteristic findings such as T2 hyperintensity in the medial thalamus, the periaqueductal area, the mammillary bodies, and the tectal plate. Wilson disease, an autosomal recessive disease characterized by the

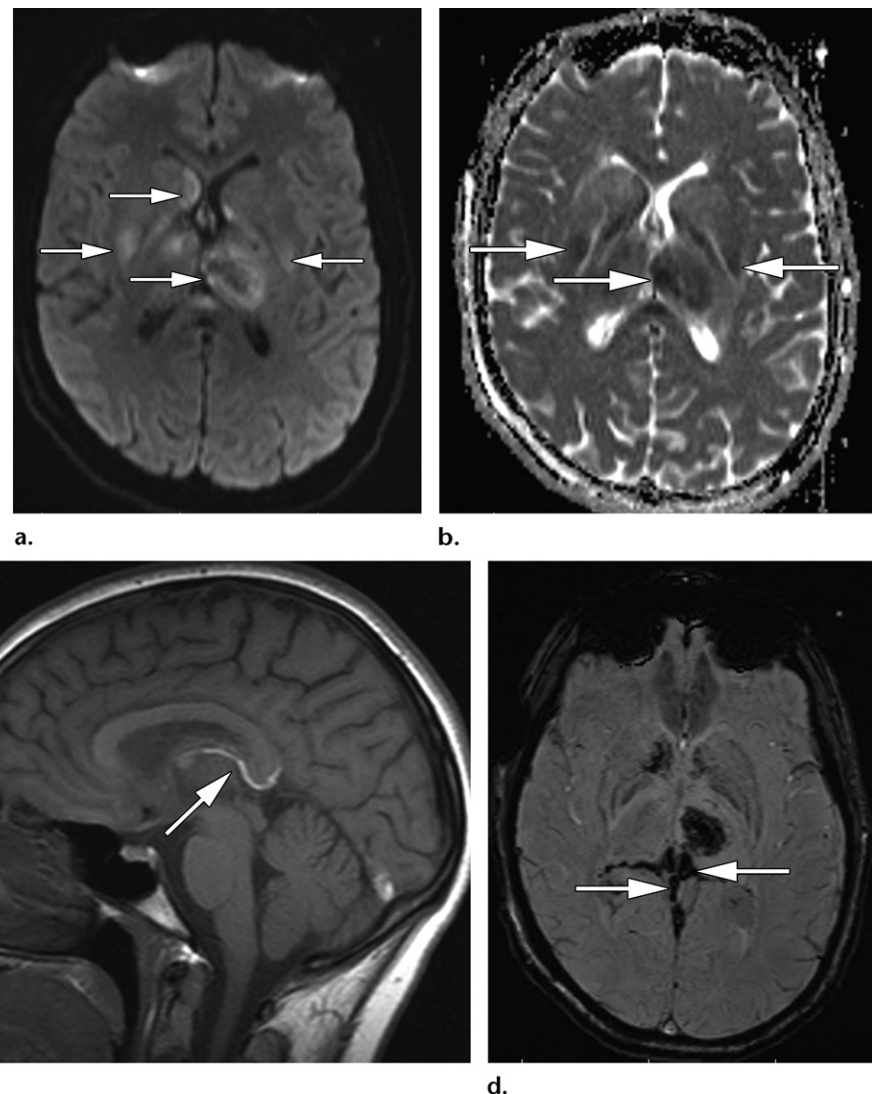
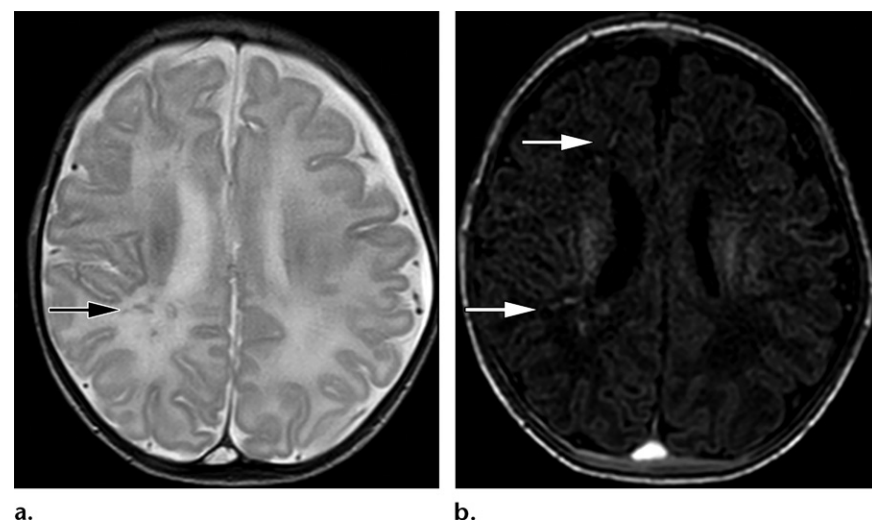


Figure 18. DCVT in a 21-year-old woman with a headache and oral contraceptive use. (a, b) Axial diffusion-weighted MR image (a) shows hyperintensity in the thalamus and basal ganglia (arrows), and the ADC map (b) shows low ADCs, which are findings consistent with cytotoxic edema. (c) Sagittal T1-weighted MR image shows an area of abnormally high signal intensity in the internal cerebral vein (arrow), which is suggestive of CVT. (d) Axial susceptibility-weighted MR image shows abnormal hypointensity corresponding to the internal cerebral veins (arrows). Note the hemorrhagic lesion in the left thalamus.

Figure 19. Engorgement or CVT of the deep medullary veins in a 12-day-old male infant. Axial T2-weighted MR image (a) shows linear hypointense white matter lesions (arrow) that correspond to linear hyperintense alterations (arrows) on an axial T1-weighted MR image (b).



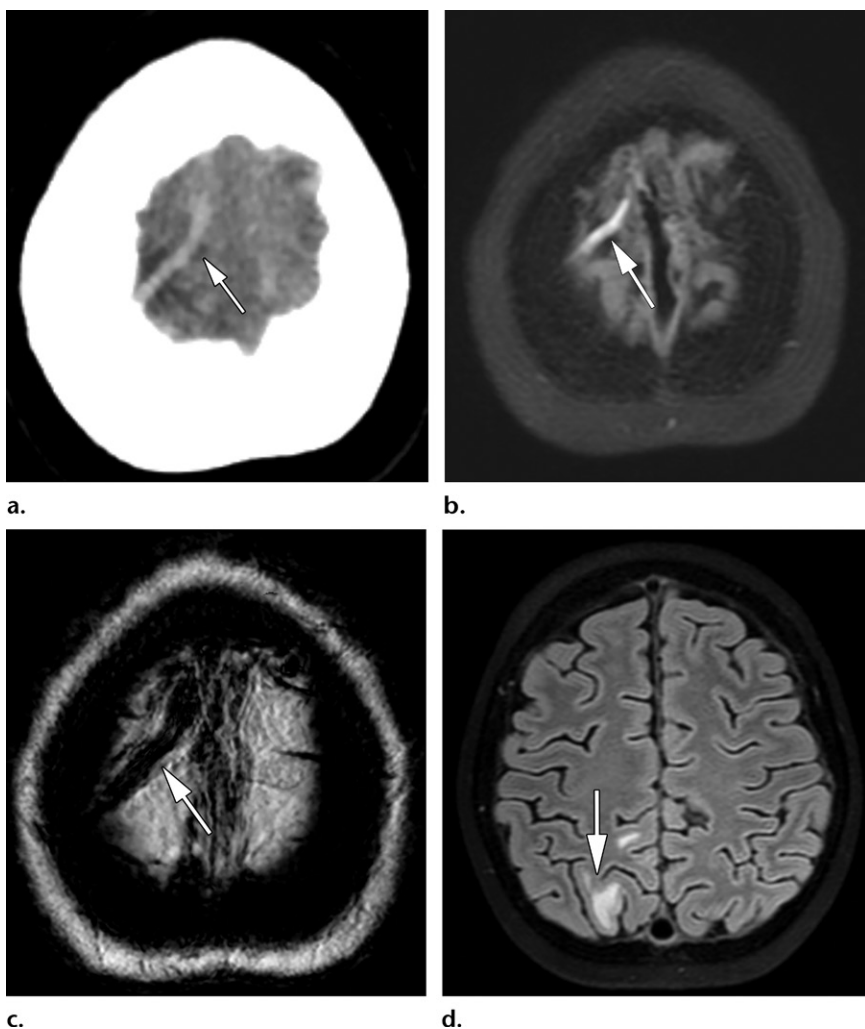


Figure 20. Isolated cortical vein CVT in an 11-year-old boy with acute lymphocytic leukemia. (a) Axial nonenhanced CT image shows hyperattenuation of a cortical vein (cord sign) (arrow). (b) Axial T1-weighted MR image shows hyperintensity of the vein (arrow). (c) Susceptibility-weighted MR image shows hypointensity of the cortical vein (arrow). (d) Axial FLAIR MR image shows an area of subcortical edema (arrow).

accumulation of copper due to ceruloplasmin deficiency, manifests at MRI as T2 hyperintensity in the putamen, pallidum, caudate nucleus, and ventrolateral region of the thalamus.

Finally, some tumors such as gliomas, neurocytomas, and germinomas can be located in the thalamus. The most important condition for evaluation in the differential diagnosis is the bilateral thalamic glioma. These neoplasms often cause a mass effect, with compression of adjacent structures, and can enhance after the administration of contrast media; furthermore, some of them have calcifications, a finding that does not occur in DCVT (72,73).

Isolated Cortical Vein CVT

Anatomy.—The superficial venous system is made up of three groups of veins: a superior group, comprising the superior cerebral veins and the vein of Trolard, which connects the superficial middle cerebral vein with the superior sagittal sinus; a medial group, comprising the superficial middle cerebral vein; and an inferior group, com-

prising the inferior cerebral veins and the vein of Labb  (which connects the middle cerebral vein with the transverse sinus).

The cortical veins drain the venous blood from the cerebral cortex and the subcortical white matter toward the dural sinuses.

Predisposing Factors and Clinical Manifestations.—The risk factors for isolated cortical vein CVT are the same as those for DST (Table 2). From the clinical point of view, isolated occlusion of a cortical vein usually causes motor or sensory neurologic deficits and seizures (34).

Imaging Findings.—Isolated cortical vein CVT is difficult to diagnose because the cortical veins are small, are located peripherally, and vary in number. Often only indirect signs can raise suspicion, such as edema or focal cortical hemorrhage, prominent collateral veins, or congestion of adjacent veins (75,76).

Nonenhanced CT shows the cord sign (Fig 20), a well-defined hyperattenuating linear structure in a cerebral sulcus, corresponding to

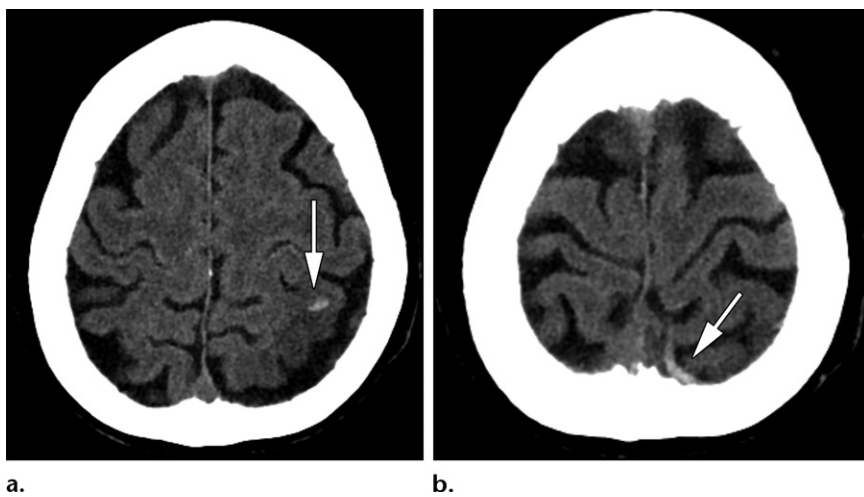


Figure 21. Isolated cortical vein CVT in a 98-year-old woman with right upper extremity paresis. (a) Axial nonenhanced CT image shows subcortical focal hemorrhage (arrow). The attenuation of the cortical veins should be evaluated when this finding is present. (b) Axial nonenhanced CT image shows hyperattenuation of a cortical vein (cord sign) (arrow), which is suggestive of CVT.

the vein with CVT. At nonenhanced T1- and T2-weighted MRI, the signal intensity of the vein with CVT varies depending on the age of the thrombus; when it is hyperintense, it is known as the hyperintense vein sign (Fig 20). Gradient-echo and susceptibility-weighted MRI sequences are very useful for detecting the CVT in the vein (Fig 20) and are even more sensitive than MR venography and CT venography (35,45,75) because the susceptibility artifact due to hemosiderin deposits can persist for months or even years (75). An area of edema or focal cortical or subcortical hemorrhage near the vein with CVT is present in up to 87% of patients with isolated cortical vein CVT (75) (Fig 21); this characteristic finding can be observed at both CT and MRI, although MRI is more sensitive in detecting it. Therefore, when edema or cortical or subcortical focal hemorrhage is detected, it is important to evaluate the attenuation and/or signal intensity of the adjacent cortical veins, especially when these lesions are not in an arterial distribution.

Pitfalls.—At nonenhanced CT, the cord sign can be mistaken for a subarachnoid hemorrhage or a subdural hematoma (77). A thorough analysis of the morphology and location will help ensure the correct diagnosis. Focal hemorrhage can mimic a hemorrhagic contusion after trauma; in this case, it is essential to correlate the imaging findings with the clinical context or to look for other findings related to trauma, such as fractures (77). A focal edema or hemorrhage can be misinterpreted as a tumor brain. It is important to evaluate the signal intensity of the adjacent cortical veins (78).

Treatment, Prognosis, and Follow-up

The standard of care treatment of CVT is anticoagulation therapy, most appropriately, administration of low-molecular-weight heparin for at least 3

months (depending on the underlying cause) (79). Endovascular treatment (chemical thrombolysis, mechanical thrombectomy, or both) may be an option in patients with more severe cases and in those who do not respond to anticoagulation treatment.

Early diagnosis and treatment improve the prognosis for patients with CVT. In recent decades, the associated mortality has decreased considerably; reported mortality rates range from 0% to 39% (16,66,80,81). The most common cause of death is transtentorial herniation, normally due to multiple lesions, diffuse edema, or mass effect. Reported factors of poor prognosis in patients with CVT include age older than 37 years, male sex, coma, intracranial hemorrhage at the time of diagnosis, DCVT, central nervous system infection, and cancer (11).

The American Heart Association (AHA) and the American Stroke Association (ASA) recommend early CT or MRI follow-up in patients with CVT and persistent symptoms or clinical deterioration despite medical treatment that suggests the propagation of the thrombus. Moreover, in patients who are in stable condition, it is reasonable to perform follow-up CT or MRI 3–6 months after the diagnosis to check the recanalization of the occluded sinus or cortical vein (13). The rates of recanalization, at least partial recanalization, are 84% at 3 months after diagnosis and 85% at 1 year after diagnosis (82); the recanalization rates are higher in patients with DCVT and CVT of the cavernous sinus than with CVT of the transverse sinus (83).

Conclusion

CVT is uncommon and difficult to diagnose because its clinical manifestations are nonspecific. Early treatment is essential to decrease the rate of complications and sequelae. Imaging techniques are fundamental to their detection, so radiologists must be familiar with the imaging findings associated with this vascular condition.

and with the potential pitfalls and conditions to consider in the differential diagnosis to reach the correct diagnosis.

Disclosures of Conflicts of Interest.—A.L.A. Activities related to the present article: disclosed no relevant relationships. Activities not related to the present article: payment for lectures from Bracco Imaging, GE, and Toshiba; royalties from Springer. Other activities: disclosed no relevant relationships.

References

- Stam J. Thrombosis of the cerebral veins and sinuses. *N Engl J Med* 2005;352(17):1791–1798.
- Coutinho JM. Cerebral venous thrombosis. *J Thromb Haemost* 2015;13(suppl 1):S238–S244.
- Devasagayam S, Wyatt B, Leyden J, Kleinig T. Cerebral Venous Sinus Thrombosis Incidence Is Higher Than Previously Thought: A Retrospective Population-Based Study. *Stroke* 2016;47(9):2180–2182.
- Gunes HN, Cokal BG, Guler SK, et al. Clinical associations, biological risk factors and outcomes of cerebral venous sinus thrombosis. *J Int Med Res* 2016;44(6):1454–1461.
- Zuurbier SM, Middeldorp S, Stam J, Coutinho JM. Sex differences in cerebral venous thrombosis: A systematic analysis of a shift over time. *Int J Stroke* 2016;11(2):164–170.
- Tsai FY, Wang AM, Matovich VB, et al. MR staging of acute dural sinus thrombosis: correlation with venous pressure measurements and implications for treatment and prognosis. *AJNR Am J Neuroradiol* 1995;16(5):1021–1029.
- Itrat A, Shoukat S, Kamal AK. Pathophysiology of cerebral venous thrombosis: an overview. *J Pak Med Assoc* 2006;56(11):506–508.
- Frerichs KU, Deckert M, Kempfki O, Schürer L, Einhäupl K, Baethmann A. Cerebral sinus and venous thrombosis in rats induces long-term deficits in brain function and morphology: evidence for a cytotoxic genesis. *J Cereb Blood Flow Metab* 1994;14(2):289–300.
- Schaller B, Graf R, Sanada Y, et al. Hemodynamic changes after occlusion of the posterior superior sagittal sinus: an experimental PET study in cats. *AJNR Am J Neuroradiol* 2003;24(9):1876–1880.
- Rhoton AL Jr. The cerebral veins. *Neurosurgery* 2002;51(4 suppl):S159–S205.
- Ferro JM, Canhão P, Stam J, Bousser MG, Barinagarrementeria F; ISCVT Investigators. Prognosis of cerebral vein and dural sinus thrombosis: results of the International Study on Cerebral Vein and Dural Sinus Thrombosis (ISCVT). *Stroke* 2004;35(3):664–670.
- Sassi SB, Touati N, Baccouche H, Drissi C, Romdhane NB, Hentati F. Cerebral venous thrombosis: a tunisian monocenter study on 160 patients. *Clin Appl Thromb Hemost* 2017;23(8):1005–1009.
- Saposnik G, Barinagarrementeria F, Brown RD Jr, et al. Diagnosis and management of cerebral venous thrombosis: a statement for healthcare professionals from the American Heart Association/American Stroke Association. *Stroke* 2011;42(4):1158–1192.
- Wasay M, Bakshi R, Bobustuc G, et al. Cerebral venous thrombosis: analysis of a multicenter cohort from the United States. *J Stroke Cerebrovasc Dis* 2008;17(2):49–54.
- de Freitas GR, Bogousslavsky J. Risk factors of cerebral vein and sinus thrombosis. *Front Neurol Neurosci* 2008;23:23–54.
- Ferro JM, Bousser MG, Canhão P, et al. European Stroke Organization guideline for the diagnosis and treatment of cerebral venous thrombosis: endorsed by the European Academy of Neurology. *Eur J Neurol* 2017;24(10):1203–1213.
- Dmytriw AA, Song JS, Yu E, Poon CS. Cerebral venous thrombosis: state of the art diagnosis and management. *Neuroradiology* 2018;60(7):669–685.
- Poon CS, Chang JK, Swarnkar A, Johnson MH, Wasenko J. Radiologic diagnosis of cerebral venous thrombosis: pictorial review. *AJR Am J Roentgenol* 2007;189(6 Suppl):S64–S75.
- Guenther G, Arauz A. Cerebral venous thrombosis: a diagnostic and treatment update. *Neurologia* 2011;26(8):488–498.
- Masuhr F, Busch M, Amberger N, et al. Risk and predictors of early epileptic seizures in acute cerebral venous and sinus thrombosis. *Eur J Neurol* 2006;13(8):852–856.
- Masuhr F, Mehraeini S, Einhäupl K. Cerebral venous and sinus thrombosis. *J Neurol* 2004;251(1):11–23.
- Chiewvit P, Piyapittayanan S, Poungvarin N. Cerebral venous thrombosis: diagnosis dilemma. *Neurol Int* 2011;3(3):e13.
- Absoud M, Hikmet F, Dey P, Joffe M, Thambapillai E. Bilateral cavernous sinus thrombosis complicating sinusitis. *J R Soc Med* 2006;99(9):474–476.
- Razek AA, Castillo M. Imaging lesions of the cavernous sinus. *AJNR Am J Neuroradiol* 2009;30(3):444–452.
- Lee JH, Lee HK, Park JK, Choi CG, Suh DC. Cavernous sinus syndrome: clinical features and differential diagnosis with MR imaging. *AJR Am J Roentgenol* 2003;181(2):583–590.
- Vijay RK. The cord sign. *Radiology* 2006;240(1):299–300.
- Virapongse C, Cazenave C, Quisling R, Sarwar M, Hunter S. The empty delta sign: frequency and significance in 76 cases of dural sinus thrombosis. *Radiology* 1987;162(3):779–785.
- Teasdale E. Cerebral venous thrombosis: making the most of imaging. *J R Soc Med* 2000;93(5):234–237.
- Walecki J, Mruk B, Nawrocka-Laskus E, Piliszek A, Przelaskowski A, Sklinda K. Neuroimaging of Cerebral Venous Thrombosis (CVT): Old Dilemma and the New Diagnostic Methods. *Pol J Radiol* 2015;80:368–373.
- Lee EJ. The empty delta sign. *Radiology* 2002;224(3):788–789.
- Leach JL, Fortuna RB, Jones BV, Gaskill-Shipley MF. Imaging of cerebral venous thrombosis: current techniques, spectrum of findings, and diagnostic pitfalls. *RadioGraphics* 2006;26(Suppl 1):S19–S41; discussion S42–S43.
- Bianchi D, Maeder P, Bogousslavsky J, Schnyder P, Meuli RA. Diagnosis of cerebral venous thrombosis with routine magnetic resonance: an update. *Eur Neurol* 1998;40(4):179–190.
- Macchi PJ, Grossman RI, Gomori JM, Goldberg HI, Zimmerman RA, Bilaniuk LT. High field MR imaging of cerebral venous thrombosis. *J Comput Assist Tomogr* 1986;10(1):10–15.
- Bousser MG, Ferro JM. Cerebral venous thrombosis: an update. *Lancet Neurol* 2007;6(2):162–170.
- Idbäck A, Boukobza M, Crassard I, Porcher R, Bousser MG, Chabriat H. MRI of clot in cerebral venous thrombosis: high diagnostic value of susceptibility-weighted images. *Stroke* 2006;37(4):991–995.
- Favrole P, Guichard JP, Crassard I, Bousser MG, Chabriat H. Diffusion-weighted imaging of intravascular clots in cerebral venous thrombosis. *Stroke* 2004;35(1):99–103.
- Lövblad KO, Bassetti C, Schneider J, et al. Diffusion-weighted MR in cerebral venous thrombosis. *Cerebrovasc Dis* 2001;11(3):169–176.
- Chu K, Kang DW, Yoon BW, Roh JK. Diffusion-weighted magnetic resonance in cerebral venous thrombosis. *Arch Neurol* 2001;58(10):1569–1576.
- Farb RI, Scott JN, Willinsky RA, Montanera WJ, Wright GA, terBrugge KG. Intracranial venous system: gadolinium-enhanced three-dimensional MR venography with auto-triggered elliptic centric-ordered sequence—initial experience. *Radiology* 2003;226(1):203–209.
- Liau L, van Buchem MA, Spilt A, et al. MR angiography of the intracranial venous system. *Radiology* 2000;214(3):678–682.
- Ayanzen RH, Bird CR, Keller PJ, McCully FJ, Theobald MR, Heiserman JE. Cerebral MR venography: normal anatomy and potential diagnostic pitfalls. *AJNR Am J Neuroradiol* 2000;21(1):74–78.
- Liang L, Korogi Y, Sugahara T, et al. Evaluation of the intracranial dural sinuses with a 3D contrast-enhanced MP-RAGE sequence: prospective comparison with 2D-TOF MR venography and digital subtraction angiography. *AJNR Am J Neuroradiol* 2001;22(3):481–492.
- Lettau M, Laible M, Barrows RJ, Heiland S, Bendszus M, Hähnel S. 3-T contrast-enhanced MR angiography with parallel imaging in cerebral venous and sinus thrombosis. *J Neuroradiol* 2011;38(5):275–282.

44. Ozsvath RR, Casey SO, Lustrin ES, Alberico RA, Hassankhani A, Patel M. Cerebral venography: comparison of CT and MR projection venography. *AJR Am J Roentgenol* 1997;169(6):1699–1707.
45. Meckel S, Reisinger C, Bremerich J, et al. Cerebral venous thrombosis: diagnostic accuracy of combined, dynamic and static, contrast-enhanced 4D MR venography. *AJNR Am J Neuroradiol* 2010;31(3):527–535.
46. Khandelwal N, Agarwal A, Kochhar R, et al. Comparison of CT venography with MR venography in cerebral sinovenous thrombosis. *AJR Am J Roentgenol* 2006;187(6):1637–1643.
47. Putaalaa J, Hiltunen S, Salonen O, Kaste M, Tattiusumak T. Recanalization and its correlation to outcome after cerebral venous thrombosis. *J Neurol Sci* 2010;292(1–2):11–15.
48. Stoltz E, Trittmacher S, Rahimi A, et al. Influence of recanalization on outcome in dural sinus thrombosis: a prospective study. *Stroke* 2004;35(2):544–547.
49. Sadigh G, Mullins ME, Saindane AM. Diagnostic Performance of MRI Sequences for Evaluation of Dural Venous Sinus Thrombosis. *AJR Am J Roentgenol* 2016;206(6):1298–1306.
50. Renowden S. Cerebral venous sinus thrombosis. *Eur Radiol* 2004;14(2):215–226.
51. Meder JF, Chiras J, Roland J, Guinet P, Bracard S, Bargy F. Venous territories of the brain. *J Neuroradiol* 1994;21(2):118–133.
52. Zubkov AY, McBane RD, Brown RD, Rabinstein AA. Brain lesions in cerebral venous sinus thrombosis. *Stroke* 2009;40(4):1509–1511.
53. Bergui M, Bradac GB, Daniele D. Brain lesions due to cerebral venous thrombosis do not correlate with sinus involvement. *Neuroradiology* 1999;41(6):419–424.
54. Forbes KPN, Pipe JG, Heiserman JE. Evidence for cytotoxic edema in the pathogenesis of cerebral venous infarction. *AJNR Am J Neuroradiol* 2001;22(3):450–455.
55. Röttger C, Trittmacher S, Gerriets T, Blaes F, Kaps M, Stoltz E. Reversible MR imaging abnormalities following cerebral venous thrombosis. *AJNR Am J Neuroradiol* 2005;26(3):607–613.
56. Manzione J, Newman GC, Shapiro A, Santo-Ocampo R. Diffusion-and perfusion-weighted MR imaging of dural sinus thrombosis. *AJNR Am J Neuroradiol* 2000;21(1):68–73.
57. Sarma D, Farb RI, Mikulis DJ, terBrugge KG. Reversal of restricted diffusion in cerebral venous thrombosis: case report. *Neuroradiology* 2004;46(2):118–121.
58. Keiper MD, Ng SE, Atlas SW, Grossman RI. Subcortical hemorrhage: marker for radiographically occult cerebral vein thrombosis on CT. *J Comput Assist Tomogr* 1995;19(4):527–531.
59. Provenzale JM, Kranz PG. Dural sinus thrombosis: sources of error in image interpretation. *AJR Am J Roentgenol* 2011;196(1):23–31.
60. Alper F, Kantarci M, Dane S, Gumustekin K, Onbas O, Durur I. Importance of anatomical asymmetries of transverse sinuses: an MR venographic study. *Cerebrovasc Dis* 2004;18(3):236–239.
61. Liang L, Korogi Y, Sugahara T, et al. Normal structures in the intracranial dural sinuses: delineation with 3D contrast-enhanced magnetization prepared rapid acquisition gradient-echo imaging sequence. *AJNR Am J Neuroradiol* 2002;23(10):1739–1746.
62. Leach JL, Jones BV, Tomsick TA, Stewart CA, Balko MG. Normal appearance of arachnoid granulations on contrast-enhanced CT and MR of the brain: differentiation from dural sinus disease. *AJNR Am J Neuroradiol* 1996;17(8):1523–1532.
63. Singh M, Nagashima M, Inoue Y. Anatomical variations of occipital bone impressions for dural venous sinuses around the torcular Herophili: with special reference to the consideration of clinical significance. *Surg Radiol Anat* 2004;26(6):480–487.
64. van den Bergh WM, van der Schaaf I, van Gijn J. The spectrum of presentations of venous infarction caused by deep cerebral vein thrombosis. *Neurology* 2005;65(2):192–196.
65. Terazzi E, Mittino D, Rudà R, et al. Cerebral venous thrombosis: a retrospective multicentre study of 48 patients. *Neurolog Sci* 2005;25(6):311–315.
66. Luo Y, Tian X, Wang X. Diagnosis and treatment of cerebral venous thrombosis: A Review. *Front Aging Neurosci* 2018;10:2.
67. Crombé D, Haven F, Gille M. Isolated deep cerebral venous thrombosis diagnosed on CT and MR imaging: A case study and literature review. *JBR-BTR* 2003;86(5):257–261.
68. Herrmann KA, Sporer B, Yousry TA. Thrombosis of the internal cerebral vein associated with transient unilateral thalamic edema: a case report and review of the literature. *AJNR Am J Neuroradiol* 2004;25(8):1351–1355.
69. Sidek S, Rahmat K, Ramli N. Imaging findings of an isolated deep cerebral venous thrombosis in the absence of superficial sinus thrombosis. *Neurol Asia* 2015;20(2):191–195.
70. Taoka T, Fukusumi A, Miyasaka T, et al. Structure of the Medullary Veins of the Cerebral Hemisphere and Related Disorders. *RadioGraphics* 2017;37(1):281–297.
71. Arrigoni F, Parazzini C, Righini A, et al. Deep medullary vein involvement in neonates with brain damage: an MR imaging study. *AJNR Am J Neuroradiol* 2011;32(11):2030–2036.
72. Menon G, Nair S, Sudhir J, Rao BR, Krishnakumar K. Bilateral thalamic lesions. *Br J Neurosurg* 2010;24(5):566–571.
73. Smith AB, Smirniotopoulos JG, Rushing EJ, Goldstein SJ. Bilateral thalamic lesions. *AJR Am J Roentgenol* 2009;192(2):W53–W62.
74. McKinney AM, Jagadeesan BD, Truwit CL. Central-variant posterior reversible encephalopathy syndrome: brainstem or basal ganglia involvement lacking cortical or subcortical cerebral edema. *AJR Am J Roentgenol* 2013;201(3):631–638.
75. Boukobza M, Crassard I, Bousser MG, Chabriat H. MR imaging features of isolated cortical vein thrombosis: diagnosis and follow-up. *AJNR Am J Neuroradiol* 2009;30(2):344–348.
76. Sagduyu A, Sirin H, Mulayim S, et al. Cerebral cortical and deep venous thrombosis without sinus thrombosis: clinical MRI correlates. *Acta Neurol Scand* 2006;114(4):254–260.
77. Krasnokutsky MV. Cerebral venous thrombosis: a potential mimic of primary traumatic brain injury in infants. *AJR Am J Roentgenol* 2011;197(3):W503–W507.
78. Yu Y, Ren M, Yao S, Zhao X, Qi X. Pathological confirmation of 4 cases with isolated cortical vein thrombosis previously misdiagnosed as brain tumor. *Oncol Lett* 2016;11(1):649–653.
79. Coutinho JM, Ferro JM, Canhão P, et al. Unfractionated or low-molecular weight heparin for the treatment of cerebral venous thrombosis. *Stroke* 2010;41(11):2575–2580.
80. Borhani Haghighi A, Edgell RC, Cruz-Flores S, et al. Mortality of cerebral venous-sinus thrombosis in a large national sample. *Stroke* 2012;43(1):262–264.
81. Nasr DM, Brinjikji W, Cloft HJ, Saposnik G, Rabinstein AA. Mortality in cerebral venous thrombosis: results from the national inpatient sample database. *Cerebrovasc Dis* 2013;35(1):40–44.
82. Dentali F, Gianni M, Crowther MA, Ageno W. Natural history of cerebral vein thrombosis: a systematic review. *Blood* 2006;108(4):1129–1134.
83. Baumgartner RW, Studer A, Arnold M, Georgiadis D. Recanalisation of cerebral venous thrombosis. *J Neurol Neurosurg Psychiatry* 2003;74(4):459–461.



Ischemic Infarction in Young Adults: A Review for Radiologists

Jennifer L. McCarty, MD

Lester Y. Leung, MD, MSc

Ryan B. Peterson, MD

Clark W. Sitton, MD

Amrou Sarraj, MD

Roy F. Riascos, MD

Waleed Brinjikji, MD

Abbreviations: CADASIL = cerebral autosomal dominant arteriopathy with subcortical infarcts and leukoencephalopathy, DSA = digital subtraction angiography, DW = diffusion-weighted, ED = emergency department, FLAIR = fluid-attenuated inversion recovery, ICA = internal carotid artery, MCA = middle cerebral artery, RCVS = reversible cerebral vasoconstriction syndrome, tPA = tissue plasminogen activator, T_{max} = time to maximum residual function, TOAST = Trial of Org 10172 in Acute Stroke Treatment, VWI = vessel wall imaging

RadioGraphics 2019; 39:1629–1648

<https://doi.org/10.1148/rg.2019190033>

Content Codes: ER MR NR VA

From the Departments of Diagnostic and Interventional Imaging (J.L.M., C.W.S., R.F.R.) and Neurology (A.S.), University of Texas Health Science Center at Houston, 6431 Fannin St, MSB 2.130B, Houston, TX 77030; Department of Neurology, Tufts Medical Center, Boston, Mass (L.Y.L.); Department of Radiology and Imaging Sciences, Emory University School of Medicine, Atlanta, Ga (R.B.P.); and Departments of Radiology and Neurosurgery, Mayo Clinic, Rochester, Minn (W.B.). Recipient of a Cum Laude award for an education exhibit at the 2018 RSNA Annual Meeting. Received February 27, 2019; revision requested May 15 and received May 17; accepted May 17. For this journal-based SA-CME activity, the authors L.Y.L. and A.S. have provided disclosures (see end of article); all other authors, the editor, and the reviewers have disclosed no relevant relationships.

Address correspondence to J.L.M. (e-mail: jennifermccartymd@gmail.com).

©RSNA, 2019

SA-CME LEARNING OBJECTIVES

After completing this journal-based SA-CME activity, participants will be able to:

- Describe how causes of ischemic infarction differ between younger and older adults.
- List the most common causes of ischemic infarction in young adults.
- Recognize key imaging features of ischemic stroke subtypes common in young adults.

See rsna.org/learning-center-rg.

Ischemic strokes in young adults are devastatingly debilitating and increasingly frequent. Stroke remains the leading cause of serious disability in the United States. The consequences of this familiar disease in this atypical age group are especially detrimental and long lasting. Ischemic stroke in young adults is now emerging as a public health issue, one in which radiologists can play a key role. The incidence of ischemic infarction in young adults has risen over the past couple of decades. Increased public awareness, increased use of MRI and angiography, and more accurate diagnosis may in part explain the increased detection of stroke in young adults. The increased prevalence of stroke risk factors in young adults (especially sedentary lifestyle and hypertension) may also contribute. However, compared with older adults, young adults have fewer ischemic infarcts related to the standard cardiovascular risk factors and large- or small-vessel disease. Instead, their infarcts most commonly result from cardioembolic disease and other demonstrated causes (ie, dissection). Thus, radiologists must expand their differential diagnoses to appropriately diagnose ischemic strokes and identify their causes in the young adult population. From the more frequent cardioembolism and dissection to the less common vasculitis, drug-related, CADASIL (cerebral autosomal dominant arteriopathy with subcortical infarcts and leukoencephalopathy), moyamoya, and hypercoagulable state-related infarcts, this article covers a wide breadth of causes and imaging findings of ischemic stroke in young adults.

©RSNA, 2019 • radiographics.rsna.org

Introduction

The incidence of ischemic infarction in young adults is increasing, and this familiar disease in this atypical age group is emerging as a public health issue (1,2). “Young adults” have been defined with different age ranges, from 18–45 to 18–55 years old (1,3,4). Stroke in all ages of adults is the fifth leading cause of death in the United States. The vast majority of infarcts (87%) are ischemic, 10%–14% of which occur in young adults (3,5,6). Stroke remains the leading cause of serious disability in the United States. Ischemic infarction can be particularly devastating in this younger population given their extended duration of disability, frequent caregiver roles, and continued exposure to complications (5).

Ischemic infarction is categorized into five subtypes: large-artery atherosclerosis, small-vessel occlusion, cardioembolic, other demonstrated cause, and undetermined cause (Table 1) (7,8). Compared with older adults, young adults have fewer ischemic infarcts from large- or small-vessel disease and more from cardioembolism (up to 46%) and other demonstrated causes (up to 34%), most commonly dissection and vasculitis or vasospasm (Fig 1) (3,4). This article reviews the epidemiology, workup, and causes of

TEACHING POINTS

- Stroke remains the leading cause of serious disability in the United States. Ischemic infarction can be particularly devastating in this younger population given their extended duration of disability, frequent caregiver roles, and continued exposure to complications.
- Compared with older adults, young adults have fewer ischemic infarcts from large- or small-vessel disease and more from cardioembolism (up to 46%) and other demonstrated causes (up to 34%), most commonly dissection and vasculitis or vasospasm.
- Posterior circulation (posterior cerebral artery, basilar artery, and vertebral artery-related) syndromes can manifest with a range of symptoms, from fluctuating responsiveness and visual field deficits to nonspecific complaints of headache, neck or jaw pain, nausea, and dizziness, that are particularly vague and easy to overlook as stroke symptoms in this young patient population.
- No universal stroke imaging algorithm exists for young adults, and protocols vary between institutions. Any imaging pathway used for ischemic infarction in young adults should, at the very least, determine the presence or absence of hemorrhage, evaluate for stroke mimics, and assess candidacy for intra-arterial therapy.
- Cervical carotid or vertebral artery dissection is one of the most common causes of stroke in young adults, accounting for 2% of strokes overall but up to 20% of strokes in patients 25 years old and younger.

ischemic infarction in young adults, focusing on how it differs from that in older adults.

Epidemiology

The reasons behind the increased frequency of acute stroke in young adults are uncertain (10,11). Several factors may explain a contemporary rise in stroke cases in young adults. First, awareness that stroke can affect people of all ages is increasing as a result of public health efforts and media coverage of famous people affected by stroke at young ages (such as former professional American football player Tedy Bruschi). This knowledge, coupled with education about common stroke symptoms (ie, “FAST”: face, arms, speech, time), may lead to earlier pursuit of emergent medical care after stroke onset.

Second, increased awareness among clinicians may lead to clinical decision making that improves the probability of an accurate diagnosis via referral to emergency departments (EDs) from primary care practices, consultation with neurologists, and performing neuroimaging (12). Notably, the increased availability and ordering of MRI has enhanced ischemic stroke diagnosis owing to the high sensitivity and specificity of diffusion-weighted (DW) imaging. Finally, there is a high prevalence of atherosclerotic risk factors (hypertension, diabetes mellitus, and sedentary lifestyle) among young adults

with stroke, and it is suspected that these conditions may contribute to the increased frequency of stroke cases (1,4,13).

Clinical Approach

Diagnosis

Studies have demonstrated that compared with older adults, young adults tend to seek medical attention later after the onset of stroke symptoms (sometimes days later) and tend to have milder severity of stroke deficits (13,14). When they do present to EDs, they are frequently misdiagnosed and are not always admitted (12). Thus, a high level of suspicion is necessary to diagnose the infarct (13,14). Clinicians are tasked with quickly assessing the patient's current symptoms, last known well time (LKWT), and pertinent medical history. The National Institutes of Health Stroke Scale is the standard of reference for quantifying severity (15).

The focus is also localization. Anterior circulation (anterior cerebral artery, middle cerebral artery [MCA], and internal carotid artery [ICA]-related) syndromes can manifest with variable contralateral hemiparesis, contralateral hemisensory loss, and aphasia (in the dominant hemisphere). Posterior circulation (posterior cerebral artery, basilar artery, and vertebral artery-related) syndromes can manifest with a range of symptoms, from fluctuating responsiveness and visual field deficits to nonspecific complaints of headache, neck or jaw pain, nausea, and dizziness, that are particularly vague and easy to overlook as stroke symptoms in this young patient population (16). Cranial nerve palsies in either circulation or a Horner syndrome can be due to ischemia or stretching or compression of nerves from an intramural hematoma (17).

Determining Cause

Determining the cause is critical in these young patients and can be straightforward (as in dissection) or require an expanded workup. Because cardioembolic stroke is the most common subtype of ischemic stroke in young adults, transthoracic and transesophageal echocardiography and electrocardiography are often performed early. Holter monitoring for 30 days may be considered if cardioembolic stroke is suspected but transesophageal echocardiography results are negative. Further workup for vasculitis entails catheter angiography, lumbar puncture, and blood testing for vasculitic inflammatory markers such as erythrocyte sedimentation rate, C-reactive protein, perinuclear antineutrophil cytoplasmic antibodies, cytoplasmic antineutrophil cytoplasmic antibodies, and lupus antibody. For other

Table 1: Subtypes of Ischemic Infarction

| Defining Features, Imaging Findings, and Causes | Cardioembolism | Other Demonstrated Causes | Undetermined Cause | Small-Vessel Occlusion (Lacunar) | Large-Artery Atherosclerosis |
|-------------------------------------------------|---------------------------------------------------------------------------------------------------------------------------------------|-----------------------------------------------------------------------------------------------------------------------------------------------------------------------------------------------|----------------------------------------------------------------------------------------------------------------|-----------------------------------------------------------------------------------------------------------------------------------------------------|----------------------------------------------------------------------------------------------------------------------------------------------------------------------------------------|
| Defining features and imaging findings | Scattered small or larger confluent infarcts, both superficial and deep, often in multiple vascular territories | Single explained stroke cause Variable appearances at imaging | Two or more potential causes or negative workup results or incomplete workup Variable appearance at imaging | Deep infarct (<1.5 cm) in basal ganglia, internal capsule, thalamus, or brainstem and no concurrent large-artery atherosclerosis in relevant vessel | Cerebral cortex, brainstem, or cerebellar infarct plus extracranial or intracranial large-artery atherosclerosis (ICA origins, carotid siphons, V4 vertebral arteries, basilar artery) |
| Causes | Septic emboli, bland emboli (from cardiac masses, right-to-left shunts, arrhythmias, and cardio-myopathy), air emboli, and fat emboli | Nonatherosclerotic vasculopathy (dissection, RCVS, moyamoya, vasculitis, drug-related, CADASIL) Prothrombotic (factor V Leiden, antiphospholipid, oral contraceptive or pregnancy related) | Unknown for each case | Lacunar infarction from small end vessel occlusion | Thromboembolic from vulnerable large-vessel plaques Decreased perfusion from parent vessel stenosis or occlusion |

Note.—CADASIL = cerebral autosomal dominant arteriopathy with subcortical infarcts and leukoencephalopathy, ICA = internal carotid artery, RCVS = reversible cerebral vasoconstriction syndrome.

patients, it may be necessary to order a hypercoagulability testing panel of functional protein C, protein S, antithrombin III, factor V Leiden mutation, and prothrombin mutations (3).

Treatment

The catchphrase for acute stroke treatment has shifted from “time is brain” to “tissue is the issue,” as more value is placed on tissue viability than on LKWT. Still, LKWT remains a crucial piece of the clinical evaluation for treatment with tissue plasminogen activator (tPA) and intra-arterial therapy (IAT). The window for tPA administration used to be 4.5 hours from LKWT in patients with ischemic stroke and no intracranial hemorrhage. Several studies over the past few years have shown IAT in patients with large-vascular occlusion to have good outcomes compared with those in control groups, with windows ranging from less than 6 hours to up to 24 hours with penumbral tissue imaging in the DAWN (DWI or CTP Assessment with Clinical Mismatch in the Triage of Wake-up and Late Presenting Strokes Undergoing Neurointervention with Trevo) trial (18–24). While these recent trials have served as the reference standards for IAT, their mean patient ages ranged from 65 to 71.5 years old.

There is no IAT trial or algorithm specifically for young adults at this time.

In young adults, medical therapy is the mainstay of treatment for many causes of ischemic infarction unrelated to large-vessel occlusion, including most cardioembolic, dissection, and prothrombotic-state strokes. Endovascular and surgical revascularization techniques are generally reserved for patients with dissection or vasospasm who have recurrent strokes despite medical therapy or for cases of severe hemodynamic compromise. The same is true of surgical procedures, which are generally reserved for patients with cardiac valve vegetations, cardiac masses, patent foramen ovale (PFO), or carotid steno-occlusive disease and recurrent strokes.

Imaging

CT versus MRI

No universal stroke imaging algorithm exists for young adults, and protocols vary between institutions. Any imaging pathway used for ischemic infarction in young adults should, at the very least, determine the presence or absence of hemorrhage, evaluate for stroke mimics, and assess candidacy for IAT. So which modality to choose,

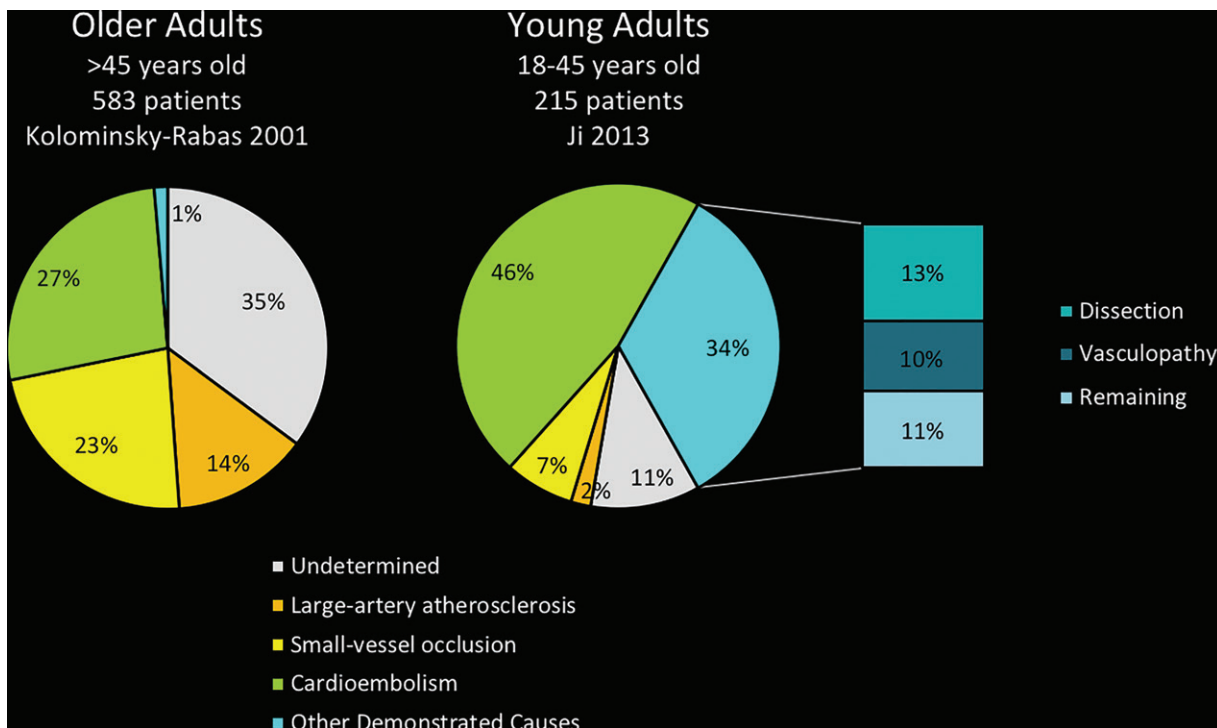


Figure 1. Ischemic infarction in older adults versus young adults. Young adults (age 18–45 years), compared with older adults (>45 years old), have more ischemic stroke from cardioembolic causes (46% vs 27%, respectively) and other determined causes (34% vs 1%, respectively). Dissection is the most common cause of the other determined cause category in young adults, accounting for 13% of ischemic infarction in patients 18–45 years old and up to 20% in patients under 25 years old. Data are from references 3 (young adults) and 9 (older adults).

Table 2: CT versus MRI for Evaluation of Acute Ischemic Stroke

| Parameter | CT | MRI |
|----------------------------------------------------|------------------------------------------------------------------------------|------------------------------------------------------------------------------------------|
| Availability | Widely available | Not available in some smaller and community hospitals |
| Proximity to ED | In or near most EDs | Potentially far away |
| Speed | Very fast: CT, CT angiography, and CT perfusion imaging performed in seconds | Becoming faster: MRI, MR angiography, and MR perfusion imaging performed in 6–15 minutes |
| Screening | None | Necessitates safety screening: pacing devices, retained metal fragments, and so on |
| Quantitative analysis | Available | Available |
| Radiation | Some | None: appealing for stroke evaluation in pediatric patients |
| Sensitivity for small infarcts and venous infarcts | Limited | High |

CT or MRI? Each has distinct advantages and disadvantages (Table 2).

We advocate using CT first in the acute setting, the most important reason being that the speed and wide availability allow faster assessment and treatment with tPA in appropriate patients (Fig 2). Notably, acute stroke evaluation with MRI is gaining popularity owing to increased sensitivity (including for small infarcts and stroke mimics), improving proximity to EDs, and decreasing imaging times. Some stroke

MRI protocols with nonenhanced DW imaging, gradient-echo imaging, and fluid-attenuated inversion-recovery (FLAIR) imaging along with contrast-enhanced MR angiography of the head and neck and postcontrast perfusion imaging can be performed in 6–15 minutes (25,26).

Cross-sectional Angiography

CT and MR angiography are critical components of the standard workup. Their noninvasive nature, wide availability, and high sensitivity allow quick

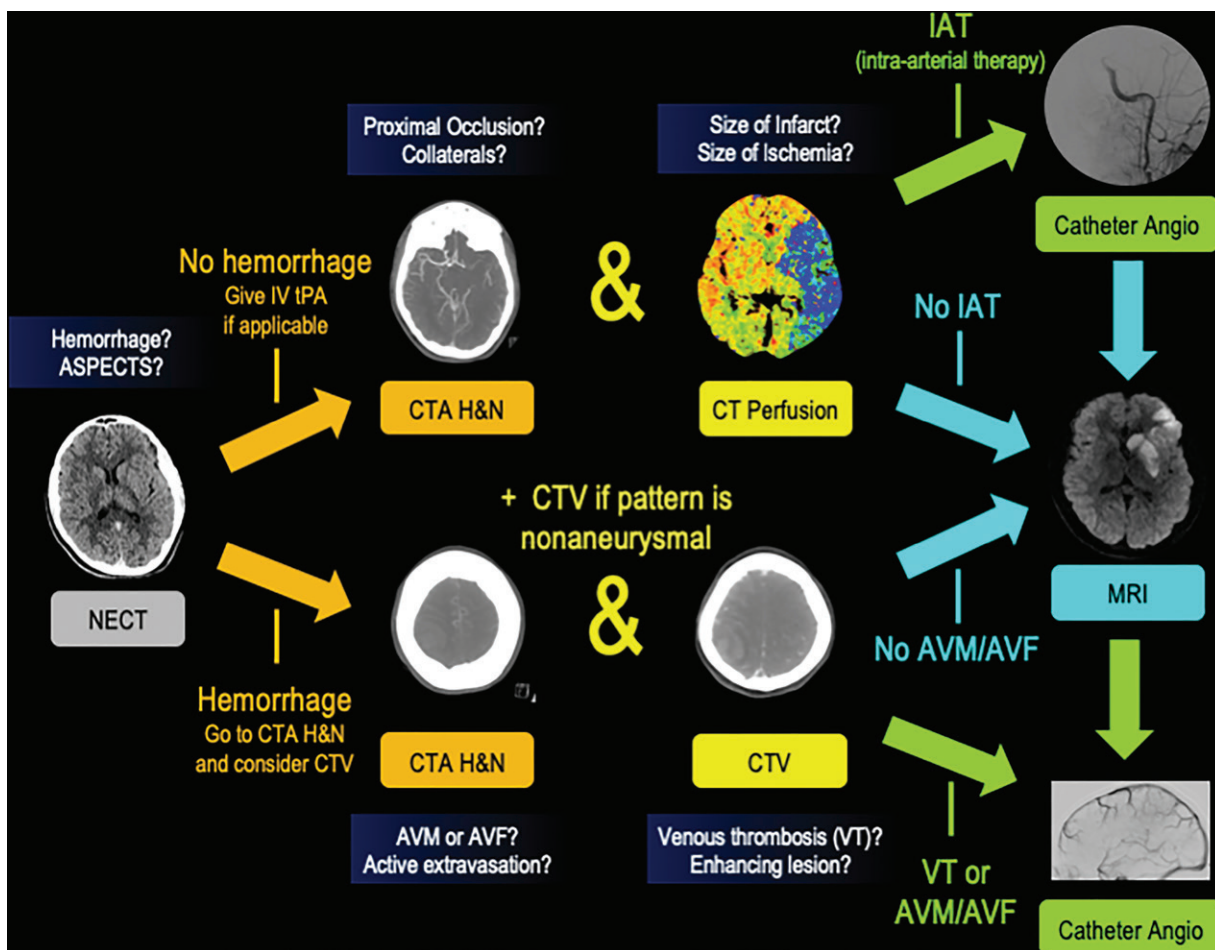


Figure 2. Flowchart shows the imaging pathway used for young adults with potential ischemic infarction that determines the presence or absence of hemorrhage, stroke mimics, and candidacy for IAT. We advocate starting with CT, as the speed and availability allow quicker tPA administration in appropriate patients. The larger intracranial veins must be closely evaluated at all modalities. For emergent evaluation in cases of intracranial hemorrhage with a nonaneurysmal pattern, we recommend including CT venography (CTV) to evaluate for venous thrombosis (VT). ASPECTS = Alberta Stroke Program Early CT Score, AVF = arteriovenous fistula, AVM = arteriovenous malformation, Catheter Angio = catheter angiography, CTA H&N = CT angiography of the head, brain, and neck, IV = intravenous, NECT = nonenhanced CT.

accurate vascular interpretation and make them preferred over catheter angiography. Additionally, CT angiography and dissection protocol MRI and MR angiography (with axial fat-saturated T1-weighted imaging) have the advantage over catheter angiography of demonstrating the vessel walls of the larger arteries in the neck in this young population with increased frequency of dissections (27,28). Overall, we recommend having a low threshold to perform urgent vascular imaging in young adults with ischemic stroke, including cross-sectional venous imaging, to allow prudent evaluation of venous thrombosis of the cortical veins or dural sinuses.

Perfusion Imaging

Perfusion imaging is essential in young stroke patients, as core infarct volume is increasingly emphasized over LKWT in selecting patients for IAT in the setting of large-vessel occlusion.

CT perfusion examination involves continuous low-dose scanning of the brain parenchyma during dynamic intravenous infusion of contrast material. This yields a first-pass time-attenuation curve for the intracranial vessels and for each voxel of brain parenchyma, from which perfusion parameters of cerebral blood flow, cerebral blood volume, time to peak, and mean transit time can be calculated.

Subjective evaluation of affected tissue volumes using these parameters can be challenging; however, automated postprocessing methods are available, providing volumes of core infarction (cerebral blood flow <30% of normal) and penumbra (time to maximum residual function [T_{max}] >6 seconds) (Fig 3) (29,30). Timing of symptom onset, clot location, and hemodynamic or metabolic compromise can all affect the reliability of software predictions, and it is important to understand the methodology of their particular

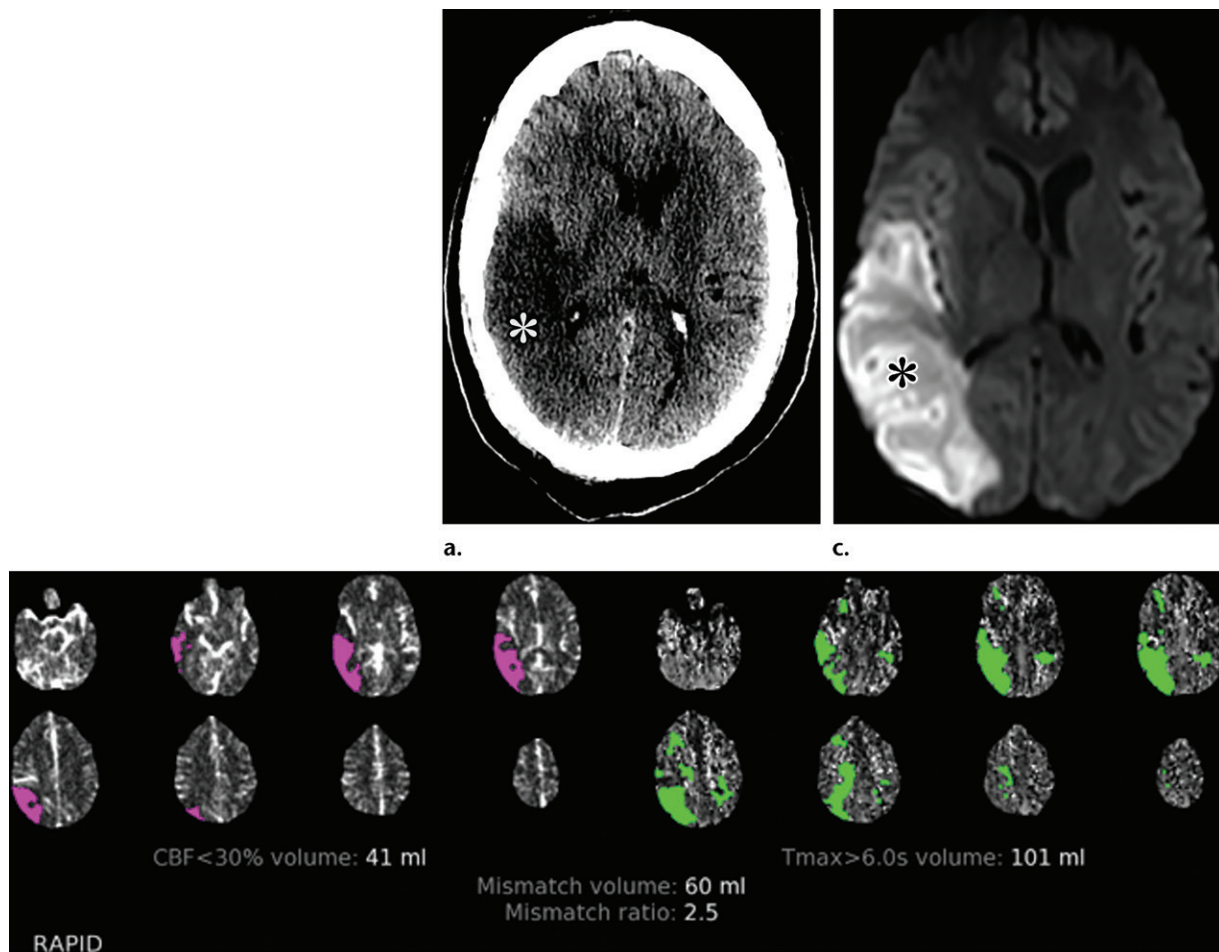


Figure 3. Bland emboli from cardiomyopathy and atrial fibrillation in a 40-year-old patient with hypertension and obesity who presented to the ED with a headache and left-sided weakness that began 2 days earlier. **(a)** Nonenhanced CT image shows a subacute right MCA ischemic infarction (*). **(b)** CT perfusion image shows a corresponding core infarct given the cerebral blood flow (CBF) of less than 30% (purple) and matching T_{max} greater than 6.0 seconds (green) abnormality, without a large penumbra. **(c)** DW image shows the final infarct size (*), which is consistent with that on the nonenhanced CT and CT perfusion images. The patient was diagnosed with atrial fibrillation in the ED. Transthoracic echocardiography 1 day after presentation showed dilated cardiomyopathy, left ventricle hypokinesis, and ejection fraction less than 20%.

perfusion processing and the clinical context in which it was developed. Nonetheless, in coordination with evaluation of anatomic imaging, particularly CT angiography, perfusion imaging can provide a valuable snapshot of information about the evolving physiology and hemodynamics of each ischemic event.

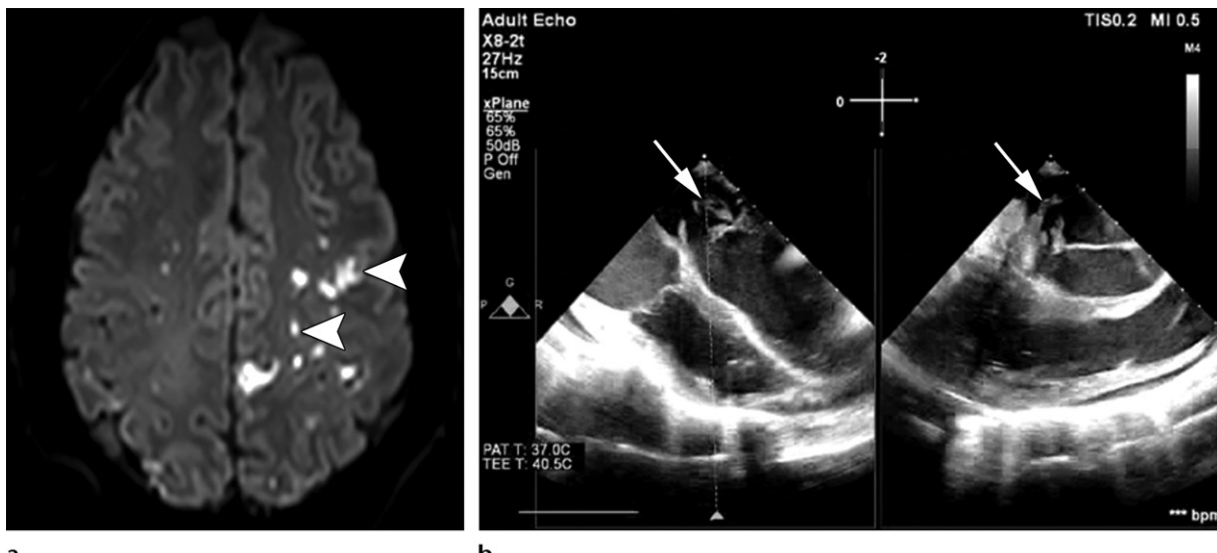
Vessel Wall Imaging

Vessel wall imaging (VWI) is a relatively new technique that uses black-blood sequences and pre- and postcontrast acquisitions to evaluate vessel walls. VWI is increasingly used to differentiate between intracranial diseases such as vasculitis, reversible cerebral vasoconstriction syndrome (RCVS), moyamoya, dissection, and atherosclerosis by evaluating stenosis, eccentric versus concentric nature, location, and enhancement (28–30). This technique has a distinct advantage over other

cross-sectional techniques and catheter angiography, which cannot depict small intracranial vessels much beyond stenosis severity and location.

Catheter Angiography

Conventional catheter angiography is infrequently indicated for workup of ischemic stroke in young adults. Still, despite the high sensitivity of CT angiography and MR angiography, catheter angiography better depicts vessels around the skull base and small distal intracranial vessels and thus remains the reference standard for diagnostic evaluation of certain causes. Appropriate indications include workup for intracranial steno-occlusive diseases such as moyamoya, diagnostic angiography for nonatherosclerotic vasculopathy, and when performing or planning interventions for revascularization of intracranial and extracranial vessel occlusions.



a.

b.

Figure 4. Septic emboli from infectious endocarditis in a 29-year-old patient who presented to the ED with right-sided weakness and a history of recent intravenous drug use. (a) Axial DW image shows numerous bilateral, small, scattered, cortical, and deep white matter ischemic infarcts (arrowheads), more pronounced on the left and most consistent with an embolic source. The patient had *Staphylococcus* septicemia. (b) Transesophageal echocardiogram reveals a large 4.0 × 2.0-cm anterior mitral valve vegetation (arrows). (Fig 4b courtesy of Patrick Kee, MBBS, PhD, University of Texas Health Science Center, Houston, Tex.)

Causes

The most common classification of subtypes of ischemic stroke is the Trial of Org 10172 in Acute Stroke Treatment (TOAST) classification (Table 1) (7,8). This scheme divides ischemic strokes into five categories, which are discussed in order from most common to least common cause of ischemic stroke in young adults.

Cardioembolic Stroke

Cardioembolic stroke is the most frequent subtype in young adults and accounts for up to 46% of ischemic infarcts in this age group (3,4). Imaging findings typically show a single large vessel occlusion from a solitary embolus or small scattered infarcts in multiple territories from showering of emboli. They may be categorized on the basis of sterility, cardiac disease, or clot composition and include septic emboli, bland emboli (from cardiac masses, right-to-left shunts, arrhythmias, and cardiomyopathy), air emboli, and fat emboli.

Septic Emboli

Intracranial complications occur in 20%–40% of patients with infective endocarditis and are most frequently ischemic stroke (Fig 4). Abscess, parenchymal hemorrhage, subarachnoid hemorrhage, or mycotic aneurysm can also occur. Occult small embolic stroke (37%) and subcortical microhemorrhages (57%) are frequent even in asymptomatic patients (31). Acute ischemic lesions manifest mostly as small scattered infarcts throughout the cerebral hemispheres, as the stroke mechanism is from tiny infectious emboli

from cardiac valve vegetations. Only a small portion of patients with infective endocarditis present with microabscesses, which show blooming on susceptibility-weighted images and gradient-echo images and usually enhance peripherally but may or may not demonstrate restricted diffusion, depending on the size of the lesion (31). While there are many causes of infectious endocarditis, one of the more common associations is intravenous drug use.

Bland Emboli

Atrial Myxoma.—Atrial myxoma is the most common primary cardiac tumor in adults and is typically seen in young adults. These patients most often present with symptoms related to mitral valve obstruction resulting in dizziness, palpitations, dyspnea, and congestive heart failure. A subset of patients (12%–46%) can present with isolated neurologic symptoms related to cerebral infarcts from embolization (Fig 5) (32). Most myxoma-related embolic infarcts primarily arise from surface thrombus surrounding the myxoma; however, direct embolization of myxomatous tumor can also occur (32).

Patent Foramen Ovale.—The foramen ovale connects the left and right atria in utero and generally closes shortly after birth. Failure to close results in patent foramen ovale (PFO). This may place a patient at increased risk for paradoxical thromboembolism through a right-to-left shunt; however, 25% of adults have PFO.

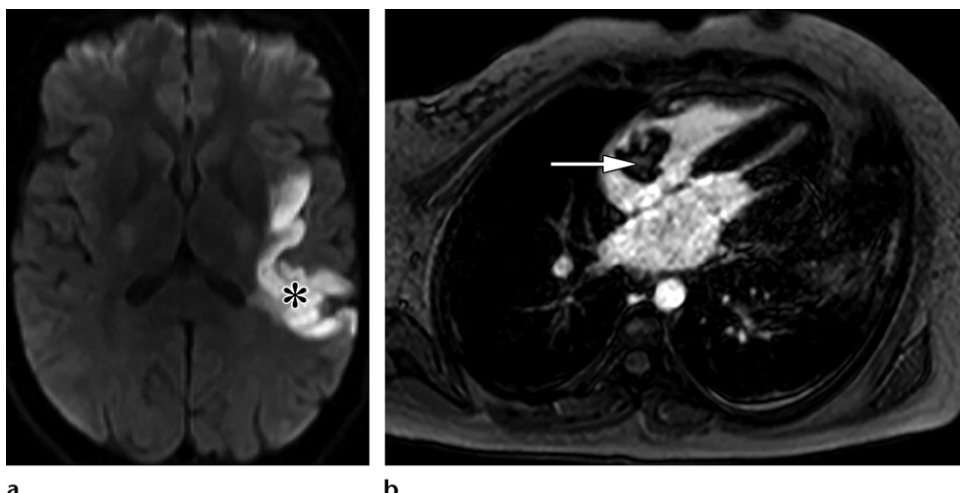


Figure 5. Bland emboli from atrial myxoma and patent foramen ovale (PFO). **(a)** Right atrial myxoma and associated ischemic infarct in a 32-year-old patient who presented to the ED with right-sided weakness and slurred speech. Axial DW image shows a confluent ischemic infarct of the left MCA (*). The patient underwent echocardiography and subsequent MRI, which revealed a PFO and an atrial myxoma. **(b)** Right atrial myxoma in a different 26-year-old patient, also with a history of ischemic infarction. Axial postcontrast MR image shows a large right atrial centrally enhancing mass (arrow). (Fig 5b courtesy of Erika Odisio, MD, and Mina Hanna, MD, University of Texas Health Science Center, Houston, Tex.)

The association between cryptogenic stroke and PFO treatment remains controversial (33–36). Some studies report that this abnormality is found in up to 50% of patients with cryptogenic stroke and is thought to account for 37% of young adult patients with cardioembolic stroke (4,33). While recent studies show reduction in risk of recurrent stroke, the number needed to treat was modest, ranging from 20 to 42 (34–36). PFO may be diagnosed with echocardiography with Doppler flow imaging and saline contrast material (bubble study).

Dilated Cardiomyopathy and Atrial Fibrillation.—Nearly one-third of cardioembolic infarcts are due to dilated cardiomyopathy (17%) and atrial fibrillation (14%), making them the second and third most common cardioembolic causes in young adults with ischemic infarction (4). Both factors pose increased risk of thromboembolism owing to stasis of blood in cardiac chambers and thrombus formation (37). They not only put patients at increased risk for a major cerebrovascular event (Fig 3) but also at risk for silent cerebral infarction syndrome (39% of patients with dilated cardiomyopathy), resulting in subclinical infarction and likely contributing to cognitive deficits, early progressive dementia, and depression (37).

Intravascular Air Emboli

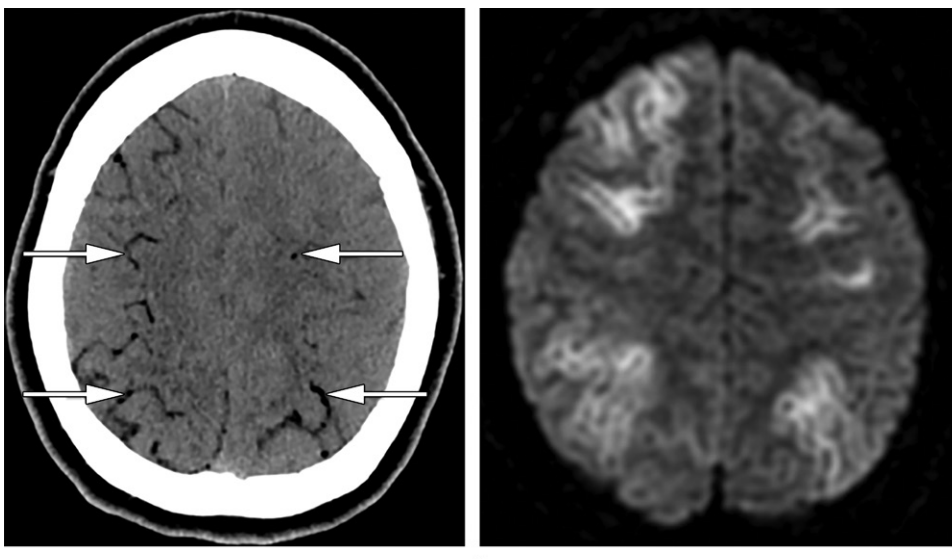
Cerebrovascular air embolism is rare but can occur during many invasive procedures, including central venous catheter placement. Any time there is access between the external environment and the vascular system with an atmospheric

pressure gradient, there is risk for air embolism (38). If the introduction of air is before the branching vessels of the aorta (ie, venous air that travels through a right-to-left shunt), the infarcts are usually smaller and scattered and involve multiple vascular territories (Fig 6). If the introduction of air is directly related to a carotid or vertebrobasilar interventional procedure, infarcts are typically confined to one vascular territory.

Fat Emboli

Cerebral fat embolism syndrome is classically seen in patients with large displaced fractures or sickle cell disease (39). Displaced fracture marrow fat droplets or fat emboli released from bone marrow necrosis in patients with sickle cell disease (usually in crisis) can traverse through a right-to-left cardiac shunt or can deform and travel through intact pulmonary capillary beds to reach the central nervous system. Patients can present with abnormal mentation or focal neurologic deficits after trauma.

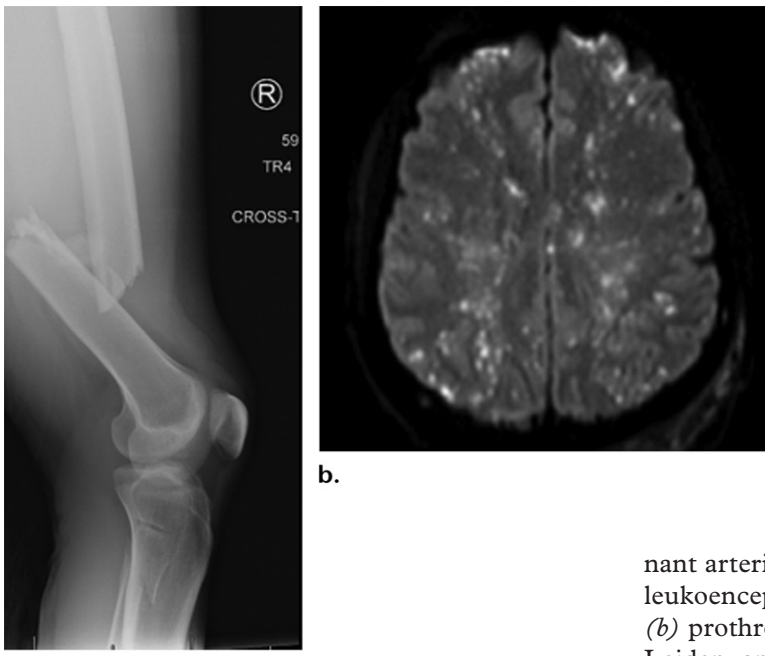
CT images are usually normal. A “starfield” pattern of innumerable tiny foci of restricted diffusion and FLAIR signal intensity abnormality scattered throughout the entire brain parenchyma is the classic pattern on MR images (Fig 7). The number of lesions can vary, and an increased number of lesions correlates with a poorer score according to the Glasgow Coma Scale (39). Traumatic axonal injury is the main differential diagnosis in a patient with traumatic injury, but these shear injuries typically have larger and more linear corresponding foci with magnetic susceptibility on susceptibility-weighted images and gradient-echo images than does fat embolization.



a.

b.

Figure 6. Intravascular air emboli in a 33-year-old patient who was nonresponsive after endoscopic retrograde cholangiopancreatography. (a) Axial nonenhanced CT image shows extensive air throughout the distal arterial branches (arrows). There was no proximal arterial air embolus and no air in the larger intradural sinuses. (b) Follow-up axial MR image shows bilateral cortical ischemic infarcts that follow the distribution of the most pronounced areas of intracranial air.



a.

Figure 7. Traumatic fat emboli in a 43-year-old patient who demonstrated continued altered mental status after being admitted for a comminuted femoral fracture. (a) Radiograph shows the fracture. (b) Axial MR image shows diffuse innumerable punctate foci of restricted diffusion throughout the cerebral hemispheres involving gray and white matter in the characteristic "starfield" pattern of fat emboli. Diffuse axonal injury is the main differential diagnosis but usually has larger and more linear associated foci of magnetic susceptibility than seen with fat emboli.

syndrome. Shear injuries also often have some CT-evident hemorrhagic foci.

Other Demonstrated Causes

This catchall category is the second most common subtype of ischemic infarction in young adults, accounting for up to 34% of cases (3,4). In the TOAST classification, these are divided into (a) nonatherosclerotic vasculopathies (dissection, carotid web, RCVS, vasculitis, drug related, CADASIL [cerebral autosomal domi-

nant arteriopathy with subcortical infarcts and leukoencephalopathy], and moyamoya) and (b) prothrombotic disorders and states (factor V Leiden, antiphospholipid syndrome, oral contraceptive use, pregnancy and puerperium) (8).

Nonatherosclerotic Vasculopathies

Vasculopathy is an all-encompassing term used to describe any disease that affects the blood vessels, including degenerative, metabolic, inflammatory, coagulopathic, and functional disorders (40). While any vasculopathy can affect any age group, there are more specific entities that should be considered in the younger population.

Dissection.—Cervical carotid or vertebral artery dissection is one of the most common causes

of stroke in young adults, accounting for 2% of strokes overall but up to 20% of strokes in patients 25 years old and younger (41,42). They can be spontaneous (Fig 8) or traumatic (Fig 9) and are associated with causes ranging from blunt cerebrovascular trauma to chiropractic adjustments, golf swings, yoga, and even coughing fits (27,43).

Dissection is a longitudinal subintimal tear in the vessel wall resulting in intramural hemorrhage collecting in the false lumen that can cause (a) progressive stenosis or occlusion of the parent vessel, (b) occlusion of perforating vessels arising from the parent vessel, or (c) creation of a double lumen, which can result in emboli. The mechanism of stroke in patients with carotid dissection includes thromboembolic stroke in about 80% of cases, hypoperfusion from high-grade stenosis or occlusion in 15%, and mixed mechanisms in 5% (44). ICA dissection typically begins 2–3 cm above the carotid bulb, while vertebral artery dissection typically occurs at the C1–C2 level.

Use of angiography is crucial. CT angiography can demonstrate a long thin irregular filiform stenosis (string of pearls sign), tapering of the true lumen to a point (flame sign), or mural thickening from the intramural hemorrhage (17,45). Fat-saturated T1-weighted MRI is the most sensitive imaging modality for depiction of a cervical arterial dissection. The intramural hematoma is typically T1 and T2 hypointense in the hyperacute phase and T1 hyperintense when subacute owing to methemoglobin in the false lumen (Fig 10) (28). Up to 10% of patients will have bilateral dissection (Fig 11).

Carotid Web.—Carotid web is an increasingly recognized cause of acute ischemic stroke in young adults. Up to 10% of stroke patients age 60 years or younger have a carotid web (46). These lesions are thought to represent an atypical form of fibromuscular dysplasia and are characterized by a shelflike projection of fibrous intimal thickening just beyond the origin of the ICA (Fig 12). There should be no or only minimal associated wall thickening, as this would suggest an atherosclerotic plaque rather than a web (46).

At VWI, the web can be seen as a thin nonenhancing fibrous band with no associated intramural hemorrhage or lipid core (47). The mechanism of stroke in these patients is thought to be due to stasis of blood distal to the carotid web and associated thrombus formation. Stroke recurrence rates in this population are high, even in the setting of antiplatelet therapy or anticoagulation, and carotid webs may be treated with angioplasty or stent placement (48–50).

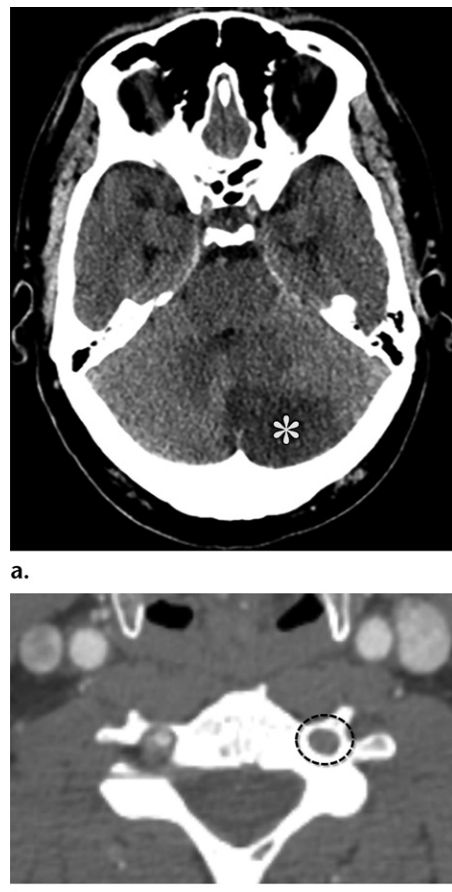


Figure 8. Spontaneous cervical vertebral artery dissection in a 44-year-old patient who presented to the ED with sudden-onset headache and dizziness and no history of trauma. (a) Axial nonenhanced CT image shows an infarct of the left inferior cerebellar hemisphere (*) and a right thalamic infarct (not shown). Given the multiple posterior circulation infarcts, vertebral artery dissection was suspected, and CT angiography was suggested. (b) Axial CT angiogram of the neck shows absent filling of the left V2 vertebral artery (dashed circle). Posterior circulation infarcts in young adults should be presumed to be from dissection until proved otherwise.

Reversible Cerebral Vasoconstriction Syndrome

RCVS.—RCVS is a combined clinical and radiographic diagnosis of unknown pathophysiology. It may occur spontaneously or after a trigger such as use of vasoactive medications, illicit or recreational drug use, trauma, postpartum state or eclampsia, neoplasm, migraine, or cervical artery dissection (51). The diagnostic criteria for RCVS include (a) severe acute thunderclap headache; (b) associated multifocal segmental cerebral artery vasoconstriction at CT angiography, MR angiography, or diagnostic angiography; (c) reversibility of vasoconstrictive abnormalities within 12 weeks; (d) normal or near-normal results of cerebrospinal fluid analysis; (e) no aneurysmal cause of subarachnoid hemorrhage;

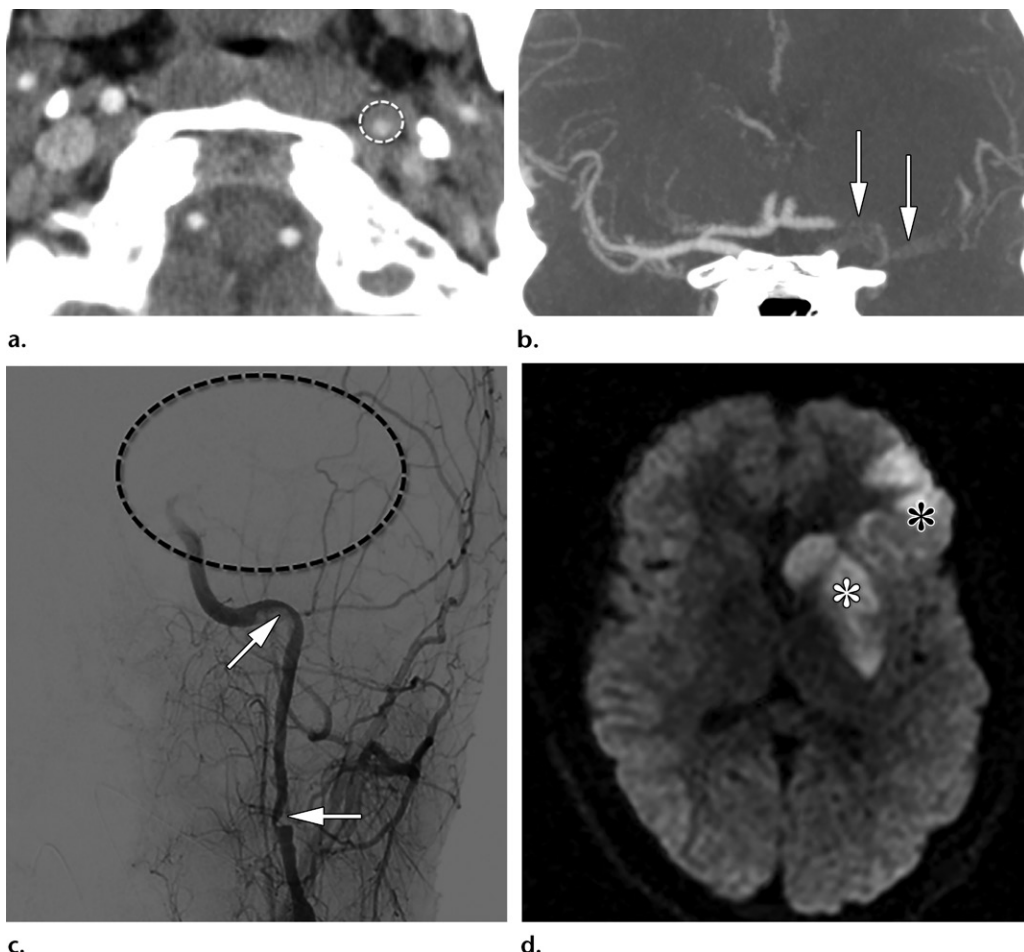


Figure 9. Traumatic cervical ICA dissection in an 18-year-old football player who presented with headache and slurred speech after being tackled. **(a)** Axial CT angiogram shows crescentic soft tissue around the left cervical ICA and asymmetrical small lumen (dashed circle). This blunt cerebrovascular traumatic dissection resulted in distal emboli. **(b)** Coronal maximum intensity projection CT angiogram shows the T-shaped occlusion (arrows) of the left carotid terminus, beginning proximal to the A1 anterior cerebral artery and M1 MCA. **(c)** Subsequent image from digital subtraction angiography (DSA) shows the left ICA with greater than 50% luminal narrowing (arrows) with carotid terminus occlusion and lack of left anterior circulation filling (dashed circle). **(d)** Axial MR image shows the final infarct in the left MCA territory, including the left inferior frontal gyrus (black *) and basal ganglia (white *).

and (f) uniphasic disease course without new symptoms after 1 month of onset (51).

Clinical workup and diagnostic imaging are used primarily to exclude alternative diagnoses, mostly infectious and inflammatory (29). Subarachnoid hemorrhage, when present, has a non-aneurysmal pattern involving the high convexities instead of the basal cisterns. The hemorrhage may not be where the vessels appear the most constricted. Multifocal beaded appearance of the larger intracranial vessels in multiple vascular territories is diagnostic of cerebral vasoconstriction but not specific for RCVS.

CT angiography and MR angiography are commonly used in the initial workup, although conventional angiography is the reference standard for diagnosing vasoconstriction with superior distal vessel evaluation. Vasoconstriction in patients with RCVS may not be visualized in the

acute setting during the thunderclap headache and may not be present in the 1st week (Fig 13). True infarcts from RCVS occur but are rare. Instead, subarachnoid hemorrhage and vasospasm are more commonly seen.

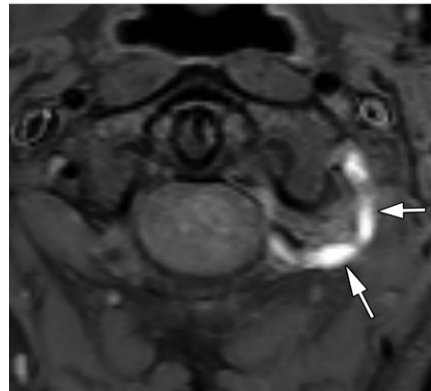
The presence of an infarct with vascular narrowing is more suggestive of central nervous system vasculitis. VWI can also be used to differentiate RCVS from other vasculopathies including vasculitis. RCVS has no or mild enhancement, while vasculitis has intense enhancement (28–30). This is of importance, as RCVS is treated with observation and calcium channel blockers, while vasculitis is treated with steroids and immunosuppressants (28).

Vasculitis.—Vasculitis is a specific vasculopathy defined as inflammation of the blood vessel wall with or without necrosis (52). The cause of

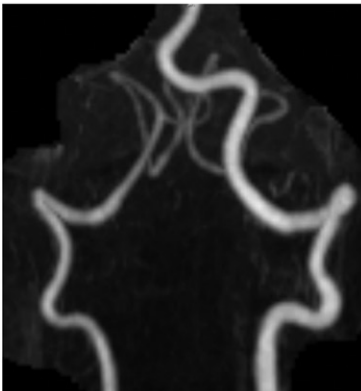
Figure 10. Spontaneous cervical vertebral artery dissection in a 40-year-old patient who presented to the ED with severe neck and jaw pain. (a) Coronal maximum intensity projection MR image of the vertebrobasilar system shows irregular filiform narrowing of the distal left vertebral artery (arrow). (b) Axial T1-weighted fat-saturated MR image shows a hyperintense intramural hematoma in the left vertebral artery (arrows) at the level of C1 and C2. (c, d) MR angiogram (c) and MR image (d) 3 months after anticoagulation therapy show resolution.



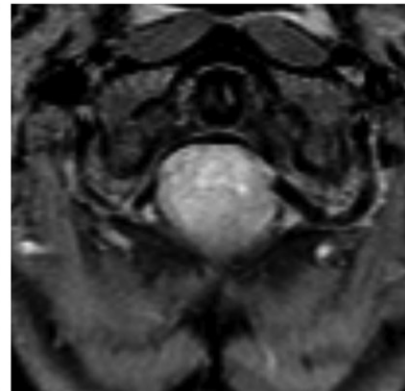
a.



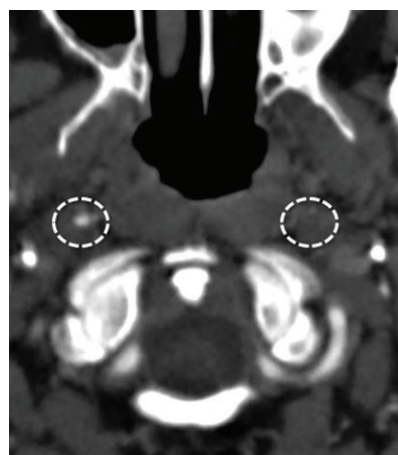
b.



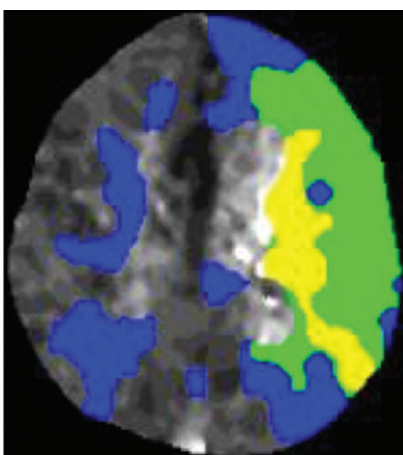
c.



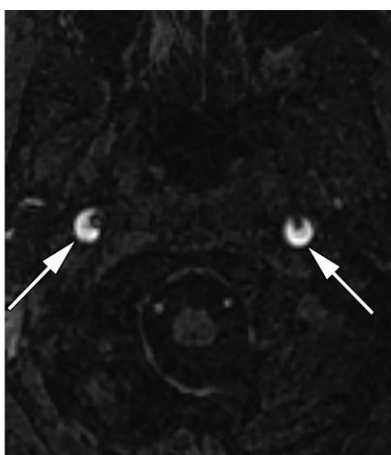
d.



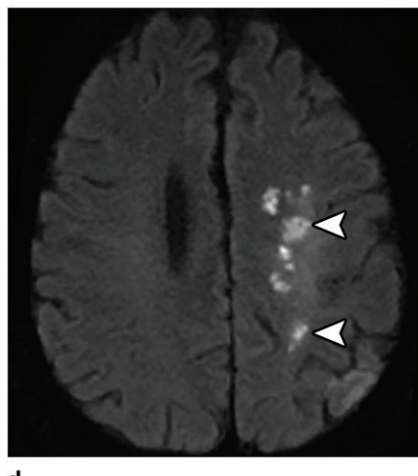
a.



b.

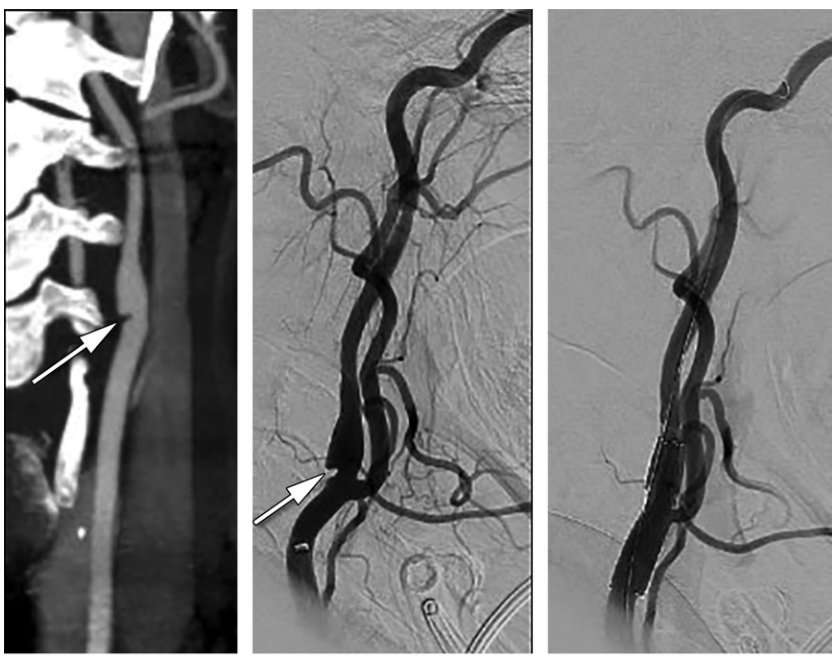


c.



d.

Figure 11. Bilateral cervical ICA dissection in a 35-year-old patient who presented to the ED with acute-onset right-sided weakness. (a) Axial CT angiogram demonstrates occlusion of the left cervical ICA and stenosis of the right cervical ICA. Note how the intramural hematomas in the bilateral cervical ICAs result in thickening of the vessel walls (dashed circles). (b) T_{\max} map from CT perfusion imaging shows hypoperfusion of the entire left cerebral hemisphere as well as hypoperfusion in the watershed territory of the right hemisphere. (c) Axial fat-saturated T1-weighted MR image shows bilateral crescentic hyperintense intramural hematomas (arrows), consistent with bilateral cervical ICA dissection. (d) Axial DW image shows scattered watershed-distribution infarcts (arrowheads) in the left cerebral hemisphere.

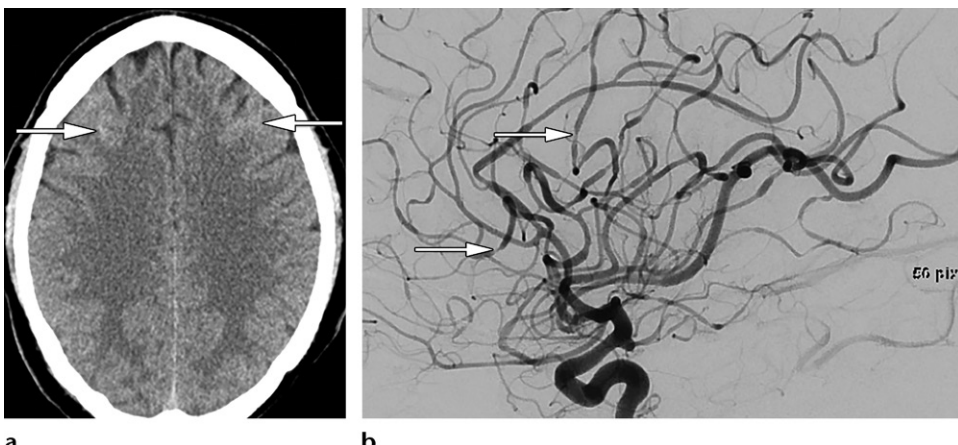


a.

b.

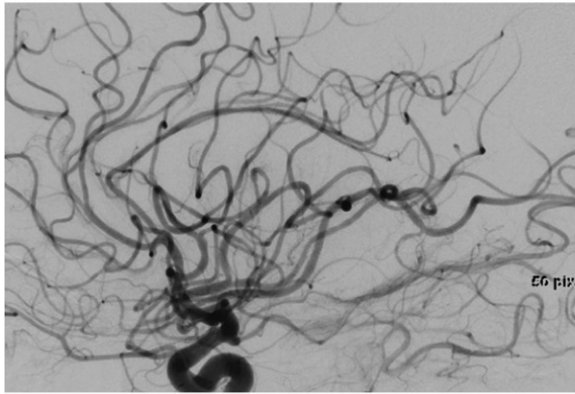
c.

Figure 12. Carotid web in a 47-year-old woman with left cerebral infarction. (a, b) Coronal maximum intensity projection CT angiogram (a) and preintervention DSA image (b) show a focal linear shelflike filling defect (arrow) along the wall of the left ICA origin without signs of atherosclerosis, consistent with a carotid web. (c) Postintervention DSA image shows that the web is no longer present. Angioplasty or stent placement may be performed.



a.

b.



c.

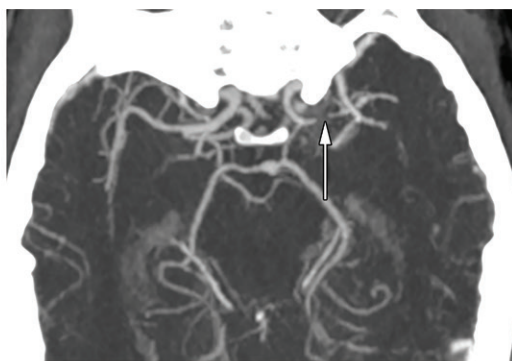
Figure 13. RCVS in a 30-year-old woman who presented to the ED with sudden-onset headache and no recent trauma. (a) Axial nonenhanced CT image shows high bilateral frontal convexity subarachnoid hemorrhage (arrows), a nonaneurysmal pattern. Initial CT angiography (not shown) showed no aneurysm or proximal narrowing. (b) DSA image 3 days later shows multifocal narrowing (arrows) and beaded appearance of the anterior cerebral arteries and MCAs. (c) Follow-up DSA image at 10 days shows near-complete resolution.

intracranial vasculitis is extensive and can range from systemic inflammatory processes such as connective tissue disease or lupus but can also be seen with infection, malignancy, irradiation, or medications. The clinical manifestation can

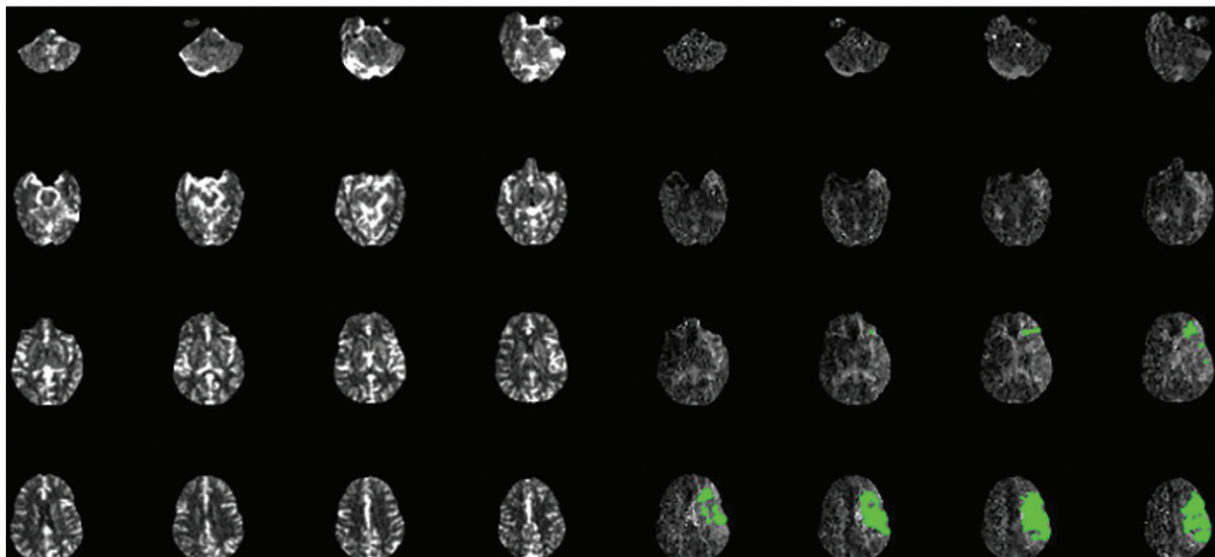
be nonspecific and difficult to differentiate from that of RCVS. Headaches associated with vasculitis are usually more subacute.

Routine workup includes evaluation of inflammatory markers such as erythrocyte sedimentation

Figure 14. Cocaine-induced vasospasm in a 25-year-old patient who presented to the ED with right hemiplegia after recent cocaine use. (a) Axial maximum intensity projection CT angiogram shows a high-grade stenosis (arrow) of the M1 segment of the left MCA. (b) Corresponding CT perfusion images show a large area of penumbra (green).



a.



b.

rate, C-reactive protein, rheumatoid factor, complement, and antineutrophil cytoplasmic antibodies and routine cerebrospinal fluid laboratory analysis. Imaging workup and findings are similar to those of other vasculopathies, but the addition of VVI may help identify concentric focal intense wall enhancement, a unique finding indicating inflammation (28,30).

Recreational Drug Use.—Illicit and recreational drugs affecting the central nervous system include cocaine, heroin, alcohol, amphetamines, toluene, cannabis, and prescribed medications (53). These substances can result in acute intracranial disease including encephalopathy, intracranial hemorrhage, or ischemic infarction and increase overall risk of ischemic stroke sevenfold (53).

For cocaine, the mechanism includes cerebral vasospasm, platelet aggregation, thrombosis, cerebral vasculitis, and thromboembolism from resultant cardiomyopathy or dysrhythmia. Typical imaging findings are multifocal vasospasm that can lead to distal cortical branch or subcortical infarcts involving multiple vascular territories or a focal large-vessel vasospasm

mimicking a large-territory infarction (Fig 14). Psychoactive stimulants, such as methamphetamines, can cause vasospasm, arteritis, and infarction (Fig 15) (53). Additionally, MDMA or ecstasy (3,4-methylenedioxymethamphetamine) results in rapid release of 5-hydroxytryptamine, a potent vasoconstrictive chemical that can lead to catastrophic ischemic injury.

Cerebral Autosomal Dominant Arteriopathy with Subcortical Infarcts and Leukoencephalopathy.—CADASIL is caused by a genetic defect in the NOTCH3 gene. Patients in their 30s typically present with migraine. Patients in their 40s and 50s may have recurrent transient ischemic attacks or strokes, resulting in dementia, cognitive decline, mood disorder, or hemiplegia (54).

The typical imaging findings are subcortical and periventricular hyperintense white matter lesions on T2-weighted or FLAIR images, classically involving the anterior temporal poles as well as the insula, centrum semiovale, and external capsule (Fig 16). The lesions are symmetric, and there is relative sparing of the fronto-orbital and occipital regions (55). Additionally, there



Figure 15. Lateral medullary syndrome related to illicit drug use in a 45-year-old patient who presented to the ED with vomiting and dysmetria that began immediately after cocaine and methamphetamine use. Axial DW image reveals a right lateral medullary infarct (arrow). CT angiography (not shown) failed to reveal any vascular abnormality.

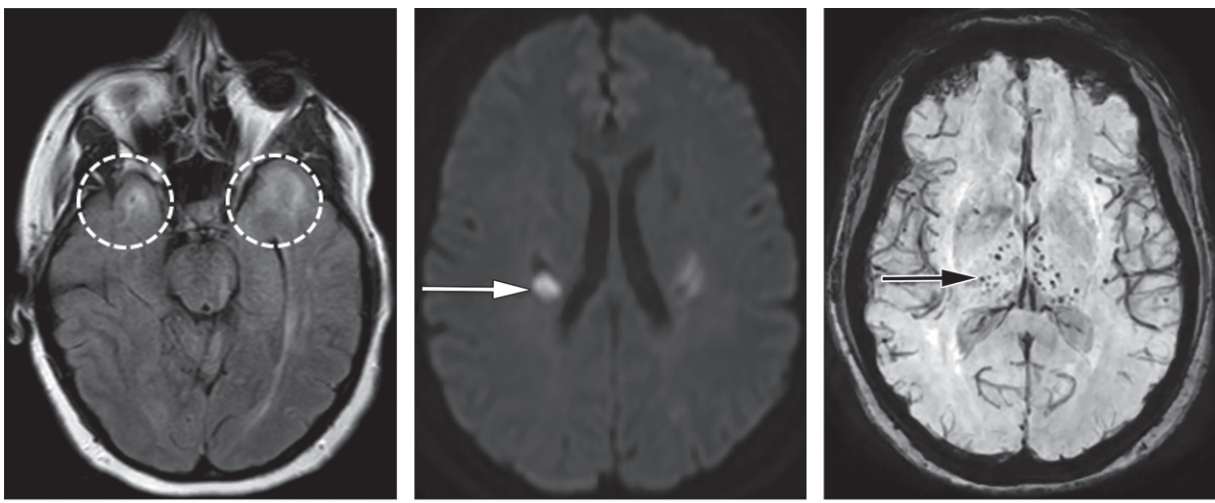


Figure 16. CADASIL in a 26-year-old woman who presented to the ED with headache and weakness. She was initially diagnosed with multiple sclerosis at an outside hospital; subsequently, CADASIL was suspected and confirmed by the presence of a *NOTCH3* genetic mutation. (a) Axial FLAIR image shows the classic temporal pole leukomalacia (dashed circles). (b) Axial DW image shows the acute or early subacute lacunar infarcts (arrow). (c) Axial susceptibility-weighted MR image shows microhemorrhages (arrow), which serve as less common radiologic features of the disease.

is usually a large number of deep gray matter microhemorrhages (54).

Moyamoya.—*Moyamoya* is Japanese for “puff of smoke,” referring to the angiographic appearance of the numerous tiny lenticulostriate collaterals that develop to compensate for steno-occlusive disease in the circle of Willis (Fig 17) (56). Moyamoya can be either the disease (an idiopathic condition) or the syndrome (a number of conditions that lead to a similar appearance). Causes of moyamoya syndrome include sickle cell disease, neurofibromatosis type 1, radiation vasculopathy, and Down syndrome.

Cerebral infarction is seen in 57% of patients with moyamoya disease (56). Stroke mechanism is due to watershed infarction from steno-occlusive disease of the ICA terminus that often

involves the anterior cerebral artery and MCA origins. Use of angiography is key to diagnosing moyamoya, although tiny lenticulostriate flow voids can be seen at T2-weighted MRI.

Prothrombotic Disorders

Prothrombotic disorders can induce venous, arterial, or microvascular thrombosis. Symptoms of arterial infarction match those in other ischemic stroke subtypes. Venous infarction stroke symptoms tend to be vague. Venous thrombosis causes mostly vasogenic edema, with usually sparse cytotoxic edema, and often manifests with intracranial hemorrhage. If there is no associated hemorrhage, findings at neuroimaging can be subtle.

Nonenhanced CT may show hyperattenuation of the larger sinuses or cortical veins. Nonenhanced MRI will show absence of the T2-hypointense



Figure 17. Known moyamoya in a young patient with prior watershed infarcts. Anteroposterior DSA image shows right ICA and proximal MCA steno-occlusive disease of the carotid termini (arrowheads), with extensive small collateral lenticulostriate arteries (arrow). (Courtesy of Rohan Samant, MD, MBA, University of Arkansas for Medical Sciences, Little Rock, Ark.)

flow voids and associated blooming from magnetic susceptibility on gradient-echo images. The classic “empty delta sign” or absent cortical venous filling can be identified at CT angiography, CT venography, or MR venography.

Factor V Leiden Mutation.—The factor V Leiden mutation is one of the most common prothrombotic disorders to cause ischemic infarction in young adults, accounting for up to 8% of other demonstrated causes in this population (4). This mutation is present in more than 95% of patients with resistance to activated protein C, an anti-thrombotic protein that inactivates coagulation factors Va and VIIIa. Appropriate antithrombotic prophylaxis is unclear (57). It is reported to be the most relevant hereditary risk factor for cerebral venous thrombosis (57).

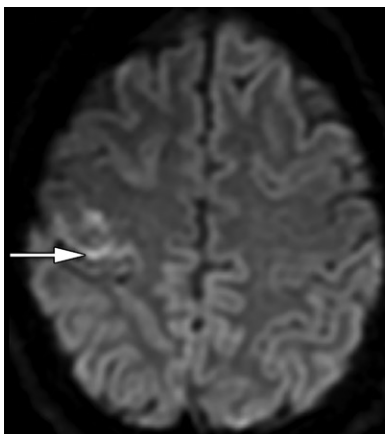
Antiphospholipid Syndrome.—Antiphospholipid syndrome is another of the more common prothrombotic disorders to cause ischemic infarction in young adults, accounting for up to 7% of other demonstrated causes in this population (4). This autoimmune disease is characterized by obstetric (classically, recurrent early miscarriages) and thrombotic (venous, arterial, or microvascular) disease in patients with persistent antiphospholipid antibodies. It can be seen with other systemic autoimmune diseases; 20%–30% of patients with systemic lupus erythematosus have moderate to high-risk antiphospholipid antibody profiles. Some studies estimate that up to 17% of patients with stroke younger than age 50 years are antiphospholipid antibody-positive (58). Treatment can be primary (no prior event) or secondary (known previous event) thrombosis prevention (58).

Oral Contraceptive Use.—Oral contraceptive use increases the risk of thrombosis, as do other states that elevate estrogen and progesterone levels, such as pregnancy. Oral contraceptive use has been seen in association with 19% of young female patients with ischemic stroke (3). This risk is greatly potentiated by smoking.

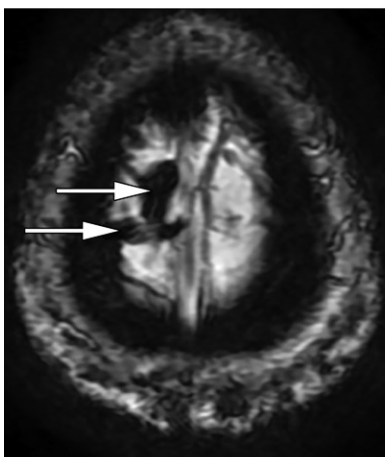
Thrombosis can be arterial or venous. Like with other venous infarcts, these patients can present with headache, papilledema, seizure, encephalopathy, or focal neurologic deficits (59). As venous infarction usually manifests with parenchymal hemorrhage and non-vascular territory edema, a very high level of suspicion is necessary to diagnose an infarct that does not follow this pattern, especially if the clinician has yet to consider the possibility and yet to request venous vascular imaging (Fig 18).

Pregnancy and Puerperium.—During pregnancy and puerperium (6 weeks after delivery), women have an increased risk of stroke due to hypercoagulability, venous stasis, vascular wall changes, elevation of cerebral perfusion pressure, and rising estrogen and progesterone levels (59). This includes hemorrhage and ischemic stroke, and both arterial (Fig 19) and venous ischemic stroke. Risk of cerebral venous thrombosis is the highest in the first 2 weeks of puerperium.

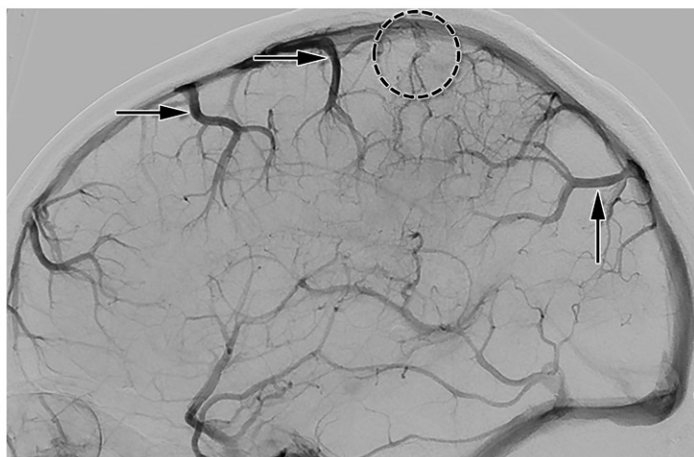
Because of the low dose to the fetus and lack of evidence of complications from iodinated contrast material, the radiation dose and iodinated contrast material used during CT examinations of the head and neck are considered safe in pregnant women. While MRI has no radiation and remains the safe preferred modality, gadolinium contrast agents are U.S. Food and Drug Administration



a.



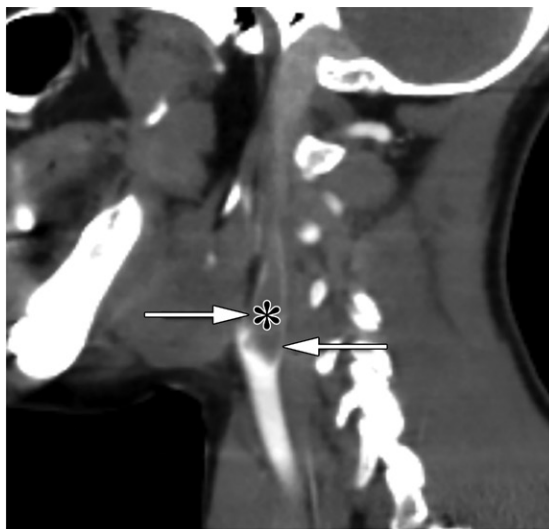
b.



c.



a.



b.

Figure 18. Venous infarction related to oral contraceptive use and hypercoagulability in a 32-year-old woman taking oral contraceptives who presented to the ED with a headache. (a) Axial DW image shows cortical restricted diffusion in the right precentral (motor) cortex (arrow). (b) Susceptibility-weighted image shows blooming artifact and magnetic susceptibility following the course of a cortical bridging vein (arrows), indicating thrombosis. (c) Lateral venous phase DSA image shows absent filling of the corresponding cortical vein (dashed circle). Compare with the normal right cortical veins (arrows).

Figure 19. Peripartum hypercoagulability in a 33-year-old woman who was 2 weeks postpartum and presented to the ED after being found unconscious. She had been complaining of generalized weakness and left-sided weakness for 2 days. (a) Axial nonenhanced CT image shows a right MCA ischemic infarction (*). (b) Sagittal CT angiogram reveals thrombus (*) filling the lumen of the right ICA and protruding into the bifurcation, with thin peripheral opacification (arrows) around the thrombus.

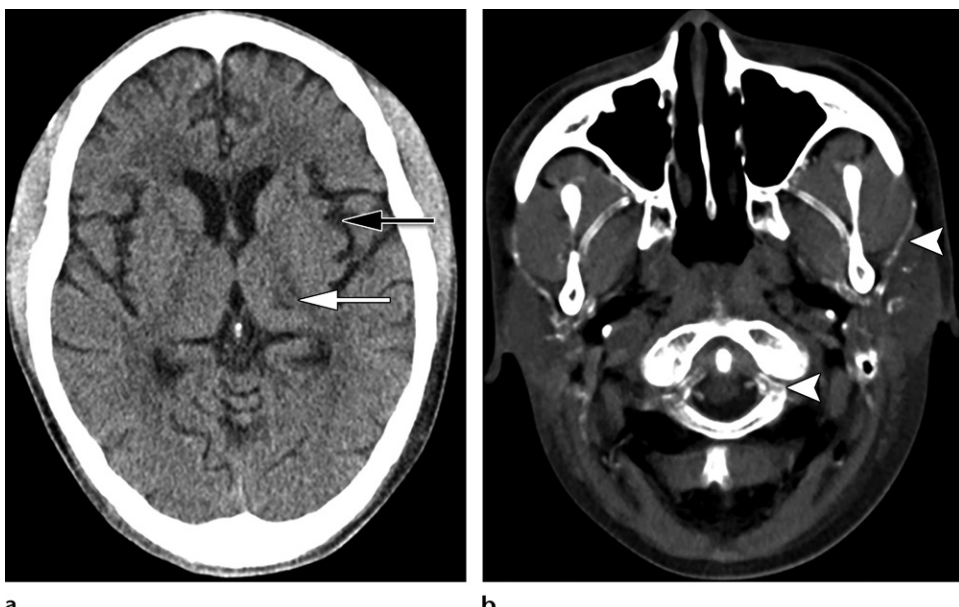


Figure 20. Ischemic infarction of undetermined cause in a 31-year-old patient with small-vessel risk factors, large-artery atherosclerosis, antiphospholipid syndrome, diabetes mellitus type 1, and end-stage renal disease who presented to the ED with left-sided facial weakness and numbness. (a) Axial nonenhanced CT image shows the left thalamic lacunar infarct (white arrow), which was found to be subacute at subsequent MRI. Sulcal prominence (black arrow) from volume loss was advanced for age. (b) Axial nonenhanced CT image shows extensive extracranial atherosclerosis of the external carotid artery branches (arrowheads) around the skull base. As there were multiple possible causes, this infarction was classified as undetermined.

Category C drugs in pregnancy, meaning that animal studies revealed adverse effects and they are to be used only when essential to the diagnosis (59). For this reason, phase-contrast or time-of-flight vascular techniques that do not use gadolinium contrast material are the standards for MR venography in pregnant patients.

Undetermined Cause

As “other demonstrated cause” was the catch-all category for ischemic strokes with known causes, “undetermined cause” is the category for those with causes that remain unknown or unclear. An ischemic infarct is considered to have an undetermined cause if it meets one of the following criteria: (a) two or more causes, (b) indeterminate cause, and (c) incomplete evaluation.

In young adults, most ischemic infarctions that fall under this subtype are of indeterminate cause, followed by multiple causes (Fig 20) and last by incomplete evaluation (3).

Small-Vessel Occlusion

Small-vessel occlusion (lacunar) infarction is less common in younger adults than in older adults, accounting for 7%–14% of ischemic strokes in young adults (3,4). Patients with lacunar infarction are likely to have known risk factors, such as hypertension or diabetes mellitus.

Imaging features include small (<1.5 cm) deep infarcts restricted to the basal ganglia, internal capsule, thalamus, or brainstem. Additionally, there should be no large-artery atherosclerosis in the clinically relevant vessel.

Large-Artery Atherosclerosis

Although large-vessel atherosclerosis-related stroke is frequent in older adults, it is the least common subtype of ischemic infarction in young adults. It accounts only for 2%–8% of ischemic stroke in young adults, compared with around double that in older adults (3,4,9). This type of infarct occurred exclusively in patients older than age 36 years in one study of 215 young adults with ischemic stroke or transient ischemic attack (3). In these young adults, the most significant stroke risk factors were sedentary lifestyle and hypertension (3).

Large-artery atherosclerosis can be extracranial or intracranial. In the TOAST classification system, a stroke can be attributed to large-artery atherosclerosis if the patient has an infarct of the cerebral cortex, brainstem, or cerebellum and evidence of accelerated atherosclerotic risk factors or symptomatic atherosclerosis in other anatomic locations (coronary artery disease or aortic disease). Supporting imaging findings include intracranial or extracranial stenosis at the usual sites for atherosclerosis (ICA origins,

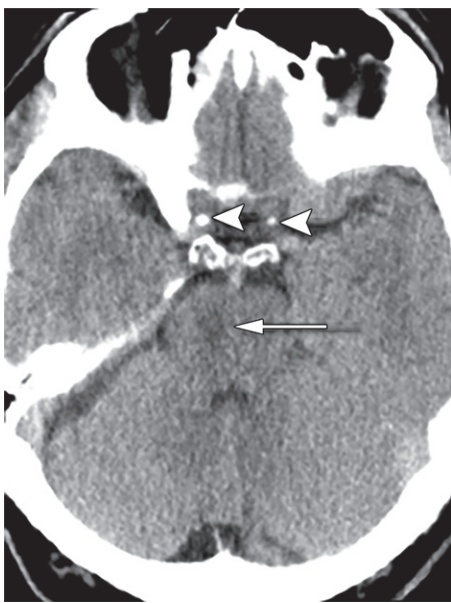


Figure 21. Large-artery atherosclerosis in a 44-year-old man with hypertension and gout who presented to the ED with a 2-day history of left-sided weakness and ataxia. He had a delayed presentation, as he initially attributed his symptoms to a gout flare. Axial nonenhanced CT image shows a right pontine infarction (arrow). Calcified atherosclerosis involves both carotid siphons (arrowheads) and the basilar artery (not shown), the latter of which likely led to pontine perforator occlusion.

carotid siphons, V4 vertebral arteries) (Fig 21) (7,8). Qualities of wall integrity and plaque content serve as important indicators for vulnerable large-vessel plaques in patients at risk for thromboembolic strokes. Plaque ulceration, fibrous cap thickness, and lipid-rich necrotic core have been used as predictors of stroke (60,61).

Conclusion

Ischemic infarction in young adults is an emerging public health issue given the rise in incidence and prolonged period of disability. Compared with older adults, young adults more often have ischemic stroke secondary to cardioembolism and other demonstrated causes (most commonly dissection). This difference must be reflected accordingly in both the imaging workup and the radiologist's differential diagnoses to ensure accurate and timely diagnoses, minimizing infarct size and complications.

Disclosures of Conflicts of Interest.—**L.Y.L.** Activities related to the present article: disclosed no relevant relationships. Activities not related to the present article: payment from Aptus Health for an educational presentation; honorarium from YoungStroke. Other activities: disclosed no relevant relationships. **A.S.** Activities related to the present article: disclosed no relevant relationships. Activities not related to the present article: consultant and speaker for and grants from Stryker Neurovascular. Other activities: disclosed no relevant relationships.

References

1. Aigner A, Grittner U, Rolfs A, Norrving B, Siegerink B, Busch MA. Contribution of Established Stroke Risk Factors to the Burden of Stroke in Young Adults. *Stroke* 2017;48(7):1744–1751.
2. Ekker MS, Boot EM, Singhal AB, et al. Epidemiology, aetiology, and management of ischaemic stroke in young adults. *Lancet Neurol* 2018;17(9):790–801.
3. Ji R, Schwamm LH, Pervez MA, Singhal AB. Ischemic stroke and transient ischemic attack in young adults: risk factors, diagnostic yield, neuroimaging, and thrombolysis. *JAMA Neurol* 2013;70(1):51–57.
4. Putaala J, Metso AJ, Metso TM, et al. Analysis of 1008 consecutive patients aged 15 to 49 with first-ever ischaemic stroke: the Helsinki Young Stroke Registry. *Stroke* 2009;40(4):1195–1203.
5. Benjamin EJ, Virani SS, Callaway CW, et al. Heart Disease and Stroke Statistics: 2018 Update—A Report From the American Heart Association. *Circulation* 2018;137(12):e67–e492 [Published correction appears in *Circulation* 2018;137(12):e493.] <https://doi.org/10.1161/CIR.0000000000000558>.
6. Stroke Facts. Centers for Disease Control and Prevention. <https://www.cdc.gov/stroke/facts.htm>. Accessed October 20, 2018.
7. Adams HP Jr, Bendixen BH, Kappelle LJ, et al. Classification of subtype of acute ischemic stroke: definitions for use in a multicenter clinical trial. TOAST: Trial of Org 10172 in Acute Stroke Treatment. *Stroke* 1993;24(1):35–41.
8. Adams HP Jr, Biller J. Classification of subtypes of ischemic stroke: history of the Trial of Org 10172 in Acute Stroke Treatment classification. *Stroke* 2015;46(5):e114–e117.
9. Kolominsky-Rabas PL, Weber M, Gefeller O, Neudoerfer B, Heuschmann PU. Epidemiology of ischemic stroke subtypes according to TOAST criteria: incidence, recurrence, and long-term survival in ischemic stroke subtypes—a population-based study. *Stroke* 2001;32(12):2735–2740.
10. Ramirez L, Kim-Tenser MA, Sanossian N, et al. Trends in Acute Ischemic Stroke Hospitalizations in the United States. *J Am Heart Assoc* 2016;5(5):e003233.
11. George MG, Tong X, Kuklina EV, Labarthe DR. Trends in stroke hospitalizations and associated risk factors among children and young adults, 1995–2008. *Ann Neurol* 2011;70(5):713–721.
12. Kuruvilla A, Bhattacharya P, Rajamani K, Chaturvedi S. Factors associated with misdiagnosis of acute stroke in young adults. *J Stroke Cerebrovasc Dis* 2011;20(6):523–527.
13. Fonarow GC, Reeves MJ, Zhao X, et al. Age-related differences in characteristics, performance measures, treatment trends, and outcomes in patients with ischemic stroke. *Circulation* 2010;121(7):879–891.
14. Leung LY, Caplan LR. Factors Associated with Delay in Presentation to the Hospital for Young Adults with Ischemic Stroke. *Cerebrovasc Dis* 2016;42(1-2):10–14.
15. NIH Stroke Scale. <http://www.nihstrokestescale.org/>. Accessed February 12, 2019.
16. Balami JS, Chen RL, Buchan AM. Stroke syndromes and clinical management. *QJM* 2013;106(7):607–615.
17. Ozdoba C, Sturzenegger M, Schroth G. Internal carotid artery dissection: MR imaging features and clinical-radiologic correlation. *Radiology* 1996;199(1):191–198.
18. Berkhemer OA, Fransen PSS, Beumer D, et al. A randomized trial of intraarterial treatment for acute ischemic stroke. *N Engl J Med* 2015;372(1):11–20.
19. Jovin TG, Chamorro A, Cobo E, et al. Thrombectomy within 8 hours after symptom onset in ischemic stroke. *N Engl J Med* 2015;372(24):2296–2306.
20. Goyal M, Demchuk AM, Menon BK, et al. Randomized assessment of rapid endovascular treatment of ischemic stroke. *N Engl J Med* 2015;372(11):1019–1030.
21. Saver JL, Goyal M, Bonafe A, et al. Stent-retriever thrombectomy after intravenous t-PA vs. t-PA alone in stroke. *N Engl J Med* 2015;372(24):2285–2295.
22. Campbell BCV, Mitchell PJ, Kleinig TJ, et al. Endovascular therapy for ischemic stroke with perfusion-imaging selection. *N Engl J Med* 2015;372(11):1009–1018.

23. Nogueira RG, Jadhav AP, Haussen DC, et al. Thrombectomy 6 to 24 Hours after Stroke with a Mismatch between Deficit and Infarct. *N Engl J Med* 2018;378(1):11–21.
24. Albers GW, Marks MP, Kemp S, et al. Thrombectomy for Stroke at 6 to 16 Hours with Selection by Perfusion Imaging. *N Engl J Med* 2018;378(8):708–718.
25. Nael K, Khan R, Choudhary G, et al. Six-minute magnetic resonance imaging protocol for evaluation of acute ischemic stroke: pushing the boundaries. *Stroke* 2014;45(7):1985–1991.
26. Shah S, Luby M, Poole K, et al. Screening with MRI for Accurate and Rapid Stroke Treatment: SMART. *Neurology* 2015;84(24):2438–2444.
27. Rodallec MH, Marteau V, Gerber S, Desmottes L, Zins M. Craniocervical arterial dissection: spectrum of imaging findings and differential diagnosis. *RadioGraphics* 2008;28(6):1711–1728.
28. Mandell DM, Mossa-Basha M, Qiao Y, et al. Intracranial Vessel Wall MRI: Principles and Expert Consensus Recommendations of the American Society of Neuroradiology. *AJNR Am J Neuroradiol* 2017;38(2):218–229.
29. Miller TR, Shivashankar R, Mossa-Basha M, Gandhi D. Reversible Cerebral Vasoconstriction Syndrome. II. Diagnostic Work-Up, Imaging Evaluation, and Differential Diagnosis. *AJNR Am J Neuroradiol* 2015;36(9):1580–1588.
30. Lindenholz A, van der Kolk AG, Zwanenburg JJM, Hendrikse J. The Use and Pitfalls of Intracranial Vessel Wall Imaging: How We Do It. *Radiotherapy* 2018;286(1):12–28.
31. Hess A, Klein I, Jung B, et al. Brain MRI findings in neurologically asymptomatic patients with infective endocarditis. *AJNR Am J Neuroradiol* 2013;34(8):1579–1584.
32. Lee VH, Connolly HM, Brown RD Jr. Central nervous system manifestations of cardiac myxoma. *Arch Neurol* 2007;64(8):1115–1120.
33. Thaler DE, Ruthazer R, Di Angelantonio E, et al. Neuroimaging findings in cryptogenic stroke patients with and without patent foramen ovale. *Stroke* 2013;44(3):675–680.
34. Wiktor DM, Carroll JD. The Case for Selective Patent Foramen Ovale Closure After Cryptogenic Stroke. *Circ Cardiovasc Interv* 2018;11(3):e004152.
35. Saver JL, Carroll JD, Thaler DE, et al. Long-Term Outcomes of Patent Foramen Ovale Closure or Medical Therapy after Stroke. *N Engl J Med* 2017;377(11):1022–1032.
36. Mas JL, Derumeaux G, Guillou B, et al. Patent Foramen Ovale Closure or Anticoagulation vs. Antiplatelets after Stroke. *N Engl J Med* 2017;377(11):1011–1021.
37. Kozdag G, Ciftci E, Ural D, et al. Silent cerebral infarction in chronic heart failure: ischemic and nonischemic dilated cardiomyopathy. *Vasc Health Risk Manag* 2008;4(2):463–469.
38. McCarthy CJ, Behravesh S, Naidu SG, Oklu R. Air Embolism: Practical Tips for Prevention and Treatment. *J Clin Med* 2016;5(11):93.
39. Simon AD, Ulmer JL, Strottman JM. Contrast-enhanced MR imaging of cerebral fat embolism: case report and review of the literature. *AJNR Am J Neuroradiol* 2003;24(1):97–101.
40. Moritani T, Ekholm S, Westesson PL, eds. Vasculopathy and Vasculitis. In: Diffusion-Weighted MR Imaging of the Brain. Berlin, Germany: Springer, 2009; 93–120.
41. Giroud M, Fayolle H, André N, et al. Incidence of internal carotid artery dissection in the community of Dijon. *J Neurol Neurosurg Psychiatry* 1994;57(11):1443.
42. Schievink WI, Mokri B, Whisnant JP. Internal carotid artery dissection in a community: Rochester, Minnesota, 1987–1992. *Stroke* 1993;24(11):1678–1680.
43. Choi MH, Hong JM, Lee JS, Shin DH, Choi HA, Lee K. Preferential location for arterial dissection presenting as golf-related stroke. *AJNR Am J Neuroradiol* 2014;35(2):323–326.
44. Morel A, Nagara O, Touzé E, et al. Mechanism of ischemic infarct in spontaneous cervical artery dissection. *Stroke* 2012;43(5):1354–1361.
45. Lévy C, Laissy JP, Raveau V, et al. Carotid and vertebral artery dissections: three-dimensional time-of-flight MR angiography and MR imaging versus conventional angiography. *Radiotherapy* 1994;190(1):97–103.
46. Coutinho JM, Derkatch S, Potvin ARJ, et al. Carotid artery web and ischemic stroke: a case-control study. *Neurology* 2017;88(1):65–69 [Published correction appears in *Neurology* 2017;89(5):521.] <https://doi.org/10.1212/WNL.0000000000003464>.
47. Boesen ME, Eswaradass PV, Singh D, et al. MR imaging of carotid webs. *Neuroradiology* 2017;59(4):361–365.
48. Phair J, Trestman EB, Yean C, Lipsitz EC. Endarterectomy for a symptomatic carotid web. *Vascular* 2017;25(5):553–556.
49. Joux J, Chausson N, Jeannin S, et al. Carotid-bulb atypical fibromuscular dysplasia in young Afro-Caribbean patients with stroke. *Stroke* 2014;45(12):3711–3713.
50. Haussen DC, Grossberg JA, Bouslama M, et al. Carotid Web (Intimal Fibromuscular Dysplasia) Has High Stroke Recurrence Risk and Is Amenable to Stenting. *Stroke* 2017;48(11):3134–3137.
51. Miller TR, Shivashankar R, Mossa-Basha M, Gandhi D. Reversible Cerebral Vasoconstriction Syndrome. I. Epidemiology, Pathogenesis, and Clinical Course. *AJNR Am J Neuroradiol* 2015;36(8):1392–1399.
52. Abdel Razek AA, Alvarez H, Bagg S, Refaat S, Castillo M. Imaging spectrum of CNS vasculitis. *RadioGraphics* 2014;34(4):873–894.
53. Tamrazi B, Almast J. Your brain on drugs: imaging of drug-related changes in the central nervous system. *RadioGraphics* 2012;32(3):701–719.
54. van den Boom R, Lesnick Oberstein SAJ, van den Berg-Huysmans AA, Ferrari MD, van Buchem MA, Haan J. Cerebral autosomal dominant arteriopathy with subcortical infarcts and leukoencephalopathy: structural MR imaging changes and apolipoprotein E genotype. *AJNR Am J Neuroradiol* 2006;27(2):359–362.
55. Yousky TA, Seelos K, Mayer M, et al. Characteristic MR lesion pattern and correlation of T1 and T2 lesion volume with neurologic and neuropsychological findings in cerebral autosomal dominant arteriopathy with subcortical infarcts and leukoencephalopathy (CADASIL). *AJNR Am J Neuroradiol* 1999;20(1):91–100.
56. Mugikura S, Takahashi S, Higano S, et al. The relationship between cerebral infarction and angiographic characteristics in childhood moyamoya disease. *AJNR Am J Neuroradiol* 1999;20(2):336–343.
57. Lüdemann P, Nabavi DG, Junker R, et al. Factor V Leiden mutation is a risk factor for cerebral venous thrombosis: a case-control study of 55 patients. *Stroke* 1998;29(12):2507–2510.
58. Garcia D, Erkan D. Diagnosis and Management of the Antiphospholipid Syndrome. *N Engl J Med* 2018;378(21):2010–2021.
59. Kanekar S, Bennett S. Imaging of Neurologic Conditions in Pregnant Patients. *RadioGraphics* 2016;36(7):2102–2122.
60. Wintermark M, Jawadi SS, Rapp JH, et al. High-resolution CT imaging of carotid artery atherosclerotic plaques. *AJNR Am J Neuroradiol* 2008;29(5):875–882.
61. Biasi GM, Froio A, Diethrich EB, et al. Carotid plaque echolucency increases the risk of stroke in carotid stenting: the Imaging in Carotid Angioplasty and Risk of Stroke (ICAROS) study. *Circulation* 2004;110(6):756–762.



Neuroimaging of Emergent and Reemergent Infections

Rafael Lourenço do Carmo, MD
 Aylla Keiner Alves Simão, MD
 Lázaro Luís Faria do Amaral, MD
 Bruno Shiguelo Yonekura Inada, MD
 Camila Filardi Silveira, MD
 Christiane Monteiro de Siqueira Campos, MD
 Leonardo Furtado Freitas, MD
 Victor Bonadio, MD
 Victor Hugo Rocha Marussi, MD

Abbreviations: ADEM = acute disseminated encephalomyelitis, CDC = Centers for Disease Control and Prevention, CHIKV = chikungunya virus, CNS = central nervous system, CSF = cerebrospinal fluid, DEN = dengue virus, DWI = diffusion-weighted imaging, EV = enterovirus, FLAIR = fluid-attenuated inversion-recovery, GBS = Guillain-Barré syndrome, JEV = Japanese encephalitis virus, SLEV = St Louis encephalitis virus, WNV = West Nile virus, ZIKV = Zika virus

RadioGraphics 2019; 39:1649–1671

<https://doi.org/10.1148/rg.2019190020>

Content Codes:

From the Department of Neuroradiology, A Beneficência Portuguesa de São Paulo, R. Maestro Cardim 769, São Paulo, SP 01323-001, Brazil. Presented as an education exhibit at the 2018 RSNA Annual Meeting. Received February 18, 2019; revision requested March 28 and received May 22; accepted July 2. For this journal-based SA-CME activity, the authors, editor, and reviewers have disclosed no relevant relationships.

Address correspondence to R.L.d.C. (e-mail: rafael.lourenco@gmail.com).

©RSNA, 2019

SA-CME LEARNING OBJECTIVES

After completing this journal-based SA-CME activity, participants will be able to:

- Recognize the importance of emergent and reemergent CNS infections as sources of morbidity and mortality worldwide.
- Identify the imaging features of some of the most prevalent emergent and re-emergent CNS infections.
- Describe clinical features, epidemiologic characteristics, and key imaging findings that may help to narrow the differential diagnosis of these CNS infections.

See rsna.org/learning-center-rg.

Infectious diseases emerge and reemerge over the years, and many of them can cause neurologic disease. Several factors contribute to the emergence and reemergence of these conditions, including human population growth, an increase in international travel, the geographic expansion of recognized pathogens to areas where they were previously nonendemic, and greater contact with wild animal reservoirs. The antivaccination social movement has played an important role in the reemergence of infectious diseases, especially some viral conditions. The authors review different viral (arboviruses such as dengue, chikungunya, and Zika virus; enterovirus 71; measles; and influenza), bacterial (syphilis, Lyme disease, and listeriosis), and parasitic (Chagas disease) diseases, focusing primarily on their neurologic complications. Although there are several additional infectious diseases with central nervous system manifestations that could be classified as emergent or reemergent, those listed here are the most relevant from an epidemiologic standpoint and are representative of important public health issues on all continents. The infections caused by these pathogens often show a variety of neuroimaging patterns that can be identified at CT and MRI, and radiology is central to the diagnosis and follow-up of such conditions. Given the increasing relevance of emerging and re-emerging infections in clinical practice and public health scenarios, radiologists should be familiar with these infections.

Online supplemental material is available for this article.

©RSNA, 2019 • radiographics.rsna.org

Introduction

Despite important advances in the prevention, diagnosis, and treatment of infectious diseases over the course of medical history, these conditions are still among the most important causes of morbidity and mortality, especially in developing countries.

The sporadic appearance of new infectious agents that affect humans is inevitable, but it is still not possible to predict the exact location and time frame in which these events will occur. *Emerging diseases* are defined as infections found in human hosts for the first time, whereas *reemerging diseases* are those that have infected humans before but occur in new locations, those for which drug-resistant variants emerge, or those that reappear after being controlled or eliminated. (1) Some well-known examples of emerging diseases include the 2009 pandemic H1N1 influenza virus and H5N1 influenza, which emerged from pigs and birds, respectively, to affect human hosts (1).

Several factors are important to the emergence and reemergence of diseases. These factors are related to the microbial agent (genetic adaptation), the environment (eg, climate changes, economic development, changes in land use, ecosystem alterations, and poverty), and/or the human host (eg, population growth, travel and migration,

TEACHING POINTS

- Emerging diseases are defined as infections found in human hosts for the first time, whereas reemerging diseases are those that have infected humans before but occur in new locations, those for which drug-resistant variants emerge, or those that reappear after being controlled or eliminated.
- MRI reveals mildly decreased gray matter volume, notably in the frontotemporal cortex, amygdala, and cingulate gyrus in the early stages of subacute sclerosing panencephalitis. In addition, multifocal T2-hyperintense lesions in the cortex, periventricular white matter, basal ganglia, and brainstem are described. As the disease progresses, diffuse cortical atrophy is noted.
- The radiologic appearance of acute necrotizing encephalopathy related to pandemic influenza is varied, but the hallmark findings are bilateral symmetric T2-hyperintense lesions that are associated with restricted diffusion and involve the thalamus, brainstem, and/or cerebellum. Additional findings are foci of magnetic susceptibility in the affected areas and adjacent leptomeningeal enhancement, which may be noted after administration of gadolinium contrast material.
- MRI is better than CT for depiction of the classic pattern of DENV encephalitis, which is T2-hyperintense lesions that affect the cortical gray matter, subcortical and deep white matter, basal ganglia, and thalamus, usually showing some degree of expansive effect. Patchy areas of restricted diffusion in the affected areas are seen in most patients, as are microhemorrhages, which are seen as small foci of blooming at susceptibility-weighted MRI.
- Vascular neurosyphilis is currently the most common form of neurologic involvement of the disease and refers to arteritis of the large- and medium-sized arteries (Heubner arteritis) and/or small-sized arteries (Nissl-Alzheimer arteritis). Although pathologic processes are different in each case, in ultimate analysis, both cause luminal narrowing and eventual vascular occlusion. Vascular neurosyphilis usually manifests 5–10 years after initial infection, usually as an ischemic syndrome that affects the territory of the middle cerebral artery in a relatively young adult who does not have risk factors for atherosclerosis.

the use of microorganisms in warfare, the misuse of antibiotics, and occupational exposure) (1,2). The advances in diagnostic methods also have allowed the identification of new pathogens (2). Antivaccination movements have gained popularity, levered by online social media, and have contributed to the reemergence of diseases that were considered controlled. This social phenomenon corresponds to outbreaks of infectious disease in Europe and North America, including measles outbreaks that led to deaths in the United Kingdom, France, and the United States (3).

An increasing number of emerging and reemerging diseases have relevance in clinical and public health scenarios. Imaging is often helpful in the diagnosis and follow-up of patients with these diseases; therefore, radiologists must be familiar with the wide range of manifestations the diseases exhibit in the brain, spine, and meninges.

Because the neurologic manifestations of infectious diseases may be nonspecific, imag-

ing is central to reaching the correct diagnosis and assists in workup and therapeutic decisions. Most of the emergent and reemergent diseases discussed in this review cause neurologic manifestations because of two distinct mechanisms. The first is secondary encephalopathy, which does not cause direct damage to the central nervous system (CNS) but is related to systemic abnormalities that cause CNS dysfunction, such as hypovolemia or metabolic disturbances. The second mechanism is direct CNS damage caused by lesions on the encephalitis-myelitis spectrum, expansive lesions such as abscesses and syphilitic gummas, or ischemic or hemorrhagic strokes. Imaging may aid in the distinction between the two mechanisms, which may be difficult to achieve on the basis of neurologic examination alone.

Distinct types of CNS lesions require different diagnostic workups and therapeutic management. Although abscesses may prompt the administration of antibiotic therapy, suspected syphilitic gummas may require biopsy for diagnostic confirmation. Imaging is paramount not only to detect but also to characterize CNS disease, and ultimately to guide decision making on further diagnostic workup or therapeutic management.

CT is useful for distinguishing secondary encephalopathy from direct CNS damage and is frequently the first imaging examination performed, given its widespread availability and fast results. However, MRI provides better soft-tissue contrast resolution and more information about CNS disease than does CT. At our institution, we use a somewhat standard MRI protocol for evaluating brain infectious diseases that comprises sagittal fast spin-echo T1-weighted, axial fast spin-echo T2-weighted, axial fluid-attenuated inversion-recovery (FLAIR), axial susceptibility-weighted, gadolinium-enhanced isotropic spoiled gradient-recalled acquisition in steady state T1-weighted, and gadolinium-enhanced fat-saturated coronal T1-weighted MRI and diffusion-weighted imaging (DWI). Whenever meningeal involvement is suspected, we also perform volumetric gadolinium-enhanced FLAIR MRI, which is often more sensitive for showing leptomeningeal enhancement than is T1-weighted MRI. Specific MRI sequences not included in this protocol may be useful to evaluate some emergent and reemergent infections.

Viral Infections

Enterovirus 71

An *enterovirus* (EV) is a single positive-stranded RNA virus that belongs to the family Picornaviridae (4,5). They are closely related to polioviruses, coxsackie groups A and B viruses, and echovi-

ruses, and are major etiologic agents of hand, foot, and mouth disease and herpangina (5).

Epidemiology.—EV71 was isolated for the first time in California in 1969 (4,5). Since then, it has emerged as an important global public health issue. Today, it is recognized as an epidemic disease that occurs mainly in Southeast Asia and the western Pacific, but it also has been reported in Australia, the United States, Japan, and Brazil (2,4,5). The latest large-scale epidemic occurred in China in 2008, with an estimated 490 000 people infected and an atypically large number of severe cases with neurologic manifestations. These severe complications were responsible for many fatal cases and were attributed to an emerging recombinant variant of EV71 (5,6).

Pathophysiologic and Clinical Issues.—Similar to other EVs, EV71 is transmitted from person to person through contact with saliva, respiratory secretions, fluid in vesicles, and feces (5). Most cases manifest in young children as a nonspecific febrile illness that lasts 3 days, with or without accompanying upper-respiratory and gastrointestinal symptoms, followed by recovery. A characteristic maculopapulovesicular rash may ensue, typically involving the hands, feet, and oral cavity; hence the name hand, foot, and mouth disease (2,5).

An estimated 10%–20% of patients who present with an EV71 infection develop CNS disease, which is responsible for most of the severe cases (2). The pathway through which the virus reaches the CNS is poorly understood, but two mechanisms have been proposed: (a) The viruses cross the blood-brain barrier or, more likely, (b) the viruses ascend through peripheral nerves by means of retrograde axonal transport (5,7). The viral presence in the CNS elicits an inflammatory response, which translates clinically to aseptic meningitis or meningoencephalitis and/or myelitis-related acute flaccid paralysis.

EV71 encephalitis usually and predominantly affects the brainstem and the cerebellum (ie, rhomboencephalitis); thus patients frequently present with myoclonus, tremor, or ataxia (2,6). Several authors (4) described other symptoms, such as cranial nerve palsies, disturbed level of consciousness, hemiparesis, or monoparesis. The prognosis of EV71 encephalitis is variable, ranging from recovery with minor neurologic sequelae to death (8). However, the most notable clinical issue associated with EV71 is acute flaccid paralysis or acute flaccid myelitis syndrome. This condition is clinically indistinguishable from poliomyelitis, and patients present with sudden-onset limb weakness and loss of muscle tone and reflexes. Some patients also have eye movement

disorders, ptosis, facial paralysis, and swallowing difficulties (2,9).

Since 2014, an increasing number of cases of acute flaccid myelitis, most of them in children (9), have been reported to the Centers for Disease Control and Prevention (CDC). No pathogen was detected in the cerebrospinal fluid (CSF) of most of these patients, but EV71, coxsackievirus A16, and/or EV D68 were isolated from the CSF in some patients (9). Since then, the CDC has been monitoring this condition, and American health professionals and health departments have been encouraged to report both confirmed and suspected cases (9). The long-term prognosis of acute flaccid paralysis or acute flaccid myelitis syndrome is poorly known (9).

Imaging.—Most types of viral encephalitides show the nonspecific brain imaging features of T2-hyperintense areas in the cortex and subcortical white matter at MRI (4). However, in EV rhomboencephalitis, a relatively specific pattern of ill-defined patchy T2- and FLAIR-hyperintense lesions (usually without substantial supratentorial lesions) in the brainstem and cerebellum is observed in most patients (4). The lesions usually are unilateral and are frequently observed in the posterior pons and medulla oblongata, the substantia nigra of the midbrain, and the dentate nucleus of the cerebellum (4,8).

The imaging features of EV71 rhomboencephalitis may be similar to those of other agents such as *Listeria monocytogenes*. Although the most common manifestation of herpes simplex encephalitis is involvement of the limbic system, a rhomboencephalitis pattern also may be observed. However, both of these conditions usually affect older patients who may be immunodeficient, whereas EV71 rhomboencephalitis usually is seen in otherwise healthy children.

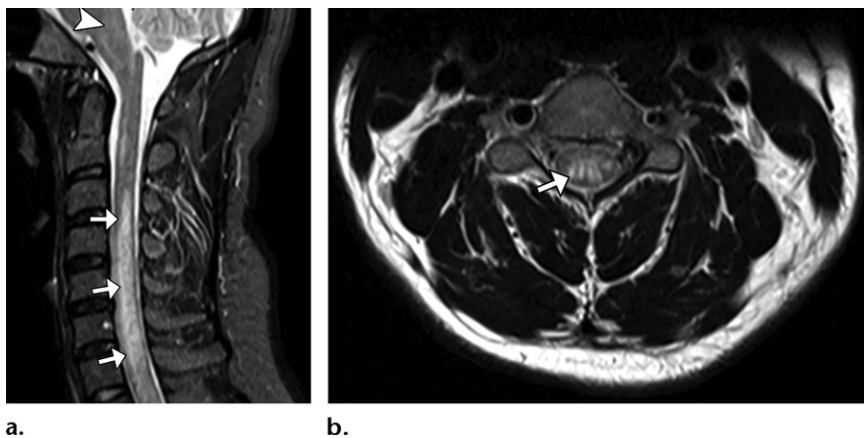
Cervical spinal cord lesions may be observed at MRI in patients with EV myelitis. Typical cord lesions are described as unilateral or bilateral T2-hyperintense areas involving the anterior horns, with or without spinal expansion (Fig 1) (8). Additional high-spatial-resolution fast imaging employing steady-state acquisition (FIESTA) may be helpful to better characterize spinal cord lesions.

Measles

Measles is an RNA virus that is a member of the *Morbillivirus* genus and the Paramyxoviridae family. It is highly contagious but preventable with a vaccine and is one of the most deadly childhood illnesses that cause a rash and fever (10).

Epidemiology.—The incidence of measles dramatically decreased in countries where vaccination

Figure 1. EV myelitis in a 30-year-old man with acute onset of paraparesis. **(a)** Sagittal short inversion time inversion-recovery (STIR) MR image shows an extensive hyperintense longitudinal cervical spinal cord lesion (arrows). Additional discrete hyperintensities are seen in the medulla oblongata (arrowhead). **(b)** Axial T2-weighted MR image reveals expansion of the spinal cord and hyperintensities in its central gray matter and surrounding white matter (arrow).



with live-attenuated measles was instituted. In the United States, the vaccine was introduced in 1963, and the number of cases of measles decreased progressively from an estimated 3–4 million annually to virtual elimination of endemic transmission in 2001 (11,12). Unfortunately, since 2004, the disease has reemerged, with a substantial increase in the number of cases reported annually (9,11). This has been attributed to factors including importation of measles virus from other countries and intentional nonvaccination. Nonvaccination has increased, particularly among some parents in the upper and middle classes in Western countries, who believe that vaccines cause health problems such as autism, although high-quality studies have found that vaccines are not associated with these conditions (9,11). According to the World Health Organization, 173 330 cases of measles were reported globally in 2017 (10).

Pathophysiologic and Clinical Issues.—Measles virus is one of the most communicable of all human diseases and spreads through direct contact with respiratory droplets, or less commonly, through contact with the airborne virus or with articles freshly soiled with nasal and throat secretions of infected patients (10–12). The virus infects the respiratory epithelium and adjacent lymph nodes, where it replicates before entering the bloodstream and reaching target organs such as the skin, lungs, liver, and in rare cases, the CNS (11).

Clinical findings include a high fever, nasal discharge, conjunctivitis, and a clustered exanthem on the buccal mucosa (Koplik sign), which usually precedes the appearance of a diffuse cutaneous rash (10).

The virus is believed to enter the CNS through cerebral endothelial cells or infected monocytes. Four different forms of encephalitis related to the measles virus have been described (11,12), each with a different pathogenesis and clinical course.

Primary measles encephalitis is the result of direct viral invasion of the brain cells during an acute systemic measles infection. It occurs in one of every 1000 patients with measles, typically during the exanthematous phase of the illness (11,12). Primary measles encephalitis causes neuronal injury and associated lymphocytic infiltrate in the brain and meninges, and the main clinical findings are fever, headache, altered mental status, motor deficits, and seizures (11,12). An estimated 10%–15% of patients who present with primary measles encephalitis die, and another 25% retain some form of permanent neurologic sequelae (11,12).

Measles-related *acute disseminated encephalomyelitis* (ADEM), which is also referred to as acute postinfectious measles encephalomyelitis, is an immune-mediated brain inflammation without viral inclusions in the CNS. ADEM also occurs after many other viral and bacterial infections and is essentially a demyelinating disorder that complicates a systemic infection. Measles ADEM occurs in one in 1000 patients with measles (11,12). More rarely, it occurs after vaccination with live attenuated measles (one to two cases per 1 million people vaccinated), in which case, it manifests with a much less severe course (11). Contrary to primary measles encephalitis, measles ADEM manifests after resolution of the acute exanthematous phase of the disease, often months after the systemic illness is over (12). Symptoms include motor and sensory deficits, ataxia, and altered mental status that may be associated with back pain and urinary bladder and bowel dysfunction when the spinal cord is involved (myelitis) (11). Treatment includes administration of corticosteroids, intravenous immunoglobulin, and plasmapheresis. The prognosis for measles ADEM is better than that for primary measles encephalitis, with 80%–90% of patients achieving full recovery and some sustaining substantial neurologic sequelae (11).

Measles inclusion body encephalitis commonly affects immunocompromised children who are not able to clear the measles virus after primary infection (11). Most reported cases have occurred in children with lymphoblastic leukemia, but it also has been associated with other causes of immunodeficiency, such as HIV infection, a solid organ or stem cell transplant, malignancies, and autoimmune diseases (11,12). Brain biopsy reveals glial cell proliferation, with areas of necrosis and perivascular inflammation associated with neuronal and glial viral inclusion bodies, which suggests that direct invasion of the brain cells is the mechanism responsible for CNS disease (11,12). Clinically, these patients present with an altered mental status and intractable seizures (11). Measles inclusion body encephalitis has a poor prognosis, with a mortality rate of 75%, while the survivors usually retain substantial neurologic deficits (11).

Subacute sclerosing panencephalitis is caused by a persistent infection of a defective measles virus and is thought to be related to an immature immune system, because it usually is observed in children who contracted the primary infection during the first 2 years of life (11,13). This complication usually manifests 6–15 years after the primary measles infection and occurs mostly in boys, although systemic measles shows no predominance in either sex (11,12). Initial symptoms may be subtle, including mild behavior alterations that progress relentlessly over 1–3 years to more obvious intellectual deficits, motor dysfunction (eg, myoclonic jerks, dyskinesia, and cerebellar ataxia), and visual abnormalities (eg, chorioretinitis and optic neuritis) (11,12). Neurologic symptoms progress inevitably to stupor, autonomic instability, and eventual death in nearly all cases (11).

Imaging.—Imaging findings of primary measles encephalitis usually reflect the inflammatory nature of this disease. The MRI appearance is usually striking but not specific, with multiple bilateral T2-hyperintense lesions in the hemispheric white matter and the cortex and a mild expansive effect (12,13). The striatum (caudate nucleus and putamen) typically is involved and also shows T2-hyperintense lesions, although this also can be seen in patients with other types of infectious encephalitis, such as those caused by mumps, echovirus 25, and mycoplasma viruses (12,13). Transient abnormalities of the splenium of the corpus callosum have been described (12), namely reversible T2 hyperintensity and restricted diffusion, which are thought to represent edema, inflammatory changes, and metabolic abnormalities. Cortical and leptomeningeal enhancement is seen in some patients after intravenous gadolinium administration (13).

ADEM shows the typical imaging findings of a demyelinating disease, which are multiple bilateral focal T2-hyperintense white matter lesions, without a substantial mass effect or vasogenic edema (12). Paramagnetic agent enhancement is variable, sometimes with the incomplete annular enhancement characteristic of demyelinating diseases (12). These findings are not specific for measles ADEM, because they are undistinguishable from those observed in ADEM related to other viral and bacterial infections.

Usually imaging findings are initially normal in patients who present with symptoms of measles inclusion body encephalitis; however, edema and eventual cerebral atrophy are noted at follow-up imaging (12).

MRI reveals mildly decreased gray matter volume, notably in the frontotemporal cortex, amygdala, and cingulate gyrus in the early stages of subacute sclerosing panencephalitis. In addition, multifocal T2-hyperintense lesions in the cortex, periventricular white matter, basal ganglia, and brainstem are described. As the disease progresses, diffuse cortical atrophy is noted (Fig 2) (11,14,15).

Influenza

Influenza viruses are negative single-stranded RNA viruses of the Orthomyxoviridae family and are responsible for worldwide epidemics and pandemics, with high morbidity and mortality rates (12,16,17). Three types of virus are recognized. Influenzas A and B cause seasonal epidemics, while influenza C generally only causes mild disease (17). Influenza A is also responsible for the pandemic form and is further classified into subtypes on the basis of the antigenic properties of its two surface glycoproteins: hemagglutinin and neuraminidase. To our knowledge at the date of publication, 18 hemagglutinin and 11 neuraminidase subtypes have been identified (H1–H18 and N1–N11, respectively) (17).

Epidemiology.—Both forms of influenza (epidemic and pandemic) occur globally (17). The epidemic form typically shows a predictable seasonality in temperate regions, whereas in tropical regions it can occur all year, with unpredictable peaks (17). The pandemic form of influenza A occurs sporadically and caused four global pandemics in the last 101 years: H1N1 Spanish influenza (1918), H2N2 Asian influenza (1957), H3N2 Hong Kong influenza (1968), and H1N1 swine influenza (2009) (12,16,17).

Pathophysiologic and Clinical Issues.—Influenza viruses spread from person to person through aerosol or direct contact with respiratory droplets (17). The epidemic forms of influenza virus are

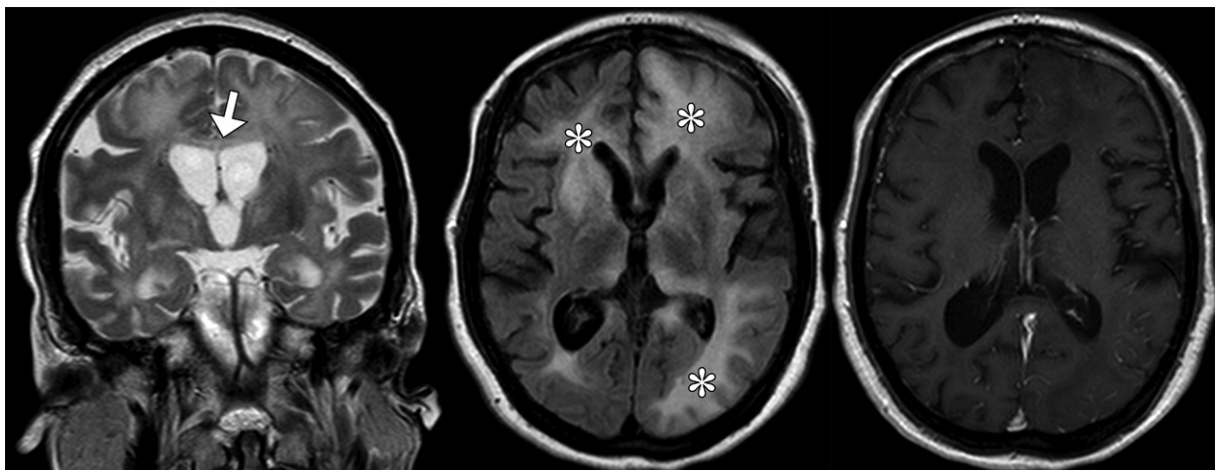
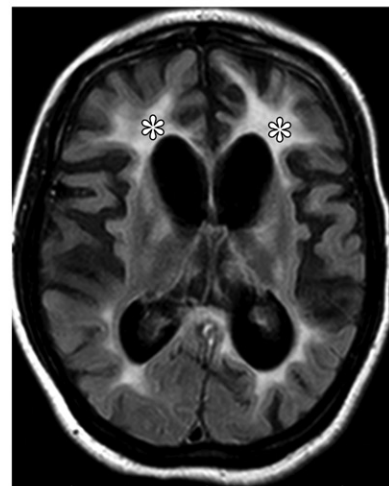
**a.**

Figure 2. Measles infection complicated by subacute sclerosing panencephalitis in an immunocompetent 24-year-old woman who presented with dizziness and fast paroxysmal contractions of the upper limbs. **(a)** Coronal T2-weighted MR image at the level of the foramina of Monro (left) shows mild cerebral volume loss and a thinned diffusely hyperintense corpus callosum (arrow). Axial FLAIR MR image (center) exhibits confluent asymmetric hyperintensities (*) in the basal ganglia, thalamus, left frontal cortex, and bilateral periventricular and subcortical white matter that mainly affect the left cerebral hemisphere. Axial gadolinium-enhanced T1-weighted MR image (right) does not show abnormal enhancement. **(b)** Axial FLAIR MR image obtained at 10-month follow-up reveals important worsening of diffuse cerebral volume loss; bilateral hyperintensities are still visible in the periventricular and subcortical white matter (*). (Case courtesy of Heliantho Lima, MD, Campinas, São Paulo, Brazil.)

not affected by vaccination or by previous exposure-induced immunity through a mechanism called antigenic drift, which permits antigenic variations in the surface glycoproteins of the virus, resulting in seasonal epidemics (16–18). Another genetic event, called antigenic shift, is restricted to influenza A viruses and is defined as the emergence of a new viral strain to which a large proportion of the population does not have immunity (17,18). This results in global pandemics if the virus strain is efficient in spreading from person to person (17).

Seasonal influenza can be asymptomatic or it can manifest as a fulminant illness, but the most typical symptoms include fever, chills, headache, myalgia, anorexia, nonproductive cough, sore throat, and nasal congestion and/or discharge (12,17).

Neurologic complications of influenza infection include meningoencephalitis, Reye syndrome, acute necrotizing encephalopathy, and myelitis (12,17,19–21). Although the pathogenesis of the influenza neurologic disease is not completely clear, pandemic strains (as opposed to epidemic influenza) are capable of down-regulating the expression of more than 30 genes involved in the CNS gene network, which presumably predisposes the host to neurologic complications, particularly when the host is a child (18). Some studies suggest that acute necrotizing encephalopathy is not related to the direct viral invasion of the brain but is triggered by an exaggerated immune response to

**b.**

the virus in the respiratory tract, with an overwhelming systemic cytokine response (19,21). The nonneurologic complications of influenza affect multiple organ systems and are beyond the scope of this review.

Imaging.—The radiologic appearance of acute necrotizing encephalopathy related to pandemic influenza is varied, but the hallmark findings are bilateral symmetric T2-hyperintense lesions that are associated with restricted diffusion and involve the thalamus, brainstem, and/or cerebellum (Fig 3) (12,19,20). Additional findings are foci of magnetic susceptibility in the affected areas and adjacent leptomeningeal enhancement, which may be noted after administration of gadolinium contrast material (19,20). Transient T2-hyperintense lesions in the splenium of the corpus callosum, which show restricted diffusion, are reported frequently, but this finding is also nonspecific for influenza and may be present in patients with other viral (eg, rotavirus, mumps virus, varicella-zoster virus, adenovirus, and measles virus) and bacterial infections, demyelinating conditions, and metabolic disturbances (12,20).

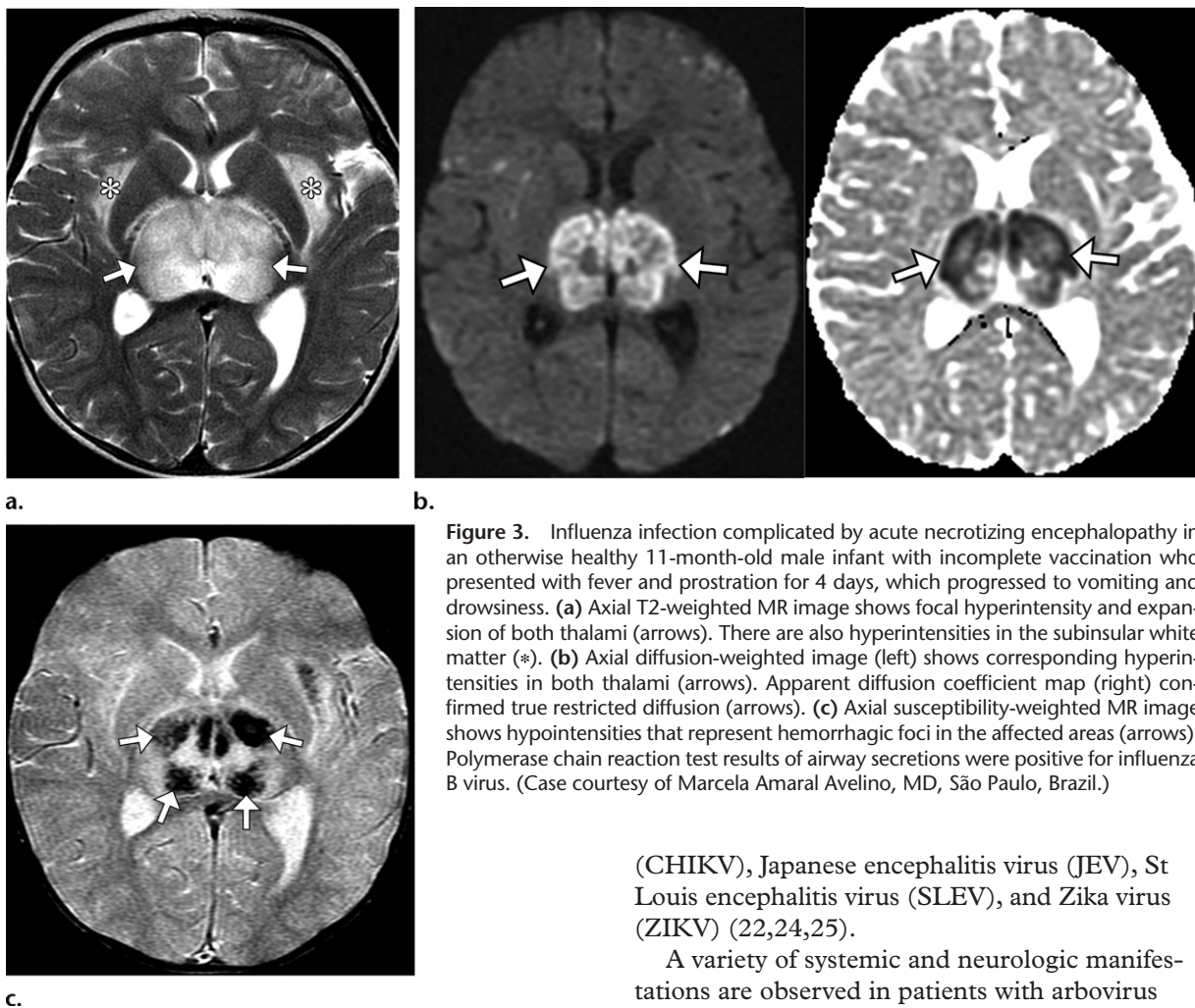


Figure 3. Influenza infection complicated by acute necrotizing encephalopathy in an otherwise healthy 11-month-old male infant with incomplete vaccination who presented with fever and prostration for 4 days, which progressed to vomiting and drowsiness. (a) Axial T2-weighted MR image shows focal hyperintensity and expansion of both thalami (arrows). There are also hyperintensities in the subinsular white matter (*). (b) Axial diffusion-weighted image (left) shows corresponding hyperintensities in both thalami (arrows). Apparent diffusion coefficient map (right) confirmed true restricted diffusion (arrows). (c) Axial susceptibility-weighted MR image shows hypointensities that represent hemorrhagic foci in the affected areas (arrows). Polymerase chain reaction test results of airway secretions were positive for influenza B virus. (Case courtesy of Marcela Amaral Avelino, MD, São Paulo, Brazil.)

(CHIKV), Japanese encephalitis virus (JEV), St Louis encephalitis virus (SLEV), and Zika virus (ZIKV) (22,24,25).

A variety of systemic and neurologic manifestations are observed in patients with arbovirus infections, ranging from asymptomatic or mildly symptomatic viremia to severe neurologic and nonneurologic complications, which eventually may lead to death (22,24,25). Some of the clinical features of the arboviruses overlap; therefore, neuroimaging findings, epidemiologic information, clinical profiles, and CSF analysis may provide clues to help distinguish among the infections (22,24,26).

Acute necrotizing encephalopathy is not associated exclusively with influenza virus. Similar clinical and imaging findings may be observed with parainfluenza, varicella-zoster virus, herpes simplex, and even measles and EVs.

Arboviruses

The term *arbovirus* means “arthropod-borne virus” and refers to RNA viruses of different families that spend part of their life cycle in arthropod hosts (mainly mosquitoes) and are spread by their bites (22–24). Arboviruses are associated with high fatality rates and a massive incidence of infection, making them the most important international infectious threat to human neurologic health, according to Rust et al (22).

Dengue virus (DENV) infects approximately 390 million people annually worldwide. The RNA genome of arboviruses permits a high genetic plasticity and frequency of mutation, granting fast adaptation to the ever-changing host and environmental conditions, and this is the main reason for the growth in the geographic range of emerging arboviruses such as DENV, chikungunya virus

DENV Infection

DENV is a mosquito-borne infection that occurs mostly in urban and suburban areas in tropical and subtropical regions of the world (26,27). DENV is an RNA virus that belongs to the *Flavivirus* genus, and the Flaviviridae family, comprising four distinct serotypes (DENV-1 to DENV-4) (28).

Epidemiology.—According to the World Health Organization, DENV is the most rapidly spreading mosquito-borne illness in the world (27,28). It has shown increasing geographic expansion, having emerged in various countries over the last 50 years, mainly in the tropical Americas, Southeast Asia, and the western Pacific (27,29). Many factors help to explain the international

spread of DENV. Some are related to the biologic characteristics of the virus (eg, the existence of four different serotypes, which prevents life-long acquired immunity against different serotypes; the virulence of some strains; and the high viral replication rate). Others concern intrinsic characteristics of the vector (eg, high reproduction rate and adaptation to the environment) or changes in human behavior and activities (eg, population growth with unplanned and uncontrolled urbanization, which creates ideal conditions for the proliferation of mosquitoes) (29–31).

In addition to the emerging outbreaks, the infection is endemic in many countries, with 3.9 billion people living in areas with high transmission risk (27). An estimated 390 million cases of DENV infection occur each year globally, and 96 million patients present clinically; thus, the public health importance of this condition cannot be overstated (27).

Pathophysiologic and Clinical Issues.—DENV is transmitted to human hosts through the bite of infected mosquitoes, predominantly those of the genus *Aedes*. Infected humans then develop viremia and spread the disease to infection-naïve mosquitoes (ie, mosquitoes that have not yet had contact with the virus), perpetuating a human-to-mosquito-to-human cycle, usually without additional hosts (27–29). The main species involved in this cycle is *A. aegypti*, a tropical and subtropical mosquito that is distributed widely around the world; however, *A. albopictus* also has been incriminated in some outbreaks in Asia, Africa, and the Americas (27,28).

The majority of DENV cases are asymptomatic or mildly symptomatic, with the most common manifestations being sudden onset of fever, accompanied by headache, retro-orbital pain, generalized myalgia and arthralgia, nausea, and abdominal pain, with or without an associated generalized rash (27). Most patients recover after a self-limited clinical course, but a small proportion progress to a more severe disease that is characterized by capillary plasma leakage and thrombocytopenia, with or without hemorrhage (28). This is the main complication of DENV infection and is referred to as *DENV hemorrhagic fever*. It is difficult to predict which patients will develop this more serious clinical condition (28).

In recent years, neurologic manifestations of DENV infection have been reported increasingly, with the incidence varying from 0.5% to 21% of cases (26,31). The most common neurologic manifestation of DENV is encephalopathy secondary to systemic disease, but an encephalitic clinical pattern can be observed, as can neuromuscular dysfunction, immune-mediated syn-

dromes (eg, DENV-related ADEM and Guillain-Barré syndrome [GBS]) and neuro-ophthalmic disorders (26,31).

The neuropathogenesis of DENV varies with the different forms of neurologic manifestations. DENV encephalopathy, which involves a diminished level of consciousness, can be caused by several factors including prolonged shock, anoxia, cerebral edema, metabolic disturbances (eg, hyponatremia), and acute liver and/or renal failure, all of which occur without direct viral injury to the brain (31). Also, vascular abnormalities characterized by increased permeability of systemic and brain blood vessels can lead to DENV-related strokes or, more frequently, intracranial hemorrhage (28,31). DENV encephalitis is related to direct CNS invasion and neurotropic effects of DENV (31). Patients with DENV encephalitis present with a variety of neurologic symptoms such as consciousness disturbances, headache, dizziness, seizures, and behavioral changes (31).

Imaging.—CT of the brain may be particularly useful in patients with DENV, because it can show spontaneously hyperattenuating intraparenchymal macrohemorrhages that are related to cerebrovascular dysfunction (ie, hemorrhage due to increased vascular permeability) or to DENV hemorrhagic encephalitis (Fig 4) (29).

However, MRI is better than CT for depiction of the classic pattern of DENV encephalitis, which is T2-hyperintense lesions that affect the cortical gray matter, subcortical and deep white matter, basal ganglia, and thalamus, usually showing some degree of expansive effect (26,29). Patchy areas of restricted diffusion in the affected areas are seen in most patients, as are microhemorrhages, which are seen as small foci of blooming at susceptibility-weighted MRI (26,29).

More rarely, similar lesions are found in less typical locations, such as the brainstem (particularly in the substantia nigra of the midbrain), hippocampus, and cerebellum (Fig E1) (29). The main conditions to consider in the differential diagnosis of DENV encephalitis are JEV, herpes simplex encephalitis, and ADEM (26). The imaging pattern in JEV may be similar to that for DENV; however, hemorrhagic findings, although described, are much less common in the former than in the latter, which may help to differentiate these two conditions (26).

Herpes simplex encephalitis characteristically manifests as bilateral asymmetric involvement of the limbic system, medial temporal lobes, insular cortices, and inferolateral frontal lobes, usually sparing the basal ganglia. ADEM is an immune complex-mediated injury to the brain that usu-

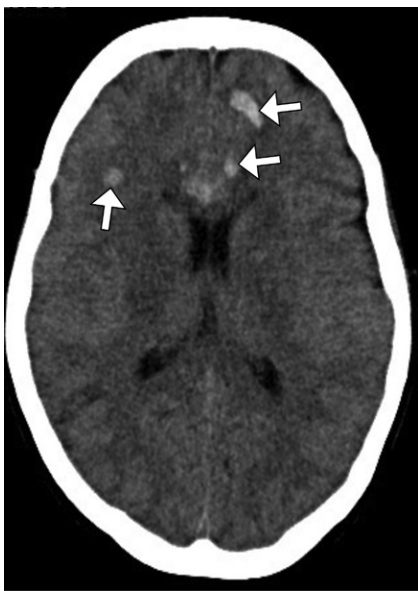


Figure 4. DENV infection with acute hemorrhage in a 40-year-old woman who presented with an altered consciousness level, a fever for 1 week, headache, and myalgia. Axial nonenhanced CT image shows multifocal hyperattenuating lesions at the gray-white matter junction in both frontal lobes and in the corpus callosum, which are findings compatible with hemorrhagic foci (arrows).

ally is observed in the convalescence phase of different viral infections, including DENV (26). It is characterized by multifocal poorly defined T2-hyperintense lesions that are observed frequently in the cerebral and/or cerebellar white matter, basal ganglia, and thalamus, with or without spinal cord lesions, but hemorrhage is uncommon (Fig E1). The temporal relationship between the detection of CNS lesions and the febrile illness may help to differentiate ADEM from DENV encephalitis, because ADEM manifests during the afebrile convalescence phase of the disease, whereas the encephalitis usually is seen during the febrile period (26).

Although rare, another pattern of CNS manifestation that has been linked to DENV is posterior reversible encephalopathy syndrome (PRES), which exhibits T2 hyperintensity that is related mostly to vasogenic edema in the occipital and parietal subcortical white matter (Fig 5; Fig E2) (29).

CHIKV Fever

CHIKV belongs to the genus *Alphavirus*, and is a member of the Togaviridae family (32–34). The origin of the word “chikungunya,” which means “those who bend up,” referring to the potentially debilitating arthritic symptoms caused by the virus (32–34), is the Makonde language, which is spoken in Tanzania and Mozambique.

Epidemiology.—Although the virus was isolated for the first time in Tanzania in 1952–1953, it is believed to have been circulating and causing outbreaks in Africa since the 18th century (32–35). CHIKV is considered an enzootic virus that is found in many tropical and subtropical regions of Africa and Asia, but a relevant number of annual cases were rarely reported before the year 2000 (34). After decades of absence, the virus reemerged in both Africa and Asia, causing large outbreaks and becoming an important public health issue (34). In February 2005, a major CHIKV outbreak occurred on the islands of the Indian Ocean. This outbreak caused many cases in Europe, most of which occurred in 2006. In the Americas, the first confirmed autochthonous cases were reported in 2013 on St Martin Island in the Caribbean Sea (32). In 2014–2015, several South American countries confirmed local transmission: Bolivia, Brazil, Ecuador, Colombia, Paraguay, Venezuela, and Argentina. The first cases of local transmission in the continental United States were reported in Florida in July 2014 (35).

Pathophysiologic and Clinical Issues.—CHIKV is transmitted most commonly to human hosts by means of the bites of mosquitoes of the species *A. aegypti* and *A. albopictus*; however, many other species of the genu *Aedes* sp have been incriminated as vectors (33–35). Although the sylvatic transmission cycle of the virus is maintained between nonhuman primates or small mammals and mosquitoes, CHIKV can circulate between humans and mosquitoes during epidemics, with no need for animal reservoirs (34). In addition to vector transmission, maternal-fetal (vertical) and blood transfer–associated transmission also have been described (34).

Clinically, CHIKV fever is similar to DENV and usually manifests with sudden-onset high fever, severe arthralgia and myalgia, headaches, photophobia, and cutaneous exanthema (34). Unlike those of DENV, most cases of CHIKV are symptomatic (34). The clinical hallmark of CHIKV infection is severe polyarthralgia, which is usually symmetric, affecting the fingers, wrists, ankles, elbows, toes, and/or knees; this is frequently the most disabling symptom of the disease (33,34). Most patients recover fully 1–2 weeks after the onset of symptoms, but the arthralgia may persist for months or even years, and some patients develop persistent arthralgia (34).

CHIKV infection may complicate and affect different organ systems, in which case it is termed *atypical CHIKV fever* (33,34). Neurologic complications described in the literature include different combinations of encephalitis and myelitis (ie, isolated encephalitis, isolated myelitis, combined

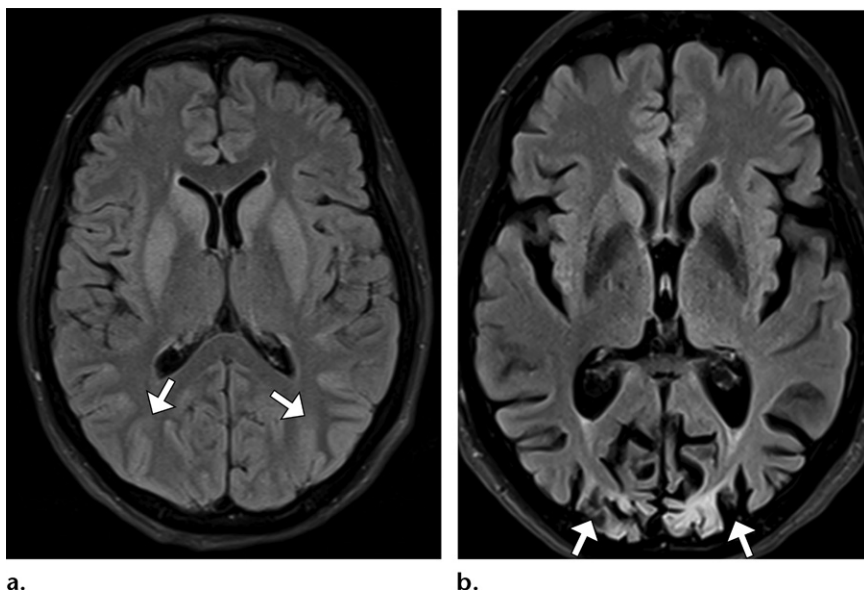


Figure 5. Serologically confirmed DENV infection with PRES in a 44-year-old woman who presented with an occipital headache and a convulsive crisis. (a) Axial FLAIR MR image acquired at presentation shows mild signal hyperintensity in the subcortical white matter of the parietal and occipital lobes (arrows). (b) Axial FLAIR MR image at 6-month follow-up shows the evolution to encephalomalacia in the parietal and occipital lobes (arrows). (Case courtesy of Juliana Souza Silva, MD, Juiz de Fora, Brazil.)

encephalomyelitis), and CHIKV-associated peripheral neuropathy manifests as GBS, which may occur without CNS involvement (32–34). The encephalitis and encephalomyelitis spectrum of neurologic disease is thought to be the result of direct viral infection of the brain, leading to neuronal degeneration, microgliosis, and perivascular cuffs, while GBS is recognized as an immune-mediated condition (32).

CHIKV encephalitis usually manifests with altered mental status and seizures and with focal neurologic deficits in some cases, while myelitis manifests with limb weakness, sensory changes, hyperreflexia, and bowel and bladder disturbances, depending on the location of the lesions in the spinal cord and the extent to which the spinal cord is involved (33). Noninflammatory encephalopathy secondary to a nonspecific manifestation of a severe systemic condition such as brain hypoperfusion related to systemic hypovolemia also may occur (33,34). CHIKV-associated GBS is similar to GBS associated with other infections (eg, *Campylobacter jejuni*) and usually manifests 3–17 days after the CHIKV infection is resolved, with symmetric bilateral flaccid weakness, with or without associated paresthesia and/or cranial nerve palsy (34). Also, similar to other acute viral conditions, CHIKV may trigger postinfectious immune-mediated ADEM (33).

Given this large spectrum of neurologic disease and the scarce epidemiologic data on the subject, it is difficult to estimate accurately the frequency of neurologic disease in patients with CHIKV fever (33).

Imaging.—The most adequate imaging method to evaluate CHIKV-related encephalitis is MRI, which shows scattered punctate T2-hyperintense

lesions distributed predominantly along the periventricular white matter, which also may exhibit restricted diffusion and T1 shortening after intravenous administration of paramagnetic agents (Fig 6) (33,36). In some cases, lesions may be confluent, showing a more extensive pattern of white matter involvement that possibly affects the subcortical regions (36). Relevant conditions to evaluate in the differential diagnosis are cerebral fat embolism and septic-embolic encephalitis, although the clinical context is usually sufficient to differentiate these conditions from CHIKV infections (eg, a febrile patient with arthralgia for a CHIKV infection, neurologic symptoms after bony fractures and/or orthopedic surgery for cerebral fat embolism, and neurologic symptoms in patients with endocarditis in septic-embolic encephalitis). Epidemiologic information also may help to distinguish CHIKV from these diagnoses, with CHIKV being more probable during known epidemics.

The radiologic appearance of CHIKV myelitis is variable, ranging from short-segment demyelinating-like T2-hyperintense lesions, with or without gadolinium enhancement at T1-weighted MRI, to longitudinally extensive T2-hyperintense lesions that usually affect the cervical segment of the spinal cord (33).

At imaging, GBS related to CHIKV is generally no different from GBS caused by other agents, and MRI usually shows gadolinium enhancement of the cauda equina nerve roots and cranial nerves (36). MRI findings of CHIKV-related ADEM are also indistinct from ADEM caused by other viral infections, which usually manifest 5–16 days after the initial onset of fever, arthralgia, and rash symptoms as focal or multifocal poorly demarcated T2-hyperintense white matter lesions (33).

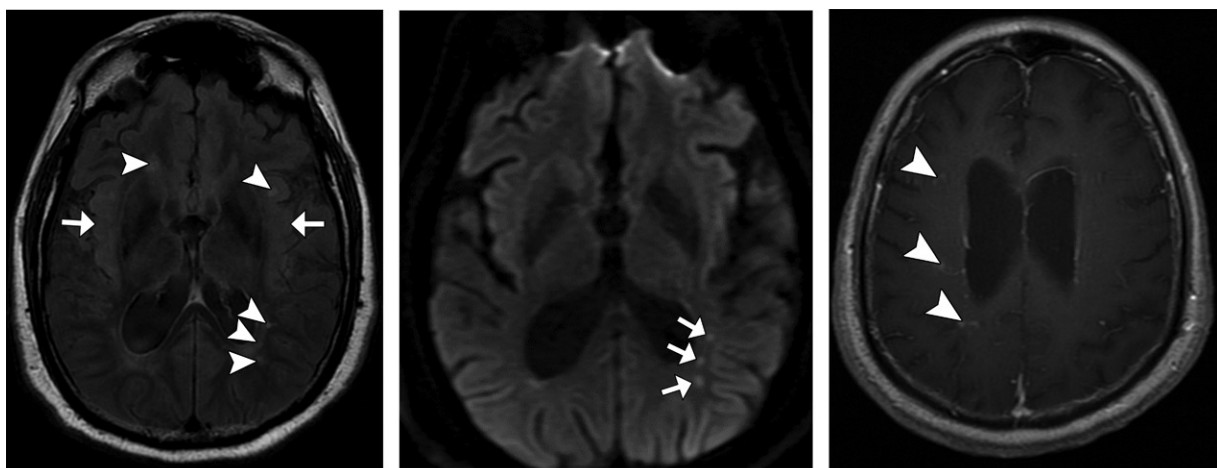


Figure 6. CHIKV encephalitis in a 62-year-old man who presented with arthralgia, headache, and fever, with worsening of symptoms in the past week; the onset of tetraplegia; and reduced level of consciousness. Serum real-time polymerase chain reaction results were positive for CHIKV. (a) Axial FLAIR MR image shows multiple bilateral punctate hyperintensities in the temporal and parietal white matter (arrowheads) and atypical involvement of both insular cortices, which show elevated signal intensity (arrows). Hyperintensities seen in the ventricular system are due to lack of complete CSF suppression due to CSF flow artifacts. (b, c) Axial diffusion-weighted image (b) and axial contrast material-enhanced T1-weighted MR image (c) show that some of the lesions exhibit high signal intensity (arrows in b) and contrast material enhancement (arrowheads in c). The apparent diffusion coefficient map (not shown) confirmed that the hyperintensities seen at DWI were true restricted diffusion. (Case courtesy of Tomás de Andrade Lourenço Freddi, MD, São Paulo, Brazil.)

ZIKV Infection

ZIKV is a mosquito-borne positive-stranded RNA virus of the genus *Flavivirus* and the family Flaviviridae and is phylogenetically closely related to DENV, yellow fever, JEV, and West Nile virus (WNV) (37–39). The name “Zika” comes from the Ziika forest of Uganda, where the virus was first isolated in 1947 (32,38,40).

Epidemiology.—ZIKV infections were confined to an equatorial zone in Africa and Asia for 60 years since it was first isolated (38). However, in 2007, it emerged on the western Pacific island of Yap, in the Federated States of Micronesia. It spread to French Polynesia and other Pacific islands in 2013–2014, quickly reaching Latin America in 2015 and North America in 2016 (32,37–39). According to the CDC, 5168 cases of symptomatic ZIKV were reported in the United States in 2016, and 224 of those were acquired through presumed local mosquito-borne transmission in Florida (41). Since November 2016, incidence of ZIKV infection has decreased in all affected countries and territories in the Americas, except for Mexico, Panama, and the islands of Turks and Caicos (38). Despite this decline, vigilance must remain high, because ZIKV may continue to spread geographically into areas with competent vectors.

Pathophysiologic and Clinical Issues.—The main form of ZIKV transmission is through bites of mosquitos of the genus *Aedes* (eg, *A. aegypti*, *A. africanus*, *A. albopictus*, *A. apicoargenteus*, *A. furcifer*) (38,39). The sylvatic cycle of ZIKV includes non-

human primates and arboreal mosquitoes in forests. It is believed that the virus occasionally was transmitted from nonhuman primates to humans by arboreal mosquitoes, thus initiating a different cycle of transmission that involves humans as hosts and urban mosquitoes as vectors (the urban cycle) (38). ZIKV also can be passed from mother to child during pregnancy (vertical transmission), or spread through sexual contact, breast-feeding, or blood transfusion (38–40).

An estimated 80% of ZIKV infections are asymptomatic (38). The symptomatic patients most commonly present with a mild self-limited illness that is characterized by transient low-grade fever, an itchy maculopapular rash, arthralgia, and nonpurulent conjunctivitis, with or without associated retro-orbital pain, headaches, myalgia, and vomiting (37–39). It is probably an underdiagnosed disease, because its symptoms resemble those of DENV and CHIKV fever, both of which are much more prevalent conditions that share similar vectors and occur in the same regions (39,40).

One of the main issues of ZIKV is the development of congenital microcephaly in newborns of infected pregnant women. *Microcephaly* is defined as a head circumference measurement obtained after birth that is less than either the mean value or the second percentile for the age and sex of the infant (38–42). This phenomenon was first noticed in Brazil in 2015, when the number of newborns with congenital microcephaly began to increase as ZIKV emerged (39,42). Subsequently, retrospective studies conducted in French Polynesia also

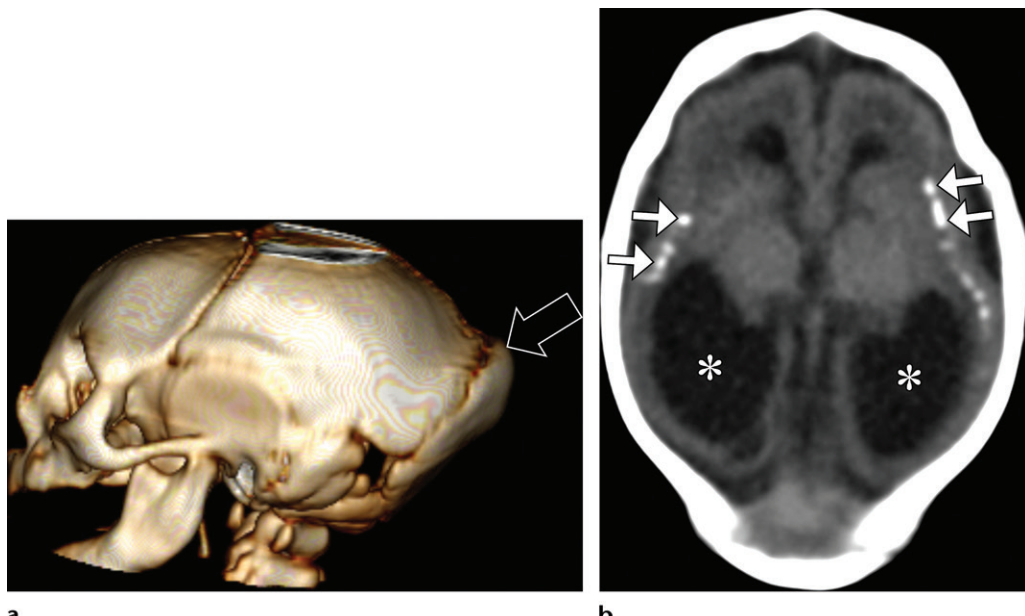


Figure 7. ZIKV infection in a male newborn. (a) Three-dimensional CT reconstruction image shows microcephaly and calvarial abnormalities including the reduction of intracranial content, which leads to a collapse of the parietal bones and occipital bone protuberance (arrow). (b) Axial nonenhanced CT image shows ventriculomegaly, which is more evident on the posterior horn of the lateral ventricles (*) and is accompanied by subcortical calcifications (arrows) and reduced white matter volume. Also note the abnormality of the calvarial shape.

suggested that ZIKV infection in pregnant women causes congenital microcephaly (38). Other congenital abnormalities such as facial disproportionality, cerebral calcifications, ventriculomegaly, corpus callosum abnormalities, brainstem hypoplasia, cutis girata, hypertonia and/or spasticity, hyperreflexia, hearing loss, and ocular anomalies also were linked to ZIKV (38,42).

In addition to congenital abnormalities, the main neurologic complication associated with ZIKV infection is GBS, which has a clinical course and outcome similar to those of classic triggers for this polyneuropathy and other arbovirus infections (38–40). Other neurologic complications include myelitis, meningoencephalitis, and ADEM; however, those occur much more rarely, and some have not been linked definitively to ZIKV infection (40).

Imaging.—A comprehensive imaging approach to congenital ZIKV infection should include pre- and postnatal evaluation for correct diagnosis, follow-up, and insight into the neurologic and cognitive development of these children (42). US is the method of choice for initial prenatal assessment, given its wide availability, low cost, and absence of fetal radiation exposure. One way to detect microcephaly prenatally is to measure head circumference, which is smaller than expected for gestational age in fetuses with microcephaly (42). US is also capable of showing other abnormalities such as brain calcifications, cerebral atrophy,

ventriculomegaly, and malformations of the posterior fossa and corpus callosum (42). In addition to US, fetal MRI may be useful to better visualize brain abnormalities before birth, to improve the identification of brainstem and cerebellar hypoplasia, and to further characterize malformations of cortical development including polymicrogyria, agyria (lissencephaly), and pachygryria (42).

Postnatal imaging modalities used for the evaluation of congenital ZIKV infection are CT and MRI. The most notable findings at CT are microcephaly and a prominent external occipital protuberance that is caused by reduced intracranial content and consequent collapse of the parietal bones (Fig 7a) (42). CT also shows brain calcifications, which usually are punctiform, linear, or coarse and are observed most frequently in the junction between the cortex and the subcortical white matter, although some occur in the basal ganglia and thalamus (Fig 7b; Fig E3) (42). Findings related to brain atrophy and decreased cerebral volume also can be seen at CT (42).

Brain calcifications appear as areas of hypointensity at susceptibility-weighted MRI and are usually hyperintense at T1-weighted MRI. However, the main advantage of MRI over CT is that it allows identification of cortical abnormalities such as a simplified pattern of cortical sulci and gyri, with normal cortical thickness alternating with areas of polymicrogyria and/or pachygryria and a thick cortex (42). Some patients also may exhibit delayed myelination, which can be seen only at MRI (42).

The conditions to consider in the differential diagnosis of congenital ZIKV infection include other congenital infections, especially cytomegalovirus and toxoplasmosis. Brain calcifications may be found in patients with all three conditions, but the distribution and shape are usually distinct, which helps in the differentiation of the causative agent. Calcifications in patients with the ZIKV infection usually are found in the cortical-subcortical junction and demonstrate a punctiform or linear pattern. Patients with cytomegalovirus classically show calcifications with a periventricular distribution, while those with congenital toxoplasmosis show cortical calcifications with a somewhat more nodular pattern. Microcephaly may be observed in patients with congenital cytomegalovirus but is not found often in those with toxoplasmosis.

Imaging also is important in the diagnosis of ZIKV-related GBS. MRI findings are usually the same as those described in classic GBS, namely nerve root enhancement of the cauda equina at gadolinium-enhanced T1-weighted MRI that usually compromises the posterior nerve roots; nevertheless, the anterior nerve root also may be seen in some cases (Fig E3) (40).

JEV Infection

JEV is an RNA virus that belongs to the family Flaviviridae and is related to other neurotropic flaviviruses such as the equine encephalitis virus and SLEV in North America; WNV in Africa, the Middle East, and North America; and Murray Valley encephalitis virus in Australia (43). These viral encephalitides share many virologic, epidemiologic, and clinical features, and the causative agents are thought to have evolved from a common ancestor approximately 10 000–20 000 years ago (43).

Epidemiology.—JEV is a severe form of viral encephalitis that is seen in Southeast Asia and northern Australia (43–45). JEV was documented in 1871, and the virus was isolated for the first time in 1935 from a human brain in Japan (43). Globally, 75% of cases occur in children and adolescents, making JEV the leading cause of viral childhood encephalitis in Asia (45).

Two distinct epidemiologic patterns of JEV are recognized: epidemic and endemic (43). Epidemic JEV infection is observed mainly in the more northern areas of Southeast Asia, comprising Bangladesh, Bhutan, the People's Republic of China, Taiwan, Japan, South Korea, North Korea, Nepal, northern Vietnam, northern India, northern Thailand, Pakistan, and Russia; in these regions, the virus shows typical seasonal characteristics, with occasional outbreaks. An endemic pattern is observed in the more south-

ern areas (Australia, Burma, Brunei Darussalam, Cambodia, Indonesia, Laos, Malaysia, Papua New Guinea, Philippines, Singapore, southern Vietnam, southern Thailand, southern India, Sri Lanka, and Timor-Leste), where cases occur sporadically throughout the year (44).

Some studies have highlighted the potential for the emergence of JEV in the United States in California. Authors have argued that the state is abundant in both potential vectors and amplifying hosts, which, combined with a JEV-naïve population, could lead to a large-scale outbreak. Thus, a high level of vigilance for JEV infections should be maintained in California (46).

Pathophysiologic and Clinical Issues.—The enzootic cycle of JEV is maintained by multiple species of mosquitoes, the most important being *Culex tritaeniorhyncus*, which find an optimal habitat for larval development in wetland rice fields (44,45). The main hosts are pigs and water birds, which explains the high levels of coinfection of JEV and neurocysticercosis, because pigs are also hosts of the latter (43). Humans are accidentally infected when bitten by an infected mosquito but only exhibit low-level transient viremia; thus, they are unlikely to transmit the virus to other mosquitoes (ie, are considered dead-end hosts) (43,45).

Most cases of JEV infection are asymptomatic. Although adults may be infected, especially in newly affected areas, most symptomatic patients are children, who present with fever, altered sensorium, headache, and vomiting (47). Some patients develop an encephalitis syndrome that is caused by direct viral invasion of the brain and is clinically characterized by behavioral abnormalities, altered mental status, seizures, and neurologic deficits in the form of hemiplegia, quadriplegia, or cerebellar signs (43).

Another reported neurologic complication of JEV infection is spinal cord involvement, which is characterized by a pattern of encephalomyelitis, instead of isolated encephalitis (43). Patients with this kind of illness frequently present with an acute flaccid paralysis syndrome, which is similar to that of poliomyelitis, and some EVs (44). Recent JEV infection also has been linked to GBS in areas where it is endemic (43).

Approximately 20%–30% of cases of JEV are fatal, and 30%–50% result in permanent neuropsychiatric sequelae (44,47,48). Currently available treatment is essentially directed symptom relief; intensive supportive care is important to avoid or reduce neurologic sequelae (47).

Imaging.—Neuroimaging shows abnormalities in most symptomatic patients with JEV (43). CT

examinations show abnormality in 56% of patients, revealing hypoattenuation in the thalamus and basal ganglia. MRI is more sensitive than CT for identification of JEV, and 94% of symptomatic patients present with abnormal findings. The most frequent abnormalities are found in the thalamus (94%), substantia nigra (58%), basal ganglia (35%), pons (26%), cerebellum, cerebral cortex, and spinal cord. They are characterized by elevated signal intensity at T2-weighted and FLAIR MRI and hypointensity at T1-weighted MRI (43). Hemorrhagic lesions in the same sites also may be observed as hypointense foci at susceptibility-weighted MRI (43).

These imaging findings are not specific for JEV infection. JEV is particularly difficult to differentiate from other arbovirus-related encephalitides, especially those caused by similar neurotropic flaviviruses, such as WNV and SLEV. Influenza virus encephalitis also may manifest with similar imaging findings. A high level of suspicion based on epidemiologic information and patient characteristics (particularly age) combined with compatible clinical evolution is required for the correct diagnosis.

SLEV Infection

SLEV is an encephalitogenic RNA arbovirus that is classified in the JEV antigenic complex and is a member of the Flaviviridae family (49,50). The virus was named after the city in which it was first isolated, St Louis, Mo, in 1933 (49,50).

Epidemiology.—SLEV is found throughout the Americas, with most of the clinically significant cases of infection reported in the United States, and to a lesser extent, in Central and South America (49,50). Although it was once considered to be virtually eliminated in many regions of the United States and many South American countries, since 2002, several outbreaks were reported in the United States, Argentina, Brazil, and Peru, and this reemergence has caused many fatal cases (49,51).

Pathophysiologic and Clinical Issues.—The transmission cycle of SLEV is maintained by *Culex* sp mosquito vectors, bird amplifiers, and mammal hosts, including humans, who are believed to be accidental hosts (49,52). Other mosquito species have been reported as alternative vectors, especially some species of the genus *Anopheles* (50,52). Epidemics of SLEV occur typically during the summer, reflecting the seasonality of most mosquito-borne infections (53). Although most SLEV infections are asymptomatic, some patients present with a nonspecific febrile syndrome (49,50).

The most common form of neurologic involvement is meningitis. Encephalitis is rare. The most

common symptoms when there is CNS involvement are fever, headache, tremors, and lethargy (53). Mortality rates in patients who present with meningitis and encephalitis are 3%–30% (49). There is no specific treatment or vaccine available for the disease (52).

Imaging.—The literature concerning brain imaging in patients with SLEV is scarce. Most reported cases showed no alterations or a few nonspecific imaging abnormalities, such as brain atrophy or chronic ischemic changes, which probably are not related to SLEV but rather to the patient's medical history (53,54). Brain MRI may show specific findings such as symmetric T2 hyperintensity selectively involving the substantia nigra of the midbrain in a small number of patients, without evidence of restricted diffusion, contrast material enhancement, or expansive effects (Fig 8). These findings are thought to represent edema caused by a local inflammatory process (53,54).

The selective involvement of the substantia nigra reflects the clinical picture of symptomatic patients, most of whom present with tremors (53,54). This is also compatible with the pathologic features of SLEV, which include severe inflammatory infiltrates in the substantia nigra (54). An extensive literature review on infectious, metabolic, and degenerative diseases did not show a similar pattern of isolated signal intensity changes in the substantia nigra in any brain diseases; therefore, any tremulous patient who presents with encephalitis should be evaluated for St Louis encephalitis (54).

The main conditions for consideration in the differential diagnosis include other arboviral encephalitides such as those caused by DENV, ZIKV, JEV, and SLEV. Clinical and epidemiologic information may be necessary to differentiate among those entities.

WNV Encephalitis

WNV is an arthropod-borne RNA *Flavivirus* that was isolated for the first time in a febrile woman in the West Nile region of Uganda in 1937 (55,56). The virus belongs to the JEV complex of the Flaviviridae family, along with JEV, SLEV, Rocio virus, and Murray Valley encephalitis virus (57). Although WNV infection technically cannot be classified as an emergent or reemergent disease, the similarity of its causative agent and vectors with other emergent and reemergent conditions make WNV a potential threat that requires constant vigilance.

Epidemiology.—Since the first identification of the virus, it has spread beyond its original

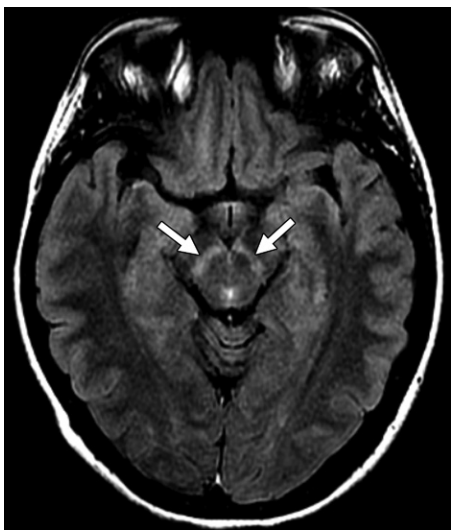


Figure 8. SLEV infection in a 35-year-old woman. Axial FLAIR MR image shows bilateral high signal intensity in the substantia nigra of the midbrain (arrows). No abnormalities were observed at DWI or on gadolinium-enhanced T1-weighted images (not shown).

geographic range and caused human diseases on every continent except Antarctica. It is the most important cause of viral encephalitis worldwide (57). The first case in the western hemisphere was recognized in 1999 in New York, when a 62-case outbreak of encephalitis was reported and caused seven deaths (55,57,58). From then on, the geographic range of the disease in the Americas has expanded to include the entire continental United States and some regions of Canada, Mexico, and Central and South America (55,57).

Pathophysiologic and Clinical Issues.—WNV infection in humans is asymptomatic in 80% of patients (55). Twenty percent of patients present with a self-limited flu-like syndrome, characterized by fever, myalgia, headache, and gastrointestinal disturbances, with or without a diffuse maculopapular rash.

Neuroinvasive disease is rare and occurs in approximately 0.66% of infections (55). It can manifest in three forms: aseptic meningitis (60%), meningoencephalitis (40%), and acute flaccid paralysis (55,56). This distinction is somewhat arbitrary, and often symptoms overlap (56).

Aseptic meningitis and meningoencephalitis related to WNV are rare in children and young adults but occur at higher rates in people older than 50 years and in immunosuppressed recipients of transplants, most likely because of a prolonged higher level of viremia in these patients (55,56). Patients who present with fever, a stiff neck, headache, photophobia, and CSF pleocytosis but with no altered mental state or focal neu-

rologic deficits are classified as having meningitis, whereas patients who show signs, symptoms, or imaging findings that suggest parenchymal involvement are classified as having meningoencephalitis (56).

Acute flaccid paralysis is reported in all age groups, and there is not a higher incidence in elderly patients (55). It usually results from direct viral infection and injury to motor neurons in the anterior horn of the spinal cord (56). Patients present clinically with acute onset (24–48 hours) of a lower motor neuron pattern of muscle weakness, with flaccid paralysis and hyporeflexia (55,56).

Imaging.—Imaging abnormalities found in neuroinvasive WNV disease are extremely variable. Studies (55,59) have shown that many patients exhibit unremarkable imaging findings. Those with detectable abnormalities at MRI most commonly show signal intensity changes in the white matter seen only on DWI MR images or true restricted diffusion that usually affects the corticospinal tract above the cerebral peduncles (55,59). This pattern is associated with a better neurologic prognosis (55). Another pattern of encephalitic WNV infection is characterized by focal areas of hyperintensity on FLAIR and T2-weighted MR images, usually involving cortical gray matter, lobar white matter, the cerebellum, basal ganglia, thalamus, pons, and midbrain. These patients usually have a worse neurologic outcome than do the former group (59). Some of those areas also may show restricted diffusion and decreased signal intensity on T1-weighted MR images (59).

The differential diagnosis for WNV encephalitis includes evaluation for encephalitis caused by other flaviviruses, such as JEV, DENV, and ZIKV. Eastern equine encephalitis virus is another rare arthropod-borne disease that causes CNS involvement and has clinical findings that resemble WNV infection. This is important to consider in the differential diagnosis, because up to one-third of all people with eastern equine encephalitis die of the disease, usually 2–10 days after the onset of symptoms (60). The imaging hallmarks of eastern equine encephalitis are asymmetric T2-hyperintense lesions classically involving the basal ganglia and the thalamus that sometimes show some mass effect, particularly in larger lesions.

WNV meningeal involvement can be seen at gadolinium-enhanced MRI as abnormal meningeal enhancement, which is an unspecific finding that may be observed with other causes of inflammatory meningeal disease (59).

Two patterns of spinal involvement have been recorded: enhancement of the cauda equina and

nerve roots at T1-weighted MRI and patchy areas of intraspinal increased signal intensity at T2-weighted MRI, which also shows contrast material enhancement that is indistinguishable from that in myelitis with other causes (59).

Bacterial Infections

Syphilis

Syphilis is a chronic venereal disease that is caused by the bacteria *Treponema pallidum* and shows multiple different clinical manifestations (61). These bacteria are gram-negative spiral-shaped microorganisms that were identified for the first time in 1905 by Schaudinn and Hoffmann (62).

Epidemiology.—The disease is an important public health issue in several developing countries (63). In most Western countries, its incidence dramatically decreased, mainly because of the use of penicillin (63). In the United States, the number of reported cases declined 90% from 1990 to 2000 (62,64). In the United States in 2000, the incidence was 11.2 per 100 000 people, which is the lowest rate since reporting began, prompting the CDC to launch a plan to eliminate syphilis (62,64). However, the incidence of the disease increased in 2001–2013, reaching a rate of 17.9 cases per 100 000 people (62,64). This pattern of reemergence happened not only in the United States but also in many other countries. In China, where the most dramatic epidemic of syphilis was reported, a rate of 33 cases per 100 000 people was registered in 2013 (62). Syphilis incidence continues to rise in many regions, requiring attention from the public health authorities. In the United States, the most recent available data are from 2017, when the incidence was 31.4 cases per 100 000 people, which is a 75% increase compared with the data from 2013 (64).

Pathophysiologic and Clinical Issues.—Syphilis is most commonly sexually transmitted (61–63), but it can spread by means of nonsexual skin contact with an infected ulcer or from mother to fetus during pregnancy (vertical transmission), resulting in congenital syphilis (61,62).

Clinically, three well-characterized stages of syphilis are described (61). Primary syphilis is defined by the presence of a chancre (sore or ulcer) at the site of inoculation, usually in the genital area, and painless regional lymphadenopathy (61). The second stage of syphilis manifests as a disseminated maculopapular rash that usually is observed 2–8 weeks after the appearance of the chancre (61). Approximately 30% of the patients who present with secondary disease progress to

the tertiary stage, which consists mainly of cardiovascular and neurologic disease (61).

Cardiovascular syphilis manifests as aortitis, which involves aortic valve insufficiency and aneurysms of the proximal aorta. Of all patients who present with tertiary syphilis, approximately one-third show some form of neurologic involvement, which also can happen during the other stages of systemic disease, although it is less common (61,65). Neurosyphilis can be asymptomatic in up to one-third of patients, with CSF abnormalities as the only indicator of CNS issues (61,63). Four major syndromes comprise symptomatic neurosyphilis: syphilitic meningitis, gummatous neurosyphilis, vascular syphilis, and parenchymatous neurosyphilis (61,63).

Syphilitic meningitis usually occurs within the 1st 2 years after infection and is characterized by widespread thickening of the meninges, meningeal lymphocytic infiltrates, and perivascular lymphocytic infiltrates. Patients usually present clinically with headaches and meningeal signs (61,65). Cranial nerve palsies also may develop, most frequently involving nerves VII and VIII, leading to facial paralysis or sensorineural hearing loss and vertigo (61).

Although they are separated for didactic purposes, gummatous syphilis is related to syphilitic meningitis and occurs as a result of an intense localized leptomeningeal inflammatory reaction early in the meningeal phase of neurosyphilis (61,63). Gummas are circumscribed masses of granulation tissue that are surrounded by mononuclear epithelial and fibroblastic cells, with occasional giant cells and perivasculitis (61). Vascular neurosyphilis is currently the most common form of neurologic involvement of the disease and refers to arteritis of the large- and medium-sized arteries (Heubner arteritis), and/or small-sized arteries (Nissl-Alzheimer arteritis) (61). Although pathologic processes are different in each case, in ultimate analysis, both cause luminal narrowing and eventual vascular occlusion (61). Vascular neurosyphilis usually manifests 5–10 years after initial infection, usually as an ischemic syndrome that affects the territory of the middle cerebral artery in a relatively young adult who does not have risk factors for atherosclerosis (61,63,65).

Parenchymatous damage of neurosyphilis causes pathologic pattern of diffuse encephalitis that manifests usually 10–20 years after the initial infection. Clinically, patients may present with psychiatric symptoms, such as modifications in personality and affect, delusions, hallucinations, loss of judgment and insight, speech disturbances, and reflex abnormalities, including Argyll Robertson pupil (a small irregular pupil that accommodates but does not react to light) (61,65).

Syphilitic encephalitis is characterized by cortical atrophy and neuronal degeneration and is associated with gliosis and scattered microglia (61).

In addition, damage to sensory nerves and the posterior column of the spinal cord may cause myelopathy associated with atrophy, degeneration, and demyelination usually 15–20 years after the initial infection. This is called *tabes dorsalis* and manifests clinically with lightning pains, dysuria, ataxia, areflexia, loss of proprioception, and Argyll Robertson pupil (61,63,65).

Imaging.—Radiologic findings of neurosyphilis reflect the abnormalities found in the four major clinical syndromes. Syphilitic meningitis is seen as meningeal enhancement that is better depicted at MRI than at CT and is radiologically indistinct from other inflammatory or noninflammatory causes of meningitis, including neoplastic disease (61,65). Associated hydrocephalus may be observed (61).

When cranial nerve palsies related to syphilitic meningitis are suspected, specific MRI sequences may be useful to evaluate cranial nerves in addition to a standard brain MRI protocol. At our institution, we use nonenhanced and gadolinium-enhanced axial T1-weighted sequences oriented to the posterior fossa and an axial 3-mm fat-saturated T1-weighted MRI sequence of the posterior fossa; we also perform 0.6-mm axial FIESTA MRI sequences from the occipital bone to the petrous ridge. This protocol is designed to evaluate cranial nerves VII and VIII, which are the nerves most commonly affected by meningeal neurosyphilis. If other cranial palsies are present or suspected, additional sequences may be necessary for an optimal imaging evaluation, and protocols should be designed on an individual basis. Imaging findings related to cranial nerve involvement are abnormal enhancement that normally affects the VII and VIII nerves, the cochlea, and the meninges lining the internal auditory canal (61). Other cranial nerves eventually may be involved and also may show abnormal enhancement (61).

Solitary or multiple syphilitic gummas are seen at imaging, usually dural-based mass lesions that are hypoattenuating or with mixed attenuation at CT. At MRI, these lesions are usually iso- to hypointense at T1-weighted and heterogeneously hyperintense at T2-weighted MRI (Fig E4) (61,65). Ring or nodular homogeneous contrast material enhancement usually is observed at both CT and MRI (61,65). An associated dural tail may be observed (61). These findings may be confused with those of primary or metastatic intracranial neoplasms, and a high level of suspicion is necessary to reach the correct diagnosis (61).

The most common imaging findings associated with vascular syphilis are lacunar infarcts, which usually are observed in the basal ganglia, thalamus, and/or brainstem and are the consequence of the subjacent arteritis caused by the condition (Fig 9a) (63). MR angiography may reveal luminal narrowing or even complete occlusion of affected arteries (65). High-spatial-resolution T1-weighted vessel wall MRI is useful to evaluate the artery walls; traditional angiographic methods, which can only show luminal abnormalities, are limited for providing information about the vessel wall. Vessel wall MRI of vascular syphilitic involvement may show abnormal enhancement of the vessel walls (Fig 9b), although this pattern may be indistinct from that observed in other causes of vasculitis (65).

Parenchymatous neurosyphilis usually is characterized at imaging by cortical atrophy, with associated preeminence of the ventricular system (61). T2-hyperintense white matter lesions without mass effect or abnormal enhancement are seen in up to 20% of patients with neurosyphilis, and its cause is still uncertain, given their nonspecific and variable appearance (Fig E4) (65).

Lyme Disease

Lyme disease, also known as *Borreliosis*, is a multisystem arthropod-borne inflammatory disease caused by the spirochete bacteria *Borrelia burgdorferi sensu stricto* in the United States and *Borrelia garinii* and *Borrelia afzelii* in Europe (61,66). The disease is named after the town of Lyme, Conn, where an epidemic of the then-unknown illness happened in 1976 and led to investigation and further understanding of the condition (61,67).

Epidemiology.—Although the disease occurs worldwide, most cases are observed in the United States, Europe, and Japan (61). The most recent data from the CDC are from 2017, when 29 513 confirmed cases were reported in the United States, resulting in an incidence of 9.1 cases per 100 000 people, which makes Lyme disease the most common vector-borne infection in the United States (66,68,69). More than 84% of the reported cases occurred in the areas in which Lyme disease is highly endemic, in New England, the Middle Atlantic, and the midwestern states of Wisconsin and Minnesota (69).

Pathophysiologic and Clinical Issues.—Lyme disease is transmitted to humans through bites of ticks of the genus *Ixodes* (61,66,67). Although many species of *Ixodes* ticks can transmit *Borrelia* sp among animals, only four species are known to bite humans: *I. scapularis* and *I. pacificus* in the United States; and *I. ricinus* and *I. persulcatus* in Europe and Asia, respectively (67). The bacteria

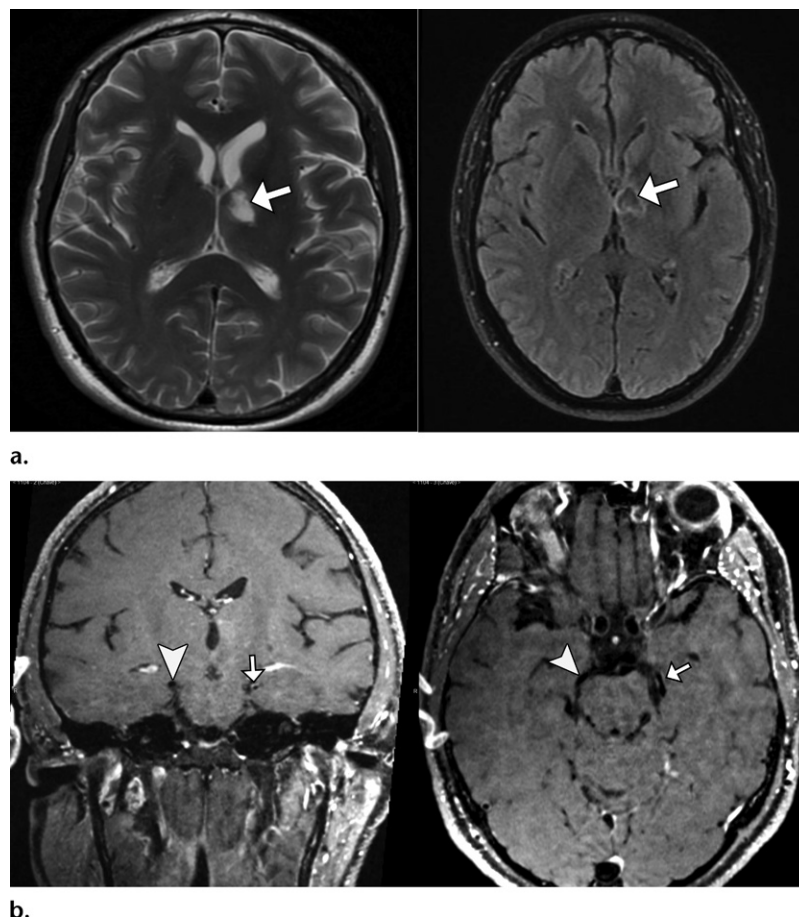


Figure 9. Meningovascular syphilis in a 47-year-old man who presented with dizziness and mental confusion and was treated for primary syphilis 4 years previously and did not have substantial atherosclerotic risk factors. (a) Axial T2-weighted (left) and axial FLAIR (right) MR images show a small encephalomalacic lesion in the left thalamus (arrow). (b) Coronal (left) and axial (right) high-spatial-resolution gadolinium-enhanced T1-weighted vessel wall MR images show enhancement of the left posterior cerebral artery wall (arrow) in comparison with the contralateral normal vessel (arrowhead).

maintain a sylvatic cycle among ticks and various species of mammals and birds. Unlike reservoir hosts, humans are considered accidental hosts and do not sustain enough spirochetes in their tissues to transmit the bacteria to noninfected ticks; therefore, humans play no part in the perpetuation of the natural cycle of the bacteria (ie, are considered dead-end hosts) (67).

Similarly to other spirochetal diseases, such as syphilis, Lyme disease manifests clinically in three different stages: early localized disease, early disseminated disease, and persisting late disease (61).

Initially, the spirochetes reproduce in the dermis at the site of the tick bite, and then spread centrifugally, creating an enlarging area of erythema, which may demonstrate central clearing, rendering an appearance similar to a bull's eye. This characteristic lesion is termed *erythema migrans* and often is accompanied by regional lymphadenopathy. Usually, this early localized phase is associated with fatigue, fever, headaches, and myalgia and/or arthralgia and lasts 4–12 weeks (61,67).

During the second phase, termed *early disseminated disease*, the spirochetes reach the bloodstream and may cause a variety of clinical symptoms, such as arthritis, cardiac disease, and the most common neurologic manifestations: lymphocytic meningitis,

radiculoneuritis, and cranial neuropathy, which usually affect the facial nerve (Bell palsy) (61,67,70).

If not treated, disease may progress to *late disseminated disease*, when chronic arthritis may ensue, with severe damage to large joints, as well as polyneuropathy and encephalitis/encephalomyelitis, which may vary from mild to debilitating (61,70).

Although CNS involvement is clinically detected in 15%–20% of patients, the underlying neuropathology remains unclear. Proposed mechanisms to explain neurologic damage include direct cytotoxicity, neurotoxic mediators secreted by leukocytes and glial cells, or triggered autoimmune reactions through molecular mimicry (61).

Both the American Academy of Neurology and the European Federation of Neurologic Societies establish criteria for the diagnosis of neurologic involvement of Lyme disease. Although the discussion of those criteria is beyond the scope of this review, both of them emphasize the need to exclude other possible causes of the clinical symptoms; therefore, neuroimaging is paramount to correctly establishing the diagnosis of Lyme disease (71).

Imaging.—CT and MRI findings of the brain and spine in patients with Lyme disease are often within normal limits, even among patients with

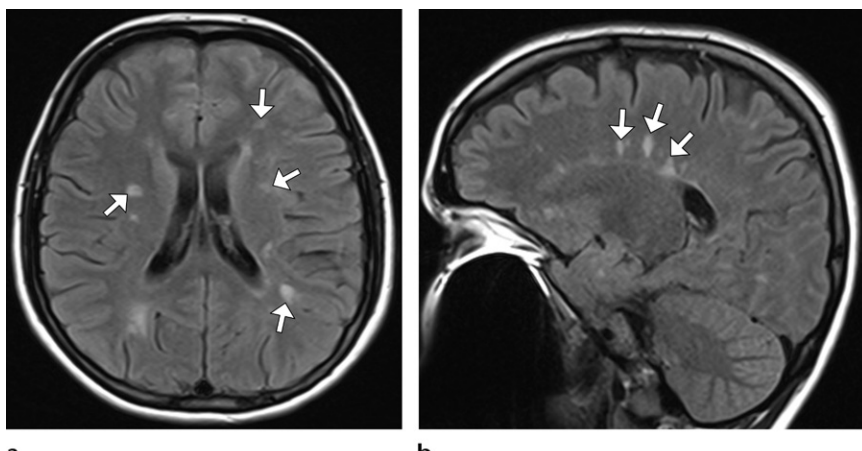
**a.****b.**

Figure 10. Lyme disease in a 31-year-old woman from the northeastern United States with a history of erythema migrans, dizziness, and a serology test result that was positive for *Borrelia burgdorferi* (immunoglobulin M and immunoglobulin G). Axial (a) and sagittal (b) FLAIR MR images show multiple bilateral hyperintense foci distributed along the ependymal surface of the lateral ventricles and in the periventricular white matter (arrows), mimicking multiple sclerosis. The patient had negative oligoclonal bands in the CSF.

known neurologic manifestations. Therefore, normal findings should not be reason to rule out the diagnosis, especially if the clinical and epidemiologic contexts are compatible (61).

In patients who present with clinical signs of meningoencephalitis, gadolinium-enhanced MRI may reveal enhancement of meninges and cranial or spinal nerves (70). Meningeal enhancement is a non-specific finding that may be observed in a variety of inflammatory and noninflammatory conditions.

Facial nerve palsy usually manifests at MRI with thin nonnodular nerve enhancement (70). Enhancement is normally expected in the geniculate ganglion and the tympanic and mastoid segments of the nerve, so only asymmetric enhancement in those segments or enhancement involving the cisternal, intracanalicular, labyrinthine, or parotid segments should be considered an imaging abnormality. A protocol similar to that described to evaluate cranial nerve involvement of neurosyphilis may be applied to patients with Lyme disease. Lyme disease-related facial nerve palsy may be indistinguishable from idiopathic facial palsies and palsies from other causes at imaging.

Brain parenchyma imaging abnormalities related to Lyme disease have been described in several studies as multiple bilateral foci of T2 hyperintensity in the periventricular or subcortical white matter that sometimes resemble the imaging pattern of multiple sclerosis, including the involvement of the callososeptal interface (Fig 10; Fig E5) (61). This is believed to be related to similar mechanisms of molecular mimicry and antigen-specific T-cell responses for both multiple sclerosis and chronic neurologic involvement of Lyme disease (61).

In addition, fluorodeoxyglucose PET has been shown to demonstrate two distinct patterns of brain hypometabolism in patients with Lyme disease: specific temporal lobe hypometabolism and diffuse cortical hypometabolism. Although no clear diagnostic pattern is described, memory

disturbances are associated with temporal lobe involvement regardless of the general pattern, and fluorodeoxyglucose PET may show the affected areas in patients who present with neurologic involvement of Lyme disease (72).

Listeriosis

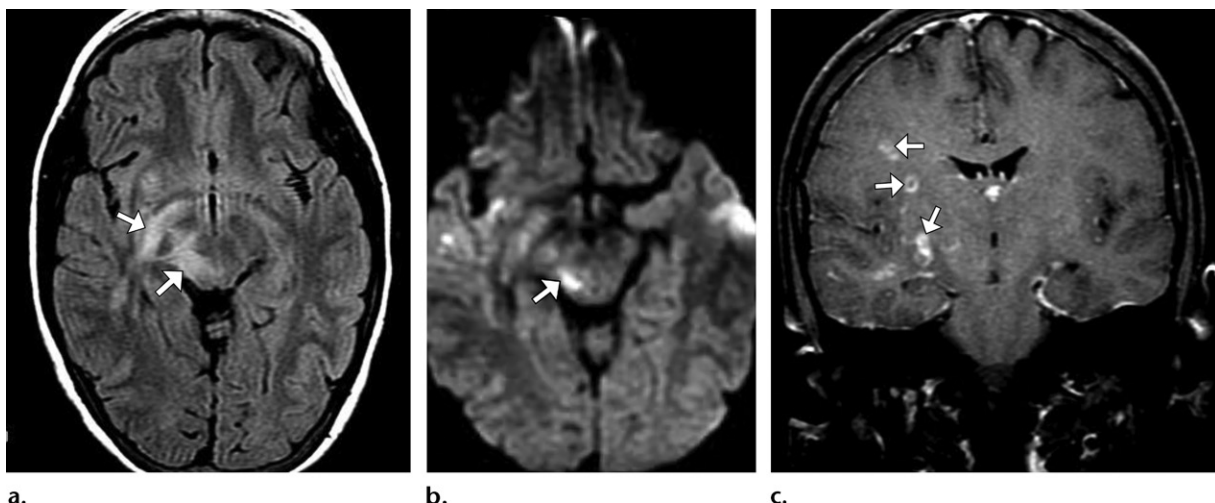
Listeriosis is a rare bacterial disease caused by *Listeria monocytogenes* that may have serious complications (73). *Listeria monocytogenes* is a gram-positive bacillus that can grow in aerobic and anaerobic conditions (74).

Transmission and Epidemiology.—*L. monocytogenes* can be found in soil, forage, water, mud, livestock food, and silage, and the main form of transmission to humans is through consumption of contaminated food (48,73). In addition, it can be transmitted from mother to child in utero or during birth (48,73). The bacteria can survive food-processing techniques that rely on acidic or salty conditions. Also, it can continue to reproduce at very low temperatures, allowing growth even in properly refrigerated foods (48,73,74).

L. monocytogenes is distributed worldwide, with most cases considered sporadic (ie, nonepidemic) (73). However, an increasing number of reported cases of human listeriosis have been reported in Europe, without a known cause (48,73). Large outbreaks also happened in the United States in 2011 and South Africa in 2017 (75–77).

Clinical Issues.—Two clinical forms of listeriosis are described: noninvasive gastrointestinal listeriosis and invasive listeriosis (73). Noninvasive disease manifests as a typically febrile gastroenteritis that usually affects immunocompetent adults and is followed by complete recovery if it is properly treated (48,73).

Immunocompromised adults, particularly elderly patients and those who receive immunosuppressive agents, are prone to develop invasive



a.

b.

c.

Figure 11. Listeriosis in a 31-year-old woman who presented with a fever and altered mental status. (a) Axial FLAIR MR image reveals hyperintense lesions in the midbrain and the posterior limb of the right internal capsule (arrows). (b) Axial diffusion-weighted image shows hyperintensity in the midbrain (arrow), which was confirmed on an apparent diffusion coefficient map (not shown) to be true restricted diffusion. (c) Coronal gadolinium-enhanced T1-weighted MR image shows nodular lesions with ring enhancement (arrows), which are suggestive of abscesses.

listeriosis, which can manifest with septicemia and/or meningoencephalitis (48,73). Patients with meningoencephalitis usually present with fever, intense headaches, nausea, vomiting, and signs of meningeal irritation. Although those symptoms may have a sudden onset, they also may initiate in an insidious subacute manner (73). Patients also may develop parenchymatous abscesses caused by invasive listeriosis (74). In rare cases, invasive listeriosis may manifest as rhomboencephalitis, which characteristically affects young healthy subjects rather than elderly and immunocompromised patients (73). Listeriosis may have specific clinical manifestations in pregnant women and newborns (neonatal listeriosis) that are beyond the scope of this review.

Imaging.—The most common brain MRI findings in invasive listeriosis are T2 hyperintensities that involve the brainstem, supratentorial white matter, cerebellar hemispheres, cerebellar peduncles, basal ganglia, or internal capsules (Fig 11a) (74). Some of those lesions may show restricted diffusion (Fig 11b). This generic encephalitic pattern may be similar to that of herpes simplex encephalitis, especially in the mesial areas of the temporal lobe and the insula.

Listeria meningitis is best seen at MRI and is characterized by nonspecific leptomeningeal enhancement that is similar to that observed in other inflammatory or noninflammatory meningeal disease. *L. monocytogenes* abscesses may appear as solitary (69%) or multiple (31%) lesions with ring enhancement located mainly in the subcortical white matter, thalamus, pons, or medulla (Fig 11c) (74,77).

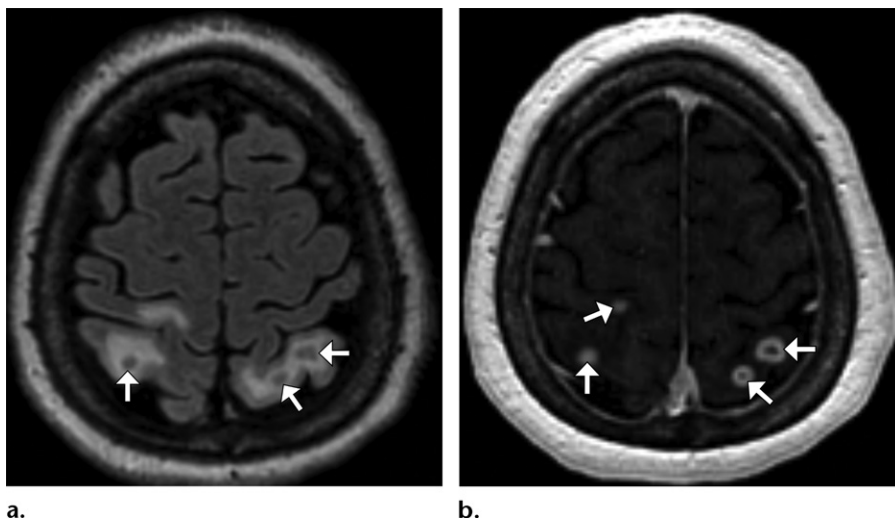
Some patients who present with rhomboencephalitis may show T2-hyperintense areas in the brainstem, cerebellum, and/or upper cervical spinal cord, sparing the supratentorial compartment (Fig E6). The findings may be similar to those of EV71 rhomboencephalitis, although EV71 mostly affects children and invasive listeriosis rhomboencephalitis affects healthy adults.

Parasitic Infection: Chagas Disease

Chagas disease, also known as American trypanosomiasis, is a zoonotic disease caused by the flagellated kinetoplastid protozoa named *Trypanosoma cruzi* (78–80). The disease is named after Brazilian physician Carlos Chagas, who discovered the condition in 1909 (80). The World Health Organization considers the disease to be one of the 13 most-neglected tropical diseases (80).

Epidemiology

Originally, Chagas disease was restricted to poor rural areas in Central and South America, where vector-borne transmission occurs (80). Over the last 3 decades, improved vector control programs and compulsory blood bank screening have substantially reduced the incidence and prevalence of the disease in Latin America. In 1980–1985, an estimated 17.4 million people were infected in that region (4% of the Latin American population); in 2005, the estimated number of people infected was 7.7 million (1.4% of that population) (80). However, during the same period the disease emerged in geographic areas where it usually was not observed, such as the United States, Canada, many parts of Europe, and the western Pacific, mainly



a.

b.

Figure 12. Reactivation of Chagas disease in a 65-year-old woman 5 years after she underwent a cardiac transplant for chagasic cardiomyopathy. (a) Axial FLAIR MR image shows hypointense nodular lesions (arrows) in the subcortical white matter that are surrounded by vasogenic edema. (b) Axial gadolinium-enhanced T1-weighted MR image reveals that the nodular lesions exhibit annular enhancement (arrows).

because immigration changed the distribution of the disease (80,81). Currently, the CDC estimates that 300 000 persons with Chagas disease live in the United States, most of whom were infected in Latin America, where the disease is still endemic (79). This shift in the disease distribution is so important that Chagas disease is now classified as both an emerging infection and a neglected tropical disease (81).

Pathophysiologic and Clinical Issues

The main form of transmission of *Trypanosoma cruzi* to humans is through contact with the feces of infected bugs of the family Reduviidae, which are members of the subfamily Triatominae (79,80,82). Different species of these blood-sucking bugs are competent vectors for the parasite.

Other mechanisms of transmission include blood transfusion from contaminated donors and vertical transmission from mother to infant (79,80,82). In rare cases, Chagas disease can be contracted by ingesting contaminated food, and this form of transmission is usually responsible for regional outbreaks in areas where the vectors are absent (80).

Chagas disease manifests with two distinct phases: an initial acute phase and a late chronic phase. The acute phase is usually asymptomatic or manifests with a self-limited febrile illness 1–2 weeks after exposure to the protozoa (80). The majority of patients never develop other signs of clinically significant disease, whereas 30%–40% develop a form of chronic disease 10–30 years after initial infection, which may be chagasic cardiopathy, digestive disease (megaeosophagus or megacolon), or associated cardiodigestive disease (80).

CNS involvement in Chagas disease may occur during both acute and chronic forms or may also be secondary to the reactivation of the disease in immunocompromised patients, such as those with

HIV infection or malignancies (83). Acute CNS involvement is rare and more frequent in children younger than 2 years old, who may present with unspecific encephalitis symptoms such as confusion, headaches, hypertonia, and seizures, with or without associated meningismus (78). During the chronic phase of the disease, CNS manifestations usually are caused by ischemic events related to hypoperfusion and/or emboli, which are secondary to cardiac Chagas disease (cardiomyopathy or cardiac arrhythmias) (84).

In immunocompromised patients, Chagas reactivation tends to manifest as cerebral mass lesions or acute diffuse meningoencephalitis, with symptoms depending largely on the number, size, and location of the lesions (78).

Imaging

The literature on Chagas CNS involvement is, to our knowledge, scarce. MRI of chagasic encephalitis may show scattered T2-hyperintense lesions, predominantly in the supratentorial white matter. Diffuse cerebral atrophy also has been reported (78). Those findings cannot be differentiated from encephalitis caused by other agents solely on the basis of imaging.

In immunocompromised patients, the most common findings that are suggestive of Chagas reactivation are single or multiple supratentorial lesions that are generally hypointense on T1-weighted images, with variable signal intensity on T2-weighted and FLAIR images, which usually show ring enhancement after gadolinium administration (Fig 12) (78,85). These lesions predominantly involve the subcortical white matter of the brain lobes, mainly the frontal lobe (83%), and are thought to represent organizing abscesses. Other locations such as the basal ganglia and/or thalamus, brainstem, cerebellum hemispheres, and spinal cord also have been reported. Imaging

findings can be indistinguishable from those of toxoplasmosis and represent a diagnostic challenge in patients with HIV infection (79,84,85). Also, T2-hypointense expansive lesions may be similar to different infectious conditions such as tuberculomas or syphilitic gummas.

Conclusion

Emerging and reemerging infections are a heterogeneous group of diseases that often present diagnostic challenges to clinicians and radiologists. A vast number of infectious agents have emerged or reemerged throughout the globe over the past decades because of changes in microorganisms and the environment and human activities. Some of these infections have the potential to affect the CNS, and imaging is important in differentiating secondary encephalopathy from direct CNS damage and in diagnostic workup and therapeutic management. Many of the emergent and reemergent CNS infections show nonspecific neuroimaging patterns, and the overlapping of findings in those diseases poses limitations to their interpretation. However, when imaging findings are analyzed along with clinical and epidemiologic information, neuroimaging can help in reaching the correct diagnosis.

Acknowledgments.—Juliana Souza Silva Elias, Juiz de Fora, Brazil; Leonardo Lopes de Macedo, Juiz de Fora, Brazil; Luís Antônio Tobaru Tibana, São Paulo, Brazil; Marcela Amaral Avelino, São Paulo, Brazil; Thiago Grunewald, Juiz de Fora, Brazil; Tomás de Andrade Lourenço Freddi, São Paulo, Brazil.

References

- Morens DM, Fauci AS. Emerging infectious diseases: threats to human health and global stability. *PLoS Pathog* 2013;9(7):e1003467.
- Chow FC, Glaser CA. Emerging and reemerging neurologic infections. *Neurohospitalist* 2014;4(4):173–184.
- Hussain A, Ali S, Ahmed M, Hussain S. The Anti-vaccination Movement: A Regression in Modern Medicine. *Cureus* 2018;10(7):e2919.
- Abdelgawad MS, El-Nekidy AE, Abouyoussef RAM, El-Faty A. MRI findings of enteroviral encephalomyelitis. *Egypt J Radiol Nucl Med* 2016;47(3):1031–1036.
- Chang PC, Chen SC, Chen KT. The Current Status of the Disease Caused by Enterovirus 71 Infections: Epidemiology, Pathogenesis, Molecular Epidemiology, and Vaccine Development. *Int J Environ Res Public Health* 2016;13(9):890.
- Zhang Y, Zhu Z, Yang W, et al. An emerging recombinant human enterovirus 71 responsible for the 2008 outbreak of hand foot and mouth disease in Fuyang city of China. *Virol J* 2010;7:94.
- Xing J, Liu D, Shen S, et al. Pathologic studies of fatal encephalomyelitis in children caused by enterovirus 71. *Am J Clin Pathol* 2016;146(1):95–106.
- Chen F, Li J, Liu T, Wang L, Li Y. MRI characteristics of brainstem encephalitis in hand-foot-mouth disease induced by enterovirus type 71: will different MRI manifestations be helpful for prognosis? *Eur J Paediatr Neurol* 2013;17(5):486–491.
- About Acute Flaccid Myelitis. Centers for Disease Control and Prevention. <https://www.cdc.gov/acute-flaccid-myelitis/about-afm.html>. Updated May 6, 2019. Accessed May 17, 2019.
- World Health Organization. Measles. https://www.who.int/immunization/monitoring_surveillance/burden/vpd/surveillance_type/active/measles/en/. Published November 2, 2018. Accessed January 2019.
- Buchanan R, Bonithus DJ. Measles virus and associated central nervous system sequelae. *Semin Pediatr Neurol* 2012;19(3):107–114.
- Koeller KK, Shih RY. Viral and prion infections of the central nervous system: radiologic-pathologic correlation: from the radiologic pathology archives. *RadioGraphics* 2017;37(1):199–233.
- Lee KY, Cho WH, Kim SH, Kim HD, Kim IO. Acute encephalitis associated with measles: MRI features. *Neuroradiology* 2003;45(2):100–106.
- Sener RN. Subacute sclerosing panencephalitis findings at MR imaging, diffusion MR imaging, and proton MR spectroscopy. *AJNR Am J Neuroradiol* 2004;25(5):892–894.
- Oztürk A, Gürses C, Baykan B, Gökyigit A, Eraksoy M. Subacute sclerosing panencephalitis: clinical and magnetic resonance imaging evaluation of 36 patients. *J Child Neurol* 2002;17(1):25–29.
- Popescu CP, Florescu SA, Lupulescu E, et al. Neurologic complications of influenza B virus infection in adults, Romania. *Emerg Infect Dis* 2017;23(4):574–581.
- Pauls C, Subbarao K. Influenza. *Lancet* 2017;390(10095):697–708.
- Bengualid V, Berger J. Neurologic Complications of Acute Influenza in Adults: Case Report and Review of the Literature. *J Neurosci Clin Res* 2017;2(1).
- Lyon JB, Remigio C, Milligan T, Deline C. Acute necrotizing encephalopathy in a child with H1N1 influenza infection. *Pediatr Radiol* 2010;40(2):200–205.
- Haktanir A. MR imaging in novel influenza A(H1N1)-associated meningoencephalitis. *AJNR Am J Neuroradiol* 2010;31(3):394–395.
- Kawada J, Kimura H, Ito Y, et al. Systemic cytokine responses in patients with influenza-associated encephalopathy. *J Infect Dis* 2003;188(5):690–698.
- Rust RS. Human arboviral encephalitis. *Semin Pediatr Neurol* 2012;19(3):130–151.
- Leibovitz EC, Jacobson S. Vaccinations for Neuroinfectious Disease: A Global Health Priority. *Neurotherapeutics* 2016;13(3):562–570.
- Beckham JD, Tyler KL. Arbovirus infections. *Continuum (Minneapolis Minn)* 2015;21(6 Neuroinfectious Disease):1599–1611.
- Sejvar JJ. Zika Virus and Other Emerging Arboviral Central Nervous System Infections. *Continuum (Minneapolis Minn)* 2018;24(5, Neuroinfectious Disease):1512–1534.
- Jugpal TS, Dixit R, Garg A, et al. Spectrum of findings on magnetic resonance imaging of the brain in patients with neurological manifestations of dengue fever. *Radiol Bras* 2017;50(5):285–290.
- Dengue vaccine: WHO position paper, September 2018—Recommendations. *Vaccine* 2018 Nov 10 [Epub ahead of print] <https://doi.org/10.1016/j.vaccine.2018.09.063>.
- Dengue: Guidelines for Diagnosis, Treatment, Prevention and Control. Geneva, Switzerland: World Health Organization, 2009 (WHO Guidelines Approved by the Guidelines Review Committee). <http://www.ncbi.nlm.nih.gov/books/NBK143157/>. Accessed January 23, 2019.
- Vanjaré HA, Mannam P, Mishra AK, et al. Brain Imaging in Cases with Positive Serology for Dengue with Neurologic Symptoms: A Clinicoradiologic Correlation. *AJNR Am J Neuroradiol* 2018;39(4):699–703.
- Teixeira MG, Costa MC, Barreto F, Barreto ML. Dengue: twenty-five years since reemergence in Brazil. *Cad Saude Publica* 2009;25(Suppl 1):S7–S18.
- Carod-Artal FJ, Wichmann O, Farrar J, Gascón J. Neurological complications of dengue virus infection. *Lancet Neurol* 2013;12(9):906–919.
- Pinheiro TJ, Guimarães LF, Silva MTT, Soares CN. Neurological manifestations of Chikungunya and Zika infections. *Arq Neuropsiquiatr* 2016;74(11):937–943.
- Mehta R, Gerardin P, de Brito CAA, Soares CN, Ferreira MLB, Solomon T. The neurological complications of chikungunya virus: A systematic review. *Rev Med Virol* 2018;28(3):e1978.
- Burt FJ, Rolph MS, Rulli NE, Mahalingam S, Heise MT. Chikungunya: a re-emerging virus. *Lancet* 2012;379(9816):662–671.
- Wilson ME, Lenschow DJ. Chikungunya fever. In: Post TW, ed. UpToDate. <https://www.uptodate.com/contents/chikungunya-fever>. Published November 9, 2018. Accessed January 20, 2019.

36. Ganesan K, Diwan A, Shankar SK, Desai SB, Sainani GS, Katrak SM. Chikungunya encephalomyeloradiculitis: report of 2 cases with neuroimaging and 1 case with autopsy findings. *AJNR Am J Neuroradiol* 2008;29(9):1636–1637.
37. Zika Virus. Fact Sheets. World Health Organization website. <https://www.who.int/en/news-room/fact-sheets/detail/zika-virus>. Published July 20, 2018. Accessed January 23, 2019.
38. Song BH, Yun SI, Woolley M, Lee YM. Zika virus: History, epidemiology, transmission, and clinical presentation. *J Neuroimmunol* 2017;308:50–64.
39. Moghadam SRJ, Bayrami S, Moghadam SJ, Golrokhi R, Pahlaviani FG, SeyedAlinaghia SA. Zika virus: A review of literature. *Asian Pac J Trop Biomed* 2016;6(12):989–994.
40. Hygino da Cruz LC Jr, Nascimento OJM, Lopes FPPL, da Silva IRF. Neuroimaging Findings of Zika Virus-Associated Neurologic Complications in Adults. *AJNRAm JNeuroradiol* 2018;39(11):1967–1974.
41. Zika Virus. Centers for Disease Control and Prevention website. <https://www.cdc.gov/zika/index.html>. Updated May 3, 2019. Accessed May 18, 2019.
42. Ribeiro BG, Werner H, Lopes FPPL, et al. Central Nervous System Effects of Intrauterine Zika Virus Infection: A Pictorial Review. *RadioGraphics* 2017;37(6):1840–1850.
43. Misra UK, Kalita J. Overview: Japanese encephalitis. *Prog Neurobiol* 2010;91(2):108–120.
44. Wang H, Liang G. Epidemiology of Japanese encephalitis: past, present, and future prospects. *Ther Clin Risk Manag* 2015;11:435–448.
45. Pearce JC, Learoyd TP, Langendorf BJ, Logan JG. Japanese encephalitis: the vectors, ecology and potential for expansion. *J Travel Med* 2018;25(suppl_1):S16–S26.
46. Netti RJ, Campbell GL, Reisen WK. Potential for the emergence of Japanese encephalitis virus in California. *Vector Borne Zoonotic Dis* 2009;9(5):511–517.
47. Kakoti G, Dutta P, Ram Das B, Borah J, Mahanta J. Clinical profile and outcome of Japanese encephalitis in children admitted with acute encephalitis syndrome. *BioMed Res Int* 2013;2013:152656.
48. A brief guide to emerging infectious diseases and zoonoses. World Health Organization website. <https://apps.who.int/iris/handle/10665/204722>. Published 2014. Accessed February 4, 2019.
49. Ortiz-Martínez Y, Vega-Useche L, Villamil-Gómez WE, Rodriguez-Morales AJ. Saint Louis Encephalitis Virus, another re-emerging arbovirus: a literature review of worldwide research. *Infez Med* 2017;25(1):77–79.
50. Heinen LB, Zuchi N, Serra OP, et al. Saint Louis Encephalitis Virus in Mato Grosso, Central-Western Brazil. *Rev Inst Med Trop Sao Paulo* 2015;57(3):215–220.
51. White GS, Symmes K, Sun P, et al. Reemergence of St. Louis Encephalitis Virus, California, 2015. *Emerg Infect Dis* 2016;22(12):2185–2188.
52. Marques RE, Del Sarto JL, Rocha RP, et al. Development of a model of Saint Louis encephalitis infection and disease in mice. *J Neuroinflammation* 2017;14(1):61.
53. Wasay M, Diaz-Arrastia R, Suss RA, et al. St Louis encephalitis: a review of 11 cases in a 1995 Dallas, Tex, epidemic. *Arch Neurol* 2000;57(1):114–118.
54. Cerna F, Mehrad B, Luby JP, Burns D, Fleckenstein JL. St. Louis encephalitis and the substantia nigra: MR imaging evaluation. *AJNR Am J Neuroradiol* 1999;20(7):1281–1283.
55. Debiasi RL, Tyler KL. West Nile virus meningoencephalitis. *Nat Clin Pract Neurol* 2006;2(5):264–275.
56. Davis LE, DeBiasi R, Goade DE, et al. West Nile virus neuroinvasive disease. *Ann Neurol* 2006;60(3):286–300.
57. Chancey C, Grinev A, Volkova E, Rios M. The global ecology and epidemiology of West Nile virus. *BioMed Res Int* 2015;2015:376230.
58. Curren EJ, Lehman J, Kolsin J, et al. West Nile Virus and Other Nationally Notifiable Arboviral Diseases – United States, 2017. *MMWR Morb Mortal Wkly Rep* 2018;67(41):1137–1142.
59. Ali M, Safril Y, Sohi J, Llave A, Weathers S. West Nile virus infection: MR imaging findings in the nervous system. *AJNR Am J Neuroradiol* 2005;26(2):289–297.
60. Eastern equine encephalitis. Centers for Disease Control and Prevention website. <https://www.cdc.gov/easternequineencephalitis/index.html>. Published December 2018. Accessed May 17, 2019.
61. Akgoz A, Mukundan S, Lee TC. Imaging of rickettsial, spirochetal, and parasitic infections. *Neuroimaging Clin N Am* 2012;22(4):633–657.
62. Stamm LV. Syphilis: Re-emergence of an old foe. *Microb Cell* 2016;3(9):363–370.
63. Khamayci Z, Bergman R, Telman G, Goldsher D. Clinical and imaging findings in patients with neurosyphilis: a study of a cohort and review of the literature. *Int J Dermatol* 2014;53(7):812–819.
64. Sexually transmitted disease surveillance 2017. Centers for Disease Control and Prevention. <https://www.cdc.gov/std/stats17/syphilis.htm>. Published July 2014. Accessed May 17, 2019.
65. Brightbill TC, Ihmeidan IH, Post MJ, Berger JR, Katz DA. Neurosyphilis in HIV-positive and HIV-negative patients: neuroimaging findings. *AJNR Am J Neuroradiol* 1995;16(4):703–711.
66. Hildenbrand P, Craven DE, Jones R, Nemeshka P. Lyme neuroborreliosis: manifestations of a rapidly emerging zoonosis. *AJNR Am J Neuroradiol* 2009;30(6):1079–1087.
67. Mead PS. Epidemiology of Lyme disease. *Infect Dis Clin North Am* 2015;29(2):187–210.
68. Schwartz AM, Hinckley AF, Mead PS, Hook SA, Kugeler KJ. Surveillance for Lyme Disease – United States, 2008–2015. *MMWR Surveill Summ* 2017;66(22):1–12.
69. Lyme disease. Centers for Disease Control and Prevention website. <https://www.cdc.gov/lyme/index.html>. Published December 2018. Accessed May 17, 2019.
70. Yoshinari NH, Mantovani E, Bonoldi VLN, Marangoni RG, Gauditano G. Brazilian lyme-like disease or Baggio-Yoshinari syndrome: exotic and emerging Brazilian tick-borne zoonosis. *Rev Assoc Med Bras* (1992) 2010;56(3):363–369.
71. Lindland ES, Solheim AM, Andreassen S, et al. Imaging in Lyme neuroborreliosis. *Insights Imaging* 2018;9(5):833–844.
72. Newberg A, Hassan A, Alavi A. Cerebral metabolic changes associated with Lyme disease. *Nucl Med Commun* 2002;23(8):773–777.
73. Allerberger F, Wagner M. Listeriosis: a resurgent foodborne infection. *Clin Microbiol Infect* 2010;16(1):16–23.
74. Bortolussi R. Listeriosis: a primer. *CMAJ* 2008;179(8):795–797.
75. do Amaral LL, Nunes RH, da Rocha AJ. Parasitic and rare spinal infections. *Neuroimaging Clin N Am* 2015;25(2):259–279.
76. Epidemiology and pathogenesis of listeria monocytogenes infection. Uptodate website. <https://www.uptodate.com/contents/epidemiology-and-pathogenesis-of-listeria-monocytogenes-infection>. Published November 15, 2018. Accessed January 8, 2019.
77. Clauss HE, Lorber B. Central nervous system infection with *Listeria monocytogenes*. *Curr Infect Dis Rep* 2008;10(4):300–306.
78. Córdova E, Maiolo E, Corti M, Orduña T. Neurological manifestations of Chagas' disease. *Neurol Res* 2010;32(3):238–244.
79. Parasites: American Trypanosomiasis (also known as Chagas Disease). Centers for Disease Control and Prevention website. <https://www.cdc.gov/parasites/chagas/epi.html>. Accessed January 12, 2013.
80. Rassi A Jr, Rassi A, Marin-Neto JA. Chagas disease. *Lancet* 2010;375(9723):1388–1402.
81. Conners EE, Vinetz JM, Weeks JR, Brouwer KC. A global systematic review of Chagas disease prevalence among migrants. *Acta Trop* 2016;156:68–78.
82. Chagas disease (American trypanosomiasis). World Health Organization website. <https://www.who.int/chagas/epidemiology/en/>. Accessed January 12, 2013.
83. Fernandes HJ, Barbosa LO, Machado TS, Campos JP, Moura AS. Meningoencephalitis Caused by Reactivation of Chagas Disease in Patient Without Known Immunosuppression. *Am J Trop Med Hyg* 2017;96(2):292–294.
84. Oliveira-Filho J, Vieira-de-Melo RM, Reis PS, et al. Chagas disease is independently associated with brain atrophy. *J Neurol* 2009;256(8):1363–1365.
85. Lury KM, Castillo M. Chagas' disease involving the brain and spinal cord: MRI findings. *AJR Am J Roentgenol* 2005;185(2):550–552.



Imaging Patterns of Toxic and Metabolic Brain Disorders

*Arthur M. de Oliveira, MD
Matheus V. Paulino, MD
Ana P. F. Vieira, MD
Alexander M. McKinney, MD, CI-CIIP
Antonio J. da Rocha, MD, PhD
Germana T. dos Santos, MD
Claudia da Costa Leite, MD, PhD
Luis F. de Souza Godoy, MD
Leandro T. Lucato, MD, PhD*

Abbreviations: ADC = apparent diffusion coefficient, AHE = acute hepatic encephalopathy, ATL = acute toxic leukoencephalopathy, CNS = central nervous system, DWI = diffusion-weighted imaging, FLAIR = fluid-attenuated inversion recovery, MBD = Marchiafava-Bignami disease, ODS = osmotic demyelination syndrome, PRES = posterior reversible encephalopathy syndrome, RSL = reversible splenial lesion, WE = Wernicke encephalopathy

RadioGraphics 2019; 39:1672–1695

<https://doi.org/10.1148/rg.2019190016>

Content Codes:

From the Neuroradiology Section, Institute of Radiology, Hospital das Clínicas, Faculdade de Medicina da Universidade de São Paulo (HC-FMUSP), R. Dr Ovidio Pires de Campos 75, São Paulo, SP 05403-010, Brazil (A.M.d.O., M.V.P., G.T.d.S., C.d.C.L., L.F.d.S.G., L.T.L.); Neuroradiology Section, Department of Radiology, Hospital Sírio-Libanês, São Paulo, Brazil (A.P.F.V.); Neuroradiology Division, Department of Radiology, University of Minnesota Medical Center, Minneapolis, Minn (A.M.M.); and Division of Neuroradiology, Santa Casa de São Paulo School of Medical Sciences, São Paulo, Brazil (A.J.d.R.). Recipient of a Magna Cum Laude award for an education exhibit at the 2018 RSNA Annual Meeting. Received February 14, 2019; revision requested April 22 and received May 16; accepted June 24. For this journal-based SA-CME activity, the authors A.M.M. and L.T.L. have provided disclosures (see end of article); all other authors, the editor, and the reviewers have disclosed no relevant relationships. **Address correspondence to** A.M.d.O. (e-mail: arthurmdeoliveira@gmail.com).

©RSNA, 2019

Toxic and metabolic brain disorders are relatively uncommon diseases that affect the central nervous system, but they are important to recognize as they can lead to catastrophic outcomes if not rapidly and properly managed. Imaging plays a key role in determining the most probable diagnosis, pointing to the next steps of investigation, and providing prognostic information. The majority of cases demonstrate bilateral and symmetric involvement of structures at imaging, affecting the deep gray nuclei, cortical gray matter, and/or periventricular white matter, and some cases show specific imaging manifestations. When an appropriate clinical situation suggests exogenous or endogenous toxic effects, the associated imaging pattern usually indicates a restricted group of diagnostic possibilities. Nonetheless, toxic and metabolic brain disorders in the literature are usually approached in the literature by starting with common causal agents and then reaching imaging abnormalities, frequently mixing many different possible manifestations. Conversely, this article proposes a systematic approach to address this group of diseases based on the most important imaging patterns encountered in clinical practice. Each pattern is suggestive of a most likely differential diagnosis, which more closely resembles real-world scenarios faced by radiologists. Basic pathophysiologic concepts regarding cerebral edemas and their relation to imaging are introduced—an important topic for overall understanding. The most important imaging patterns are presented, and the main differential diagnosis for each pattern is discussed.

Online supplemental material is available for this article.

©RSNA, 2019 • radiographics.rsna.org

SA-CME LEARNING OBJECTIVES

After completing this journal-based SA-CME activity, participants will be able to:

- Identify the imaging features of some of the most prevalent CNS toxic and metabolic disorders.
- Describe imaging findings that are highly specific for the diagnosis of particular toxic and metabolic brain disorders.
- Recognize the most important types of cerebral edema and their imaging characteristics.

See rsna.org/learning-center-rg.

Introduction

This article addresses some of the most challenging diagnostic issues in neuroimaging. Toxic and metabolic brain disorders manifest secondary to derangements of a well-balanced environment encompassing metabolic substrates, neurotransmitters, electrolytes, physiologic pH levels, and blood flow, either by endogenous malfunctions or exogenous toxic effects. Patients with these disorders often present

TEACHING POINTS

- Toxic and metabolic disorders affecting the CNS usually manifest imaging characteristics and topographic distributions that should raise suspicion for such diagnoses when the clinical context is compatible. Bilateral and symmetric lesions with restricted diffusion, no or mild mass effects, and no enhancement are often depicted. In addition, sites with higher susceptibility include the cortical gray matter, deep gray nuclei, thalami, periventricular white matter, and corpus callosum. Therefore, lesions with such features and distributions can be secondary to underlying toxic effects. However, such manifestations are unspecific without adequate clinical context and can represent other conditions. Inborn errors of metabolism and hypoxia may have similar imaging features, but the presented context is usually different for these possibilities. Thus, correlations with clinical history are of particular importance in guiding imaging analysis.
- A clinical finding of acute diffuse white matter impairment corroborated by bilateral symmetric confluent areas of true restricted diffusion involving the periventricular white matter and sparing the basal ganglia at DWI signals ATL as an underlying cause. Subsequent normalization of findings is related to intramyelinic edema.
- Common sites involved in WE include the regions surrounding the third ventricle (the medial thalamus in 85% of cases, the mammillary bodies in 60% of cases, and the hypothalamus), the tectal plate and the periaqueductal gray matter in two-thirds of cases, and the putamina.
- In nearly all cases of metronidazole-induced brain toxicity (up to 93%), MR images show bilateral symmetric lesions in the cerebellum, particularly involving the dentate nuclei. A majority of cases (86%) show a characteristic pattern of bilateral symmetric involvement of the dentate nuclei, vestibular nuclei, tegmenta, and superior olivary nuclei.
- ODS affecting extrapontine cerebral regions, including the cortex, has been extensively described. Approximately 50% of cases manifest isolated pontine lesions, with pontine and extrapontine lesions in 30% of cases. There are only extrapontine lesions in 20% of ODS cases, which makes diagnosing this condition even more challenging and underscores the importance of recognizing the spectrum of ODS symptoms.

to the emergency department and are diagnosed with global cerebral dysfunction presenting as acute confusional state and delirium, but commonly they are also critically ill inpatients. These cases often demand a fast and effective management approach because they may result in permanent structural brain damage. Imaging plays a key role in these cases, as imaging findings can be used to diagnose the condition or narrow the differential diagnosis (1).

In addition to providing a final diagnosis, imaging can provide prognostic information. Extensive lesions involving gray matter are often related to poor prognosis and outcomes, while lesions restricted to white matter, sparing cortical and deep gray matter, can point to a reversible cause.

Toxic and metabolic disorders affecting the central nervous system (CNS) usually manifest imaging characteristics and topographic distribu-

Table 1: Major Causes of Toxic and Metabolic Disorders

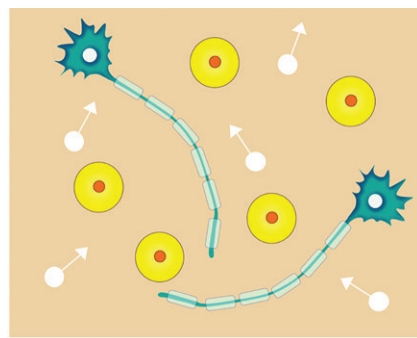
| |
|--------------------------------------------------------------------------|
| Most common endogenous metabolic derangements related to CNS involvement |
| Hypertensive encephalopathies |
| Glucose disorders |
| Parathyroid disorders |
| Hepatic encephalopathy (manganese and/or ammonia levels) |
| Uremic encephalopathy |
| ODS |
| Cobalamin deficiency |
| Major exogenous causes of toxic encephalopathy |
| Alcohol-related disorders (WE, MBD) |
| Industrial agents (methanol, toluen) |
| Inhaled gases (carbon monoxide, pesticides) |
| Illicit drug use (heroin, cocaine) |
| Chemotherapeutic agents (methotrexate, fludarabine, 5-fluorouracil) |
| Immunosuppressive agents (TNF- α blockers, cyclosporine) |
| Other potentially neurotoxic medications (metronidazole, vigabatrine) |

Note.—MBD = Marchiafava-Bignami disease, ODS = osmotic demyelination syndrome, TNF = tumor necrosis factor, WE = Wernicke encephalopathy.

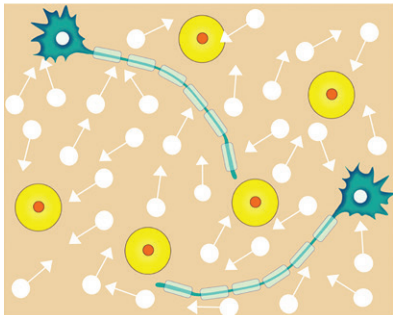
tions that should raise suspicion for such diagnoses when the clinical context is compatible. Bilateral and symmetric lesions with restricted diffusion, no or mild mass effects, and no enhancement are often depicted. In addition, sites with higher susceptibility include the cortical gray matter, deep gray nuclei, thalami, periventricular white matter, and corpus callosum. Therefore, lesions with such features and distributions can be secondary to underlying toxic effects. However, such manifestations are unspecific without adequate clinical context and can represent other conditions. Inborn errors of metabolism and hypoxia may have similar imaging features, but the presented context is usually different for these possibilities. Thus, correlations with clinical history are of particular importance in guiding imaging analysis. By allying imaging patterns with some clinical findings, it is possible to reach a hypothesis with good accuracy (2).

The brain is highly susceptible to a number of acquired metabolic abnormalities, and the list of toxins and poisons that affect the CNS is long (Table 1). Some agents accumulate slowly such that their clinical manifestations are insidious, while others cause profound almost immediate CNS toxic effects. Aiming at a more practical and easier line of attack to address this group of diseases, this article proposes an approach

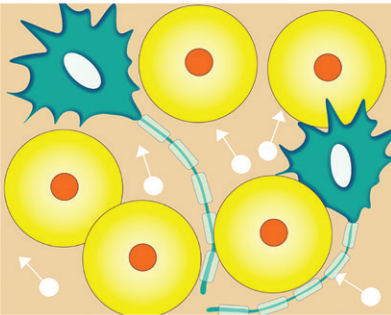
Figure 1. Types of cerebral edema. Teal shapes = neurons and axons with myelin sheaths, white circles with arrows = water molecules, yellow circles = glial cells. (a) Illustration depicts the normal relationship between brain cells and extracellular space, which contains water molecules with freedom of movement. (b) Illustration depicts brain tissue in a vasogenic edema situation, with an increased number of water molecules occupying the extracellular space but maintaining freedom of movement. (c) Illustration depicts a cytotoxic brain edema situation, represented by the swelling of brain cells (increased volume) without primarily affecting the extracellular space. Water molecules inside the brain cells lose their freedom of movement. (d) Illustration depicts intramyelinic edema, with swelling of periaxonal space and spaces between myelin layers, without primarily affecting other extracellular spaces or involving brain cells. Water molecules inside the myelin layers cannot move to other extracellular spaces, losing their freedom of movement.



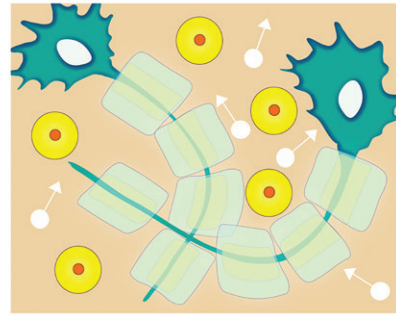
a.



b.



c.



d.

beginning with a given general imaging pattern and discussing its most important possible differential diagnoses, highlighting imaging findings or clinical information that can lead to a specific diagnosis.

Cerebral Edema

Vasogenic and cytotoxic edema have been traditionally related to alterations encountered in toxic and metabolic brain disorders. Each one encompasses many causes that share similar interconnected processes resulting in abnormal shifts in water among various compartments of the brain parenchyma. Each type of cerebral edema leads to particular imaging findings. Recently, other pathologic concepts have been used in neuroimaging to describe and explain some specific imaging findings and disorders, such as the concepts of excitotoxic injury and intramyelinic edema (3,4). Figure 1 depicts a schematic representation of the most important alterations affecting brain tissue in each type of edema.

Vasogenic cerebral edema refers to a process induced by mechanical or chemical insults that leads to blood-brain barrier disruption, whether by physical damage or endothelial activation by blood mediators, resulting in leakage of fluid from capillaries into the extracellular space in the white matter. Images show T2-weighted and fluid-attenuated inversion-recovery (FLAIR) hyperintensities owing to water accumulation in the extracellular space, without restricted diffusion, as the freedom of movement of water molecules is not affected.

Vasogenic edema can produce mass effect, with dislocation of structures and defacement of the cerebral sulci. The gray matter is maintained, as this type of edema mainly involves the white matter, extending in a fingerlike fashion. Common examples include edemas associated with tumors and abscesses, as well as posterior reversible encephalopathy syndrome (PRES) (3,4).

Cytotoxic cerebral edema, the classic edema associated with cerebral ischemia, is a condition in which extracellular water passes into cells, causing them to swell. In brief, prior ischemic or hypoxic insults impair mitochondrial function and adenosine triphosphate production and cause failure of ion pumps and accumulation of metabolites (such as lactate), resulting in cellular edema. This process does not compromise the blood-brain barrier and mainly affects gray matter, although white matter is also involved. The imaging features of cytotoxic cerebral edema appear primarily as changes at diffusion-weighted imaging (DWI) caused by restricted water diffusivity within brain cells, without T1- or T2-weighted changes, as the entire process is a redistribution of water. Importantly, the changes are not completely reversible (cell death), and as the pathologic process progresses, alterations in T2-weighted signal intensity and contrast enhancement can appear secondarily (3,4).

Excitotoxic brain injury is a final common pathway of many cerebral disorders, such as infarction, hypoxic-ischemic encephalopathy, and status epilepticus, but it is also closely related to

Table 2: Most Common Causes of ATL

| |
|-----------------------------------------------------|
| Chemotherapeutic agents (methotrexate, fludarabine) |
| Opioid use (heroin, opiates) |
| AHE |
| Immunosuppressive agents (cyclosporine, tacrolimus) |
| Carbon monoxide poisoning (subacute presentation) |
| Other (uremia, cocaine use, metronidazole use) |

Note.—AHE = acute hepatic encephalopathy.

toxic and metabolic disorders. Excitotoxicity is the excessive release of excitatory amino acids in the synaptic cleft, with glutamate being the most important neurotransmitter responsible for many neurologic functions (memory, cognition, movement, and sensation). Excessive glutamate in the synaptic cleft can lead to cell swelling and subsequent death (ie, cytotoxic edema) in the event of ischemia and cell failure with disruption of glutamate reuptake. If the reuptake of glutamate is maintained, cell swelling and death may not occur. Instead, the process known as intramyelinic edema may occur instead.

The myelin sheath is composed of layers of myelin around axons that form tight junctions with axons and isolate the periaxonal space and spaces between myelin layers from other extracellular spaces. Such sites are virtual but potential extracellular spaces. Thus, intramyelinic edema refers to non-neurotoxic edema in these virtual spaces, which is characterized by restricted diffusion (as water molecules are unable to shift to other extracellular spaces) and reversibility of the condition (without cell death). Consequently, the imaging hallmark is true and reversible diffusion-weighted restriction. It is believed that intramyelinic edema alone results in completely reversible edema, while irreversible or partially reversible conditions manifest when cellular edema is concurrently present. The periventricular white matter and the splenium, which are known to have higher metabolism, are especially susceptible to these changes (5,6).

Imaging Patterns

Toxic and metabolic disorders are closely related to excitotoxic brain injury, as they often induce intense glutamate release. Although receptors related to excitotoxic injury are widely distributed in the brain, there are classic CNS sites that are particularly susceptible to this mechanism, such as the basal ganglia and thalamus, cortical gray matter, periventricular white matter, and the corpus callosum. This differential susceptibility is important because it

indicates some possible characteristic imaging patterns that could lead to the consideration of toxic and metabolic causes during diagnosis (5–7).

Another important concept to be introduced is acute toxic leukoencephalopathy (ATL). ATL, which has been recently described in terms of its clinical, radiologic, and pathologic features, relates to cerebral white matter alterations secondary to various toxic agents and has great potential for reversibility if rapidly and correctly approached, highlighting the importance of its recognition (8). A clinical finding of acute diffuse white matter impairment corroborated by bilateral symmetric confluent areas of true restricted diffusion involving the periventricular white matter and sparing the basal ganglia at DWI signals ATL as an underlying cause. Subsequent normalization of findings is related to intramyelinic edema, as described previously (8,9). Table 2 summarizes the most common causes of ATL.

Toxic and metabolic disorders affecting the CNS are usually depicted on images following some patterns of involvement that are closely related to the pathophysiologic mechanism of damage, which is important to recognize because each pattern can point to a most likely diagnosis and even indicate the prognosis. Note that each pattern indicates the most commonly involved sites for a group of diseases but each disease can manifest more than one pattern and can affect other structures. The most important patterns are as follows (Fig 2):

1. Basal ganglia and/or thalami involvement. The periventricular white matter and the cortical gray matter may be also involved. This pattern is usually related to cytotoxic brain edema, poor outcomes, and irreversibility.
 2. Dentate nuclei involvement.
 3. Prominent cortical gray matter involvement. Although cortical lesions can coexist with basal ganglia- and white matter-associated involvement, they are the most distinguishing feature.
 4. Symmetric periventricular white matter involvement with gray matter sparing. This is a pattern that includes ATL causes and is more related to intramyelinic edema and higher possibilities of reversibility and better outcomes.
 5. Corticospinal tract region involvement.
 6. Corpus callosum involvement.
 7. Asymmetric white matter involvement in a demyelinating disease pattern.
 8. Parieto-occipital subcortical vasogenic edema.
 9. Central pons involvement.
- The pattern of involvement, damage extension, and possibility of reversion (mainly in cases of ATL) are related primarily to the

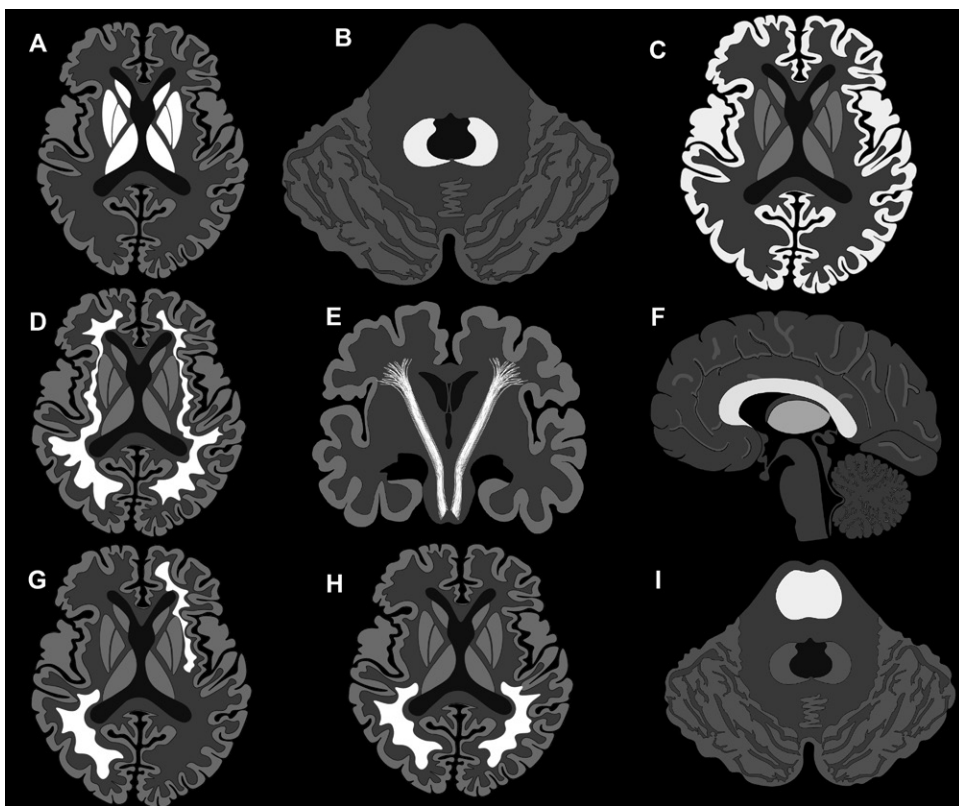


Figure 2. Illustration shows the most important general imaging patterns in toxic and metabolic brain disorders. White areas = areas of involvement. These include symmetric basal ganglia and/or thalami involvement (axial view) (A); symmetric dentate nuclei involvement (axial view) (B); prominent cortical gray matter involvement (axial view) (C); symmetric periventricular white matter involvement (with gray matter sparing) (axial view) (D); corticospinal tract involvement (axial view) (E); corpus callosum involvement (coronal view) (F); asymmetric white matter involvement (demyelinating disease pattern) (axial view) (G); parieto-occipital subcortical vasogenic edema (axial view) (H); and central pons involvement (axial view) (I).

intensity and duration of exposure to a determined agent (2,7–9).

Keep in mind that such patterns of involvement are unspecific and comprise various possible diagnoses, but they can be used as a guide since each pattern is related to a minor number of diagnostic possibilities and can be a prognostic factor.

Pattern 1: Basal Ganglia and/or Thalami Involvement

Pattern 1a: T2-weighted and FLAIR Hyperintensity

Wernicke Encephalopathy.—WE is usually related to chronic and frequent alcohol intake, but it is important to remember that almost 50% of WE cases are unrelated to alcohol use (10). The underlying pathophysiology is associated with nutritional deficiencies, notably thiamine (vitamin B1). Thiamine is important in maintaining osmotic gradients across the cell membrane, ensuring its integrity (2).

Aside from alcohol abuse, other important causes of WE include hyperemesis (pregnancy-

related, chemotherapy), eating disorders, and bariatric surgery, any of which can lead to secondary malnutrition (2,10,11). Although most cases occur in adults, it is important to emphasize that WE can also occur in children (2). The classic clinical triad of symptoms, including ocular dysfunction (nystagmus, ophthalmoplegia), ataxia, and confusion, manifests in only 30% of patients (11).

Imaging plays an important role in early WE diagnosis. MRI is much more sensitive than CT for evaluating alterations related to WE. Importantly, remember that cerebral atrophy and microhemorrhages can manifest owing to chronic alcohol intake. During the acute phase, symmetric bilateral T2-weighted and FLAIR hyperintensities and restricted diffusion can be observed in affected areas, with 50% of cases showing enhancement following the administration of contrast material (postcontrast). Common sites involved in WE include the regions surrounding the third ventricle (the medial thalami in 85% of cases, the mammillary bodies in 60% of cases, and the hypothalamus), the tectal plate and the periaqueductal gray matter in two-thirds of cases, and the putamina (Fig 3) (2,10,11). Other sites that can be altered, albeit less

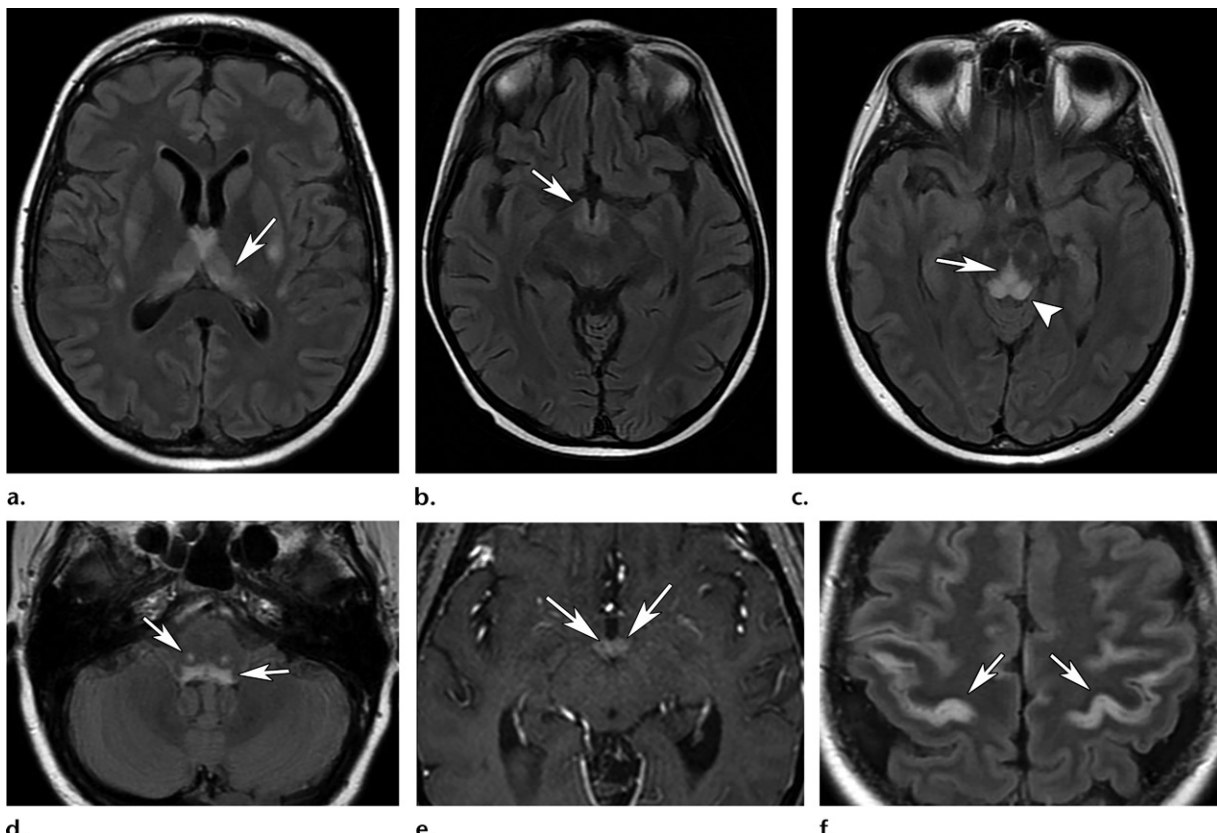


Figure 3. WE in a patient with diplopia and impaired mental status after long-term parenteral nutrition. (a–d) Axial FLAIR MR images show bilateral and symmetric hyperintensities involving the medial thalamus (arrow in a), hypothalamus (arrow in b), periaqueductal gray matter (arrow in c), tectum (arrowhead in c), and dorsal pons (arrows in d). (e) Axial contrast-enhanced T1-weighted MR image shows symmetric enhancement of the mammillary bodies (arrows). (f) Axial FLAIR MR image shows periorolanic cortical involvement (arrows).

commonly, are the dorsal medulla, cerebellum, and cranial nerve nuclei. There may also exist cortical involvement, which can be asymmetric and usually involves the periorolanic cortex (Fig 3f) (2,10,11). Strong uniform postcontrast enhancement of the mammillary bodies is observed in up to 80% of cases and is considered a pathognomonic finding for WE (Fig 3e). In the chronic phase, the mammillary bodies are atrophied (2,10,11).

Methanol Poisoning.—Methanol is a strong CNS depressant and a common component in solvents, perfumes, paint removers, and gasoline mixtures. This substance can be accidentally inhaled or ingested, with some cases of methanol poisoning resulting from the intake of adulterated alcoholic drinks (moonshine) (2,12,13).

Methanol causes severe metabolic acidosis, with patients commonly presenting in a comatose state after preceding visual and gastrointestinal symptoms. Diagnosis is often delayed, contributing to the high mortality of this condition. Important clinical clues include an increased anion gap and a latent period between ingestion and clinical symptom onset (ethanol ingested simultaneously slows methanol metabolism).

Imaging can play an important role in making this diagnosis (2,12–14).

Bilateral symmetric basal ganglia necrosis is the most characteristic imaging feature of methanol poisoning. Selective or predominant involvement of the putamina with relative sparing of the globi pallidi is suggestive of methanol poisoning (Fig 4). Variable degrees of subcortical white matter and cerebellar involvement and optic nerve necrosis are depicted, dependent on the severity of the intoxication (12–14). Hemorrhagic necrosis appears as an area of hyperattenuation on CT images. MR images show T2-weighted and FLAIR hyperintensity, and susceptibility-weighted imaging sequences sometimes show associated changes owing to the presence of hemorrhage (sometimes occurring during the evolution of the disease and not in the acute phase). Restricted diffusion is depicted in the acute phases, and MR spectroscopy shows reduced N-acetylaspartate and elevated lactate peaks (Fig 4e) (2,12–14).

Carbon Monoxide Poisoning.—Carbon monoxide is an odorless and colorless gas usually produced by the incomplete combustion of fuels and can cause poisoning by accidental inhalation. The

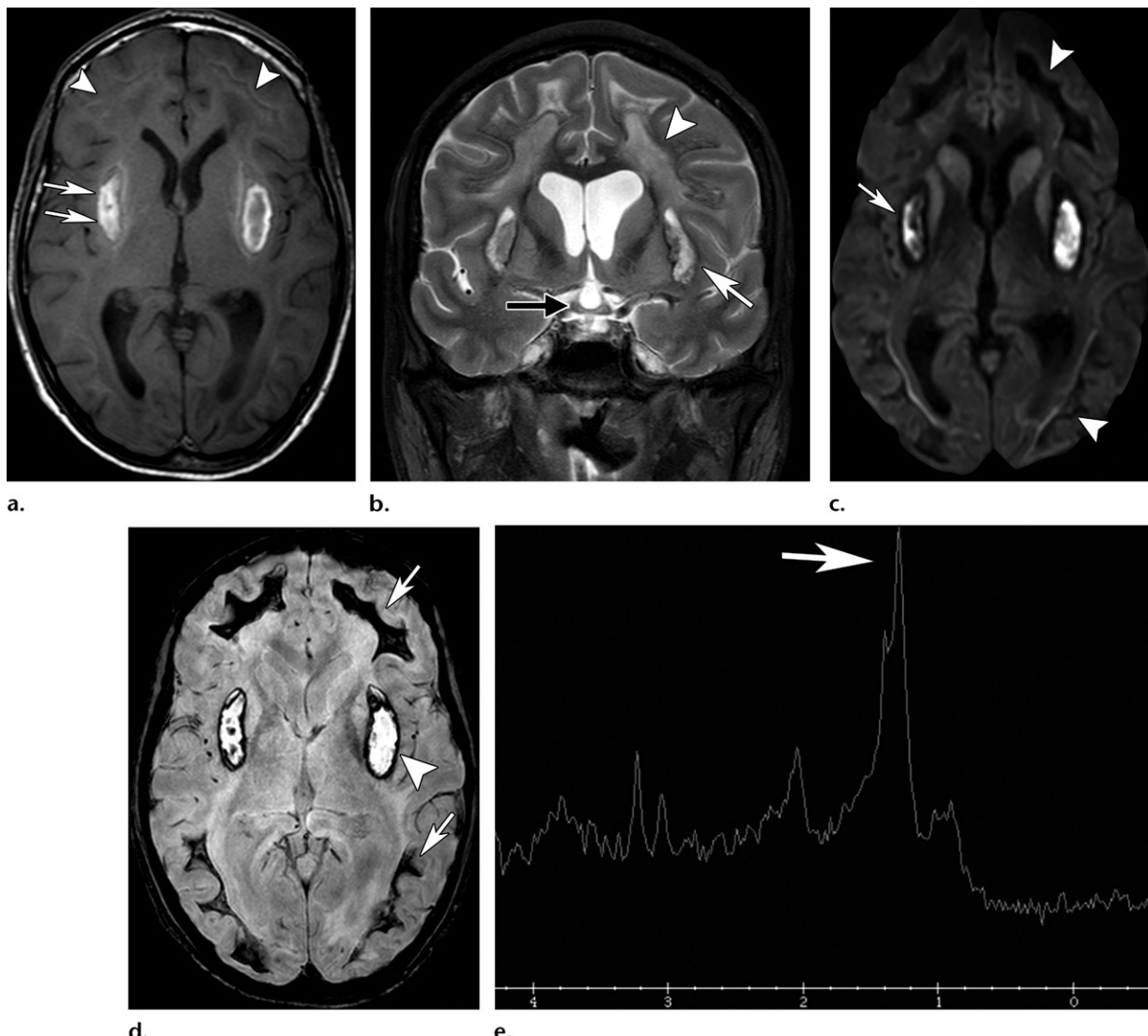


Figure 4. Methanol poisoning after moonshine intake. (a) Axial T1-weighted MR image shows hyperintensities involving the putamina (arrows) owing to necrotic hemorrhage. Note the subtle hyperintensities (arrowheads) involving the anterior and posterior white matter. (b) Coronal T2-weighted MR image shows chiasma involvement (black arrow) in addition to putamina (white arrow) and diffuse white matter (arrowhead) hyperintensities. (c) Axial diffusion-weighted MR image shows restricted diffusion involving the putamina (arrow). There are magnetic susceptibility artifacts involving the white matter owing to hemorrhage (arrowheads). (d) Axial T2*-weighted MR image shows necrotic hemorrhage, which is better demonstrated than on b, characterized by a rim of low signal intensity involving the putamina (arrowhead) and extensive low signal intensity involving the anterior and posterior white matter (arrows). (e) MR spectroscopic image with short echo time shows a huge lactate peak at 1.3 ppm (arrow).

toxic mechanism is secondary to impaired oxygen transportation, as carbon monoxide combines with hemoglobin with over 200 times higher affinity than that of oxygen (2,15,16).

Because the globus pallidus is sensitive to hypoxia, its bilateral symmetric necrotic involvement is the hallmark of carbon monoxide poisoning (Fig 5). Hypoattenuation in both globi pallidi can be visualized on CT images, with hyperintensities on T2-weighted and FLAIR images and a thin hypointense rim around the lesion caused by hemorrhage (hyperintense on T1-weighted images). Diffusion-weighted images show restricted diffusion, and susceptibility-weighted sequences may show areas of hypointensity corresponding

to hemorrhage (2,15). In addition to the globi pallidi, less common sites that may be involved are the hippocampi, caudate nuclei, putamina, thalami, cerebellum, corpus callosum, and cerebral cortex (2,15,16).

The second most commonly affected site is the cerebral white matter (up to one-third of patients), which can show delayed leukoencephalopathy in the subacute phase of carbon monoxide poisoning. This effect, which appears weeks after the initial insult, is characterized by progressive white matter demyelination with extensive bilateral symmetric confluent areas of hyperintensity on T2-weighted and FLAIR images and subsequent (months later) complete or partial resolution (Fig 5) (2,17).

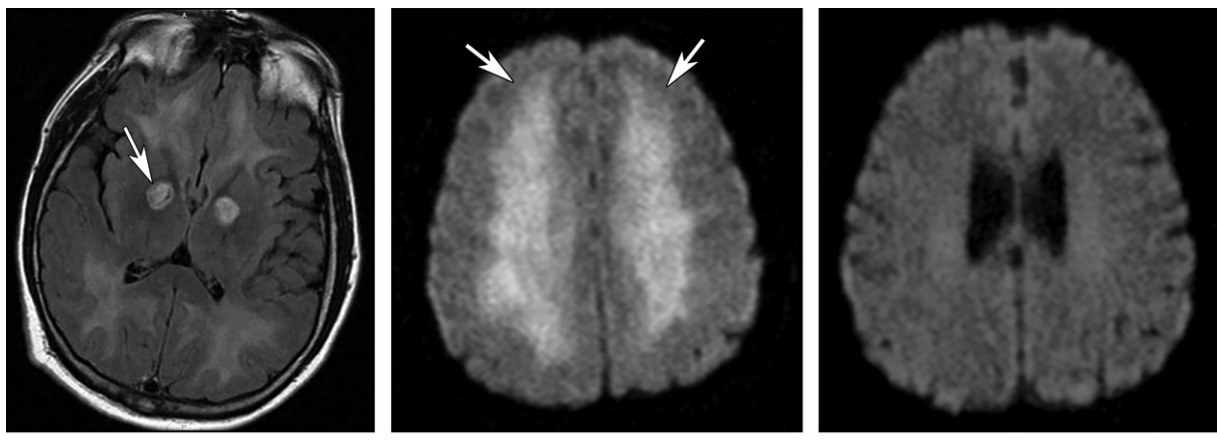


Figure 5. Carbon monoxide poisoning in two patients. (a) Axial FLAIR MR image shows symmetric hyperintensity involving both globi pallidi (arrow) and sparing the putamina, a classic finding of this condition. Note that there is also white matter involvement. (b, c) Axial diffusion-weighted MR images in another patient show subacute extensive bilateral and symmetric areas of restricted diffusion involving the periventricular white matter (arrows in b), with posterior normalization on the 1-year follow-up image (c).

At that point, it is important to remember the importance of correlation with clinical history, as some conditions may mimic carbon monoxide poisoning with bilateral globi pallidi involvement, such as hypoxic-ischemic encephalopathy and drug use (15,16).

Vigabatrin-associated Toxicity.—Vigabatrin is an antiepileptic drug used for the treatment of infantile spasms. The potential risk of developing brain abnormalities during the course of treatment is well known. Approximately one-third of patients develop such abnormalities, with little variation among current studies (17,18). The younger the patient, the higher the risk, with patients younger than 1 year being the most commonly affected (17,18).

Important characteristics of this entity are a frequently asymptomatic course and reversibility through drug discontinuation. Recent studies demonstrate that affected children received higher doses than unaffected children, but the duration of treatment was not an important factor (17,18).

Images depict classic findings of toxic encephalopathy, with symmetric restricted diffusion and T2-weighted and FLAIR hyperintensity in involved areas, subsequently normalized after vigabatrin withdrawal. The major affected areas are the globi pallidi, thalamus, dorsal brainstem, and dentate nuclei (Fig 6) (17,18).

Uremic Encephalopathy.—Uremic encephalopathy, a metabolic disorder that occurs in the context of both acute and chronic renal failure, is a complication resulting from the presence of endogenous uremic toxins in patients with severe renal failure. The pathogenesis is complex and unclear, and the condition is likely caused by the effects

of neurotoxicity from the accumulation of uremic toxins such as guanidine compounds (19–21). Clinical manifestations include various neurologic symptoms, such as movement disorders (tremor, asterixis, myoclonus), seizures, cognitive disorders, and impaired mental status (21).

Uremic encephalopathy has three patterns of imaging findings: basal ganglia involvement (most common), cortical or subcortical involvement (PRES-like), and white matter involvement (caused by ATL). Imaging findings are unspecific, and the patient's clinical history and laboratory findings are indispensable for diagnosis. Imaging can also aid in clinical management because it can shed light on the severity and possible reversibility.

The most common finding is bilateral symmetric involvement of the basal ganglia with variable white matter and cortical-associated involvement (19,20). The lentiform fork sign can be identified in patients with uremic encephalopathy and may be indicative of underlying metabolic acidosis coexisting with uremia, a typically encountered association. This sign is characterized on T2-weighted and FLAIR images by hyperintensity of the white matter that surrounds the lentiform nuclei (internal and external capsules and the medullary laminae), delineating the lateral and medial boundaries of both putamina, giving its peculiar appearance that is more commonly found in patients with diabetes (Fig 7) (19,22).

Pattern 1b: T2 Hypointensity

Toluene Use.—Toluene is the most important component of industrial solvents. This lipid-soluble product, found in glues, paint thinners, and inks, can be rapidly absorbed by the CNS. Clinical and imaging findings usually manifest

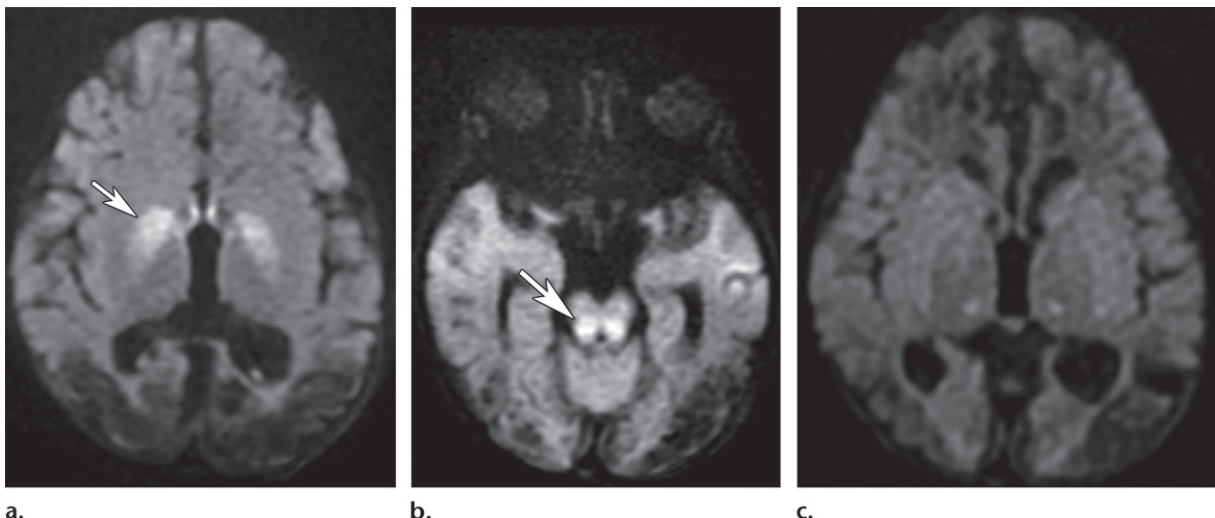


Figure 6. Vigabatrin-associated toxicity. Axial diffusion-weighted MR images show restricted diffusion symmetrically involving the globi pallidi (arrow in **a**) and dorsal brainstem (arrow in **b**), with normalization on the 6-month follow-up image (**c**).

after chronic use (years), and thus the condition is termed *chronic solvent encephalopathy* (2,23,24).

Continued toluene use leads to severe irreversible cognitive impairment, which is an important clue for diagnosis in adolescents and young adults because this population is not usually affected by dementia, and toluene use is widespread in this population. Alterations depicted on images include diffuse periventricular white matter lesions that are hyperintense on T2-weighted and FLAIR images and significant T2 hypointensity involving the thalamus, basal ganglia, and substantiae nigrae (Fig 8) (23,24). The cause for such hypointensity is still not known. It has been hypothesized to be secondary to excessive iron deposition (25). Generalized cerebral and cerebellar atrophy also manifest, with ventricular dilatation and thinning of the corpus callosum (2).

Parathyroid-Hypofunction Disorders and Hyperparathyroidism-related Disorders—Parathyroid-hypofunction disorders are characterized by hypofunction of the parathyroid glands or their products. There are three main types, differentiated by clinical and laboratory findings: (*a*) hypoparathyroidism, (*b*) pseudohypoparathyroidism, and (*c*) pseudopseudohypoparathyroidism (2,26).

The main imaging findings are the same for all conditions and are related to calcium deposition in the basal ganglia. CT images show coarse bilateral and symmetric calcifications in the globi pallidi, putamina, and caudate nuclei, emphasizing that the thalamus, subcortical white matter, and dentate nuclei may also be affected (Fig 9). MR images can depict hyperintensity on T1-weighted images and hypointensity on T2-weighted images. T2*- or susceptibility-weighted

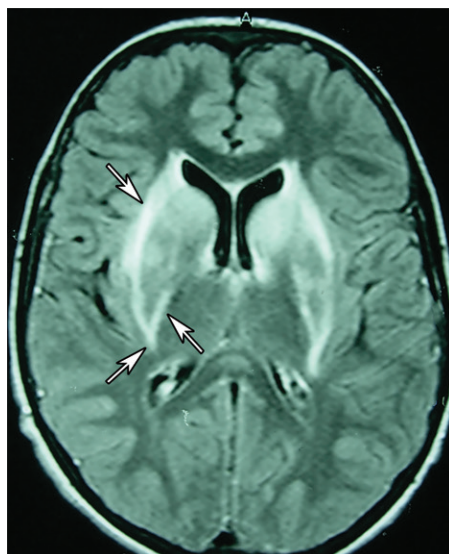
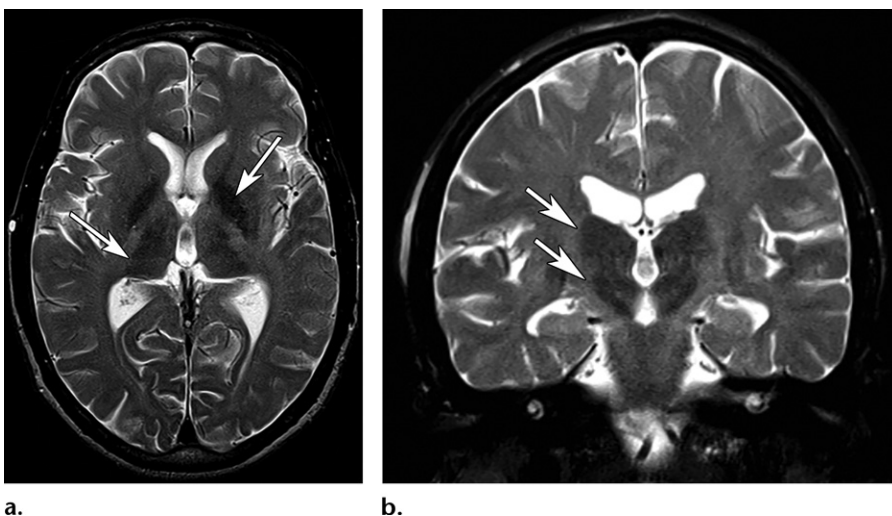


Figure 7. Uremic encephalopathy. Axial FLAIR MR image shows symmetric involvement of the basal ganglia, with hyperintensities (arrows) affecting the white matter that surrounds the basal ganglia, delineating the lateral and medial boundaries of both putamina (ie, lentiform fork sign).

images can depict blooming artifacts related to calcium deposition (2,26).

An important differential diagnosis is Fahr disease, a genetic condition characterized by idiopathic basal ganglia calcification with a similar imaging pattern to that of parathyroid-hypofunction disorders but without laboratory alterations (2).

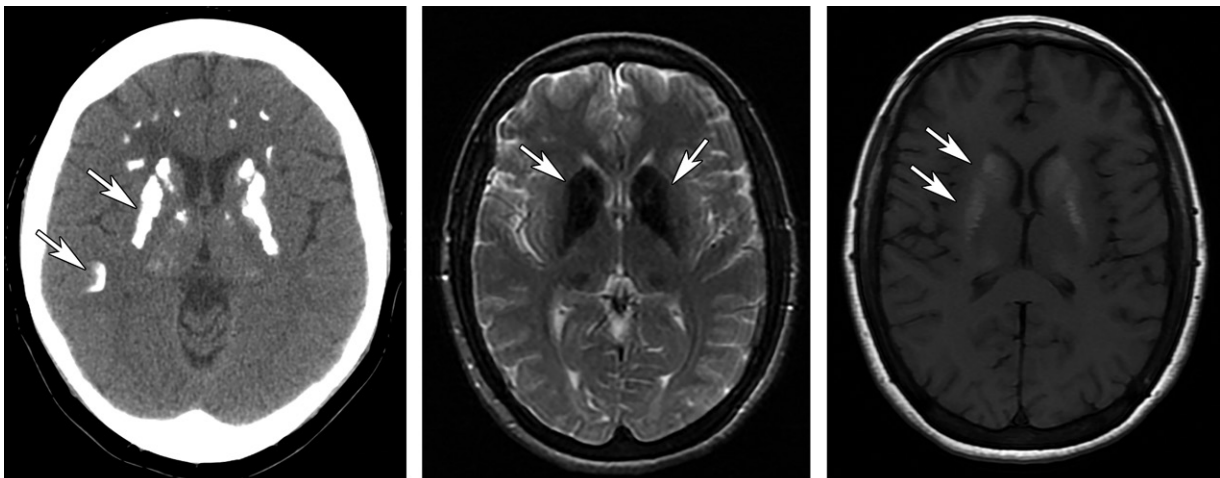
Disorders related to hyperparathyroidism are characterized by hyperfunction of the parathyroid glands or high serum levels of parathyroid hormone. Primary hyperparathyroidism is caused by parathyroid adenoma (75%–85%), parathyroid hyperplasia (10%–20%), or carcinoma (1%–5%) and is characterized by high serum levels of



a.

b.

Figure 8. Effects of chronic toluene use. (a) Axial T2-weighted MR image shows accentuated symmetric hypointensities (arrows) involving the globi pallidi and thalami. (b) Coronal T2-weighted MR image shows symmetric hypointensities (arrows) involving the thalami and substantiae nigrae.



a.

b.

c.

Figure 9. Primary hypoparathyroidism in a 10-year-old boy who presented with tetany and hyperreflexia and was diagnosed with concomitant low levels of calcium and parathyroid hormone. (a) Axial CT image (soft-tissue window) shows coarse and symmetric calcifications (arrows) in the basal ganglia and periventricular white matter. (b, c) Axial T2-weighted (b) and T1-weighted (c) MR images show low-signal-intensity abnormalities in b and high-signal-intensity abnormalities in c, involving the basal ganglia produced by the calcifications (arrows).

parathyroid hormone and calcium serum levels. Secondary hyperparathyroidism is related to chronic renal failure, in which the kidneys fail to convert vitamin D to the active form and excrete phosphate, leading to high parathyroid hormone levels, normal or low calcium levels, and high phosphate serum levels (2,27,28).

In hyperparathyroid disturbances, as in hypoparathyroid disorders, bilateral symmetric calcifications are depicted in the basal ganglia. In primary hyperparathyroidism, the salt-and-pepper appearance (ie, multiple well-defined hypointensities in the skull owing to trabecular bone resorption) can be observed, while in secondary hyperparathyroidism, diffuse thickening of the skull, plaque-like dural thickening, calcification, and pipestem calcifications of carotid arteries are found. Brown tumors can manifest in both types

of hyperparathyroidism and are described as well-defined round lytic lesions without sclerotic margins or cortical involvement (27,28).

Pattern 1c: T1 Hyperintensity

Diabetic Striatopathy.—Diabetic striatopathy is also known as *hyperglycemia-induced hemichorea-hemiballismus*, and patients with this condition present with characteristic involuntary nonpatterned movements. This is a nonketotic delayed hyperglycemia complication and can sometimes lead to a diagnosis of diabetes mellitus type 2. At presentation, the mean age is 71 years, and the mean glycemia level is 431 mg/dL (2,29,30). Nevertheless, it must be noted that symptoms of this condition can manifest acutely or even weeks after normalization of the hyperglycemic event (2,29).

Imaging findings are virtually pathognomonic and depict a usually unilateral T1 hyperintensity involving the striatum and hyperattenuation in the same region on CT images (Fig 10). Diabetic striatopathy is completely reversible in 73% of patients (29,30).

Chronic Hepatic Encephalopathy.—Chronic hepatic encephalopathy is a potentially reversible clinical syndrome that occurs in the context of chronic severe liver dysfunction. Most patients have a long history of cirrhosis accompanied by portal hypertension or portosystemic shunting (2,31,32). Neurotoxic substances accumulate within brain tissue, and manganese is the substance most related to alterations, usually observed in chronic hepatic encephalopathy (31).

Patients may have no clinical findings or only subtle cognitive and motor impairment, but they can also present with periods of decompensation of symptoms during the course of the disease that are more related to higher ammonia levels and acute hepatic encephalopathy (32).

The characteristic imaging finding is bilateral and symmetric T1 hyperintensity involving the globi pallidi and substantiae nigrae (reported in 80%–90% of patients with chronic liver failure), most likely due to manganese accumulation (Fig 11a). High signal intensity on T1-weighted images of the pituitary gland and the hypothalamus can be depicted but is less common. After liver transplant, changes can decrease or even disappear, typically normalizing after 1 year (2,31,32).

Patients receiving total parenteral nutrition, patients with occupational exposure to manganese from welding, and those with noncirrhotic portal vein thrombosis can also demonstrate similar imaging findings (32). Notably, such patients may show glutamine-glutamate peak at MR spectroscopy with short echo times, resonating at 2.1–2.4 ppm, which is probably related to chronic accumulation of glutamine levels in the brain tissue owing to recurrent alterations in ammonia levels in chronic hepatic disease. The conversion of glutamate and ammonia into glutamine serves as a method of ammonia detoxification (32,33).

Recent studies have noted signs of brain edema, even in cases of chronic hepatic encephalopathies. Excess glutamine in cerebral tissue leads to the edema of astrocytes. For this reason, fast FLAIR sequences can show bilateral vasogenic edema (without restriction at DWI) in cerebral white matter, mainly involving the corticospinal tract (Fig 11b) (31,32).

On T2-weighted images, laminar hyperintensities involving the deep layers of periolan-dic cortices have been histologically related to chronic hepatic encephalopathy. It is well known

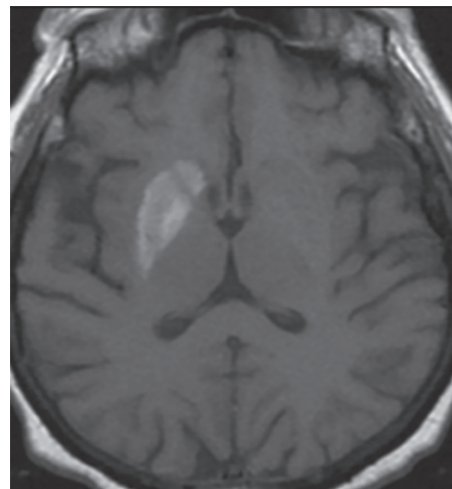


Figure 10. Diabetic striatopathy (hyperglycemia-induced hemichorea hemiballismus). Axial T1-weighted MR image shows unilateral hyperintensity in the striatum. CT images showed hyperattenuation in the same region (not shown).

that similar cortical laminar T2 hyperintensities are also depicted in cases of hypoxic-ischemic brain injury. In hypoxic-ischemic encephalopathy, however, these are frequently located in the boundary zones of the cerebral cortices, reflecting the influence of hemodynamic factors, whereas in chronic hepatic encephalopathy these are most striking in the superior parietal and posterior frontal convexities (Fig 11c) (34).

Parathyroid-Related Disorders.—T1 hyperintensities involving the basal ganglia, thalamus, and dentate nuclei may be secondary to calcifications (Fig 9c). In such cases, calcium metabolism disorders are more likely to have manifested (2).

Figure E1 summarizes the disorders associated with pattern 1.

Pattern 2: Dentate Nuclei Involvement

Metronidazole-induced Brain Toxicity

Metronidazole is an antibiotic that is used to treat a wide variety of bacterial and protozoal infections and was recently reported to rarely cause CNS toxic effects. These toxic effects can affect patients of all ages, usually appearing during prolonged treatment, frequently over 25 days of use (mean duration, 54 days), but it is important to emphasize that shorter periods, such as 7 days, have also been described to cause such toxic effects (35,36).

Patients present with symptoms of cerebellar dysfunction, such as dysarthria, ataxia, and dysmetria (75% of cases), confusion (33%), and seizures (13%) (35).

In nearly all cases of metronidazole-induced brain toxicity (up to 93%), MR images show

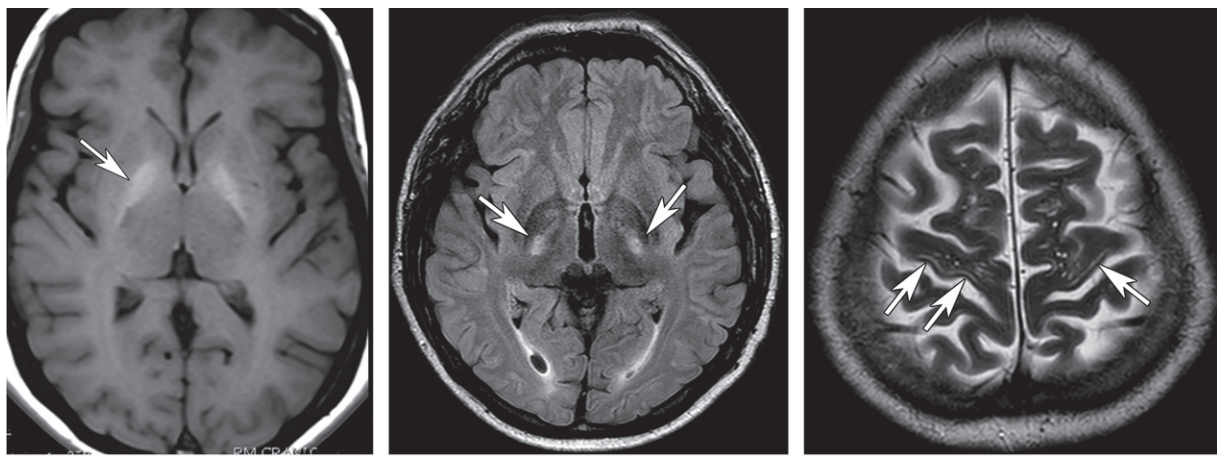


Figure 11. Chronic hepatic encephalopathy. (a) Axial T1-weighted MR image shows symmetric hyperintensity (arrow) involving the globi pallidi. (b) Axial FLAIR MR image shows high-signal-intensity abnormalities (arrows) along the corticospinal tracts, at the level of the posterior limb of the internal capsule. (c) Axial T2-weighted MR image shows linear hyperintensities (arrows) involving the deep layers of the perirolandic cortex.



Figure 12. Metronidazole-induced brain toxicity. Axial FLAIR MR image shows a symmetric hyperintensity (arrow) involving the dentate nuclei.

bilateral symmetric lesions in the cerebellum, particularly involving the dentate nuclei (Fig 12). A majority of cases (86%) show a characteristic pattern of bilateral symmetric involvement of the dentate nuclei, vestibular nuclei, tegmenta, and superior olivary nuclei. A lack of enhanced lesions with T2-weighted and FLAIR hyperintensity is the most common finding. However, not all cases affect the dentate nuclei, with some cases demonstrating periventricular white matter involvement or affecting the splenium (ATL and reversible splenial lesion [RSL]-like appearance), sparing the dentate nuclei (35,36).

It is important to note if T2 hyperintensity of the dentate nuclei occurs in patients undergoing treatment of tuberculosis with isoniazid, which

occurs mainly in countries where tuberculosis is an endemic infection. MR images obtained in this population may show a pattern similar to that of metronidazole-induced brain toxicity (37). Calcium metabolism disorders can manifest calcifications involving the dentate nuclei (2).

Methyl Bromide–induced Toxicity

Methyl bromide is one of the most common components used in pesticides and is usually involved in toxicity related to directed occupational inhalation in agricultural use (38). Methyl bromide–induced toxicity usually manifests with symptoms that are delayed months after initial exposure and are characterized by cranial neuropathy, pyramidal tract dysfunction, and behavioral changes. On T2-weighted and FLAIR images, bilateral symmetric reversible hyperintensities involving the cerebellum and the brainstem can be visualized, including mainly the periaqueductal midbrain, dorsal pons, and dentate nuclei (Fig 13). These imaging findings have a pattern similar to those of WE and metronidazole-induced brain toxicity (38).

Figure E2 summarizes the disorders associated with pattern 2.

Pattern 3: Prominent Cortical Involvement

Adult Hypoglycemic Encephalopathy

Adult hypoglycemic encephalopathy or hypoglycemic brain injury is caused by an imbalance between supply and use of glucose by cerebral cells, leading to brain injury (39). The clinical manifestation is characterized by seizures, a depressed level of consciousness, and even coma in patients

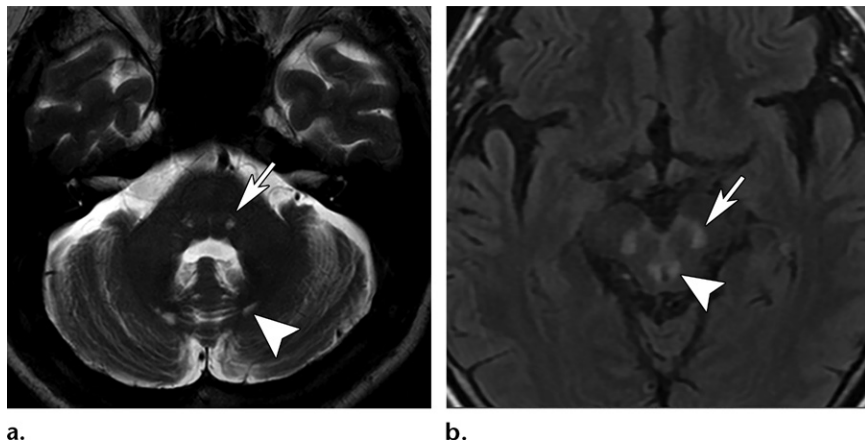
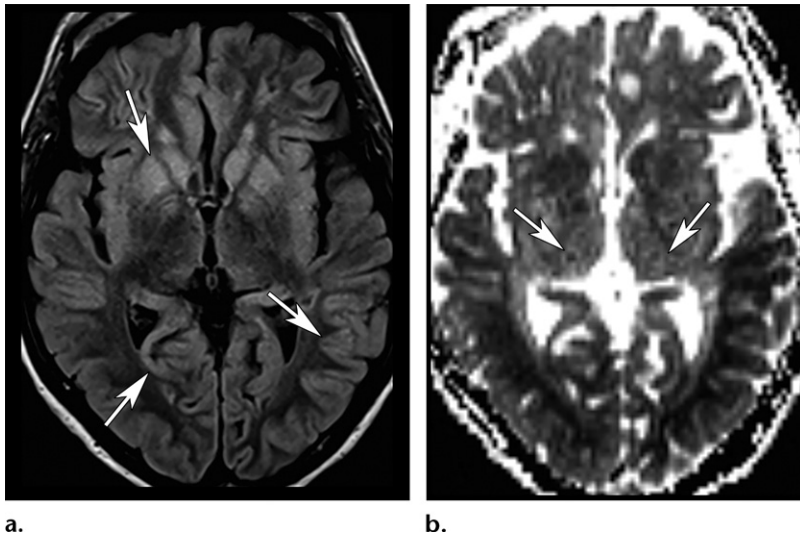


Figure 13. Methyl bromide-induced toxicity. (a) Axial T2-weighted MR image shows symmetric hyperintensities involving the dentate nuclei (arrowhead) and dorsal pons (arrow). (b) Axial FLAIR MR image shows high-signal-intensity abnormalities involving the periaqueductal gray matter (arrowhead) and subthalamic nuclei (arrow).

a.

b.

Figure 14. Hypoglycemia in a man with cirrhosis who presented in a coma with a glucose level of 20 mg/dL. (a) Axial FLAIR MR image shows symmetric hyperintensities involving the temporal and parieto-occipital cortex and the basal ganglia (arrows) and sparing the white matter and thalamus. (b) Axial apparent diffusion coefficient (ADC) map shows true restricted diffusion (hypointensity) affecting the same regions and better depicts the thalamic sparing (arrows).



a.

b.

with diabetes (commonly in those patients undergoing insulin replacement therapy) (2,39).

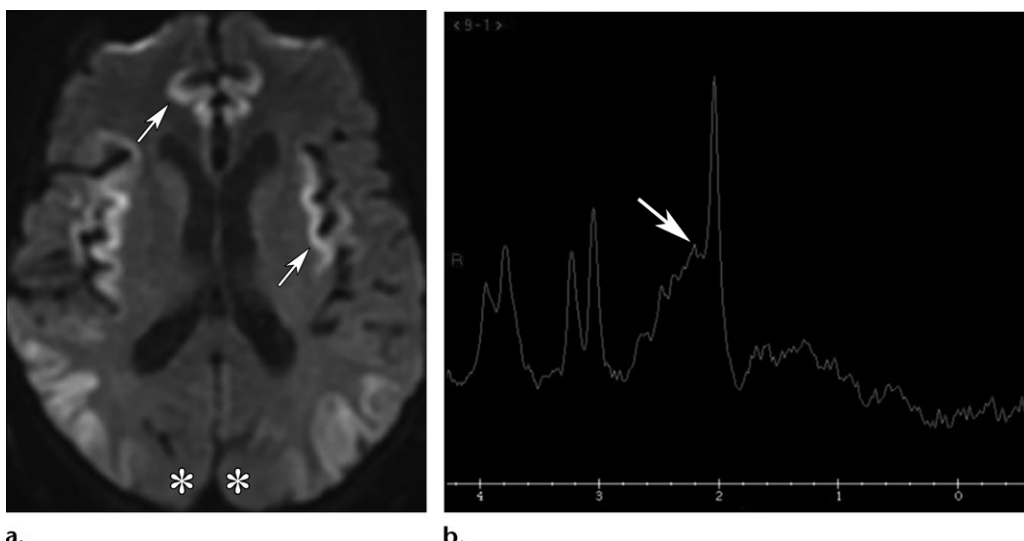
Hypoglycemic encephalopathy has a predilection for posterior and deep regions. The most common imaging findings are symmetric hyperintensities on T2-weighted and FLAIR images and strong restricted diffusion affecting the gyri in the parieto-occipital and temporal regions on diffusion-weighted images. The basal ganglia can be involved, and this involvement may point to poor outcomes. Another suggestive characteristic finding is the sparing of the thalamus, white matter, and cerebellum (Fig 14). Earlier signs are better depicted on T1-weighted images as sulcal effacement owing to gyral swelling and can be visualized on CT images as hypoattenuation (2,39).

In newborns, the most common cause is maternal diabetes, which usually manifests in the first 3 postnatal days. The most characteristic pattern of neonatal hypoglycemia is symmetric posterior parieto-occipital gray and white matter signal abnormality with diffusion restriction involving the optic radiations and frequently the posterior thalamus (2,40).

An important differential diagnosis for hypoglycemic injury is hypoxic-ischemic brain injury, which has similar imaging findings to those of hypoglycemic encephalopathy. An important piece of information that may help narrow the differential diagnosis is that hypoxic-ischemic brain injury usually manifests with a history of cardiac arrest and usually involves the thalamus and cerebellum symmetrically (2,39).

Hyperammonemic Encephalopathy and AHE

Hyperammonemic encephalopathy is primarily caused by hyperammonemia, which has a direct toxic effect on the brain and causes osmotic imbalance (which can lead to ODS) (2,32,41,42). Acute liver failure is the major cause of hyperammonemia, sometimes called AHE (caused by viral infections and other acute hepatic dysfunctions or by AHE superimposed with chronic hepatic failure), but it can manifest in nonhepatic conditions, the most important of which are drug toxicities (valproate and acetaminophen), sepsis, bone marrow transplant, and parenteral nutrition.



a.

b.

Figure 15. Hyperammonemic encephalopathy in a 54-year-old man on the 10th day after liver transplant. (a) Axial diffusion-weighted MR image shows bilateral and symmetric restricted diffusion affecting the insular and cingulate gyri (arrows) and sparing the parieto-occipital region (*). (b) MR spectroscopic image with an echo time of 30 msec shows a glutamine-glutamate peak at approximately 2.1–2.4 ppm (arrow).

Additionally, such patients usually have a serious condition and other metabolic-associated disorders, such as hypoglycemia and osmotic imbalance, exacerbating brain injury. Rapid recognition and treatment are fundamental for improved patient outcome (32,41,42). Early symptoms can be observed with plasma ammonia levels of 60 $\mu\text{mol/L}$. Lethargy and vomiting progress to seizures and coma (2,42).

Classic and suggestive imaging characteristics related to hyperammonemic encephalopathy are characterized by strongly restricted diffusion on diffusion-weighted images, accompanied by high signal intensity symmetrically and bilaterally in the insular and cingulate gyri on T2-weighted and FLAIR images (Fig 15a), with relative sparing of the occipital lobes and perirolandic region. The basal ganglia are usually also affected, but hemispheric white matter is typically preserved. Hyperammonemic encephalopathy (owing to AHE or other causes) most commonly involves the insula and thalamus (42,43).

Another characteristic finding at MR spectroscopy with short echo times is a glutamate-glutamine peak resonating between 2.1 and 2.4 ppm (Fig 15b). As in cases of chronic hepatic encephalopathy, an increase in glutamine levels is a response to hyperammonemia as glutamine is used to metabolize ammonia (32,33,42).

Less severe cases of AHE with lower ammonia serum levels can manifest at imaging without affecting the cortex and with T2-weighted and FLAIR as well as DWI changes involving the thalamus, posterior limb of the internal capsule, and dorsal brainstem, with variable periventricular white matter involvement. It seems that there is a

strong correlation between MRI severity and serum ammonia levels and between serum ammonia levels and clinical outcomes (cortical involvement results in more severe cases and with poor outcomes) (34). Note that AHE is a described cause of ATL, manifesting as solely symmetric periventricular white matter involvement, which occurs in 15% of cases (43). After therapy, clinical features and abnormalities at MR spectroscopy improve first, followed 3–6 months later by possible normalization of the signal intensity in the basal ganglia and cortex (32,41,42).

Figure E3 summarizes the disorders associated with pattern 3.

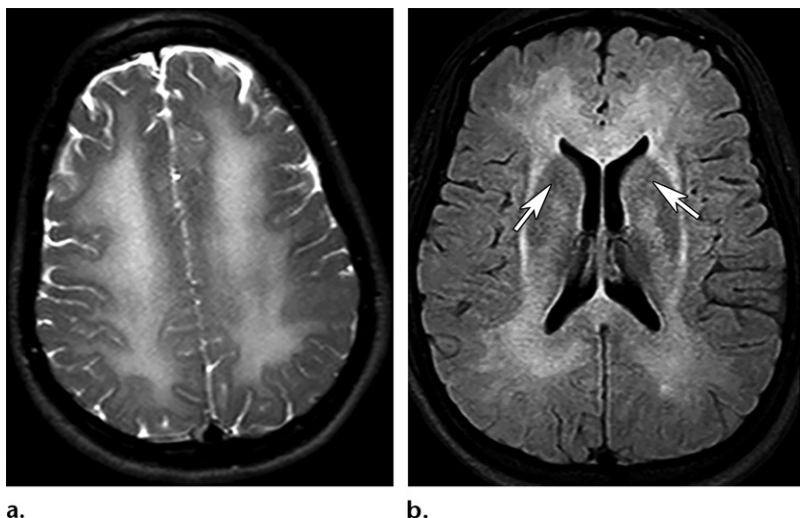
Pattern 4: Symmetric Periventricular White Matter Involvement

Heroin Toxic Leukoencephalopathy

Heroin is an opioid that is most commonly used as a recreational drug for its euphoric effects. This substance is also the most commonly abused opioid and one of the most common drugs used in overdose-related deaths worldwide (2,44,45). Heroin is typically injected intravenously. However, it can also be inhaled. Symptoms usually have rapid onset and last for hours (2,44).

The most common acute complication of injected heroin is stroke, typically involving the globi pallidi (up to 10% of cases), which has a similar imaging manifestation to that depicted in cases of carbon monoxide poisoning (2,45,46). Nonetheless, the most dramatic acute effects occur with inhaled heroin. The freebase form is heated on aluminum foil, and the vapors are inhaled (commonly known as *chasing the dragon*)

Figure 16. Inhaled heroin (chasing the dragon) toxicity in two patients. (a) Axial T2-weighted MR image shows confluent symmetric hyperintensity in the cerebral white matter. Diffusion-weighted images and ADC maps showed restricted diffusion (not shown), and 6-month control images showed normalization (not shown). (b) Axial FLAIR MR image in another patient shows bilateral and symmetric hyperintensity affecting the periventricular white matter, with selective involvement of the posterior limb of the internal capsule and sparing of the anterior limb of the internal capsule (arrows).



(2). Toxic leukoencephalopathy related to this method of inhalation has a nonlinear progression and can have a latent period before onset. The disease continues to progress for up to 6 months after cessation of heroin use (2,44,45).

Heroin toxic leukoencephalopathy manifests as confluent, widespread, bilateral, symmetric white matter T2-weighted and FLAIR hyperintensities involving both the supra- and infratentorial compartments (Fig 16). Supratentorial white matter hyperintensities often selectively involve the posterior limb of the internal capsule and periventricular white matter, usually sparing the anterior limb of the internal capsule and subcortical U fibers (Fig 16b). The basal ganglia are rarely involved. Cerebellar involvement manifests as symmetric white matter hyperintensities with dentate nuclei sparing, a pattern sometimes described as a butterfly-wing pattern. Diffusion-weighted images show diffusion restriction in the affected areas during the acute phase (44,45).

Methotrexate and Other Chemotherapeutic Agents

Methotrexate has been associated with CNS toxic effects and the development of leukoencephalopathy after its administration. The general incidence is approximately 0.8%–4.5%, but there are some described risk factors that can elevate these rates, such as intrathecal administration (the major risk factor, with some studies reporting a relative risk of 66%) and high doses (the higher the dose, the higher the risk). Methotrexate-related toxic leukoencephalopathy is most common in pediatric patients (47–49).

There are three main patterns that are classically described for methotrexate-related CNS toxicity: (a) toxic leukoencephalopathy, (b) disseminated necrotizing encephalopathy, and (c) subacute combined degeneration. This final

pattern is related to vitamin B12 deficiency, which is addressed further in the article (47–49).

Methotrexate-related toxic leukoencephalopathy is the most common manifestation, with a wide range of clinical and imaging findings. This condition often manifests acutely between 2 and 14 days after methotrexate administration, but manifestation can occur on a delay, even years after use (43–45). The majority of patients are asymptomatic, and imaging findings are mild and transient (47).

The most important imaging finding is true diffusion restriction, bilaterally asymmetric across multiple vascular territories, affecting the centrum semiovale and sparing the subcortical U fibers. These changes are thought to be early signs of acute toxic methotrexate-related leukoencephalopathy (Fig 17a, 17b). The same regions appear on T2-weighted and FLAIR images as hyperintensities and can disappear or persist after symptom resolution (47–49).

Disseminated necrotizing encephalopathy is a rare manifestation and complication of intrathecal methotrexate therapy combined with whole-brain radiation therapy but has more aggressive findings and consequences and is typically fatal (47,49). Clinically, necrotizing encephalopathy is characterized by rapidly progressive subcortical dementia with motor and autonomic deficits (urinary incontinence, gait disturbance, memory difficulty, and hemiparesis) (47,49). MR images show extensive white matter involvement, with multiple low-signal-intensity foci within the disseminated areas of T2 hyperintensity (pointing to hemorrhage). The low-signal-intensity foci have peripheral or solid enhancement, as they are associated with mass effect (tumorlike pattern) (Fig 17c–17e) (47). Lesions and enhancement can disappear completely without any treatment. No reliable imaging features are described to differentiate necrotizing encephalopathy from a recurrent

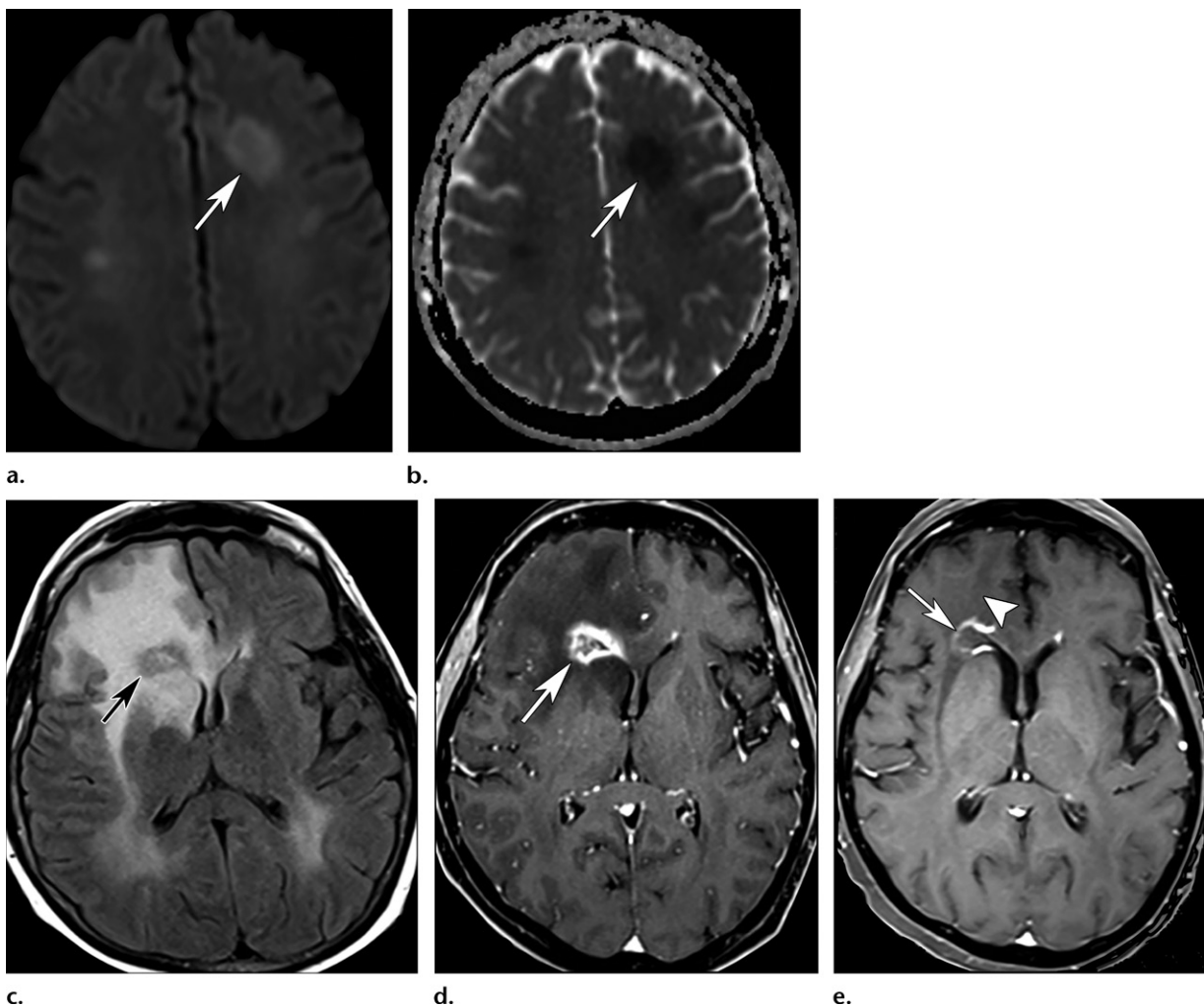


Figure 17. Methotrexate-related CNS toxicity in two patients. (a, b) Axial diffusion-weighted image (a) and ADC map (b) in a patient with toxic leukoencephalopathy show multiple lesions (arrow) with true restricted diffusion affecting the centrum semiovale and crossing vascular territories while sparing the subcortical U fibers. (c) Axial FLAIR MR image in another patient with a more severe case of necrotizing encephalopathy after undergoing intrathecal methotrexate therapy combined with whole-brain radiation therapy shows a hypointense lesion (arrow) involved by an extensive confluent area of vasogenic edema (hyperintensity). (d) Axial contrast-enhanced T1-weighted MR image in the same patient as in c shows peripheral enhancement of the lesion (arrow) and a circumjacent hypointense area of edema. (e) Axial contrast-enhanced T1-weighted control MR image obtained 3 months later shows a reduction in the lesion enhancement (arrow) and surrounding edema (arrowhead).

mass, but knowledge or suspicion of this condition prevents unnecessary invasive therapies (49).

Importantly, it is necessary to emphasize that many other chemotherapeutic and immunosuppressive drugs can cause leukoencephalopathy with reversible restricted diffusion (ATL), such as cyclosporine, 5-fluorouracil, and fludarabine (Fig 18). The use of chemotherapeutic agents is the major cause of ATL, and immunosuppressive agents are another group of drugs usually involved with such conditions. The most important pattern to recognize is bilateral symmetric white matter involvement (8,9,43).

Carbon Monoxide Poisoning

Brain toxic effects of carbon monoxide poisoning can appear in a subacute manifestation weeks after initial insult as delayed leukoencephalopathy

(ATL) with restricted diffusion and posterior reversibility. Up to one-third of cases demonstrate such findings (Fig 5). All aspects of carbon monoxide poisoning (15) are discussed earlier in this article.

Uremic Encephalopathy

Up to 10% of cases of uremic encephalopathy, discussed previously, can manifest as a classic cause of ATL at imaging, with confluent bilateral and symmetrical periventricular white matter involvement and posterior normalization on follow-up images (19,43).

Acute Hepatic Encephalopathy

As discussed previously, AHE is a cause of ATL in up to 15% of cases, manifesting solely as symmetric periventricular white matter involvement.

AHE is the third most common cause of ATL in a series of 101 cases (43).

Pattern 5: Corticospinal Tract Involvement

Cobalamin Deficiency

Cobalamin deficiency, or vitamin B12 deficiency, can have many causes, such as insufficient intrinsic factor (pernicious anemia, atrophic gastritis, or gastrectomy), ileal malabsorption (Crohn disease, resection of ileum, and infective ileitis), malnutrition (alcohol excess, veganism, and strict vegetarianism), and prolonged use of some medications, such as H₂-receptor histaminergic antagonists, metformin, proton pump inhibitors, and methotrexate (50,51). Vitamin B12 deficiency is usually associated with both megaloblastic anemia and subacute combined degeneration. Neurologic symptoms can precede anemia and may not completely resolve after treatment (50,51).

Subacute combined degeneration selectively affects the dorsal and lateral spinal cord columns, depicted as hyperintensities symmetrically affecting such sites at T2-weighted imaging (Fig 19a). The selective involvement of the dorsal columns creates a characteristic appearance of an inverted V shape. With indistinguishable clinical and imaging findings, the less common copper deficiency is a differential diagnosis for subacute combined degeneration. Excessive zinc intake can produce secondary copper deficiency, leading to the same manifestation. Imaging alterations in the brain are nonspecific but are characterized by bilateral hyperintensities on T2-weighted and FLAIR images following the path of the corticospinal tract (Fig 19b) (50,51). Usually there is complete resolution within 3 months after treatment, and permanent residual functional deficit occurs in only a minority of cases (51).

Chronic Hepatic Encephalopathy

Chronic hepatic encephalopathy, discussed previously, is classically recognized by its alterations at T1-weighted imaging. Recent studies show that this condition can lead to the development of variable vasogenic brain edemas during the disease course. It usually affects the white matter in the corticospinal tract regions, most likely due to glutamine accumulation within brain tissue (Fig 11b) (32).

Pattern 6: Corpus Callosum Involvement

Marchiafava-Bignami Disease

MBD is a rare disorder characterized by osmotic demyelination and subsequent necrosis of the

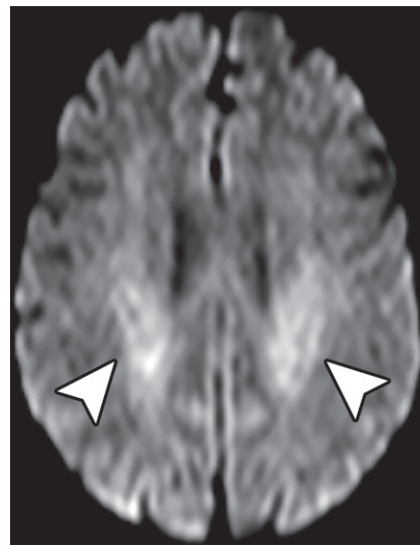


Figure 18. Fludarabine-related toxicity leading to ATL. Axial diffusion-weighted MR image shows symmetric restricted diffusion (arrowheads) involving the periventricular white matter.

corpus callosum. Such conditions are primarily associated with chronic ethanol use and vitamin B complex deficiency (not exclusively B1 deficiency, as in cases of WE) (2,52,53).

MBD manifests in two clinical forms. The first is type A (acute), in which patients present with seizures and/or in a coma, with involvement of the entire corpus callosum, and which usually progresses to death within several days. The second is type B (chronic), in which patients are diagnosed with mild encephalopathy and focal lesions in the corpus callosum (most commonly in the genu). MBD is usually accompanied by other alcohol-related pathologic conditions, with some reports of WE and MBD occurring together. Associated brain volume loss is common (52,53).

The diagnosis of MBD at imaging is based on corpus callosum involvement. Selective involvement of the middle layers of the corpus callosum in the context of chronic ethanol use is a highly suggestive finding of MBD. The initial changes associated with acute MBD are best visualized on sagittal FLAIR images. Central callosal involvement sparing the periphery is referred to as the sandwich sign (Fig 20a). Alterations in cases of type B appear first in the genu and frontoparietal cortex followed by splenial involvement. There is variable white matter involvement (53). DWI is initially negative, with diffusion restriction occurring later. Acute lesions may show contrast enhancement (2). Chronic MBD appears as thinning of the corpus callosum with central linear hypointensities on T1-weighted images. Diffusion-tensor images show a reduction in callosal fibers (Fig 20b) (2,52,53).

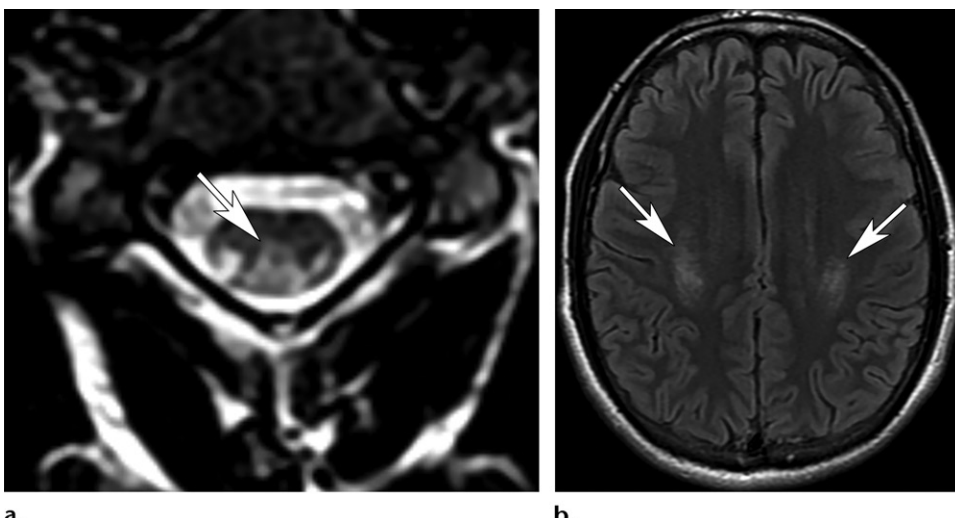
**a.****b.**

Figure 19. Cobalamin deficiency with combined subacute degeneration of the spinal cord. **(a)** Axial T2-weighted MR image of the cervical spine shows involvement of the dorsal and lateral columns (arrow) in an inverted V shape. **(b)** Axial FLAIR MR image of the head shows bilateral hyperintensities (arrows) involving the region of the corticospinal tract.

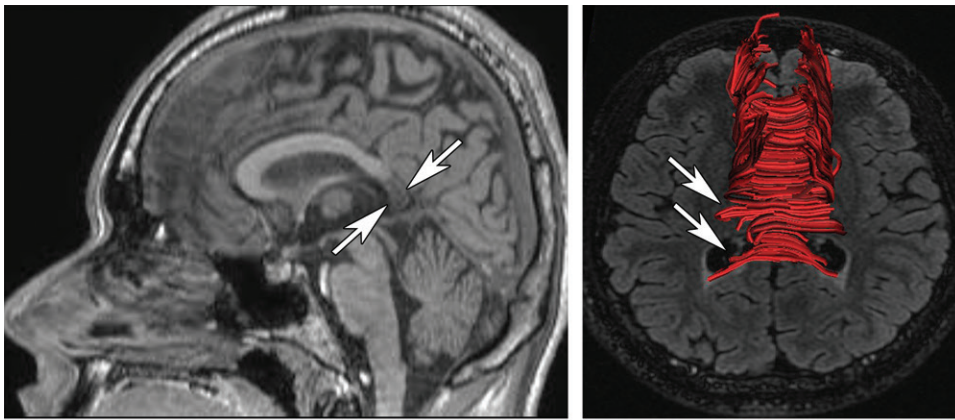
**a.****b.**

Figure 20. MBD in a 30-year-old man with a history of multiple binge drinking episodes who presented with apraxia, hemianesthesia, and symptoms of dementia. **(a)** Sagittal FLAIR MR image shows demyelinating and necrosis of the central portion of the splenium (hypointensity), sparing the periphery (arrows) (sandwich sign). **(b)** Axial diffusion-tensor reconstructed MR image shows reduction in the callosal fibers (red area) in the same splenial region (arrows).

Reversible Splenial Lesion

The so-called RSLs or cytotoxic lesions of the corpus callosum, which are secondary lesions that are associated with several different entities, are an important imaging differential diagnosis for MBD. These lesions are usually reversible and involve the splenium of the corpus callosum (2,8,9,43,54). The precise pathophysiology of RSLs is unknown but is probably due to excitotoxic intracellular and/or intramyelinic edema, as the splenium has a high density of excitatory receptors that render it vulnerable to cytotoxic edema (2,9,54).

The use and subsequent withdrawal of anti-epileptic drugs is most commonly associated with RSLs, which typically manifest between 24 hours and 3 weeks after drug discontinuation. Aside

from that, other conditions related to RSLs are viral infection (mild encephalopathy with RSL) and metabolic abnormalities (hypoglycemia, hypernatremia, and acute alcohol poisoning), although there are many other related causes and withdrawal from other types of drugs can lead to RSLs (2,8,9,43,54).

Patients are often asymptomatic, a different clinical presentation from those patients with MBD. Imaging findings include ovoid lesions involving the central splenium, hyperintense lesions on T2-weighted and FLAIR images, and hypointense lesions on T1-weighted images, with restricted diffusion and no enhancement (Fig 21) (2,8,9,54). RSL is considered a subtype of ATL because there is an overlap of

causes between these two entities and owing to its appearance with reversible restricted diffusion. RSL appears to be the mildest severity of ATL, only involving the splenium and with complete posterior resolution (43). The lesions are not always strictly splenial and can involve the entire corpus callosum in a minority of cases. In addition, patients can be diagnosed with severe encephalopathy and sometimes the lesion is not completely reversible, which is why the use of the term *cytotoxic lesions of the corpus callosum* is currently preferred (55).

Figure E4 summarizes the disorders associated with patterns 4, 5, and 6.

Pattern 7: Asymmetric White Matter Involvement (Demyelinating Disease Pattern)

Levamisole-induced Leukoencephalopathy

Levamisole is a medication with anthelmintic and immunomodulatory properties, but its use has been suspended in most countries because of its collateral effects. It has been recognized as a cocaine adulterant because it can induce effects similar to those of cocaine on the CNS. It is estimated that approximately 69% of commercialized cocaine worldwide is adulterated (56–58). Patients are usually adolescents or young adults and present with a strokelike episode, which makes it an important differential diagnosis in this population and affects patient management (56,57).

Imaging characteristically shows lesions with a tumefactive demyelinating pattern, represented as one or a few randomly distributed oval or round lesions in the centrum semiovale, with no mass effect or edema, with smooth and incomplete enhancement peripherally (C-shaped appearance, the incomplete portion is related to the cortex) and strongly restricted diffusion (Fig 22). T2-weighted and diffusion-weighted images can depict concentric layers of hyperintensities. Another important characteristic is that after treatment with steroids, lesions tend to regress and even disappear. Recognizing this entity is of great importance in guiding management approaches and treatment (56–58).

One should remember the important well-known and extensively described intracranial vascular effects of cocaine and of many other illicit drugs. Blood pressure imbalance induces ischemic and/or hemorrhagic stroke or even reversible cerebral vasoconstriction syndrome and PRES (46).

Chemotherapeutic Agents

Many chemotherapeutic agents have been related to neurotoxic effects and induce a demye-

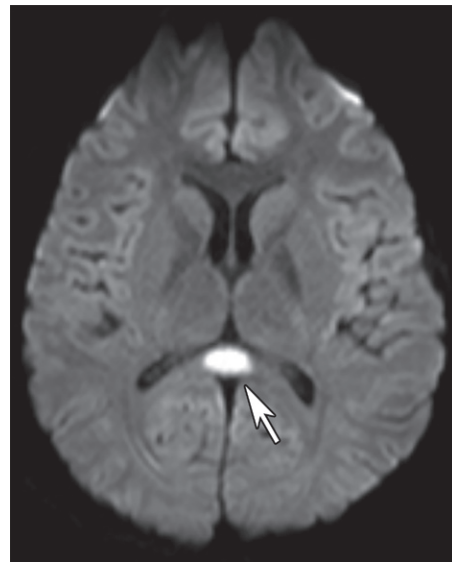


Figure 21. Ovoid lesion in a patient who presented to the emergency department after using a large amount of cannabis. No abnormal symptoms other than those that are expected after cannabis use were seen. Axial diffusion-weighted MR image shows a single ovoid central lesion (arrow) affecting the splenium, with true restricted diffusion (ADC map not shown). MRI (not shown) performed months later was normal.

linating leukoencephalopathy pattern during the course of treatment, characterized at imaging as multiple ovoid asymmetric white matter hyperintensities in a perivenular distribution (59). The most common agents related to this pattern are tumor necrosis factor- α blockers (infliximab, adalimumab), which are currently widely used to treat immune-mediated conditions and some cancers (59). Vincristine, a chemotherapeutic agent used to treat some types of leukemia, Hodgkin disease, and small cell lung cancer, has also been associated with this pattern of neurotoxicity (59).

Pattern 8: Parieto-occipital Subcortical Vasogenic Edema

Posterior Reversible Encephalopathy Syndrome

PRES, also known as *reversible posterior leukoencephalopathy syndrome*, refers to a clinicoradiologic disorder of potentially reversible subcortical vasogenic brain edema in patients with classic acute neurologic symptoms (seizure in 60%–75%, altered mental function and headache in 20%–25%) in the setting of several conditions, such as hypertension, preeclampsia, renal failure, sepsis, thrombocytopenia, the administration of cytotoxic or immunosuppressive medications, and many other potential causes. Symptoms and imaging findings usually normalize after treatment (2,60–62).

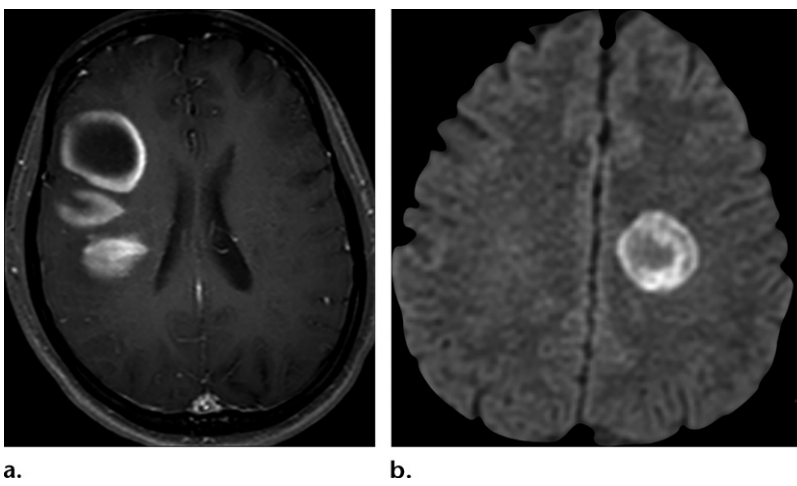


Figure 22. Levamisole-induced leukoencephalopathy in two patients. (a) Axial contrast-enhanced T1-weighted MR image shows hypointense lesions within the centrum semiovale with incomplete peripheral enhancement, without edema or mass effect. (b) Axial diffusion-weighted MR image shows a lesion centered in the centrum semiovale with strong restricted diffusion and different concentric layers of hyperintensities. Both cases depict lesions with a tumefactive demyelinating pattern.

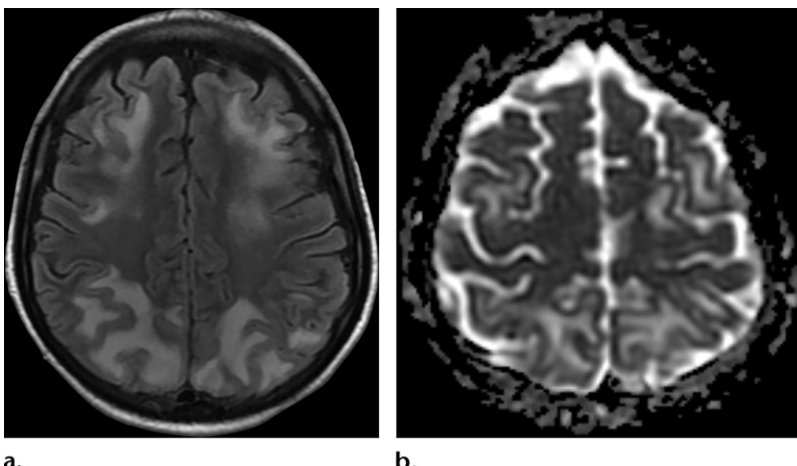


Figure 23. PRES. (a) Axial FLAIR MR image shows bilateral asymmetric hyperintensity involving the subcortical white matter of the parieto-occipital and frontal lobes, sparing the cortex. (b) Axial ADC map shows no true restricted diffusion affecting these areas, indicating a vasogenic edema mechanism. A postcontrast T1-weighted MR image (not shown) showed no enhancement. Such findings are compatible with vasogenic edema in a typical PRES distribution. Clinical and epidemiologic findings can favor this diagnosis.

PRES was classically described as a cerebrovascular autoregulatory disorder caused by hypertension, but this pathophysiologic theory does not explain the manifestation of all the clinical and imaging findings. In addition, most patients present with only mild blood pressure elevation, and 20%–30% of patients are normotensive. Current theories have a similar shared mechanism, advocating endothelial injury and dysfunction secondary to different causes (cytotoxic, immunogenic), ultimately resulting in vasogenic edema. Interstitial fluid accumulates in the subcortical white matter, with a predilection for the parietal and occipital lobes (2,61,62). This condition occurs at all ages but is most common in young women (2).

Imaging findings include changes associated with vasogenic edema, commonly bilateral and asymmetric high signal intensity on T2-weighted and FLAIR images and hypoattenuation on CT images involving the subcortical white matter (Fig 23). Diffusion-weighted images and apparent diffusion coefficient maps are often negative (differentiating the condition from cytotoxic and intramyelinic edema) or at least have a smaller

extension than those changes depicted on FLAIR images. Postcontrast enhancement is not a typical feature, but some studies report that up to 37% of cases depict contrast enhancement (61,62).

Proposed algorithms for PRES diagnosis usually involve the presence of suggestive clinical symptoms associated with known risk factors and typical imaging findings (61).

There are many patterns of involvement that have been described, including (a) parieto-occipital involvement, the most common and suggestive pattern (up to 90%, also known as *classic PRES*); (b) the superior frontal sulcus pattern (70%); (c) the holohemispheric watershed pattern (50%); and (d) involvement in other less common sites, such as the cerebellum, basal ganglia, and brainstem (2). Combinations of patterns are common (more than 90% of cases). Note that PRES, despite its name, is not always reversible and not always posterior (2,61,63).

Prompt suspicion and recognition of PRES is important because delayed diagnosis can progress to subarachnoid hemorrhage and/or infarction owing to diffuse vascular contraction secondary to endothelial dysautoregulation (2,61–63).

The administration of many drugs can lead to PRES or PRES-like symptoms and imaging presentation, the most important of which are cyclosporine and tacrolimus. An important tip is that in these drug-related cases, an atypical PRES is the rule, with symmetric lesions in unusual sites and possible contrast enhancement at imaging (61–63).

Pattern 9: Symmetric Central Pontine Involvement

Osmotic Demyelination Syndrome

ODS is an acute form of demyelination caused by rapid shifts in serum osmolality. The classic and most common cause is a rapid correction of hyponatremia. However, it is important to remember that ODS may occur in patients who are normonatremic. In fact, this heterogeneous disorder has osmotic stress as its basic cause. Many other conditions that lead to ODS have been described, and there are known comorbid conditions that predispose patients to its development. These causes and predisposing conditions are described in Table 3 (2,64).

In the classic context of rapid hyponatremia correction leading to ODS, sodium levels are usually lower than 115 mmol/L, and correction rates are higher than 12 mmol/L per day (2).

Oligodendrocytes are especially vulnerable to osmotic changes (particularly at the pons) leading to demyelination that most commonly involves the brainstem region, which is why this entity was classically called *central pontine myelinolysis*. Nevertheless, any brain cell can be affected by osmotic imbalance, and ODS affecting extrapontine cerebral regions, including the cortex, has been extensively described. Approximately 50% of cases manifest isolated pontine lesions, with pontine and extrapontine lesions in 30% of cases. There are only extrapontine lesions in 20% of ODS cases, which makes diagnosing this condition even more challenging and underscores the importance of recognizing the spectrum of ODS symptoms (2,64,65).

The main signs or symptoms are seizures and altered mental status, often biphasic, with altered mental status when hyponatremia has manifested and subsequent improvement after natremia restoration followed by new rapid deterioration after approximately 1 week (2,64).

The classic and most common imaging appearance consists of well-demarcated and symmetric, rounded, or trident-shaped lesions on the central pons that characteristically spare the peripheral pons and corticospinal tract regions (Fig 24a). Sparing of the transverse pontine fibers is described and can be visualized at imaging as fine lines of normal signal intensity

Table 3: Causes and Predisposing Conditions of ODS

Causes

- Rapid hyponatremia correction
- Alcoholism
- Liver transplant (hyperammonemia)
- Malnutrition
- Hyper- or hypoglycemia
- Azotemia and hemodialysis

Predisposing conditions

- Renal, adrenal, and pituitary disease
- Hyperemesis
- History of transplantation
- Severe burns
- Prolonged use of diuretics
- Paraneoplastic disease

crossing the lesion. Alterations are depicted on conventional images 1–2 weeks after symptom onset as a hypoattenuating lesion on CT images, a hypointense lesion on T1-weighted images, and a hyperintense lesion on T2-weighted and FLAIR images. Importantly, diffusion-weighted images can depict restricted diffusion in the acute phase as soon as 24 hours after the onset of ODS, which is an important finding for early diagnosis (2,64,65).

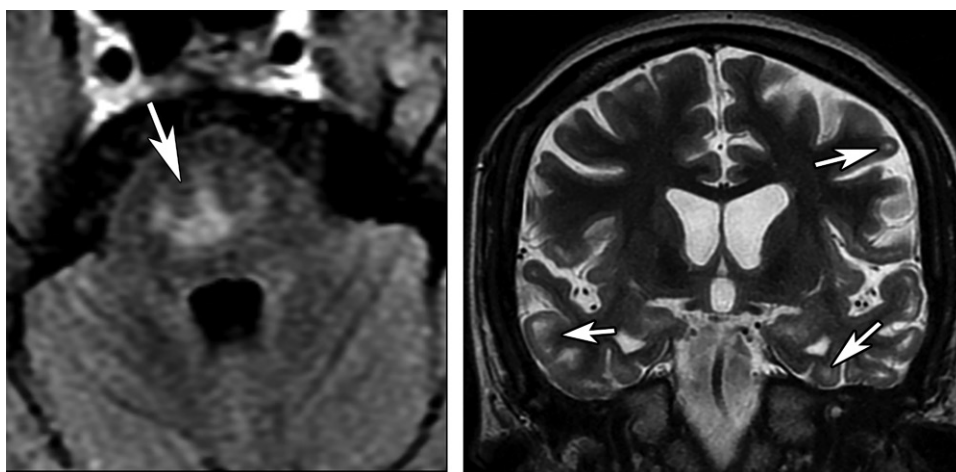
The most commonly involved extrapontine sites are the basal ganglia, thalamus, and hemispheric white matter, often symmetrically. Some cases show laminar necrosis of the cortex (2,64). There is an uncommon but suggestive manifestation of extrapontine ODS. Studies have shown that the white matter immediately underlying the gray matter is especially susceptible to osmotic distress, leading to alterations in these sites that are depicted on images as multiple and diffuse punctate lesions on juxtacortical white matter or delineating the transition line between cortical gray matter and subjacent white matter (Fig 24b) (65).

Suggestive Sites of Involvement

Some sites of involvement more specifically suggest a reduced number of conditions and may point to subjacent diagnoses (Fig 25). Remember that most findings are not pathognomonic. However, by considering the patient's clinical history, it is possible to reduce the number of conditions in the differential diagnosis. These correlations refer only to toxic and metabolic causes and can be used for orientation in a suitable clinical context.

Conclusion

Diagnosing toxic and metabolic brain disorders remains challenging and refers to a heterogeneous group of diseases. Although many imaging manifestations are unspecific, some imaging



a.

b.

Figure 24. ODS in two patients. (a) Axial FLAIR MR image shows classic findings of ODS, characterized by a trident-shaped lesion (arrow) affecting the central pons and sparing of the periphery and the region of the corticospinal tract. (b) Coronal T2-weighted MR image with extrapontine findings shows multiple juxtacortical (white matter–gray matter transition) hyperintense lesions (arrows).

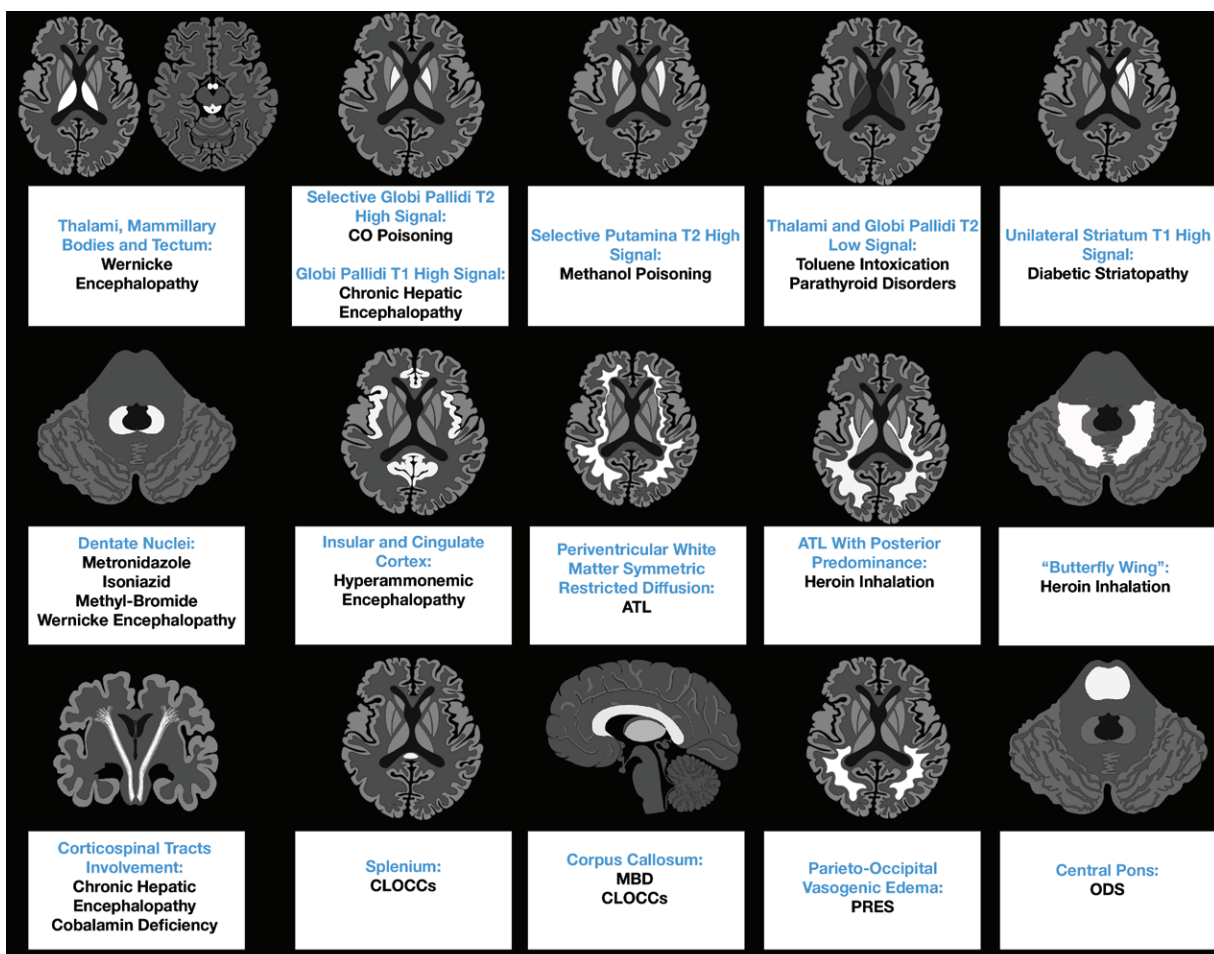


Figure 25. Chart demonstrates the correlation between more specific sites of involvement in toxic and metabolic brain disorders and their most likely diagnoses. CLOCCs = cytotoxic lesions of the corpus callosum, CO = carbon monoxide.

findings can be quite specific for a few conditions. Nonetheless, some prognostic information can be obtained from imaging studies, suggesting a reversible subjacent cause or indicating severe involvement of cerebral structures.

Approaching these conditions by considering the patterns at imaging can add to the radiologist's daily routine. Depending on the pattern, pathophysiologic information can be inferred and a reduced number of conditions in the differential diagnosis can be considered.

Many other causes related to toxic and metabolic disorders exist, and there are other possible uncommon presentations for each cause. The proposed patterns and online supplements describe the majority of the most common conditions and presentations encountered in clinical practice and can be helpful when diagnosing such a group of diseases. One should always look for the accessible clinical history as it points to subjacent toxic and metabolic causes over other groups of diseases that can show the same imaging characteristics. Combining clinical issues with imaging findings can make it possible to reach a specific diagnosis.

Disclosures of Conflicts of Interest.—**A.M.M.** Activities related to the present article: disclosed no relevant relationships. Activities not related to the present article: chief executive officer of VEEV; payment from VEEV for informatics solutions consulting. **Other activities:** pending informatics patent from Radnysis, VEEV. **L.T.L.** Activities related to the present article: disclosed no relevant relationships. Activities not related to the present article: payment for a 2017 lecture from Bracco Imaging. Other activities: disclosed no relevant relationships.

References

- Valk J, van der Knaap MS. Toxic encephalopathy. AJNR Am J Neuroradiol 1992;13(2):747–760.
- Osborn AG, Hedlund GL, Salzman KL. Toxic, metabolic, degenerative and CSF disorders. In: Osborn's Brain. 2nd ed. Philadelphia, Pa: Elsevier; 2017: 905–1155.
- Schaefer PW, Buonanno FS, Gonzalez RG, Schwamm LH. Diffusion-weighted imaging discriminates between cytotoxic and vasogenic edema in a patient with eclampsia. Stroke 1997;28(5):1082–1085.
- Na DG, Kim EY, Ryoo JW, et al. CT sign of brain swelling without concomitant parenchymal hypotattenuation: comparison with diffusion- and perfusion-weighted MR imaging. Radiology 2005;235(3):992–998.
- Lipton SA, Rosenberg PA. Excitatory amino acids as a final common pathway for neurologic disorders. N Engl J Med 1994;330(9):613–622.
- Moritani T, Smoker WRK, Sato Y, Numaguchi Y, Westesson PL. Diffusion-weighted imaging of acute excitotoxic brain injury. AJNR Am J Neuroradiol 2005;26(2):216–228.
- Chokshi FH, Aygun N, Mullins ME. Imaging of acquired metabolic and toxic disorders of the basal ganglia. Semin Ultrasound CT MR 2014;35(2):75–84.
- McKinney AM, Kieffer SA, Paylor RT, SantaCruz KS, Kendi A, Lucato L. Acute toxic leukoencephalopathy: potential for reversibility clinically and on MRI with diffusion-weighted and FLAIR imaging. AJR Am J Roentgenol 2009;193(1):192–206.
- Rimkus Cde M, Andrade CS, Leite Cda C, McKinney AM, Lucato LT. Toxic Leukoencephalopathies, Including Drug, Medication, Environmental, and Radiation-Induced Encephalopathic Syndromes. Semin Ultrasound CT MR 2014;35(2):97–117.
- Santos Andrade C, Tavares Lucato L, da Graça Morais Martin M, et al. Non-alcoholic Wernicke's encephalopathy: broadening the clinicoradiological spectrum. Br J Radiol 2010;83(989):437–446.
- Kim TE, Lee EJ, Young JB, Shin DJ, Kim JH. Wernicke encephalopathy and ethanol-related syndromes. Semin Ultrasound CT MR 2014;35(2):85–96.
- Blanco M, Casado R, Vázquez F, Pumar JM. CT and MR imaging findings in methanol intoxication. AJNR Am J Neuroradiol 2006;27(2):452–454.
- Hegde AN, Mohan S, Lath N, Lim CC. Differential diagnosis for bilateral abnormalities of the basal ganglia and thalamus. RadioGraphics 2011;31(1):5–30.
- Vaneckova M, Zakharov S, Klempir J, et al. Imaging findings after methanol intoxication (cohort of 46 patients). Neuroendocrinol Lett 2015;36(8):737–744.
- Sener RN. Acute carbon monoxide poisoning: diffusion MR imaging findings. AJNR Am J Neuroradiol 2003;24(7):1475–1477.
- Lo CP, Chen SY, Lee KW, et al. Brain injury after acute carbon monoxide poisoning: early and late complications. AJR Am J Roentgenol 2007;189(4):W205–W211.
- Pearl PL, Veizina LG, Saneto RP, et al. Cerebral MRI abnormalities associated with vigabatrin therapy. Epilepsia 2009;50(2):184–194.
- Hussain SA, Tsao J, Li M, et al. Risk of vigabatrin-associated brain abnormalities on MRI in the treatment of infantile spasms is dose-dependent. Epilepsia 2017;58(4):674–682.
- Kim DM, Lee IH, Song CJ. Uremic Encephalopathy: MR Imaging Findings and Clinical Correlation. AJNR Am J Neuroradiol 2016;37(9):1604–1609.
- Donnerstag F, Ding X, Pape L, et al. Patterns in early diffusion-weighted MRI in children with haemolytic uraemic syndrome and CNS involvement. Eur Radiol 2012;22(3):506–513.
- Murray AM, Tupper DE, Knopman DS, et al. Cognitive impairment in hemodialysis patients is common. Neurology 2006;67(2):216–223.
- Kumar G, Goyal MK. Lentiform Fork sign: a unique MRI picture—Is metabolic acidosis responsible? Clin Neurol Neurosurg 2010;112(9):805–812.
- Aydin K, Sencer S, Demir T, Ogel K, Tunaci A, Minareci O. Cranial MR findings in chronic toluene abuse by inhalation. AJNR Am J Neuroradiol 2002;23(7):1173–1179.
- Caldemeyer KS, Pascuzzi RM, Moran CC, Smith RR. Toluene abuse causing reduced MR signal intensity in the brain. AJR Am J Roentgenol 1993;161(6):1259–1261.
- Hurley RA, Taber KH. Occupational exposure to solvents: neuropsychiatric and imaging features. J Neuropsychiatry Clin Neurosci 2015;27(1):1–6.
- Shoback DM, Bilezikian JP, Costa AG, et al. Presentation of Hypoparathyroidism: Etiologies and Clinical Features. J Clin Endocrinol Metab 2016;101(6):2300–2312.
- de la Plaza Llamas R, Ramírez Ángel JM, Arteaga Peralta V, Hernández Cristóbal J, López Marcano AJ. Brain calcifications and primary hyperparathyroidism. Cir Esp 2016;94(1):e5–e7.
- Piciucchi S, Barone D, Gavelli G, Dubini A, Oboldi D, Matteuci F. Primary hyperparathyroidism: imaging to pathology. J Clin Imaging Sci 2012;2(1):59.
- Lai PH, Tien RD, Chang MH, et al. Chorea-ballismus with nonketotic hyperglycemia in primary diabetes mellitus. AJNR Am J Neuroradiol 1996;17(6):1057–1064.
- Bathla G, Policeni B, Agarwal A. Neuroimaging in patients with abnormal blood glucose levels. AJNR Am J Neuroradiol 2014;35(5):833–840.
- Alonso J, Córdoba J, Rovira A. Brain magnetic resonance in hepatic encephalopathy. Semin Ultrasound CT MR 2014;35(2):136–152.
- Rovira A, Alonso J, Córdoba J. MR imaging findings in hepatic encephalopathy. AJNR Am J Neuroradiol 2008;29(9):1612–1621.
- Ramadan S, Lin A, Stanwell P. Glutamate and glutamine: a review of *in vivo* MRS in the human brain. NMR Biomed 2013;26(12):1630–1646.
- Matsusue E, Kinoshita T, Ohama E, Ogawa T. Cerebral cortical and white matter lesions in chronic hepatic en-

- cephalopathy: MR-pathologic correlations. *AJNR Am J Neuroradiol* 2005;26(2):347–351.
35. Kuriyama A, Jackson JL, Doi A, Kamiya T. Metronidazole-induced central nervous system toxicity: a systematic review. *Clin Neuropharmacol* 2011;34(6):241–247.
 36. Kim E, Na DG, Kim EY, Kim JH, Son KR, Chang KH. MR imaging of metronidazole-induced encephalopathy: lesion distribution and diffusion-weighted imaging findings. *AJNR Am J Neuroradiol* 2007;28(9):1652–1658.
 37. Peter P, John M. Isoniazid-induced cerebellitis: a disguised presentation. *Singapore Med J* 2014;55(1):e17–e19.
 38. Geyer HL, Schaumburg HH, Herskovitz S. Methyl bromide intoxication causes reversible symmetric brainstem and cerebellar MRI lesions. *Neurology* 2005;64(7):1279–1281.
 39. Kang EG, Jeon SJ, Choi SS, Song CJ, Yu IK. Diffusion MR imaging of hypoglycemic encephalopathy. *AJNR Am J Neuroradiol* 2010;31(3):559–564.
 40. Wong DS, Poskitt KJ, Chau V, et al. Brain injury patterns in hypoglycemia in neonatal encephalopathy. *AJNR Am J Neuroradiol* 2013;34(7):1456–1461.
 41. McKinney AM, Lohman BD, Sarikaya B, et al. Acute hepatic encephalopathy: diffusion-weighted and fluid-attenuated inversion recovery findings, and correlation with plasma ammonia level and clinical outcome. *AJNR Am J Neuroradiol* 2010;31(8):1471–1479.
 42. U-King-Im JM, Yu E, Bartlett E, Soobrah R, Kucharczyk W. Acute hyperammonemic encephalopathy in adults: imaging findings. *AJNR Am J Neuroradiol* 2011;32(2):413–418.
 43. Özütemiz C, Roshan SK, Kroll NJ, et al. Acute Toxic Leukoencephalopathy: Etiologies, Imaging Findings, and Outcomes in 101 Patients. *AJNR Am J Neuroradiol* 2019;40(2):267–275.
 44. Keogh CF, Andrews GT, Spacey SD, Forkheim KE, Graeb DA. Neuroimaging features of heroin inhalation toxicity: “chasing the dragon”. *AJR Am J Roentgenol* 2003;180(3):847–850.
 45. Geibprasert S, Gallucci M, Krings T. Addictive illegal drugs: structural neuroimaging. *AJNR Am J Neuroradiol* 2010;31(5):803–808.
 46. Tamrazi B, Almasti J. Your brain on drugs: imaging of drug-related changes in the central nervous system. *RadioGraphics* 2012;32(3):701–719.
 47. Inaba H, Khan RB, Laningham FH, Crews KR, Pui CH, Daw NC. Clinical and radiological characteristics of methotrexate-induced acute encephalopathy in pediatric patients with cancer. *Ann Oncol* 2008;19(1):178–184.
 48. Reddick WE, Glass JO, Helton KJ, et al. Prevalence of leukoencephalopathy in children treated for acute lymphoblastic leukemia with high-dose methotrexate. *AJNR Am J Neuroradiol* 2005;26(5):1263–1269.
 49. Kim JY, Kim ST, Nam DH, Lee JI, Park K, Kong DS. Leukoencephalopathy and disseminated necrotizing leukoencephalopathy following intrathecal methotrexate chemotherapy and radiation therapy for central nerve system lymphoma or leukemia. *J Korean Neurosurg Soc* 2011;50(4):304–310.
 50. Morita S, Miwa H, Kihira T, Kondo T. Cerebellar ataxia and leukoencephalopathy associated with cobalamin deficiency. *J Neurol Sci* 2003;216(1):183–184.
 51. Briani C, Dalla Torre C, Citton V, et al. Cobalamin deficiency: clinical picture and radiological findings. *Nutrients* 2013;5(11):4521–4539.
 52. Tung CS, Wu SL, Tsou JC, Hsu SP, Kuo HC, Tsui HW. Marchiafava-Bignami disease with widespread lesions and complete recovery. *AJNR Am J Neuroradiol* 2010;31(8):1506–1507.
 53. Arbelaez A, Pajon A, Castillo M. Acute Marchiafava-Bignami disease: MR findings in two patients. *AJNR Am J Neuroradiol* 2003;24(10):1955–1957.
 54. Lin D, Rheinboldt M. Reversible splenial lesions presenting in conjunction with febrile illness: a case series and literature review. *Emerg Radiol* 2017;24(5):599–604.
 55. Starkey J, Kobayashi N, Numaguchi Y, Moritani T. Cytotoxic Lesions of the Corpus Callosum That Show Restricted Diffusion: Mechanisms, Causes, and Manifestations. *RadioGraphics* 2017;37(2):562–576.
 56. Yan R, Wu Q, Ren J, et al. Clinical features and magnetic resonance image analysis of 15 cases of demyelinating leukoencephalopathy induced by levamisole. *Exp Ther Med* 2013;6(1):71–74.
 57. Lucia P, Pocek M, Passacantando A, Sebastiani ML, De Martinis C. Multifocal leucoencephalopathy induced by levamisole. *Lancet* 1996;348(9039):1450.
 58. Kemanetzoglou E, Andreadou E. CNS Demyelination with TNF- α Blockers. *Curr Neurol Neurosci Rep* 2017;17(4):36.
 59. Eiden C, Diot C, Mathieu O, Mallaret M, Peyrière H. Levamisole-adulterated cocaine: what about in European countries? *J Psychoactive Drugs* 2014;46(5):389–392.
 60. Stone JB, DeAngelis LM. Cancer-treatment-induced neurotoxicity: focus on newer treatments. *Nat Rev Clin Oncol* 2016;13(2):92–105.
 61. Gao B, Lyu C, Lerner A, McKinney AM. Controversy of posterior reversible encephalopathy syndrome: what have we learnt in the last 20 years? *J Neurol Neurosurg Psychiatry* 2018;89(1):14–20.
 62. McKinney AM, Short J, Truwit CL, et al. Posterior reversible encephalopathy syndrome: incidence of atypical regions of involvement and imaging findings. *AJR Am J Roentgenol* 2007;189(4):904–912.
 63. Rykken JB, McKinney AM. Posterior reversible encephalopathy syndrome. *Semin Ultrasound CT MR* 2014;35(2):118–135.
 64. Alleman AM. Osmotic demyelination syndrome: central pontine myelinolysis and extrapontine myelinolysis. *Semin Ultrasound CT MR* 2014;35(2):153–159.
 65. Tatewaki Y, Kato K, Tanabe Y, Takahashi S. MRI findings of corticosubcortical lesions in osmotic myelinolysis: report of two cases. *Br J Radiol* 2012;85(1012):e87–e90.



Imaging-based Selection for Endovascular Treatment in Stroke

Kambiz Nael, MD

Yu Sakai, BA

Pooja Khatri, MD, MSc

Charles J. Prestigiacomo, MD

Josep Puig, MD, PhD

Achala Vagal, MD, MS

Abbreviations: AHA = American Heart Association, AIS = acute ischemic stroke, ASA = American Stroke Association, ASPECTS = Alberta Stroke Program Early CT Score, CBF = cerebral blood flow, DWI = diffusion-weighted imaging, EVT = endovascular treatment, LVO = large-vessel occlusion, MCA = middle cerebral artery, MIP = maximum intensity projection, NIHSS = National Institutes of Health Stroke Scale, TICI = Thrombolysis in Cerebral Infarction, T_{max} = time to maximum

RadioGraphics 2019; 39:1696–1713

<https://doi.org/10.1148/rg.2019190030>

Content Codes: **CT** **ER** **MR** **NR** **VA**

From the Neuroimaging Advanced and Exploratory Laboratory, Department of Radiology, Icahn School of Medicine at Mount Sinai, One Gustave L. Levy Place, Box 1234, New York, NY 10029 (K.N., Y.S.); Departments of Neurology (P.K.), Neurosurgery (C.J.P.), and Radiology (A.V.), University of Cincinnati Medical Center, Cincinnati, Ohio; and Department of Radiology, University of Manitoba, Winnipeg, MB, Canada (J.P.). Presented as an education exhibit at the 2018 RSNA Annual Meeting. Received February 28, 2019; revision requested June 13 and received July 9; accepted July 25. For this journal-based SA-CME activity, the authors K.N., P.K., and A.V. have provided disclosures (see end of article); all other authors, the editor, and the reviewers have disclosed no relevant relationships.

Address correspondence to K.N. (e-mail: Kambiznael@gmail.com).

See discussion on this article by Leslie-Mazwi (pp 1714–1716).

©RSNA, 2019

SA-CME LEARNING OBJECTIVES

After completing this journal-based SA-CME activity, participants will be able to:

- Describe the imaging paradigms for patient selection for EVT of AIS according to the recent AHA-ASA guidelines.
- List imaging criteria used for EVT selection in patients with AIS who present in the early (<6 hours) or late (6–24 hours) window.
- Discuss subgroups of patients with AIS in whom there currently is not sufficient evidence for performance of EVT.

See rsna.org/learning-center-rg.

Treatment of acute ischemic stroke (AIS) has evolved significantly in the past few years. Endovascular treatment (EVT) is now proved to be efficacious up to 24 hours from onset in properly selected patients. The recently updated 2018 American Heart Association–American Stroke Association guidelines reflect the important role of imaging in triage and patient selection for EVT of AIS.

Pretreatment imaging in patients with acute stroke should (*a*) allow assessment for intracranial hemorrhage and demonstrate (*b*) the extent of early ischemic changes, (*c*) the presence of large arterial occlusion, and (*d*) in some cases potential salvageable tissue before the decision to proceed with EVT. The authors review how multimodality imaging can be used for EVT selection in the context of the recent guidelines. They highlight the importance of having streamlined imaging workflows that are integrated with clinical decision making to maximize treatment efficiency. Knowledge of the various imaging criteria including perfusion imaging used for EVT selection is highlighted. The authors discuss variable imaging paradigms used for selection of patients in the early and late windows (who present before vs after 6 hours from onset of symptoms), as reflected in the latest guidelines and in relation to their level of evidence. Finally, they focus on challenges in the subgroups of patients who were excluded from recent EVT trials and with limited evidence to prove the efficacy of EVT, such as patients with low NIHSS (National Institutes of Health Stroke Scale) score, distal occlusion, or large ischemic core.

©RSNA, 2019 • radiographics.rsna.org

Introduction

Endovascular treatment (EVT) is now established as a potent treatment option for patients with acute ischemic stroke (AIS) with large-vessel occlusion (LVO) involving the anterior circulation. In 2015, six randomized trials—MR CLEAN (1), ESCAPE (2), REVASCAT (3), SWIFT PRIME (4), EXTEND-IA (5), and THRACE (6)—revolutionized acute stroke care by demonstrating that EVT is an effective treatment for patients with AIS and LVO in the “early window” (ie, within 6 hours from symptom onset). In 2018, two additional successful trials—DAWN (7) and DEFUSE 3 (8)—extended EVT into the “late window” (ie, up to 24 hours from symptom onset) (Table). The overwhelmingly positive results of these trials have led to changes in treatment guidelines and widespread adoption of EVT (9).

Although trials varied in eligibility criteria, such as time of symptom onset, prestroke level of functioning, and clinical severity of stroke symptoms, all the trials had a clear focus on fast, effective, and safe reperfusion in AIS patients selected with well-integrated imaging strategies. Use of multimodal imaging for patient selection and triage was a critical component, thereby placing imaging data in the center of treatment decisions.

TEACHING POINTS

- The ultimate goal of neuroimaging in patients with AIS is to optimize patient selection for safe and efficient EVT. The value of imaging is directly dependent on whether the information gained is worth the time spent, given the time sensitivity of reperfusion therapies for efficacy.
- In patients with suspected anterior circulation LVO of less than 6 hours, nonenhanced CT and CT angiography can provide sufficient imaging information to determine EVT candidacy.
- In late-window patients with LVO presenting 6–24 hours after symptom onset or with unknown stroke onset, perfusion imaging provides additional information about the predicted core, salvageable penumbra, and mismatch to select patients who are more likely to benefit from treatment at later times from onset. The success of the late-window DAWN and DEFUSE 3 trials has catapulted perfusion imaging into routine clinical practice.
- Another imaging parameter that can be used in patient selection is collateral circulation. A growing body of literature suggests that collateral status allows prediction of tissue outcome. The role of collateral flow in treatment selection may be most relevant in the extended window to distinguish ischemia with fast versus slow progression to irreversibility.
- In the era of endovascular therapy, advanced imaging plays a critical role in selection of patients with AIS for treatment. Consistent with current guidelines, nonenhanced CT and CT angiography are likely sufficient for EVT selection in the early window (<6 hours). For the late window (6–24 hours), additional perfusion imaging (perfusion CT or DWI and perfusion MRI) is helpful to assess the ischemic core—and possibly the penumbra and mismatch—for treatment decision making. Subgroups of patients remain for whom evidence is lacking about optimal treatment, including those with low NIHSS score, large ischemic core, or distal occlusion. Regardless of the imaging modalities and strategies at individual institutions, efficient imaging workflow must be established to provide faster treatment.

In this article, we summarize the imaging modalities available for AIS patients with a focus on the updated 2018 American Heart Association (AHA)–American Stroke Association (ASA) guidelines. We also discuss how available imaging strategies can guide treatment selection in the new era of EVT. All physicians involved in management of stroke patients (radiologists, neurologists, emergency physicians, and neurointerventionalists) need to be familiar with the most recent guidelines and understand how to use imaging for treatment selection in patients with AIS.

Neuroimaging

Neuroimaging for acute stroke encompasses parenchymal imaging to assess the ischemic changes and the presence of intracranial hemorrhage, vascular imaging to assess the patency of major arterial branches of the neck and brain, and perfusion imaging to assess salvageable brain. A wide variety of imaging techniques—CT or MRI based—are available to assess eligibility for EVT. Important considerations for the choice of

technique include level of clinical evidence for its use in patient selection, constraints of time and cost, ease of access and availability, and institutional preference. The ultimate goal of neuroimaging in patients with AIS is to optimize patient selection for safe and efficient EVT. The value of imaging is directly dependent on whether the information gained is worth the time spent (10), given the time sensitivity of reperfusion therapies for efficacy.

Computed Tomography

Since earlier treatment leads to greater benefit (11,12), the AHA recommended that initial brain imaging be performed within 20 minutes of arrival in the emergency department in at least 50% of patients who may be candidates for thrombolysis or thrombectomy (9). A multimodal CT-based workup (13,14) consists of nonenhanced CT to rule out intracranial hemorrhage and depict early ischemic changes, CT angiography to detect LVO, and perfusion CT to assess the ischemic core and penumbra.

For determination of the extent of early ischemic changes at nonenhanced CT, the Alberta Stroke Program Early CT Score (ASPECTS) is commonly used (www.aspectsinstroke.com). The ASPECTS scale uses a 10-point negative ordinal scoring system for the middle cerebral artery (MCA) territory, with a score of 10 indicating a normal result and with one point subtracted for each abnormal region (15). Despite successful application of ASPECTS in several clinical trials, there remains some concern about interobserver variability even for experienced neuroradiologists (16–18).

In potential candidates for EVT, a noninvasive vascular study of intracranial circulation (level Ia) and extracranial arteries (level IIa) is recommended during the initial imaging evaluation (9). CT angiography was used as the primary vascular imaging method in the recent endovascular trials to identify LVO as the target for EVT (19). Also, CT angiography provides useful additional information about the aortic arch anatomy, tortuosity of the supra-aortic arteries, and the possibility of tandem proximal stenosis to facilitate treatment planning and achieve safer and faster reperfusion in patients with acute stroke (20).

Finally, perfusion CT can be performed to assess the extent of the penumbra and also the ischemic core. The perfusion CT maps can be visually evaluated for subjective assessment of the ischemic core (ie, severe decrease in cerebral blood volume [CBV]) (21,22) and operational penumbra (eg, CBV-MTT [mean transit time] mismatch) (20,23). To provide more objective assessment of the ischemic core and penumbra and reduce observer variability, several investigators

Enrollment and Imaging Criteria Used in Eight Trials of EVT for AIS

| Trial | Treatment Window (h) | Imaging Modalities | Defining Early Ischemic Changes or Core | Vascular Imaging | Perfusion Imaging and Criteria (if Used) |
|-------------|----------------------|--------------------|-----------------------------------------------------------------------------------------------------------------------------------|------------------------------------------------------------|----------------------------------------------------------------------------------------------------------------------------------------------|
| MR CLEAN | 6 | CT | 1/3 of MCA territory, no ASPECTS | CTA | No |
| EXTEND-IA | 6 | CT | Core < 70 mL using perfusion CT | CTA | Perfusion CT Core < 70 mL Absolute mismatch volume > 10 mL Mismatch ratio > 1.2 |
| ESCAPE | up to 12 | CT | ASPECTS ≥ 6 | Multiphasic CTA: collateral ≥ 50% of MCA pial circulation* | No |
| SWIFT PRIME | 6 | MRI, CT | CT or MRI ASPECTS ≥ 6 | CTA or MRA | Perfusion CT or perfusion MRI Core < 50 mL, mismatch > 1.8† |
| REVASCAT | up to 8 | MRI, CT | CT ASPECTS ≥ 7 MRI ASPECTS ≥ 6 | CTA or MRA | Perfusion CT–CBV ASPECTS or perfusion CT–SI ASPECTS in patients >4.5 h from onset |
| THRACE | 5 | MRI, CT | 1/3 of MCA territory, no ASPECTS | CTA or MRA | No |
| DAWN | 6–24 | MRI, CT | Core ≤ 20 mL if age > 80 y Core ≤ 30 mL if age < 80 y and NIHSS score 10–20 Core ≤ 50 mL if age < 80 y and NIHSS score > 20 | CTA or MRA | Core at MRI: ADC < 620 × 10 ⁻³ mm ² /sec Core at perfusion CT: relative CBF < 30% |
| DEFUSE 3 | 6–16 | MRI, CT | Core ≤ 70 mL Mismatch ≥ 15 mL, mismatch ratio ≥ 1.8 | CTA or MRA | Core at MRI: ADC < 620 × 10 ⁻³ mm ² /sec Core at perfusion CT: relative CBF < 30% T_{max} > 6 sec for penumbra |

Note.—ADC = apparent diffusion coefficient, ASPECTS = Alberta Stroke Program Early CT Score, CBF = cerebral blood flow, CBV = cerebral blood volume, CTA = CT angiography, MCA = middle cerebral artery, MRA = MR angiography, NIHSS = National Institutes of Health Stroke Scale, SI = source image, T_{max} = time to maximum.

*Dichotomized as good or moderate versus poor or absent.

†Used only initially before the criteria were revised to use ASPECTS.

A few important points about these trials in terms of imaging utilization:

- One consistent imaging criteria across all of the trials was use of vascular imaging to identify LVO, which was defined as intracranial carotid or M1 occlusion in all of the trials. Some trials included M2 occlusion for enrollment (SWIFT PRIME and EXTEND-IA), and MR CLEAN included both anterior cerebral artery (ACA) and M2 occlusions.
- In determination of ischemic changes and the ischemic core, MR CLEAN had the most minimalistic imaging approach, using nonenhanced CT just to ensure that no large infarction existed (without using ASPECTS). EXTEND-IA was the only trial that used perfusion imaging to define the ischemic core (<70 mL) consistently for enrollment of all patients. SWIFT PRIME also used perfusion imaging to calculate the ischemic core (<50 mL) during the early enrollment stage before revision was made to switch to ASPECTS.
- Among trials that used nonenhanced CT ASPECTS as an enrollment criterion, CT ASPECTS ≥ 6 was used in ESCAPE and SWIFT PRIME and CT ASPECTS ≥ 7 was used in REVASCAT. Three trials encouraged MRI use when available, although the only trial that predominantly enrolled patients using MRI was THRACE.
- The only trial that used CT angiography collateral status as an enrollment criterion was ESCAPE.

have worked on providing quantitative perfusion CT with automated software.

Most recent work has suggested use of relative cerebral blood flow (CBF) for defining the ischemic core, with threshold values ranging between 30% and 45% (24–26). For definition of the ischemic penumbra, T_{max} (time to maximum) > 6 seconds has been proposed as an indication of critical hypoperfusion (24,27). The EVT trials that used perfusion imaging as a selection criterion used automated software to quantify the core and mismatch in a time-efficient manner. We further discuss perfusion CT later in the article and how it can be used for treatment selection in the late window (6–24 hours from symptom onset or last known well).

Comprehensive stroke imaging with nonenhanced CT, CT angiography, and perfusion CT takes only a few minutes and can be performed with almost all current scanners. CT has distinct advantages over MRI, such as widespread availability, speed of acquisition, and cost-effectiveness. For this reason, CT is the imaging workhorse in the vast majority of stroke centers.

MR Imaging

To be comparable to CT, a comprehensive MRI protocol should include diffusion-weighted imaging (DWI) for detecting early ischemic changes, fluid-attenuated inversion-recovery (FLAIR) and gradient-echo (GRE) imaging for detecting intracranial hemorrhage (28), MR angiography for assessing vessel status, and perfusion MRI for assessing penumbral tissue. The major advantage of MRI is the DWI sequence, which is the most sensitive imaging modality for evaluating early ischemia and provides level I evidence for assessing the ischemic core (29,30). DWI is the recommended sequence in patient selection for late-window thrombectomy.

Automated software can calculate the volume of the ischemic core using quantitative ADC (apparent diffusion coefficient) values of $<600 \times 10^{-3} \text{ mm}^2/\text{sec}$ (31–33). After thrombectomy or spontaneous reperfusion, there is a variable rise in ADC values of the ischemic bed; therefore, the infarct volume should ideally be assessed using DWI or FLAIR images rather than ADC maps. GRE imaging alone or in combination with FLAIR imaging has excellent diagnostic accuracy in detection of acute intracranial hemorrhage, comparable to that of CT (28,34).

As with CT angiography, MR angiography can provide essential information about the LVO. Large-field-of-view vascular imaging of the neck and brain using contrast-enhanced MR angiography also depicts extracranial vascular anatomy and pathologic conditions such as tandem

stenosis or dissection, thus informing the interventionalist of the procedural strategy or excluding patients from EVT on the basis of undue risk. However, MR angiography without contrast material (such as time-of-flight MR angiography) can be limited by motion-related artifact and longer acquisition time and sometimes results in inadequate image quality for assessing the origin of supra-aortic arteries.

As with CT, perfusion MRI can also be performed in a comprehensive stroke protocol to assess the penumbra. One major advantage of MRI is that, by obtaining an accurate estimate of the ischemic core with DWI, perfusion MRI is used only to estimate the penumbra, often by using $T_{max} > 6$ seconds (35). This is advantageous over perfusion CT, where additional information is needed to identify both the ischemic core and penumbra, sometimes with mixed results (36–39).

The biggest practical disadvantages of MRI protocols include sparse availability and delayed workflow related to required patient screening and longer acquisition time (40,41). Although fast 6-minute MRI stroke protocols have been described (42), there are often delays related to the logistical challenges of implementing MRI in everyday clinical practice. The general consensus is that MRI should be used for EVT selection only in institutions that are capable of achieving speed and triaging efficiency similar to what can be accomplished with CT-based imaging.

With the recent positive results of the WAKE-UP trial (43), which used DWI–FLAIR imaging mismatch to select patients for extending the time window for intravenous thrombolysis, stroke centers now need the capability of performing timely MRI studies in a subset of the patients who would be eligible for delayed thrombolytic treatment (Fig 1). An earlier study also showed that quantitative mismatch of DWI and FLAIR imaging results can be used as the basis for safe thrombolytic treatment of patients with unwitnessed stroke (44). In addition, perfusion imaging (perfusion CT or perfusion MRI) has been used for successful treatment of wake strokes with thrombolytic treatment, according to recently published results of the EXTEND trial (45).

Collateral Status

Collateral flow status information can also be assessed noninvasively with vascular imaging such as CT angiography (46,47) or MR angiography (48,49). It is now well known that poor baseline collaterals are associated with a larger ischemic core and worse functional outcomes (50,51).

CT angiography is the most commonly used imaging modality for assessing the extent of collaterals, given its broad use in the prethrombectomy

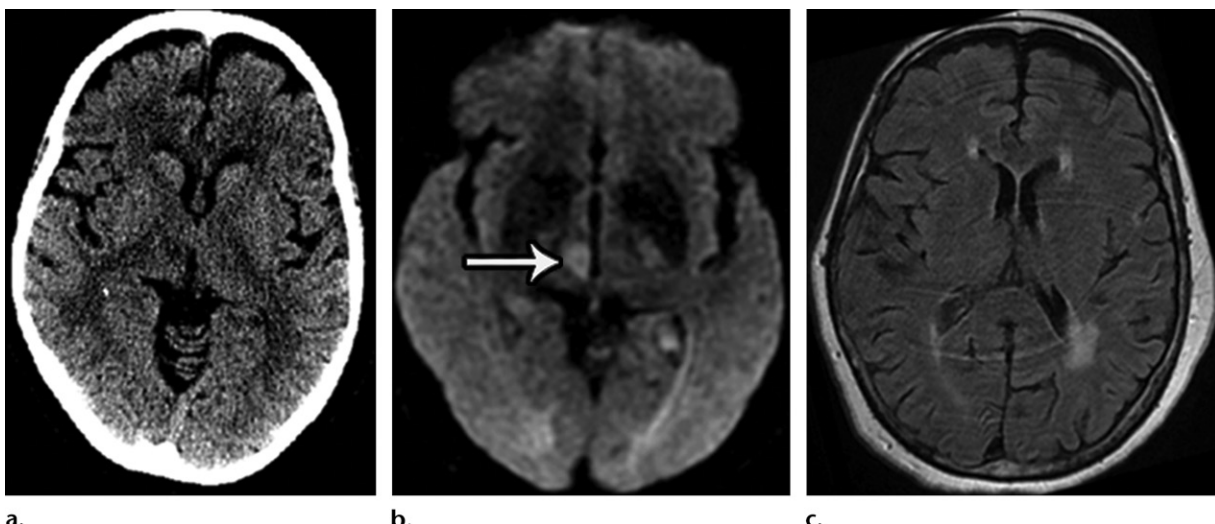


Figure 1. DWI–FLAIR imaging mismatch in an 84-year-old woman with unknown onset of acute stroke who presented with left-sided weakness and a baseline NIHSS (National Institutes of Health Stroke Scale) score of 10. (a) Axial nonenhanced CT image obtained on arrival is negative for infarction. Results of CT angiography were also normal (not shown). (b, c) Axial diffusion-weighted image (b) shows restricted diffusion in the right thalamus (arrow) without associated T2 hyperintensity on an axial FLAIR image (c), consistent with DWI–FLAIR imaging mismatch. The patient received an infusion of tissue plasminogen activator on the basis of the WAKE-UP trial results and improved to an NIHSS score of 3.

setting. Two commonly used scoring systems are the Tan score (0 = no collaterals, 1 = <50% of the affected MCA territory, 2 = ≥50% but <100%, 3 = 100%) (52,53) and the Maas scale (1 = absent, 2 = less than contralateral side, 3 = equal to contralateral side, 4 = greater than contralateral side, 5 = exuberant) (54). While the prognostic importance of collateral assessment with CT angiography in patients with AIS has been established, consensus is lacking on the optimal imaging technique and number of phases required and its role in modifying treatment effect. Some investigators have shown variable degrees of improvement by using multiphase CT angiography (55–57); others suggest that single-phase CT angiography may be sufficient (51,58).

Contrast-enhanced MR angiography provides similar performance as CT angiography in terms of delineation of intracranial arteries and collateral assessment after a dynamic acquisition with injection of gadolinium contrast material (48,49,59). On the other hand, the flow-related signal of time-of-flight MR angiography is mainly depicted via antegrade flow; therefore, this technique provides only modest information about the collateral flow (49,59). Maximum intensity projection (MIP) images from CT angiography or MR angiography are useful to provide rapid visual assessment of the extent of collaterals (Fig 2).

Recent analyses of the MR CLEAN and Interventional Management of Stroke III trials, while underpowered, suggest a potential role for collateral assessment in identifying patients likely or unlikely to benefit from EVT (1,60).

Also, the ESCAPE investigators successfully used moderate-to-good collateral scores at multiphase CT angiography as a criterion to enroll patients for EVT and showed treatment benefit over medical therapy (2). It is well known that patients with poor collaterals have a faster infarct growth rate (fast progressors) (Fig 2), and those with good collaterals are able to sustain the ischemic bed longer (slow progressors). For thrombectomy candidates who are being transferred from primary care to a comprehensive stroke center, repeat imaging may sometimes be warranted to identify the fast progressors with poor collaterals.

Collateral information can also be assessed with perfusion imaging, including perfusion CT (61,62) or perfusion MRI (63,64). A recent study showed no significant association between collaterals and penumbral volume, indicating that although collaterals have good negative correlation with the final infarct volume, they have limited significance as a marker of salvageable tissue (65).

Quantitative assessment of cerebral blood volume (CBV) within the ischemic bed allows prediction of angiographic collaterals. Relative CBV, obtained by comparing the CBV of the purported ischemic bed to the CBV in normally perfused brain regions, has been shown to correlate with angiographic collateral status (66). In addition, the perfusion collateral index has been defined as relative CBV times the volume of moderate hypoperfusion—defined by a tissue delay of 2–6 seconds—as an indication of robust collaterals (64).

The main purpose of a perfusion study using perfusion CT or perfusion MRI is to outline the

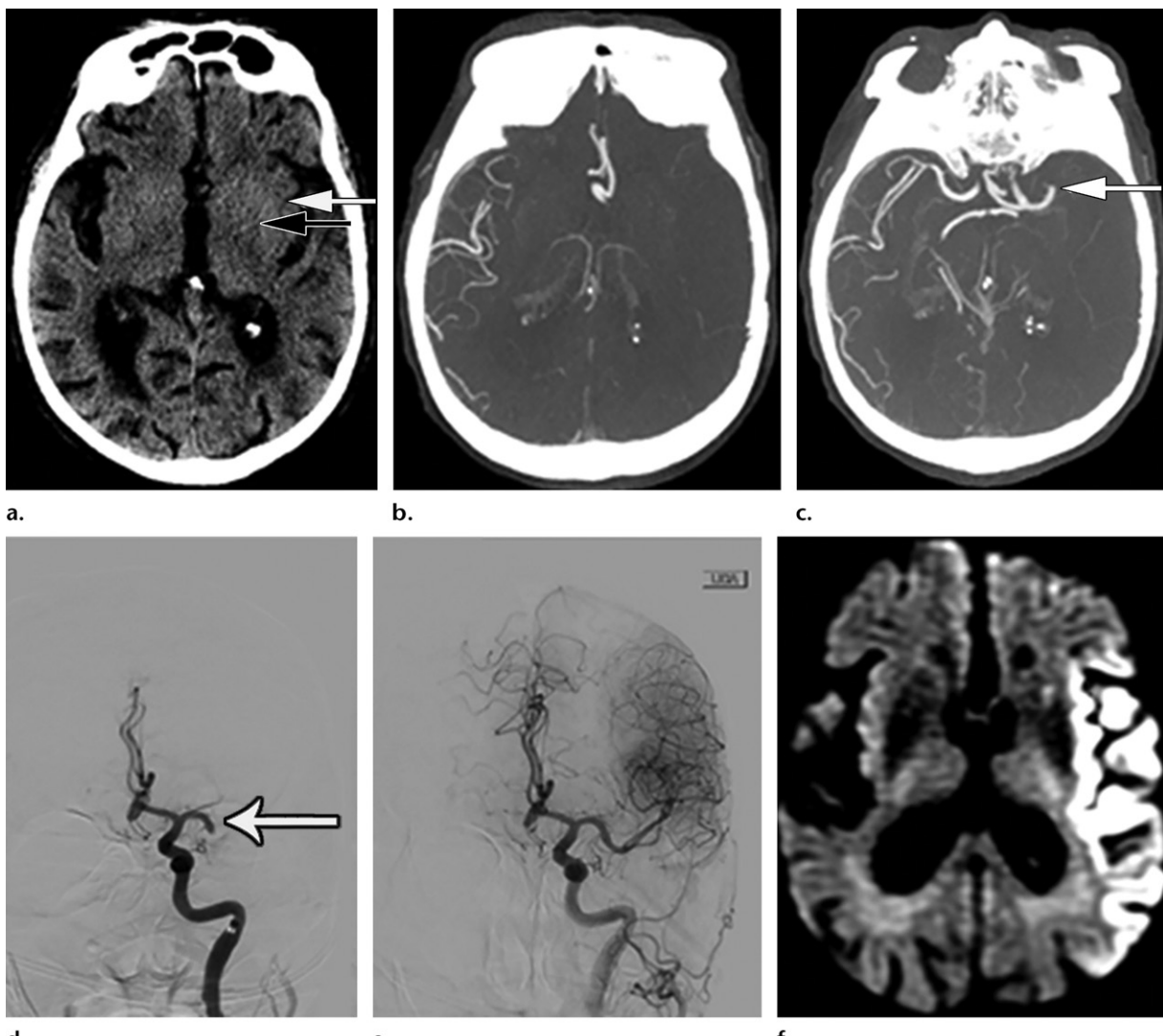


Figure 2. Poor collaterals resulting in rapid infarct progression in a 78-year-old man with left MCA syndrome and baseline NIHSS score of 21. (a) Axial nonenhanced CT image obtained within 1 hour from symptom onset shows ASPECTS of 8 (subtle hypoattenuation in the left insular cortex [white arrow] and the posterior limb of the internal capsule [black arrow]). (b, c) Axial thick-slab MIP CT angiograms show left M1 occlusion (arrow in c) with poor collaterals in the left MCA territory. (d) Coronal digital subtraction angiogram shows the left M1 occlusion (arrow). (e) Angiogram shows successful thrombectomy (TICI [Thrombolysis in Cerebral Infarction] scale grade 2c) performed within 90 minutes from initial CT. (f) Follow-up axial diffusion-weighted image shows a large established left MCA territorial infarct despite successful EVT, demonstrating the importance of collateral circulation.

salvageable brain tissue (ischemic penumbra) and ischemic core. The relevance of perfusion imaging varies on the basis of the time window since symptom onset.

Imaging Workflow

Regardless of the type of imaging modality, it is imperative for stroke centers to have an optimal imaging workflow that is integrated with clinical decision making to minimize the time penalty and maximize the efficiency of treatment delivery to stroke patients. It is recommended that intravenous thrombolysis be performed in qualified patients using a parallel process (in imaging units) while further advanced imaging such as CT angiography and perfusion CT is being performed.

It is critical that CT angiography–perfusion CT or MR angiography–perfusion MRI is performed as quickly as possible, and performance of vascular or perfusion imaging should not delay performance of intravenous thrombolysis in eligible patients. According to the 2018 AHA-ASA recommendations, it is reasonable to perform vascular imaging before performing a renal function test in patients without a history of renal impairment (level IIb) (12). This stems from evidence demonstrating a relatively low risk of transient contrast material–induced nephropathy secondary to CT angiography in the absence of a history of renal impairment (67–69).

Radiologists and technologists play a pivotal role in streamlining the workflows of both image

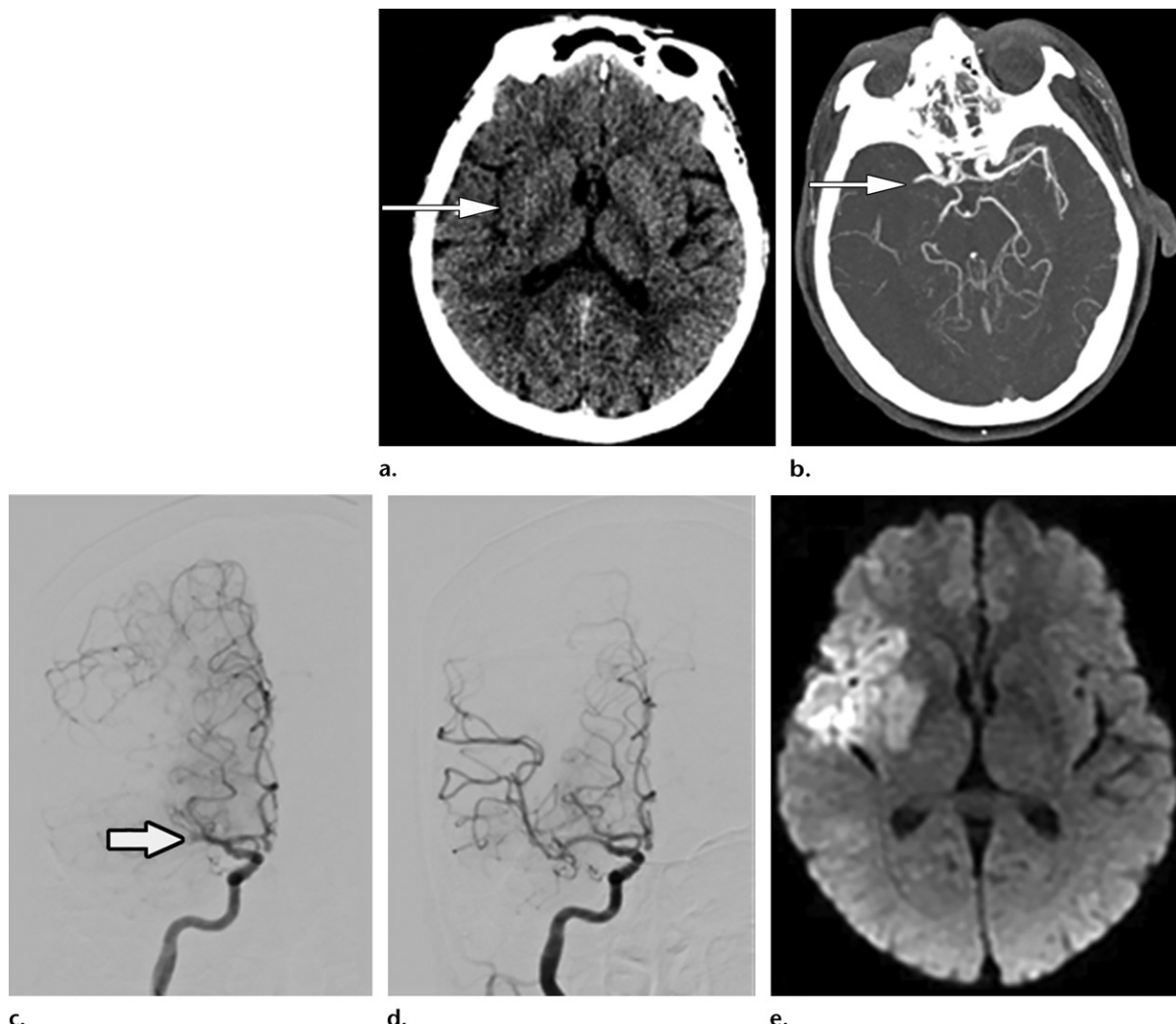


Figure 3. EVT selection in the early time window (<6 hours) using nonenhanced CT and CT angiography in a 74-year-old woman with right MCA syndrome and baseline NIHSS score of 26. Time from onset to CT was 47 minutes. (a) Axial nonenhanced CT image shows ASPECTS of 9 (hypoattenuating insula [arrow]). (b) Axial thick-slab MIP CT angiogram shows right M1 occlusion (arrow). (c) Coronal digital subtraction angiogram shows the right M1 occlusion (arrow). (d) Angiogram shows successful mechanical thrombectomy (TICI scale grade 2c) achieved within 78 minutes from nonenhanced CT. (e) Follow-up diffusion-weighted image shows infarction along the right MCA distribution.

acquisition and interpretation and should be an integral part of the stroke team. Having multi-component quality improvement programs and multidisciplinary engagement of emergency physicians, neurologists, radiologists, and neuro-interventionalists improves treatment times and outcomes.

Imaging-based Treatment Selection

As we enter the paradigm-shifting era of acute stroke care, the pressing question is how to deliver this time-critical therapy to patients who need it and how to optimize stroke imaging. On the basis of the most recent AHA-ASA guidelines, any AIS patient with significant neurologic deficits (NIHSS score ≥ 6) who presents with LVO within 24 hours may be a potential candidate for EVT, depending on his or her imaging profile.

The primary purpose of imaging in patient selection is to identify patients with favorable risk-benefit ratios. The 2015 and 2018 EVT trials have now established care in two broad time categories: the early window (<6 hours from symptom onset or last known well) and late window (6–24 hours from symptom onset or last known well). In this section, we describe imaging selection based on time from stroke onset to presentation of less than 6 hours versus 6–24 hours.

Early Window (<6 Hours)

In patients with suspected anterior circulation LVO of less than 6 hours, nonenhanced CT and CT angiography can provide sufficient imaging information to determine EVT candidacy (Fig 3). Patients with occlusion of the intracranial internal carotid artery (ICA) and/or M1 and absence of a

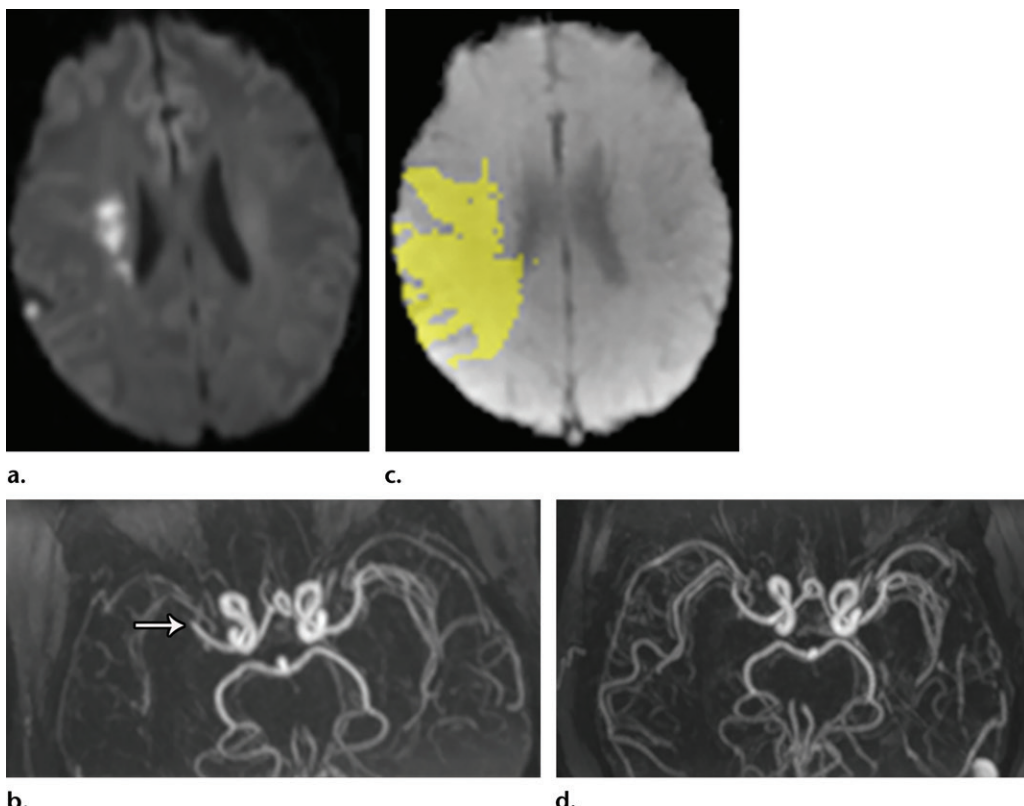


Figure 4. MRI for EVT selection in the early window in a 61-year-old woman with left hemiparesis and NIHSS score of 12 approximately 3 hours from last known well. **(a)** Axial diffusion-weighted image show small areas of infarction along the right MCA distribution. **(b)** Axial contrast-enhanced thick-slab MIP MR angiogram shows occlusion of right M1 (arrow). **(c)** Axial T_{\max} map from perfusion MRI using a 6-second threshold shows a large penumbra (yellow). **(d)** Axial contrast-enhanced thick-slab MIP MR angiogram after thrombectomy shows recanalization of the right MCA.

large infarct core at nonenhanced CT (ASPECTS ≥ 6) are considered safe candidates for EVT. If MRI workup is used, DWI ASPECTS ≥ 6 and establishing LVO with MR angiography can be used (3,4). Enrollment and imaging criteria used in eight EVT trials are summarized in the Table.

Additional imaging beyond nonenhanced CT and CT angiography may be performed for patients presenting within 6 hours of symptom onset (Fig 4). Several early-window trials used some form of additional imaging other than nonenhanced CT and CT angiography to determine EVT candidacy. These included perfusion imaging (perfusion CT or perfusion MRI) to estimate ischemic core volume of <50 mL in a subset of SWIFT PRIME (4) and <70 mL in EXTEND-IA (5) or multiphase CT angiography to determine moderate to good collaterals in ESCAPE (2). However, MR CLEAN (1) and THRACE (6) did not use any advanced imaging criteria other than nonenhanced CT and CT angiography, and REVASCAT (3) used nonenhanced CT ASPECTS ≥ 6 only for patient selection. Hence, according to the AHA-ASA guidelines, additional imaging other than nonenhanced CT and CT angiography may not be necessary in patients presenting within 6 hours.

The disadvantages of additional imaging (including perfusion imaging) in the early window include potential for delay of treatment and inappropriate exclusion of patients who may benefit from EVT if additional imaging-based eligibility criteria are applied. However, in the 2018 updated AHA guidelines, the statement “no necessity for perfusion imaging in <6 hours group” was removed for reevaluation (70). Since the majority of patients with LVO presenting in the early window may have penumbral mismatch, it is unclear whether performance of perfusion imaging is worth the time, and the role of perfusion imaging in the early time window will require clarification in future studies.

Late Window (6–24 Hours)

Current data do not definitively support using nonenhanced CT alone in treatment selection. The HERMES pooled analysis (11), which included the five trials MR CLEAN, ESCAPE, REVASCAT, SWIFT PRIME, and EXTEND-IA, showed a decline in treatment effect with time beyond 7 hours after symptom onset when nonenhanced CT and ASPECTS were used for treatment selection. REVASCAT, which randomized patients by

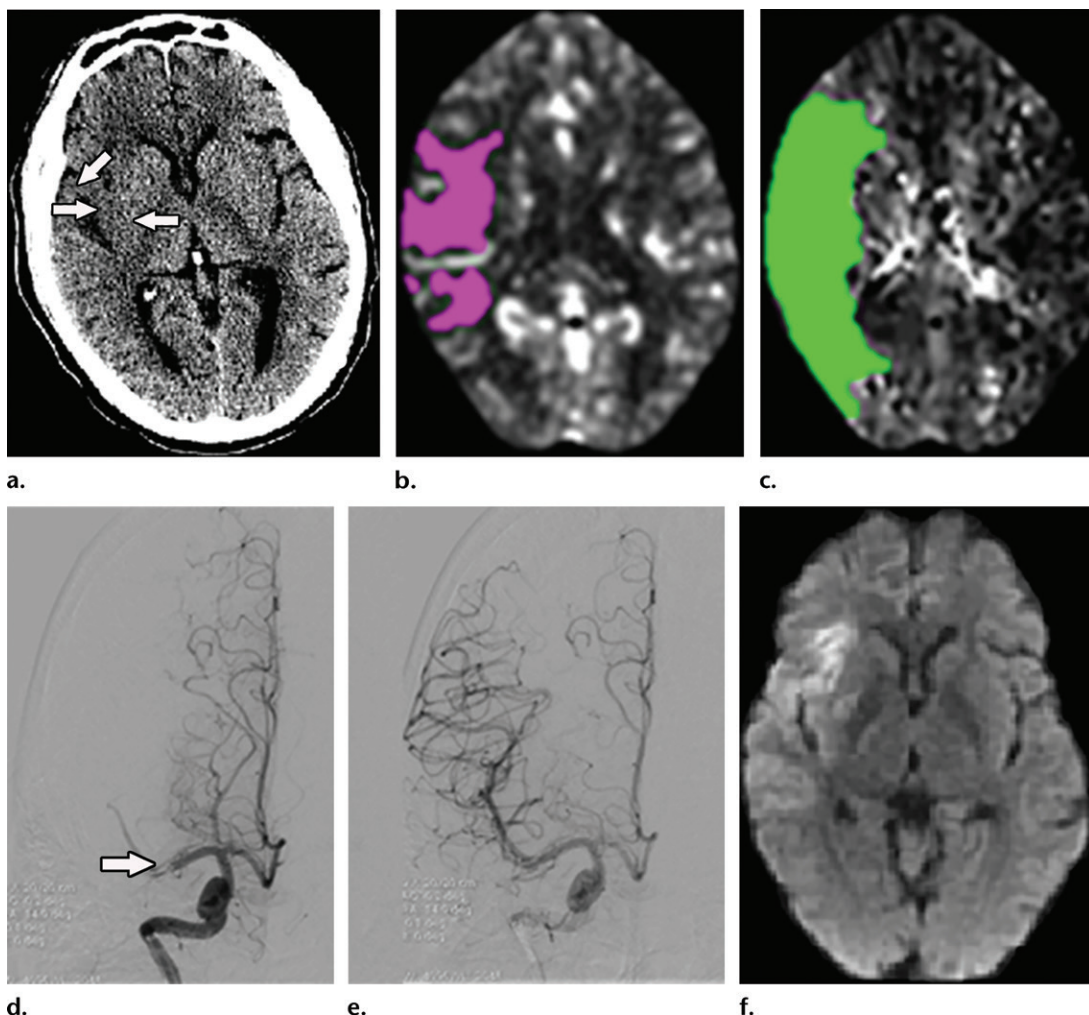


Figure 5. EVT selection in extended window (6–24 hours) in a 57-year-old man with right MCA syndrome and baseline NIHSS score of 10–11 who presented 18 hours after last known well. **(a)** Axial nonenhanced CT image shows hypotenuation in the putamen, insula, and temporal lobe (arrows) (ASPECTS of 7). **(b, c)** Axial perfusion CT images with application of two thresholds (relative CBF < 30% for ischemic core and $T_{max} > 6$ seconds for penumbra) shows 30 mL of ischemic core (purple in **b**) and penumbra of 102 mL (green in **c**). On the basis of the extended-window results in DAWN, the patient underwent EVT. **(d)** Coronal digital subtraction angiogram shows right distal M1 occlusion (arrow). **(e)** Angiogram shows successful thrombectomy (TICI scale grade 3). **(f)** Follow-up diffusion-weighted image shows a stable infarct without growth.

ASPECTS ≥ 6 , also showed a substantial decrease in treatment effect with time (71). MR CLEAN, which used nonenhanced CT for parenchymal imaging, demonstrated that the effect of treatment was lost when the time from symptom onset to reperfusion was longer than 6 hours (72).

In late-window patients with LVO presenting 6–24 hours after symptom onset or with unknown stroke onset, perfusion imaging provides additional information about the predicted core, salvageable penumbra, and mismatch to select patients who are more likely to benefit from treatment at later times from onset. The success of the late-window DAWN and DEFUSE 3 trials has catapulted perfusion imaging into routine clinical practice. According to the updated AHA-ASA guidelines, perfusion CT (in addition to nonenhanced CT and CT angiography) or MRI (DWI,

perfusion MRI) is recommended to aid in patient selection for EVT when patients meet the eligibility criteria of DAWN and DEFUSE 3 (level I).

DAWN used clinical (NIHSS score) and imaging (estimated ischemic core volume using perfusion CT or DWI up to 50 mL) mismatch to determine EVT candidacy between 6 and 24 hours from symptom onset (7). DEFUSE 3 used perfusion-core mismatch and maximum core size estimated up to 70 mL as imaging criteria to select patients with anterior circulation LVO 6–16 hours from symptom onset (8). Both DAWN and DEFUSE 3 used automated perfusion CT with thresholds of CBF < 30% for the ischemic core and $T_{max} > 6$ seconds for penumbral volume (Figs 5, 6). The imaging criteria used in DAWN and DEFUSE 3 are summarized in the Table. However, the reliability of quantitative perfusion CT

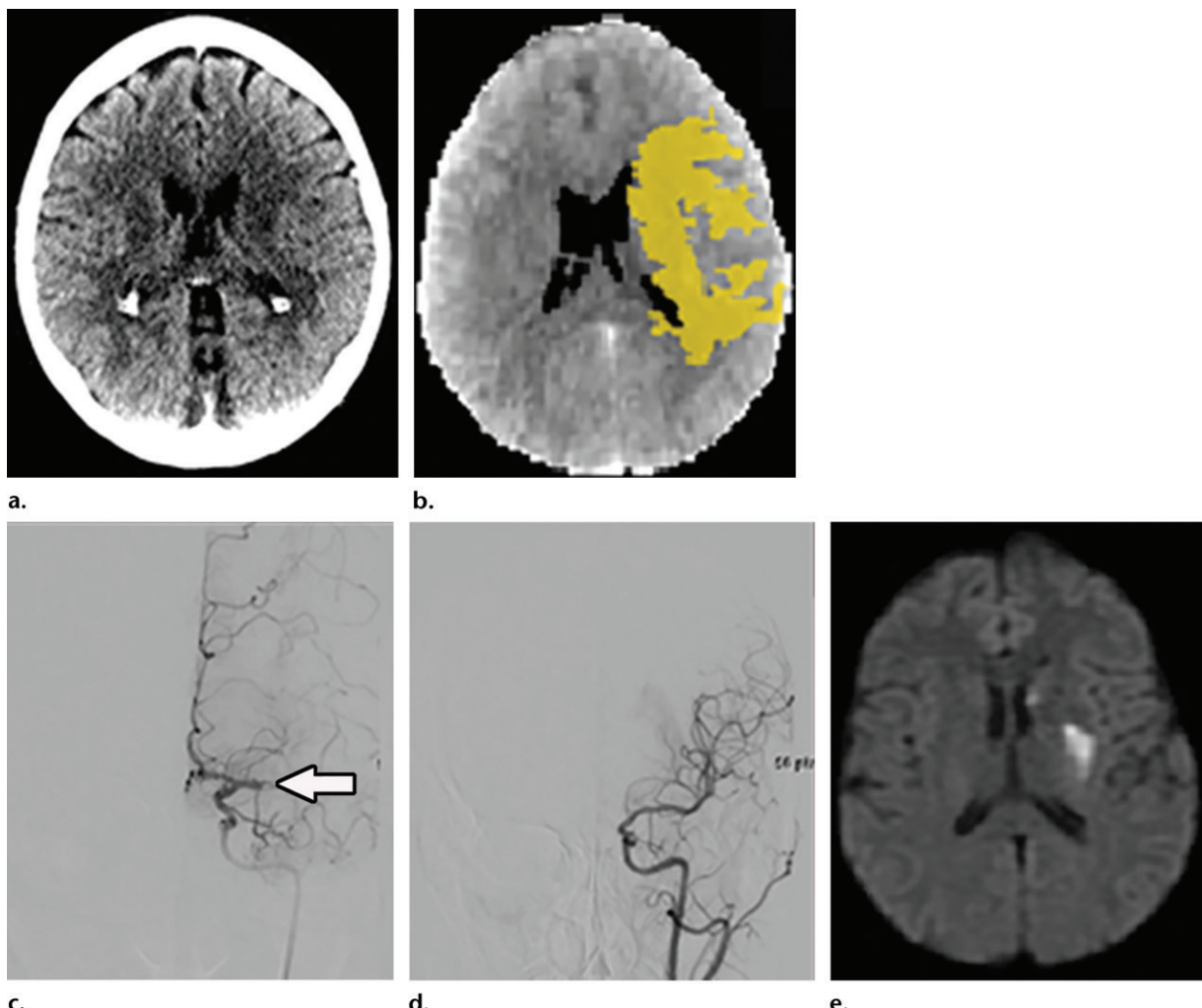


Figure 6. Perfusion imaging for EVT selection in extended window in a 54-year-old woman with left M1 occlusion (not shown) and baseline NIHSS score of 11 who presented 9 hours after symptom onset. (a) Axial nonenhanced CT image shows a normal ASPECTS of 10. (b) Axial perfusion CT image after application of two thresholds (relative CBF < 30% for ischemic core and $T_{max} > 6$ seconds for penumbra) shows 41 mL of penumbra (yellow) with no detectable ischemic core. (c) Coronal digital subtraction angiogram shows left M1 occlusion (arrow). (d) Angiogram shows successful thrombectomy (TICI scale grade 3) within 1 hour of initial CT. (e) Follow-up axial diffusion-weighted image shows a small infarct.

needs further improvement in terms of accuracy (38,73) and interrater agreement among different postprocessing software (74).

Figure 7 shows an example of MRI selection for EVT in the late window.

Restrictive imaging criteria used in DAWN and DEFUSE 3 may limit the generalizability of their results in routine daily practice. There is growing evidence that patients with LVO within 6–24 hours may still benefit from EVT outside the eligibility criteria of DAWN and DEFUSE 3 (75) (level IIB, nonrandomized data); however, current AHA-ASA guidelines (9) state that these eligibility criteria should be strictly adhered to in clinical practice pending the results of future randomized clinical trials in this subgroup. Figure 8 shows an example of wake-up stroke with perfusion CT and DAWN criteria used for selection of EVT for M2 occlusion.

Another imaging parameter that can be used in patient selection is collateral circulation. A growing body of literature suggests that collateral status allows prediction of tissue outcome (60,76,77). The role of collateral flow in treatment selection may be most relevant in the extended window to distinguish ischemia with fast versus slow progression to irreversibility. Good collaterals can sustain ischemic tissue, resulting in smaller volume of established core and decreased infarct growth in the extended window (78). At CT angiography, moderate-to-good collateral circulation is generally defined as filling of 50% or more of the MCA pial arterial circulation.

This dichotomized criterion was used in ESCAPE to enroll early-window patients for EVT with a successful result (2). ESCAPE investigators also used the same criterion to enroll 49 patients with stroke beyond 6 hours (up to 12

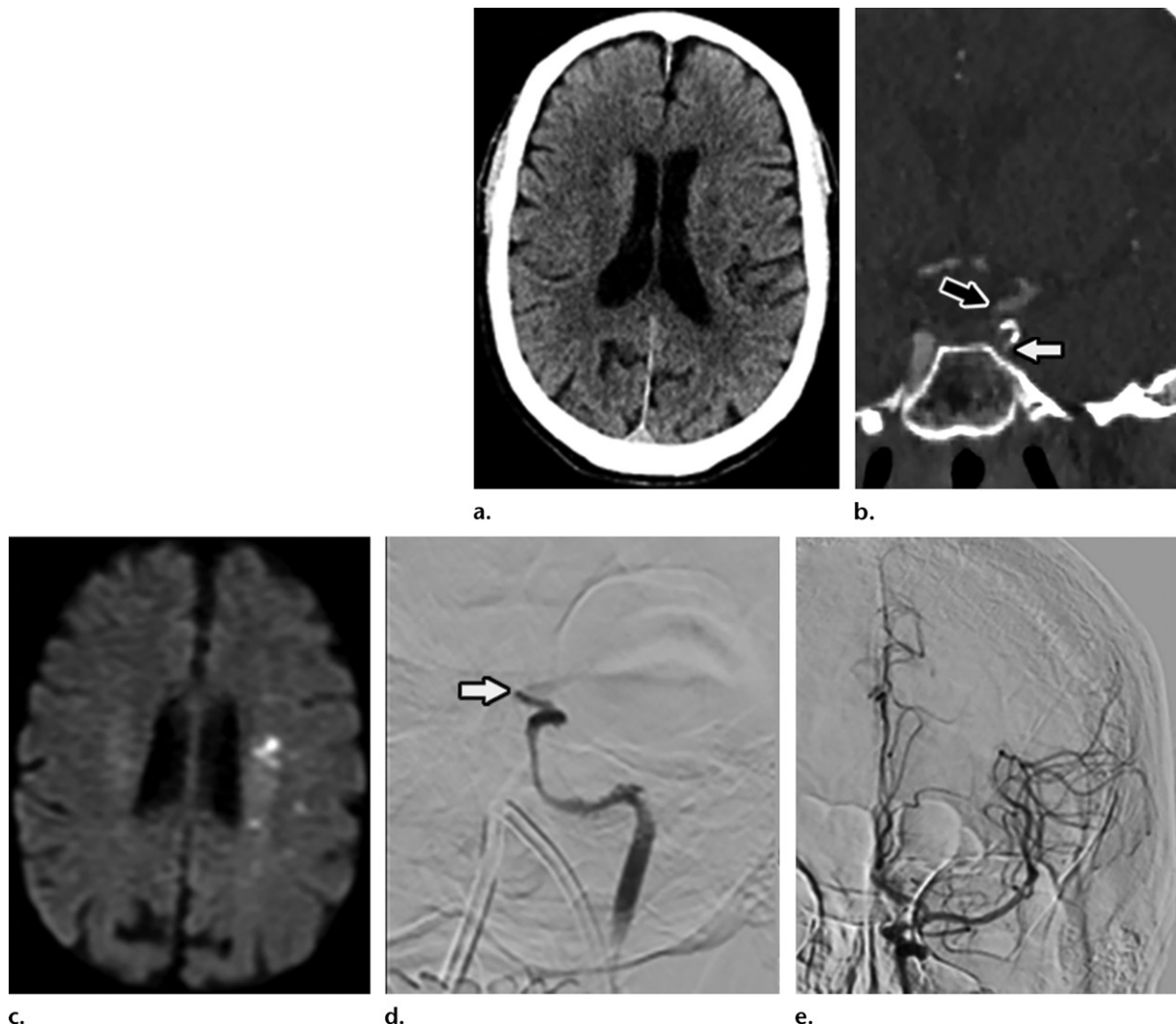


Figure 7. Use of MRI to determine ischemic core for EVT selection in late window in a 74-year-old man with right-sided weakness and baseline NIHSS score of 7. Time from onset to initial CT was 17 hours. **(a)** Axial nonenhanced CT image shows no infarction with ASPECTS of 10. **(b)** Coronal thin-section MIP CT angiogram shows complete occlusion of the petrocavernous and clinoid segments of the left internal carotid artery (white arrow) with reconstitution of flow at the carotid bifurcation (black arrow). The patient was transferred to our institution for possible mechanical thrombectomy. MRI was performed to determine the ischemic core. **(c)** Axial diffusion-weighted image shows multiple punctate border zone infarcts in the left hemisphere. **(d)** Coronal digital subtraction angiogram shows the occlusion of the left internal carotid artery (arrow). **(e)** Angiogram shows successful thrombectomy (TICI scale grade 2c). The patient was discharged with an NIHSS score of 0.

hours from onset). The treatment effect in this group favored the EVT group but did not reach statistical significance in this small group of patients. The 2018 AHA-ASA guidelines suggest that it may be reasonable to incorporate collateral flow status into clinical decision making in some candidates to determine eligibility for mechanical thrombectomy (level IIB). Additional trials are required to fully establish use of collateral flow status to determine eligibility for EVT (79).

Patient Subgroups with Limited Evidence

In this section, we highlight challenges in subgroups that were excluded from recent EVT trials

or in which there is not enough evidence to prove the efficacy of EVT.

Low NIHSS Score

Most thrombectomy trials used an NIHSS score threshold of greater than 6 as a selection criterion for determination of EVT candidacy. Only 14 of 1740 patients in the recent randomized controlled trials had a low baseline NIHSS score (≤ 5) (11,80). The discrepancy between having an LVO and a low NIHSS score less than 6 is often due to excellent collateral circulation. Although natural history data are limited, several studies suggest a poor outcome in this cohort due to later neurologic deterioration (81,82). Multiple nonrandomized studies have also suggested a

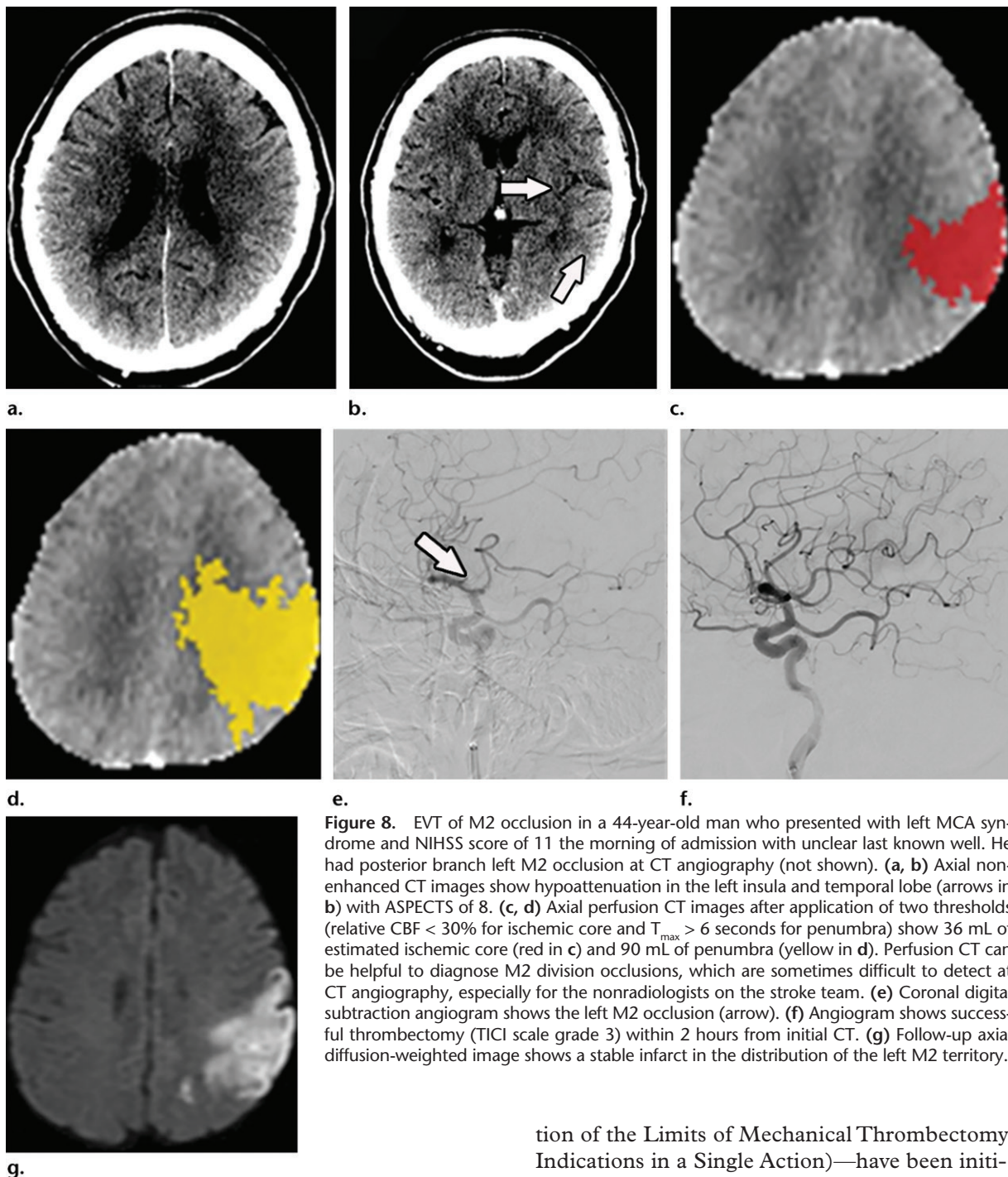


Figure 8. EVT of M2 occlusion in a 44-year-old man who presented with left MCA syndrome and NIHSS score of 11 the morning of admission with unclear last known well. He had posterior branch left M2 occlusion at CT angiography (not shown). (a, b) Axial non-enhanced CT images show hypoattenuation in the left insula and temporal lobe (arrows in b) with ASPECTS of 8. (c, d) Axial perfusion CT images after application of two thresholds (relative CBF < 30% for ischemic core and $T_{max} > 6$ seconds for penumbra) show 36 mL of estimated ischemic core (red in c) and 90 mL of penumbra (yellow in d). Perfusion CT can be helpful to diagnose M2 division occlusions, which are sometimes difficult to detect at CT angiography, especially for the nonradiologists on the stroke team. (e) Coronal digital subtraction angiogram shows the left M2 occlusion (arrow). (f) Angiogram shows successful thrombectomy (TICI scale grade 3) within 2 hours from initial CT. (g) Follow-up axial diffusion-weighted image shows a stable infarct in the distribution of the left M2 territory.

benefit of EVT in LVO patients with low NIHSS score (83).

Some centers perform CT angiography in all stroke patients, irrespective of baseline NIHSS score, thus identifying LVO patients with low NIHSS score, who could potentially benefit from immediate EVT rather than rescue thrombectomy later after neurologic deterioration (Fig 9). Two prospective randomized trials—ENDOLOW (Endovascular Therapy for Low NIHSS Ischemic Strokes) and MOSTE IN EXTREMIS (Minor Stroke Therapy Evaluation in Explora-

tion of the Limits of Mechanical Thrombectomy Indications in a Single Action)—have been initiated to compare immediate mechanical thrombectomy versus initial medical management in patients with AIS and low NIHSS score of 0–5 due to LVO. The results of these trials will likely provide more clarity regarding the benefit of EVT in this subgroup.

Distal Occlusion

Current data support EVT in patients with LVO including of the internal carotid artery (intra-cranial or extracranial) and MCA M1 segment. Patients with M2 occlusions were included in several trials (1–3,5); however, they were a minority. Post hoc HERMES analysis of EVT

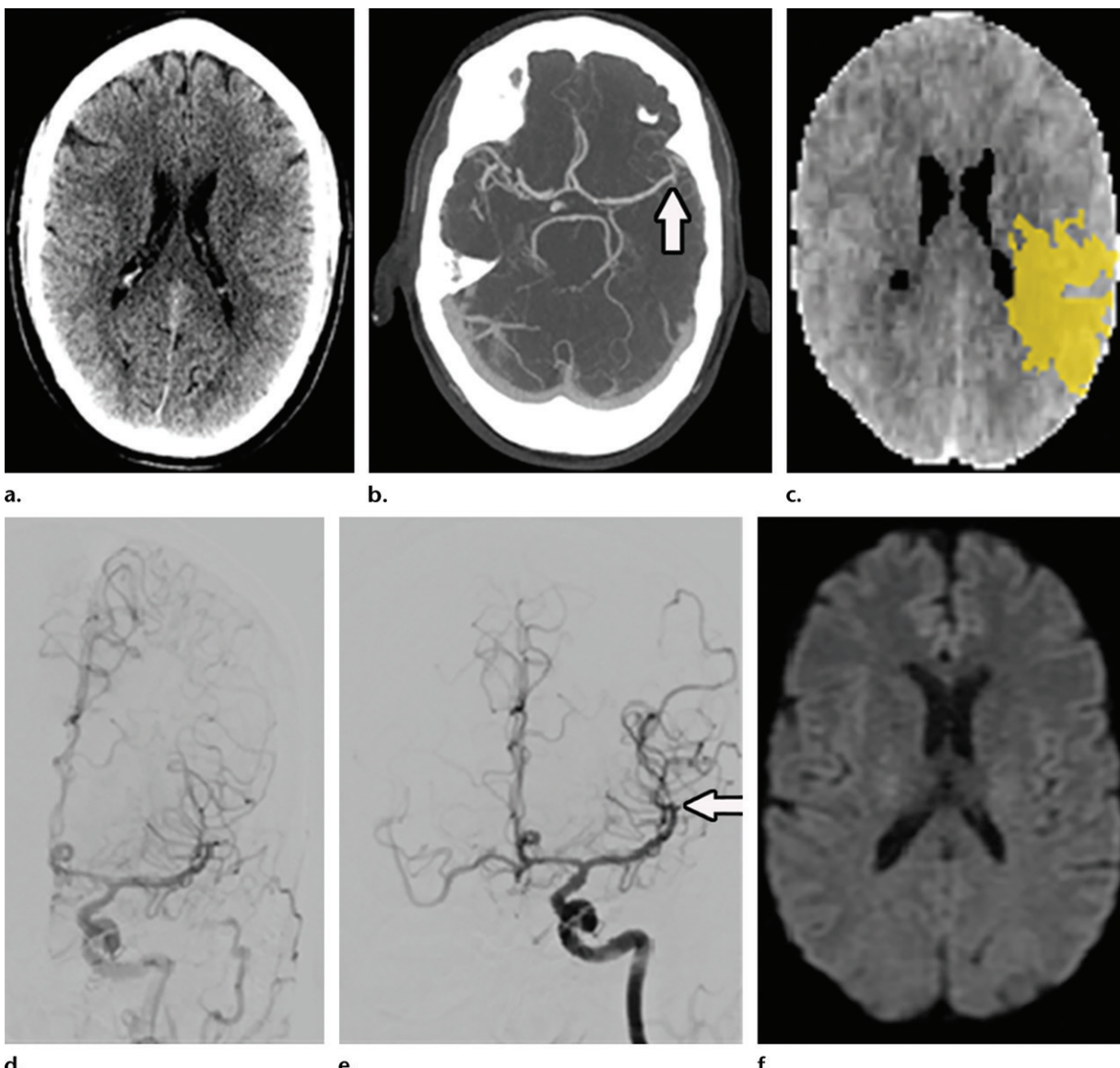


Figure 9. EVT of stroke with low NIHSS score in a 53-year-old man with aphasia and baseline NIHSS score of 1. Time from onset to CT was 2.5 hours. (a) Axial nonenhanced CT image shows normal ASPECTS of 10. (b) Axial CT angiogram shows left M2 occlusion (arrow). (c) Axial perfusion CT image after application of two thresholds (relative CBF < 30% for ischemic core and $T_{max} > 6$ seconds for penumbra) shows 56 mL of penumbra (yellow) with no detectable ischemic core. The patient received tissue plasminogen activator but had worsening aphasia 30 minutes later. (d) Coronal digital subtraction angiogram shows the left M2 occlusion. (e) Angiogram shows successful thrombectomy (TICI scale grade 2b) (arrow) within 3 hours from initial CT. (f) Follow-up axial diffusion-weighted image shows no restricted diffusion along the described distribution.

of M2 occlusions (67 of 818 patients vs 64 of 828 treated with medical therapy) showed better functional outcome in those treated with EVT, although the difference did not reach statistical significance (84). A sizable M2 occlusion (M1-like M2 occlusion) will likely benefit from EVT (85,86) (Figs 8, 9).

For more distal MCA occlusions, such as of M3, and anterior cerebral artery occlusions, consensus is lacking on the effectiveness and safety of EVT. As skill levels increase even further and devices become even safer, distal occlusions including M2 occlusions may become even more amenable to EVT.

Large Ischemic Core

Currently, there is no level I evidence on treating AIS patients with a large ischemic core, often defined as ASPECTS < 6 or ischemic core volume greater than 50–70 mL (Fig 10). However, growing evidence suggests that EVT may be beneficial in patients with a large ischemic core, including those with CT or MRI ASPECTS of 3–5 or estimated core volume greater than 50–70 mL at DWI or perfusion CT (87–89). Recent post hoc HERMES analyses, based on individual patient data from early-window trials, demonstrated improved outcome after EVT for the small subset of patients enrolled with large ischemic cores,

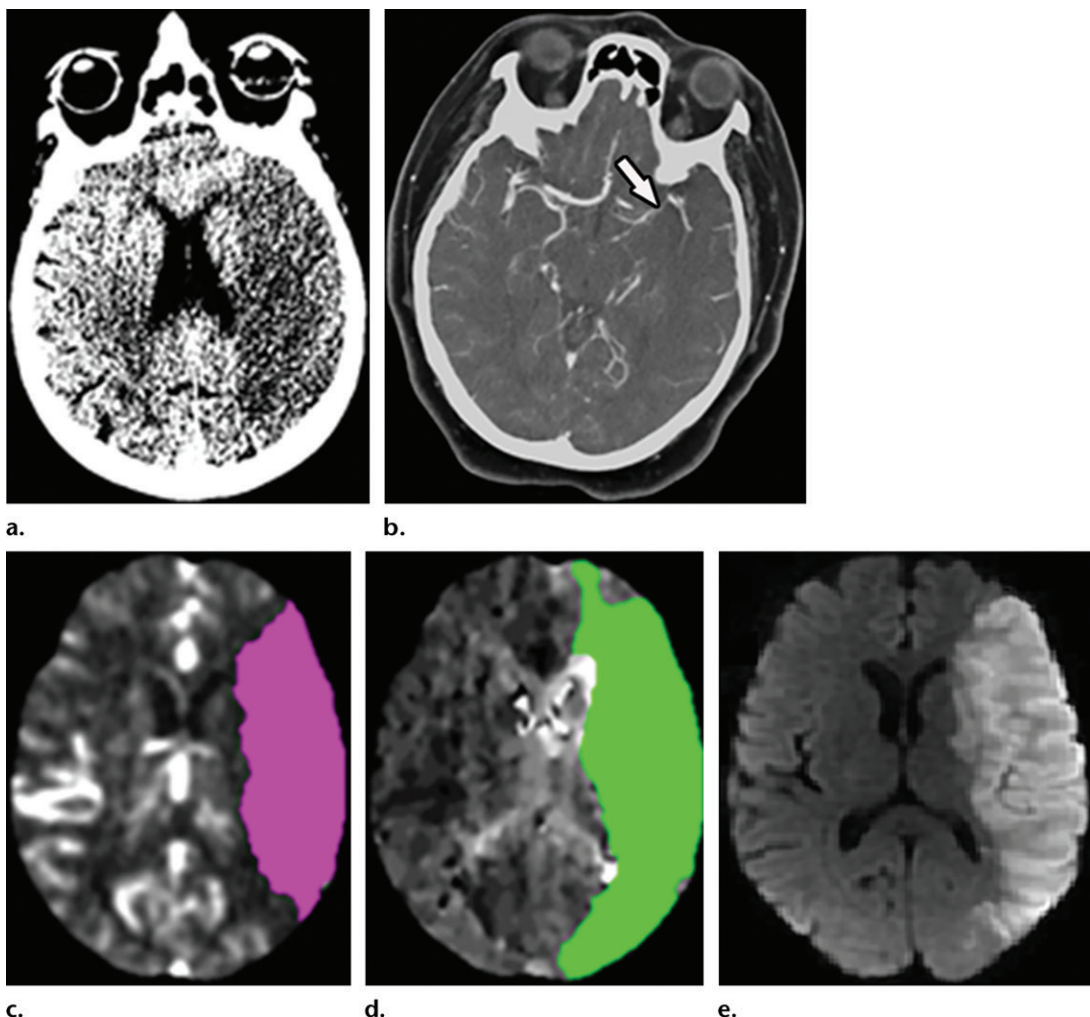


Figure 10. Large ischemic core with no EVT in a 68-year-old woman who presented with left MCA syndrome in the morning (wake-up stroke) and baseline NIHSS score of 14. (a) Axial nonenhanced CT image shows widespread hypotenuation and loss of gray-white matter differentiation throughout the left MCA distribution (ASPECTS of 3). (b) Axial CT angiogram shows M1 occlusion (arrow) and poor collaterals to the infarcted area. (c) Axial perfusion CT image after application of two thresholds (relative CBF < 30% for ischemic core and $T_{max} > 6$ seconds for penumbra) shows 71 mL of estimated ischemic core (purple). (d) Axial perfusion CT image after application of two thresholds (relative CBF < 30% for ischemic core and $T_{max} > 6$ seconds for penumbra) shows 122 mL of penumbra (green). EVT was not performed given the large core. (e) Follow-up axial diffusion-weighted image shows the final infarct, which involves almost the entire MCA distribution.

measured as ASPECTS < 6 and infarct greater than one-third of the MCA territory (84) and ischemic core greater than 70 mL at perfusion CT or MRI (90) (Fig 11).

Further randomized controlled trials are needed to determine whether advanced imaging paradigms using perfusion CT, CT angiography, perfusion MRI, and DWI, including measures of infarct core, collateral flow status, and penumbra, will be beneficial for selecting patients with large predicted cores. Results of the ongoing LASTE (Large Stroke Therapy Evaluation) IN EXTREMIS trial are likely to provide further data on this subset of patients. Another important factor to consider beyond the core volume is infarct topography and whether the predicted core involves eloquent cortex, again a fertile area for future research.

Posterior Circulation LVO

Posterior circulation LVOs are rare and represent only 5% of all LVOs (91–93). To our knowledge, there are no randomized controlled trials of EVT for acute stroke caused by posterior circulation LVO.

In the basilar artery, mechanical thrombectomy has been associated with lower recanalization rate and more procedural complications than in anterior circulation strokes (94,95). In a retrospective review of 24 basilar artery occlusions, successful recanalization was associated with a more favorable mRS (modified Rankin scale) score at 90 days (96). A meta-analysis of 31 studies summarizing 1358 patients with basilar artery occlusion who were treated with EVT and/or fibrinolysis failed to show sufficient evidence to make a

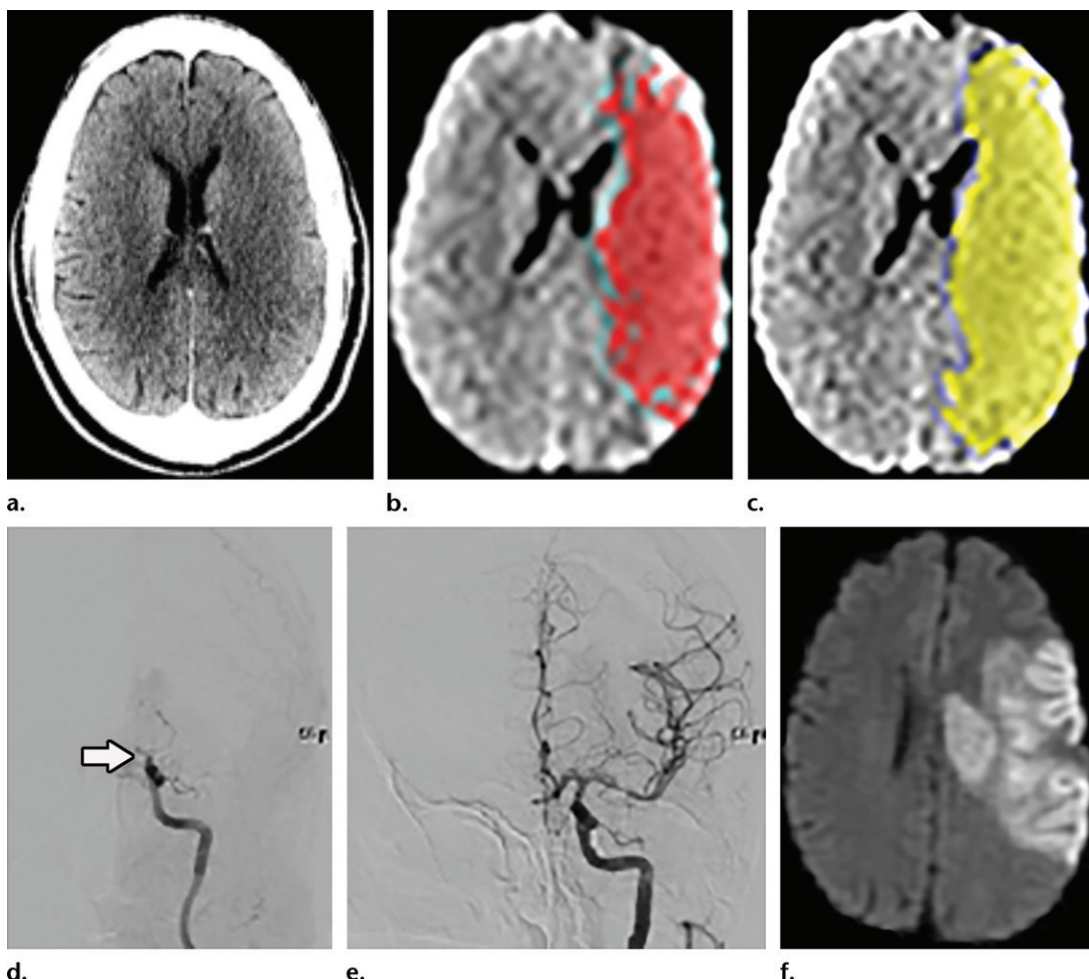


Figure 11. Large ischemic core treated with EVT in a 48-year-old man with left MCA syndrome and baseline NIHSS score of 26. Time from onset to CT was 4 hours. (a) Axial nonenhanced CT image shows an evolving acute infarct with ASPECTS of 5. (b, c) Axial perfusion CT images after application of two thresholds (relative CBF < 30% for ischemic core and $T_{max} > 6$ seconds for penumbra) show 72 mL of estimated ischemic core (red in b) and 122 mL of penumbra (yellow in c). Given the patient's young age, the decision was made to proceed with mechanical thrombectomy despite the large core. (d) Coronal digital subtraction angiogram shows left carotid terminus occlusion (arrow). (e) Angiogram shows successfully recanalization (TICI scale grade 3) within 97 minutes from initial CT. (f) Follow-up axial diffusion-weighted image shows the large infarct along the left MCA distribution.

management recommendation; however, the EVT group nonetheless had a significantly higher rate of independence (90-day mRS score, 0–2) than the group without EVT (95).

The primary results of the randomized Basilar Artery Occlusion Chinese Endovascular Trial (BEST, NCT02737189) were presented at the 2018 World Stroke Congress and suggested that patients treated with EVT achieved significantly better outcomes than patients treated with medical management alone. However, these results have not been published at this time. Currently, emergent EVT is reasonable for posterior circulation LVOs to maximize the chance of a good clinical outcome (AHA class IIa, level of evidence B-NR) (93).

LVO beyond 24 Hours

Experience with EVT of anterior circulation LVO after 24 hours is limited (97). The evidence

is insufficient to guide recommendations. Although there are evidence-based guidelines for imaging strategies for EVT selection, real-world practice regarding imaging paradigms varies substantially. A recent study surveying experts in the field including experienced vascular neurologists and neurointerventionalists highlighted this discordance (98). However, there is consensus that time is of paramount importance and that imaging needs to be efficient in terms of both performance and interpretation of results to give individual AIS patients the best chance for benefit from this powerful treatment.

Conclusion

In the era of endovascular therapy, advanced imaging plays a critical role in selection of patients with AIS for treatment. Consistent with current guidelines, nonenhanced CT and CT angiogra-

phy are likely sufficient for EVT selection in the early window (<6 hours). For the late window (6–24 hours), additional perfusion imaging (perfusion CT or DWI and perfusion MRI) is helpful to assess the ischemic core—and possibly the penumbra and mismatch—for treatment decision making. Subgroups of patients remain for whom evidence is lacking about optimal treatment, including those with low NIHSS score, large ischemic core, or distal occlusion. Regardless of the imaging modalities and strategies at individual institutions, efficient imaging workflow must be established to provide faster treatment.

Disclosures of Conflicts of Interest.—K.N. Activities related to the present article: disclosed no relevant relationships. Activities not related to the present article: board member for Olea Medical. Other activities: disclosed no relevant relationships. P.K. Activities related to the present article: disclosed no relevant relationships. Activities not related to the present article: consultant for Genentech, Lumosa Therapeutics, and NeuroSpring; grants from Nervive and Cerenovus. Other activities: disclosed no relevant relationships. A.V. Activities related to the present article: disclosed no relevant relationships. Activities not related to the present article: grants from Cerenovus and GE Healthcare. Other activities: disclosed no relevant relationships.

References

- Berkhemer OA, Fransen PS, Beumer D, et al. A randomized trial of intraarterial treatment for acute ischemic stroke. *N Engl J Med* 2015;372(1):11–20.
- Goyal M, Demchuk AM, Menon BK, et al. Randomized assessment of rapid endovascular treatment of ischemic stroke. *N Engl J Med* 2015;372(11):1019–1030.
- Jovin TG, Chamorro A, Cobo E, et al. Thrombectomy within 8 hours after symptom onset in ischemic stroke. *N Engl J Med* 2015;372(24):2296–2306.
- Saver JL, Goyal M, Bonafe A, et al. Stent-retriever thrombectomy after intravenous t-PA vs. t-PA alone in stroke. *N Engl J Med* 2015;372(24):2285–2295.
- Campbell BC, Mitchell PJ, Kleinig TJ, et al. Endovascular therapy for ischemic stroke with perfusion-imaging selection. *N Engl J Med* 2015;372(11):1009–1018.
- Bracard S, Ducrocq X, Mas JL, et al. Mechanical thrombectomy after intravenous alteplase versus alteplase alone after stroke (THRACE): a randomised controlled trial. *Lancet Neurol* 2016;15(11):1138–1147.
- Nogueira RG, Jadhav AP, Haussen DC, et al. Thrombectomy 6 to 24 Hours after Stroke with a Mismatch between Deficit and Infarct. *N Engl J Med* 2018;378(1):11–21.
- Albers GW, Marks MP, Kemp S, et al. Thrombectomy for Stroke at 6 to 16 Hours with Selection by Perfusion Imaging. *N Engl J Med* 2018;378(8):708–718.
- Powers WJ, Rabinstein AA, Ackerson T, et al. 2018 Guidelines for the Early Management of Patients With Acute Ischemic Stroke: A Guideline for Healthcare Professionals From the American Heart Association/American Stroke Association. *Stroke* 2018;49(3):e46–e110. [Published corrections appear in *Stroke* 2018;49(3):e138 and *Stroke* 2018;49(6):e233–e234.] <https://doi.org/10.1161/STR.0000000000000158>.
- Saver JL. Time is brain—quantified. *Stroke* 2006;37(1):263–266.
- Saver JL, Goyal M, van der Lugt A, et al. Time to Treatment With Endovascular Thrombectomy and Outcomes From Ischemic Stroke: A Meta-analysis. *JAMA* 2016;316(12):1279–1288.
- Lees KR, Emberson J, Blackwell L, et al. Effects of Alteplase for Acute Stroke on the Distribution of Functional Outcomes: A Pooled Analysis of 9 Trials. *Stroke* 2016;47(9):2373–2379.
- van Seeters T, Biessels GJ, Kappelle LJ, et al. The Prognostic Value of CT Angiography and CT Perfusion in Acute Ischemic Stroke. *Cerebrovasc Dis* 2015;40(5–6):258–269.
- Kim EY, Shin DH, Noh Y, Goh BH, Lee YB. Comparison of Imaging Selection Criteria for Intra-Arterial Thrombectomy in Acute Ischemic Stroke with Advanced CT. *Eur Radiol* 2016;26(9):2974–2981.
- Barber PA, Demchuk AM, Zhang J, Buchan AM; ASPECTS Study Group. Validity and reliability of a quantitative computed tomography score in predicting outcome of hyperacute stroke before thrombolytic therapy: Alberta Stroke Programme Early CT Score. *Lancet* 2000;355(9216):1670–1674.
- McTaggart RA, Jovin TG, Lansberg MG, et al. Alberta Stroke Program early computed tomographic scoring performance in a series of patients undergoing computed tomography and MRI: reader agreement, modality agreement, and outcome prediction. *Stroke* 2015;46(2):407–412.
- Kobkitsuksakul C, Tritanon O, Suraratdecha V. Interobserver agreement between senior radiology resident, neuroradiology fellow, and experienced neuroradiologist in the rating of Alberta Stroke Program Early Computed Tomography Score (ASPECTS). *Diagn Interv Radiol* 2018;24(2):104–107.
- Maegerlein C, Fischer J, Mönch S, et al. Automated Calculation of the Alberta Stroke Program Early CT Score: Feasibility and Reliability. *Radiology* 2019;291(1):141–148.
- Menon BK, Demchuk AM. Computed Tomography Angiography in the Assessment of Patients With Stroke/TIA. *Neurohospitalist* 2011;1(4):187–199.
- Goyal M, Menon BK, Hill MD, Demchuk A. Consistently achieving computed tomography to endovascular recanalization <90 minutes: solutions and innovations. *Stroke* 2014;45(12):e252–e256.
- Srinivasan A, Goyal M, Al Azri F, Lum C. State-of-the-art imaging of acute stroke. *RadioGraphics* 2006;26(suppl 1):S75–S95.
- Heiss WD. Flow thresholds of functional and morphological damage of brain tissue. *Stroke* 1983;14(3):329–331.
- Murphy BD, Fox AJ, Lee DH, et al. Identification of penumbra and infarct in acute ischemic stroke using computed tomography perfusion-derived blood flow and blood volume measurements. *Stroke* 2006;37(7):1771–1777.
- Campbell BC, Christensen S, Levi CR, et al. Cerebral blood flow is the optimal CT perfusion parameter for assessing infarct core. *Stroke* 2011;42(12):3435–3440.
- Cereda CW, Christensen S, Campbell BCV, et al. A benchmarking tool to evaluate computer tomography perfusion infarct core predictions against a DWI standard. *J Cereb Blood Flow Metab* 2016;36(10):1780–1789.
- Bivard A, McElduff P, Spratt N, Levi C, Parsons M. Defining the extent of irreversible brain ischemia using perfusion computed tomography. *Cerebrovasc Dis* 2011;31(3):238–245.
- Lin L, Bivard A, Krishnamurthy V, Levi CR, Parsons MW. Whole-Brain CT Perfusion to Quantify Acute Ischemic Penumbra and Core. *Radiology* 2016;279(3):876–887.
- Fiebach JB, Schellinger PD, Gass A, et al. Stroke magnetic resonance imaging is accurate in hyperacute intracerebral hemorrhage: a multicenter study on the validity of stroke imaging. *Stroke* 2004;35(2):502–506.
- Hjort N, Christensen S, Sølling C, et al. Ischemic injury detected by diffusion imaging 11 minutes after stroke. *Ann Neurol* 2005;58(3):462–465.
- Chalela JA, Kidwell CS, Nentwich LM, et al. Magnetic resonance imaging and computed tomography in emergency assessment of patients with suspected acute stroke: a prospective comparison. *Lancet* 2007;369(9558):293–298.
- Schaefer PW, Hassankhani A, Putman C, et al. Characterization and evolution of diffusion MR imaging abnormalities in stroke patients undergoing intra-arterial thrombolysis. *AJNR Am J Neuroradiol* 2004;25(6):951–957.
- Dardzinski BJ, Sotak CH, Fisher M, Hasegawa Y, Li L, Minematsu K. Apparent diffusion coefficient mapping of experimental focal cerebral ischemia using diffusion-weighted echo-planar imaging. *Magn Reson Med* 1993;30(3):318–325.
- Nael K, Meshksar A, Liebeskind DS, et al. Periprocedural arterial spin labeling and dynamic susceptibility contrast

- perfusion in detection of cerebral blood flow in patients with acute ischemic syndrome. *Stroke* 2013;44(3):664–670.
- 34. Verma RK, Kottke R, Anderegg L, et al. Detecting subarachnoid hemorrhage: comparison of combined FLAIR/SWI versus CT. *Eur J Radiol* 2013;82(9):1539–1545.
 - 35. Wheeler HM, Mlynash M, Inoue M, et al. Early diffusion-weighted imaging and perfusion-weighted imaging lesion volumes forecast final infarct size in DEFUSE 2. *Stroke* 2013;44(3):681–685.
 - 36. Copen WA, Morais LT, Wu O, et al. In Acute Stroke, Can CT Perfusion-Derived Cerebral Blood Volume Maps Substitute for Diffusion-Weighted Imaging in Identifying the Ischemic Core? *PLoS One* 2015;10(7):e0133566.
 - 37. Bandera E, Botteri M, Minelli C, Sutton A, Abrams KR, Latronico N. Cerebral blood flow threshold of ischemic penumbra and infarct core in acute ischemic stroke: a systematic review. *Stroke* 2006;37(5):1334–1339.
 - 38. Schaefer PW, Souza L, Kamalian S, et al. Limited reliability of computed tomographic perfusion acute infarct volume measurements compared with diffusion-weighted imaging in anterior circulation stroke. *Stroke* 2015;46(2):419–424.
 - 39. Geuskens RR, Borst J, Lucas M, et al. Characteristics of Misclassified CT Perfusion Ischemic Core in Patients with Acute Ischemic Stroke. *PLoS One* 2015;10(11):e0141571.
 - 40. Sheth KN, Terry JB, Nogueira RG, et al. Advanced modality imaging evaluation in acute ischemic stroke may lead to delayed endovascular reperfusion therapy without improvement in clinical outcomes. *J Neurointerv Surg* 2013;5(suppl 1):i62–i65.
 - 41. Ma H, Parsons MW, Christensen S, et al. A multicentre, randomized, double-blinded, placebo-controlled phase III study to investigate EXtending the time for Thrombolysis in Emergency Neurological Deficits (EXTEND). *Int J Stroke* 2012;7(1):74–80.
 - 42. Nael K, Khan R, Choudhary G, et al. Six-minute magnetic resonance imaging protocol for evaluation of acute ischemic stroke: pushing the boundaries. *Stroke* 2014;45(7):1985–1991.
 - 43. Thomalla G, Simonsen CZ, Boutitie F, et al. MRI-Guided Thrombolysis for Stroke with Unknown Time of Onset. *N Engl J Med* 2018;379(7):611–622.
 - 44. Schwamm LH, Wu O, Song SS, et al. Intravenous thrombolysis in unwitnessed stroke onset: MR WITNESS trial results. *Ann Neurol* 2018;83(5):980–993.
 - 45. Ma H, Campbell BCV, Parsons MW, et al. Thrombolysis Guided by Perfusion Imaging up to 9 Hours after Onset of Stroke. *N Engl J Med* 2019;380(19):1795–1803.
 - 46. Menon BK, O'Brien B, Bivard A, et al. Assessment of leptomeningeal collaterals using dynamic CT angiography in patients with acute ischemic stroke. *J Cereb Blood Flow Metab* 2013;33(3):365–371.
 - 47. Lima FO, Furie KL, Silva GS, et al. The pattern of leptomeningeal collaterals on CT angiography is a strong predictor of long-term functional outcome in stroke patients with large vessel intracranial occlusion. *Stroke* 2010;41(10):2316–2322.
 - 48. Hernández-Pérez M, Puig J, Blasco G, et al. Dynamic Magnetic Resonance Angiography Provides Collateral Circulation and Hemodynamic Information in Acute Ischemic Stroke. *Stroke* 2016;47(2):531–534.
 - 49. Ernst M, Forkert ND, Brehmer L, et al. Prediction of infarction and reperfusion in stroke by flow- and volume-weighted collateral signal in MR angiography. *AJR Am J Neuroradiol* 2015;36(2):275–282.
 - 50. Souza LC, Yoo AJ, Chaudhry ZA, et al. Malignant CTA collateral profile is highly specific for large admission DWI infarct core and poor outcome in acute stroke. *AJR Am J Neuroradiol* 2012;33(7):1331–1336.
 - 51. Tong E, Patric J, Tong S, et al. Time-resolved CT assessment of collaterals as imaging biomarkers to predict clinical outcomes in acute ischemic stroke. *Neuroradiology* 2017;59(11):1101–1109.
 - 52. Tan IY, Demchuk AM, Hopyan J, et al. CT angiography clot burden score and collateral score: correlation with clinical and radiologic outcomes in acute middle cerebral artery infarct. *AJR Am J Neuroradiol* 2009;30(3):525–531.
 - 53. Tan JC, Dillon WP, Liu S, Adler F, Smith WS, Wintermark M. Systematic comparison of perfusion-CT and CT-angiography in acute stroke patients. *Ann Neurol* 2007;61(6):533–543.
 - 54. Maas MB, Lev MH, Ay H, et al. Collateral vessels on CT angiography predict outcome in acute ischemic stroke. *Stroke* 2009;40(9):3001–3005.
 - 55. Menon BK, d'Esterre CD, Qazi EM, et al. Multiphase CT Angiography: A New Tool for the Imaging Triage of Patients with Acute Ischemic Stroke. *Radiology* 2015;275(2):510–520.
 - 56. van den Wijngaard IR, Holswilder G, Wermer MJ, et al. Assessment of Collateral Status by Dynamic CT Angiography in Acute MCA Stroke: Timing of Acquisition and Relationship with Final Infarct Volume. *AJNR Am J Neuroradiol* 2016;37(7):1231–1236.
 - 57. van den Wijngaard IR, Boiten J, Holswilder G, et al. Impact of Collateral Status Evaluated by Dynamic Computed Tomographic Angiography on Clinical Outcome in Patients With Ischemic Stroke. *Stroke* 2015;46(12):3398–3404.
 - 58. Schregel K, Tsogkas I, Peter C, et al. Outcome Prediction Using Perfusion Parameters and Collateral Scores of Multi-Phase and Single-Phase CT Angiography in Acute Stroke: Need for One, Two, Three, or Thirty Scans? *J Stroke* 2018;20(3):362–372.
 - 59. Yang JJ, Hill MD, Morrish WF, et al. Comparison of pre- and postcontrast 3D time-of-flight MR angiography for the evaluation of distal intracranial branch occlusions in acute ischemic stroke. *AJR Am J Neuroradiol* 2002;23(4):557–567.
 - 60. Menon BK, Qazi E, Nambiar V, et al. Differential Effect of Baseline Computed Tomographic Angiography Collaterals on Clinical Outcome in Patients Enrolled in the Interventional Management of Stroke III Trial. *Stroke* 2015;46(5):1239–1244.
 - 61. Shuaib A, Butcher K, Mohammad AA, Saqqur M, Liebeskind DS. Collateral blood vessels in acute ischaemic stroke: a potential therapeutic target. *Lancet Neurol* 2011;10(10):909–921.
 - 62. Wintermark M, Rowley HA, Lev MH. Acute stroke triage to intravenous thrombolysis and other therapies with advanced CT or MR imaging: pro CT. *Radiology* 2009;251(3):619–626.
 - 63. Campbell BC, Christensen S, Tress BM, et al. Failure of collateral blood flow is associated with infarct growth in ischemic stroke. *J Cereb Blood Flow Metab* 2013;33(8):1168–1172.
 - 64. Nael K, Doshi A, De Leacy R, et al. MR Perfusion to Determine the Status of Collaterals in Patients with Acute Ischemic Stroke: A Look Beyond Time Maps. *AJR Am J Neuroradiol* 2018;39(2):219–225.
 - 65. Nannoni S, Cereda CW, Sirimarco G, et al. Collaterals are a major determinant of the core but not the penumbra volume in acute ischemic stroke. *Neuroradiology* 2019 May 23 [Epub ahead of print].
 - 66. Arenillas JF, Cortijo E, García-Bermejo P, et al. Relative cerebral blood volume is associated with collateral status and infarct growth in stroke patients in SWIFT PRIME. *J Cereb Blood Flow Metab* 2018;38(10):1839–1847. [Published correction appears in *J Cereb Blood Flow Metab* 2018 Mar 9:271678X18765354.] <https://doi.org/10.1177/0271678X17740293>.
 - 67. Krolikowski A, Dzialowski I, Roy J, et al. Incidence of radiocontrast nephropathy in patients undergoing acute stroke computed tomography angiography. *Stroke* 2007;38(8):2364–2366. [Published correction appears in *Stroke* 2007;38(9):e97.] <https://doi.org/10.1161/STROKEAHA.107.482778>.
 - 68. Ehrlich ME, Turner HL, Currie LJ, Wintermark M, Worrall BB, Southerland AM. Safety of Computed Tomographic Angiography in the Evaluation of Patients With Acute Stroke: A Single-Center Experience. *Stroke* 2016;47(8):2045–2050.
 - 69. Lima FO, Lev MH, Levy RA, et al. Functional contrast-enhanced CT for evaluation of acute ischemic stroke does not increase the risk of contrast-induced nephropathy. *AJR Am J Neuroradiol* 2010;31(5):817–821.
 - 70. Correction to: 2018 Guidelines for the Early Management of Patients With Acute Ischemic Stroke: A Guideline for Healthcare Professionals From the American Heart Association/American Stroke Association. *Stroke* 2018;49(6):e233–e234.

71. Ribo M, Molina CA, Cobo E, et al. Association Between Time to Reperfusion and Outcome Is Primarily Driven by the Time From Imaging to Reperfusion. *Stroke* 2016;47(4):999–1004.
72. Fransen PS, Berkhemer OA, Lingsma HF, et al. Time to Reperfusion and Treatment Effect for Acute Ischemic Stroke: A Randomized Clinical Trial. *JAMA Neurol* 2016;73(2):190–196.
73. Haussen DC, Dehkhanghani S, Rangaraju S, et al. Automated CT Perfusion Ischemic Core Volume and Noncontrast CT ASPECTS (Alberta Stroke Program Early CT Score): Correlation and Clinical Outcome Prediction in Large Vessel Stroke. *Stroke* 2016;47(9):2318–2322.
74. Kudo K, Sasaki M, Yamada K, et al. Differences in CT perfusion maps generated by different commercial software: quantitative analysis by using identical source data of acute stroke patients. *Radiology* 2010;254(1):200–209.
75. Desai SM, Rocha M, Molyneaux BJ, et al. Thrombectomy 6–24 hours after stroke in trial ineligible patients. *J Neurointerv Surg* 2018;10(11):1033–1037.
76. Liebeskind DS, Jahan R, Nogueira RG, Zaidat OO, Saver JL; SWIFT Investigators. Impact of collaterals on successful revascularization in Solitaire FR with the intention for thrombectomy. *Stroke* 2014;45(7):2036–2040.
77. Bang OY, Saver JL, Buck BH, et al. Impact of collateral flow on tissue fate in acute ischaemic stroke. *J Neurol Neurosurg Psychiatry* 2008;79(6):625–629.
78. Vagal A, Aviv R, Sucharew H, et al. Collateral Clock Is More Important Than Time Clock for Tissue Fate. *Stroke* 2018;49(9):2102–2107.
79. Amiri H, Bluhmki E, Bendszus M, et al. European Cooperative Acute Stroke Study-4: EXTending the time for Thrombolysis in Emergency Neurological Deficits ECASS-4—ExTEND. *Int J Stroke* 2016;11(2):260–267.
80. Goyal M, Menon BK, van Zwam WH, et al. Endovascular thrombectomy after large-vessel ischaemic stroke: a meta-analysis of individual patient data from five randomised trials. *Lancet* 2016;387(10029):1723–1731.
81. Haussen DC, Lima FO, Bouslama M, et al. Thrombectomy versus medical management for large vessel occlusion strokes with minimal symptoms: an analysis from STOPStroke and GESTOR cohorts. *J Neurointerv Surg* 2018;10(4):325–329.
82. Dargazanli C, Arquizan C, Gory B, et al. Mechanical Thrombectomy for Minor and Mild Stroke Patients Harboring Large Vessel Occlusion in the Anterior Circulation: A Multicenter Cohort Study. *Stroke* 2017;48(12):3274–3281.
83. Nagel S, Bouslama M, Krause LU, et al. Mechanical Thrombectomy in Patients With Milder Strokes and Large Vessel Occlusions. *Stroke* 2018;49(10):2391–2397.
84. Román LS, Menon BK, Blasco J, et al. Imaging features and safety and efficacy of endovascular stroke treatment: a meta-analysis of individual patient-level data. *Lancet Neurol* 2018;17(10):895–904.
85. Sarraj A, Sangha N, Hussain MS, et al. Endovascular Therapy for Acute Ischemic Stroke With Occlusion of the Middle Cerebral Artery M2 Segment. *JAMA Neurol* 2016;73(11):1291–1296.
86. Coutinho JM, Liebeskind DS, Slater LA, et al. Mechanical Thrombectomy for Isolated M2 Occlusions: A Post Hoc Analysis of the STAR, SWIFT, and SWIFT PRIME Studies. *AJNR Am J Neuroradiol* 2016;37(4):667–672.
87. Gilgen MD, Klimek D, Liesirova KT, et al. Younger Stroke Patients With Large Pretreatment Diffusion-Weighted Imaging Lesions May Benefit From Endovascular Treatment. *Stroke* 2015;46(9):2510–2516.
88. Mourand I, Abergel E, Mantilla D, et al. Favorable revascularization therapy in patients with ASPECTS \leq 5 on DWI in anterior circulation stroke. *J Neurointerv Surg* 2018;10(1):5–9.
89. Rebello LC, Bouslama M, Haussen DC, et al. Endovascular Treatment for Patients With Acute Stroke Who Have a Large Ischemic Core and Large Mismatch Imaging Profile. *JAMA Neurol* 2017;74(1):34–40.
90. Campbell BCV, Majoe CBLM, Albers GW, et al. Penumbral imaging and functional outcome in patients with anterior circulation ischaemic stroke treated with endovascular thrombectomy versus medical therapy: a meta-analysis of individual patient-level data. *Lancet Neurol* 2019;18(1):46–55.
91. Greving JP, Schonewille WJ, Wijman CA, et al. Predicting outcome after acute basilar artery occlusion based on admission characteristics. *Neurology* 2012;78(14):1058–1063.
92. Mattle HP, Arnold M, Lindsberg PJ, Schonewille WJ, Schroth G. Basilar artery occlusion. *Lancet Neurol* 2011;10(11):1002–1014.
93. Kayan Y, Meyers PM, Prestigiacomo CJ, Kan P, Fraser JF; Society of NeuroInterventional Surgery. Current endovascular strategies for posterior circulation large vessel occlusion stroke: report of the Society of NeuroInterventional Surgery Standards and Guidelines Committee. *J Neurointerv Surg* 2019 May 18 [Epub ahead of print]. <https://doi.org/10.1136/neurintsurg-2019-014873>.
94. Alonso de Leciñana M, Kawiorski MM, Ximénez-Carrillo Á, et al. Mechanical thrombectomy for basilar artery thrombosis: a comparison of outcomes with anterior circulation occlusions. *J Neurointerv Surg* 2017;9(12):1173–1178.
95. Wyszomirski A, Szczyrba S, Tomaka D, Karaszewski B. Treatment of acute basilar artery occlusion: systematic review and meta-analysis. *Neurol Neurochir Pol* 2017;51(6):486–496.
96. Hu SY, Yi HJ, Lee DH, Hong JT, Sung JH, Lee SW. Effectiveness and Safety of Mechanical Thrombectomy with Stent Retrievers in Basilar Artery Occlusion: Comparison with Anterior Circulation Occlusions. *J Korean Neurosurg Soc* 2017;60(6):635–643.
97. Desai SM, Haussen DC, Aghaebrahim A, et al. Thrombectomy 24 hours after stroke: beyond DAWN. *J Neurointerv Surg* 2018;10(11):1039–1042.
98. Fisher M, Goyal M. Variance of Imaging Protocols for Patients With Suspected Acute Ischemic Stroke Because of Large-Vessel Occlusion. *Stroke* 2018;49(8):1805–1808.

Invited Commentary on "Imaging-based Selection for Endovascular Treatment in Stroke"

From:

Thabele M. Leslie-Mazwi, MD

Departments of Neurology and Neurosurgery, Massachusetts General Hospital, Harvard Medical School
Boston, Massachusetts

In the preceding article, Nael and colleagues (1) present a broad and excellent review of current imaging recommendations for EVT selection in acute stroke, using as their basis the 2018 AHA-ASA Guidelines for the Early Management of Patients with Acute Ischemic Stroke (2). These guidelines generated some controversy on their release. This was predominantly (in this author's opinion) because they were produced as a strictly evidence-based document, as opposed to one based on a combination of evidence and expert consensus. This represented a change from prior AHA-ASA guidelines.

By hewing to the evidence-based principle, the 2018 acute stroke guidelines reflect what we know, how well we know it, and what we need to learn in acute stroke. However, clinical evaluation and treatment require a pragmatic approach that may merge multiple sources of evidence. Imaging plays a central role in this, and one that continues to evolve.

Always critical, the role of imaging in treatment selection has gained newfound prominence. Driving this is a renewed vigor in stroke treatment heralded by the ability to recanalize LVO stroke using highly efficient thrombectomy tools. The potential benefit of effective widespread LVO treatment at a societal level is tremendous: LVO contributes the vast majority of disability and death in stroke (3) and represents a huge financial health care burden. Therefore, identifying treatment candidates is a care imperative. Our imaging selection should rapidly and accurately identify patients with target lesions and exclude those who may be harmed by treatment.

The two prevailing imaging modalities in EVT selection for stroke are CT and MRI. The superiority of MRI in providing detailed tissue information in stroke is beyond dispute. The quality of vessel imaging (time-of-flight imaging with the advantage of no contrast material or contrast-enhanced imaging) is less robust. However, as discussed by Nael et al (1), the tissue imaging precision of MRI comes at a cost, in time, candidacy (aggressive prescreening is required), and logistics. Focus on process can accelerate MRI times to approximate CT times

(4), but no direct randomized head-to-head comparisons exist of the two imaging modalities.

CT as a modality is demonstrably sufficient for identifying EVT candidates, despite concerns about imprecision and the variability inherent in modern perfusion imaging. CT-based selection paradigms also possess a range of advantages, including widespread availability and candidacy, fast image acquisition, more options for automated processing, and excellent vessel resolution. Unsurprisingly, therefore, CT is what Nael et al (1) refer to as the workhorse of stroke treatment selection.

Imaging-based treatment selection consumes time. Time is brain (5). Therefore, a balance needs to be struck between the information required for decisions to be made and the time taken to acquire that information. The impact of the time consumed by imaging-based treatment selection is different in the early and late treatment windows. On the basis of the HERMES data, that distinction normally occurs at 6 hours from time last known well (6).

In the early window, candidacy is broad and CT and CT angiography suffice for most treatment decisions, with a wide net cast; speed is prioritized over precision. This balance shifts in later treatment windows. To maintain a treatment effect in late windows, data suggest that greater precision in patient selection is required. At those later time points, besides identifying LVO, the volume of affected tissue must be measured.

In this, we are guided by evidence from DEFUSE 3 (7) and DAWN (8), the randomized late-window trials. DEFUSE 3 was a more permissive trial than DAWN, using a higher established core infarct volume across all age categories but measuring the volume of penumbra instead of inferring it from the patient's clinical deficit. Given the maintained clinical effect in the DEFUSE 3 non-DAWN population (9), it is likely that more permissive criteria are reasonable for treatment selection in later windows.

EVT chosen with currently defined imaging-based selection has a dramatic effect on patient functional outcomes. With the remarkable treatment effects and astonishingly low NNT (number needed to treat) values of the recent

trials (10), a sound argument can be made for expansion of treatment and therefore less selective imaging paradigms. What reasons would lead us to be restrictive in application of this incredibly powerful therapeutic intervention for these incredibly at-risk patients?

The first is patient harm. Permissive imaging-based selection approaches could result in treatment of patients at risk for injury (eg, those with large necrotic infarct cores at risk for reperfusion hemorrhage). However, to my knowledge, no data are currently available that indicate that any contemporary selection paradigm investigated by the recent randomized trials leads to patient harm. In fact, mortality and hemorrhagic complications were similar and statistically insignificant in the endovascular and medical treatment arms in all recent trials. Even in the least selective trials (MR CLEAN, THRACE, and REVASCAT) (11–13), there was no increase in harm.

The second rationale for restriction is absence of benefit or—applying different terminology—cost-effectiveness. If multiple patients are treated with minimal or no improvement in the majority, is the treatment still cost-effective? What is an acceptable NNT if we worry that an NNT of 3 is overly selective? The cost of protracted and severe disability is high, weighting this consideration in favor of intervention, despite the cost of thrombectomy devices and treatment requirements (14).

Considering both of these concerns, there seems to be a strong rationale for expanding imaging and clinical inclusion criteria for LVO patients. Trials are actively assessing this point. Nael et al (1) explore this in their discussion of the current fringes of thrombectomy: LVO patients with low NIHSS score, pretreatment large core infarcts, or more distal occlusions. It seems likely that expansion of candidacy into one of these domains is imminent. Perhaps the most tantalizing possibility is EVT of patients with established large core infarcts.

LVO patients with existing large core infarcts at imaging are currently excluded from most EVT. They represent the majority of LVO patients not offered thrombectomy. However, the potential for benefit is being assessed in at least two active trials discussed by Nael et al (1). Benefit for this group may look different from the conventional independent functional outcome that benchmarks stroke treatment trials.

For instance, reduction in mortality or severe disability may be a treatment goal worth pursuing, if more moderate degrees of disability are acceptable. If EVT of patients with large established core infarcts demonstrates benefit, as many suspect, imaging-based selection paradigms will

play a central role in helping to prove this and will need to evolve further clinically in response. For instance, we may see simplification of imaging needs.

Regardless of horizons to come, the simple issue of workflow presents a contemporary challenge, as Nael et al (1) emphasize. LVO is a disease of exquisite time sensitivity (15). Despite the evidence that in later windows treatment candidates can still be identified, treatment must be delivered as rapidly as possible. Irrespective of the imaging paradigm chosen, the process by which the patient is imaged must be as streamlined as possible. Preparation for and performance of imaging and interpretation of the results has the potential for significant loss of time.

Achieving speed involves a critical evaluation of existing processes, reduction of required process steps, parallel processing wherever possible, and adherence to protocols. Ongoing data collection, review, and improvement allow further refinements to be made. The recommendation in the AHA-ASA guidelines to proceed to CT angiography without waiting for measurements of serum creatinine level is a stellar example of saving time by reducing unnecessary process steps (2).

Finally, as we consider imaging-based selection for EVT and LVO patients, we must consider it at the level of systems. The imperative to identify LVO patients holds true across the entire spectrum of stroke care. In the prehospital space, this has taken the form of mobile stroke units (some of which have attempted CT angiography in the field) and a variety of prehospital technologies for detecting hemispheric asymmetry as a possible clue to LVO (16). These prehospital imaging modalities augment the clinical examination to aid in selecting patients for EVT. The ability to make this determination accurately in the field has implications for triage, including the possibility of bypass to thrombectomy-capable centers.

Many patients present first to centers without thrombectomy capability. For these individuals, CT angiography allows local imaging-based selection before subsequent transfer for EVT (17). Such paradigms shift imaging triage for possible LVO patients to the referring hospital, minimizing futile transfers. In the current era of late-window treatment with expanded numbers of patients to screen, this becomes especially important. At the level of thrombectomy-capable centers, more advanced imaging (eg, for evidence-based identification of late-window treatment candidates) is now a system-of-care expectation. Tremendous gains remain to be realized by coordinated delivery of stroke care at a system level.

Acute stroke care is in the midst of a renaissance, driven by efficient EVT techniques for LVO patients. Imaging-based selection has catalyzed this renaissance through accurate identification of LVO patients, as elegantly described by Nael and colleagues (1). Without a doubt, it will continue to play a central role in the exciting future evolution of the field of stroke care.

References

- Nael K, Sakai Y, Khatri P, Prestigiacomo CJ, Puig J, Vagal A. Imaging-based selection for endovascular treatment in stroke. *RadioGraphics* 2019;39(6):1696–1713.
- Powers WJ, Rabinstein AA, Ackerson T, et al. 2018 guidelines for the early management of patients with acute ischemic stroke: a guideline for healthcare professionals from the American Heart Association/American Stroke Association. *Stroke* 2018;49(3):e46–e110. [Published corrections appear in *Stroke* 2018;49(3):e138 and *Stroke* 2018;49(6):e233–e234.] <https://doi.org/10.1161/STR.0000000000000158>.
- Malhotra K, Gornbein J, Saver JL. Ischemic strokes due to large-vessel occlusions contribute disproportionately to stroke-related dependence and death: a review. *Front Neurol* 2017;8:651.
- Simonsen CZ, Yoo AJ, Rasmussen M, et al. Magnetic resonance imaging selection for endovascular stroke therapy: workflow in the GOLIATH trial. *Stroke* 2018;49(6):1402–1406.
- Desai SM, Rocha M, Jovin TG, Jadhav AP. High variability in neuronal loss. *Stroke* 2019;50(1):34–37.
- Goyal M, Menon BK, van Zwam WH, et al. Endovascular thrombectomy after large-vessel ischaemic stroke: a meta-analysis of individual patient data from five randomised trials. *Lancet* 2016;387(10029):1723–1731.
- Albers GW, Marks MP, Kemp S, et al. Thrombectomy for stroke at 6 to 16 hours with selection by perfusion imaging. *N Engl J Med* 2018;378(8):708–718.
- Nogueira RG, Jadhav AP, Hassen DC, et al. Thrombectomy 6 to 24 hours after stroke with a mismatch between deficit and infarct. *N Engl J Med* 2018;378(1):11–21.
- Leslie-Mazwi TM, Hamilton S, Mlynash M, et al. DEFUSE 3 non-DAWN patients. *Stroke* 2019;50(3):618–625.
- Martinez-Gutierrez JC, Leslie-Mazwi T, Chandra RV, et al. Number needed to treat: a primer for neurointerventionalists. *Interv Neuroradiol* 2019 Jun 27:1591019919858733 [Epub ahead of print]. <https://doi.org/10.1177/1591019919858733>.
- Berkhemer OA, Fransen PS, Beumer D, et al. A randomized trial of intraarterial treatment for acute ischemic stroke. *N Engl J Med* 2015;372(1):11–20.
- Jovin TG, Chamorro A, Cobo E, et al. Thrombectomy within 8 hours after symptom onset in ischemic stroke. *N Engl J Med* 2015;372(24):2296–2306.
- Bracard S, Ducrocq X, Mas JL, et al. Mechanical thrombectomy after intravenous alteplase versus alteplase alone after stroke (THRACE): a randomised controlled trial. *Lancet Neurol* 2016;15(11):1138–1147.
- Sevick LK, Ghali S, Hill MD, et al. Systematic review of the cost and cost-effectiveness of rapid endovascular therapy for acute ischemic stroke. *Stroke* 2017;48(9):2519–2526.
- Saver JL, Goyal M, van der Lugt A, et al. Time to treatment with endovascular thrombectomy and outcomes from ischemic stroke: a meta-analysis. *JAMA* 2016;316(12):1279–1288.
- Martinez-Gutierrez JC, Chandra RV, Hirsch JA, Leslie-Mazwi T. Technological innovation for prehospital stroke triage: ripe for disruption. *J Neurointerv Surg* 2019 Jun 14 [Epub ahead of print].
- Boulouis G, Siddiqui KA, Lauer A, et al. Immediate vascular imaging needed for efficient triage of patients with acute ischemic stroke initially admitted to nonthrombectomy centers. *Stroke* 2017;48(8):2297–2300.

CT for Treatment Selection in Acute Ischemic Stroke: A Code Stroke Primer

Christopher A. Potter, MD

Achala S. Vagal, MD

Mayank Goyal, MD, FRCPC

Diego B. Nunez, MD, MPH

Thabele M. Leslie-Mazwi, MD

Michael H. Lev, MD

Abbreviations: ACA = anterior cerebral artery, ASPECTS = Alberta Stroke Program Early CT Score, CBV = cerebral blood volume, DWI = diffusion-weighted imaging, EVT = endovascular thrombectomy, GWD = gray-white matter differentiation, ICA = internal carotid artery, ICH = intracranial hemorrhage, LVO = large-vessel occlusion, MCA = middle cerebral artery, MIP = maximum intensity projection, tPA = tissue plasminogen activator

RadioGraphics 2019; 39:1717–1738

<https://doi.org/10.1148/rg.2019190142>

Content Codes: **CT** **ER** **NR** **VA**

From the Department of Radiology, Brigham and Women's Hospital, 75 Francis St, Boston, MA 02115 (C.A.P., D.B.N.); Department of Radiology, University of Cincinnati, Cincinnati, Ohio (A.S.V.); Department of Diagnostic Imaging, University of Calgary, Calgary, AB, Canada (M.G.); and Department of Radiology, Massachusetts General Hospital, Boston, Mass (T.M.L., M.H.L.). Presented as an education exhibit at the 2018 RSNA Annual Meeting. Received February 28, 2019; revision requested June 13 and received July 12; accepted July 25. For this journal-based SA-CME activity, the authors A.S.V., M.G., and M.H.L. have provided disclosures (see end of article); all other authors, the editor, and the reviewers have disclosed no relevant relationships. **Address correspondence to** C.A.P. (e-mail: cpotter3@bwh.harvard.edu).

©RSNA, 2019

SA-CME LEARNING OBJECTIVES

After completing this journal-based SA-CME activity, participants will be able to:

- Describe CT findings that are early indicators of ischemia and infarction.
- Compare stroke imaging patterns that are favorable or unfavorable for treatment.
- Recognize pitfalls in interpretation of nonenhanced CT images.

See rsna.org/learning-center-rg.

CT is the primary imaging modality used for selecting appropriate treatment in patients with acute stroke. Awareness of the typical findings, pearls, and pitfalls of CT image interpretation is therefore critical for radiologists, stroke neurologists, and emergency department providers to make accurate and timely decisions regarding both (a) immediate treatment with intravenous tissue plasminogen activator up to 4.5 hours after a stroke at primary stroke centers and (b) transfer of patients with large-vessel occlusion (LVO) at CT angiography to comprehensive stroke centers for endovascular thrombectomy (EVT) up to 24 hours after a stroke. Since the DAWN and DEFUSE 3 trials demonstrated the efficacy of EVT up to 24 hours after last seen well, CT angiography has become the operational standard for rapid accurate identification of intracranial LVO. A systematic approach to CT angiographic image interpretation is necessary and useful for rapid triage, and understanding common stroke syndromes can help speed vessel evaluation. Moreover, when diffusion-weighted MRI is unavailable, multiphase CT angiography of collateral vessels and source-image assessment or perfusion CT can be used to help estimate core infarct volume. Both have the potential to allow distinction of patients likely to benefit from EVT from those unlikely to benefit. This article reviews CT-based workup of ischemic stroke for making tPA and EVT treatment decisions and focuses on practical skills, interpretation challenges, mimics, and pitfalls.

©RSNA, 2019 • radiographics.rsna.org

Introduction

CT is the first-line imaging modality used in neurologic emergencies owing to its speed, accurate depiction of acute intracranial disease, and availability (1). The critical role of nonenhanced CT for stroke evaluation began in 1996, when the U.S. Food and Drug Administration (FDA) approved intravenous tissue plasminogen activator (tPA) for clot thrombolysis (2). Nonenhanced CT should be performed rapidly in patients with signs and symptoms of acute stroke to exclude intracranial hemorrhage (ICH) and identify large (ie, >100 mL or more than one-third of a brain territory at risk) well-established infarcts. However, the revised 2018 American Heart Association (AHA) guidelines state that the extent or severity of the hypoattenuation seen at CT should not be used as a criterion for withholding tPA owing to insufficient evidence (3). Early signs of proximal middle cerebral artery (MCA) large-vessel occlusive infarction seen at nonenhanced CT include loss of gray-white matter differentiation (GWD) at the insula, basal ganglia, and caudate head as well as sulcal effacement (4–7).

TEACHING POINTS

- Since the DAWN (Clinical Mismatch in the Triage of Wake Up and Late Presenting Strokes Undergoing Neurointervention with Trevo) and DEFUSE 3 (Endovascular Therapy Following Imaging Evaluation for Ischemic Stroke) trials showed the efficacy of endovascular thrombectomy (EVT) up to 24 hours after the onset of stroke, CT angiography has become the operational standard for rapid accurate identification of intracranial large-vessel occlusion (LVO).
- To expedite the decision to transfer a patient to a stroke center that is capable of performing EVT, all patients should undergo CT angiography immediately after undergoing nonenhanced CT without being removed from the CT scanner.
- The insula, caudate heads, and basal ganglia show early findings of proximal MCA thrombosis at nonenhanced CT and should be carefully evaluated.
- Knowledge of common stroke syndromes is part of an efficient evaluation in conjunction with interpreting CT angiograms and identifying vessel occlusions.
- Potential acute stroke mimics include intracranial masses due to primary or metastatic malignancy, cerebritis, cerebral abscess, and posterior reversible encephalopathy syndrome (PRES).

Since the DAWN (Clinical Mismatch in the Triage of Wake Up and Late Presenting Strokes Undergoing Neurointervention with Trevo) (8) and DEFUSE 3 (Endovascular Therapy Following Imaging Evaluation for Ischemic Stroke) (9) trials showed the efficacy of endovascular thrombectomy (EVT) up to 24 hours after the onset of stroke, CT angiography has become the operational standard for rapid accurate identification of intracranial large-vessel occlusion (LVO). The proximal intracranial vessels are evaluated to identify LVOs suitable for catheter thrombectomy, whereas the cervical vessels are evaluated for the presence of dissection, critical stenoses, or other vascular variants or abnormalities that may complicate EVT.

At primary stroke centers, nonenhanced CT is essential in the decision-making process by helping rule out ICH and large well-established infarct. CT angiography helps identify proximal LVOs in patients with acute MCA or intracranial internal carotid artery (ICA) syndromes, aiding in the decision of whether to transfer a patient to a comprehensive stroke center accredited to perform EVT.

However, some measure of core infarct volume is required before proceeding with EVT to determine both ICH risk and the likelihood of treatment benefit (5). Small cores (<50–70 mL or in a symmetric collateral pattern) are considered favorable for EVT treatment, and large cores (>100 mL or in a collateral pattern typical of malignancy) are considered unfavorable to treat. Core volume can be estimated from cross-sectional images (ie, dif-

fusion-weighted images, CT angiography source images as [length × width × height]/2) (10).

Diffusion-weighted imaging (DWI) remains the unequivocal reference standard used to assess core infarct volume (3,11). When MRI is unavailable, multimodal CT assessment is helpful. Perfusion CT or multiphase CT angiography collateral and source image assessment are emerging as important tools for treating stroke in eligible patients, especially those with delayed presentation (>6 hours from symptom onset) or stroke of unknown onset (from time last seen well) (3).

This review focuses exclusively on the current role of CT in management of acute stroke. We present an overview of CT-based workup in evaluation of acute ischemic stroke that emphasizes practical considerations in nonenhanced CT, CT angiography, and perfusion CT, including key aspects of interpretation, pitfalls, and challenges.

Imaging Rationale and Code Stroke Workflow

Although an in-depth discussion of the pathophysiology of acute ischemic stroke is beyond the scope of this review, the concepts of ischemic core and penumbra are essential to understanding the role of the different components of imaging evaluation. In ischemic stroke, arterial occlusion due to embolism or less commonly *in situ* thrombosis leads to a cascade of cellular events. These events cause local dysfunction and ultimately cell death, leading to development of an infarct core, which is defined as brain tissue likely to die despite immediate reperfusion. The infarct core is surrounded by the ischemic penumbra, the ischemic tissue at risk for infarction that may be salvaged with timely reperfusion (12,13). In the setting of a proximal MCA or ICA LVO, if there is persistent insufficient tissue reperfusion as time passes, there is continued core infarct growth with penumbral loss (12).

The rate of penumbral loss in untreated stroke does not appear to be directly time dependent but appears to depend primarily on the quality and maintenance of collateral flow (9,10). Regardless of whether stroke patients are classified as rapid or slow progressors, failure of collateral flow with associated penumbral loss will continue up to 24 or even 48 hours after stroke onset in the absence of LVO recanalization, necessitating imaging approaches for selecting patients that may benefit from EVT (13). Accurate identification of the infarct core has therefore been a target of intense scientific investigation.

In determining a patient's eligibility for treatment of acute stroke, imaging must rapidly answer the following three essential questions: (a) Is there an ICH seen at nonenhanced CT that is a

contraindication to intravenous tPA or EVT, or is there a large well-established hypoattenuating infarct? (b) Is there a proximal LVO seen at CT angiography that can be treated with EVT? (c) Is there a large core infarct seen at DWI, at CT angiography of collateral vessels or on CT angiographic source images, or at perfusion CT that is a relative contraindication to intravenous tPA or EVT?

Rapidly acquiring and interpreting nonenhanced CT images of a patient suspected of having acute stroke is critical to expedite administration of intravenous tPA. Optimally, evaluation of the nonenhanced CT images of a patient designated with “code stroke” occurs at the scanner console at the time of acquisition and findings are directly communicated to the stroke team.

To expedite the decision to transfer a patient to a stroke center that is capable of performing EVT, all patients should undergo CT angiography immediately after undergoing nonenhanced CT without being removed from the CT scanner.

Performing CT angiography in this setting should never delay the administration of intravenous tPA. If a pharmacist is present as part of the code stroke team, imaging and medication preparation may occur simultaneously. Once the nonenhanced CT images have been reviewed and the decision has been made to administer tPA, CT angiography may be performed during the several minutes needed to mix and prepare the tPA.

Efficient imaging workflow is essential. Ideally, a code stroke page should be initiated as soon as the patient is identified, which may be during transportation or at presentation to the emergency department. The page notifies the stroke team, radiologists, and CT and MRI technologists about an incoming patient. This allows the technologists to accommodate the patient as quickly as possible in the scanner, minimizing the door-to-imaging time to no more than the 25 minutes recommended by the American Heart Association’s Get With The Guidelines program (3,14), which can be seen at <https://www.heart.org/en/professional/quality-improvement/get-with-the-guidelines/get-with-the-guidelines-stroke/get-with-the-guidelines-stroke-overview>.

Nonenhanced CT

Technique

There has been rapid development of CT technology over the past decades, enabling rapid imaging with a relatively low dose of radiation. Current American College of Radiology recommendations for CT of the brain include a reconstructed axial section thickness of no more than 5 mm using overlapping or contiguous sections. Imaging times should be no greater than 2 seconds, with a mini-

mum acquired section thickness of 2 mm or less and a table pitch no greater than 2:1 (15). Reformatted coronal and sagittal images is routine at many institutions, although not universal.

Dual-energy CT is available with different system architectures, the most popular being dual-source and fast kilovolt peak-switching systems. Because dual-energy CT acquires data using high and low x-ray energy spectra, materials can be characterized on the basis of their x-ray absorption characteristics and contrast can be optimized. Using the data from the low and high kilovolt peak x-ray spectra, dual-energy CT post-processing can generate virtual monochromatic images that display the expected attenuation at a single virtual x-ray spectrum, which is not possible in conventional nonenhanced CT using a single polychromatic spectrum. Spectral absorption curves can be plotted at different energy levels and can be used to optimize the contrast of GWD on images (16,17).

Image Review

Initial Image Review.—During the initial imaging evaluation in a patient with stroke, it must be determined rapidly whether there is ICH or a large, well-established, hypoattenuating territorial infarct.

Revised 2018 American Heart Association guidelines recommend that at least 50% of stroke treatment candidates undergo nonenhanced CT imaging within 25 minutes of arrival (3). Initial rapid nonenhanced CT evaluation within 4.5 hours from onset in patients without other contraindications to intravenous tPA administration should focus on identification of a large territorial infarct and exclusion of ICH, which is an absolute contraindication to intravenous tPA treatment (3).

These results should be communicated immediately after imaging to enable rapid intravenous tPA administration, which should never be delayed by CT angiography for EVT triage. Currently, guidelines for treatment with intravenous tPA within 4.5 hours and EVT within 6 hours are based only on nonenhanced CT relative and absolute exclusion criteria (3,14).

The sensitivity and specificity of nonenhanced CT for depiction of ICH is estimated to be high with modern CT scanners, likely exceeding 95%–98% depending on the patient cohort and level of training of the radiologists (18). Indeed, recent work published in *Nature Biomedical Engineering* has suggested that even subtle hemorrhages can be sensitively depicted with artificial intelligence platforms, with accuracy approaching that of experienced subspecialty-trained neuroradiologists and exceeding that of less experienced nonsubspecialty-trained readers (19).

Nonenhanced CT is much less sensitive compared with DWI for depiction of both the cytotoxic edema and low cerebral blood volume (CBV) that accompany early ischemia (13). Despite this, the widespread availability and speed of CT make it the most practical first-line imaging strategy at most institutions, as it can be performed in minutes and requires no prescreening or patient exclusion.

The sensitivity and specificity for acute infarction at nonenhanced CT likely depend on the duration, infarct size, and degree of ischemia. Sensitivity and specificity for depiction of early ischemic change are also likely better for the anterior circulation than the posterior circulation, primarily owing to artifact at the skull base from thick surrounding bone, although this has not been definitively demonstrated.

Several areas of the brain including the insula, basal ganglia, and caudate head are early indicators of acute infarct owing to their vascular anatomy in relation to the most common patterns of proximal MCA LVO distribution (4,5,20). Special attention should therefore be directed to these regions during initial image review (Fig 1).

Well-established frank ischemia seen at CT in these regions as an area of low attenuation with loss of GWD is typically attributed to vasogenic edema from blood-brain barrier breakdown. This imaging finding indicates irreversible infarction in the clinical setting of an acute MCA occlusion and is not attributable to cytotoxic edema from membrane pump failure and low CBV with poor collateral flow (21). Cytotoxic edema is a more subtle hyperacute finding and is typically attributable to membrane pump failure and low CBV.

The Alberta Stroke Program Early CT Score (ASPECTS) was developed to establish a reproducible scoring system for early ischemic changes at nonenhanced CT due to MCA stroke, since estimation of one-third of the MCA territory can be challenging in practice (22).

In the ASPECTS system, the brain is separated into 10 discrete labeled areas of the deep and superficial gray matter on each side. Starting with a maximum of 10 points on each side, the patient's score is decreased by one point for each area of the brain with early ischemic change (Fig 2). As it is a topographic scoring strategy, it requires only axial images for implementation.

The nonenhanced CT ASPECTS is often used by stroke neurologists to identify the extent of early ischemic change. Patients with ASPECTS of less than 7 have been shown to have a lower chance of independent recovery after a stroke (22). Automated quantification of ASPECTS using machine learning is being implemented at some sites (23). More information

about ASPECTS can be found at the educational website www.aspectsinstroke.com.

Identification of vessel occlusion is limited at nonenhanced CT, although an "attenuating vessel sign" is highly specific when it is present. The attenuating vessel sign due to thrombus in the M1 segment of the MCA has relatively low sensitivity of 17%–52% but high specificity of 95% (24,25).

Considered an equivalent of the attenuating vessel sign in the M1 segment, the MCA "dot" sign in the proximal M2 vessels is often associated with early insular GWD loss (26). At imaging, the dot sign appears in the vessels in the lateral sylvian fissure adjacent to the insula wall.

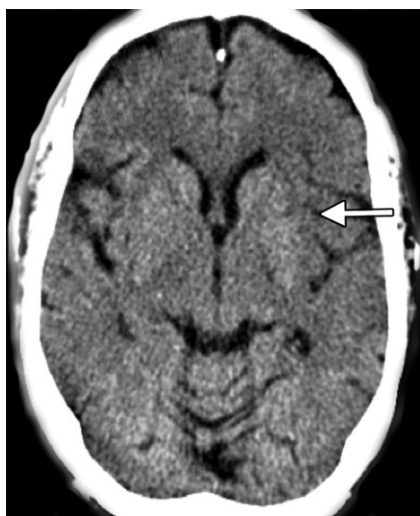
The mixed images obtained with dual-energy CT are produced by blending both high and low kilovolt peak datasets. Dual-energy CT can be used in the initial examination similar to the way conventional nonenhanced CT is used. Monochromatic imaging is not widely used in this context, since image reconstruction is not typically automated and it is too time-consuming. Nevertheless, optimization of GWD has been reported to occur at a virtual kilo-electron voltage of 66–75 (17).

Tip or Pearl for Image Review.—A methodical search pattern is important because the imaging findings in acute ischemic stroke can be subtle on nonenhanced CT images.

Gray-White Matter Differentiation.—Loss of GWD is the imaging hallmark of acute infarct at nonenhanced CT. Use of a narrow stroke window while performing soft-tissue sequences has been studied, and recommended values have been reported (window width, 8 HU; window level, 32 HU) (27).

Evaluation of coronal and sagittal images is essential because signs of sulcal hemorrhage on axial images are subtle and can easily be missed. The imaging findings of acute infarct can be difficult to notice in the following locations: the extreme vertex owing to volume averaging; the inferior temporal lobes, where the gray-white matter junction is oriented axially; the occipital lobes owing to frequent artifact caused by the irregular contours of the skull; and the deep gray matter, particularly the caudate heads (Fig 3) (4). The insula, caudate heads, and basal ganglia show early findings of proximal MCA thrombosis at nonenhanced CT and should be carefully evaluated.

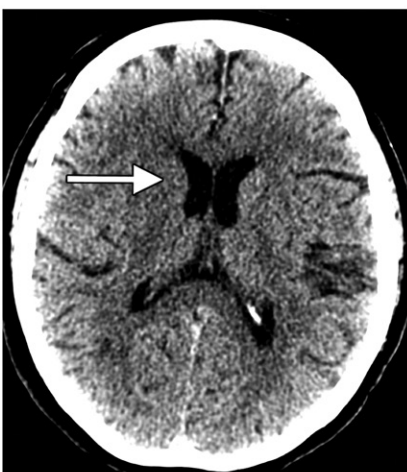
However, nonenhanced CT has low sensitivity for depiction of hyperacute and early acute hypoattenuating ischemic changes (28). Even large territorial infarcts may not be seen until the subacute phase. An acute territorial infarct visible at nonenhanced CT that is greater than one-



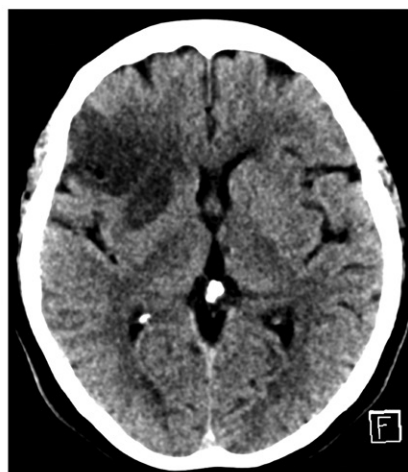
a.



b.



c.



d.

F

Figure 1. Left MCA infarction. (a) Axial nonenhanced CT image shows subtle hypoattenuation of the gray matter of the left insula in an “insular ribbon” configuration (arrow), resulting in loss of GWD. In the setting of persistent proximal MCA occlusion, the insular ribbon sign is an early indicator of a proximal MCA infarct and is predictive of core infarct growth due to penumbral loss (15). More extensive loss of GWD is seen throughout the left frontal lobe. (b) Nonenhanced CT image obtained at follow-up demonstrates well-established left insular and extensive left MCA hypoattenuation due to vasogenic edema, indicating infarction. (c) Nonenhanced CT image depicts loss of GWD in the right caudate head (arrow) and basal ganglia, which are also important early indicators of infarction. (d) Nonenhanced CT image obtained at follow-up shows the established right caudate and anterior frontal lobe infarcts.

third of the MCA territory has been considered a relative contraindication for administration of intravenous tPA, but the revised 2018 American Heart Association guidelines state that the extent or severity of the hypoattenuation should not be used as a criterion for withholding intravenous tPA owing to lack of sufficient evidence (3).

Sulci.—Focal sulcal effacement is also an important early secondary sign of acute ischemia and can help identify subtle acute infarcts.

Vessels.—The hyperattenuating vessel sign can be seen in the intracranial ICA, M1 and M2 segments of the MCA, and A1 and A2 segments of the anterior cerebral artery (ACA) as well as the basilar and vertebral arteries (29) (Fig 4). This sign typically indicates the need for intervention. Although CT angiography should always be performed for definitive diagnosis in LVO, identification of a hyperattenuating MCA sign greater than 8 mm in length also indicates that administration of intravenous tPA alone is not likely to achieve

successful recanalization. This is not an indication to withhold intravenous tPA according to the revised 2018 American Heart Association guidelines (3,30).

In addition to reviewing the nonenhanced CT images for acute infarct, it is important to remember that mimics of acute stroke are common in the emergent setting. A full routine evaluation of the nonenhanced CT images is essential to identify alternative diagnoses such as intracranial masses, infection, and hemorrhage, all of which can cause focal and nonspecific neurologic findings.

Pitfalls of Image Review.—Challenges in evaluation of nonenhanced CT images in stroke are often caused by artifact from patient motion that can be associated with alterations in consciousness as well as from streak artifact from bone or hardware (26). Skull base artifact at the petrous apices or posterior fossa often limits the visibility of subtle hypoattenuation in acute infarct (Fig 3). Skull base streak artifact can also mimic the

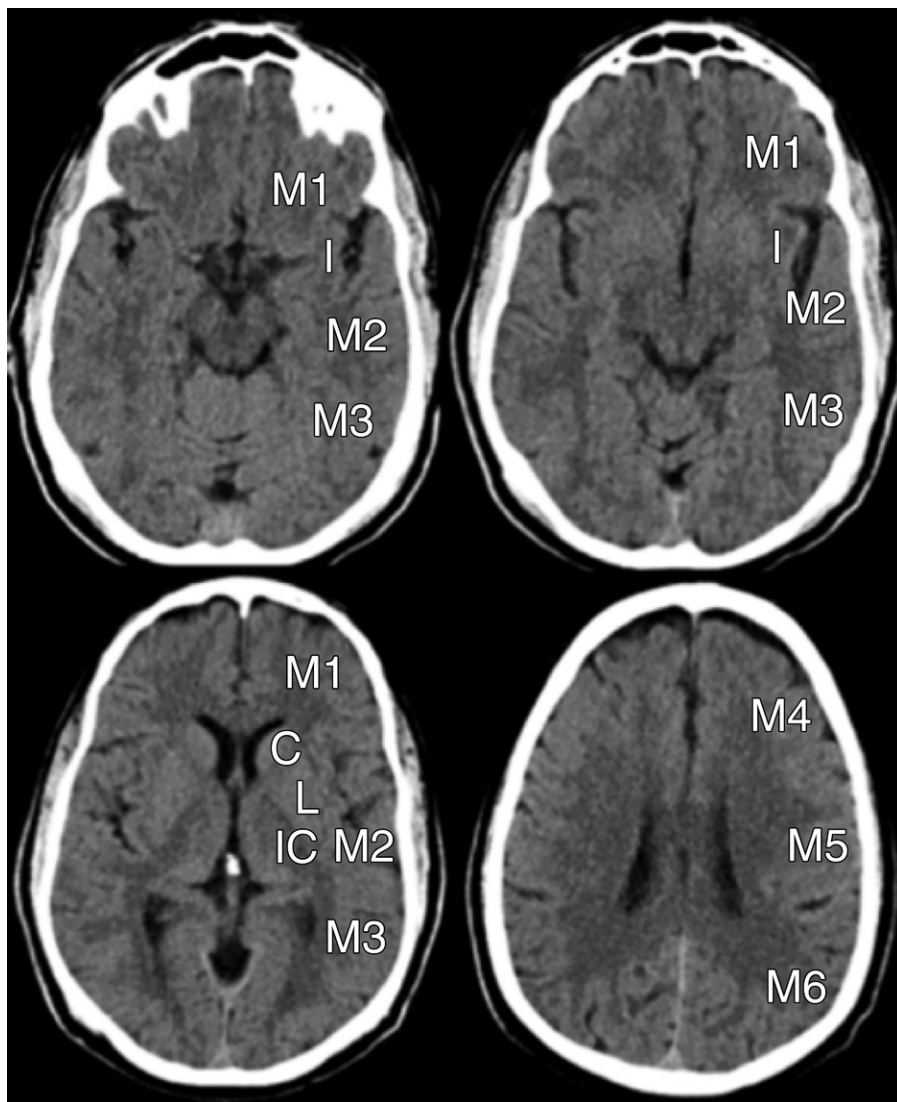


Figure 2. Regions of the brain used to calculate ASPECTS. Axial nonenhanced CT images show the labeled MCA territories that are given one point each for a score out of 10 points by using the ASPECTS system. C = caudate, I = insula, IC = internal capsule, L = lentiform nucleus, M1–M6 = cortical regions.

hyperattenuating MCA sign. Comparison with the contralateral side will typically help resolve any ambiguity.

Coronal and sagittal reformations can improve visualization and help one distinguish artifact, infarct, and hemorrhage in some cases, especially at locations such as the sylvian fissure, where axial volume averaging can mimic GWD loss. In situations where axial images are tilted off axis, coronal and sagittal reformations can display areas of nonanatomic linear hyperattenuation that cross through different brain regions and structures.

Evaluation of the basilar artery for acute thrombus is another example where coronal and sagittal reformations can be helpful for distinguishing artifact from thrombus.

CT Angiography

Technique

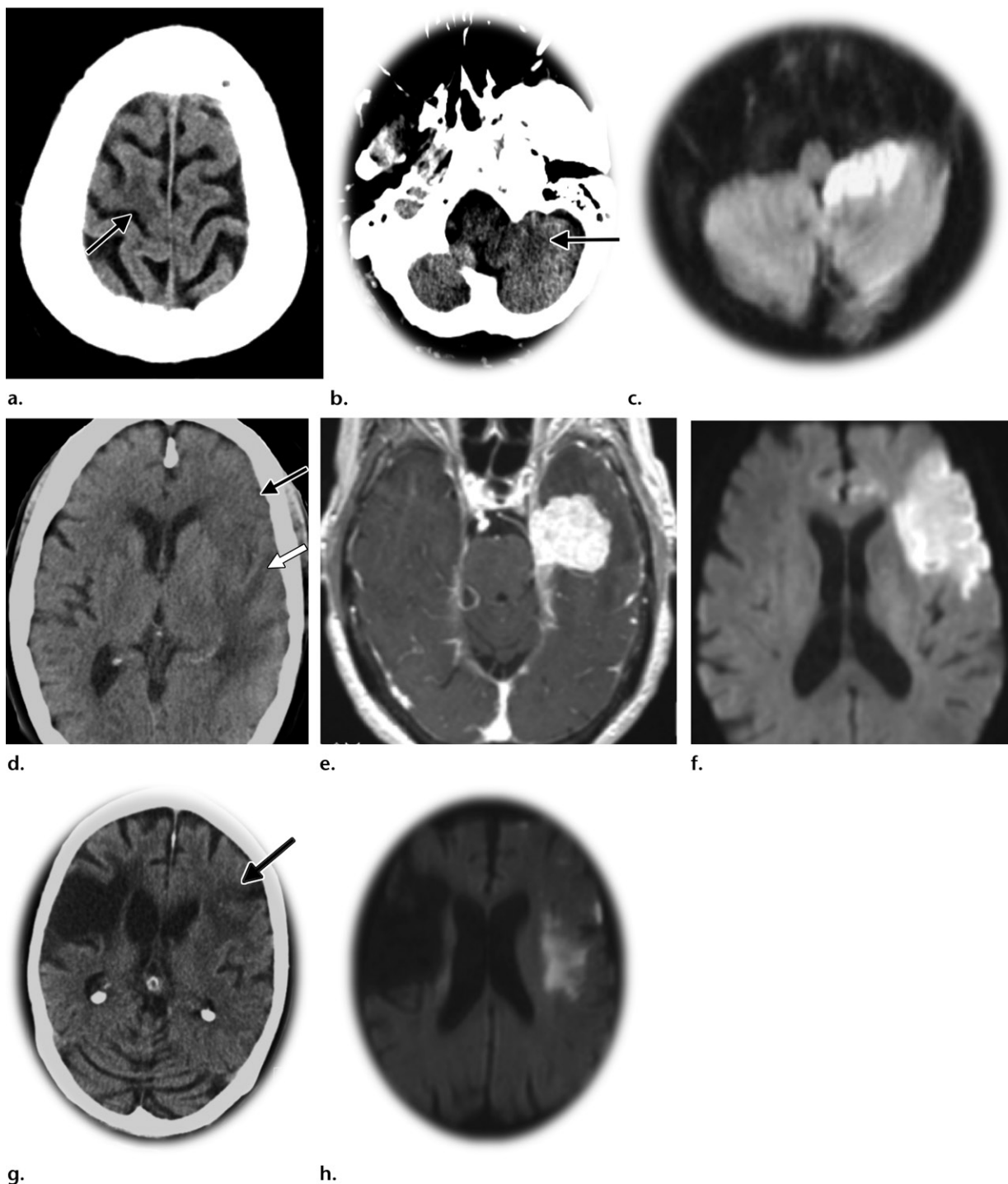
Intravenous tPA administration should never be delayed to perform advanced CT, and CT angi-

graphy should also never be delayed by removing the patient from the CT table for additional clinical evaluation or to review the nonenhanced CT images at the scanner.

An 18–20-gauge needle should be confirmed before the patient arrives, as power injection of contrast material is required. The right arm should be used to limit streak artifact from hyperattenuating contrast material crossing the midline, since the flow from the left brachiocephalic vein enters the superior vena cava at an average rate of 4–5 mL/sec in adults.

Administration of iodinated contrast material without first testing renal function in candidates for EVT is acceptable, as the likelihood of contrast material-induced nephropathy has been shown to be very low relative to the potential for brain injury from stroke (3,31). Correct timing of the injection of contrast material can be achieved by using a test bolus to calculate the imaging delay or by using semiautomated or automated triggering after injection of the full dose of contrast material.

Figure 3. Potential pitfalls that can cause missed infarcts at nonenhanced CT. (a) Small focus of GWD loss at the right frontal vertex (arrow), which could be missed owing to atypical location just deep to the skull, especially with thick (≥ 5 -mm) axial sections. (b) Left inferior cerebellar GWD loss (arrow) might also be overlooked owing to skull base beam-hardening artifact in this region. (c) Subsequent diffusion-weighted image shows the evolving infarct. (d–f) The presence of nonstroke disease can also distract the reader owing to satisfaction of search or anchoring bias, as well as nonspecific findings. (d, e) In another patient, low attenuation due to vasogenic edema from a left temporal meningioma (white arrow in d) distracts from and overlaps with hypoattenuation from an acute left anterior frontal infarct (black arrow in d). (f) Diffusion-weighted image shows the acute left anterior frontal infarct. (g, h) Similarly, encephalomalacia from prior infarcts makes evaluation for new infarction difficult. (g) In a patient with old right MCA-distribution encephalomalacia, CT image shows new left frontal GWD loss (arrow) due to an acute left MCA infarct, which might be considered “age-indeterminate.” (h) Subsequent MR image shows the acute left MCA infarct.



Images should be acquired at a maximum thickness of 1.5 mm and reconstructed in sections overlapping by 50% or less. Anatomic cov-

erage should begin at the origins of the cervical vessels at the aortic arch and extend through the vertex (32). Multiplanar and maximum intensity

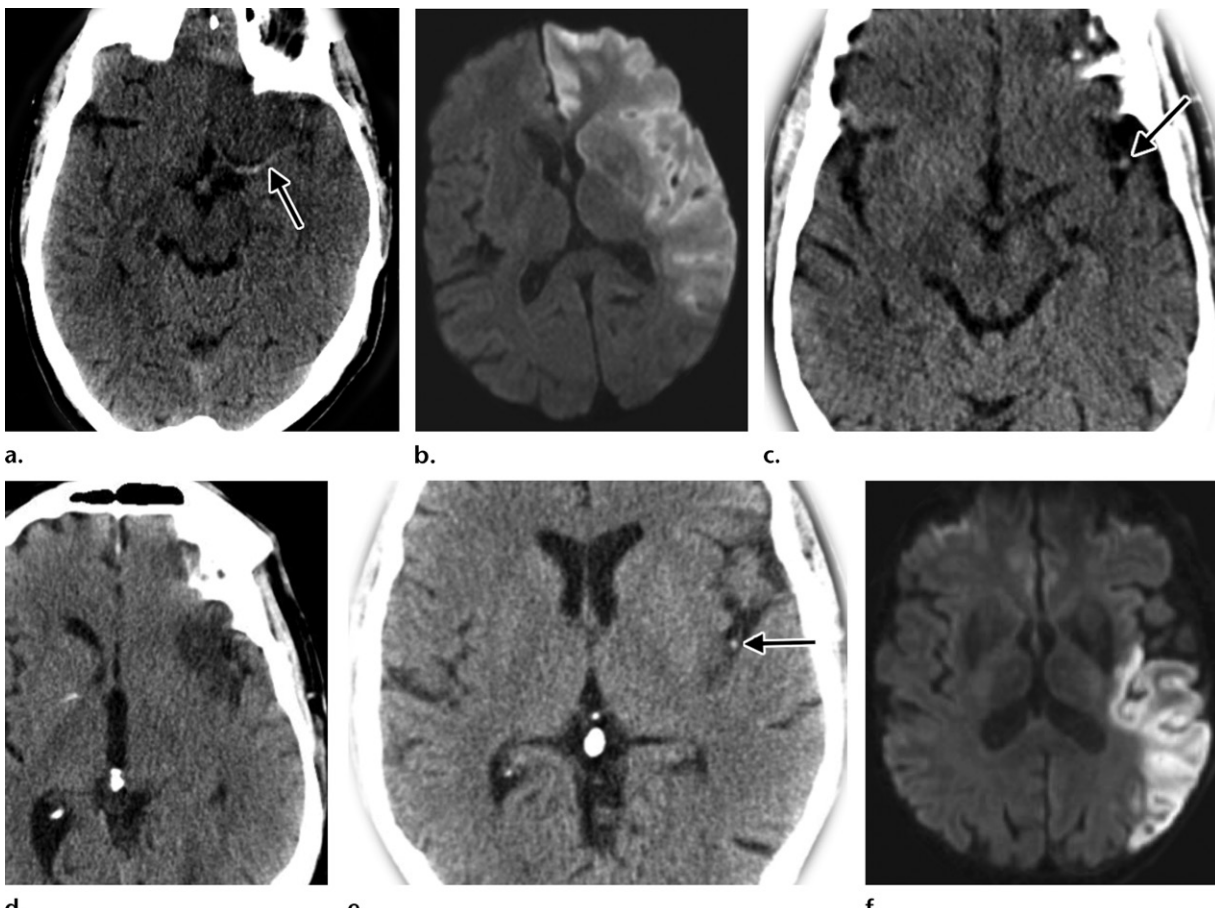


Figure 4. Attenuating vessel sign. This is an early hyperacute ischemic finding at nonenhanced CT that can be seen before changes of vasogenic edema are visible and allows anticipation of the presence of a clot at CT angiography for both anterior and posterior circulation strokes (24). (a) A hyperattenuating MCA sign (arrow) is seen in the M1 segment. (b) Diffusion-weighted image shows a large left MCA infarct. (c) Thrombus in an M2 branch vessel can create an MCA dot sign, seen in the left anterior sylvian fissure (arrow). (d) Subsequent nonenhanced CT image shows a left MCA infarct in the territory of the left anterior temporal artery. (e) An MCA dot sign is seen in another patient in the posterior sylvian fissure (arrow). (f) Follow-up diffusion-weighted image shows the extent of the infarct, which corresponds to the occlusion of the inferior MCA M2 division.

projection (MIP) reformations can be acquired at orthogonal planes for optimal evaluation, depending on the institution.

CT angiography can be performed as a single, delayed, or multiphasic study. Multiphasic CT angiography begins with an arterial imaging sequence spanning from the aortic arch to the vertex. The next two imaging sequences are performed after a single contrast material bolus and are timed to depict the peak and late venous phases in the head (33). The images acquired with multiphasic CT angiography can be rapidly and automatically reformatted into sequential axial MIP images that can be used for collateral flow assessment and EVT decision making (33).

Four-dimensional CT angiography is performed at some centers. This is a dynamic CT angiographic technique in which bone-subtracted MIP images can be viewed like digital subtraction angiograms are viewed over time. The images are used to evaluate collateral filling or in a condensed three-dimensional MIP image of all time points

(Fig 5) (34). Automated delineation of LVOs is under investigation as well, which may help to speed detection, particularly in busy centers.

CT angiographic data can be acquired at dual-energy CT as well, which has the potential to provide robust three-dimensional vessel reconstruction using bone subtraction techniques (16,35,36). The lengthy postprocessing time has largely limited its clinical application. In addition, iodine maps are reconstructions that can be used to show attenuating contrast material throughout an image. The attenuation can also be subtracted from an image to create a virtual nonenhanced CT image (37).

Image Review

Tips or Pearls for Image Review.—Patients suspected of having LVO should undergo CT angiography to expedite treatment with EVT. Although the entire intracranial vasculature is depicted well at current-generation CT angiography, occlusions of the intracranial ICA and

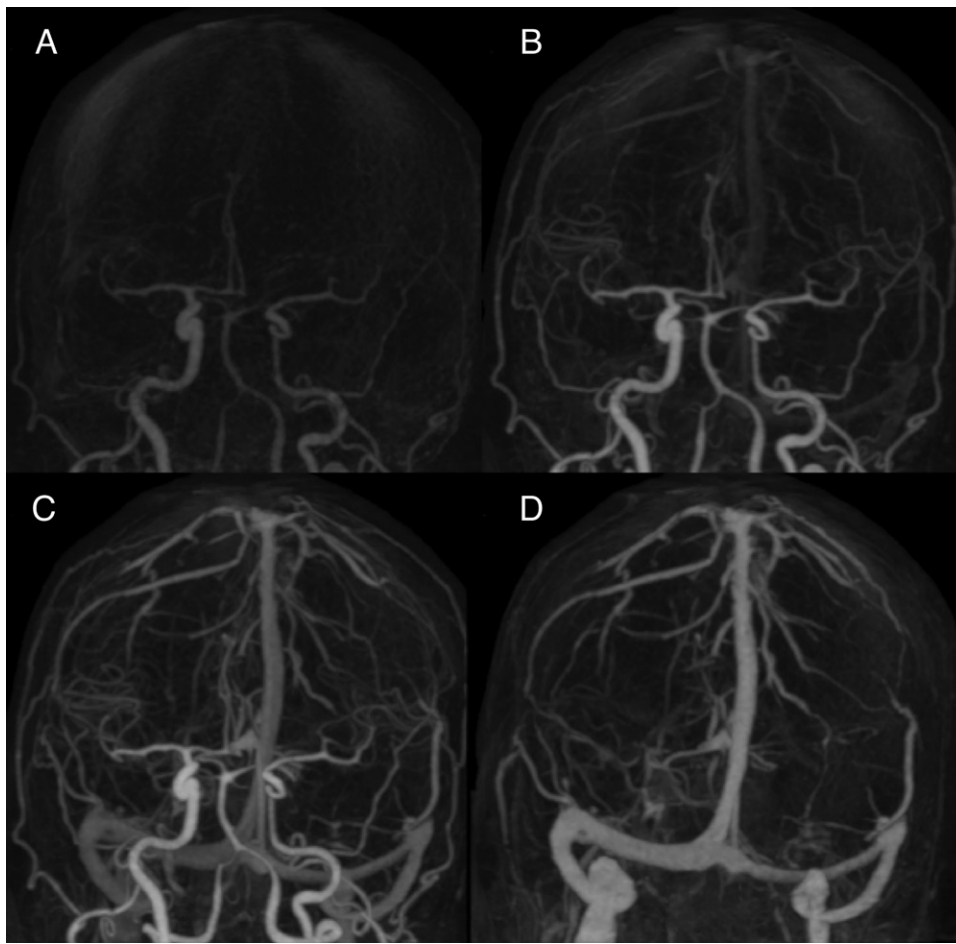


Figure 5. Four-dimensional CT angiography. Dynamic four-dimensional CT angiography data can be reconstructed into time-resolved MIP reconstructions that appear similar to conventional catheter digital subtraction angiograms. The earliest images show the arteries (*A*), followed by increased venous filling over time (*B*, *C*) and dense opacification of the venous sinuses without visible arterial enhancement (*D*).

proximal MCA segments should be the focus at imaging, since these vessels are the targets for EVT (3). The skull base and neck vessels are largely orthogonal to the axial imaging plane, and their patency can be assessed quickly by viewing the axial CT angiography source images at the scanner console at the time of acquisition.

Overlapping thick-section MIP images of the circle of Willis in axial, coronal, and sagittal planes can help expedite identification of LVOs (3-cm section thickness at overlapping intervals of 5 mm). The more distal branches of the circle of Willis can be difficult to interpret on thin-section CT angiography source images, and using thick-section reconstructions increases their visibility. CT technologists can produce MIP reformations at the scanner console in less than 1 minute (28,38).

Collateral flow assessment of the intracranial circulation at CT angiography can be used to help assess the potential risks (ie, ICH) versus benefits (ie, limited infarct growth and improved clinical outcomes) of EVT. The quality of collat-

eral flow is an important determinant of the rate of infarct progression (12).

Multiple groups and studies have described systems that help define collateral flow, including ASPECTS, the Miteff and Maas systems, and the modified Tan scale (39–41). There is no consensus on which standardized scoring system is optimal for collateral grading.

Several groups consider a malignant collateral pattern at delayed phase CT to be characterized by contrast material failing to reach more than 50% of the intracranial vessels and tissue bed of the at-risk MCA territory (42). Conversely, a good collateral pattern can be defined as a symmetric or nearly symmetric leptomeningeal flow when comparing the hemisphere affected by ischemia with the contralateral hemisphere. In the setting of an intracranial ICA or proximal MCA occlusion, infarct core growth and penumbral loss progress more rapidly in patients with malignant collateral patterns (ie, fast progressors), whereas infarct core growth and penumbral loss progress more slowly in patients

with good collateral patterns (ie, slow progressors) (43,44).

ASPECTS is one of the best-known collateral score systems and compares the filling of the intracranial arteries at all three phases of multiphase CT angiography. When there are no or just a few vessels visible in the ischemic territory at any phase, the collateral score is given a 0 or 1, indicating poor collaterals. If there is normal symmetric vessel filling, or a delay of a single phase with similar extent of vessel filling, collaterals are given a score of 5 or 4, respectively, indicating good collaterals. Intermediate collaterals with scores of 2 or 3 demonstrate a delay of two phases with either a similar or decreased extent of perfused vessels (Fig 6) (45).

Modified by the time of stroke onset, the degree of collateral flow is an important indicator of the potential efficacy of EVT. Malignant or poor collateral flow is associated with a low probability of penumbral salvage or clinical benefit from EVT unless thrombectomy is performed very quickly after onset of stroke (33,46) (Fig 7).

Complete assessment of the intracranial vasculature can seem daunting. MIP and multiplanar reformations are indispensable for efficient assessment. Coronal reformations rapidly depict the proximal MCA, ACA, and terminal ICA, while sagittal reformations demonstrate the ACA and distal MCA vessels. Evaluating the overall symmetry of vessels can help identify regions of relative hypoperfusion, particularly in the cerebral convexities. Assessing hypoperfused regions can help differentiate stroke from mimics such as seizure and directs the reader's attention to likely areas of vessel occlusion.

Knowledge of common stroke syndromes is part of an efficient evaluation in conjunction with interpreting CT angiograms and identifying vessel occlusions. Although a patient's signs and symptoms may not be available at the time of their imaging orders, discussing the results of the initial nonenhanced CT with referring providers often offers the opportunity to obtain a brief clinical history that can help focus the CT angiography assessment. Knowledge of symptoms such as laterality, acuity of onset, and specific functional involvement (eg, aphasia, hemiparesis, hemisensory deficit, and hemineglect) is essential to correlate specific imaging findings with the acute manifestation of stroke.

For example, contralateral arm and face weakness with or without a sensory disturbance, which might also include an expressive aphasia (Broca aphasia) in the dominant hemisphere (typically the left hemisphere), suggests occlusion of the superior M2 division or anterior temporal MCA branches (Fig 8a). The superior

M2 division is located anteriorly in the sylvian fissure and primarily supplies the superior frontal-parietal regions. A receptive aphasia (Wernicke aphasia) in the dominant hemisphere or visual field problems from disruption of the visual tracts suggest occlusion of the inferior M2 division of the MCA (Fig 8b). The inferior M2 division is in the posterior sylvian fissure and supplies the temporal-parietal regions.

A combination of these symptoms suggests occlusion more proximally at the MCA bifurcation (Fig 8c). Complete hemiplegia and hemisensory loss suggest a proximal M1 segment MCA occlusion, which includes occlusion of the lenticulostriate vessels that supply the internal capsule (Fig 8d).

Isolated focal arm, hand, and face weakness suggests a more distal occlusion, usually in an M3 or M4 branch. These occlusions are depicted well on sagittal thick-section MIP images.

Complete hemiplegia and hemisensory loss can also be caused by occlusion of the intracranial ICA. Dense monocular blindness can also occur and is due to an occlusion of the ophthalmic artery. However, occlusion of the ICA may be more difficult to detect. The symptoms can range from subtle to severe, and there may be no symptoms if the circle of Willis is intact and there is good contralateral flow (47).

Contralateral lower extremity weakness and sensory loss suggest occlusion of the ACA (Fig 8e). Occlusion of the A1 segment of the ACA is an easily overlooked cause of infarct in the anterior lentiform nuclei and caudate head.

Visual changes are the most frequent sign of posterior cerebral arterial occlusion. These changes typically manifest as homonymous hemianopsia owing to infarction of the occipital visual cortex.

Profound alteration of consciousness or cranial nerve deficits suggest brainstem involvement and basilar thrombosis. Readers should always check for the presence of these conditions, and they are usually clearly depicted at CT angiography.

Although symptoms of ataxia, vertigo, and dizziness are nonspecific, they should prompt careful evaluation of the posterior circulation, including the posterior inferior cerebellar artery (PICA) (Fig 8f) and anterior inferior cerebellar artery (AICA). The distribution of vessels supplying the cerebellum is highly variable. The AICA and PICA develop in a reciprocal relationship, and a single artery or side could be dominant. If the ipsilateral PICA and AICA are not visible at imaging, this may indicate vascular occlusion and prompts careful evaluation (47).

The degree and location of vessel narrowing or partial obstruction should be included in the final interpretation. Intracranial arterial stenosis

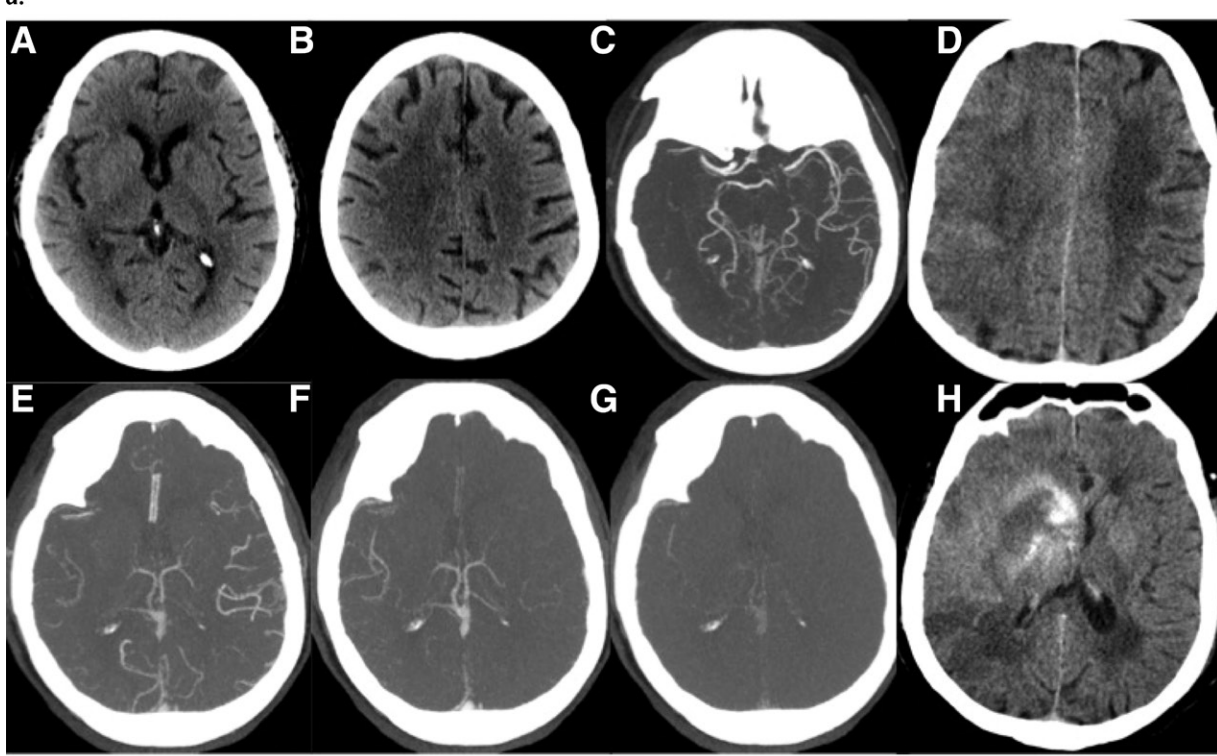
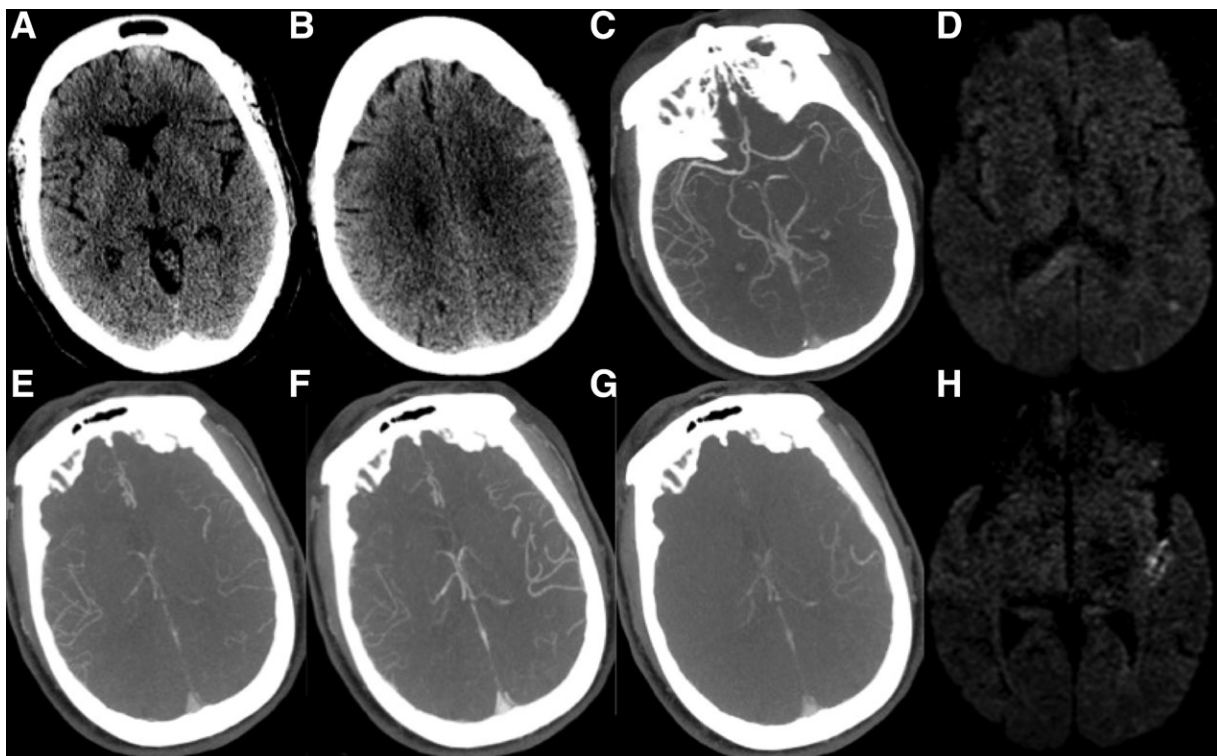
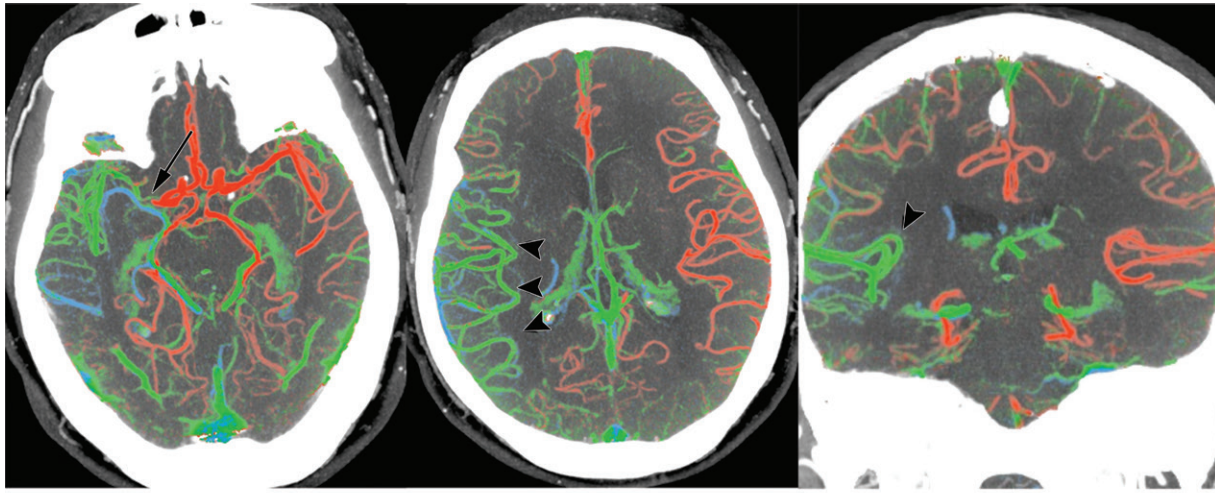
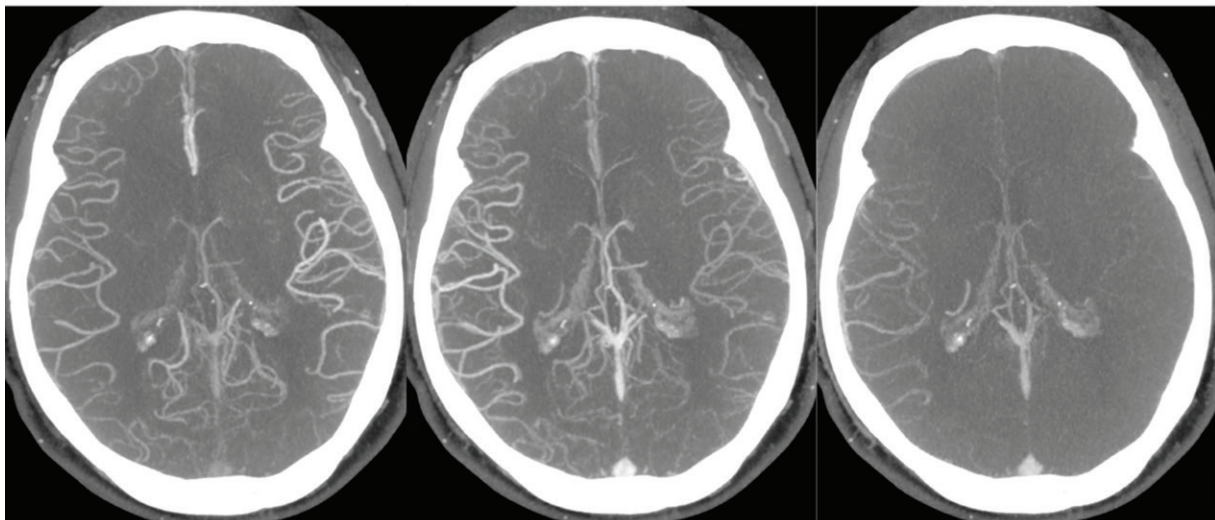


Figure 6. (a) Good collateral flow. *A* and *B*, Initial nonenhanced CT images show some patchy GWD loss in the left anterior frontal lobe. *C*, Axial MIP CT angiogram shows occlusion at the left MCA bifurcation. *E–G*, MIP images of the three sequential CT angiography phases show that the extent of the visualized vessels on the affected side has a single phase delay, consistent with good collaterals. *D* and *H*, Diffusion-weighted images after treatment with intravenous tPA and EVT demonstrate that only a small focus of acute infarct remains. (b) Poor collateral flow. *A* and *B*, Initial nonenhanced CT images depict no loss of GWD. *C*, Axial MIP image from CT angiography shows occlusion of distal right M1. *E–G*, MIP images of the three sequential CT angiography phases show few opacified vessels on the affected side, consistent with poor collaterals. The patient was treated with intravenous tPA and EVT. *D* and *H*, Follow-up nonenhanced CT images show a large right MCA infarct that developed after treatment.

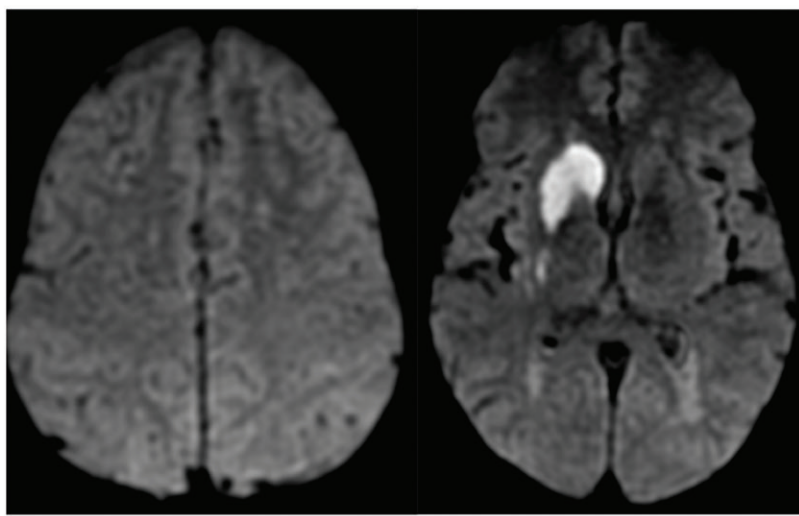
Figure 7. Collateral flow at multiphase CT angiography with right-sided M1 occlusion. (a) ColorViz software summation images—with color-coded early arterial (red), late arterial or venous (green), and delayed venous (blue) phases—show predominantly green vessels (arrowheads) ipsilateral to the right MCA occlusion (arrow), indicating symmetric but delayed collaterals relative to the predominantly red vessels in the unaffected hemisphere and suggesting good pial arterial filling collateral flow. (b) Corresponding conventional multiphase CT angiograms. The patient received intravenous tPA. (c) Follow-up diffusion-weighted images 24 hours after ictus show hyperintense signal consistent with acute infarction in the caudate head and lentiform nucleus only with sparing of the cortex, where good collateral flow was present.



a.



b.



c.

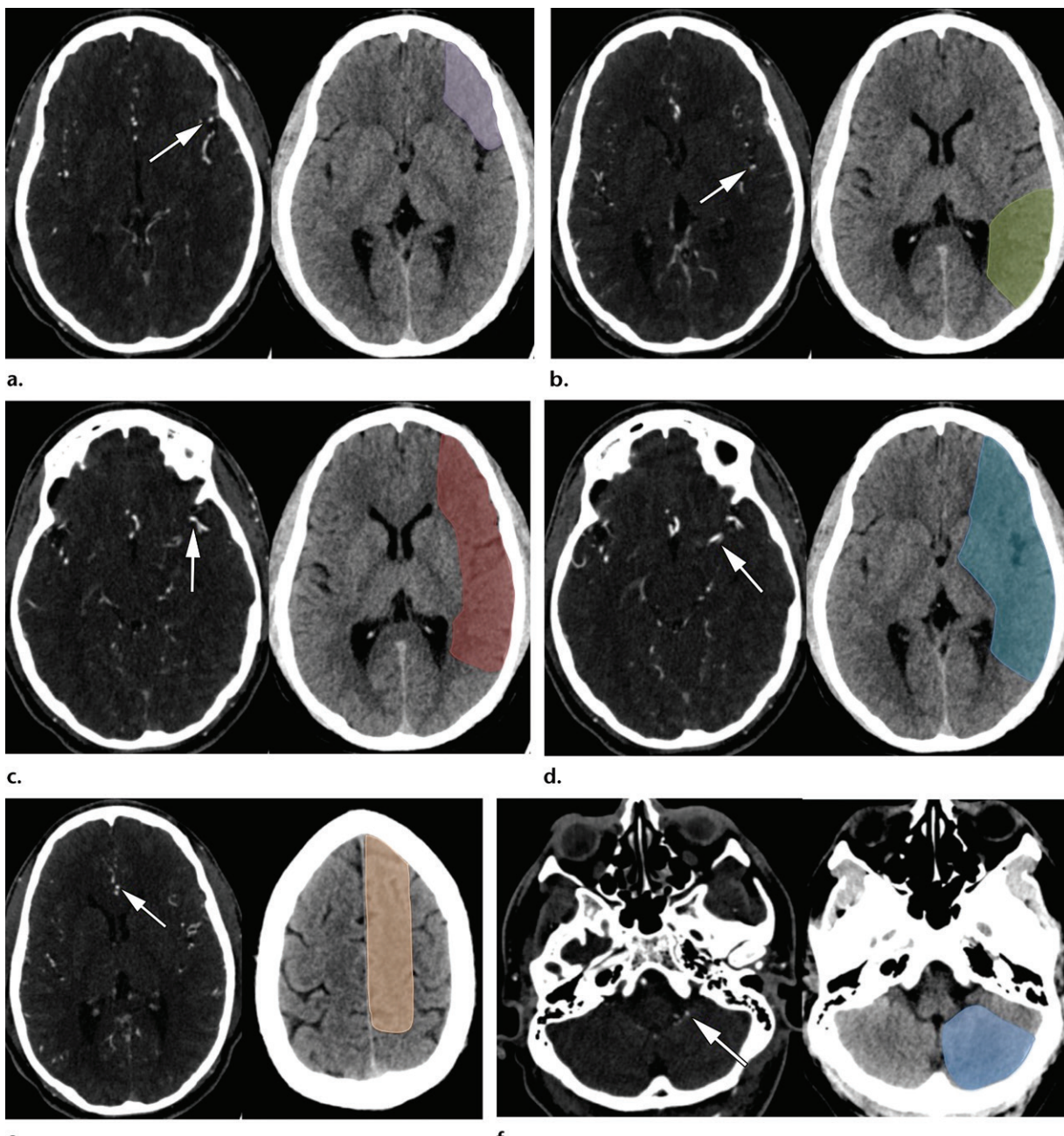


Figure 8. Common stroke syndromes. (a) Axial CT angiogram (left) shows the left superior M2 vessel (arrow). Along with the anterior temporal artery, the M2 segment perfuses the left frontal lobe and frontal operculum (purple region on nonenhanced CT image [right]). The frontal operculum contains the Broca area in the dominant hemisphere, and infarction may cause a nonfluent aphasia. (b) Axial CT angiogram (left) shows the left inferior M2 vessel (arrow), which typically perfuses the inferior parietal and temporal lobes (yellow region on nonenhanced CT image [right]). Infarction in this region in the dominant hemisphere could cause a fluent (Wernicke) aphasia. (c) Axial CT angiogram (left) shows the left MCA bifurcation (arrow). Occlusion can cause a pattern similar to occlusion of both M2 vessels but without significant involvement of the deep gray matter structures (red region on nonenhanced CT image [right]). (d) Axial CT angiogram (left) shows the proximal left M1 segment of the MCA (arrow). Occlusion in this segment typically causes hemiplegia and hemisensory loss owing to involvement of the cortex, basal ganglia, and internal capsule (blue region on nonenhanced CT image [right]). (e) Axial CT angiogram (left) shows the proximal left A2 segment of the ACA (arrow). The vascular territory of the ACA is parafalcine, and occlusion can cause contralateral lower extremity weakness and sensory loss (orange region on nonenhanced CT image [right]). (f) Axial CT angiogram (left) shows the left posterior inferior cerebellar artery (PICA) (arrow). The PICA often supplies the inferior medial cerebellum (blue region on nonenhanced CT image [right]), and infarction can cause a variety of symptoms, including ataxia.

may be clinically significant and can create falsely delayed arrival time values on perfusion CT images (48–50). However, management of proximal intracranial vascular stenoses is beyond the scope

of this review. Thrombus density, distance to the terminal ICA, and length longer than 8 mm have been associated with worse functional outcome but are not used as criteria for EVT (51).

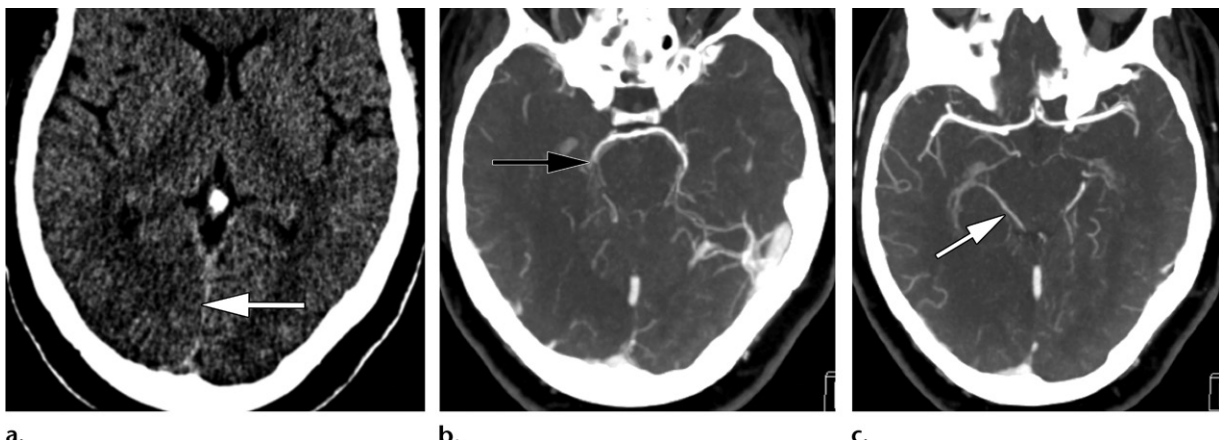


Figure 9. Potential false-negative interpretation of a posterior cerebral artery (PCA) occlusion in a patient with new-onset vision changes. (a) Axial nonenhanced CT image shows mild hypoattenuation with loss of GWD in the medial right occipital lobe (arrow). (b) CT angiogram shows a patent proximal right PCA and a more distal and possibly contiguous enhanced vascular structure lateral to the midbrain and pons (arrow). (c) Axial thin-section source image from CT angiography shows that the distal structure is the basal vein of Rosenthal (arrow), a common confounder when assessing the patency of the PCA, which is occluded in this case.

It is important to evaluate initial CT angiograms of the neck at the scanner console to identify areas of critical stenosis, dissection, or vessel tortuosity. These findings can help inform the plan for EVT. CT angiograms can depict clinically relevant severe ICA stenosis at the cervical ICA origin ($>70\%$ narrowing), although heavy circumferential calcifications can lead to overestimation of the degree of narrowing.

Atherosclerotic disease of carotid origin and embolus associated with untreated atrial fibrillation are some of the most common causes of stroke in adults (52). Spontaneous arterial dissection is more common in patients younger than 40 years or after acute vascular trauma.

Multiplanar and MIP reconstructions aid in rapid screening of patency and vessel contour of the cervical carotid arteries as well as in demonstrating underlying vascular abnormalities, such as fibromuscular dysplasia. However, MIP images may poorly depict small intimal flaps in the carotid arteries, and evaluation of the vertebral arteries is complicated by the bony foramina. Evaluation of the cervical arteries in multiple planes is important, as pseudoaneurysms and dissections may be better visualized in the coronal and sagittal planes than on axial images.

At perfusion CT, it is important to identify extracranial narrowing that decreases the rate of intracranial flow. This can cause an abnormal appearance at perfusion CT and lead to misinterpretation of imaging findings, as discussed in the next section (48, 49).

Pitfalls of Image Review.—CT angiography can be challenging owing to the complexity of the anatomy, the number of images obtained, and patient cooperation. Images obtained before a

stroke can be indispensable, particularly in confirmation of chronic vessel occlusions.

Late-phase CT angiography can lead to extensive venous attenuation that complicates interpretation by introducing distracting vessels and veins that can be confused with patent arteries. When venous contamination is present, it is essential to carefully trace the arteries, particularly the posterior cerebral arteries (PCAs) to avoid mistaking a patent basal vein of Rosenthal for a patent distal PCA segment (Fig 9).

Hypoattenuation on CT angiography source images has been studied as a correlate of low CBV in brain regions. CT angiography may be superior to nonenhanced CT alone for identification of parenchymal ischemic change (28). Studies have also shown that CT angiography source images and diffusion-weighted images are more accurate at depicting core infarct volume than nonenhanced CT images (28, 53).

Like perfusion CT, CT angiography is flow and timing dependent and demonstrates tissue viability on the basis of hemodynamic parameters. For this reason, CT angiography source images have the potential to overestimate core infarct volume in regions of poor but not critical hypoperfusion. This overestimation can lead to inaccurate patient selection and underuse of EVT in patients who might benefit from treatment (28, 54, 55).

Collateral vessels can be viewed at single-phase, dual-phase, or multiphase CT angiography. Images must be acquired and reviewed by using at least arterial and delayed phases. The vessels can then be classified as good or poor by comparing the attenuation to that of the contralateral uninvolved hemisphere (33).

In regions of ischemia caused by long-segment proximal vascular occlusion, there may be a de-

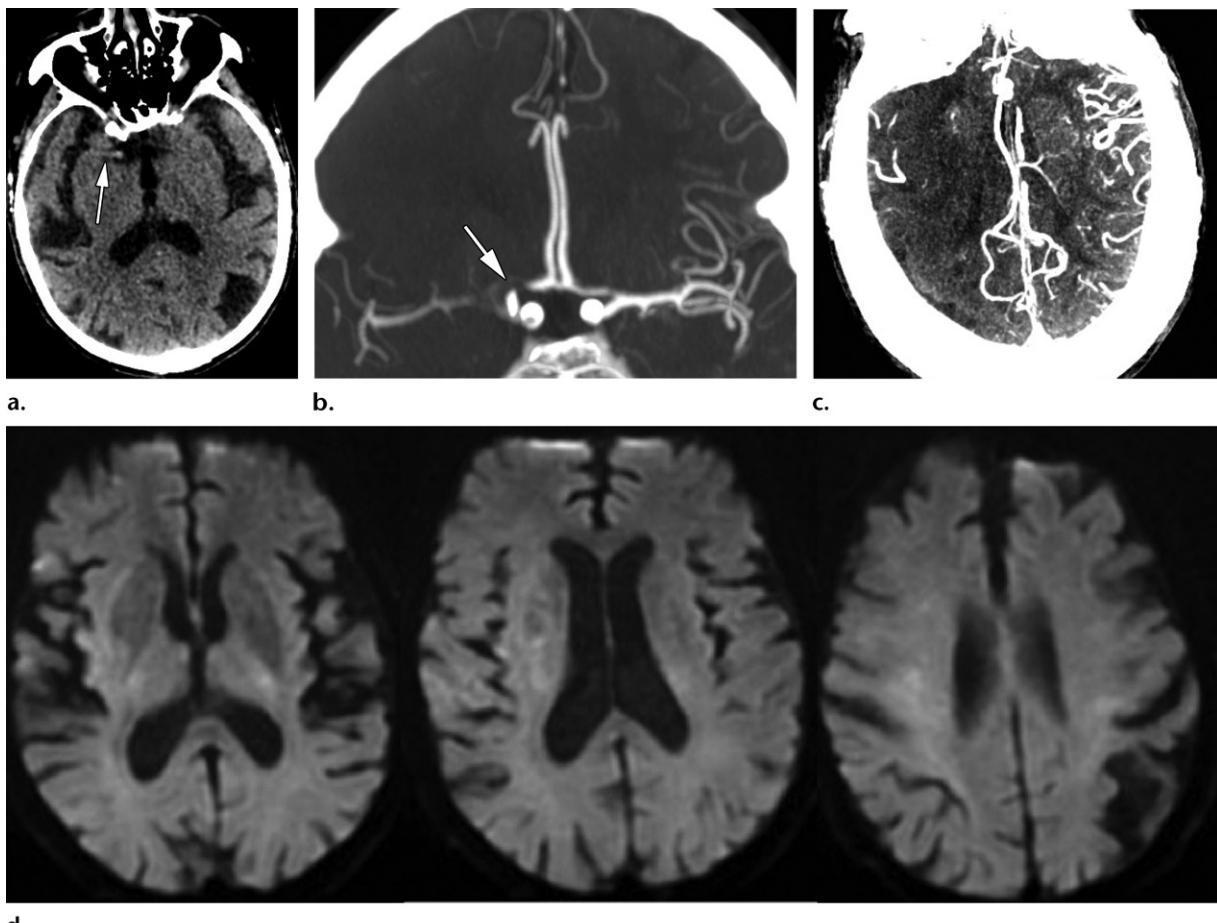


Figure 10. Poor collateral flow with early ischemia in a hospital visitor who collapsed after abrupt onset of left hemiparesis. (a) Non-enhanced CT image less than 30 minutes after stroke shows a hyperattenuating MCA sign (arrow) but is otherwise normal without subtle or well-established ischemic hypoattenuation, not surprising given the hyperacute manifestation. (b) Coronal thick-section MIP CT angiogram shows a T occlusion of the right ICA terminus involving the proximal M1 and A1 segments (arrow). (c) Axial thick-section MIP image of collateral vessels obtained in the arterial phase shows absent enhancement in over 50% of the territory at risk, suggestive of a malignant pattern with both vascular and parenchymal window and level settings. Given the hyperacute manifestation, normal nonenhanced CT findings, and immediate availability of the interventional team in a patient with a poor collateral pattern likely to progress to a large infarction, the decision was made to perform rapid EVT after thrombolysis with intravenous tPA. (d) Diffusion-weighted images obtained after removal of a right M1 thrombus show only trace final infarct in the right MCA territory.

layed arrival time of contrast material with relatively maintained collateral flow. In this context, reviewing arterial single-phase MIP images may be misleading.

For example, a region with intermediate collaterals distal to a long-segment occlusion might be labeled incorrectly as a poor or malignant pattern if the images are obtained too early in the arterial phase. This may inappropriately exclude some patients from receiving treatment with EVT (56,57) (Fig 10).

The ASPECTS system partially addresses this pitfall by using multiphase CT angiography. Collateral flow is categorized as good, intermediate, or poor on the basis of interhemispheric comparisons corrected for contrast material arrival time.

Other advantages of multiphase CT angiography include low cost of implementation and relative insensitivity to patient motion (33).

Perfusion CT

Technique

Dynamic or first-pass perfusion CT is performed by sequentially imaging a defined section of tissue after a single high-flow bolus of contrast material is administered. The same section is imaged multiple times in cine mode as the bolus passes to track the degree of attenuation at both the tissue and arterial levels as a function of time.

Older CT scanners with narrow detectors provided craniocaudal coverage of a limited section of the brain only. Modern scanners with helical capability and broader z-direction detectors can perform whole-brain perfusion CT.

As with CT angiography, an 18- or 20-gauge peripheral needle is preferred to achieve optimal contrast agent flow rates with a saline chaser of at least 15–20 mL. A minimum contrast material

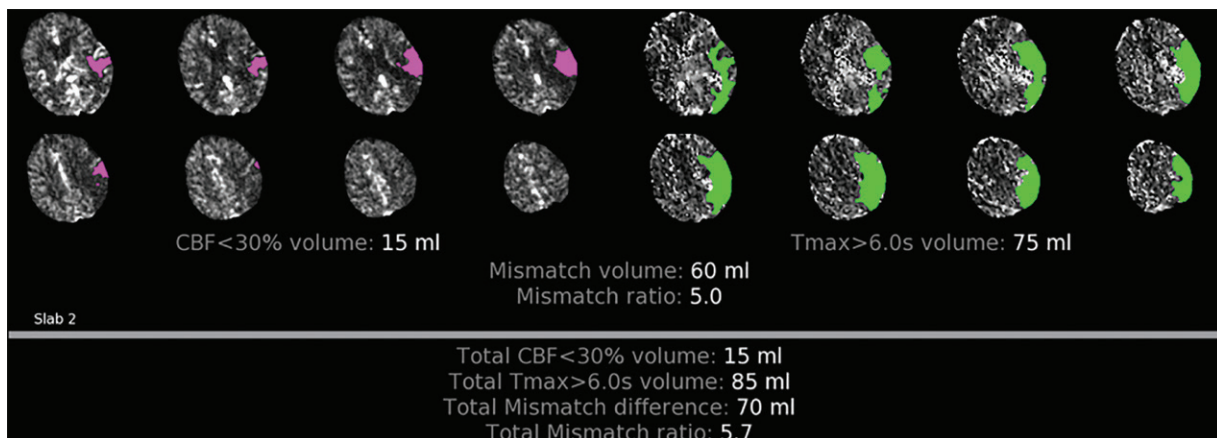


Figure 11. Perfusion CT findings favorable for EVT in an 85-year-old woman with atrial fibrillation who had received intravenous tPA for right MCA syndrome. CT angiography showed a right M1 occlusion extending to the inferior M2 division (not shown). CT perfusion images 10 hours after last known normal show a small 15-mL region of critical cerebral blood flow (CBF) reduction (CBF < 30% [purple]) surrounded by a larger 75-mL region of delayed transit time (time to maximum of the tissue residue function [T_{\max}] > 6 seconds [green]) for a T_{\max} -CBF mismatch ratio of 5. On the basis of these favorable perfusion CT findings, the patient was referred for EVT.

injection of 40 mL with a minimum rate of 4 mL/sec by using power injection is recommended. A higher rate of injection forms a tighter bolus and helps improve hemodynamic maps.

Technique should be optimized to the particular scanner, but 70–90 kVp and 100–200 mAs are recommended to keep the total radiation dose as low as reasonably achievable. In cine mode, one image per second should be acquired over a period of at least 50–60 seconds. Perfusion CT can be performed concurrently with or separately from CT angiography (58,60–62).

Automated or semiautomated postprocessing of the CT perfusion data generates multiple perfusion maps (38,58,59). Perfusion parameter calculations are performed using deconvolution approaches. The methodologies of different deconvolution algorithms are beyond the scope of this review (63).

Because attenuation change is linearly associated with the concentration of iodinated contrast material in a region, absolute values of perfusion parameters can be calculated. Cerebral blood flow (CBF) and time to maximum enhancement are among the most accurate values for use in acute stroke evaluation (64,65). Automated software platforms can generate qualitative and quantitative maps of ischemic lesion volumes from perfusion CT data with automatically selected arterial and venous inputs. The arterial inflow region of interest (ROI) is usually located in the A2 segment of the ACA or the M2 segment of the MCA. The venous ROI is selected over the dural venous confluence.

Even small differences in vessel ROI selection can result in substantial differences on the maps and in reported tissue values, so assessing the imaging input quality is important. To ensure high-

quality perfusion CT images, it is also important to assess for patient motion, adequate attenuation of the contrast material bolus, and sufficiently long acquisition time to avoid truncation of the tissue and vessel time-attenuation curves (36,63).

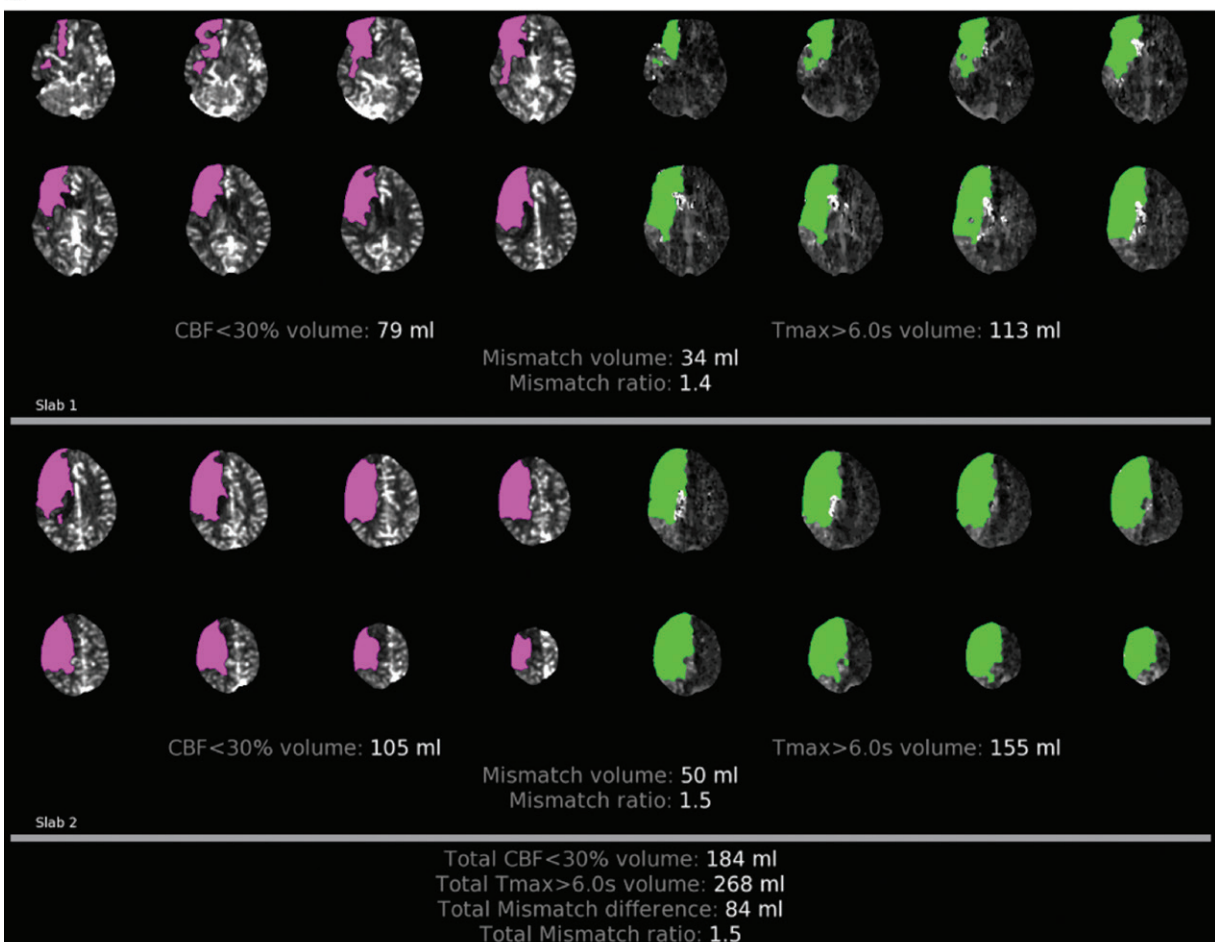
Image Review

Tips and Pearls for Image Review.—Using the time-attenuation curves generated from initial ROI selection, color-coded perfusion parameter maps can be generated automatically or semiautomatically. Parameters demonstrated on these maps include CBF, time to maximum of the tissue residue function (T_{\max}), CBV, and mean transit time. Only CBF and T_{\max} have been widely studied in recent randomized clinical trials.

For example, in the CT arms of the DAWN and DEFUSE 3 trials, automated perfusion CT software estimated core infarct volume on the basis of a less than 30% threshold for CBF reduction and penumbral volume on the basis of a threshold greater than 6 seconds for prolongation of T_{\max} (8,9). Mismatch ratios and ischemic volumes can be calculated, displayed, and used for clinical trial enrollment, depending on the specific eligibility criteria (Figs 11, 12).

The accuracy of perfusion CT for helping distinguish large (>100 mL) from small (<50–70 mL) core infarct volumes in EVT selection has been studied compared with a DWI reference standard (55,66–68). Use of perfusion CT has been increasing since its successful use in helping determine eligibility for enrollment in subsets of patients in the recent late-window DAWN and DEFUSE 3 trials (8,9).

Perfusion CT is grouped with MRI in the updated 2018 American Heart Association–

**a.****b.**

American Stroke Association guidelines for early management of patients with acute ischemic stroke, which states, “in selected patients with AIS [acute ischemic stroke] within 6 to 24 hours of last known normal who have LVO in the anterior circulation, obtaining CTP [CT perfusion imaging], DW-MRI [diffusion-weighted MRI], or MRI perfusion is recommended to aid in patient selection for mechanical thrombectomy, but only

when imaging and other eligibility criteria from RCTs [randomized controlled trials] showing benefit are being strictly applied in selecting patients for mechanical thrombectomy” (3, p e59).

However, in the recent Hermes meta-analysis of early-window EVT trials and in a subgroup analysis of the DEFUSE 3 late-window trial that were presented at the 2018 American Heart Association International Stroke Conference,

DWI was found to be more efficient than perfusion CT when used to help select candidates for EVT. DWI was found to have higher odds ratios for selecting patients more likely to experience clinical improvement and functional independence (69).

Given this, it is not surprising that there is currently little consensus on the optimal imaging strategy for late-window EVT selection. Use of DWI, CT angiography of collateral vessels, and perfusion CT for core infarct volume assessment varies widely between different comprehensive stroke centers and in different clinical situations (8,9,66,70).

Additionally, recent trials have suggested that advanced CT and MRI can be used to extend the time window for intravenous tPA administration (71,72). The recent EXTEND (Extending the Time for Thrombolysis in Emergency Neurological Deficits) trial results have shown that patients benefit from treatment with intravenous tPA at 9 hours or after a wake-up stroke when they are selected using perfusion CT or perfusion MRI (73).

Tenecteplase is a newer intravenous tPA that is currently being investigated in late-window clinical trials. When perfusion CT is used for treatment selection, tenecteplase may provide stronger benefits up to 6 hours after symptom onset (74).

Pitfalls of Image Review.—Potential pitfalls of perfusion CT include motion artifact, poor signal-to-noise ratio from a suboptimal contrast material bolus, faulty arterial and venous input functions, and truncation of the tissue and vascular time-attenuation flow curves from a shortened acquisition time.

It is important to identify the degree of motion to decide whether the images are of adequate quality. Moderate-to-severe motion artifact occurs frequently, and one study reported that it occurred in 25% of patients (75).

Although automated perfusion software generates volumetric data for core and penumbra, it is important to be aware of its potential technical and clinical pitfalls. The time-attenuation curves should be evaluated to ensure appropriate location of the ROI in a vessel that runs nearly perpendicular to the imaging plane to avoid volume averaging with the vessel wall and surrounding structures. Slow flow in a stenotic major vessel selected for the arterial input function (eg, chronic carotid occlusion) will result in inaccurate relative parameter values.

The effect of truncated time-attenuation curves has also been a concern (68,69,79). Perfusion CT protocols less than 60 seconds in length can

overestimate infarct core volume, since perfusion parameter values may be underestimated in voxels with incomplete bolus tracking (77-79).

Poor signal-to-noise ratio can result when insufficient contrast material reaches the imaging voxel. This can be caused by factors such as poor cardiac output associated with atrial fibrillation (commonly associated with acute embolic stroke) or unsuspected venous or arterial stenoses delaying the arrival of contrast material at the circle of Willis (48,63,49).

Moreover, thresholds for determining core and penumbra can vary between vendors and between postprocessing platforms (68,69). Thresholds for determining irreversible ischemia likely vary with time after stroke, quality of collateral flow, and ischemic preconditioning (11,55). Perfusion CT thresholds can also be unreliable in the presence of old infarcts, partial reperfusion, or hyperemia associated with compensatory vasodilatation.

Stroke Mimics

Potential acute stroke mimics include intracranial masses due to primary or metastatic malignancy, cerebritis, cerebral abscess, and posterior reversible encephalopathy syndrome (PRES). Most of these pathologic processes cause vasogenic edema and accentuation of—rather than loss of—GWD. Low-grade gliomas and other hypoattenuating lesions without surrounding vasogenic edema may require use of MRI for definitive diagnosis (Fig 13).

Increased gyriform enhancement with mass effect in subacute infarction may be indistinguishable from high-grade glioma. Metastases, cerebritis, abscess, demyelinating disease, and PRES can all mimic subacute infarction by blurring or effacing GWD owing to mass effect and displacement (Fig 13).

Contrast material staining after EVT can mimic acute hemorrhage. Dual-energy CT iodine maps and virtual nonenhanced CT images can help confirm that intracranial hyperattenuation is due to iodine leakage through a nonintact blood-brain barrier (16,79).

Perfusion CT can also be useful in stroke differential diagnosis by helping distinguish wedge-shaped perfusion deficits caused by arterial occlusive emboli from other flow derangements, such as those caused by seizure, hypoglycemia, or hyperglycemia (49).

Conclusion

CT evaluation of acute ischemic stroke is robust, rapid, and widely available. The DAWN and DEFUSE 3 trials proved that EVT results in improved outcomes and functional independence

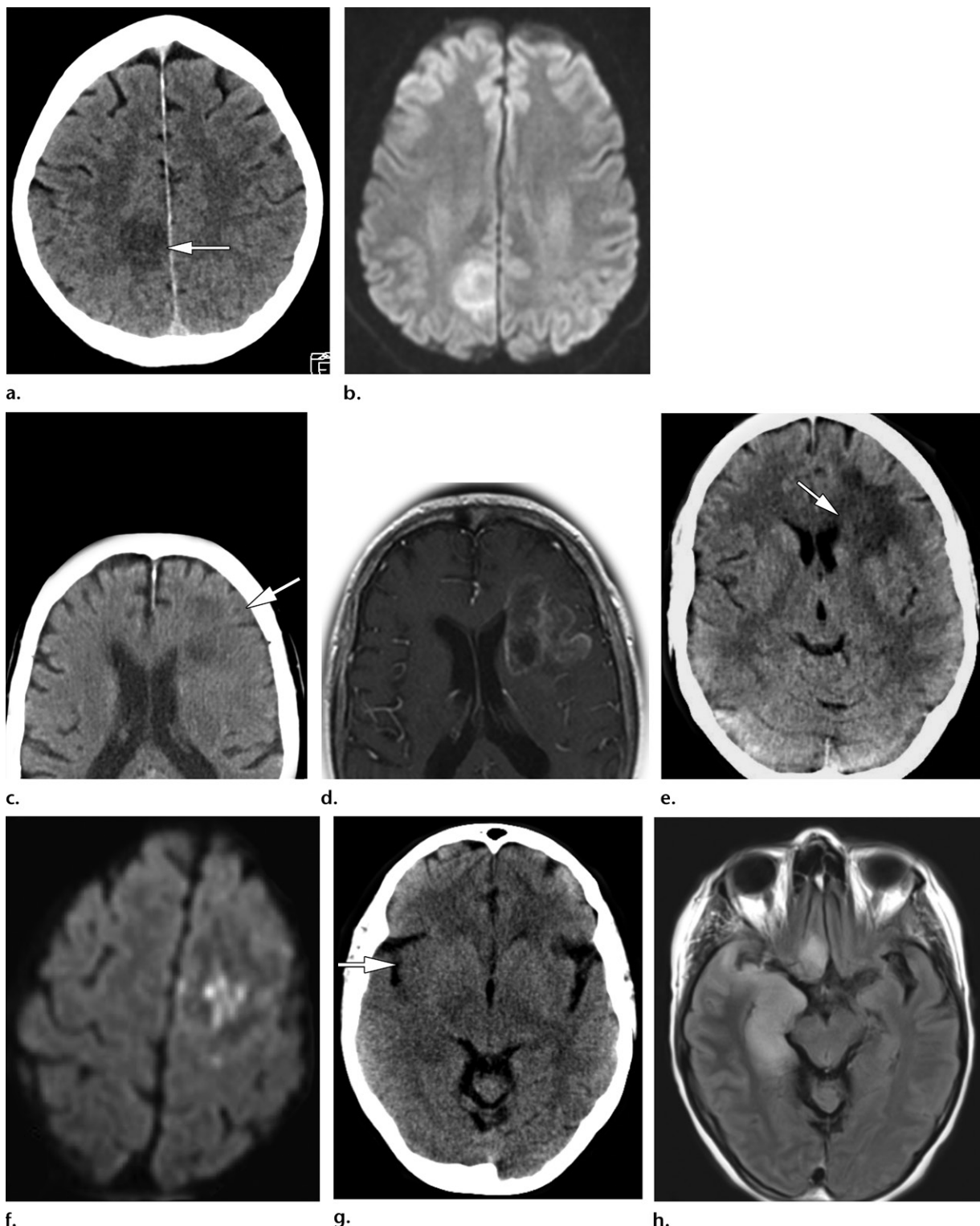


Figure 13. Stroke mimics caused by nonspecific hypoattenuating lesions at nonenhanced CT. (a) Nonenhanced CT image in a 58-year-old man with confusion shows cortical effacement from a well-circumscribed rounded area of hypoattenuation with loss of GWD in the medial right parietal lobe (arrow). (b) Subsequent FLAIR (fluid-attenuated inversion-recovery) image shows that the lesion is hyperintense. DWI showed no diffusion restriction in the lesion, which was confirmed at biopsy to be a low-grade glioma. (c) Admission nonenhanced CT image in another patient shows an irregular lesion with patchy hypoattenuation (arrow). (d) Contrast-enhanced T1-weighted MR image shows serpentine irregular surrounding enhancement. These findings are suggestive of a subacute evolving infarct, but the lesion was proved to represent a left frontal glioblastoma multiforme. (e) Nonenhanced CT image in another patient shows subcortical and gray-white matter junction left frontal lobe hypoattenuation (arrow), which is suggestive of vasogenic edema but nonspecific. (f) Diffusion-weighted image shows diffusion restriction. Along with peripheral enhancement on postcontrast T1-weighted images (not shown), these findings helped confirm the final diagnosis of cerebral abscess. (g) Nonenhanced CT image in a young patient shows loss of GWD in the right insula and external capsule (arrow). (h) FLAIR image shows additional involvement of the right mesial temporal lobe, amygdala, and hypothalamic regions. The final diagnosis was herpes encephalitis.

even up to 24 hours after a stroke. Because of this, nonenhanced CT and CT angiography have become the community standards for selecting patients for intravenous tPA and EVT in both early and late time windows.

Although DWI is the reference standard for determining core infarct lesion volume, CT angiography and perfusion CT may be used when DWI is not available. These uses of CT may help distinguish patients with large infarct cores—who are least likely to benefit from and most likely to be harmed by EVT—from patients with small infarct cores.

Awareness of common findings, pearls, and pitfalls of multimodal stroke CT evaluation and interpretation has therefore become essential for providers caring for patients with acute stroke.

Disclosures of Conflicts of Interest.—**A.S.V.** Activities related to the present article: disclosed no relevant relationships. Activities not related to the present article: institution received grants from Cerenovus, ENDOLOW trial, GE Healthcare, Imaging Core Lab, and Johnson & Johnson. Other activities: disclosed no relevant relationships. **M.G.** Activities related to the present article: disclosed no relevant relationships. Activities not related to the present article: author received payment from Medtronic, Menticor, Microvention, and Stryker for consulting; institution received grants from Medtronic and Stryker; author received payment from GE Healthcare for a licensing agreement. Other activities: disclosed no relevant relationships. **M.H.L.** Activities related to the present article: disclosed no relevant relationships. Activities not related to the present article: received grant from GE Healthcare; consultant to Takeda Pharmaceuticals and GE Healthcare; institution received research funding from GE Healthcare; institution received research software license from Siemens Healthineers. Other activities: patents pending for portable electrical impedance spectroscopy device, artificial intelligence for use in CT of brain hemorrhage, and artificial intelligence to depict collaterals.

References

- Tomandl BF, Klotz E, Handschu R, et al. Comprehensive imaging of ischemic stroke with multisector CT. *RadioGraphics* 2003;23(3):565–592.
- National Institute of Neurological Disorders and Stroke tPA Stroke Study Group. Tissue plasminogen activator for acute ischemic stroke. *N Engl J Med* 1995;333(24):1581–1587.
- Powers WJ, Rabinstein AA, Ackerson T, et al. 2018 Guidelines for the Early Management of Patients With Acute Ischemic Stroke: A Guideline for Healthcare Professionals From the American Heart Association/American Stroke Association. *Stroke* 2018;49(3):e46–e110. [Published corrections appear in *Stroke* 2018;49(3):e138 and *Stroke* 2018;49(6):e233–e234.] <https://doi.org/10.1161/STR.0000000000000158>.
- Tomura N, Uemura K, Inugami A, Fujita H, Higano S, Shishido F. Early CT finding in cerebral infarction: obscuration of the lentiform nucleus. *Radiology* 1988;168(2):463–467.
- Truwit CL, Barkovich AJ, Gean-Marton A, Hibri N, Norman D. Loss of the insular ribbon: another early CT sign of acute middle cerebral artery infarction. *Radiology* 1990;176(3):801–806.
- Dippel DW, Du Ry van Beest Holle M, van Kooten F, Koudstaal PJ. The validity and reliability of signs of early infarction on CT in acute ischaemic stroke. *Neuroradiology* 2000;42(9):629–633.
- Wardlaw JM, Mielke O. Early signs of brain infarction at CT: observer reliability and outcome after thrombolytic treatment—systematic review. *Radiology* 2005;235(2):444–453.
- Nogueira RG, Jadhav AP, Haussen DC, et al. Thrombectomy 6 to 24 Hours after Stroke with a Mismatch between Deficit and Infarct. *N Engl J Med* 2018;378(1):11–21.
- Albers GW, Marks MP, Kemp S, et al. Thrombectomy for Stroke at 6 to 16 Hours with Selection by Perfusion Imaging. *N Engl J Med* 2018;378(8):708–718.
- Sims JR, Ghai LR, Schaefer PW, et al. ABC/2 for rapid clinical estimate of infarct, perfusion, and mismatch volumes. *Neurology* 2009;72(24):2104–2110.
- Schellinger PD, Bryan RN, Caplan LR, et al. Evidence-based guideline: the role of diffusion and perfusion MRI for the diagnosis of acute ischemic stroke: report of the Therapeutics and Technology Assessment Subcommittee of the American Academy of Neurology. *Neurology* 2010;75(2):177–185. [Published correction appears in *Neurology* 2010;75(10):938.] <https://doi.org/10.1212/WNL.0b013e3181e7c9dd>.
- González RG. Imaging-guided acute ischemic stroke therapy: from “time is brain” to “physiology is brain.” *AJNR Am J Neuroradiol* 2006;27(4):728–735.
- Kanekar SG, Zacharia T, Roller R. Imaging of stroke. II. Pathophysiology at the molecular and cellular levels and corresponding imaging changes. *AJR Am J Roentgenol* 2012;198(1):63–74.
- Kelly AG, Hellkamp AS, Olson D, Smith EE, Schwamm LH. Predictors of rapid brain imaging in acute stroke: analysis of the Get with the Guidelines—Stroke program. *Stroke* 2012;43(5):1279–1284.
- ACR-ASNR-SPR Practice Parameter for the Performance of Computed Tomography (CT) of the Brain. <https://www.acr.org/-/media/ACR/Files/Practice-Parameters/CT-Brain.pdf>. Revised 2015. Accessed April 2, 2019.
- Potter CA, Sodickson AD. Dual-Energy CT in Emergency Neuroimaging: added Value and Novel Applications. *RadioGraphics* 2016;36(7):2186–2198.
- Pomerantz SR, Kamalian S, Zhang D, et al. Virtual monochromatic reconstruction of dual-energy unenhanced head CT at 65–75 keV maximizes image quality compared with conventional polychromatic CT. *Radiology* 2013;266(1):318–325.
- Perry JJ, Stiell IG, Sivilotti ML, et al. Sensitivity of computed tomography performed within six hours of onset of headache for diagnosis of subarachnoid haemorrhage: prospective cohort study. *BMJ* 2011;343:d4277.
- Lee H, Yune S, Mansouri M, et al. An explainable deep-learning algorithm for the detection of acute intracranial haemorrhage from small datasets. *Nat Biomed Eng* 2019;3(3):173–182.
- Kamalian S, Kemmling A, Borgie RC, et al. Admission insular infarction >25% is the strongest predictor of large mismatch loss in proximal middle cerebral artery stroke. *Stroke* 2013;44(11):3084–3089.
- Kucinski T. Unenhanced CT and acute stroke physiology. *Neuroimaging Clin N Am* 2005;15(2):397–407, xi–xii.
- Pexman JH, Barber PA, Hill MD, et al. Use of the Alberta Stroke Program Early CT Score (ASPECTS) for assessing CT scans in patients with acute stroke. *AJNR Am J Neuroradiol* 2001;22(8):1534–1542.
- Kuang H, Najm M, Chakraborty D, et al. Automated ASPECTS on Noncontrast CT Scans in Patients with Acute Ischemic Stroke Using Machine Learning. *AJNR Am J Neuroradiol* 2019;40(1):33–38.
- Leys D, Pruvost JP, Godefroy O, Rondepierre P, Leclerc X. Prevalence and significance of hyperdense middle cerebral artery in acute stroke. *Stroke* 1992;23(3):317–324.
- Mair G, Boyd EV, Chappell FM, et al. Sensitivity and specificity of the hyperdense artery sign for arterial obstruction in acute ischemic stroke. *Stroke* 2015;46(1):102–107.
- Barber PA, Demchuk AM, Hudon ME, Pexman JH, Hill MD, Buchan AM. Hyperdense sylvian fissure MCA “dot” sign: a CT marker of acute ischemia. *Stroke* 2001;32(1):84–88.
- Lev MH, Farkas J, Gemmette JJ, et al. Acute stroke: improved nonenhanced CT detection—benefits of soft-copy interpretation by using variable window width and center level settings. *Radiology* 1999;213(1):150–155.
- Camargo EC, Furie KL, Singhal AB, et al. Acute brain infarct: detection and delineation with CT angiographic

- source images versus nonenhanced CT scans. *Radiology* 2007;244(2):541–548.
29. Goldmakher GV, Camargo EC, Furie KL, et al. Hyperdense basilar artery sign on unenhanced CT predicts thrombus and outcome in acute posterior circulation stroke. *Stroke* 2009;40(1):134–139.
 30. Riedel CH, Jensen U, Rohr A, et al. Assessment of thrombus in acute middle cerebral artery occlusion using thin-slice nonenhanced computed tomography reconstructions. *Stroke* 2010;41(8):1659–1664.
 31. Dittrich R, Akdeniz S, Kloska SP, et al. Low rate of contrast-induced nephropathy after CT perfusion and CT angiography in acute stroke patients. *J Neurol* 2007;254(11):1491–1497.
 32. ACR-ASNR-SPR Practice Parameter for the Performance and Interpretation of Cervicocerebral Computed Tomography Angiography (CTA) of the Brain. <https://www.acr.org/-/media/ACR/Files/Practice-Parameters/CervicoCerebralCTA.pdf>. Revised 2015. Accessed April 2, 2019.
 33. Menon BK, d'Esterre CD, Qazi EM, et al. Multiphase CT Angiography: a New Tool for the Imaging Triage of Patients with Acute Ischemic Stroke. *Radiology* 2015;275(2):510–520.
 34. Kortman HG, Smit EJ, Oei MT, Manniesing R, Prokop M, Meijer FJ. 4D-CTA in neurovascular disease: a review. *AJNR Am J Neuroradiol* 2015;36(6):1026–1033.
 35. Deng K, Liu C, Ma R, et al. Clinical evaluation of dual-energy bone removal in CT angiography of the head and neck: comparison with conventional bone-subtraction CT angiography. *Clin Radiol* 2009;64(5):534–541.
 36. Buerke B, Puesken M, Wittkamp G, et al. Bone subtraction CTA for transcranial arteries: intra-individual comparison with standard CTA without bone subtraction and TOF-MRA. *Clin Radiol* 2010;65(6):440–446.
 37. McCollough CH, Leng S, Yu L, Fletcher JG. Dual- and Multi-Energy CT: principles, Technical Approaches, and Clinical Applications. *Radiology* 2015;276(3):637–653.
 38. de Lucas EM, Sánchez E, Gutiérrez A, et al. CT protocol for acute stroke: tips and tricks for general radiologists. *RadioGraphics* 2008;28(6):1673–1687.
 39. Yeo LL, Paliwal P, Teoh HL, et al. Assessment of intracranial collaterals on CT angiography in anterior circulation acute ischemic stroke. *AJNR Am J Neuroradiol* 2015;36(2):289–294.
 40. Maas MB, Lev MH, Ay H, et al. Collateral vessels on CT angiography predict outcome in acute ischemic stroke. *Stroke* 2009;40(9):3001–3005.
 41. Miteff F, Levi CR, Bateman GA, Spratt N, McElduff P, Parsons MW. The independent predictive utility of computed tomography angiographic collateral status in acute ischaemic stroke. *Brain* 2009;132(Pt 8):2231–2238.
 42. Souza LC, Yoo AJ, Chaudhry ZA, et al. Malignant CTA collateral profile is highly specific for large admission DWI infarct core and poor outcome in acute stroke. *AJNR Am J Neuroradiol* 2012;33(7):1331–1336.
 43. Goyal M, Menon BK, Almekhlafi MA, Demchuk A, Hill MD. The Need for Better Data on Patients with Acute Stroke Who Are Not Treated Because of Unfavorable Imaging. *AJNR Am J Neuroradiol* 2017;38(3):424–425.
 44. Rocha M, Jovin TG. Fast Versus Slow Progressors of Infarct Growth in Large Vessel Occlusion Stroke: Clinical and Research Implications. *Stroke* 2017;48(9):2621–2627.
 45. ASPECTS Collateral Score. <http://www.aspectstroke.com/collateral-scoring/>. Accessed April 2, 2019.
 46. Sun CH, Connelly K, Nogueira RG, et al. ASPECTS decay during inter-facility transfer predicts patient outcomes in endovascular reperfusion for ischemic stroke: a unique assessment of dynamic physiologic change over time. *J Neurointerv Surg* 2015;7(1):22–26.
 47. Aminoff MJ, Josephson SA, eds. Aminoff's Neurology and General Medicine. 5th ed. London, England: Academic Press/Elsevier, 2014.
 48. Allmendinger AM, Tang ER, Lui YW, Spektor V. Imaging of stroke. I. Perfusion CT: overview of imaging technique, interpretation pearls, and common pitfalls. *AJR Am J Roentgenol* 2012;198(1):52–62.
 49. Lui YW, Tang ER, Allmendinger AM, Spektor V. Evaluation of CT perfusion in the setting of cerebral ischemia: patterns and pitfalls. *AJNR Am J Neuroradiol* 2010;31(9):1552–1563.
 50. Holmstedt CA, Turan TN, Chimowitz MI. Atherosclerotic intracranial arterial stenosis: risk factors, diagnosis, and treatment. *Lancet Neurol* 2013;12(11):1106–1114.
 51. Borst J, Berkhemer OA, Santos EMM, et al. Value of Thrombus CT Characteristics in Patients with Acute Ischemic Stroke. *AJNR Am J Neuroradiol* 2017;38(9):1758–1764.
 52. Benjamin EJ, Virani SS, Callaway CW, et al. Heart Disease and Stroke Statistics—2018 Update: A Report From the American Heart Association. *Circulation* 2018;137(12):e67–e492. [Published correction appears in *Circulation* 2018;137(12):e493.] <https://doi.org/10.1161/CIR.0000000000000558>.
 53. Schramm P, Schellinger PD, Fiebach JB, et al. Comparison of CT and CT angiography source images with diffusion-weighted imaging in patients with acute stroke within 6 hours after onset. *Stroke* 2002;33(10):2426–2432.
 54. Pulli B, Schaefer PW, Hakimelahi R, et al. Acute ischemic stroke: infarct core estimation on CT angiography source images depends on CT angiography protocol. *Radiology* 2012;262(2):593–604.
 55. Schaefer PW, Souza L, Kamalian S, et al. Limited reliability of computed tomographic perfusion acute infarct volume measurements compared with diffusion-weighted imaging in anterior circulation stroke. *Stroke* 2015;46(2):419–424.
 56. Christoforidis GA, Mohammad Y, Kehagias D, Avutu B, Slivka AP. Angiographic assessment of pial collaterals as a prognostic indicator following intra-arterial thrombolysis for acute ischemic stroke. *AJNR Am J Neuroradiol* 2005;26(7):1789–1797.
 57. Reid M, Famuyide AO, Forkert ND, et al. Accuracy and Reliability of Multiphase CTA Perfusion for Identifying Ischemic Core. *Clin Neuroradiol* 2018 Aug 21. [Epub ahead of print] [Published correction appears in *Clin Neuroradiol* 2019 Jun 3.] <https://doi.org/10.1007/s00062-018-0717-x>.
 58. Hoeffner EG, Case I, Jain R, et al. Cerebral perfusion CT: technique and clinical applications. *Radiology* 2004;231(3):632–644.
 59. Sriniwasan A, Goyal M, Al Azri F, Lum C. State-of-the-art imaging of acute stroke. *RadioGraphics* 2006;26(suppl 1):S75–S95.
 60. Eastwood JD, Lev MH, Provenzale JM. Perfusion CT with iodinated contrast material. *AJR Am J Roentgenol* 2003;180(1):3–12.
 61. Christensen S, Lansberg MG. CT perfusion in acute stroke: practical guidance for implementation in clinical practice. *J Cereb Blood Flow Metab* 2018 Oct 22:271678X18805590 [Epub ahead of print].
 62. ACR-ASNR-SPR Practice Parameter for the Performance of Computed Tomography (CT) Perfusion in Neuroradiologic Imaging. <https://www.acr.org/-/media/ACR/Files/Practice-Parameters/ct-perfusion.pdf>. Revised 2017. Accessed April 2, 2019.
 63. Konstas AA, Goldmakher GV, Lee TY, Lev MH. Theoretic basis and technical implementations of CT perfusion in acute ischemic stroke. II. Technical implementations. *AJNR Am J Neuroradiol* 2009;30(5):885–892.
 64. Bivard A, Levi C, Spratt N, Parsons M. Perfusion CT in acute stroke: a comprehensive analysis of infarct and penumbra. *Radiology* 2013;267(2):543–550.
 65. Campbell BC, Mitchell PJ, Kleinig TJ, et al. Endovascular therapy for ischemic stroke with perfusion-imaging selection. *N Engl J Med* 2015;372(11):1009–1018.
 66. Goyal M, Menon BK, Derdeyn CP. Perfusion imaging in acute ischemic stroke: let us improve the science before changing clinical practice. *Radiology* 2013;266(1):16–21.
 67. Kamalian S, Kamalian S, Maas MB, et al. CT cerebral blood flow maps optimally correlate with admission diffusion-weighted imaging in acute stroke but thresholds vary by postprocessing platform. *Stroke* 2011;42(7):1923–1928.
 68. Kamalian S, Kamalian S, Konstas AA, et al. CT perfusion mean transit time maps optimally distinguish benign oligemia from true “at-risk” ischemic penumbra, but thresholds vary by postprocessing technique. *AJNR Am J Neuroradiol* 2012;33(3):545–549.

69. Campbell BCV, Majoie CBLM, Albers GW, et al. Penumbbral imaging and functional outcome in patients with anterior circulation ischaemic stroke treated with endovascular thrombectomy versus medical therapy: a meta-analysis of individual patient-level data. *Lancet Neurol* 2019;18(1):46–55.
70. Leslie-Mazwi TM, Hirsch JA, Falcone GJ, et al. Endovascular Stroke Treatment Outcomes After Patient Selection Based on Magnetic Resonance Imaging and Clinical Criteria. *JAMA Neurol* 2016;73(1):43–49.
71. Thomalla G, Simonsen CZ, Boutitie F, et al. MRI-Guided Thrombolysis for Stroke with Unknown Time of Onset. *N Engl J Med* 2018;379(7):611–622.
72. Ma H, Campbell BCV, Parsons MW, et al. Thrombolysis Guided by Perfusion Imaging up to 9 Hours after Onset of Stroke. *N Engl J Med* 2019;380(19):1795–1803.
73. Schwamm LH, Wu O, Song SS, et al. Intravenous thrombolysis in unwitnessed stroke onset: MR WITNESS trial results. *Ann Neurol* 2018;83(5):980–993.
74. Parsons M, Spratt N, Bivard A, et al. A randomized trial of tenecteplase versus alteplase for acute ischemic stroke. *N Engl J Med* 2012;366(12):1099–1107.
75. Fahmi F, Beenens LF, Streekstra GJ, et al. Head movement during CT brain perfusion acquisition of patients with suspected acute ischemic stroke. *Eur J Radiol* 2013;82(12):2334–2341.
76. Borst J, Marquering HA, Beenens LF, et al. Effect of extended CT perfusion acquisition time on ischemic core and penumbra volume estimation in patients with acute ischemic stroke due to a large vessel occlusion. *PLoS One* 2015;10(3):e0119409.
77. Copen WA, Deipolyi AR, Schaefer PW, Schwamm LH, González RG, Wu O. Exposing hidden truncation-related errors in acute stroke perfusion imaging. *AJNR Am J Neuroradiol* 2015;36(4):638–645.
78. Schaefer PW, Mui K, Kamalian S, Nogueira RG, Gonzalez RG, Lev MH. Avoiding “pseudo-reversibility” of CT-CBV infarct core lesions in acute stroke patients after thrombolytic therapy: the need for algorithmically “delay-corrected” CT perfusion map postprocessing software. *Stroke* 2009;40(8):2875–2878.
79. Phan CM, Yoo AJ, Hirsch JA, Nogueira RG, Gupta R. Differentiation of hemorrhage from iodinated contrast in different intracranial compartments using dual-energy head CT. *AJNR Am J Neuroradiol* 2012;33(6):1088–1094.



Acute Headache in the Emergency Setting

Melike Guryildirim, MD

Marinos Kontzialis, MD

Merve Ozen, MD

Mehmet Kocak, MD

Abbreviations: AV = arteriovenous, AVM = arteriovenous malformation, CAD = carotid artery dissection, CSF = cerebrospinal fluid, CVT = cerebral venous thrombosis, ED = emergency department, FLAIR = fluid-attenuated inversion-recovery, ICH = intracerebral hemorrhage, IIH = idiopathic intracranial hypertension, PRES = posterior reversible encephalopathy syndrome, RCVS = reversible cerebral vasoconstriction syndrome, SAH = subarachnoid hemorrhage, VAD = vertebral artery dissection

RadioGraphics 2019; 39:1739–1759

<https://doi.org/10.1148/rg.2019190017>

Content Codes: **CT** **ER** **HN** **MR** **NR** **VA**

From the Department of Diagnostic Radiology and Nuclear Medicine, Rush University Medical Center, 1653 W Congress Pkwy, Chicago, IL 60612. Presented as an education exhibit at the 2018 RSNA Annual Meeting. Received February 26, 2019; revision requested May 29 and received July 11; accepted July 25. For this journal-based SA-CME activity, the authors, editor, and reviewers have disclosed no relevant relationships. **Address correspondence to** M.K. (e-mail: Mehmet_Kocak@rush.edu).

©RSNA, 2019

SA-CME LEARNING OBJECTIVES

After completing this journal-based SA-CME activity, participants will be able to:

- Recognize the indications and select the appropriate imaging techniques for evaluation of acute headache in the emergency setting.
- Describe the CT and MRI features of common and less-common causes of acute headache.
- Formulate a differential diagnosis on the basis of clinical and imaging manifestations.

See rsna.org/learning-center-rg.

Acute headache is a common symptom and is reported by approximately 2%–4% of patients who present to the emergency department. Many abnormalities manifest with headache as the first symptom, and it is crucial to obtain a patient's complete clinical history for correct diagnosis. Headache onset, duration, and severity; risk factors such as hypertension, immunosuppression, or malignancy; and the presence of focal neurologic deficits or systemic symptoms may aid the radiologist in deciding whether imaging is appropriate and which modality to choose. Imaging findings are more likely to be abnormal in patients with a “thunderclap” headache than in those with headaches of lesser severity. The causes of headache in the emergency setting are various. They may manifest at imaging as subarachnoid hemorrhage (ruptured aneurysm, reversible vasoconstriction syndrome, or pituitary apoplexy), parenchymal hemorrhage (hypertension, ruptured arteriovenous malformation, cerebral amyloid angiopathy, dural arteriovenous fistula, or sinus thrombosis), or parenchymal edema (posterior reversible encephalopathy syndrome, reversible cerebral vasoconstriction syndrome, sinus thrombosis, or encephalitis). Alterations in intracranial pressure that are related to idiopathic intracranial hypertension or spontaneous intracranial hypotension and prior lumbar puncture or epidural injection may manifest with specific imaging findings. With accumulating knowledge of disease pathophysiology, radiologists have started to play a more central role in making the correct diagnosis. This article reviews multiple causes of acute headache and their characteristic appearances at multimodality imaging and familiarizes the reader with current concepts in imaging.

Online supplemental material is available for this article.

©RSNA, 2019 • radiographics.rsna.org

Introduction

Headache is one of the most common patient concerns in the emergency department, and approximately 2%–4% of all patients who present to the emergency department (ED) report symptoms of headache that are unrelated to trauma (1–3). Appropriate selection of patients who require diagnostic workup is important. Studies (1,3–5) have shown that secondary (pathologic) causes of headache are diagnosed in 4% of all patients with headaches and in greater than 14% of those with sudden-onset severe headaches.

According to the Choosing Wisely initiative of the American Board of Internal Medicine Foundation, no imaging should be performed in patients with an uncomplicated headache. The American Headache Society similarly does not recommend neuroimaging studies in patients with stable headaches that meet the criteria for migraine. The American College of Radiology (ACR) developed evidence-based guidelines, the ACR Appropriateness Criteria (6), to assist providers in making imaging decisions for patients who present with headache.

TEACHING POINTS

- Convexity SAH is the earliest complication of RCVS; however, it is seen in only 20%–25% of cases.
- Angiographic studies including MR angiography, CT angiography, and catheter angiography can be normal during the 1st week after clinical onset of RCVS. This is likely related to centripetal progression of cerebral vasoconstriction that appears in small peripheral arterioles and proceeds centrally to involve medium and large cerebral arteries.
- Two-dimensional time-of-flight MR venography is the most commonly used technique to evaluate CVT and is most sensitive to the flow that is perpendicular to the plane of acquisition.
- Headache is the earliest symptom and is reported by 68% of patients with spontaneous internal carotid artery (ICA) dissection (ICAD) and by 69% of those with spontaneous vertebral artery dissection (VAD).
- Transverse sinus stenosis has been shown in more than 90% of patients with IIH, rendering venous outflow obstruction as one of the possible underlying pathophysiologic mechanisms.

Indications for neuroimaging are strongly based on the patient's clinical history and a detailed physical examination. Studies have shown that several clinical signs, symptoms, and types of headache are associated with increased likelihood of the patient having a serious intracranial abnormality. These include abnormal findings at neurologic examination, a cluster-type headache, the patient seeing an aura or vomiting, a headache that the clinician cannot define as being caused by a common primary headache disorder, and a headache aggravated by exertion or performance of a Valsalva maneuver. Among these findings, the highest association with serious intracranial abnormality was found to be with the presence of any abnormal finding at neurologic examination. Other helpful clinical information includes pain radiating to the face or neck, Horner syndrome, cranial nerve palsies, systemic symptoms such as fever or weight loss, immunosuppression, known malignancy or HIV infection, pregnancy, vision loss, or pulsatile tinnitus. Imaging of patients with a headache related to trauma is beyond the scope of this article.

Special consideration is given to the "thunderclap" headache, which is a severe headache for which the patient reports a pain score of 7 on a 0–10 pain scale and during which the pain peaks within 60 seconds of onset. Thunderclap headaches have a higher imaging yield in the ED. A large Norwegian study (7) showed subarachnoid hemorrhage (SAH) in 16% of patients who presented with acute severe headache in the ED; however, the percentage was dramatically higher, at 47%, in patients who presented with a thunderclap headache or reported having experienced "the worst headache of my life." The location and type of pain are not specific. It may be a single

headache or may recur over a few days. It may start spontaneously or during performance of the Valsalva maneuver, exertion, sexual activity, emotional stress, bathing, or showering. Neurovascular disorders including ruptured cerebral aneurysms or reversible cerebral vasoconstriction syndrome (RCVS) are the most common causes of thunderclap headaches. Less commonly, intracranial hypertension and hypotension syndromes, infections, cervical artery dissections, cerebral venous thrombosis (CVT), or pituitary apoplexy may also manifest with a thunderclap headache (8).

Pregnancy requires that special emphasis be given to multiple precipitating factors that are unique to the peri- and postpartum periods. The most common causes of headache during these periods are posterior reversible encephalopathy syndrome (PRES), sinus CVT, postepidural headache, and Sheehan syndrome.

Imaging Modality Decisions

Diagnostic imaging workup of patients who present with acute headache in the ED starts with nonenhanced CT, which readily shows intracranial hemorrhage, edema, or mass effect and may be sufficient to exclude many causes (9).

When nonenhanced CT shows no abnormality in patients with a thunderclap headache, a lumbar puncture should be performed to rule out SAH. However, despite this traditional teaching, there is an increasing trend to skip lumbar puncture because of its invasiveness, low diagnostic yield, and potential to cause a more severe postpuncture headache (10,11). A traumatic lumbar puncture further reduces specificity. Xanthochromia of the cerebrospinal fluid (CSF) is pathognomonic for SAH; however, more than 12 hours must pass after SAH for xanthochromia to develop. In addition, ex vivo hemolysis and hyperbilirubinemia may cause a false-positive result (12,13).

When SAH is confirmed, CT angiography, MR angiography, and/or catheter angiography should be the next step. In most institutions, CT angiography is the preferred modality, given its shorter examination time and noninvasiveness. A sudden unilateral headache accompanied by neck and facial pain or ipsilateral Horner syndrome in a young patient may warrant CT angiography or MR angiography of the neck to evaluate for cervical artery dissection. In patients with a skull base, orbital, or periorbital headache who have accompanying cranial nerve palsies (likely related to involvement of the cranial nerves at the skull base, cavernous sinus, or orbital apex), contrast material-enhanced MRI is indicated. Heavily T2-weighted sequences should be performed to better delineate the cisternal segments of the cranial nerves (14).

In patients with suspected headache of rhinogenic origin and clinical visual confirmation of sinonasal disease, no imaging may be necessary in the ED, whereas MRI of the brain or paranasal sinuses may be indicated if there is any suspicion for intracranial complications or invasive fungal sinusitis (15).

In patients with immunosuppression, cancer, suspected encephalitis, or papilledema who have a new-onset headache or a positional headache, nonenhanced CT and MRI with and without intravenous contrast material usually are appropriate for initial imaging (16). If there is any suspicion for dural venous sinus CVT, initial evaluation starts with a nonenhanced CT study. It is appropriate to perform CT venography while the patient is still on the table. MR venography with and without intravenous contrast material is otherwise preferred and can be combined with MRI of the brain to evaluate for parenchymal abnormalities (17). In patients with odontogenic pain, contrast-enhanced maxillofacial CT is performed in our institution to guide treatment. Patients older than 55 years with a new-onset headache in the temple regions, particularly with tenderness of the superficial temporal arteries, should be evaluated for temporal (giant cell) arteritis and MRI or MR angiography are the preferred modalities, although imaging investigation for giant cell arteritis is not commonly performed in the ED. The cluster headache, a subtype of trigeminal autonomic headache, has an increased association with pituitary macroadenomas in 5%–10% of patients, thereby justifying the need for contrast-enhanced MRI of the brain (6).

In this article, we review the etiology of acute headache in the ED and classify abnormalities according to the predominant imaging manifestations as hemorrhage, vascular abnormality, or edema or mass effect. Other abnormalities that do not necessarily fall under these categories are discussed in the “Miscellaneous Manifestations” section.

Hemorrhage

SAH due to Nontraumatic Rupture of an Aneurysm

Most intracranial aneurysms are saccular (berry aneurysms). Ruptured saccular aneurysms are the most common cause of nontraumatic SAH and represent approximately 85% of cases of spontaneous SAH (18). The epicenter of the extravasated blood may allow prediction of the site of ruptured aneurysm.

Intraventricular hemorrhage can coexist; for instance, an anterior communicating artery aneurysm may rupture into the third ventricle through the lamina terminalis.

The differential diagnosis of diffuse SAH includes conditions such as ruptured nonsaccular aneurysm, arteriovenous (AV) malformation (AVM), and dural AV fistula. The most common locations of intracranial aneurysms are the anterior communicating artery (30%–35%), the posterior communicating artery (30%–35%), the middle cerebral artery bifurcation (20%), the basilar artery (5%), the internal carotid artery terminus or posterior wall, the superior cerebellar artery, and the posterior inferior cerebellar artery (Fig 1a, 1b).

The accuracy of CT for reliable detection of SAH is 98%–99%, with the use of a 64-detector-row CT scanner and the current highest spatial resolution for CT angiography of 0.4–0.7 mm. CT angiography has specificity rates of 90%–94% for aneurysms smaller than 3 mm and up to 100% for aneurysms larger than 4 mm. CT angiography should be performed with a section thickness of 1.5 mm or less.

MR angiography is used mostly in nonemergency settings in patients with clinical features that are suspicious for or a family history of SAH. Three-dimensional time-of-flight MR angiography is the most widely used technique and provides good spatial resolution; however, it can, at times, be of limited value because of its susceptibility to motion artifacts and the intrinsic T1 hyperintensity of methemoglobin-containing hematomas, which could appear on source images. In those cases, contrast-enhanced MR angiography, which has higher sensitivity (approaching that of CT angiography) may be preferred (19).

Vessel wall MRI is an emerging technique for evaluating intracranial vascular disease (20). Although it is not commonly used in the ED, vessel wall MRI may help in determining which aneurysm has ruptured in patients with acute SAH and multiple aneurysms. In these patients, neurologic interventional radiologists may not always place coils or stents successfully in all aneurysms. In these cases, to decide whether a surgical intervention is necessary, vessel wall MRI is performed to investigate inflammation and/or enhancement of the aneurysm wall. In autopsy studies, inflammatory changes such as macrophage and leukocyte invasion, which may manifest as circumferential aneurysm wall enhancement at vessel wall MRI, were encountered more commonly in the vessel walls of ruptured aneurysms than in those of their unruptured counterparts (21, 22) (Fig 1c, 1d).

Infected (Mycotic) Aneurysms

Cerebral arteries are the third most common site of infected (mycotic) aneurysms, after those of the aorta and peripheral arteries. Infectious arteritis destroys the vessel wall, with resultant contained

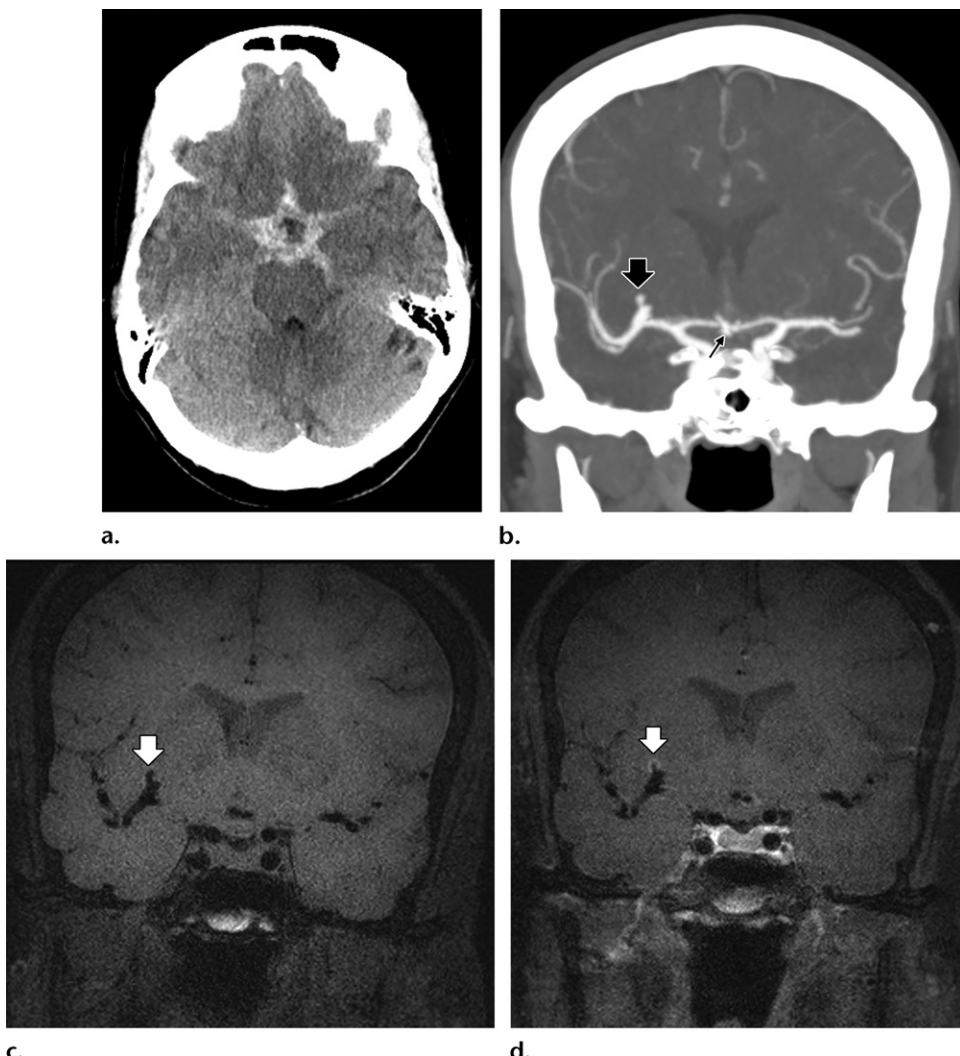


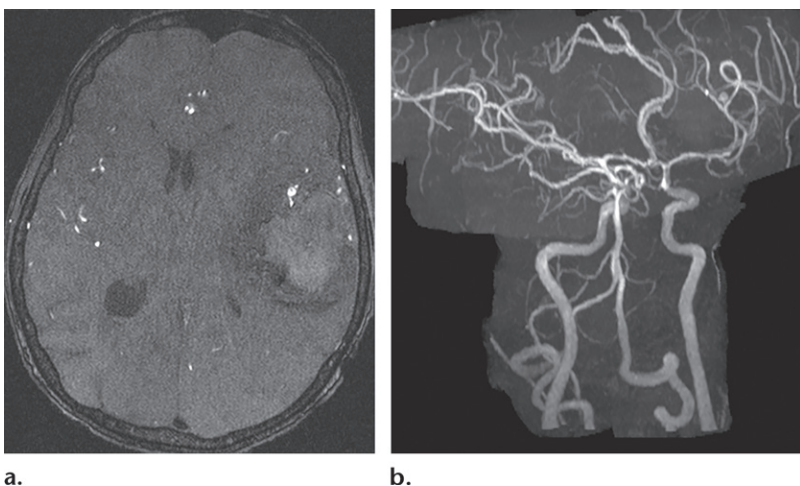
Figure 1. Aneurysm in a 64-year-old woman who presented with a thunderclap headache. **(a)** Initial axial nonenhanced CT image shows subarachnoid hemorrhage in the basal cisterns. **(b)** Coronal maximum intensity projection CT angiogram that was subsequently obtained shows a bilobed aneurysm arising from the right middle cerebral artery bifurcation (thick arrow) and another smaller aneurysm arising from the anterior communicating artery and projecting inferiorly (thin arrow). **(c, d)** Nonenhanced (**c**) and contrast-enhanced (**d**) vessel wall MR images show wall enhancement in the right middle cerebral artery bifurcation aneurysm (arrow). There was no enhancement around the anterior communicating artery aneurysm (not shown).

rupture and pseudoaneurysm formation. Although most cases are asymptomatic, patients may present with a headache, seizures, or focal neurologic deficits. Anterior circulation is more commonly involved than is posterior circulation (23). They tend to be located peripherally (segment 2 and beyond) and are fusiform in appearance (Fig 2). The A2 segment courses superiorly along the genu of the corpus callosum. The M2 segment refers to the sylvian segment of the middle cerebral artery after it trifurcates into an anterior division, posterior division, and the anterior temporal artery.

Nonaneurysmal Perimesencephalic SAH

In up to 15% of patients with SAH, no source of bleeding is identified. Two-thirds of these cases are

related to perimesencephalic SAH (18). Nonaneurysmal perimesencephalic SAH is characterized by the presence of subarachnoid blood immediately anterior to the midbrain and pons, most commonly in the interpeduncular and preoptic cisterns (Fig 3). Hemorrhage may extend into the ambient or quadrigeminal plate cisterns or to the basal part of the sylvian fissures. In rare cases, there is further extension along the lateral sylvian fissures or the posterior part of the interhemispheric falx. Frank intraventricular hemorrhage does not occur, except for a small amount of sediment in the occipital horns. This pattern at nonenhanced CT is reliable only within the first 3 days after onset of symptoms, given that substantial redistribution occurs after 3 days. Angio-



a.

b.

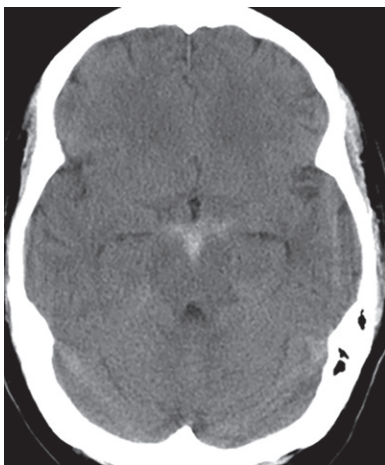


Figure 3. Acute SAH in a 44-year-old woman with a history of alcoholic hepatitis and an elevated international normalized ratio who presented to the ED with a headache after a fall. Axial nonenhanced CT image of the brain shows acute SAH in the interpeduncular cistern. CT angiography was performed and was negative for aneurysms. The patient recovered fully.

graphic studies are normal, without any underlying aneurysm. Recognition of this type of SAH is important, given its excellent prognosis, without rebleeding, vasospasm, or hydrocephalus.

A ruptured vertebrobasilar aneurysm may show a similar imaging appearance in 5% of cases (18). Clues to diagnosis at nonenhanced CT are extension of the blood into the anterior interhemispheric or lateral sylvian fissures or the presence of frank intraventricular blood. The distinction is important, because basilar artery aneurysms carry a 50% risk of rehemorrhage within 4 years after the initial hemorrhage. Other rare causes of perimesencephalic hemorrhage include cervicomedullary junction tumors such as hemangioblastomas, posterior fossa and cervical spine AVM, acute arterial dissection, and dural AV fistulas (18).

Figure 2. Ruptured saccular aneurysm in a 52-year-old woman with a history of Crohn disease, opiate use, and known osteomyelitis of the humerus who presented with headache and altered mental status. Axial three-dimensional time-of-flight MR angiogram source image (a) and maximum intensity projection image (b) show a ruptured saccular aneurysm arising from the left M2 segment. Moderate-sized intraparenchymal hemorrhage is noted in the left temporal lobe.

Intracerebral Hemorrhage

The incidence of intracerebral hemorrhage (ICH) is approximately 25 per 100 000 person-years, with a mortality rate of 40% at 1 month after presentation (24). Risk factors include male sex, older age, low to middle income, alcohol consumption, hypercholesterolemia, anticoagulation, and drug abuse. Headache is more common in patients presenting with ICH than in those with SAH and ischemic stroke. Additional clinical manifestations of ICH include focal neurologic deficit that develops within minutes to hours. This gradual occurrence of functional loss is uncommon in patients with ischemic stroke or acute SAH. Vomiting is also more common in ICH than in ischemic stroke and SAH (25).

Spontaneous nontraumatic ICH is presumably an end result of small vessel diseases (microangiopathies), which include arteriolosclerosis, liophyalinosis, and cerebral amyloid angiopathy.

After initial diagnosis of an ICH, CT angiography, CT venography, MRI, MR angiography, or MR venography are considered to investigate the underlying cause. Findings that are suspicious for a vascular abnormality or lesions include enlarged vessels or calcifications along the margins of the ICH, associated SAH, hyperattenuation in a dural sinus or cortical vein, disproportionately large surrounding edema, and hematoma with an unusual shape and heterogeneous intensity (26). Patients with ICH who have lobar hemorrhage, are younger than 55 years, and have no history of hypertension benefit from MRI for identification of a secondary cause (27).

Hypertension is the most common cause of nontraumatic ICH in elderly patients. Hypertensive cerebral microangiopathy affects the small deep perforating arteries that supply the basal ganglia and deep white matter. The most commonly affected sites are the basal ganglia, thalamus, pons, and cerebellum (Fig 4). Microbleeding has been

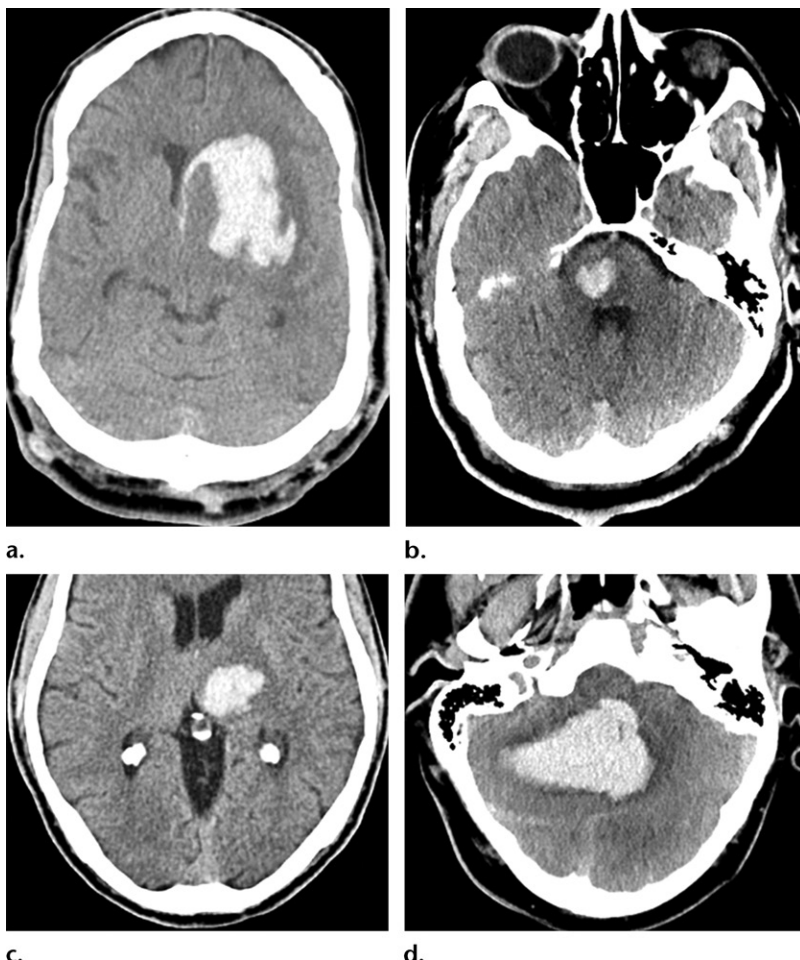


Figure 4. Characteristic locations of hypertensive intraparenchymal hemorrhage in four different patients. Axial nonenhanced CT images show hypertensive intraparenchymal hemorrhage in the basal ganglia (a), pons (b), thalamus (c), and cerebellum (d).

linked to subsequent intracerebral hemorrhage, which is seen most commonly in the same locations (28) and is best viewed with gradient-echo and susceptibility-weighted MRI sequences. Expansion of the hematoma is characterized by the “spot sign” on a CT angiogram or contrast-enhanced CT images.

Cerebral amyloid angiopathy is a major cause of lobar hemorrhage in elderly patients. This entity is characterized histopathologically by amyloid deposition in the small- to medium-sized cortical and leptomeningeal vessel walls, which leads to fibrinoid necrosis and vascular fragility that appear at imaging as multiple microbleeds in lobar distribution. Less commonly, cerebral amyloid angiopathy is associated with cerebellar involvement. The lobar distribution tends to favor the posterior cortical regions, particularly the occipital lobe. As in hypertensive microbleeds, cerebral amyloid angiopathy microbleeds have been linked to increased risk of intraparenchymal hemorrhage (Fig 5). In a 2004 study (29) among 94 survivors of primary lobar hemorrhage, a higher total number of hemorrhages (initial ICH plus other micro- and macrobleeds detected at T2*-weighted MRI at baseline) allowed prediction of an increased

risk of future symptomatic hemorrhage, with a 3-year cumulative risk of 14% for those with only one hemorrhage, 17% for those with two lesions, 38% for those with three to five lesions, and 51% for those with six or more lesions. Convexal SAH is described increasingly in patients with cerebral amyloid angiopathy, especially in those who present with symptoms similar to those of a transient ischemic attack (18).

Gradient-echo weighted T2*- and susceptibility-weighted MRI are the best methods for evaluation of cerebral microbleeds, with true-positive rates of 48%–89%, false-positive rates of 11%–24%, and false-negative rates of 18%–48%. False-positive imaging features that mimic those of cerebral microbleeds include microaneurysms, microcalcifications, and arteriolar pseudocalcifications (28).

AVM, or more specifically, pial AVM, is a major cause of lobar hemorrhage in patients up to 40 years old. Hemorrhage rates are 2%–4% per year for all patients with AVM, with higher rates in those who initially present with hemorrhage (30). AVMs consist of abnormal connections between the arteries and veins, resulting in an intervening network of vessels. The fistulous connec-

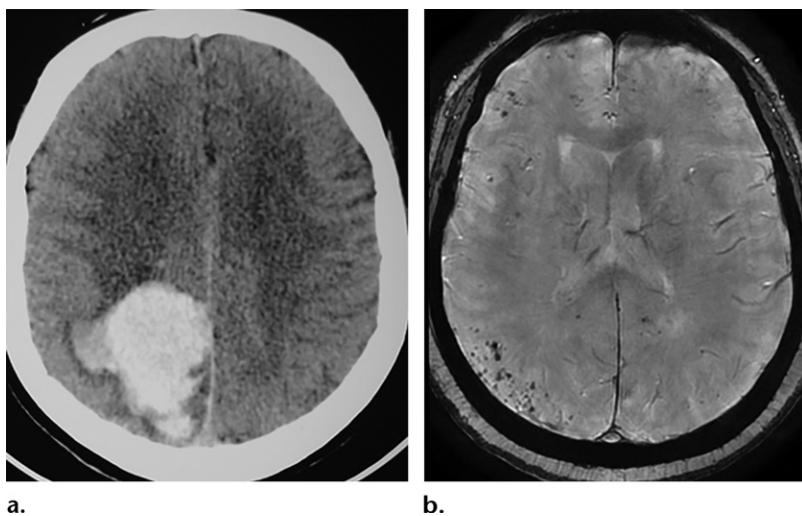


Figure 5. Intraparenchymal hematoma in a 72-year-old man who presented to the ED with a headache and altered mental status. **(a)** Initial axial nonenhanced CT image shows an intraparenchymal hematoma in the right parietal lobe. **(b)** Axial susceptibility-weighted MR image obtained a few months earlier in the same patient shows multiple subcortical microbleeds, particularly in the right parieto-occipital region.

tion between the artery and the vein occurs via a nidus, an abnormal tangle of vessels in the AVM. Spetzler and Martin (31) developed a grading system for AVMs based on their size, the pattern of venous drainage, and the eloquence of the adjacent brain to estimate the risk of open surgery. The nidus size could be small (1–3 cm), medium (3–6 cm), or large (greater than 6 cm), which correspond to 1, 2, and 3 points on the grading scale, respectively. If the nidus is adjacent to an eloquent site, 1 point is allocated. The presence of deep venous drainage adds 1 point, whereas superficial drainage is worth 0 points. Therefore, the grade of an operable AVM varies between grades 1 and 5. Grade 6 lesions are considered nonoperable (31).

The diagnosis is made on the basis of the appearance of the nidus at CT, MRI, and catheter angiography and early venous drainage at dynamic imaging such as conventional catheter angiography. Nonenhanced CT may show a hematoma due to rupture or a slightly hyperattenuating mass due to microbleeding or blood pooling in the AVM. Mass effect is not expected in AVMs, because they tend to replace rather than displace the brain parenchyma. The presence of calcifications associated with the hematoma at nonenhanced CT should raise suspicion for an underlying AVM. At conventional T2-weighted MRI, the nidus is seen as a cluster of signal voids. Draining veins are seen on susceptibility-weighted magnitude images as hyperintense vessels because of higher oxyhemoglobin content in the draining vein. CT angiography is effective for evaluating the AVM nidus, feeding arteries, and draining veins. CT angiography is 90% sensitive for the diagnosis of AVM. CT angiography better shows the feeding artery and intranidal aneurysms than does 1.5-T time-of-flight MR angiography (32).

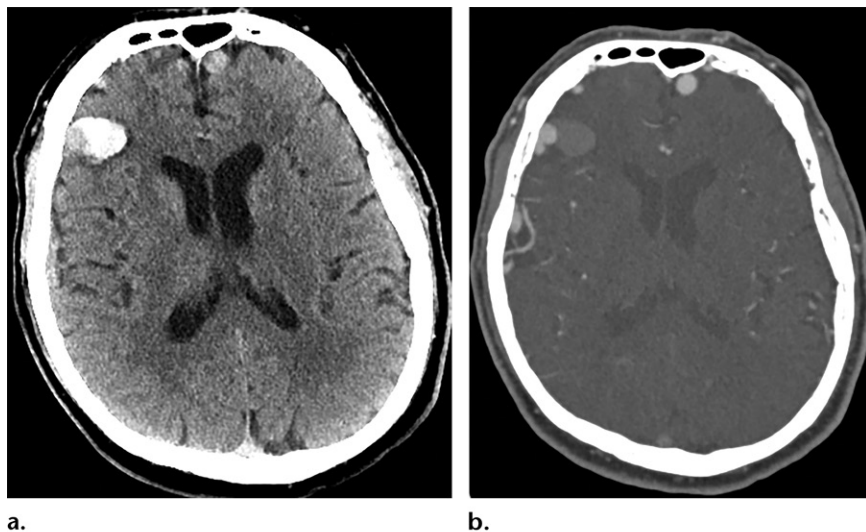
Dural AV fistulas are abnormal connections between the arteries feeding the meninges, bone,

or muscles and small venules in the dura mater. They account for 10%–15% of all intracranial AV shunts (33). The presence or absence of cortical venous reflux allows the prognosis of an AV fistula to be determined. The lack of cortical venous drainage is associated with a benign course and extremely low risk of intracranial hemorrhage (Borden type I, Cognard types I or IIa). Borden types II and III or Cognard types IIb–V fistulas have cortical venous reflux and are regarded as malignant fistulas. The reported annual risk of intracranial hemorrhage is 8.1%. In the ED, nonenhanced CT can show the ICH and edema related to venous congestion. Depending on the presence of venous reflux, dilated veins or venous ectasia may appear as hyperattenuating tubules overlying the cortex. MRI helps in determining coexisting parenchymal abnormalities such as white matter T2-weighted or fluid-attenuated inversion-recovery (FLAIR) hyperintensity or venous ischemia. At MRI, a cluster of flow voids around the venous dural sinuses should lead to evaluation with CT angiography, MR angiography, or digital subtraction angiography (34). CT angiography or MR angiography shows dilated cortical veins as abnormal enhancing tubular structures or flow voids. No true nidus is identified in the brain parenchyma (Fig 6) (35).

Spontaneous Retroclival Hematoma

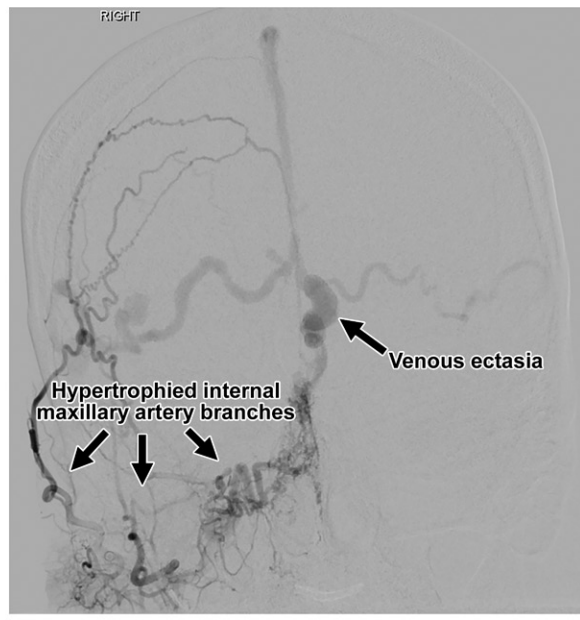
All patients with spontaneous retroclival hematoma present with a sudden-onset severe headache. This condition is characterized by a contained blood collection that crosses the basi-occipital synchondrosis that remains in a nondependent configuration in the retroclival region (Fig 7). The nondependent configuration may be related to the meningeal coverings in this region,

Figure 6. Ethmoidal dural AV fistula in a 62-year-old man with hypertension, hyperlipidemia, and diabetes who presented to the ED with headache, confusion, and diaphoresis. (a) Axial nonenhanced CT image shows a right frontal lobe hematoma and prominent hyperattenuating cortical veins. (b) Subsequently obtained CT angiogram shows dilated tortuous veins along the right frontal and temporal convexities and the left frontal convexity. Multiple areas of venous aneurysmal dilatation are also seen, one of which is adjacent to the right frontal lobe hemorrhage. (c) Conventional angiogram shows an ethmoidal dural AV fistula fed primarily by hypertrophic internal maxillary artery branch vessels with superficial venous drainage and substantial bilateral venous ectasia draining bilaterally to the Labbe veins.



a.

b.



c.

given that the basilar plexus exists in the interdural (subdural) space between the two-layered dura and that a separately named layer called the *anterior pontine membrane* (or free arachnoid membrane) separates the clival dura from the subarachnoid space (36).

Spontaneous retroclival hematoma is more common in pediatric patients than in adults and usually occurs as a result of trauma. The location of the hemorrhage is epidural in trauma patients. An epidural clival hematoma does not extend beyond the tectorial membrane, whereas a subdural clival hematoma can enter the spinal subarachnoid space. Retroclival subdural hematomas are less common compared with their epidural counterparts and are more commonly seen in adults. A spontaneous retroclival subdural hematoma is believed to occur as a result of disruption of petrosal and bridging cortical veins at the foramen magnum. The prognosis is favorable in patients with no angiographic abnormalities; most patients recover completely and have no risk of vasospasm or rebleeding.

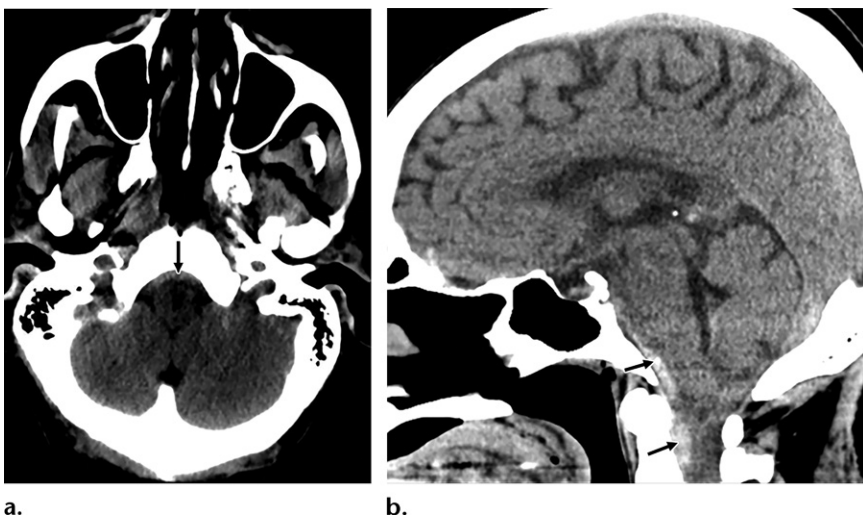
Vascular Abnormalities

Reversible Cerebral Vasoconstriction Syndrome

RCVS is not a single disease, but rather is the end result of multiple abnormal processes that cause reversible vasoconstriction in the cerebral vasculature. The pathophysiology is not clearly

understood, but a disturbance in the cerebral vascular tone appears to be the final common pathway (37). The concept of transient and fully reversible arterial vasoconstriction was initially described in 1988 by Call and Fleming, hence the less commonly used name is *Call-Fleming syndrome*. PRES can coexist with RCVS, which suggests a common pathogenetic mechanism.

RCVS is commonly the correct diagnosis in patients who present with a thunderclap headache, and its symptoms mimic those of aneurysmal SAH. The headache usually starts



a.

b.

Figure 7. Retroclival blood collection in a 43-year-old woman who presented to the ED with a sudden headache. Axial (a) and sagittal (b) nonenhanced CT images show a retroclival blood collection that crosses the basiocipital synchondrosis and remains in a nondependent configuration along the retroclival dura (arrows). The patient recovered without any complications.

posteriorly and may become diffuse over time. It is often triggered by sexual activity, exertion, Valsalva maneuver, emotion, postpartum state, or vasoactive substances such as illicit drugs, α -sympathomimetics, and serotoninergic drugs. It has been shown to be associated with pheochromocytoma, porphyria, and thrombotic thrombocytopenic purpura (38). The headache recurs over a few days or weeks, although in rare cases, it progresses rapidly over hours or more slowly over days. In up to 75% of patients, the headache is the only symptom; however, fluctuating neurologic deficits and seizures have also been described. Conversely, the headache may be absent in some patients with RCVS.

Primary angiitis of the central nervous system (PACNS) may overlap clinically and radiographically with RCVS. The distinction is important, because the management is different. The onset of headache is more insidious and is seen predominantly in older men with PACNS, whereas the thunderclap headache is seen more commonly in young to middle-aged women with RCVS. At imaging, approximately 90% of patients with PACNS show multifocal infarcts of varying ages, whereas initial imaging may appear normal in patients with RCVS. Hemorrhagic complications or concomitant PRES are not seen as commonly in PACNS as they are in RCVS (39).

Imaging is important to confirm the diagnosis of RCVS, to exclude other causes such as aneurysmal SAH or cerebral vasculitis, and to monitor potential complications. Nonenhanced CT of the brain is the initial modality of evaluation and shows intracranial hemorrhage, cerebral edema, and in some cases, infarcts. However, the initial CT examination appears normal in most patients. Various patterns of intracranial hemorrhage (convexity SAH, ICH, and/or subdural) are seen. Convexity SAH is the earliest complication of RCVS;

however, it is seen in only 20%–25% of cases (18) (Fig 8a, 8b). CT angiography can be helpful for exclusion of other potential diagnoses such as aneurysms, vasculitis, or arterial dissections.

The key imaging feature of RCVS is segmental arterial vasoconstriction characterized as a “string of beads” pattern, with alternating areas of arterial stenosis and dilatation. Angiographic studies including MR angiography, CT angiography, and catheter angiography can be normal during the 1st week after clinical onset. This is likely related to the centripetal progression of cerebral vasoconstriction. The small peripheral arterioles are affected first, and the medium and large cerebral arteries may not yet show vasoconstriction at the time of initial imaging. Segmental arterial vasoconstriction can lead to ischemic or hemorrhagic infarcts that can cause permanent disability, and in severe cases, death. Infarcts often are seen in the arterial border zones. By definition and also included in the diagnostic criteria, the cerebrovascular abnormalities are transient and resolve in 3 months (40) (Fig 8c, 8d).

Transcranial Doppler US is used to monitor the course of vasoconstriction in RCVS. A crescendo-decrescendo pattern of flow velocities has been shown in affected vessels.

Posterior Reversible Encephalopathy Syndrome

There is substantial overlap in the clinical and radiologic presentations of PRES and RCVS, which suggests a common physiologic pathway, and likely, altered vascular tone (40,41). PRES is seen in patients with preeclampsia or eclampsia, renal failure, hypertension, sepsis, or alcohol withdrawal and those who take cytotoxic or immunosuppressive medications (42,43). The pathophysiology of PRES remains unclear; however, dysregulation of cerebral vascular tone

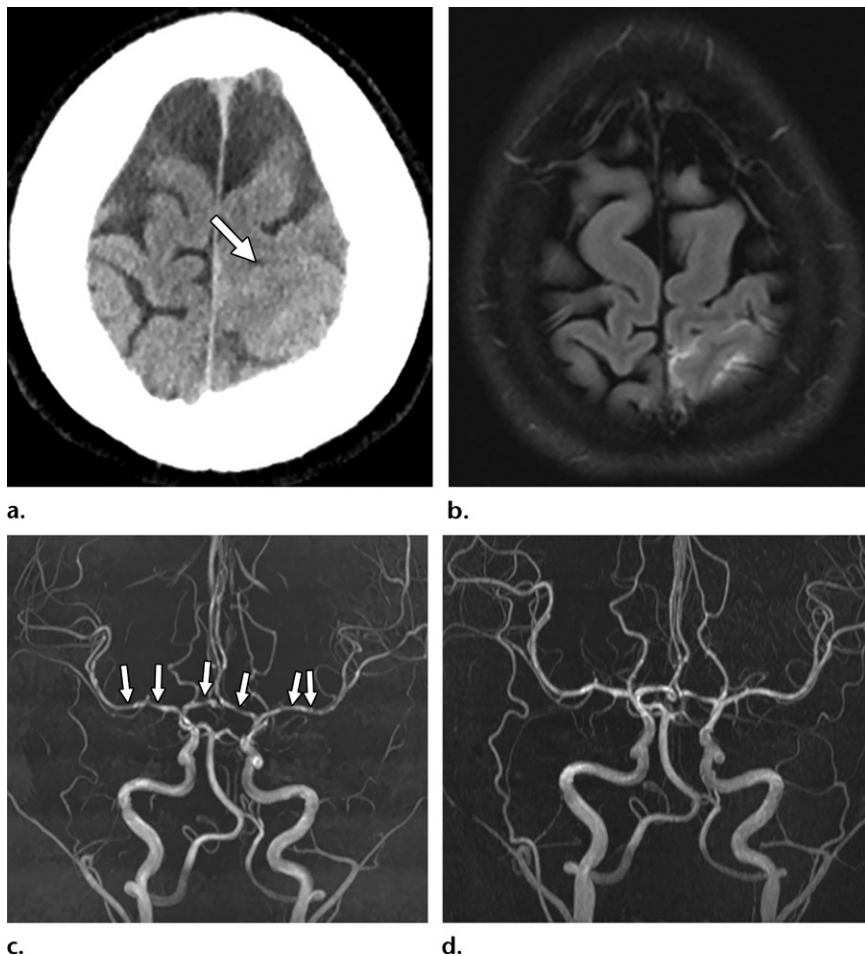


Figure 8. RCVS in a 21-year-old woman who presented to the ED with a headache. (a, b) Axial nonenhanced CT image (a) and axial FLAIR MR image (b) show a hyperintense left convexity sulci hemorrhage (arrow in a) and corresponding sulcal hyperintensities. (c, d) MR angiograms show segmental vasoconstriction of bilateral A1 and M1 segments (arrows in c) that subsequently resolved (d). Review of the patient's medications revealed selective serotonin reuptake inhibitor use.

due to sympathetic overactivity and subsequent endothelial dysfunction likely are involved (44).

The clinical and imaging findings are usually reversible. The symptoms may vary from confusion to status epilepticus. Because of the involvement of the occipital lobes, patients usually have visual symptoms including disturbances, hallucinations, or blindness (41). Nonenhanced CT is often the initial imaging modality in these patients and usually shows low attenuation in the cortical-subcortical regions, with loss of differentiation between gray and white matter due to vasogenic edema. At MRI, FLAIR signal hyperintensity is seen primarily in the cortex and subcortical white matter. Parieto-occipital involvement is classic and is seen in approximately 70% of cases (Fig 9). The other imaging patterns include a holohemispheric watershed pattern and a superior frontal sulcus pattern. Atypical locations such as the basal ganglia, cerebellum, or brain stem also may be involved. Intracranial hemorrhage (eg, SAH, parenchymal hematomas, or microhemorrhages) can be seen in approximately 15% of cases (45) (Figs 10, 11). Restricted diffusion in a punctate or gyral pattern is another atypical finding that is seen in approximately 17% of

cases (42). Contrast enhancement can be seen in 21%–44% of patients and may be leptomeningeal, gyral, or nodular (42,46,47).

Cerebral Venous Thrombosis

Headache is the most frequent and often the first symptom of CVT; however, it is associated almost invariably with other symptoms such as papilledema, focal deficits, seizures, altered consciousness, or cranial nerve palsies. Headache as the sole presentation of CVT is rare. Headache type is nonspecific and can be thunderclap, acute, or progressive (48).

The superior sagittal sinus is involved most commonly. Cortical venous involvement is seen in 6% of patients; however, it is likely to be overlooked when there is accompanying dural sinus involvement. Parenchymal imaging abnormalities reflect increased venous pressure and comprise vasogenic or cytotoxic edema or parenchymal hemorrhages (in one-third of cases). Substantially increased venous pressure may impede arterial perfusion, and cell death may occur. The initial imaging evaluation starts with nonenhanced CT. The sinus CVT may appear to be hyperattenuating, which is a finding present in only 20%–25% of cases (49,50).

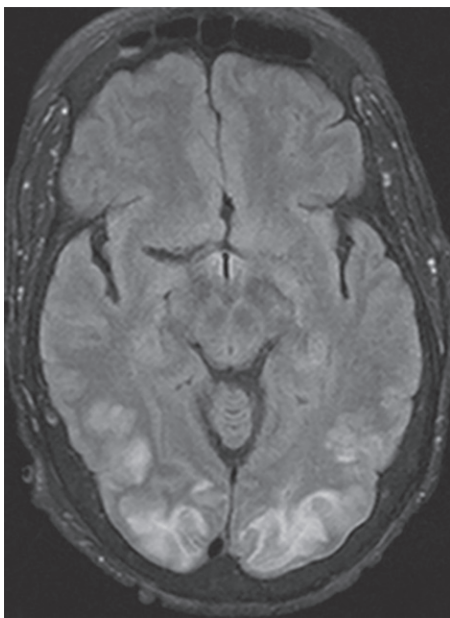


Figure 9. PRES in a 45-year-old man with a history of kidney transplant and hypertension who presented with a headache. Axial FLAIR MR image shows hyperintensities in the gyri and juxtacortical white matter of the bilateral occipital lobes. The patient was diagnosed with PRES, and the imaging findings resolved over time.

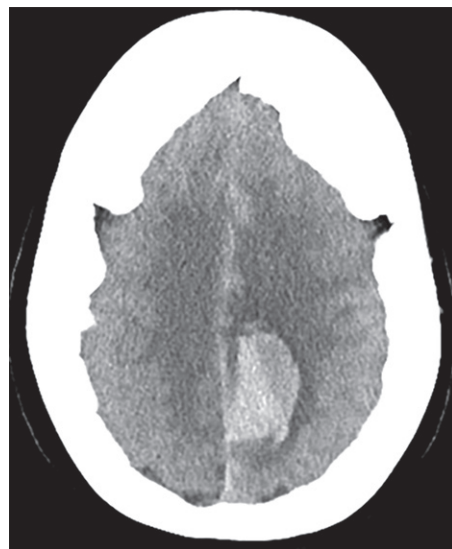


Figure 10. Parenchymal hemorrhage in a 68-year-old woman with a history of hypertension who presented with headache. Axial non-enhanced CT image shows parenchymal hemorrhage in the left parasagittal parietal lobe.

Measuring the attenuation value of the sinus CVT at nonenhanced CT may provide additional diagnostic value (51). Buyck et al (52) found a mean attenuation value of 73.9 HU in sinus CVT, and they suggested a threshold of 62 HU for the differentiation of CVT from parenchymal abnormalities. Further studies (53,54) suggested similar thresholds of 64 HU and 58 HU in adult and pediatric patients, respectively. Parenchymal hemorrhage is seen only in one-third of cases. Lobar hemorrhage in the parasagittal frontal and parietal lobes is typical in patients with superior sagittal sinus CVT, whereas hemorrhage in the temporal or occipital lobes is more typical of transverse sinus CVT. Hemorrhage is typically cortical, with subcortical extension (Fig 12a). Venous pressures beyond the durability of venous walls and continued arterial perfusion are believed to contribute to the development of parenchymal hemorrhages (55). Nonenhanced MRI is superior to nonenhanced CT for the detection of CVT. The absence of a flow void or asymmetric altered flow signal intensity should alert the radiologist to an underlying CVT. The T1 and T2 signal intensity characteristics of CVT depend on the interval between the onset of CVT and the time of imaging. Acute CVT (0–5 days) appears as T1 isointensity and T2 hypointensity at MRI. The T2 hypointensity may be misinterpreted as a normal flow void; therefore, assessment should

be made with multiple sequences. Contrast material administration and application of venographic techniques allow confirmation of the diagnosis (55). MRI also is preferred for evaluation of parenchymal abnormalities. In the brain parenchyma, focal vasogenic or cytotoxic edema may be detected, or both types may coexist. The use of the term *venous infarct* is not desired, because CVT-related parenchymal abnormalities may be reversible. Affected brain parenchyma appears hyperintense at T2-weighted or FLAIR MRI, with or without associated hemorrhage. Restricted diffusion or T2-weighted “shine-through” may be seen at diffusion-weighted MRI, depending on the type of edema.

The most commonly used venographic techniques are nonenhanced time-of-flight MR venography, contrast-enhanced MR venography, and CT venography. Phase-contrast MR venography is used less often. Two-dimensional time-of-flight MR venography is the most commonly used technique to evaluate CVT and is most sensitive to the flow that is perpendicular to the plane of acquisition. Therefore, axial, coronal, or oblique planes may be used for image acquisition. Potential pitfalls of time-of-flight MR venography are the nulling of the venous signal that is parallel to the plane of imaging and T1 shortening of methemoglobin. CT venography is a rapid and reliable technique, with 95% sensitivity (Fig 12b). A 45-second prescanning delay is ideal, and a shorter prescanning delay (<30 seconds) may result in a nondiagnostic scan because of inadequate venous enhancement (56).

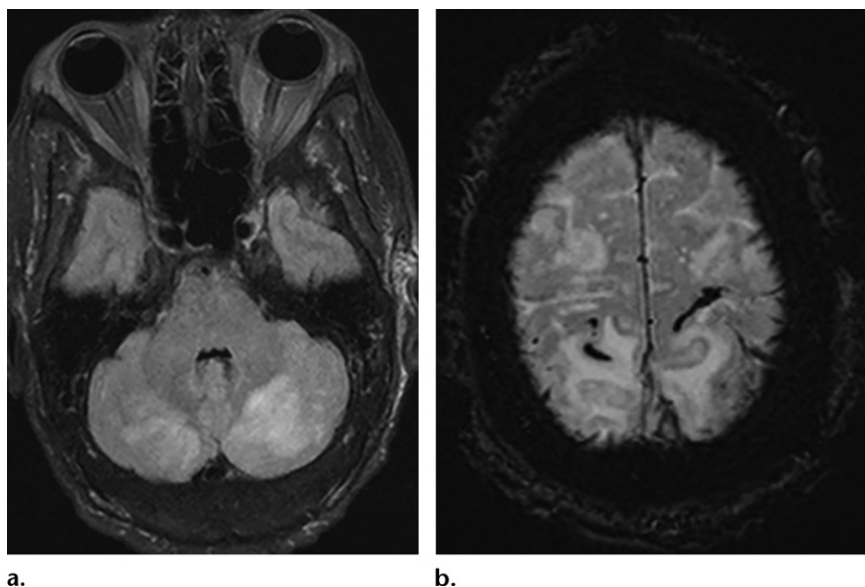


Figure 11. SAH in a 48-year-old man with a history of end-stage renal disease who presented with a headache. (a) Axial FLAIR MR image shows bilateral abnormal signal hyperintensity in the cerebellar hemispheres. (b) Axial susceptibility-weighted MR image shows convexity SAH.

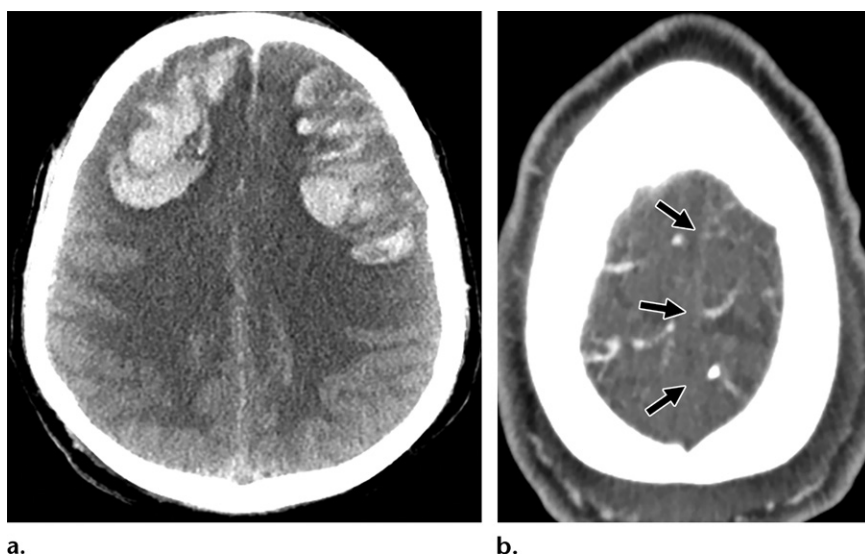


Figure 12. CVT in a 57-year-old man who presented to the ED with headache and subsequently lost consciousness. (a) Axial non-enhanced CT image shows parenchymal hemorrhage in the bilateral frontal lobes in a symmetric distribution. (b) Axial CT venogram obtained later shows the filling defect in the superior sagittal sinus (arrows).

Carotid and Vertebral Artery Dissections

Spontaneous craniocervical dissections occur in patients with underlying arteriopathy and can be triggered by minor activities such as coughing, vomiting, or cervical manipulation. Headache is the earliest symptom and is reported by 68% of patients with spontaneous internal carotid artery (ICA) dissection (ICAD) and by 69% of those with spontaneous vertebral artery dissection (VAD). When headache was present, it was the initial manifestation in 47% of those with ICAD and in 33% of those with VAD (57). Nearly 10% of patients with cervical artery dissection present with isolated headache or neck pain (58). The thunderclap headache is uncommon and is seen in only 3.6% of patients with ICAD and 9.2% of patients with VAD. The relatively higher incidence in VAD is partly explained by the more common occurrence of SAH in those with VAD. Von

Babo et al (59) showed a 10-fold increase in the development of SAH in patients with VAD compared with those with ICAD. Pulsatile tinnitus is more common in patients with ICAD, whereas ischemic stroke is more common in patients with VAD; however, the ischemic stroke associated with ICAD is more severe.

Extracranial CAD is most commonly seen distal to the carotid bulb, extending toward the skull base and terminating before the petrous segment. ICADs are most common in the supraclinoid segment. VADs are often seen in the pars transversaria or the atlas loop in 35% and 34% of patients, respectively. Nonenhanced CT may show a hyperattenuating crescent-shaped intramural hematoma in cervical CADs (60).

The accuracy of MRI and CT angiography for diagnosis of ICADs and VADs are relatively similar, with 83%–99% sensitivity and specificity

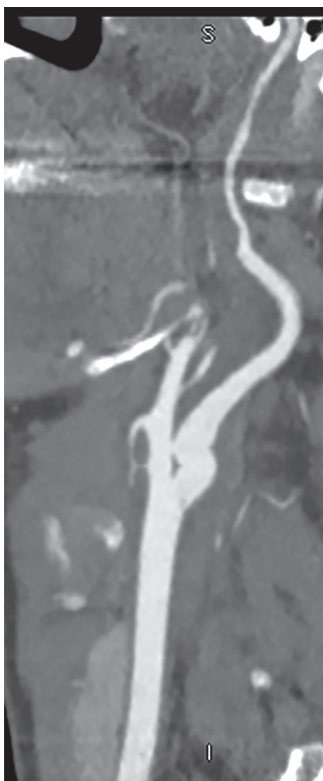


Figure 13. Spontaneous ICAD in a 39-year-old woman who presented with a headache and neck pain for 2 weeks. Reformatted CT angiogram of the carotid artery shows a long segment and distal tapering of the right cervical internal carotid artery from its middle segment to the skull base. *I* = inferior, *S* = superior.

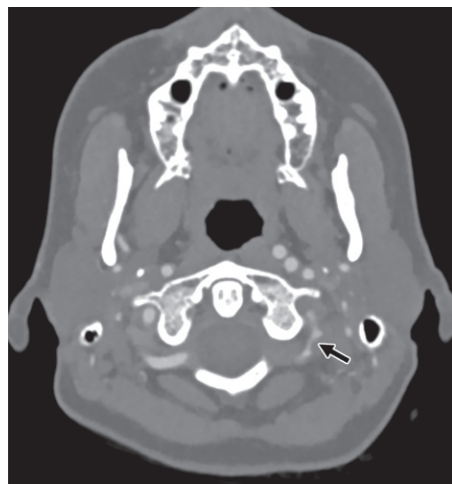


Figure 14. VAD in a 37-year-old woman who presented to the ED with a right-sided headache and neck pain. Initial nonenhanced CT (not shown) was negative. CT angiogram of the neck shows wall irregularity and luminal narrowing involving the atlas loop and distal pars transversaria segments of the left vertebral artery (arrow).

(61). Angiographic findings of CAD include an intimal flap, elongated tapered stenosis or occlusion, and a dissecting aneurysm (pseudoaneurysm) (Fig 13).

The string sign is caused by diminished antegrade flow into the ICA and appears as a trickle of contrast material in the lumen (62,63). It can be seen with CADs; however, it can also be seen with other abnormalities including preocclusive atherosclerosis at the carotid artery bifurcation, carotid artery disease resulting from radiation, subacute partial thrombosis of the ICA, and partial recanalization of an occluded artery (63).

CT angiographic findings of VAD include irregularity and/or stenosis of the vessel, the string sign, the double lumen sign, dissecting aneurysm formation, or complete occlusion. The most common imaging finding of VAD is stenosis caused by formation of subintimal hematoma (Fig 14; Fig E1). The double lumen sign is a direct sign of dissection and is formed by the presence of an intimal flap that divides the lumen (Fig E1). Dissecting aneurysms occur

when the tear extends into the subadventitial region, widening the weakened adventitia and forming an aneurysm.

The pathognomonic crescent sign is seen classically at axial fat-suppressed T1-weighted MRI and represents an eccentric rim of T1-hyperintense subintimal hematoma, surrounding a hypointense arterial lumen (Fig 15). This sign is seen more commonly in CADs than in VADs likely because of the horizontal course of the atlas loop segment in relation to the imaging plane and the presence of the adjacent vertebral venous plexus. Dorsal vessel wall thickening against the adjacent fat with a normal luminal caliber, which is described as the *suboccipital rind sign*, is sometimes the only imaging finding in atlas loop segment dissections. This finding can be missed if only lumen-enhancing techniques are used (64). Also, inherent strong background suppression at contrast-enhanced MR angiography substantially limits evaluation of the vessel wall.

Edema or Mass Effect

Intracranial Infections

Headache is the most common and often the first manifestation of intracranial infections caused by bacterial, viral, and fungal and other parasitic agents. Intracranial extension of a paranasal sinus infection and otitis may result in epidural empyemas, meningitis, cerebritis, or abscess. Intracranial infection should be suspected whenever a headache is associated with fever, altered mental state, focal neurologic deficits, or generalized seizures. The most common bacterial causes of

adult meningitis are *Streptococcus pneumoniae*, *Neisseria meningitidis*, and *Listeria monocytogenes*.

Nonenhanced CT usually shows no abnormalities in patients with uncomplicated meningitis. Contrast-enhanced CT or MRI may show lepto-meningeal enhancement. At MRI, FLAIR hyperintensity of the cerebral sulci is typical. Complications of meningitis include cerebritis or cerebral abscess, subdural empyema, hydrocephalus, CVT, ventriculitis, and vasculopathy or infarcts.

Subdural empyema is a purulent fluid collection in the subdural space. It may arise from hematogenous dissemination of infection, osteomyelitis of the adjacent bone, sinus or ear infections, thrombophlebitis, or as a complication of bacterial meningitis. An iso -or hypoattenuating fluid collection is seen at nonenhanced CT. The distinctive features are hyperintensity at FLAIR MRI and diffusion-weighted imaging with low apparent diffusion coefficients. Rim enhancement may be seen. In ventriculitis, ventricles enlarge with a rim of surrounding T2-weighted FLAIR hyperintensity, or there may be hyperintense layering material in the ventricles at diffusion-weighted imaging. Contrast-enhanced images show ependymal enhancement.

In patients with HIV infection, infectious causes including cryptococcal meningoencephalitis or toxoplasmosis may cause headache. Toxoplasmosis tends to favor the basal ganglia and shows ill-defined areas of hypoattenuation at nonenhanced CT that correspond to hyperintensity at T2-weighted or FLAIR MRI. Rim or solid enhancement can be seen (Fig 16; Fig E2).

Herpes simplex encephalitis is one of the most important causes of viral encephalitis and requires timely treatment to prevent catastrophic results. People of all ages may be affected and there is no seasonal predilection (65). Hyperintense areas at FLAIR and T2-weighted MRI and abnormalities in the temporal lobe, insulae, and inferior frontal lobes are typical. The basal ganglia are characteristically spared. The disease may be bilateral but asymmetric. Hemorrhage and necrosis may develop throughout the course of the disease (Fig 17).

Petrosus apicitis develops when acute suppurative otitis media spreads into a pneumatized petrous apex (Fig 18; Fig E3). Gradenigo syndrome is the triad of abducens nerve palsy (causing diplopia), deep facial pain (involving the first and second divisions of the trigeminal nerve), and acute otitis media. In addition, patients may present with headache and tinnitus. This entity has been rare since the widespread use of antibiotics and is easily overlooked if the patient's clinical presentation is incomplete and atypical (66,67).

Headache may be the initial and isolated symptom of intracranial tumors including pri-

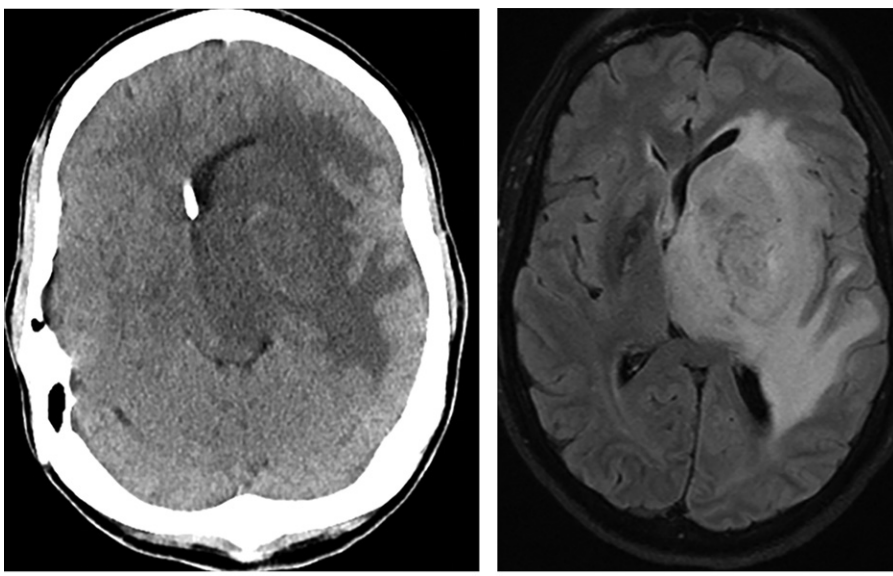


Figure 15. ICAD in a 37-year-old woman who presented with a headache and left-sided neck pain. Initial nonenhanced CT (not shown) was negative. Axial nonenhanced T1-weighted fat-suppressed MR angiogram shows a crescent-shaped T1-hyperintense intramural hematoma along the left internal carotid artery. The crescent sign (arrow) is more commonly seen in ICADs than in VADs.

mary brain tumors or intracranial metastases in the supra- or infratentorial compartments. Headache was reported by 47%–71% of patients with intracranial tumors (68–70).

Colloid cysts of the third ventricle are benign tumors that comprise 1% of all intracranial neoplasms. The most common manifestation is headache in 68%–100% of patients. Headaches may be relieved by a change in position, and this is likely related to intermittent foraminal obstruction due to the pendulous nature of the lesion. There is a reported risk of sudden death due to obstruction of the foramen of Monro, resulting in acute hydrocephalus. The imaging appearance depends on the composition of the cyst contents (the amount of cholesterol and protein). At nonenhanced CT, the colloid cysts typically appear as a well-defined hyperattenuating lesion at the anterosuperior aspect of the third ventricle. Usually they are hyperintense at T1-weighted MRI and vary from hypointense to hyperintense at T2-weighted MRI, depending on the content of the cyst. Contrast-enhanced images may show a thin rim of enhancement related to the cyst capsule. Calcifications are rare; however, they can be seen in the walls of larger cysts (71).

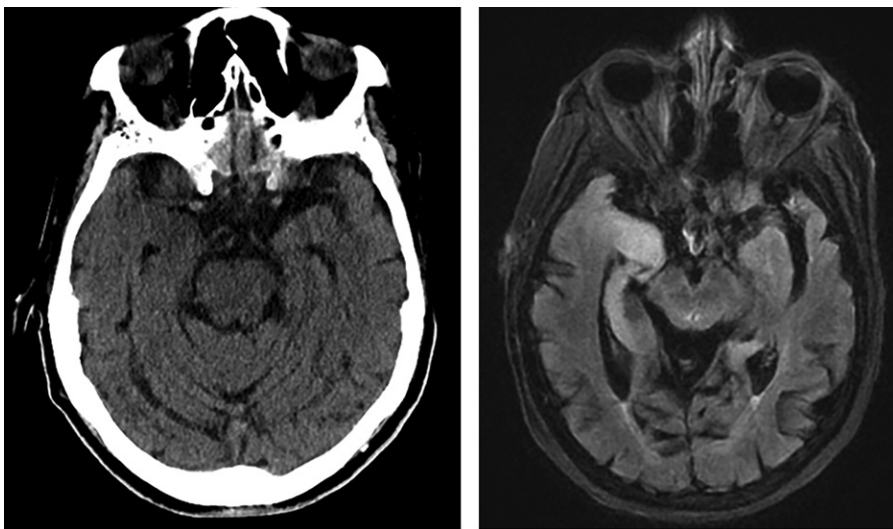
Hemorrhagic metastasis is another commonly encountered abnormality in the ED in patients who present with a headache. Tumors that manifest most commonly and show spontaneous hemorrhage include metastases (eg, melanoma, renal, thyroid, carcinoid, and choriocarcinoma) and high-grade gliomas, particularly glioblastomas.



a.

b.

Figure 16. Toxoplasmosis in a 45-year-old man with a history of HIV infection and a CD4 count of 23 who presented to the ED with a headache and confusion. (a) Initial axial nonenhanced CT image shows a large area of hypoattenuation centered in the left basal ganglia with mass effect and a rightward midline shift. (b) Axial FLAIR MR image shows the hyperintense lesion. Polymerase chain reaction results confirmed the diagnosis of toxoplasmosis.



a.

b.

Figure 17. Herpes simplex virus-1 encephalitis in a 93-year-old woman who presented to the ED with a headache. (a) Initial axial nonenhanced CT image shows subtle hypoattenuation in the right anteromedial temporal lobe. (b) Axial FLAIR MR image shows corresponding abnormal hyperintensity and mild swelling in the anteromedial right temporal lobe and parahippocampal gyrus. Lumbar puncture results confirmed the diagnosis.

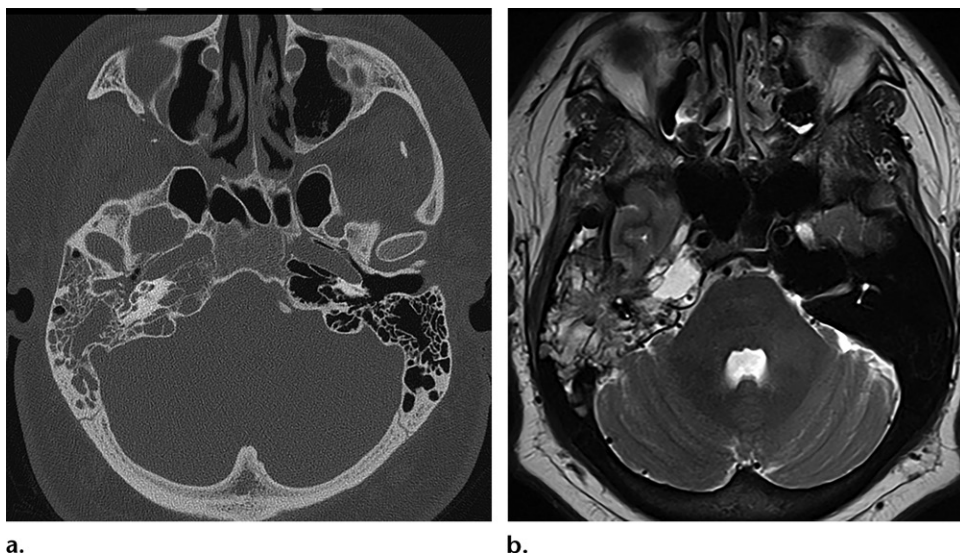
Metastases account for 2%–15% of nontraumatic intracranial hemorrhages.

Miscellaneous Manifestations

Idiopathic Intracranial Hypertension

Idiopathic intracranial hypertension (IIH) is elevated intracranial pressure without evidence of an intracranial mass, hydrocephalus, or abnormal meningeal enhancement. *Pseudotumor cerebri* is

another commonly used name for this entity. Although it has also been referred to as “benign intracranial hypertension,” this name is not accurate and should be avoided, given the risk of vision loss and reduced quality of life with this condition. Transverse sinus stenosis has been shown in more than 90% of patients with IIH, rendering venous outflow obstruction as one of the possible underlying pathophysiologic mechanisms. The typical patient is an obese adolescent



a.

b.

Figure 18. Meningitis in a 32-year-old man who presented with a 1-week history of sinus pressure followed by right ear pain, muffled hearing, and drainage. (a) Axial CT image (bone window) of the temporal bones shows diffuse opacification of the right mastoid air cells, mastoid antrum, tympanic cavity, and pneumatized petrous apex. (b) Axial T2-weighted MR image shows extensive fluid signal intensity in the same anatomic regions.

or adult woman who presents with papilledema. IIH is rare in children younger than 3 years and patients older than 60 years of age.

The diagnostic criteria for IIH, which were revised in 2013, include (*a*) papilledema; (*b*) normal neurologic examination results, with the exception of cranial nerve abnormalities (eg, dysfunction of cranial nerves VI or VII); (*c*) no evidence of a mass, hydrocephalus, or meningeal enhancement at neuroimaging; (*d*) normal CSF composition (eg, no pleocytosis, elevated protein level, low glucose level, abnormal cytologic results, or other evidence of infection or malignancy); and (*e*) elevated lumbar puncture opening pressure (greater than 250 mm in adults and greater than 280 mm in children) (72).

IIH without papilledema also is well recognized. These patients tend to have lower opening pressure levels than those who present with papilledema. In the absence of papilledema, the other criteria should be met, with the additional symptom of unilateral or bilateral abducens nerve palsies. If there is no abducens nerve palsy, three of the following neuroimaging criteria should be met: (*a*) empty sella, (*b*) flattening of the posterior aspect of the globe, (*c*) distention of the subarachnoid space with or without a tortuous optic nerve, and (*d*) transverse sinus stenosis (Fig 19; Fig E4). The right transverse sinus is dominant in most individuals, and unilateral artifactual irregularities may be seen in the transverse sinuses at MR venography. Tonsillar descent can be seen in patients with both intracranial hypertension and hypotension, and therefore it is not included in the neuroimaging criteria (72).

CSF pressure is most accurately measured with the patient in the lateral decubitus position; however, most fluoroscopically guided procedures are performed with the patient in the prone position. The benefits of removing a large volume of CSF (>20 mL) from the patient to aid relief is controversial. A normal opening pressure level does not exclude the diagnosis of IIH when the patient has other typical symptoms such as bilateral papilledema. Conversely, an increased opening pressure level without appropriate symptoms should not be interpreted as IIH.

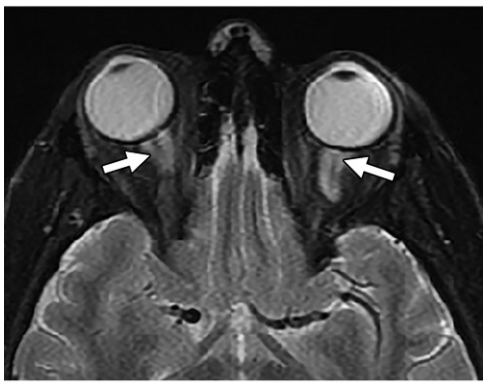
Meningoceles and CSF leaks also are associated with increased intracranial pressure (73–75). Some patients who undergo repair of a CSF leak may later present with symptoms of increased intracranial pressure. Therefore, the skull base defects and resultant CSF leaks are believed to have a role in decompression of increased intracranial pressure. Meningoceles are protrusions of meninges through points of weakness and are conceptually similar to empty sella; both entities represent enlarged subarachnoid spaces that result in decompression of the increased intracranial pressure. *Petrosus apex cephaloceles* are posterolateral protrusions of Meckel's cave into the petrous apex and may be seen in patients with IIH (73,76).

Spontaneous Intracranial Hypotension

Spontaneous intracranial hypotension is an important cause of new persistent daily headaches and is much more common in the ED than it was previously understood to be. In an ED-based study (77), spontaneous intracranial hypotension



a.



b.

Figure 19. IIH in a 38-year-old woman who presented with a headache and vision changes. (a) Coronal T2-weighted MR image shows an enlarged and partially empty sella (arrow). (b) Axial fat-suppressed T1-weighted MR image shows bilateral dilatation of the optic sheaths (arrows).

was found to be half as common as spontaneous SAH, with an estimated annual incidence of five cases per 100 000 patients. In some patients, the headache is acute and mimics acute SAH. A positional or orthostatic headache is a characteristic symptom that gets worse when the patient is in an upright position and improves with recumbency. International Classification of Headache Disorders (ICHD-3) diagnostic criteria for spontaneous intracranial hypotension include (*a*) a headache that develops in temporal relation to low CSF pressure or CSF leakage or led to its discovery, (*b*) low CSF pressure (<60 mm) or signs of a CSF leak at imaging, and (*c*) no known cause of CSF leakage (eg, a procedure or trauma). Spontaneous CSF leakage is associated with generalized connective tissue disorders (78–83). Therefore, patients with CSF leaks should be screened for connective tissue and vascular abnormalities. CSF leaks may occur along the skull base or in the spinal canal. Typical intracranial imaging features include sagging of the

brain (misinterpreted as a Chiari malformation), subdural fluid collections, diffuse pachymeningeal enhancement, and pituitary gland hyperemia (Fig 20; Fig E5). Objective measurements including mamillopontine distance and pontomesencephalic angle are also helpful in the diagnosis of intracranial hypotension. The mamillopontine distance is the distance between the inferior aspect of the mammillary bodies and the superior aspect of the pons. The pontomesencephalic angle is the angle between the anterior aspect of the midbrain and the superior aspect of the pons on a sagittal image. A mamillopontine distance of 5.5 mm or less and pontomesencephalic angle of 50° or less were found to be sensitive and specific for diagnosis of spontaneous intracranial hypotension (84).

Patients also may present with spinal longitudinal extradural fluid collections (Fig 20), which are associated most commonly with dural tears along the thecal sac. In these patients, the dural tears are most commonly ventral. There may be laterally placed CSF leaks that are related to either a CSF venous fistula or a distal nerve root sleeve tear in patients who do not have spinal extradural fluid collections (85). Conventional myelography with subsequent CT myelography may help to identify the site of the dural tear in most patients. Dynamic CT myelography may be the preferred modality to identify the site of a high-flow CSF leak (86).

Similar to spontaneous intracranial hypotension, postdural puncture headache is attributed to low CSF pressure and is characterized by a headache that occurs within 5 days of a lumbar puncture and is caused by CSF leakage through the dural puncture. Risk factors include female sex, age of 31–50 years, a history of postdural puncture headache, and orientation of the needle bevel perpendicular to the long axis of the spinal column at the time of the dural puncture.

Aida et al (87) described two main mechanisms for postspinal puncture headache: intrathecal air and CSF leak, with the latter evident in the majority of cases. Headache onset in the intrathecal air group is short, beginning within 1 hour of the procedure and lasting less than 3 days, whereas headache onset related to CSF leak is relatively delayed. Epidural patch block is unsuccessful if the cause of postdural puncture headache is intrathecal air (88). Imaging findings are similar for both causes and resemble those of spontaneous intracranial hypotension.

Pituitary Apoplexy

Pituitary apoplexy is a severe and potentially fatal medical condition that is characterized by a sudden-onset severe headache, vomiting, ophthalmoplegia, and altered mental status, followed by

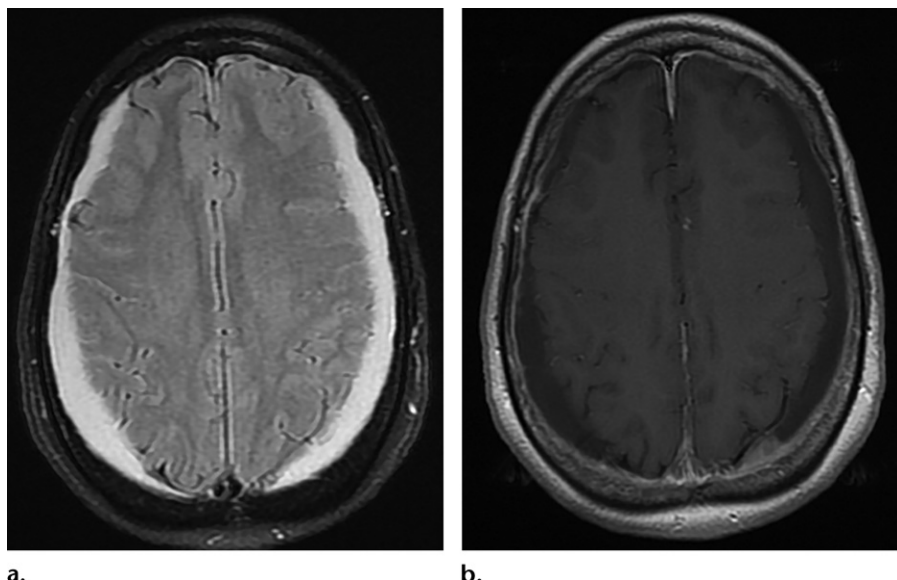


Figure 20. Spontaneous intracranial hypotension in a 76-year-old woman who presented with a headache and double vision. (a) Axial FLAIR MR image shows hyperintense subdural fluid collections overlying both cerebral convexities. (b) Axial contrast-enhanced MR image shows diffuse mild pachymeningeal enhancement. Additional entire spine MRI showed subdural fluid collections in the lumbar spine (not shown).

panhypopituitarism. The most common cause is the hemorrhagic infarction of a known pituitary macroadenoma in approximately 1.6%–2.8% of patients with pituitary macroadenomas (89). In some cases, pituitary apoplexy may be the initial manifestation of a pituitary macroadenoma. Less commonly, it may occur as necrosis of the pituitary gland due to massive bleeding in the postpartum period, which is a condition that is known as *Sheehan syndrome* (90). Risk factors include hypertension, diabetes, anticoagulation therapy, estrogen therapy, use of bromocriptine, radiation therapy, conventional angiography, open heart surgery, and pituitary function dynamic tests.

The term *pituitary apoplexy* should only be used if the clinical syndrome develops. Hemorrhage may coexist in asymptomatic patients with large macroadenomas. The most common symptom at presentation is headache, which is seen in approximately 90%–97% of patients. The headache is usually sudden, severe, and retro-orbital. The second most common symptom is visual deficit, which occurs in 50%–82% of patients. These are followed by nausea, vomiting, ocular palsy, and meningism. The superior aspect of the pituitary gland is covered by the diaphragma sellae, which is a fold of dura mater that separates the subarachnoid space from the pituitary. In pituitary apoplexy, when the pressure gradient in the sella exceeds the resistance of the surrounding structures, blood is expelled into the subarachnoid space, resulting in SAH. Thus, pituitary apoplexy is included in the differential diagnosis for thunderclap headache and SAH in patients with angiographic studies that show no vascular abnormalities (91).

In most cases, the clinical diagnosis may be something other than pituitary apoplexy; therefore, radiologists should be alert for early

and prompt diagnosis of this entity, given the potentially severe prognosis. Nonenhanced CT may show a hyperattenuating sellar mass with suprasellar extension. The appropriate clinical manifestations (including acute vision loss or ophthalmoplegia) must accompany these imaging findings. The differential diagnosis of a hyperattenuating lesion of the sella includes evaluation for aneurysms, Rathke cleft cysts, meningioma, germinoma, and lymphoma. CT with intravenous contrast material may reveal rim enhancement. MRI is the most important tool in diagnosis and may help to differentiate blood from hyperintensity related to other causes. MRI signal intensity may be heterogeneous and depends on the age of the blood products. Acute hemorrhagic lesions are isointense at T1-weighted MRI and hypointense at T2-weighted MRI. Gradient-echo and susceptibility-weighted MRI depict hemorrhage and blooming around the mass. At contrast-enhanced MRI, thin rim enhancement can be seen (92) (Fig E6). Fluid-fluid levels in the area of infarction or sphenoid sinus mucosal wall thickening also have been described as useful imaging features (93,94). The latter is believed to be due to venous engorgement.

Carbon Monoxide Poisoning

Carbon monoxide poisoning should be considered when patients present to the ED with a headache, especially during the winter months. The diagnosis is suggested when multiple family members or coworkers are affected simultaneously, when patients are brought from an enclosed space with a carbon monoxide source such as a gasoline or kerosene generator, and when patients experience rapid improvement when they are removed from the source without other intervention. Standard

pulse oximetry does not allow differentiation of carboxyhemoglobin from oxyhemoglobin (95). Chronic low-dose carbon monoxide exposure may also cause headaches, more often during winter months. Formation of carboxyhemoglobin in the blood causes a state of anoxia or hypoxia, coupled with the direct toxic effects of carbon monoxide on mitochondria, leading to anoxic-ischemic encephalopathy. Lesions are usually bilateral.

The most commonly affected site is the globus pallidus. Less commonly, the putamen and caudate nucleus, thalamus, periventricular and subcortical white matter, corpus callosum, cerebral cortex, and hippocampus of the temporal lobe also may be affected (96).

In the acute stage, symmetric hypointensities in the bilateral globus pallidi are seen at nonenhanced CT. At MRI, restricted diffusion is noted because of cytotoxic edema. The lesions are hypointense at T1-weighted MRI and hyperintense at T2-weighted MRI, with patchy contrast enhancement. (Fig E7). Diffuse brain atrophy and cerebral white matter demyelination may occur in the chronic stage (97,98). Cerebral white matter involvement is associated with the development of chronic symptoms. Diffusion-weighted MRI may show abnormal signal intensity in the cerebral white matter before symptoms manifest (96).

Conclusion

Many patients present to the ED with a headache, and radiologists play a key role in timely diagnosis and guidance of treatment. Awareness of subtle imaging findings that suggest potential diagnoses is important and can help facilitate efficient problem solving. Knowledge of common associations can help the radiologist to choose the appropriate imaging modalities and develop a patient-based treatment plan.

References

- Ramirez-Lassepas M, Espinosa CE, Cicero JJ, Johnston KL, Cipolle RJ, Barber DL. Predictors of intracranial pathologic findings in patients who seek emergency care because of headache. *Arch Neurol* 1997;54(12):1506–1509.
- Torelli P, Campana V, Cervellin G, Manzoni GC. Management of primary headaches in adult Emergency Departments: a literature review, the Parma ED experience and a therapy flow chart proposal. *Neurol Sci* 2010;31(5):545–553.
- Goldstein JN, Camargo CA Jr, Pelletier AJ, Edlow JA. Headache in United States emergency departments: demographics, work-up and frequency of pathological diagnoses. *Cephalgia* 2006;26(6):684–690.
- Locker T, Mason S, Rigby A. Headache management: are we doing enough? An observational study of patients presenting with headache to the emergency department. *Emerg Med J* 2004;21(3):327–332.
- Linn FH, Wijdicks EF, van der Graaf Y, Weerdesteyn-van Vliet FA, Bartelds AI, van Gijn J. Prospective study of sentinel headache in aneurysmal subarachnoid hemorrhage. *Lancet* 1994;344(8922):590–593.
- Douglas AC, Wippold FJ 2nd, Broderick DF, et al. ACR Appropriateness Criteria Headache. *J Am Coll Radiol* 2014;11(7):657–667.
- Bø SH, Davidsen EM, Gulbrandsen P, Dietrichs E. Acute headache: a prospective diagnostic work-up of patients admitted to a general hospital. *Eur J Neurol* 2008;15(12):1293–1299.
- Ducros A, Bousser MG. Thunderclap headache. *BMJ* 2013;346:e8557.
- Rizk B, Platon A, Tasu JP, et al. The role of unenhanced CT alone for the management of headache in an emergency department. A feasibility study. *J Neuroradiol* 2013;40(5):335–341.
- Taylor RA, Singh Gill H, Marcolini EG, Meyers HP, Faust JS, Newman DH. Determination of a Testing Threshold for Lumbar Puncture in the Diagnosis of Subarachnoid Hemorrhage after a Negative Head Computed Tomography: A Decision Analysis. *Acad Emerg Med* 2016;23(10):1119–1127.
- Gill HS, Marcolini EG, Barber D, Wira CR. The Utility of Lumbar Puncture After a Negative Head CT in the Emergency Department Evaluation of Subarachnoid Hemorrhage. *Yale J Biol Med* 2018;91(1):3–11.
- Brisman JL, Song JK, Newell DW. Cerebral aneurysms. *N Engl J Med* 2006;355(9):928–939.
- Carpenter CR, Hussain AM, Ward MJ, et al. Spontaneous Subarachnoid Hemorrhage: A Systematic Review and Meta-analysis Describing the Diagnostic Accuracy of History, Physical Examination, Imaging, and Lumbar Puncture With an Exploration of Test Thresholds. *Acad Emerg Med* 2016;23(9):963–1003.
- Expert Panel on Neurologic Imaging, Polliceni B, Corey AS, et al. ACR Appropriateness Criteria® Cranial Neuropathy. *J Am Coll Radiol* 2017;14(11S):S406–S420.
- Expert Panel on Neurologic Imaging, Kirsch CFE, Bykowski J, et al. ACR Appropriateness Criteria® Sinonasal Disease. *J Am Coll Radiol* 2017;14(11S):S550–S559.
- Whitehead MT, Cardenas AM, Corey AS. ACR Appropriateness Criteria® Headache. <https://acsearch.acr.org/docs/69482/Narrative/>. Revised 2019. Accessed September 4, 2019.
- Expert Panel on Neurologic Imaging, Salmela MB, Mortazavi S, et al. ACR Appropriateness Criteria® Cerebrovascular Disease. *J Am Coll Radiol* 2017;14(5S):S34–S61.
- Marder CP, Narla V, Fink JR, Tozer Fink KR. Subarachnoid hemorrhage: beyond aneurysms. *AJR Am J Roentgenol* 2014;202(1):25–37.
- Hacein-Bey L, Provenzale JM. Current imaging assessment and treatment of intracranial aneurysms. *AJR Am J Roentgenol* 2011;196(1):32–44.
- Kontzialis M, Wasserman BA. Intracranial vessel wall imaging: current applications and clinical implications. *Neurovasc Imaging* 2016;2(4).
- Kataoka K, Taneda M, Asai T, Kinoshita A, Ito M, Kuroda R. Structural fragility and inflammatory response of ruptured cerebral aneurysms. A comparative study between ruptured and unruptured cerebral aneurysms. *Stroke* 1999;30(7):1396–1401.
- Matouk CC, Mandell DM, Günel M, et al. Vessel wall magnetic resonance imaging identifies the site of rupture in patients with multiple intracranial aneurysms: proof of principle. *Neurosurgery* 2013;72(3):492–496; discussion 496.
- Lee WK, Mossop PJ, Little AF, et al. Infected (mycotic) aneurysms: spectrum of imaging appearances and management. *RadioGraphics* 2008;28(7):1853–1868.
- van Asch CJ, Luitse MJ, Rinkel GJ, van der Tweel I, Algra A, Klijn CJ. Incidence, case fatality, and functional outcome of intracerebral haemorrhage over time, according to age, sex, and ethnic origin: a systematic review and meta-analysis. *Lancet Neurol* 2010;9(2):167–176.
- Broderick J, Connolly S, Feldmann E, et al. Guidelines for the management of spontaneous intracerebral hemorrhage in adults: 2007 update: a guideline from the American Heart Association/American Stroke Association Stroke Council, High Blood Pressure Research Council, and the Quality of Care and Outcomes in Research Interdisciplinary Working Group. *Circulation* 2007;116(16):e391–e413.

26. Hemphill JC 3rd, Greenberg SM, Anderson CS, et al. Guidelines for the Management of Spontaneous Intracerebral Hemorrhage: A Guideline for Healthcare Professionals From the American Heart Association/American Stroke Association. *Stroke* 2015;46(7):2032–2060.
27. Kamel H, Navi BB, Hemphill JC 3rd. A rule to identify patients who require magnetic resonance imaging after intracerebral hemorrhage. *Neurocrit Care* 2013;18(1):59–63.
28. Haller S, Vernooyj MW, Kuijer JPA, Larsson EM, Jäger HR, Barkhof F. Cerebral Microbleeds: Imaging and Clinical Significance. *Radiology* 2018;287(1):11–28.
29. Greenberg SM, Eng JA, Ning M, Smith EE, Rosand J. Hemorrhage burden predicts recurrent intracerebral hemorrhage after lobar hemorrhage. *Stroke* 2004;35(6):1415–1420.
30. Rutledge WC, Ko NU, Lawton MT, Kim H. Hemorrhage rates and risk factors in the natural history course of brain arteriovenous malformations. *Transl Stroke Res* 2014;5(5):538–542.
31. Spetzler RF, Martin NA. A proposed grading system for arteriovenous malformations. *J Neurosurg* 1986;65(4):476–483.
32. Tranvinh E, Heit JJ, Hacein-Bey L, Provenzale J, Wintermark M. Contemporary Imaging of Cerebral Arteriovenous Malformations. *AJR Am J Roentgenol* 2017;208(6):1320–1330.
33. Newton TH, Cronqvist S. Involvement of dural arteries in intracranial arteriovenous malformations. *Radiology* 1969;93(5):1071–1078.
34. Gandhi D, Chen J, Pearl M, Huang J, Gemmete JJ, Kathuria S. Intracranial dural arteriovenous fistulas: classification, imaging findings, and treatment. *AJNR Am J Neuroradiol* 2012;33(6):1007–1013.
35. Geibprasert S, Pongpech S, Jiarakongmun P, Shroff MM, Armstrong DC, Krings T. Radiologic assessment of brain arteriovenous malformations: what clinicians need to know. *RadioGraphics* 2010;30(2):483–501.
36. Ayberk G, Ozveren MF, Aslan S, et al. Subarachnoid, subdural and interdural spaces at the clival region: an anatomical study. *Turk Neurosurg* 2011;21(3):372–377.
37. Calabrese LH, Dodick DW, Schwedt TJ, Singhal AB. Narrative review: reversible cerebral vasoconstriction syndromes. *Ann Intern Med* 2007;146(1):34–44.
38. Paliwal PR, Teoh HL, Sharma VK. Association between reversible cerebral vasoconstriction syndrome and thrombotic thrombocytopenic purpura. *J Neurol Sci* 2014;338(1–2):223–225.
39. de Boysson H, Parienti JJ, Mawet J, et al. Primary angiitis of the CNS and reversible cerebral vasoconstriction syndrome: A comparative study. *Neurology* 2018;91(16):e1468–e1478.
40. Miller TR, Shivashankar R, Mossa-Basha M, Gandhi D. Reversible Cerebral Vasoconstriction Syndrome, Part 2: Diagnostic Work-Up, Imaging Evaluation, and Differential Diagnosis. *AJR Am J Neuroradiol* 2015;36(9):1580–1588.
41. Hinckley J, Chaves C, Appignani B, et al. A reversible posterior leukoencephalopathy syndrome. *N Engl J Med* 1996;334(8):494–500.
42. McKinney AM, Short J, Truwit CL, et al. Posterior reversible encephalopathy syndrome: incidence of atypical regions of involvement and imaging findings. *AJR Am J Roentgenol* 2007;189(4):904–912.
43. Kontzialis M, Huisman TAGM. Toxic-Metabolic Neurologic Disorders in Children: A Neuroimaging Review. *J Neuroimaging* 2018;28(6):587–595.
44. Fugate JE, Rabinstein AA. Posterior reversible encephalopathy syndrome: clinical and radiological manifestations, pathophysiology, and outstanding questions. *Lancet Neurol* 2015;14(9):914–925.
45. Stevens CJ, Heran MK. The many faces of posterior reversible encephalopathy syndrome. *Br J Radiol* 2012;85(1020):1566–1575.
46. Fugate JE, Claassen DO, Cloft HJ, Kallmes DF, Kozak OS, Rabinstein AA. Posterior reversible encephalopathy syndrome: associated clinical and radiologic findings. *Mayo Clin Proc* 2010;85(5):427–432.
47. Karia SJ, Rykken JB, McKinney ZJ, Zhang L, McKinney AM. Utility and Significance of Gadolinium-Based Contrast Enhancement in Posterior Reversible Encephalopathy Syndrome. *AJR Am J Neuroradiol* 2016;37(3):415–422.
48. Botta R, Donirpathi S, Yadav R, Kulkarni GB, Kumar MV, Nagaraja D. Headache Patterns in Cerebral Venous Sinus Thrombosis. *J Neurosci Rural Pract* 2017;8(5 Suppl 1):S72–S77.
49. Alvis-Miranda HR, Milena Castellar-Leones S, Alcalá-Cerra G, Rafael Moscote-Salazar L. Cerebral sinus venous thrombosis. *J Neurosci Rural Pract* 2013;4(4):427–438.
50. Chiewwut P, Piyapittayanan S, Poungvarin N. Cerebral venous thrombosis: diagnosis dilemma. *Neurol Int* 2011;3(3):e13.
51. Black DF, Rad AE, Gray LA, Campeau NG, Kallmes DF. Cerebral venous sinus density on noncontrast CT correlates with hematocrit. *AJNR Am J Neuroradiol* 2011;32(7):1354–1357.
52. Buyck PJ, De Keyzer F, Vanneste D, Wilms G, Thijs V, Demaerel P. CT density measurement and H:H ratio are useful in diagnosing acute cerebral venous sinus thrombosis. *AJNR Am J Neuroradiol* 2013;34(8):1568–1572.
53. Avsenik J, Oblak JP, Popovic KS. Non-contrast computed tomography in the diagnosis of cerebral venous sinus thrombosis. *Radiol Oncol* 2016;50(3):263–268.
54. de la Vega Muns G, Quencer R, Ezuddin NS, Saigal G. Utility of Hounsfield unit and hematocrit values in the diagnosis of acute venous sinus thrombosis in unenhanced brain CTs in the pediatric population. *Pediatr Radiol* 2019;49(2):234–239.
55. Leach JL, Fortuna RB, Jones BV, Gaskill-Shipley MF. Imaging of cerebral venous thrombosis: current techniques, spectrum of findings, and diagnostic pitfalls. *RadioGraphics* 2006;26(Suppl 1):S19–S41; discussion S42–S43.
56. Rodallec MH, Krainik A, Feydy A, et al. Cerebral venous thrombosis and multidetector CT angiography: tips and tricks. *RadioGraphics* 2006;26(Suppl 1):S5–S18; discussion S42–S43.
57. Silbert PL, Mokri B, Schievink WI. Headache and neck pain in spontaneous internal carotid and vertebral artery dissections. *Neurology* 1995;45(8):1517–1522.
58. Arnold M, Cumurciuc R, Staph C, Favrole P, Berthet K, Bousser MG. Pain as the only symptom of cervical artery dissection. *J Neurol Neurosurg Psychiatry* 2006;77(9):1021–1024.
59. von Babo M, De Marchis GM, Sarikaya H, et al. Differences and similarities between spontaneous dissections of the internal carotid artery and the vertebral artery. *Stroke* 2013;44(6):1537–1542.
60. Rodallec MH, Marteau V, Gerber S, Desmottes L, Zins M. Craniocervical arterial dissection: spectrum of imaging findings and differential diagnosis. *RadioGraphics* 2008;28(6):1711–1728.
61. Provenzale JM, Sarikaya B. Comparison of test performance characteristics of MRI, MR angiography, and CT angiography in the diagnosis of carotid and vertebral artery dissection: a review of the medical literature. *AJR Am J Roentgenol* 2009;193(4):1167–1174.
62. Lippman HH, Sundt TM Jr, Holman CB. The poststenotic carotid slim sign: spurious internal carotid hypoplasia. *Mayo Clin Proc* 1970;45(11):762–767.
63. Pappas JN. The angiographic string sign. *Radiology* 2002;222(1):237–238.
64. Lum C, Chakraborty S, Schlossmacher M, et al. Vertebral artery dissection with a normal-appearing lumen at multisector CT angiography: the importance of identifying wall hematoma. *AJNR Am J Neuroradiol* 2009;30(4):787–792.
65. Dorsett M, Liang SY. Diagnosis and Treatment of Central Nervous System Infections in the Emergency Department. *Emerg Med Clin North Am* 2016;34(4):917–942 [Published correction appears in *Emerg Med Clin North Am* 2017;35(2):xix.] <https://doi.org/10.1016/j.emc.2016.06.013>.
66. Pedroso JL, de Aquino CC, Abrahão A, et al. Gradenigo's Syndrome: Beyond the Classical Triad of Diplopia, Facial Pain and Otorrhea. *Case Rep Neurol* 2011;3(1):45–47.
67. Taklalsingh N, Falcone F, Velayudhan V. Gradenigo's Syndrome in a Patient with Chronic Suppurative Otitis Media, Petrous Apicitis, and Meningitis. *Am J Case Rep* 2017;18:1039–1043.

68. Forsyth PA, Posner JB. Headaches in patients with brain tumors: a study of 111 patients. *Neurology* 1993;43(9):1678–1683.
69. Vázquez-Barquero A, Ibáñez FJ, Herrera S, Izquierdo JM, Berciano J, Pascual J. Isolated headache as the presenting clinical manifestation of intracranial tumors: a prospective study. *Cephalgia* 1994;14(4):270–272.
70. Suwanwela N, Phanthumchinda K, Kaorophum S. Headache in brain tumor: a cross-sectional study. *Headache* 1994;34(7):435–438.
71. Armao D, Castillo M, Chen H, Kwock L. Colloid cyst of the third ventricle: imaging-pathologic correlation. *AJR Am J Neuroradiol* 2000;21(8):1470–1477.
72. Friedman DI, Liu GT, Digre KB. Revised diagnostic criteria for the pseudotumor cerebri syndrome in adults and children. *Neurology* 2013;81(13):1159–1165.
73. Bialer OY, Rueda MP, Bruce BB, Newman NJ, Bioussse V, Saindane AM. Meningoceles in idiopathic intracranial hypertension. *AJR Am J Roentgenol* 2014;202(3):608–613.
74. Pérez MA, Bialer OY, Bruce BB, Newman NJ, Biousses V. Primary spontaneous cerebrospinal fluid leaks and idiopathic intracranial hypertension. *J Neuroophthalmol* 2013;33(4):330–337.
75. Yang Z, Wang B, Wang C, Liu P. Primary spontaneous cerebrospinal fluid rhinorrhea: a symptom of idiopathic intracranial hypertension? *J Neurosurg* 2011;115(1):165–170.
76. O’Connell BP, Yawn RJ, Hunter JB, Haynes DS. Bilateral Petrous Apex Cephaloceles and Skull Base Attenuation in Setting of Idiopathic Intracranial Hypertension. *Otol Neurotol* 2016;37(8):e256–e257.
77. Schievink WI. Spontaneous spinal cerebrospinal fluid leaks and intracranial hypotension. *JAMA* 2006;295(19):2286–2296.
78. Schievink WI, Gordon OK, Tourje J. Connective tissue disorders with spontaneous spinal cerebrospinal fluid leaks and intracranial hypotension: a prospective study. *Neurosurgery* 2004;54(1):65–70; discussion 70–71.
79. Schievink WI, Meyer FB, Atkinson JL, Mokri B. Spontaneous spinal cerebrospinal fluid leaks and intracranial hypotension. *J Neurosurg* 1996;84(4):598–605.
80. Schievink WI, Morreale VM, Atkinson JL, Meyer FB, Piepgras DG, Ebersold MJ. Surgical treatment of spontaneous spinal cerebrospinal fluid leaks. *J Neurosurg* 1998;88(2):243–246.
81. Schievink WI, Reimer R, Folger WN. Surgical treatment of spontaneous intracranial hypotension associated with a spinal arachnoid diverticulum. Case report. *J Neurosurg* 1994;80(4):736–739.
82. Schrijver I, Schievink WI, Godfrey M, Meyer FB, Francke U. Spontaneous spinal cerebrospinal fluid leaks and minor skeletal features of Marfan syndrome: a microfibrillopathy. *J Neurosurg* 2002;96(3):483–489.
83. Mokri B, Maher CO, Sencakova D. Spontaneous CSF leaks: underlying disorder of connective tissue. *Neurology* 2002;58(5):814–816.
84. Shah LM, McLean LA, Heilbrun ME, Salzman KL. Intracranial hypotension: improved MRI detection with diagnostic intracranial angles. *AJR Am J Roentgenol* 2013;200(2):400–407.
85. Farb RI, Nicholson PJ, Peng PW, et al. Spontaneous Intracranial Hypotension: A Systematic Imaging Approach for CSF Leak Localization and Management Based on MRI and Digital Subtraction Myelography. *AJR Am J Neuroradiol* 2019;40(4):745–753.
86. Dobrocky T, Mosimann PJ, Zibold F, et al. Cryptogenic Cerebrospinal Fluid Leaks in Spontaneous Intracranial Hypotension: Role of Dynamic CT Myelography. *Radiology* 2018;289(3):766–772.
87. Aida S, Taga K, Yamakura T, Endoh H, Shimoji K. Headache after attempted epidural block: the role of intrathecal air. *Anesthesiology* 1998;88(1):76–81.
88. Somri M, Teszler CB, Vaida SJ, et al. Postdural puncture headache: an imaging-guided management protocol. *Anesth Analg* 2003;96(6):1809–1812.
89. Dubuisson AS, Beckers A, Stevenaert A. Classical pituitary tumour apoplexy: clinical features, management and outcomes in a series of 24 patients. *Clin Neurol Neurosurg* 2007;109(1):63–70.
90. Sheehan HL. Post-partum necrosis of the anterior pituitary. *Ir J Med Sci* 1948;(270):241–255.
91. Ju YE, Schwedt TJ. Abrupt-onset severe headaches. *Semin Neurol* 2010;30(2):192–200.
92. Goyal P, Utz M, Gupta N, et al. Clinical and imaging features of pituitary apoplexy and role of imaging in differentiation of clinical mimics. *Quant Imaging Med Surg* 2018;8(2):219–231.
93. Semple PL, Jane JA, Lopes MB, Laws ER. Pituitary apoplexy: correlation between magnetic resonance imaging and histopathological results. *J Neurosurg* 2008;108(5):909–915.
94. Waqar M, McCreary R, Kearney T, Karabatsou K, Gnanalingham KK. Sphenoid sinus mucosal thickening in the acute phase of pituitary apoplexy. *Pituitary* 2017;20(4):441–449.
95. Zorbalar N, Yesilaras M, Aksay E. Carbon monoxide poisoning in patients presenting to the emergency department with a headache in winter months. *Emerg Med J* 2014;31(e1):e66–e70.
96. Beppu T. The role of MR imaging in assessment of brain damage from carbon monoxide poisoning: a review of the literature. *AJR Am J Neuroradiol* 2014;35(4):625–631.
97. Lo CP, Chen SY, Lee KW, et al. Brain injury after acute carbon monoxide poisoning: early and late complications. *AJR Am J Roentgenol* 2007;189(4):W205–W211.
98. Kim DM, Lee IH, Park JY, Hwang SB, Yoo DS, Song CJ. Acute carbon monoxide poisoning: MR imaging findings with clinical correlation. *Diagn Interv Imaging* 2017;98(4):299–306.

CT of the Neck: Image Analysis and Reporting in the Emergency Setting

Alain Cunqueiro, MD

William A. Gomes, MD, PhD

Peter Lee, MD

R. Joshua Dym, MD

Meir H. Scheinfeld, MD, PhD

Abbreviations: EAC = external auditory canal,
PTA = peritonsillar abscess

RadioGraphics 2019; 39:1760–1781

<https://doi.org/10.1148/rg.2019190012>

Content Codes: **CT** **ER** **HN** **IN** **NR**

From the Division of Emergency Radiology (M.H.S.), Department of Radiology (A.C., P.L.), Montefiore Medical Center, Albert Einstein College of Medicine, 111 E 210 St, Bronx, NY 10467; Department of Radiology, Westchester Medical Center, Valhalla, NY (W.A.G.); and Department of Radiology, Rutgers New Jersey Medical School, Newark, NJ (R.J.D.). Presented as an education exhibit at the 2018 RSNA Annual Meeting. Received February 25, 2019; revision requested March 28 and received April 1; accepted April 11. For this journal-based SA-CME activity, the authors, editor, and reviewers have disclosed no relevant relationships. **Address correspondence to** M.H.S. (e-mail: mscheinf@montefiore.org).

©RSNA, 2019

SA-CME LEARNING OBJECTIVES

After completing this journal-based SA-CME activity, participants will be able to:

- Describe how to systematically interpret the findings of neck CT performed in the emergency department.
- Identify common pathologic entities found at neck CT in the emergency department.
- Compose a report detailing and synthesizing the findings seen at emergency neck CT.

See rsna.org/learning-center-rg.

Interpreting findings seen at CT of the neck is challenging owing to the complex and nuanced anatomy of the neck, which contains multiple organ systems in a relatively small area. In the emergency department setting, CT is performed to investigate acute infectious or inflammatory symptoms and chronic processes. With few exceptions, neck CT should be performed with intravenous contrast material, which accentuates abnormally enhancing phlegmonous and neoplastic tissues and can be used to delineate any abscesses or necrotic areas. As part of the evaluation, the vascular structures and aerodigestive tract must be scrutinized, particularly for patency. Furthermore, although the patient may present because of symptoms that suggest non-life-threatening conditions involving structures such as the teeth or salivary glands, there may be serious implications for other areas, such as the orbits, brain, and spinal cord, that also may be revealed at the examination. With a focus on the emergency setting, the authors propose using an approach to interpreting neck CT findings whereby 12 areas are systematically evaluated and reported on: the cutaneous and subcutaneous soft tissues, aerodigestive tract and adjacent soft tissues, teeth and periodontal tissues, thyroid gland, salivary glands, lymph nodes, vascular structures, bony airspaces, cervical spine, orbits and imaged brain, lung apices, and superior mediastinum. The use of a systematic approach to interpreting neck CT findings is essential for identifying all salient findings, recognizing and synthesizing the implications of these findings to formulate the correct diagnosis, and reporting the findings and impressions in a complete, clear, and logical manner.

Online supplemental material is available for this article.

©RSNA, 2019 • radiographics.rsna.org

Introduction

In the emergency setting, CT of the neck is often performed to investigate symptoms of acute infection or inflammation or symptoms of aerodigestive tract compromise referable to the neck. A neck mass or adenopathy also may be investigated, particularly when it results in airway or vascular compromise. In a recent single-center study (1), neck CT had a positivity rate of 87%, indicating that it is generally performed for good reason and, therefore, imaging findings should be expected. Interpretation of neck CT findings can be challenging, primarily because of the multiple organ systems in the neck. Because there are components of the respiratory, digestive, vascular, endocrine, skeletal, and neurologic systems in the neck, the radiologist is required to have knowledge and an understanding of how disease manifests and how an abnormality in one system can spread and affect other systems.

TEACHING POINTS

- A checklist approach similar to that used for interpreting abdominopelvic CT images, in which all imaged organs such as the lung bases, heart, liver, gallbladder, biliary tree, spleen, pancreas, adrenal glands, and other organs are systematically evaluated, also seems prudent for interpreting neck CT images.
- CT images in patients with epiglottitis show thickening of the mucosa of the epiglottis, aryepiglottic folds, and/or arytenoids. As the epithelium is tightly bound to the vocal cords, edema does not spread inferior to them. Also, because the epithelium and lamina propria are loosely bound to the epiglottic cartilage on the lingual side, there may be initial thickening of only the anterior surface.
- With Ludwig angina, CT images show inflammatory stranding and fluid in the submandibular and sublingual spaces, with or without abscesses or gas. As Ludwig angina is a "cellulitis," rim-enhancing components are not required to make the diagnosis.
- An intracranial aneurysm is a particularly important finding that may be incidentally encountered at neck CT. The prevalence of intracranial aneurysm in the general population without comorbidities has been estimated to be 3.2%. Owing to the risk of aneurysmal rupture with devastating subarachnoid hemorrhage and the availability of effective treatment options, the intracranial arteries should be scrutinized in every case.
- Epidural abscesses are collections of pus in the epidural space and are most commonly due to sinus infections. CT images show a rim-enhancing collection with characteristics of an epidural collection (eg, lentiform in shape, usually not crossing sutures). When these abscesses result from a temporal bone infection such as mastoiditis, a rim-enhancing epidural collection may be seen between the mastoid bone and the cerebellum or temporal lobe.

The traditional approach to neck CT analysis is focused on an understanding of the fascial spaces of the neck (2–4). Knowledge of this complex anatomy is necessary when a mass or inflammatory process is identified, and a strategy for determining which structures are deviated and the direction of the deviations must be used to make a diagnosis or differential diagnosis. Still, having a systematic approach to evaluating the common locations of disease is beneficial for efficient and consistent detection of all salient imaging findings. A checklist approach similar to that used for interpreting abdominopelvic CT images, in which all imaged organs such as the lung bases, heart, liver, gallbladder, biliary tree, spleen, pancreas, and adrenal glands are systematically evaluated, also seems prudent for interpreting neck CT images.

In this article, we describe a 12-item checklist-based approach, informed by the space-based approach, that can be used to address the complex anatomy and variety of possible abnormalities that can be seen in the nontraumatic emergency setting (Table). It should be emphasized that once a specific disease process is

Twelve Areas of Assessment on the Neck CT Analysis Checklist

1. Cutaneous and subcutaneous soft tissues
2. Aerodigestive tract and adjacent soft tissues
3. Teeth and periodontal tissues
4. Thyroid gland
5. Salivary glands
6. Lymph nodes
7. Vascular structures
8. Bony airspaces
9. Cervical spine
10. Orbita and imaged brain
11. Lung apices
12. Superior mediastinum

suspected, its pathophysiologic features should be used to guide the search for other areas of involvement and validate or reject the suspicion. Ultimately, individual findings must be synthesized to derive a diagnosis or differential diagnosis that can guide further management.

We begin by describing a protocol for CT of the neck. Then, for each item on the checklist, we describe the structures being evaluated and common (and some uncommon but important) pathologic conditions that are seen in the acute setting. We conclude by describing an approach to integrating the findings of the individual checklist items to derive a coherent diagnosis, which is reported in the "Impression" section of the report.

Neck CT Protocol

Whenever possible, neck CT should be performed with intravenous contrast material to maximize the ability to detect and characterize abscesses, masses, and vascular complications of infectious, inflammatory, and neoplastic conditions. As an exception, contrast material is not required to identify a suspected retained aerodigestive tract foreign body (5). In fact, contrast material may obscure or confound the detection of a small foreign body. Therefore, at many institutions, intravenous contrast material is not administered for this indication. When there is a palpable or focal abnormality, the CT technologist places a BB marker on that area.

At our institution, when contrast material is administered, we use a biphasic contrast agent injection protocol to achieve good parenchymal and vascular opacification, although a monophasic protocol also can be used. Sixty milliliters of iodinated contrast material is injected at 2 mL/sec for 30 seconds. Following a 60-second delay, an additional 40 mL of the agent is administered at 2 mL/sec for 20 seconds. Following a 10-second delay,

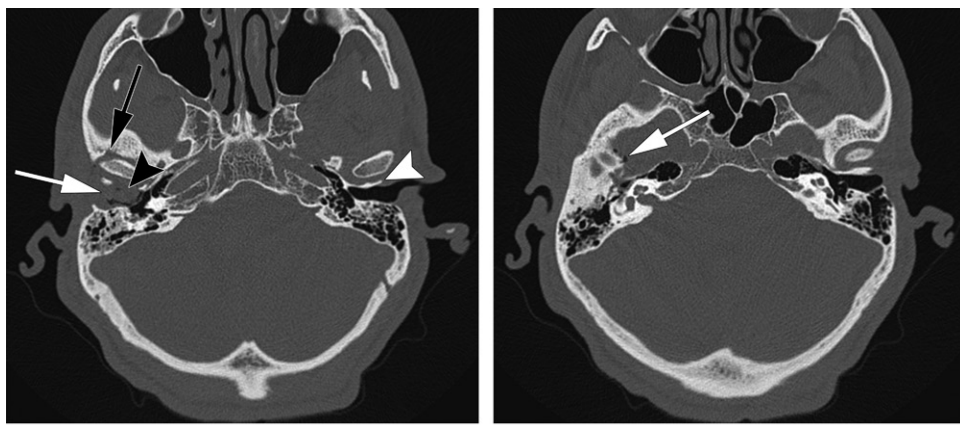
**a.****b.**

Figure 1. Malignant otitis externa of the right ear in a 55-year-old man. **(a)** Axial nonenhanced CT image shows an opacified right EAC (white arrow). There is bone erosion of the anterior wall of the right EAC, which is also the posterior wall of the temporomandibular joint (black arrowhead). In comparison, the left anterior wall of the left EAC (white arrowhead) is complete. There is also erosion of the anterior margin of the glenoid fossa (black arrow). **(b)** Axial nonenhanced CT image obtained superior to **a** shows foci of gas (arrow) in the right middle cranial fossa.

imaging is commenced. CT images are acquired helically, from the orbital roofs to the aortic arch, by using 120 kVp and 100–300 mA, with the exact tube current varying according to patient factors. Images with a thickness of 2.5 mm are constructed in the axial, sagittal, and coronal planes by using a soft-tissue kernel and in the axial plane by using a bone kernel. Axial 0.625-mm images constructed by using bone and soft-tissue kernels also are sent to the picture archiving and communication system.

Neck CT Checklist

Cutaneous and Subcutaneous Soft Tissues

The cutaneous and subcutaneous soft tissues include the skin, subcutaneous fat, and superficial muscles (eg, platysma muscle and facial expression muscles). The subcutaneous tissues may be the primary site of inflammation or an indication of adjacent inflammation. Primary cellulitis of the subcutaneous tissues of the face may be caused by disruption of the skin due to chronic skin conditions (such as eczema and psoriasis), infection of a hair follicle (folliculitis), a retained foreign body, or minimal trauma. On CT images, the subcutaneous fat and muscular structures should have sharp definition without infiltration of the subcutaneous fat.

At CT, cellulitis manifests as skin thickening and infiltration of the subcutaneous fat and is sometimes associated with abscess formation, which appears as a rim-enhancing fluid collection (Fig E1). Thickening of the platysma muscle is commonly seen secondary to inflammation or infection of adjacent structures and serves as a beacon to draw attention to the adjacent area. Injectable filler agents such as collagen, silicone, and

hyaluronic acid can mimic subcutaneous infection or inflammation, and this possibility should be considered when isolated subcutaneous infiltration or highly symmetric infiltration is detected (6).

Otitis externa, also called swimmer's ear, is a superficial infection of the external auditory canal (EAC) that is related to minor trauma or liquid exposure such as that from swimming. It is seen most commonly in children and manifests as pain, discharge, and edema of the ear canal. Although the diagnosis is usually made by means of physical examination, otitis externa manifests at contrast material–enhanced neck CT as thickening of the EAC and pinna without involvement of the underlying bone (Fig E2).

With malignant otitis externa, the more severe and invasive form of otitis externa, aggressive infection of the EAC penetrates into the adjacent bone, causing osteomyelitis of the bony EAC, temporomandibular joint, adjacent parts of the temporal bone, and skull base, with involvement of the adjacent soft tissues (7). Malignant otitis externa is a life-threatening disease that is typically seen in elderly patients with diabetes, and it is caused by *Pseudomonas aeruginosa* infection in more than 90% of cases (8). Owing to the permeative nature of this process, it may mimic a tumor (9).

Contrast-enhanced CT of malignant otitis externa will reveal extension of the infection to the bone and soft tissue outside of the EAC, with bone erosion of the EAC; soft-tissue infiltration of the infratemporal fossa; erosion, widening, and infiltration of the temporomandibular joint; soft-tissue infiltration along the eustachian tube and within the nasopharynx; and bone erosion within the petrous apex and mastoid process (Fig 1) (7,10). Among the cranial nerves, the facial nerve

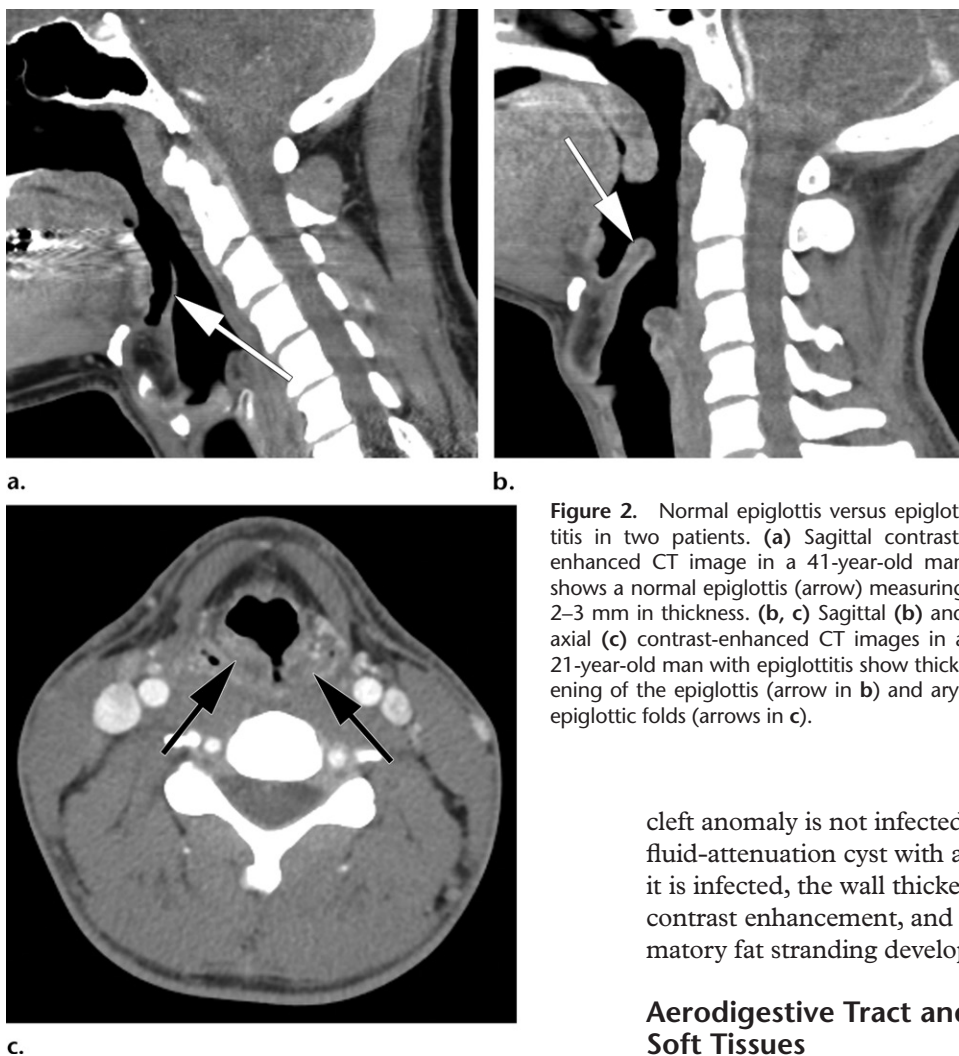


Figure 2. Normal epiglottis versus epiglottitis in two patients. (a) Sagittal contrast-enhanced CT image in a 41-year-old man shows a normal epiglottis (arrow) measuring 2–3 mm in thickness. (b, c) Sagittal (b) and axial (c) contrast-enhanced CT images in a 21-year-old man with epiglottitis show thickening of the epiglottis (arrow in b) and aryepiglottic folds (arrows in c).

cleft anomaly is not infected, it appears at CT as a fluid-attenuation cyst with a thin wall (12). When it is infected, the wall thickens and demonstrates contrast enhancement, and surrounding inflammatory fat stranding develops (12).

Aerodigestive Tract and Adjacent Soft Tissues

The aerodigestive tract and surrounding soft tissues must be evaluated from the mouth through the most caudal imaged portions of the esophagus and trachea. Evaluating these structures in a systematic manner, from the superior to inferior aspect, ensures that all findings will be identified. From a practical standpoint, this entails examination of the nasal cavity and nasopharynx, oral cavity and oropharynx, hypopharynx, larynx, and imaged portions of the trachea and esophagus.

At imaging, the epiglottis and aryepiglottic folds should be thin (Fig 2). There should be no thickening of the mucosa of the aerodigestive tract and no adjacent collections. Although mucosal and other types of neoplasms may be discovered incidentally, even in the acute setting (1), neoplastic disease of the neck is beyond the scope of this review and is well covered elsewhere (13–15). An important reminder regarding the imaging of all airway lesions is that imaging should not delay definitive airway management for patients with tenuous airways.

Epiglottitis and *supraglottitis* refer to life-threatening acute inflammation of the epiglottis, aryepiglottic folds, and/or arytenoids. Although

is the most commonly affected owing to involvement at the stylomastoid foramen. Cranial nerves V, VI, and IX–XII also may be affected as infection spreads in the soft tissues (7). Rare intracranial manifestations include sigmoid sinus thrombosis, meningitis, and brain abscess. Therefore, when a soft-tissue abnormality is detected in the EAC, adjacent bone, soft tissue, and intracranial structures should be examined for the possibility of contiguous spread.

Branchial cleft anomalies can manifest as a cyst where there is no internal or external connection, as a sinus where there is only an external connection, or as a fistula where there are openings on the skin and pharyngeal surfaces (11). Second branchial cleft anomalies account for 95% of these anomalies, and cysts are the most common anomaly at this location (11). The classic location of second branchial cleft anomalies is anterior to the sternocleidomastoid muscle, at the angle of the mandible; however, different types may manifest along a line between the oropharynx and the supraclavicular region (11). When a branchial

classically thought of as a disease of children, epiglottitis also affects adults, being most famously the likely cause of the death of George Washington in 1799 (16). Since the advent of the *Haemophilus influenzae* type B vaccine, there has been a dramatic reduction in epiglottitis cases among children. Epiglottitis is now more commonly seen in adults, with an incidence of one to two cases per 100 000 adults, as a result of other bacterial (*Streptococcus pneumoniae*), viral (herpes simplex), and fungal infections, or noninfectious causes such as trauma or chemicals (17,18).

Children with epiglottitis generally are in respiratory distress when they present and are diagnosed at clinical or radiographic examination. In adults who present with symptoms such as severe sore throat, dysphagia, and fever, with a more gradual onset, CT can be performed as the initial imaging investigation. CT images in patients with epiglottitis show thickening of the mucosa of the epiglottis, aryepiglottic folds, and/or arytenoids (Fig 2). As the epithelium is tightly bound to the vocal cords, edema does not spread inferior to them (16). Also, because the epithelium and lamina propria are loosely bound to the epiglottic cartilage on the lingual side, there may be initial thickening of only the anterior surface (Fig E3).

With epiglottitis, in adults in particular, only some of the supraglottic structures may be thickened (Fig E4). Identification of an epiglottic abscess increases the risk of airway obstruction, so one should carefully search for this finding (16,19).

A peritonsillar abscess (PTA) or peritonsillar phlegmon develops following tonsillitis or pharyngitis and is the most common pediatric head and neck abscess (20). A PTA is an accumulation of pus in the loose tissue around the palatine tonsil. This accumulation is due to the spread of infection from the tonsil or the obstruction of Weber glands, which are minor salivary glands that lie superior to the palatine tonsils (20). The abscess or phlegmon most commonly develops superior to the palatine tonsil, between the capsule of the tonsil (which lies medial to the abscess) and the superior pharyngeal constrictor muscle (which lies peripheral to the abscess) (21). CT can depict a spectrum of tonsillar and peritonsillar abnormalities. In tonsillitis, the tonsils are enlarged and demonstrate a striated enhancement pattern (Fig 3). Peritonsillar phlegmon appears as a vague hypoenhancing area without a well-formed rim of enhancement.

CT is 100% sensitive and 75% specific for detection of PTA, which on CT images most commonly appears as a rim-enhancing collection superolateral to the palatine tonsil (Fig 4) (21).

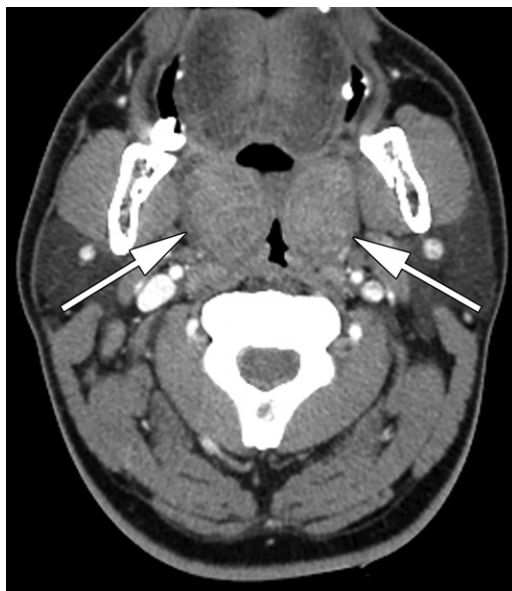


Figure 3. Tonsillitis in a 34-year-old man. Axial contrast-enhanced CT image shows enlarged palatine tonsils (arrows) that are in contact with each other ("kissing" tonsils) at the midline. The classic striated enhancement pattern is seen in the right tonsil.

When possible, a PTA should be differentiated from an intratonsillar abscess, which may not require drainage and is associated with a lower recurrence rate (22). Also, when the carotid artery has a medial course, this variant should be noted because it may be mistaken clinically for tonsil-related disease, or the artery may be injured in a tonsillar intervention (23). Therefore, we recommended documenting the distance from the closest margin of the abscess to the carotid artery and whether there are any trajectories that are particularly safe or unsafe if an intraoral drainage is performed.

Retropharyngeal abscess is an accumulation of pus posterior to the pharynx, with the potential to spread inferiorly into the mediastinum via the "danger" space. The danger space is a potential space that extends from the skull base to the diaphragm. It is bound by the alar fascia anteriorly and the prevertebral fascia posteriorly (discussed in greater detail in the "Superior Mediastinum" section) (24). In children, most commonly those between the ages of 2 and 4 years, retropharyngeal abscess is due to an upper respiratory infection or otitis that leads to enlarged lateral retropharyngeal nodes, which lie between the distal cervical internal carotid artery laterally and the prevertebral musculature medially (Fig 5), with subsequent suppuration and intranodal abscess formation (25).

If the infected nodes rupture, a retropharyngeal abscess forms. Because these lymph nodes atrophy before puberty, retropharyngeal abscess

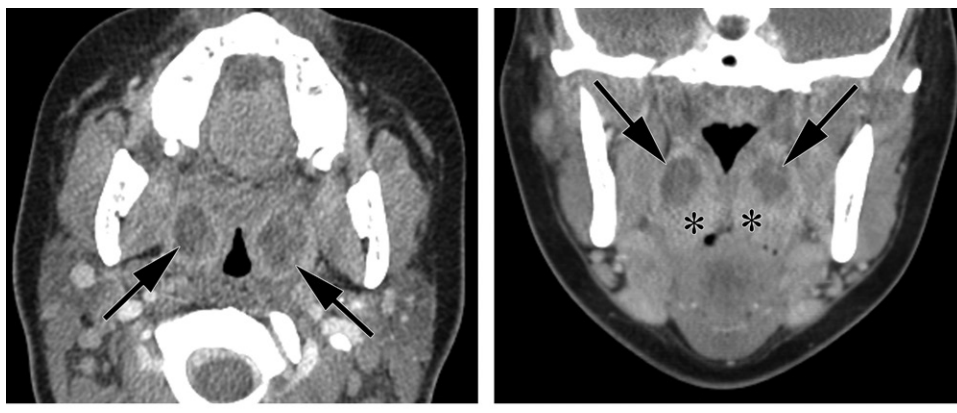


Figure 4. Bilateral PTAs in a 21-year-old woman. Axial (a) and coronal (b) contrast-enhanced CT images show bilateral low-attenuation collections (arrows) superolateral to the palatine tonsils (* in b).

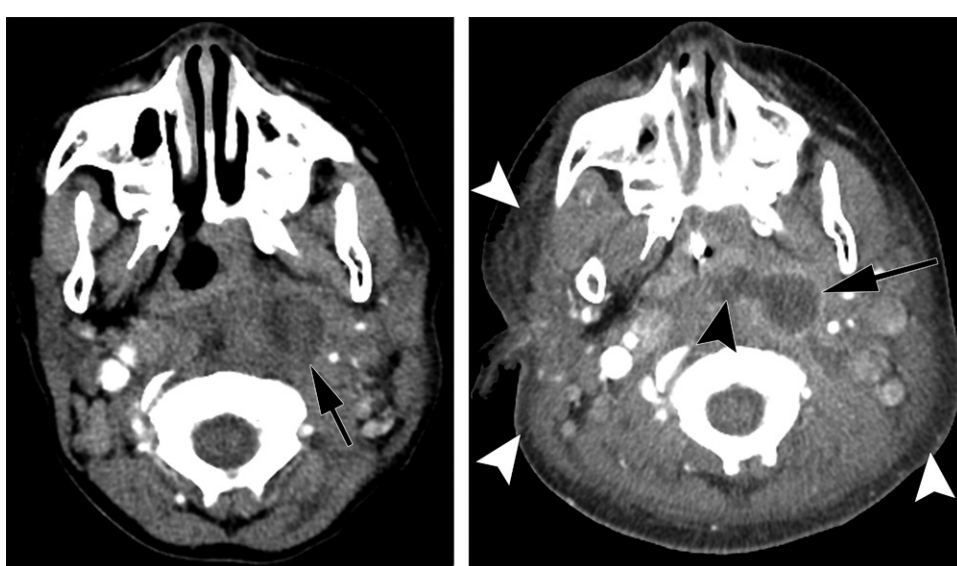


Figure 5. Left retropharyngeal suppurated lymph node and retropharyngeal abscess in a 5-year-old boy. (a) Axial contrast-enhanced CT image shows a left retropharyngeal low-attenuation lymph node (arrow), consistent with internal suppuration. (b) Axial contrast-enhanced CT image obtained 3 days later, by which time the patient's condition had worsened such that intubation was required, shows that the suppurated lymph node (arrow) has ruptured into the retropharyngeal space (black arrowhead). Subcutaneous edema (white arrowheads) also is present.

is rare in adults. The adult cases that do occur usually are due to foreign body perforation (26).

In children, contrast-enhanced CT of the neck depicts suppurated lymph nodes as round structures posterior to the pharynx, with decreased internal attenuation and a rim of enhancement (Fig 5). A retropharyngeal abscess is a larger rim-enhancing collection that is not confined by the boundaries of the lymph node; rather, it extends across the retropharyngeal space (Fig 5) (24).

Retropharyngeal abscess must be differentiated from retropharyngeal edema, which may be an accessory finding due to other infectious processes or represent inflammation such as that due to prior radiation therapy or calcific tendinitis of the longus colli. Calcific tendinitis

of the longus colli, technically a prevertebral process, results from an inflammatory reaction to hydroxyapatite deposits within the longus colli muscle or tendon (27). The CT diagnosis is dependent on the identification of abnormal calcific attenuation, which is usually seen within the longus colli tendon, inferior to the anterior arch of C1. Retropharyngeal edema involves the retropharyngeal space from side to side, with tapered superior and inferior ends; however, there is no rim enhancement (Fig 6) (24).

Angioedema refers to increased capillary permeability and extravasation of fluid that result in localized and transient edematous swelling of the skin or mucosa. Most cases are idiopathic; other cases involve hereditary, drug-related,

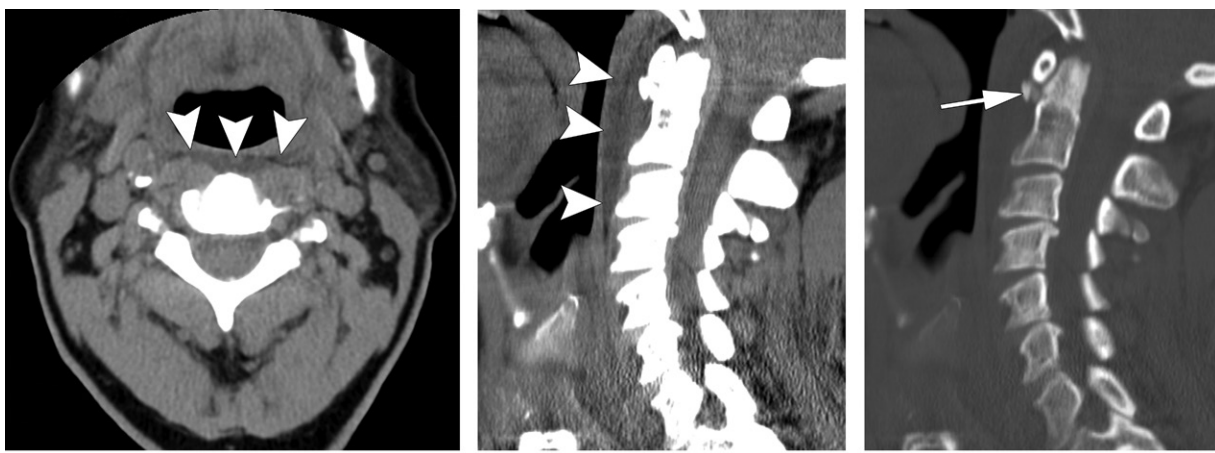


Figure 6. Retropharyngeal edema due to calcific tendinitis of the longus colli in a 71-year-old woman. (a, b) Axial (a) and sagittal (b) nonenhanced CT images show retropharyngeal edema (arrowheads). Note the tapered superior and inferior margins in b. (c) Sagittal nonenhanced CT image (bone window) shows calcification (arrow) inferior to the anterior arch of C1, in the typical location for calcific tendinitis of the longus colli.

and/or allergy-related causes (28). The most commonly implicated drugs are angiotensin-converting enzyme inhibitors (either immediate or after months to years of taking the drug) and nonsteroidal anti-inflammatory agents (28). Manifestations may be minor conditions such as lip swelling or severe conditions such as laryngeal edema. Symptoms may develop over minutes to hours and resolve over 1–3 days.

The diagnosis of angioedema as the cause of head and neck swelling is usually based on clinical examination findings and the exclusion of other serious diagnoses. Therefore, neck CT may be performed to rule out treatable diagnoses. Neck CT images show focal or diffuse low-attenuation swelling of all or some of the soft tissues of the upper airway. For example, focal involvement may be seen in the tongue (Fig E5) (particularly in association with angiotensin-converting enzyme inhibitors), subcutaneous fat, lips (Fig 7), or soft palate, and it may be unilateral (28). Diffuse pharyngeal or laryngeal edema may be seen at CT, but it generally follows intubation, with the swollen soft tissues surrounding a previously placed endotracheal tube.

Evaluation for the presence of a foreign body is one of the few indications for which neck CT is performed without contrast material. In a large series (29), 76% of pharyngeal and esophageal foreign bodies were impacted just below the cricopharyngeus muscle, at approximately the C6 level. Also, fish bones (60% of cases) and chicken bones (16% of cases) were the most commonly retained foreign bodies in that series (29). Radiography may be unreliable, yielding false-positive and false-negative results. CT of the neck enables definitive identification and localization of potential foreign bodies. A bone will appear as a thin or

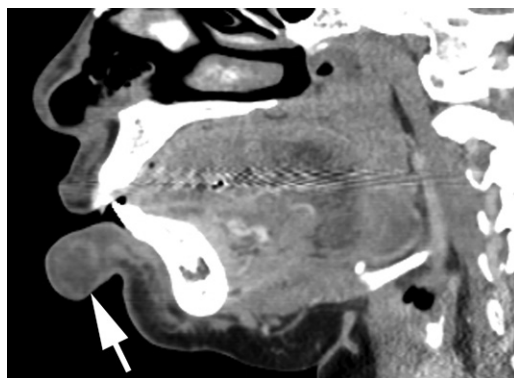
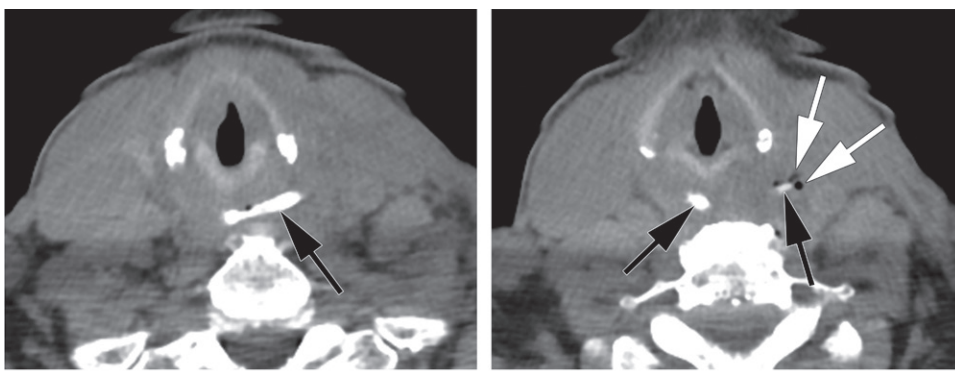


Figure 7. Sagittal contrast-enhanced CT image in a 45-year-old woman shows edema of the lower lip (arrow), consistent with angioedema.

flat radiopaque attenuating lesion lodged within the oropharynx, hypopharynx, or esophagus (Fig 8). Wooden foreign bodies have air attenuation in the acute phase and therefore are best detected by using lung windows, and they may mineralize and increase in attenuation with time (30). If there has been a perforation, extraluminal gas and fluid may be present. In this situation, repeat CT with intravenous contrast material may be necessary to delineate an abscess. A food bolus (commonly meat) in the esophagus will appear as a mixed-attenuation focus (Fig E6).

Teeth and Periodontal Tissues

The teeth and surrounding structures are common culprits in cases of head and neck infection and are linked to systemic disorders such as cardiovascular disease (31,32). Infection may be localized to the tooth and its surrounding structures, or it may spread to distant locations. Primary causes of odontogenic infection include



a.

b.

Figure 8. Impacted chicken bone in a 78-year-old woman. Axial nonenhanced CT images show the radiodense bone (black arrows) in the cervical esophagus, posterior to the larynx. There is gas (white arrows in b) within the adjacent left lateral soft tissues, consistent with perforation. Rim enhancement cannot be assessed because contrast material was not administered.

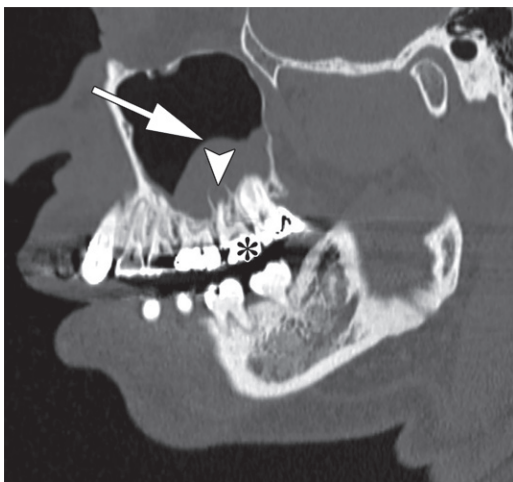


Figure 9. Odontogenic sinusitis in a 50-year-old man. Sagittal nonenhanced CT image shows a carious lesion in the second maxillary molar (*), obscured by streak artifact from dental amalgam. At the tooth apex, there is a periapical lucency and dehiscence of the bone plate (arrowhead) between the tooth and the maxillary sinus. There is associated adjacent polypoid mucosal disease within the maxillary sinus (arrow).

dental carious lesions, periodontal disease, and periapical disease. Dental caries appear on CT images as a defect or channel in the highly mineralized enamel of the tooth (Fig E7). When the caries are severe, large parts of the tooth crown or the entire crown may be absent. Tooth decay is a slow process and may be asymptomatic at first. When decay reaches the pulp chamber of the tooth, the pulp becomes infected, pressurized, ischemic, and ultimately necrotic. The infected material may be released at the apex of the tooth into the periapical region, causing periapical periodontitis, which may then develop into a periapical abscess, granuloma, or cyst. The development of osteomyelitis of the jaw is uncommon, unless there are other complicating factors such as prior radiation treatment or an open fracture.

Periodontal disease—that is, inflammation of the gingiva (gums)—can progress to periodontitis, in which the periodontal ligament that connects the tooth to the alveolar process, as well as the bone of the alveolar process, is lost (Fig E8). The last category of dental infection is pericoronitis, in which food material becomes trapped under a gum flap, commonly in the setting of a partially erupted third molar, and causes acute inflammation and infection (Fig E9). When reporting dental lesions, the amount of detail should be tailored to the given clinical setting. If the dental lesions are incidental and the extent of disease is limited, the lesions should be reported. If there is diffuse disease, a general statement should be made and may be followed by a description of the worst one or two lesions. If the dental disease is directly related to the reason that the examination was performed, a complete discussion is warranted.

Although the inflammatory process begins in or adjacent to a specific tooth, it may spread to nearby areas, including the orbits or intracranial compartment. For maxillary teeth whose roots abut the maxillary sinuses, a periapical inflammatory process may dehisce the bony separation between the tooth apex and the sinus and thereby cause odontogenic sinusitis. At CT, this condition appears as a soft-tissue-attenuation tract between the tooth apex and the sinus, with adjacent opacification of the sinus (Fig 9).

A periodontal abscess is a focal pocket of pus that forms adjacent to a tooth owing to the direct spread of infection, such as pericoronitis, or following a bony breakthrough of periapical disease into adjacent soft tissues. Bony breakthrough occurs at weak points of the alveolar process, which include the buccal surface throughout the maxilla and the lingual surface in the area of the mandibular molars. Infection may spread into the periodontal or more distant tissues as a result of

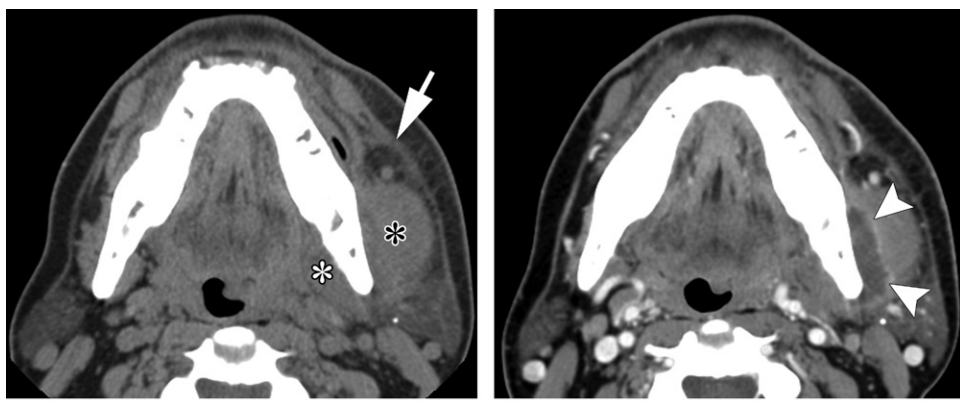


Figure 10. Periodontal abscess in a 50-year-old man. (a) Axial nonenhanced CT image shows asymmetric soft-tissue thickening (white *) medial to the left mandibular ramus, as well as thickening of the left masseter muscle (black *). Owing to the lack of contrast enhancement, an abscess cannot be discerned. Note the thickening of the left platysma muscle (arrow). (b) Twelve hours later, the CT examination was repeated with intravenous contrast material administration, and the abscess (arrowheads) could be delineated between the mandibular ramus and masseter muscle.

dental procedures such as tooth extraction (33). If left untreated, there may be subsequent spread into adjacent muscle and deep spaces of the neck. To diagnose this condition, it is essential to administer intravenous contrast material to delineate the extent of disease and determine whether there is a drainable collection (Fig 10). There is typically a rim-enhancing hypoattenuating fluid collection adjacent to the involved tooth (Fig 10).

Ludwig angina is one of the most feared complications of dental infection. *Ludwig angina*, derived from the Latin word *angere*, meaning choke, refers to a polymicrobial infectious cellulitis involving the sublingual space above the mylohyoid muscle and the submandibular (ie, submylohyoid) space below the mylohyoid muscle. There is usually bilateral involvement, which may lead to airway obstruction at the level of the oral cavity and oropharynx (4). Ludwig angina manifests with fever, firm neck swelling, and difficulty swallowing or speaking (31). Most cases of Ludwig angina are related to dental infection (4) or recent extraction of the second or third molars, whose roots extend below the attachment of the mylohyoid muscle to the mandible (31). Regardless of whether the infection begins above or below the mylohyoid muscle or on the left or right side, it may spread around the free posterior edge of the mylohyoid muscle between these spaces and from left to right (34).

Oral piercings also may cause Ludwig angina (35). Infection spreads by means of contiguous extension and can lead to mediastinitis if left untreated. With Ludwig angina, CT images show inflammatory stranding and fluid in the submandibular and sublingual spaces, with or without abscesses or gas (Fig 11). As Ludwig angina is a “cellulitis,” rim-enhancing components are not required to make the diagnosis. Lymphadenopa-

thy is generally absent. The report should state the tooth of origin (when it can be determined), extent of infection, presence (or absence) of drainable collections, and degree of mass effect on the airway. Treatment consists of a combination of airway protection and antibiotics, and surgical drainage when necessary (4). When there are complications such as mediastinitis and mandibular osteomyelitis, these too must be addressed.

Thyroid Gland

The thyroid gland synthesizes the hormones triiodothyronine and thyroxine. At nonenhanced CT, the thyroid is hyperattenuating owing to its high iodine concentration. The thyroid normally enhances homogeneously following intravenous contrast material administration. Thyroid nodules are commonly encountered at neck imaging. Although a discussion of this topic, including characterization and workup, is beyond the scope of this review, this subject has been reviewed previously in this and other journals (36–38).

The reporting of thyroid enlargement should include a description of the extent of the enlargement and of any mass effect on the trachea, esophagus, and neck vessels (39). If there is tracheal compression, the craniocaudal length of the compression and the degree of reduction of the cross-sectional area should be estimated. The vocal cords should be evaluated for signs of asymmetry, as paralysis may occur owing to compression of the recurrent laryngeal nerve (40). The paralysis manifests as dilatation of the ipsilateral piriform sinus and laryngeal ventricle, medial rotation and thickening of the ipsilateral aryepiglottic fold, and anteromedial displacement of the ipsilateral arytenoid cartilage. Most cases

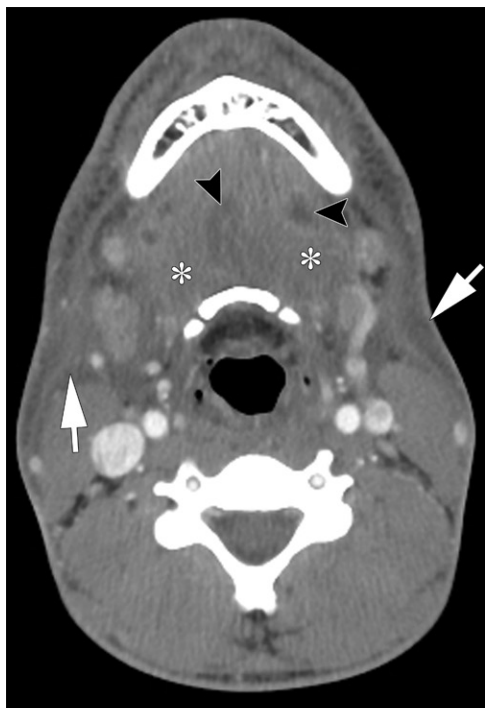
**a.****b.**

Figure 11. Ludwig angina in a 26-year-old man. Axial (a) and coronal (b) contrast-enhanced CT images show submandibular and sublingual edema (white *) with internal fluid pockets (arrowheads) consistent with pus. The oral cavity (black * in b) is obliterated. Subcutaneous edema (arrows) also is present. When possible, specific involvement of the sublingual and submandibular spaces should be described owing to potential implications for drainage. However, owing to associated edema, as in this case, this may not always be possible.

of mediastinal extension are substernal, although a fraction of cases are posterior mediastinal. The degree of mediastinal extension, which is important when surgery is being planned, is measured from the sternal notch (39).

Graves disease is the most common autoimmune disease and the most common cause of hyperthyroidism. With this disease, autoantibodies stimulate the thyroid-stimulating hormone

receptors on follicular cells, in effect mimicking thyroid-stimulating hormone. CT images show a diffusely enlarged and hyperenhancing gland (Fig 12). Thyroid gland infection is rare owing to the surrounding capsule, good vascularity, good lymphatic drainage, and internal iodine content (41). Still, risk factors for development of thyroid abscesses include immunodeficiency and underlying gland abnormalities such as thyroid nodules, thyroid cancer, and fourth branchial cleft anomalies. Fourth branchial cleft fistulas or sinus tracts, which are usually on the left, begin at the apex of the piriform sinus and descend along the tracheoesophageal groove to the cranial portion of the thyroid gland, and they may lead to recurrent infection (12).

Goiter refers to enlargement of the thyroid gland. Iodine deficiency is an important cause of goiter worldwide, but it is uncommon in the United States. In the United States, the most common cause of goiter is Hashimoto thyroiditis, whereby the gland is unable to produce an adequate amount of thyroid hormone and is continuously stimulated by thyroid-stimulating hormone to enlarge. Other causes of goiter include Graves disease and toxic or nontoxic nodular goiter. Factors that predispose individuals to having nodular goiter include iodine deficiency and genetics; the exact causal mechanism is uncertain. Nodular goiter usually begins as diffuse gland enlargement and progresses to the nodular form. On CT images, goiter appears as an enlarged nodular heterogeneous gland with regions of hemorrhage, cysts, necrosis, and calcification (Fig 13). The enlargement may be asymmetric (39).

The two superior parathyroid glands are most commonly located dorsal to the superior poles of the thyroid gland, and the two inferior parathyroid glands are most commonly located inferior, dorsal, or lateral to the inferior thyroid pole (42). They measure up to 5 mm in diameter and, owing to their small size, generally are not well seen at routine CT of the neck (42). When these glands are enlarged owing to hyperplasia or adenoma, they may be detected at CT. Therefore, when a parathyroid gland is identified and the patient has an elevated serum calcium level, it is prudent to recommend endocrine evaluation to determine whether parathyroid disease is the underlying cause.

Salivary Glands

The major salivary glands include the parotid, submandibular, and sublingual glands. At CT, the attenuation of the parotid gland in adults is usually intermediate, between the attenuation of fat and that of muscle, owing to its fat content. In children and some adults, the parotid gland

is isoattenuating to muscle. Intraparotid ducts typically are not visible unless they are dilated. The parotid gland is the only salivary gland that contains lymph nodes. Accessory parotid tissue often can be seen along the course of its duct (Stensen duct) superficial to the masseter muscle. The submandibular and sublingual glands have higher attenuation than does the parotid gland owing to their lower fat content.

Sialadenitis refers to inflammation of a salivary gland. The populations that are most at risk for acute sialadenitis are elderly persons and neonates. Acute unilateral sialadenitis most commonly involves the parotid gland and is usually caused by an ascending bacterial infection from the oral cavity in the setting of salivary stasis and dehydration (25). *Staphylococcus aureus* is the most common infecting organism (43). Sialolithiasis with an obstructing ductal stone is an important cause of submandibular sialadenitis; 80%–90% of sialoliths occur in the submandibular glands, while 10%–20% occur in the parotid glands. The higher rate of stone formation in the submandibular gland is due to the small papillary orifice, ascending course of the (Wharton) duct, higher viscosity of saliva, and slow salivary flow rate (25). Causes of bilateral sialadenitis include viral infection, radiation, immunoglobulin G4-related sialadenitis (of the submandibular glands), and Sjögren syndrome (of the parotid glands). Viral sialadenitis, most commonly mumps, typically (in 85% of cases) occurs in children younger than 15 years and is bilateral in 90% of cases (44). Ninety percent of cases of viral sialadenitis involve the parotid glands, while 10% also involve the submandibular glands (44).

In the acute phase, sialadenitis manifests at contrast-enhanced CT as enlargement and heterogeneous hyperenhancement of the affected gland(s), with surrounding fat stranding (Fig 14). If there is an obstructing ductal stone (Fig 14), ductal dilatation also is present. The involved glands and their ducts should be inspected for stones. However, occasionally this may be difficult because these structures are obscured by streak artifact from dental amalgam. Bacterial sialadenitis may be complicated by the formation of a rim-enhancing abscess or multiple small abscesses.

Lymph Nodes

Adenopathy in the neck can be caused by many different entities, including infection, inflammatory disease, and malignancy. Although acute conditions are the first that come to mind, malignancy must remain in the differential diagnosis. Normal lymph nodes demonstrate an ovoid morphology, a fatty hilum, smooth margins, and

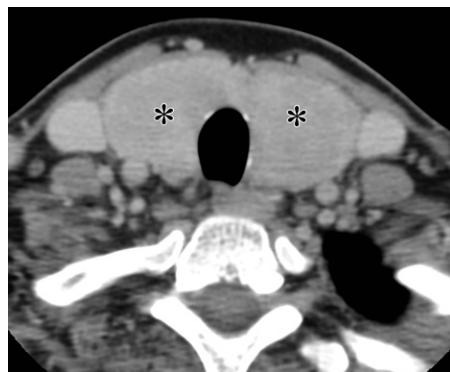


Figure 12. Graves disease in a 29-year-old woman. Axial contrast-enhanced CT image shows a homogeneously enlarged thyroid gland (*).

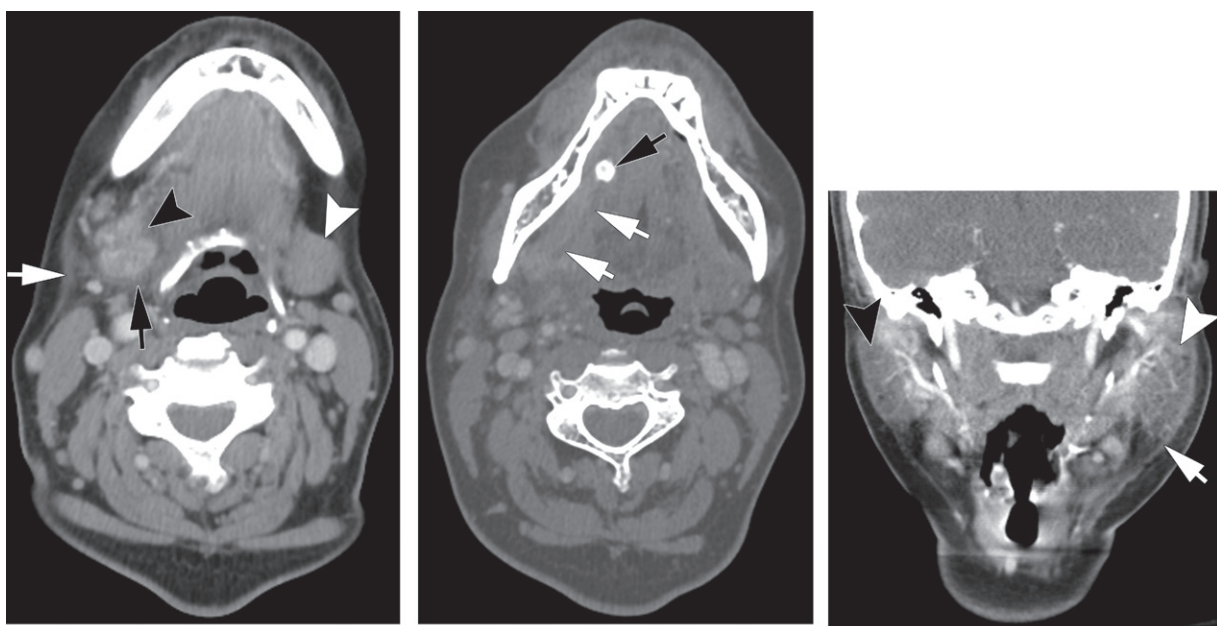


Figure 13. Thyroid goiter in a 56-year-old woman. Axial nonenhanced CT image shows an enlarged thyroid gland (black *) surrounding the trachea (arrow), which is narrowed to 8 × 5 mm. Internal cysts and a calcification also are noted. In addition, there is an indeterminate low-attenuation nodule or complex cyst (white *) in the isthmus.

homogeneous isoattenuation to muscle at CT. Cervical lymph nodes can be classified into levels (I–VII) and anatomic groups (supraclavicular, parotid, retropharyngeal, and occipital stations) according to established criteria (45).

Viral infections are the most common cause of reactive adenopathy in children and young adults. CT reveals mildly enlarged and enhancing nodes without surrounding fat stranding. Bacterial infections typically cause more prominent nodal enlargement and also cause surrounding inflammatory change. In children, lymph nodes may suppurate, and these nodes become centrally hypodense with peripheral enhancement (46).

Mycobacterial cervical lymphadenitis, referred to as scrofula, may be tuberculous or nontuberculous (47). Seventy-five percent of the time, scrofula is unilateral. In the acute phase, the lymph nodes are enlarged and homogeneously enhance at CT. As caseation occurs, the nodes become



a.

b.

c.

Figure 14. Sialadenitis in two patients. (a, b) Acute right submandibular sialadenitis in a 57-year-old woman. Axial contrast-enhanced CT image (a) shows an enlarged hyperenhancing right submandibular gland (black arrowhead) with internal and surrounding edema (black arrow) and overlying thickening of the platysma muscle (white arrow). In comparison, the left submandibular gland (white arrowhead) is normal. Axial contrast-enhanced CT image (b) obtained superior to a shows a stone (black arrow) in the distal portion of the dilated right submandibular duct (white arrows). (c) Coronal contrast-enhanced CT image at the level of the parotid glands in a 22-year-old woman with acute left parotiditis shows edema, enlargement, and hyperenhancement of the left parotid gland (white arrowhead). There is also thickening of the left platysma muscle (arrow). In comparison, the right parotid gland (black arrowhead) is normal. Additional images (not shown) did not show a stone within or along the course of the parotid duct.



Figure 15. Mycobacterial lymphadenitis (scrofulula) in the left side of the neck in a 43-year-old man. Axial contrast-enhanced CT image shows a centrally hypoattenuating cystic lymph node (black arrow) with minimal surrounding fat stranding. Another lymph node (white arrow) has ruptured and fistulized to the skin.

centrally hypoattenuating and cystic, with perinodal fat stranding that is milder than what is seen with bacterial adenitis (Fig 15). If the capsules of individual lymph nodes rupture, they may coalesce

into a single nodal mass (47). Fistulization and drainage to the skin also may occur (Fig 15).

A comprehensive discussion of malignant lymphadenopathy is beyond the scope of this article and has been reviewed elsewhere (14,48). However, a few points should be made to differentiate malignant adenopathy from infectious adenopathy. Nodal metastasis is a common feature of squamous cell carcinoma of the head and neck. At CT, these nodes are enlarged, rounder than the normally elongated cervical nodes, and centrally necrotic. Nodal metastases usually lack the surrounding inflammatory stranding that is seen with bacterial adenitis. However, extracapsular tumor extension can mimic inflammatory stranding where there are indistinct nodal margins or after biopsy and radiation when the lymph node may have poorly defined margins (45). In keeping with lymphatic drainage patterns, the location of a nodal metastasis can suggest the site of a primary head and neck malignancy. Cervical lymph node involvement is the most common manifestation of Hodgkin disease involving the head and neck (48). Disease may be unilateral or bilateral, with enlarged lymph nodes or a confluent soft-tissue mass (48). In contrast to squamous cell carcinoma-related adenopathy, central necrosis is an uncommon feature of lymphoma (48). As a last point, either clinical or imaging

follow-up or tissue sampling may be necessary to make a definitive diagnosis.

Vascular Structures

The common carotid, internal carotid, and vertebral arteries traverse the neck and can be readily evaluated at standard contrast-enhanced neck CT. While dedicated CT angiography is generally superior for the specific evaluation of arterial disease, many arterial abnormalities can be identified on standard soft-tissue neck CT images. Therefore, the carotid and vertebral arteries should be traced at every neck CT examination. Normally, the walls of the carotid and vertebral arteries have a smooth contour along their external and luminal surfaces and are uniform in thickness, measuring 1–2 mm (49). The arterial lumens generally are uniform in diameter, except in the carotid bulb, a region of normal luminal widening at the origin of the internal carotid artery. The vertebral arteries course along the posterior neck, passing through the transverse foramina of the C2–C6 vertebrae.

Atherosclerosis of the cervical arteries, particularly at the carotid bulbs, is extremely common in middle-aged and older adults and can be evaluated by using multiple modalities, including CT (50). Arterial dissection is characterized by a defect in the intimal layer of the artery that allows passage of blood into the arterial wall. This defect leads to the formation of a false lumen, which is frequently accompanied by narrowing or occlusion of the true lumen (51).

Although primary vascular inflammation is a relatively rare cause of neck pain, it is occasionally identified at neck CT. Cervical arterial inflammation may reflect a systemic large-vessel vasculitis such as Takayasu arteritis. In this setting, extensive arterial wall thickening may be seen and usually also involves the visualized mediastinal arteries (Fig E10). In contrast, carotidynia is a poorly understood idiopathic condition characterized by neck pain and focal tenderness in the region of the carotid bifurcation. Associated imaging abnormalities may include mural thickening of the affected carotid artery and stranding of surrounding fat (Fig 16) (52).

Portions of the circle of Willis are typically included at CT examinations of the neck, and consequently, intracranial arterial abnormalities may be visualized. An intracranial aneurysm is a particularly important finding that may be incidentally encountered at neck CT. The prevalence of intracranial aneurysm in the general population without comorbidities has been estimated to be 3.2% (53). Owing to the risk of aneurysmal rupture with devastating subarachnoid hemorrhage and the availability of effective treatment

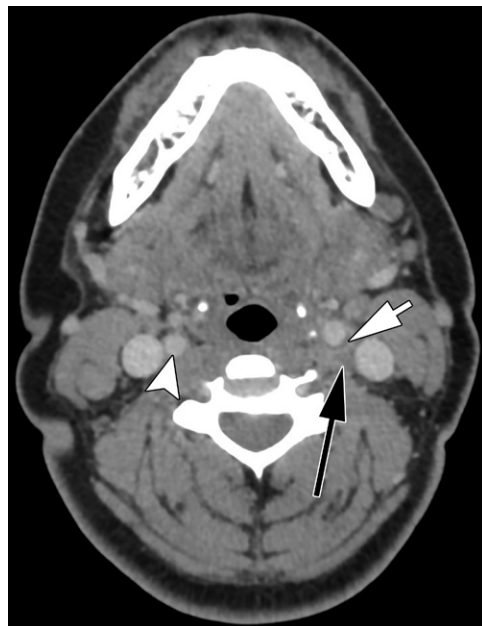


Figure 16. Carotidynia in a 29-year-old woman. Axial contrast-enhanced CT image shows pericarotid infiltration (black arrow). A soft plaque (white arrow) causing mild luminal narrowing also is present at the carotid bulb, with possible enhancement of the adjacent vessel wall. In comparison, the right internal carotid artery (arrowhead) is normal.

options, the intracranial arteries should be scrutinized in every case.

Numerous veins are visible on contrast-enhanced neck CT images. The largest and most important veins are the internal jugular veins, which arise from the intracranial dural venous sinuses and extend to the mediastinum. Normal internal jugular veins are frequently asymmetric in caliber. Valves, which are visible in the internal jugular veins occasionally, and heterogeneous enhancement due to the mixing of opacified and nonopacified blood should not be mistaken for thrombosis.

Jugular thrombosis may be complete, in which case the vein is nonopacified and usually enlarged (when acute), or partial, in which case a sharply marginated filling defect is seen. Edema of adjacent fat planes may be present. At nonenhanced CT, there may be abnormally increased attenuation in the thrombosed vein. The thrombus may extend superiorly to the sigmoid sinuses or inferiorly to the mediastinal veins. Additional imaging of the head or chest may be necessary to completely visualize the clot.

A jugular venous thrombus may be bland, tumorous, or septic. Bland thrombus is frequently associated with indwelling venous catheters, such as hemodialysis catheters, and can also be seen in thrombophilic conditions. In Lemierre syndrome, septic thrombophlebitis of the internal jugular vein

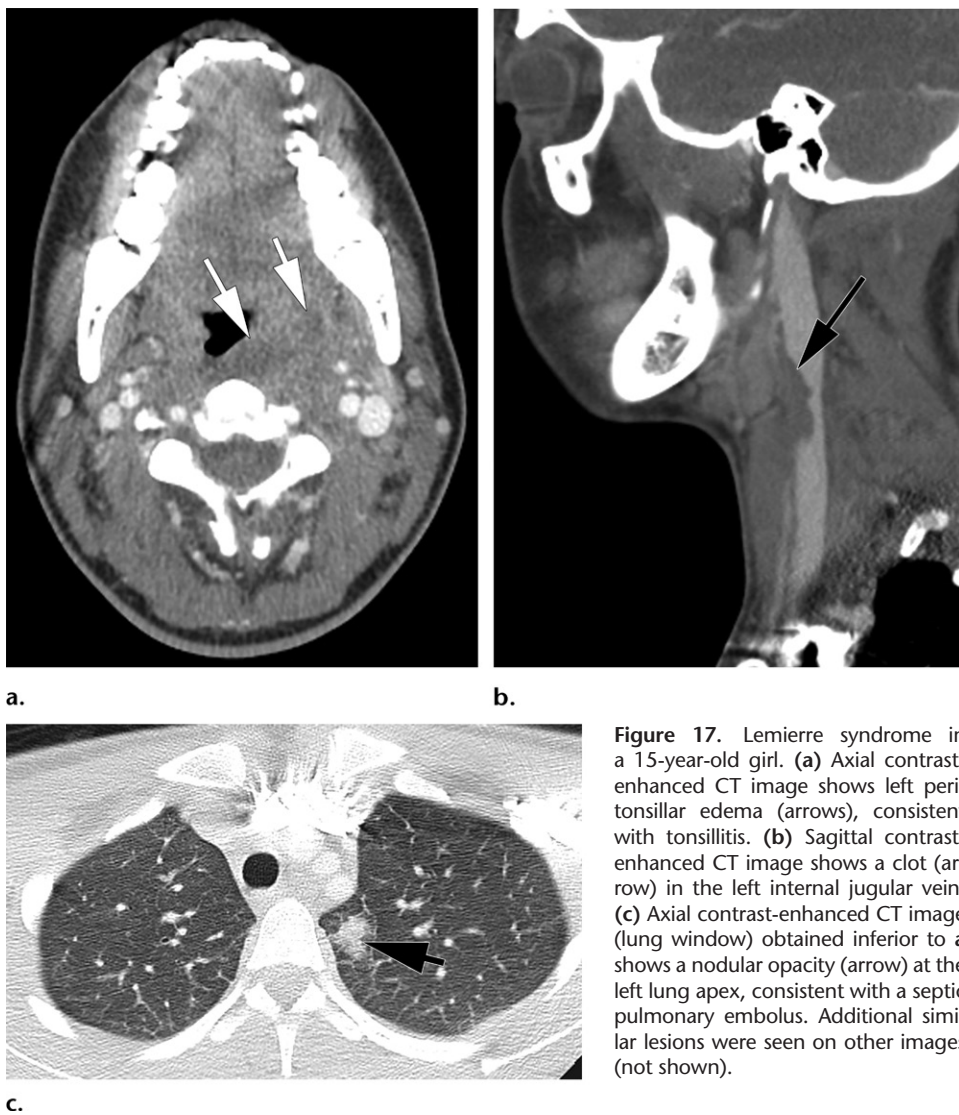


Figure 17. Lemierre syndrome in a 15-year-old girl. (a) Axial contrast-enhanced CT image shows left peritonsillar edema (arrows), consistent with tonsillitis. (b) Sagittal contrast-enhanced CT image shows a clot (arrow) in the left internal jugular vein. (c) Axial contrast-enhanced CT image (lung window) obtained inferior to a shows a nodular opacity (arrow) at the left lung apex, consistent with a septic pulmonary embolus. Additional similar lesions were seen on other images (not shown).

occurs secondary to a pharyngeal infection such as pharyngitis or PTA (Fig 17). Associated septic pulmonary emboli are frequently present. Systemic dissemination of infection may occur, particularly if treatment is delayed, and is associated with significant mortality, even with antimicrobial treatment (54). Therefore, identification of a peritonsillar or retropharyngeal abscess should prompt a reflex search for a jugular venous thrombus and septic pulmonary emboli in the included lung apices.

Bony Airspaces

The pneumatized spaces of the head and neck include the paranasal sinuses, which communicate with the nasal cavity, and the mastoid air cells, which communicate with the tympanic (middle ear) cavity. The paranasal sinuses consist of the maxillary, sphenoid, and frontal sinuses, as well as the ethmoid air cells. The mastoid air cells lie predominantly within the mastoid portion of the temporal bone but vary in extent considerably between

individuals. In some people, pneumatized spaces extend to the apical (medial) portion of the temporal bone and are termed *petrous apex air cells*. The normally aerated paranasal sinuses and mastoid air cells have an imperceptibly thin mucosal lining.

Sinusitis may be acute or chronic and have an allergy-related, viral, bacterial, or fungal cause. Most patients with acute sinusitis do not require imaging. However, if there is concern regarding a possible alternative diagnosis or spread to the orbits or brain, contrast-enhanced maxillofacial or neck CT is indicated (26). At CT, acute bacterial sinusitis is characterized by the presence of fluid and mucosal thickening in one or more sinuses (55). Fluid within the sinus may layer dependently, resulting in an air-fluid level, or it may have a frothy (bubbly) appearance.

It is important to note that the presence of intrasinus fluid or mucosal thickening is not specific for acute sinusitis and may also be seen, for example, in the setting of upper respiratory

tract infection or nasogastric tube placement. Forty-four percent of adults and 50% of children have imaging findings of sinusitis, although they undergo imaging for other reasons (56). Furthermore, mucosal thickening can persist for 8 weeks following the resolution of sinusitis (56). Therefore, for the diagnosis of acute sinusitis, supporting clinical signs and symptoms such as fever and pain overlying the affected sinuses must be present.

Complications of acute bacterial sinusitis include extension into the orbit with development of a subperiosteal abscess and orbital cellulitis; extension into the overlying soft tissues (eg, Pott puffy tumor); and intracranial extension with development of an epidural abscess, subdural empyema, or cerebritis with or without brain abscess. Cavernous sinus thrombosis is seen occasionally. These complications are discussed in greater detail in the following sections.

Fungal sinus disease includes allergic fungal sinusitis and invasive fungal sinusitis. Allergic fungal sinusitis is a chronic inflammatory condition that is characterized at CT by extensive opacification of multiple sinuses, which are typically expanded. Hyperattenuating material, reflecting allergic mucin, is frequently seen in the affected sinuses. Acute invasive fungal sinusitis typically occurs in immunocompromised patients and can be rapidly progressive and life-threatening (57). Zygomycetes fungi such as *Mucor* species cause up to 80% of cases in patients with diabetes, while *Aspergillus* species cause up to 80% of cases in patients with neutropenia—for example, in cases of chemotherapy, bone marrow transplant, and acquired immunodeficiency syndrome (57). Acute invasive fungal sinusitis is characterized by unilateral destruction of the osseous margins of the sinus, with extension into adjacent structures such as the orbits, intracranial compartment, and subcutaneous tissues. It is important to note that due to the angioinvasive nature of this process, extension to adjacent structures may occur even with intact bony sinus walls and minimal mucosal thickening (57).

Infiltration of the periantral fat is a classic finding of acute invasive fungal sinusitis (Fig 18) (58). A chronic form of invasive fungal sinusitis may occur in immunocompetent patients, in whom the condition progresses over months to years (57). A masslike hyperattenuating focus is typically seen in a sinus or multiple sinuses, and there is gradual sinus wall destruction. Involvement of the periantral fat, orbits, or intracranial compartment indicates invasion (57). As a final note regarding this disease, when fungal sinusitis is suspected, this should be mentioned in the report, as the pathologist can use special stains, such as silver and periodic acid–Schiff stains, to highlight organisms that have invaded the vessel walls and lumen (59).



Figure 18. *Mucor* sinusitis in a 59-year-old woman with diabetes. Axial contrast-enhanced CT image shows an air-fluid level (confirmed on other images, not shown) in the left maxillary sinus (*), consistent with sinusitis. Classic periantral fat stranding (black arrow) is seen on the left, as compared with the normal periantral fat (white arrow) on the right. The findings in this case show that minimal sinus opacification does not exclude the diagnosis of invasive fungal sinusitis.

Acute otomastoiditis predominantly affects children, and it occurs when otitis media spreads to involve the mastoid air cells. Uncomplicated otomastoiditis manifests at CT as opacification of the middle ear cavity and mastoid air cells, without osseous destruction. Although the presence of mastoid air cell fluid is common, it does not necessarily indicate mastoiditis. The presence of supportive clinical features, such as tenderness over the mastoid prominence of the temporal bone, is required for diagnosis.

As mastoiditis progresses, the mastoid septa become eroded. The condition involving mastoid effusion in conjunction with septal erosion is referred to as coalescent mastoiditis (60). Comparing the side of the clinical symptoms with the contralateral side can be helpful in determining whether there is erosion of the mastoid septa. Complications of mastoiditis include erosion of the outer cortex of the mastoid bone with development of a neck abscess (ie, Bezold abscess) (Fig 19), as well as erosion of the inner cortex of the mastoid bone, which can lead to sigmoid sinus thrombosis, epidural abscess, or cerebritis with or without brain abscess (60). MRI is useful for evaluating intracranial extension of mastoiditis.

In patients with pneumatized petrous apices, petrous apicitis, a condition analogous to mastoiditis, can develop in the petrous apex (61). Infection typically spreads from the tympanic cavity

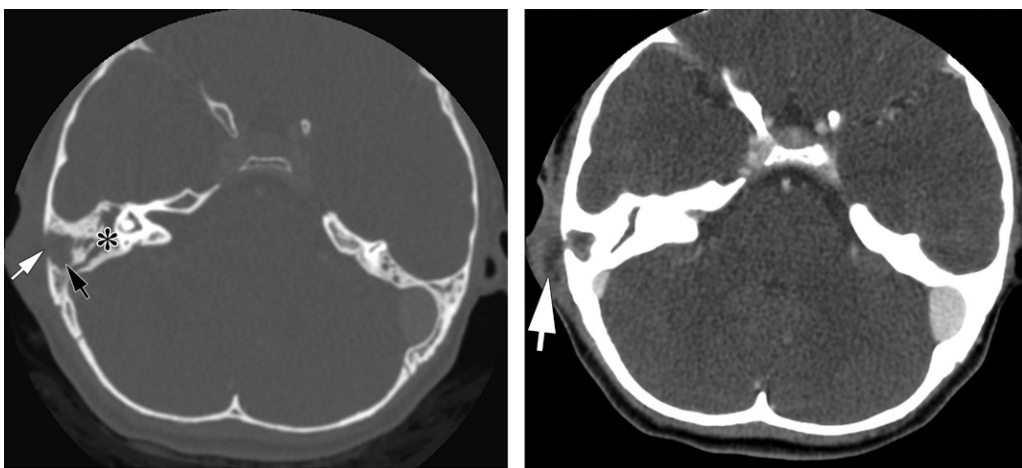
**a.****b.**

Figure 19. Right coalescent mastoiditis with extracranial abscess in a 13-year-old girl. (a) Axial contrast-enhanced CT image (bone window) shows tympanomastoid opacification (*). There is coalescence of the right mastoid air cells (black arrow) with breakthrough of the overlying cortex (white arrow). (b) Image in a obtained in soft-tissue windows shows an overlying or developing abscess (arrow).

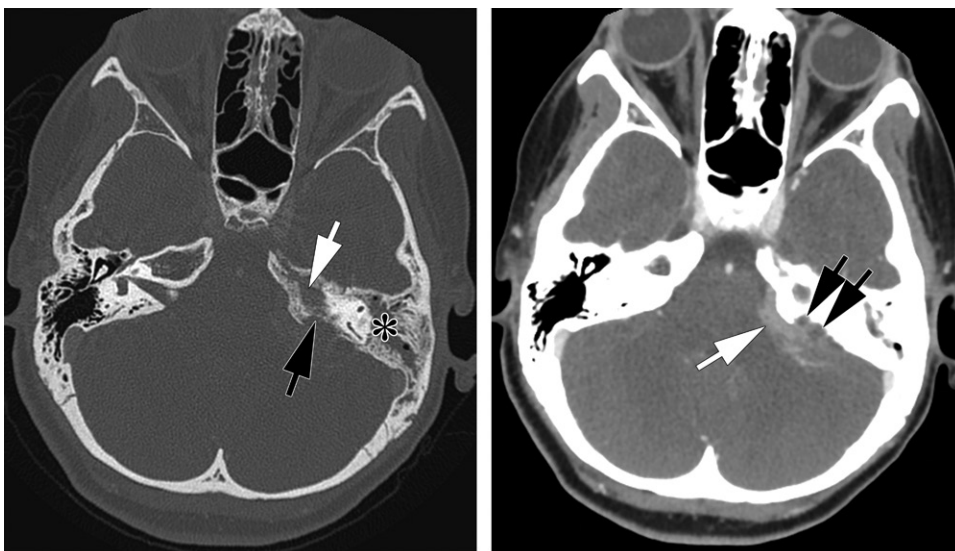
**a.****b.**

Figure 20. Left petrous apicitis in an 11-year-old girl who presented with ear drainage and diplopia. (a) Axial contrast-enhanced CT image (bone window) shows left tympanomastoid opacification (*), as well as opacification and coalescence of air cells at the petrous apex (white arrow). There is also bone dehiscence (black arrow) along the dorsal aspect of the petrous apex. (b) Image in a obtained in soft-tissue windows shows epidual phlegmon (white arrow) and nonenhanced foci (black arrows), consistent with abscess.

to the air cells in the petrous apex, and it may lead to osseous erosion and subsequent involvement of adjacent skull base structures. Gradenigo syndrome is a classic manifestation of petrous apicitis and constitutes the triad of facial pain (reflecting involvement of the trigeminal nerve in Meckel's cave), ophthalmoplegia (reflecting involvement of the sixth cranial nerve in Dorello's canal), and otalgia and otorrhea (reflecting otomastoiditis).

With petrous apicitis, CT images show opacification of the petrous apex air cells, which may also demonstrate coalescence, with more extensive ero-

sion of the petrous apex in advanced cases (Fig 20). The intracranial extension may result in cavernous sinus or sigmoid sinus venous thrombosis, epidural abscess, subdural empyema, meningitis, or cerebritis with or without brain abscess. MRI should be performed when intracranial extension is suspected.

Cervical Spine

At standard CT evaluation of the neck, the crano-cervical junction and the entire cervical spine are included, and abnormalities of the cervical spine are commonly seen. In the setting of suspected cervical spine disease, dedicated CT or MRI of

the spine is preferred over neck CT. However, the symptoms of cervical spine disease may mimic those of extraspinal entities, prompting the use of neck CT with a soft-tissue protocol. Therefore, in the acute setting, careful inspection of the cervical spine is mandatory at neck CT.

Bacterial infection of an intervertebral disk, or discitis, is typically accompanied by infection of the adjoining vertebrae (osteomyelitis) and may be due to hematogenous seeding, direct spread from retropharyngeal or paraspinal infection, or inoculation by way of spinal instrumentation. CT findings of bacterial discitis and osteomyelitis include loss of disk space height and erosion of the adjacent vertebral endplates (62). Inflammatory changes of the paraspinal soft tissues also are usually present and include obscuration of paraspinal fat planes, paraspinal abscesses, and retropharyngeal edema (Fig E11). Eventually, severe bone destruction and deformity can develop. Noninfectious processes occasionally mimic the findings of discitis and osteomyelitis and should be considered if paraspinal inflammatory changes or abscesses are absent (63). MRI is superior to CT for the diagnosis of discitis and osteomyelitis, particularly early in the course of disease, and should be performed if discitis or osteomyelitis is suspected.

Infection of the spinal facet (zygapophyseal) joints is an uncommon cause of neck pain. In this condition, CT may demonstrate irregularity and erosion of the articular bone, fluid in and around the joint, and/or infiltration of adjacent paraspinal fat planes. Infectious involvement of the epidural space may occur in isolation or within the context of vertebral infection. Visualization of the spinal canal is quite limited with CT, even with administration of contrast material. However, one can often distinguish the lower-attenuation cerebrospinal fluid from the higher-attenuation spinal cord with use of narrow window settings, and it may be possible to identify an abnormal peripheral (epidural) area of attenuation adjacent to evidence of discitis or septic arthritis (Fig 21).

Degenerative disease of the cervical spine is commonly seen at neck CT and frequently incidental. However, in the setting of neck pain, degenerative disease may be relevant with regard to the symptoms reported by the patient. The presence of degenerative changes should be noted, at least in general terms, and if severe spinal canal stenosis or an alignment abnormality is present, a more detailed description is warranted. Anterior spinal osteophytes are frequently seen in the setting of degenerative disease and are usually asymptomatic. However, large anterior osteophytes, as seen in the setting of diffuse idiopathic skeletal hyperostosis, can cause dysphagia owing to compression of the esophagus (64).



Figure 21. Epidural phlegmon in a 59-year-old man with human immunodeficiency virus infection and a history of intravenous drug use. Sagittal contrast-enhanced CT image shows prevertebral edema (*). There is also thin enhancing material in the anterior epidural space extending from the C1–C5 vertebrae (arrows), consistent with epidural phlegmon. Surgical drainage was performed.

Orbits and Imaged Brain

The orbits are included in all CT examinations of the neck. The reader is referred to the relatively recent article regarding orbital emergencies published in this journal (65).

Progression of intraorbital infection can result in thrombosis of the superior ophthalmic vein, which can then propagate to the cavernous sinus. Superior ophthalmic vein thrombosis appears on contrast-enhanced CT images as enlargement of the superior ophthalmic vein, with a central filling defect, and surrounding fat stranding. When cavernous sinus thrombosis occurs, there is outward bulging of the normally straight or concave lateral wall of the cavernous sinus, with filling defects in the sinus that correspond to clots (66). If the superior ophthalmic vein is not thrombosed, it becomes enlarged owing to impaired drainage into the cavernous sinus (Fig 22).

Infection involving the orbits, paranasal sinuses, or temporal bones can spread to the intracranial compartment by means of bone dehiscence or through valveless diploic veins. While intracranial extension is often clearly visible on contrast-enhanced CT images, once

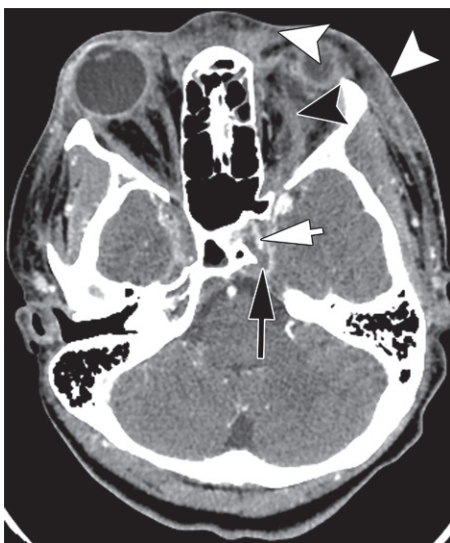


Figure 22. Cavernous sinus thrombosis in a 14-year-old girl. Axial contrast-enhanced CT image shows incomplete enhancement of the left cavernous sinus (black arrow), through which the enhancing internal carotid artery (white arrow) is coursing. The left superior ophthalmic vein (black arrowhead) is dilated and not enhanced. There is associated subcutaneous edema (white arrowheads) of the face and edema in the left orbit.

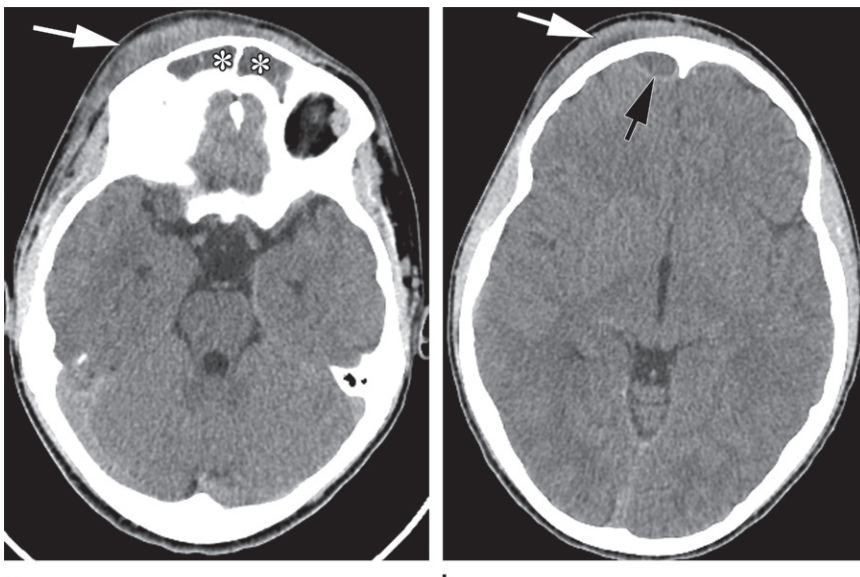


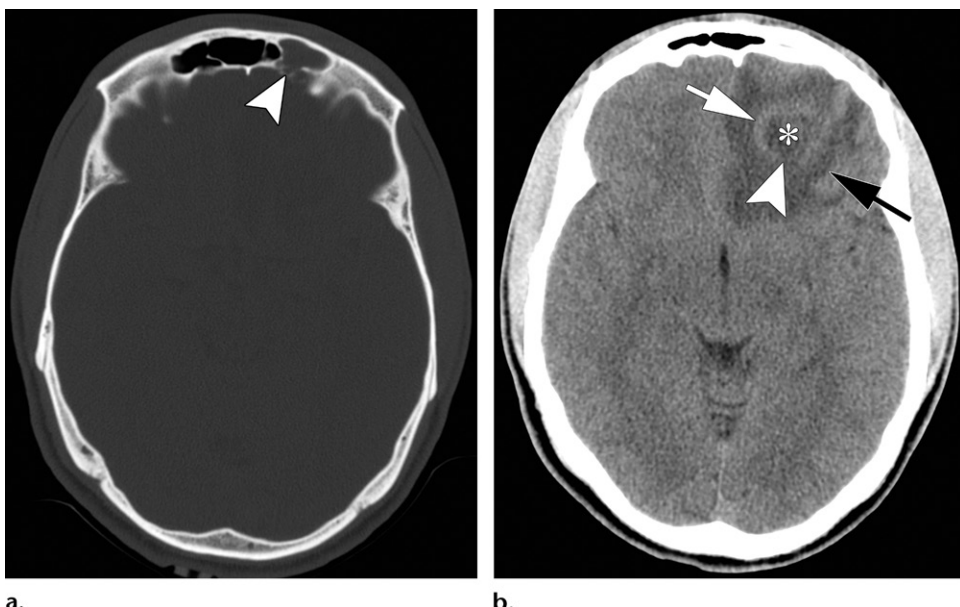
Figure 23. Epidural abscess and subgaleal phlegmon in a 13-year-old boy. Axial contrast-enhanced CT images show opacification of the frontal sinuses (* in a) and a rim-enhancing epidural fluid collection (black arrow in b) just superior to the frontal sinus, which is consistent with an epidural abscess. There is also enhancing subgaleal soft tissue (white arrow), consistent with phlegmon.

there is concern regarding possible intracranial extension of infection, contrast-enhanced MRI should be performed, as it is more sensitive and can facilitate better delineation of the extent of disease. In addition, there should be a low threshold for MRI when an invasive fungal infection is suspected in an immunocompromised patient, as long as imaging does not cause a delay in performing a potentially life-saving surgical intervention (67).

Epidural abscesses are collections of pus in the epidural space and are most commonly due to sinus infections (68). CT images show a rim-enhancing collection with characteristics of an epidural collection (eg, lentiform in shape, usually not crossing sutures) (Fig 23). When these abscesses result from a temporal bone infection such as mastoiditis, a rim-enhancing epidural collection may be seen between the mastoid bone and the

cerebellum or temporal lobe (Fig 20). Subdural empyemas, like epidural abscesses, are often secondary to sinusitis or mastoiditis and appear as rim-enhancing collections or confluent enhancement in the subdural space. Ultimately, infection in the meninges can extend to involve the brain parenchyma, with cerebritis appearing on CT images as an area of low attenuation adjacent to sinus or mastoid infection. A brain abscess appears as an intraparenchymal hyperattenuating ring that enhances after contrast material administration, with the internal and surrounding hypoattenuating areas representing purulent material and edema, respectively (Fig 24).

In addition to evaluating for intracranial extension of infection, one must also scrutinize the imaged brain for incidental findings. On a typical neck CT image, a substantial portion of the inferior frontal and temporal lobes, along with the



a.

b.

Figure 24. Left frontal sinusitis and left frontal lobe abscess in a 22-year-old man. (a) Axial nonenhanced CT image (bone window) shows an opacified left frontal sinus, with thinning of the posterior wall of the sinus (arrowhead). (b) Axial nonenhanced CT image obtained just superior to a shows an abscess with a low-attenuation center (*), a thicker abscess rim (white arrow), and surrounding edema (black arrow). Typical thinning of the abscess capsule (arrowhead) is present on the side facing the ventricle. These findings were confirmed at contrast-enhanced MRI (not shown). Culture analysis revealed α -hemolytic *Streptococcus* as the causative organism.

brainstem, posterior fossa, and suprasellar cistern, which includes the circle of Willis, is visible. Intracranial masses, large aneurysms of the circle of Willis, acute infarcts, and intracranial hemorrhages are additional examples of intracranial anomalies that can be seen on neck CT images.

Lung Apices

The lung apices are visible on all CT scans of the neck. Visible structures include the upper lobe lung parenchyma and pleural surfaces, as well as the upper lobe pulmonary arteries, veins, and airways. Numerous common and clinically significant pathologic conditions may be seen in the lung apices at neck CT. Although many of these conditions are identified incidentally, recognizing them can still be vital for patient management.

Pneumonia appears as nodular and/or consolidative opacities in the lung parenchyma. CT is more sensitive than chest radiography for detection of pneumonia. As such, it is possible that pneumonia that was not appreciated on a previously obtained chest radiograph may be visible in the lung apices on a neck CT image. It is also possible that perceived opacities in the lung apices seen on a chest radiograph may not be present on a subsequently obtained CT image (69). Given the limitations of chest radiography in the diagnosis of pneumonia, one must take advantage of any opportunity to scrutinize a portion of the lungs with a more sensitive imaging modality.

Nodules or masses are frequently encountered on CT images, and the detection of them in the lung apices at neck CT can be helpful for the analysis of other examination findings. For example, identification of nodules representing septic emboli in the presence of internal jugular vein thrombosis can confirm the diagnosis of Lemierre syndrome (discussed earlier). The presence of metastases in the lung apices can aid in characterizing nonspecific neck CT findings as likely neoplastic rather than infectious or inflammatory. Incidentally detected nodules or masses may also represent previously unknown lung malignancy. Study findings have shown that a significant proportion of lung cancers missed at chest radiography are in the upper regions of the lung (70). When they are detected, appropriate follow-up should be recommended and communicated.

Finally, important information regarding the fluid status of the patient can be gleaned from an assessment of the lung apices. Findings of pulmonary edema include interlobular septal thickening and nodular or confluent ground-glass opacities, which are often accompanied by pleural effusions (Fig E12). This information can be helpful to the emergency and admitting physicians, particularly when the diagnosis was not made at chest radiography.

Superior Mediastinum

Typically, the area imaged at neck CT extends inferiorly as far as the aortic arch and therefore

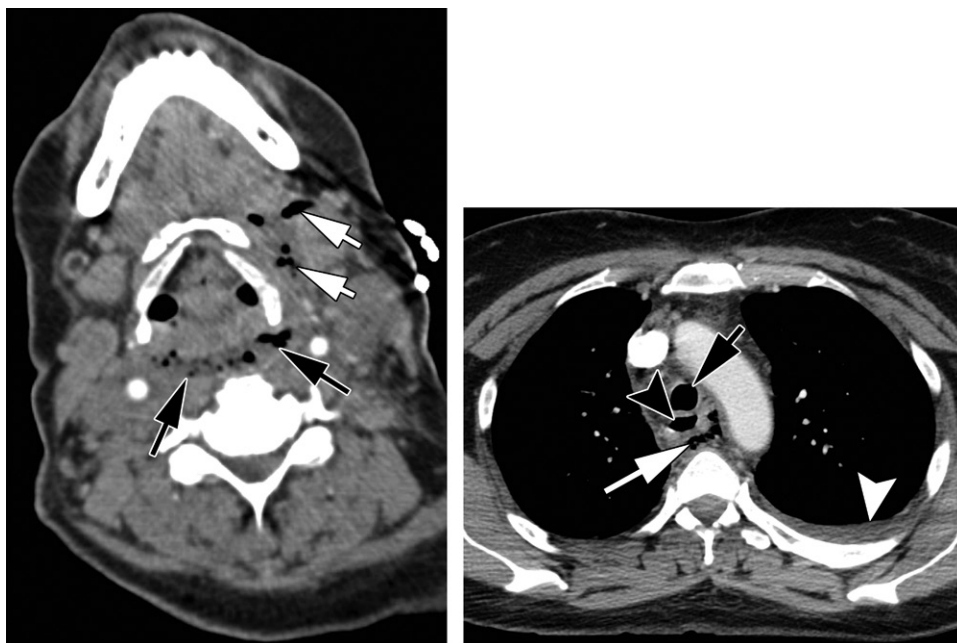
**a.****b.**

Figure 25. Descending mediastinitis in a 50-year-old woman who recently underwent a dental procedure. (a) Axial contrast-enhanced CT image shows foci of gas and fluid (white arrows) in the left submandibular space, with extension to the danger space (black arrows). (b) Axial contrast-enhanced CT image obtained inferior to a shows continued extension into the mediastinum (white arrow) and a small left pleural effusion (white arrowhead). The trachea (black arrow) and esophagus (black arrowhead) also are seen.

includes the superior mediastinum. Visualized structures include the trachea, esophagus, aortic arch, and arch vessels, as well as the distal internal jugular veins, brachiocephalic veins, and superior vena cava. Under normal circumstances, the superior mediastinal fat should be homogeneous, without fat stranding or a pneumomediastinum. Residual thymic tissue should not be confused for disease, particularly in children and young adults (71). The vessels should exhibit normal opacification, without filling defects. The esophageal wall should not be thickened.

Suspected oropharyngeal or dental infection is a common indication for neck CT. Rarely, such infections extend into the mediastinum and result in a life-threatening complication known as descending necrotizing mediastinitis. The longitudinal orientation of the deep cervical fascia allows routes of infection spread from the head and neck into the mediastinum. The danger space is a well-described potential space between the alar fascia anteriorly and the prevertebral fascia posteriorly. It extends from the skull base to the diaphragm, through which head and neck infection can extend into the mediastinum (24). CT findings of descending necrotizing mediastinitis include fat stranding, myositis, mediastinal fluid collections, pleural and pericardial fluid collections, cervical adenopathy, and vascular thrombosis (Fig 25) (72,73).

Important aortic disease can be detected incidentally at neck CT performed in the emer-

gency department. The incidental discovery and reporting of a thoracic aortic aneurysm seen on a neck CT image can affect the long-term survival of the patient (Fig E13) (74). Aortic dissections, penetrating ulcers, and large atherosomas are other aortic pathologic conditions that can be seen at neck CT and are important to recognize. Mediastinal masses also may be detected on neck CT scans. Noting an anterior mediastinal mass in a patient with cervical adenopathy can help the clinician diagnose lymphoma. Goiters with mediastinal extension, thymomas, congenital cysts, esophageal masses, and neurogenic tumors are among the most common mediastinal masses that can be discovered incidentally at neck CT.

Synthesis of Findings

After specific findings are evaluated and reported in the proper sections of the report, the “Impression” section provides the opportunity to synthesize these findings into a unified diagnosis (Figure E14). The diagnosis of Lemierre syndrome (discussed earlier) is used to illustrate this synthesis process (Figure E15). Subcutaneous edema of the involved side should be included in the “Cutaneous and Subcutaneous Soft Tissues” section. The primary infection—for example, tonsillitis—is included in the “Aerodigestive Tract” section. Vascular clot or occlusion should be included in the “Vascular Structures” section.

Septic pulmonary emboli should be included in the “Lung Apices” section. These findings are merged in the “Impression” section, with the final diagnosis being Lemierre syndrome (Figure E15).

Conclusion

CT findings of the neck should be interpreted systematically, in a manner similar to that used to interpret other radiologic studies, such as abdominopelvic CT images and chest radiographs. The described approach involving evaluation of the 12 areas listed in Table 1 is recommended, particularly for the evaluation of acute infectious or inflammatory processes. Findings in these individual areas can then be synthesized into a coherent impression that describes the source and relationship of the disease in individual areas. Interpreting imaging findings in this fashion enables consistent identification of all findings and clear reporting of the disease process.

References

- Giannitto C, Esposito AA, Casiraghi E, Biondetti PR. Epidemiological profile of non-traumatic emergencies of the neck in CT imaging: our experience. *Radiol Med (Torino)* 2014;119(10):784–789.
- Maroldi R, Farina D, Ravanelli M, Lombardi D, Nicolai P. Emergency imaging assessment of deep neck space infections. *Semin Ultrasound CT MR* 2012;33(5):432–442.
- Gamss C, Gupta A, Chazen JL, Phillips CD. Imaging evaluation of the suprathyroid neck. *Radiol Clin North Am* 2015;53(1):133–144.
- Vieira F, Allen SM, Stocks RM, Thompson JW. Deep neck infection. *Otolaryngol Clin North Am* 2008;41(3):459–483, vii.
- Marco De Lucas E, Sádaba P, Lastra García-Barón P, et al. Value of helical computed tomography in the management of upper esophageal foreign bodies. *Acta Radiol* 2004;45(4):369–374.
- Ginat DT, Schatz CJ. Imaging features of midface injectable fillers and associated complications. *AJR Am J Neuroradiol* 2013;34(8):1488–1495.
- Sudhoff H, Rajagopal S, Mani N, Moumoulidis I, Axon PR, Moffat D. Usefulness of CT scans in malignant external otitis: effective tool for the diagnosis, but of limited value in predicting outcome. *Eur Arch Otorhinolaryngol* 2008;265(1):53–56.
- Rosenfeld RM, Schwartz SR, Cannon CR, et al. Clinical practice guideline: acute otitis externa. *Otolaryngol Head Neck Surg* 2014;150(1 Suppl):S1–S24.
- Michalowicz M, Ramanathan M Jr. Clival osteomyelitis presenting as a skull base mass. *J Neurol Surg Rep* 2017;78(2):e93–e95.
- Rubin J, Curtin HD, Yu VL, Kamerer DB. Malignant external otitis: utility of CT in diagnosis and follow-up. *Radiology* 1990;174(2):391–394.
- Koeller KK, Alamo L, Adair CF, Smirniotopoulos JG. Congenital cystic masses of the neck: radiologic-pathologic correlation. *RadioGraphics* 1999;19(1):121–146; quiz 152–153.
- Adams A, Mankad K, Offiah C, Childs L. Branchial cleft anomalies: a pictorial review of embryological development and spectrum of imaging findings. *Insights Imaging* 2016;7(1):69–76.
- Seeburg DP, Baer AH, Aygun N. Imaging of Patients with Head and Neck Cancer: From Staging to Surveillance. *Oral Maxillofac Surg Clin North Am* 2018;30(4):421–433.
- Kelly HR, Curtin HD. Chapter 2 Squamous Cell Carcinoma of the Head and Neck: Imaging Evaluation of Regional Lymph Nodes and Implications for Management. *Semin Ultrasound CT MR* 2017;38(5):466–478.
- Razek AA, Huang BY. Soft tissue tumors of the head and neck: imaging-based review of the WHO classification. *RadioGraphics* 2011;31(7):1923–1954.
- Baxter FJ, Dunn GL. Acute epiglottitis in adults. *Can J Anaesth* 1988;35(4):428–435.
- Charles R, Fadden M, Brook J. Acute epiglottitis. *BMJ* 2013;347:f5235.
- Lee SH, Yun SJ, Kim DH, Jo HH, Ryu S. Do we need a change in ED diagnostic strategy for adult acute epiglottitis? *Am J Emerg Med* 2017;35(10):1519–1524.
- Berger G, Landau T, Berger S, Finkelstein Y, Bernheim J, Ophir D. The rising incidence of adult acute epiglottitis and epiglottic abscess. *Am J Otolaryngol* 2003;24(6):374–383.
- Smith MM, Heubi CH. Infections of the Neck and Pharynx in Children. *Curr Treat Options Pediatr* 2018;4(2):211–220.
- Scott PM, Loftus WK, Kew J, Ahuja A, Yue V, van Hasselt CA. Diagnosis of peritonsillar infections: a prospective study of ultrasound, computerized tomography and clinical diagnosis. *J Laryngol Otol* 1999;113(3):229–232.
- Ali SA, Kovatch KJ, Smith J, et al. Predictors of intratonsillar versus peritonsillar abscess: A case-control series. *Laryngoscope* 2019;129(6):1354–1359.
- Lo CC, Luo CM, Fang TJ. Aberrant internal carotid artery in the mouth mimicking peritonsillar abscess. *Am J Emerg Med* 2010;28(2):259.e5–259.e6.
- Hoang JK, Branstetter BF 4th, Eastwood JD, Glastonbury CM. Multiplanar CT and MRI of collections in the retropharyngeal space: is it an abscess? *AJR Am J Roentgenol* 2011;196(4):W426–W432.
- Brucker JL, Gentry LR. Imaging of head and neck emergencies. *Radiol Clin North Am* 2015;53(1):215–252.
- Chalifoux JR, Vachha B, Moonis G. Imaging of Head and Neck Infections: Diagnostic Considerations, Potential Mimics, and Clinical Management. *Semin Roentgenol* 2017;52(1):10–16.
- Offiah CE, Hall E. Acute calcific tendinitis of the longus colli muscle: spectrum of CT appearances and anatomical correlation. *Br J Radiol* 2009;82(978):e117–e121.
- Ishigami K, Averill SL, Pollard JH, McDonald JM, Sato Y. Radiologic manifestations of angioedema. *Insights Imaging* 2014;5(3):365–374.
- Nandi P, Ong GB. Foreign body in the oesophagus: review of 2394 cases. *Br J Surg* 1978;65(1):5–9.
- Prabhu SM, Irodi A, George PP, Sundaresan R, Anand V. Missed intranasal wooden foreign bodies on computed tomography. *Indian J Radiol Imaging* 2014;24(1):72–74.
- Scheinfeld MH, Shifteh K, Avery LL, Dym H, Dym RJ. Teeth: what radiologists should know. *RadioGraphics* 2012;32(7):1927–1944.
- Merchant AT, Virani SS. Evaluating periodontal treatment to prevent cardiovascular disease: challenges and possible solutions. *Curr Atheroscler Rep* 2017;19(1):4.
- Sakamoto H, Aoki T, Kise Y, Watanabe D, Sasaki J. Descending necrotizing mediastinitis due to odontogenic infections. *Oral Surg Oral Med Oral Pathol Oral Radiol Endod* 2000;89(4):412–419.
- Som PM, Curtin HD. Fascia and spaces of the neck. In: Som PM, Curtin HD, eds. *Head and neck imaging*. 5th ed. St Louis, Mo: Mosby, 2011: 2203–2234.
- Yu CH, Minnema BJ, Gold WL. Bacterial infections complicating tongue piercing. *Can J Infect Dis Med Microbiol* 2010;21(1):e70–e74.
- Kumbhar SS, O’Malley RB, Robinson TJ, et al. Why thyroid surgeons are frustrated with radiologists: lessons learned from pre- and postoperative US. *RadioGraphics* 2016;36(7):2141–2153.
- Nachiappan AC, Metwalli ZA, Hailey BS, Patel RA, Ostrowski ML, Wynne DM. The thyroid: review of imaging features and biopsy techniques with radiologic-pathologic correlation. *RadioGraphics* 2014;34(2):276–293.
- Tessler FN, Middleton WD, Grant EG. Thyroid Imaging Reporting and Data System (TI-RADS): A User’s Guide. *Radiology* 2018;287(1):29–36.
- Bin Saeedan M, Aljohani IM, Khushaim AO, Bukhari SQ, Elnaas ST. Thyroid computed tomography imaging:

- pictorial review of variable pathologies. *Insights Imaging* 2016;7(4):601–617.
40. Paquette CM, Manos DC, Psooy BJ. Unilateral vocal cord paralysis: a review of CT findings, mediastinal causes, and the course of the recurrent laryngeal nerves. *RadioGraphics* 2012;32(3):721–740.
 41. Yedla N, Pirela D, Manzano A, Tuda C, Lo Presti S. Thyroid abscess: challenges in diagnosis and management. *J Investig Med High Impact Case Rep* 2018;6:2324709618778709.
 42. Johnson NA, Tublin ME, Ogilvie JB. Parathyroid imaging: technique and role in the preoperative evaluation of primary hyperparathyroidism. *AJR Am J Roentgenol* 2007;188(6):1706–1715.
 43. Li RM, Kiemeneij M. Infections of the Neck. *Emerg Med Clin North Am* 2019;37(1):95–107.
 44. Abdel Razek AAK, Mukherji S. Imaging of sialadenitis. *Neuroradiol J* 2017;30(3):205–215.
 45. Hoang JK, Vanka J, Ludwig BJ, Glastonbury CM. Evaluation of cervical lymph nodes in head and neck cancer with CT and MRI: tips, traps, and a systematic approach. *AJR Am J Roentgenol* 2013;200(1):W17–W25.
 46. Ludwig BJ, Wang J, Nadgir RN, Saito N, Castro-Aragon I, Sakai O. Imaging of cervical lymphadenopathy in children and young adults. *AJR Am J Roentgenol* 2012;199(5):1105–1113.
 47. Hanson RA, Thoongsuwan N. Scrofula. *Curr Probl Diagn Radiol* 2002;31(6):227–229.
 48. Lee YY, Van Tassel P, Nauert C, North LB, Jing BS. Lymphomas of the head and neck: CT findings at initial presentation. *AJR Am J Roentgenol* 1987;149(3):575–581.
 49. Saba L, Sanfilippo R, Montisci R, Suri JS, Mallarini G. Carotid artery wall thickness measured using CT: inter- and intraobserver agreement analysis. *AJNR Am J Neuroradiol* 2013;34(2):E13–E18.
 50. Saba L, Anzidei M, Sanfilippo R, et al. Imaging of the carotid artery. *Atherosclerosis* 2012;220(2):294–309.
 51. Rodalec MH, Marteau V, Gerber S, Desmottes L, Zins M. Craniocervical arterial dissection: spectrum of imaging findings and differential diagnosis. *RadioGraphics* 2008;28(6):1711–1728.
 52. Lecler A, Obadia M, Savatovsky J, et al. TIPIC Syndrome: Beyond the Myth of Carotidynia, a New Distinct Unclassified Entity. *AJNR Am J Neuroradiol* 2017;38(7):1391–1398.
 53. Vlak MH, Algra A, Brandenburg R, Rinkel GJ. Prevalence of unruptured intracranial aneurysms, with emphasis on sex, age, comorbidity, country, and time period: a systematic review and meta-analysis. *Lancet Neurology* 2011;10(7):626–636.
 54. Eilbert W, Singla N. Lemierre's syndrome. *Int J Emerg Med* 2013;6(1):40.
 55. Som PM, Brandwein MS, Wang BY. Inflammatory disease of the sinonal cavities. In: Som PM, Curtin HD, eds. *Head and neck imaging*. 5th ed. St Louis, Mo: Mosby, 2011; 167–251.
 56. Wyler B, Mallon WK. Sinusitis Update. *Emerg Med Clin North Am* 2019;37(1):41–54.
 57. Aribandi M, McCoy VA, Bazan C 3rd. Imaging features of invasive and noninvasive fungal sinusitis: a review. *RadioGraphics* 2007;27(5):1283–1296.
 58. Middlebrooks EH, Frost CJ, De Jesus RO, Massini TC, Schmalzluss IM, Mancuso AA. Acute Invasive Fungal Rhinosinusitis: A Comprehensive Update of CT Findings and Design of an Effective Diagnostic Imaging Model. *AJNR Am J Neuroradiol* 2015;36(8):1529–1535.
 59. Montone KT. Pathology of fungal rhinosinusitis: a review. *Head Neck Pathol* 2016;10(1):40–46.
 60. Vazquez E, Castellote A, Piqueras J, et al. Imaging of complications of acute mastoiditis in children. *RadioGraphics* 2003;23(2):359–372.
 61. Ludwig BJ, Foster BR, Saito N, Nadgir RN, Castro-Aragon I, Sakai O. Diagnostic imaging in nontraumatic pediatric head and neck emergencies. *RadioGraphics* 2010;30(3):781–799.
 62. Tali ET, Oner AY, Koc AM. Pyogenic spinal infections. *Neuroimaging Clin N Am* 2015;25(2):193–208.
 63. Morales H. Infectious Spondylitis Mimics: Mechanisms of Disease and Imaging Findings. *Semin Ultrasound CT MR* 2018;39(6):587–604.
 64. Egerter AC, Kim ES, Lee DJ, et al. Dysphagia Secondary to Anterior Osteophytes of the Cervical Spine. *Global Spine J* 2015;5(5):e78–e83.
 65. Nguyen VD, Singh AK, Altmeyer WB, Tantiwongkosi B. Demystifying orbital emergencies: A pictorial review. *RadioGraphics* 2017;37(3):947–962.
 66. Absoud M, Hikmet F, Dey P, Joffe M, Thambapillai E. Bilateral cavernous sinus thrombosis complicating sinusitis. *J R Soc Med* 2006;99(9):474–476.
 67. Expert Panel on Neurologic Imaging; Kennedy TA, Corey AS, et al. ACR Appropriateness Criteria: Orbitis Vision and Visual Loss. *J Am Coll Radiol* 2018;15(5S):S116–S131.
 68. Ziegler A, Patadia M, Stankiewicz J. Neurological Complications of Acute and Chronic Sinusitis. *Curr Neurol Neurosci Rep* 2018;18(2):5.
 69. Self WH, Courtney DM, McNaughton CD, Wunderink RG, Kline JA. High discordance of chest x-ray and computed tomography for detection of pulmonary opacities in ED patients: implications for diagnosing pneumonia. *Am J Emerg Med* 2013;31(2):401–405.
 70. Monnier-Cholley L, Arrivé L, Porcel A, et al. Characteristics of missed lung cancer on chest radiographs: a French experience. *Eur Radiol* 2001;11(4):597–605.
 71. Drabkin MJ, MeyerJI, Kanth N, et al. Age-stratified patterns of thymic involution on multidetector CT. *J Thorac Imaging* 2018;33(6):409–416.
 72. Scaglione M, Pinto A, Giovine S, Di Nuzzo L, Giuliano V, Romano L. CT features of descending necrotizing mediastinitis: a pictorial essay. *Emerg Radiol* 2007;14(2):77–81.
 73. Capps EF, Kinsella JJ, Gupta M, Bhatki AM, Opatowsky MJ. Emergency imaging assessment of acute, nontraumatic conditions of the head and neck. *RadioGraphics* 2010;30(5):1335–1352.
 74. Kuzmik GA, Sang AX, Elefteriades JA. Natural history of thoracic aortic aneurysms. *J Vasc Surg* 2012;56(2):565–571.

Dental Emergencies: A Practical Guide

Rafael M. Loureiro, MD

Erica A. Naves, MD

Rafael F Zanello, MD

Daniel V. Sumi, MD

Regina L. E. Gomes, MD, PhD

Mauro M. Daniel, MD, PhD

Abbreviations: PLS = periodontal ligament space, 3D = three-dimensional

RadioGraphics 2019; 39:1782–1795

<https://doi.org/10.1148/rg.2019190019>

Content Codes: **CT** **ER** **HN**

From the Department of Radiology and Diagnostic Imaging, Hospital Israelita Albert Einstein, Av Albert Einstein 627/701, 05652-900 São Paulo, Brazil. Recipient of a Certificate of Merit award for an education exhibit at the 2018 RSNA Annual Meeting. Received February 18, 2019; revision requested April 22 and received May 16; final version accepted June 24. For this journal-based SA-CME activity, the authors, editor, and reviewers have disclosed no relevant relationships. **Address correspondence to** E.A.N. (e-mail: eanaves@hotmail.com).

©RSNA, 2019

SA-CME LEARNING OBJECTIVES

After completing this journal-based SA-CME activity, participants will be able to:

- Recognize the most frequent causes of dental emergencies.
- Describe the imaging findings of the most common types of odontogenic infection, dental trauma, and dental procedure complications.
- Identify imaging hallmarks and pitfalls of dental emergencies.

See rsna.org/learning-center-rg.

Dental disease is a frequent finding on head and neck images, especially in the context of emergencies, and can be a challenge for radiologists who are inexperienced with findings of dental trauma or disease. Dental abnormalities can be subtle and therefore must be included in the systematic approach to these images. Although dedicated dental images are not acquired in most emergency cases, the teeth are included on many different images of the head and neck, and their initial evaluation seldom requires a specific protocol. The high prevalence of craniofacial trauma, sinus infection, and maxillomandibular procedures, among other conditions, frequently requires interpretation of dental images in daily emergency practice. The imaging findings can be categorized into infection, trauma, and complications of procedures, although sometimes these categories can overlap. Such categories can help the radiologist decide which imaging protocol and dynamic maneuvers should be used and are also useful when reading images and proposing differential diagnoses. Familiarity with the imaging findings of dental emergencies improves the radiologist's diagnostic confidence and role in guiding patient care, avoiding progression to life-threatening conditions, and reducing aesthetic problems, dental loss, and related conditions. Information about the imaging protocols is provided, the relevant anatomy of the teeth and related structures is reviewed, and the key imaging findings of dental emergencies are presented.

©RSNA, 2019 • radiographics.rsna.org

Introduction

Dental emergency is a common problem observed in hospital emergency departments. Over the past decades, there has been a rise in emergency department visits for dental problems in the United States (1). Pain, trauma, and infection are among the most common concerns during such visits. For the most part, dental emergencies are not life threatening but can be painful and/or cosmetically significant (2).

Dental disease is a frequent finding on head and neck images, especially in the context of emergencies (2), and can be a challenge for the radiologist who is inexperienced with findings of dental trauma or disease. Dental abnormality can be subtle and therefore must be included in the systematic approach to these images (3). Although dedicated dental images are not acquired in most emergency cases, the teeth are included on many different images of the head and neck. Their initial evaluation seldom requires a specific protocol.

In this article, the imaging findings are categorized into infection, trauma, and complications of procedures, although sometimes these categories can overlap. They can help the radiologist decide which imaging protocol should be used and are also useful when reading images and proposing differential diagnoses. The goal of this article is to provide information about the imaging protocols, review relevant anatomy of the teeth and related structures, and present key imaging findings of dental emergencies.

TEACHING POINTS

- In the context of dental infection, the most indicated maneuver is the “puffed cheek” technique, which the patient performs by pursing the lips and puffing out the cheeks. This maneuver distends the oral cavity and separates the gingival and buccal mucosal surfaces, helping to more accurately locate mucosal lesions and small abscesses.
- It is essential to understand the route of dissemination of dental infections into the deep spaces of the neck. Their spread usually depends on their position relative to the mylohyoid line, which represents the attachment of the mylohyoid muscle to the mandible.
- In particular, unilateral maxillary sinusitis is highly indicative of odontogenic sinusitis; more than 70% of these cases can be attributed to dental disease.
- Luxation is the most common traumatic dental injury in the primary dentition, whereas crown fracture is most frequently reported in the permanent teeth. The maxillary incisors are the teeth most affected by traumatic injury.
- Infection related to a dental implant may lead to “peri-implantitis,” a condition in which peri-implant osteolysis can threaten the hold of a dental implant, often associated with inflammation of adjacent soft tissues.

Imaging Protocols

The role of the radiologist begins with selection of the most appropriate imaging protocol. This is an essential step in the process and is necessary for an accurate diagnosis.

Cone-beam CT allows evaluation of the teeth and alveolar bone with high spatial resolution, three-dimensional (3D) images, and less radiation exposure compared with multidetector CT. Its main drawback is poor image quality of soft tissues and limited availability in emergency centers. In most cases, multidetector CT is the modality of choice to help evaluate dental emergencies because of its wide availability, scanning speed, and high spatial resolution (4,5). The obtained image sections should be as thin as possible to allow identification of subtle abnormalities. Isotropic datasets, when available, permit reformation into axial, coronal, and sagittal planes, as well as 3D surface-rendered and panoramic reconstructions that can be of great value during image interpretation (3,6). Contrast-enhanced images improve the evaluation in cases of suspected infection or in investigations of active bleeding after a dental procedure (7).

Some dynamic maneuvers provide more image details and thus enhance accuracy. In the context of dental infection, the most indicated maneuver is the “puffed cheek” technique, which the patient performs by pursing the lips and puffing out the cheeks. This maneuver distends the oral cavity and separates the gingival and buccal mucosal surfaces, helping to more accurately locate mucosal lesions and small abscesses (Fig 1) (8). If metal artifacts degrade images of the oral cavity, another

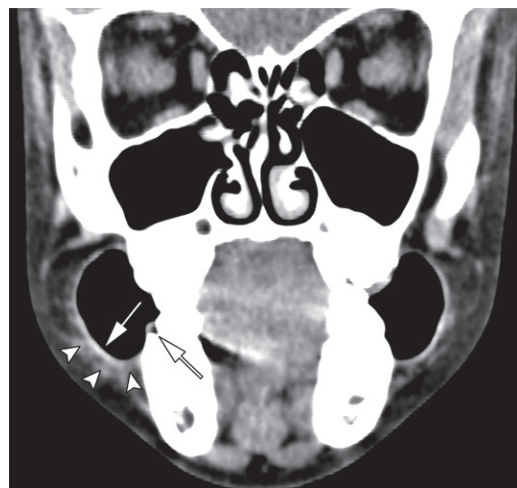


Figure 1. Puffed cheek technique. Coronal nonenhanced CT image (soft-tissue window) shows the oral cavity distended by air, with mucosal thickening (arrows) and subcutaneous edema (arrowheads), which could be difficult to depict without the technique.

technique that may be useful is to acquire images with the mouth closed and open, therefore moving the metal artifacts to a different area in the second acquisition (8).

Anatomy and Nomenclature

The tooth is formed by two main parts composed of different tissues. The portion that can be observed at oral inspection is called the crown, while the portion covered by the alveolar bone ridge is called the root. The crown is composed of two mineralized layers (one external harder layer, called enamel, and a deeper layer, called dentin) and an inner structure known as pulp. The dentin and pulp extend apically and form the root, which is surrounded by a thin layer of cementum, a third mineralized layer (Fig 2). The pulp contains the neurovascular elements (9). The transition between enamel and cementum marks the boundary between crown and root and is named the cementoenamel junction or neck (10).

The teeth are attached in bone sockets called alveolar processes and are fixed to these cavities by ligaments called periodontal ligaments that exert a damping role, allowing slight mobility during chewing.

Human dentition develops in two overlapping stages, resulting in formation of two dental sets that are called primary and secondary dentition. The primary set, also known as deciduous, is composed of 20 temporary teeth that begin to erupt at 6 months of age and are shed by about 12 years of age, giving rise to a secondary set of 32 permanent teeth that begin to appear around 7 years of age (3,10,11).

Extending distally from the midline, the quadrants of the primary teeth are named as follows:

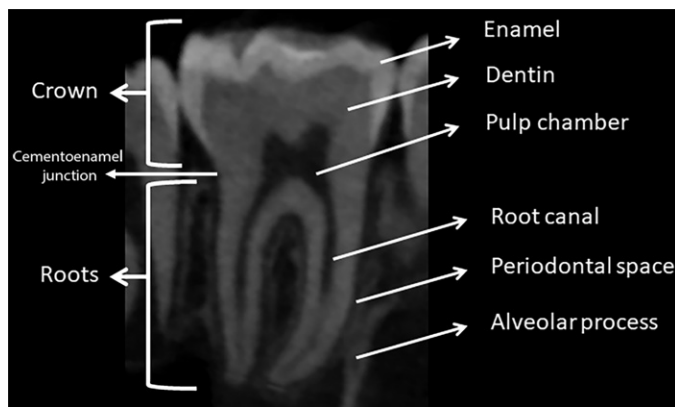
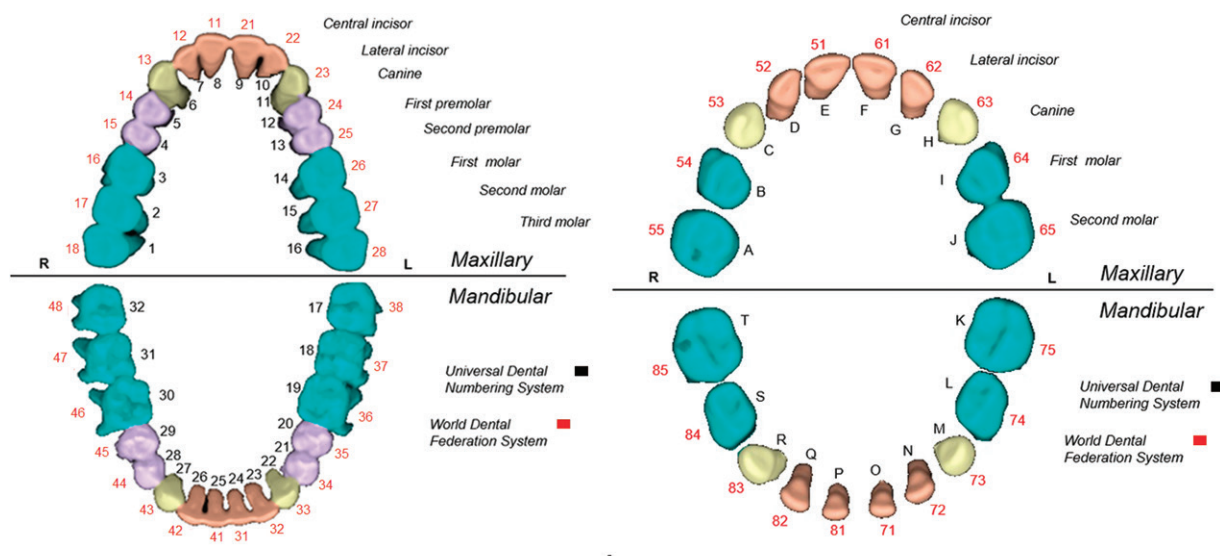


Figure 2. Tooth anatomy. Sagittal cone-beam CT image demonstrates the two main parts of the tooth and its layers, attached to the alveolar process.



a.

b.

Figure 3. Tooth numbering and nomenclature. Color reconstruction of a 3D volume-rendered CT image shows the Universal Dental (black) and World Dental Federation (red) numbering systems and dental nomenclature for the permanent (a) and deciduous (b) dentition.

central incisor, lateral incisor, canine, first molar, and second molar. In the permanent dentition, the teeth are named as follows: central incisor, lateral incisor, canine, first premolar, second premolar, first molar, second molar, and third molar (Fig 3) (10).

The teeth can be numbered by two major classification systems: the Universal System and the World Dental Federation System (3). Despite its name, the Universal System is most commonly used in the United States. In this system, the upper right, upper left, lower left, and lower right quadrants are arranged in a circle in the clockwise direction. This system identifies the primary teeth with letters in alphabetical order, progressing from A to T clockwise, and the permanent teeth with numbers, from 1 to 32, also clockwise.

The World Dental Federation System is better known globally and uses a combination of two numbers, the first of which indicates the quadrant of the tooth and the second number the position

of the tooth in each respective quadrant. Thus, the upper right, upper left, lower right, and lower left quadrants receive the numbers 5, 6, 7, and 8 in the primary dentition and 1, 2, 3, and 4 in the permanent dentition. The second number refers to the position of the tooth from medial to lateral, ranging from number 1 (central incisor) to number 5 (second molar) in the primary dentition and to number 8 (third molar) in the permanent dentition (Fig 3) (11).

Infections

Odontogenic infection arises from any part of the tooth or adjacent structures and can directly spread into adjacent bone and soft tissues through superficial and deep neck spaces. Imaging plays a crucial role in identifying the source of infection and the extent of the disease process, as well as depicting any complications.

It is essential to understand the route of dissemination of dental infections into the deep

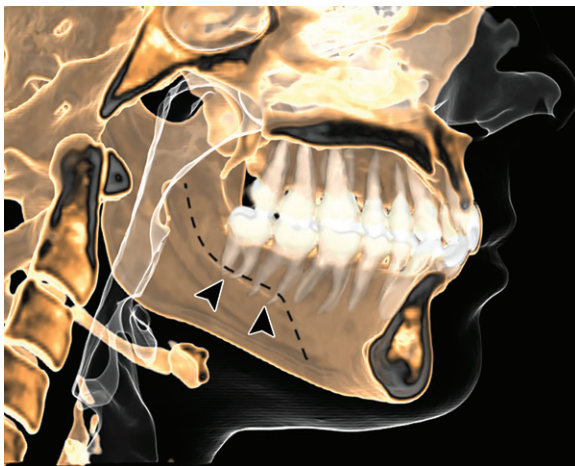
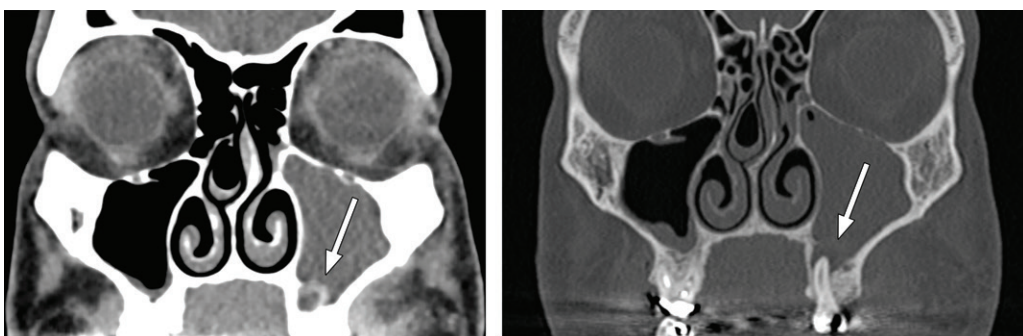


Figure 4. Mylohyoid line. Three-dimensional volume-rendered CT image shows the attachment of the mylohyoid muscle to the internal surface of the mandible (dashed line). It lies above the root apices of the second and third molars (arrowheads) and below the root apices of the other teeth. (Courtesy of Fábio Augusto Ribeiro Dalprá, MD, Hospital Israelita Albert Einstein, São Paulo, Brazil.)



a.

b.

Figure 5. Periapical abscess. (a) Coronal contrast-enhanced CT image (soft-tissue window) demonstrates a hypoattenuating fluid collection with peripheral enhancement (arrow). (b) Coronal CT image (bone window) shows bone loss around the root apex with discontinuity of the maxillary sinus floor (arrow). Both images show complete opacification of the left maxillary sinus, consistent with odontogenic sinusitis.

spaces of the neck. Their spread usually depends on their position relative to the mylohyoid line, which represents the attachment of the mylohyoid muscle to the mandible. The mylohyoid line divides the submandibular and sublingual spaces, so that lesions involving the root apices of the second and third molars disseminate directly to the submandibular space, while lesions involving other teeth disseminate to the sublingual space (Fig 4) (4,12).

Periapical and Subperiosteal Abscesses

Inflammation of periapical tissues is caused by infection of the root canal with pulp devitalization, arising from carious lesions on the crown (12). Widening of the periodontal space adjacent to the root apex leads to bone erosion and produces periapical lucency, which can be observed on radiographs and CT images. Periapical abscess is the organized infection of apical periodontitis. When prolonged, this condition increases bone erosion and can lead to cortical discontinuity and spread of infection beyond the alveolar bone (6).

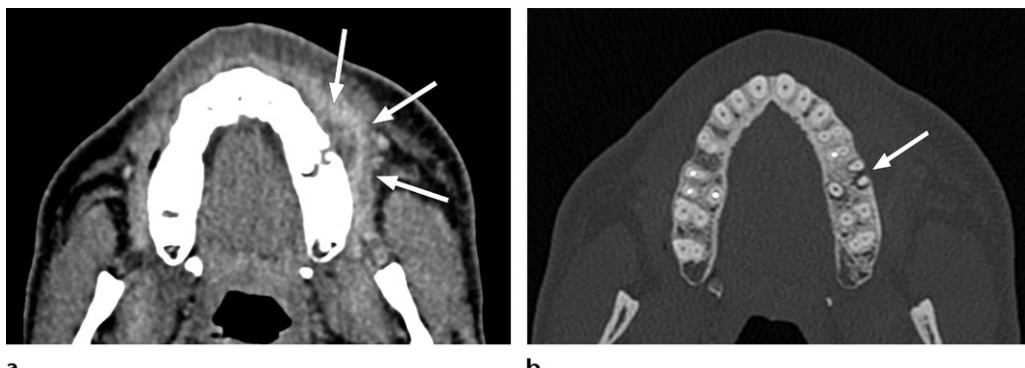
When this process arises from the upper dental arch with rupture of the cortical bone, the infec-

tion can extend into the overlying maxillary sinus, sometimes causing odontogenic sinusitis, which can progress to an abscess inside the sinus (Fig 5). When the infection progresses with rupture of the cortical bone, it usually penetrates along the bone margin and extends as an extraosseous abscess, either confined by the periosteum, forming a subperiosteal abscess (Fig 6), or disseminating into deep neck planes (6).

Pericoronitis

Pericoronitis is the inflammation around the crown of a partially erupted tooth, affecting the pericoronal tissue, most commonly in the mandibular third molars (12).

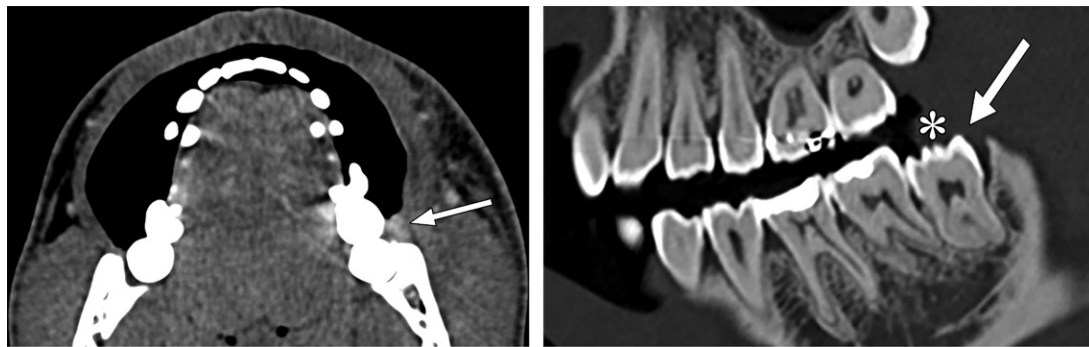
Those teeth usually erupt without opposition, thus being more prone to the impaction of food particles between the gingiva and crown, which forms a source of infection and inflammation. The process manifests initially with local gingivitis and can spread to the surrounding tissues, including the alveolar bone or even culminating in abscess formation (2). At imaging, pericoronitis typically appears as thickening and enhancement of the pericoronal tissues of a partially erupted tooth (Fig 7).



a.

b.

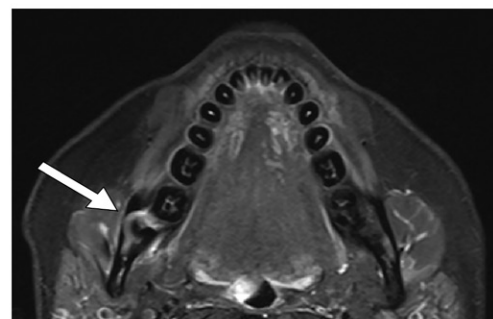
Figure 6. Subperiosteal abscess. (a) Axial contrast-enhanced CT image (soft-tissue window) shows a hypodense fluid collection with peripheral enhancement and stranding of the adjacent fat tissues (arrows). (b) Axial CT image (bone window) demonstrates that the collection is continuous with periapical disease and erosion of the vestibular cortical bone (arrow).



a.

b.

Figure 7. Pericoronitis. (a) Axial contrast-enhanced CT image (soft-tissue window) demonstrates enhancement of the pericoronal tissues (arrow). (b) Sagittal CT image (bone window) shows that the affected tooth is partially erupted (arrow) and partially covered by gingiva (*).



c.

Odontogenic Sinusitis

Odontogenic sinusitis substantially differs from sinusitis of other causes in its pathophysiology, microbiology, and treatment. Injury of the mucoperiosteum of the maxillary sinus is the basis of odontogenic sinusitis pathophysiology. Dental procedures are considered to be the most common cause of odontogenic sinusitis, followed by periapical and periodontal disease (13).

On images, the diagnosis is made when an interruption of the maxillary sinus floor, frequently associated with periodontal or carious disease, is associated with sinusitis (Fig 8). In particular, unilateral maxillary sinusitis is highly indicative of odontogenic sinusitis; more than 70% of these cases can be attributed to dental disease (14,15). Anaerobic bacteria are more frequent in odontogenic sinusitis than in nonodontogenic sinusitis, which warrants a different treatment approach (16,17). Furthermore, because the mucoperiosteum and mucociliary function are compromised in odontogenic sinusitis, endoscopic sinus surgery

may be required in addition to treatment of the dental condition (18).

Ludwig Cellulitis

Ludwig cellulitis, also called Ludwig angina, is infectious cellulitis of the subcutaneous and deep neck spaces that extends bilaterally, generally involving the sublingual, submental, and submandibular spaces (Fig 9) (19). The infection more commonly arises from the second and third mandibular molars, although it can originate from any other oral or adjacent infected structures. It is more frequent in patients in an immunocompromised state or in individuals with other comorbidities, such as diabetes mellitus and hypertension (20,21). The potential risk of airway obstruction

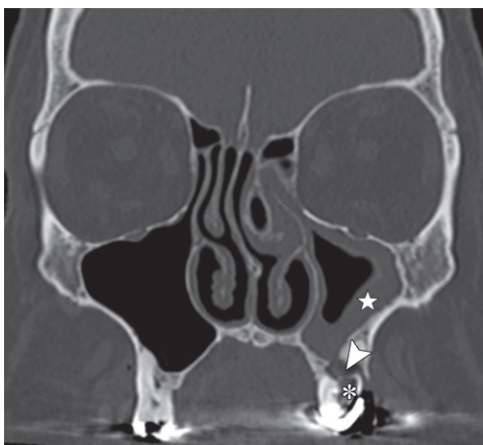


Figure 8. Odontogenic sinusitis. Coronal nonenhanced CT image (bone window) demonstrates unilateral maxillary sinusitis (☆) associated with a bone discontinuity that communicates the sinus floor with periodontal disease (arrowhead) around a tooth with a large carious lesion (*).

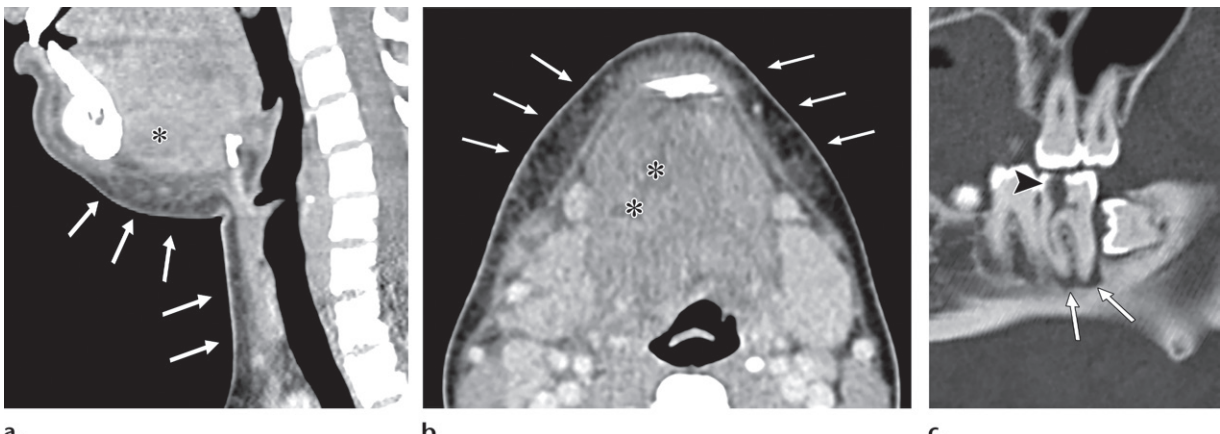


Figure 9. Ludwig cellulitis. (a, b) Sagittal (a) and axial (b) contrast-enhanced CT images (soft-tissue window) reveal a small fluid collection with peripheral enhancement (*), with fat stranding and edema extending bilaterally within the submandibular, sublingual, and submental spaces (arrows). (c) Sagittal CT image (bone window) demonstrates a carious lesion affecting the pulp chamber (arrowhead) of the lower second molar with apical periodontitis (arrows), therefore revealing the cause of the infectious process.



Figure 10. Chronic osteomyelitis of the mandible. Axial nonenhanced CT image (bone window) demonstrates a sequestrum (arrow), periosteal reaction (white arrowhead), and linear bone radiolucencies consistent with a sinus tract (black arrowheads).

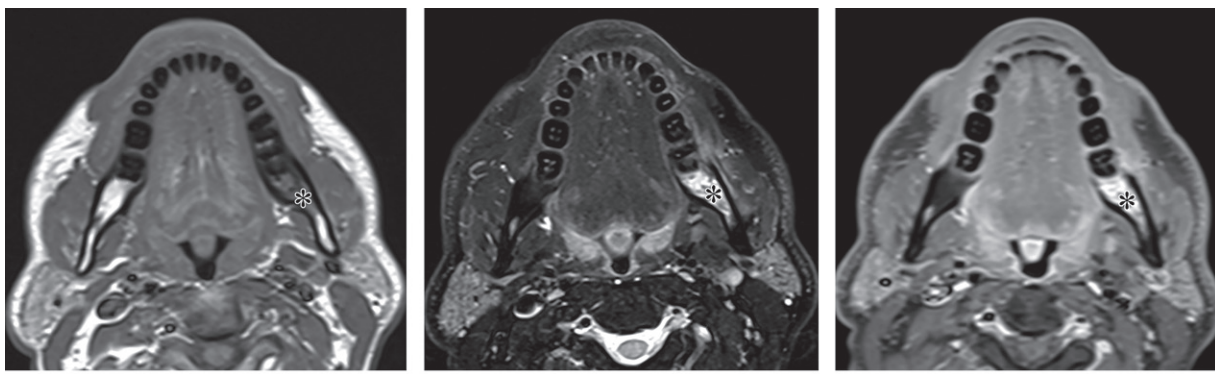
due to the rapid spread of the cellulitis makes this condition life threatening, requiring prompt evaluation. CT is useful for diagnosis and to determine airway patency, the source of infection, and the presence of drainable abscesses (7,19).

Osteomyelitis

Osteomyelitis of the jaw is most often caused by a bacterial focus that can originate from an odontogenic infection (periapical or periodontal lesion), surgical site, foreign body, or fracture (12). It occurs more commonly in the mandible, as the maxilla has significant collateral blood flow and bone marrow with struts that make it less prone to infection (22,23).

The first signs of osteomyelitis are bone marrow edema and loss of the trabecular structure, which can progress to fragmentation of the cortices and spread of the infection to adjacent soft parts (12,24). In the acute phase, there is predominantly bone lysis, whereas in the chronic phase, more sclerosis of trabecular bone occurs. A sequestrum is characteristic of chronic osteomyelitis and represents a segment of necrotic bone that is separated from living bone by granulation tissue and bone resorption (Fig 10) (25,26).

CT is the best modality for assessing fine bone detail, periosteal bone formation, the sequestrum, and the source of infection; however, bone marrow



a.

b.

c.

Figure 11. Acute osteomyelitis of the mandible. Axial T1-weighted (a), T2-weighted (b), and contrast-enhanced T1-weighted (c) MR images demonstrate signal intensity changes and enhancement of the bone marrow (*).

changes are not well depicted with this method. Compared with CT, MRI has worse spatial resolution; however, it is the modality of choice for depicting bone marrow edema in the early stages, which appears as high signal intensity on T2-weighted and short τ inversion-recovery (STIR) images. On T1-weighted images, low signal intensity of the affected areas reflects loss of normal fatty marrow signal (Fig 11) (26). Soft-tissue extension, abscess formation, and sinus tracts are also accurately depicted on MR images (12,25,27).

Imaging is used in osteomyelitis to help the radiologist localize the condition, determine its source and extent, and evaluate response after treatment.

Dental Trauma

Dental trauma is extremely common, with approximately one-third of all individuals experiencing a dental injury during their lifetime (28). Dental trauma can be classified into fracture, luxation, and avulsion (29,30). Luxation is the most common traumatic dental injury in the primary dentition, whereas crown fracture is most frequently reported in the permanent teeth (31). The maxillary incisors are the teeth most affected by traumatic injury (2,32).

A fracture is a discontinuity of any dental component and can result in loss of tooth structure. It can be classified according to the affected segment of the tooth: crown, crown-root, and root fractures. It is fundamental to assess the extent of the fracture through the tooth layers (Figs 12–14), since fractures affecting the pulp (pulp chamber or root canal) place the tooth vitality at risk and thus carry a worse prognosis. When the fracture involves the alveolar process, it is called a dentoalveolar fracture.

Dental luxation is a general term that covers multiple types of injuries to the tooth support structures, particularly the periodontal ligament. Dental luxation injuries are divided into concussion, subluxation, extrusive luxation, intrusive luxation,

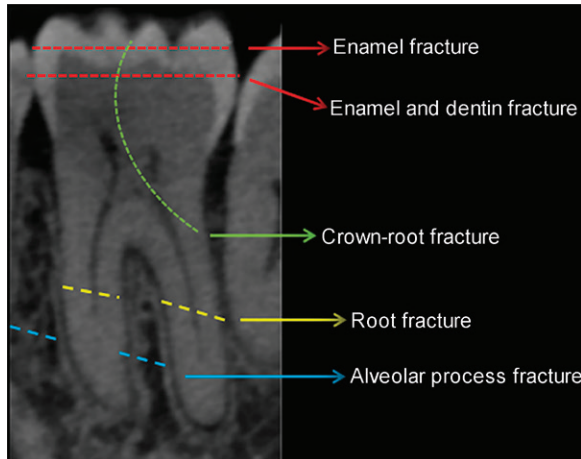


Figure 12. Dental fractures. Cone-beam CT image of a molar tooth shows lines representing different types of dental fractures.

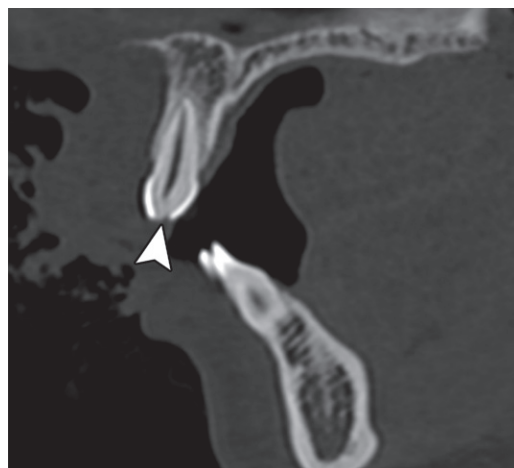


Figure 13. Dental crown fracture. Sagittal CT image (bone window) shows a fracture of enamel and dentin without pulp involvement (arrowhead).

and lateral luxation (Table, Fig 15). They can be associated with dental fracture but can also manifest without dental fracture.

While radiologic abnormalities are not expected in concussion and subluxation, tooth displacement

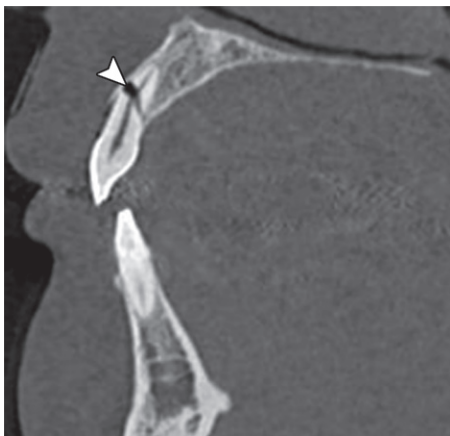


Figure 14. Dental root fracture. Sagittal CT image (bone window) shows a root fracture with pulp involvement (arrowhead).

Clinical Manifestation and Imaging Findings of Luxation and Avulsion Injuries

| Type of Injury | Clinical Manifestation | Imaging Findings | Figures |
|--------------------|--------------------------------------------------------------|-----------------------------------------------------------|---------|
| Concussion | Tooth is tender to touch, without loosening or displacement | No abnormalities | 15a |
| Subluxation | Tooth is tender to touch, with loosening but no displacement | Abnormalities are not expected | 15a |
| Extrusive luxation | Tooth appears longer and displaced, with marked loosening | Widening of PLS,* usually in apical region | 15b, 16 |
| Lateral luxation | Tooth is displaced, without loosening | Asymmetric widening of PLS with fracture of alveolar bone | 15c, 17 |
| Intrusive luxation | Tooth is displaced into alveolar bone | Tooth intrusion into alveolar bone, PLS reduced or absent | 15d |
| Avulsion | Tooth is completely out of socket | Empty socket | 15e |

*PLS = periodontal ligament space.

and widening of the periodontal ligament space (PLS) are observed in extrusive luxation (Fig 16) and lateral luxation (Fig 17), the latter accompanied by fracture of the alveolar process. Despite its name, lateral luxation consists of eccentric displacement of the tooth, usually in the palatal, lingual, or labial direction. On the other hand, intrusive luxation appears on images as a narrowed or absent PLS, with a tooth displaced into the alveolar bone (Table) (29,33,34).

A potential pitfall to be aware of is that a widened PLS can develop in patients receiving orthodontic treatment, usually in multiple teeth, mimicking extrusive luxations (35). In these cases, the brackets and wires are easily seen on CT images and radiographs.

Finally, *avulsion* is the term used when the tooth is completely displaced from the alveolar socket (Fig 18) (30,36).

Complications of Dental Procedures

Complications of dental procedures are widely seen in daily practice. Some complications may require imaging assessment, and the radiologist must be prepared to evaluate them. To better understand

the imaging findings, it is essential to ask the patient about the specific procedure that was previously performed and when. Knowledge of the elapsed time between procedure and imaging examination is also useful to help determine the type of lesion.

Complications of Tooth Extraction

The main reasons for extraction of permanent teeth are caries, periodontal disease, and dental impaction, the latter mainly involving the third molars, also called wisdom teeth (37). Postoperative complications after tooth removal may range from mild discomfort to major complications requiring hospitalization or resulting in permanent damage (38).

Typical imaging findings in the first few days after a noncomplicated dental extraction are soft-tissue material filling the tooth socket (often with gas bubbles) and thickening and stranding of the adjacent tissues, mainly the gingiva, buccal mucosa, and buccal space. These structures are better depicted with the puffed cheek technique on multidetector CT images (Fig 19) (39).

Infection is among the most common complications after tooth extraction (40). It may spread

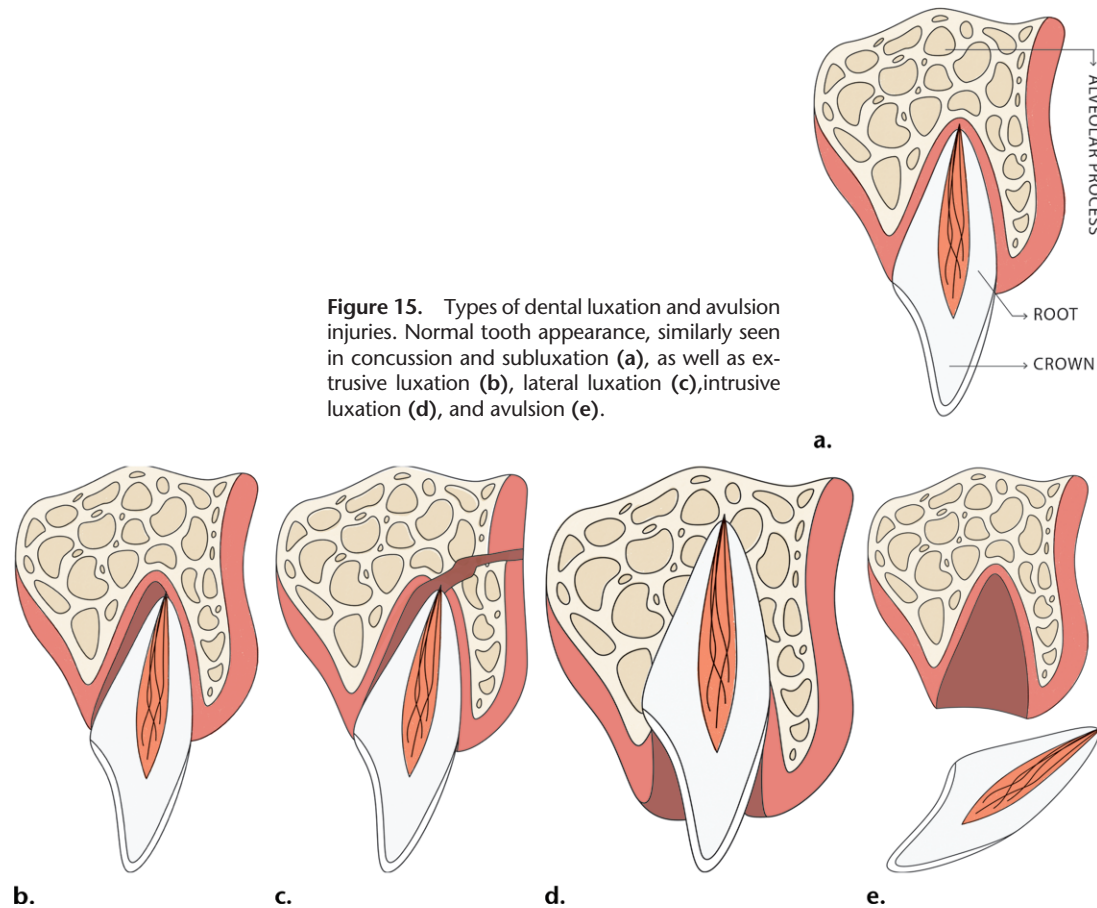


Figure 15. Types of dental luxation and avulsion injuries. Normal tooth appearance, similarly seen in concussion and subluxation (**a**), as well as extrusive luxation (**b**), lateral luxation (**c**), intrusive luxation (**d**), and avulsion (**e**).



Figure 16. Dental extrusive luxation. Sagittal (**a**), axial (**b**), and coronal (**c**) CT images (bone window) show tooth displacement with widening of the PLS (arrows).

from the surgical site to the adjacent tissues and lead to development of cellulitis, abscess, and even life-threatening deep neck infection. It usually manifests as an increase in facial or neck swelling beyond the 3rd or 4th postoperative day, with increasing pain. In these cases, stranding and thickening of the adjacent tissues are more widespread (Fig 20), with the parapharyngeal, submandibular, anterior visceral, masticator, and sublingual spaces being the most involved (3). Abscess appears as a fluid collection with rim enhancement. If the infection spreads

into the medullary alveolar bone, osteomyelitis may develop.

Noninfectious complications include traumatic displacement of an impacted tooth (either a fragment or the entire tooth) (Fig 21), bone fracture (Fig 22), hematoma, and oroantral fistulas.

Hematoma may be associated with a focus of active bleeding, which can be observed at contrast-enhanced CT as an area of extravasation near the extraction site, often inside the tooth socket (Fig 23).

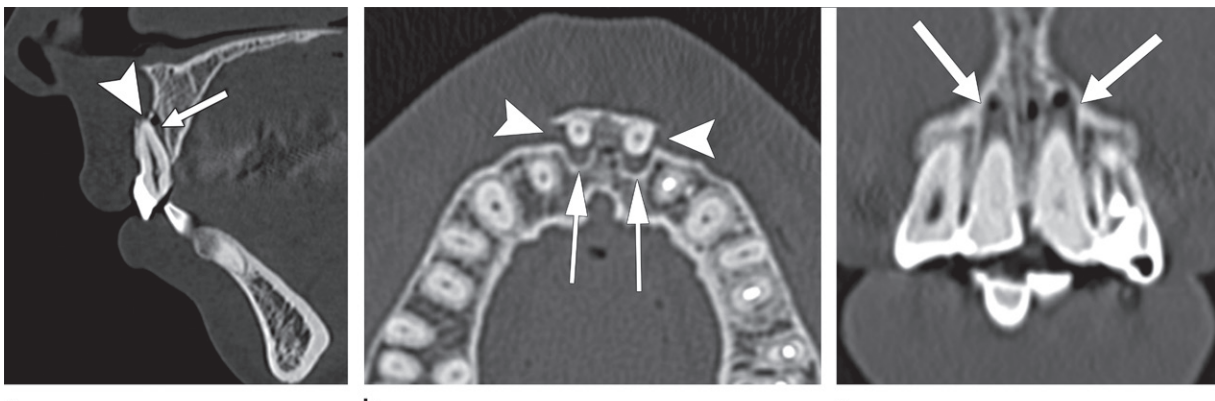


Figure 17. Dental lateral luxation. Sagittal (a), axial (b), and coronal (c) CT images (bone window) show tooth displacement, widening of the PLS (arrows), and fracture of the alveolar process (arrowheads in a and b).

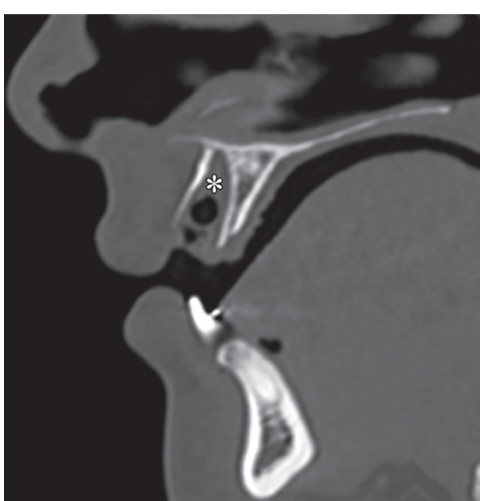


Figure 18. Dental avulsion. Sagittal CT image (bone window) shows an empty alveolar socket (*).



Figure 20. Cellulitis after third molar extraction. Axial contrast-enhanced CT image (soft-tissue window) a few days after left inferior third molar extraction (*) shows thickening of the gingival and buccal mucosa, masseter muscle, and perimandibular soft tissues, with gas bubbles and extensive stranding of the subcutaneous fat (arrows).



Figure 19. Noncomplicated third molar extraction. Axial contrast-enhanced CT image (soft-tissue window) a few days after a dental extraction shows soft-tissue material filling the alveolar cavity (*), thickening and enhancement of gingival and buccal mucosal surfaces (arrowheads), and mild stranding of the buccal fat space.

Oroantral fistula is an abnormal defect of the maxillary sinus floor, communicating the antrum with the oral cavity. It can be a complication of tooth extraction, most commonly of the maxillary molars (41). At imaging, identification of bony disruption of the maxillary sinus floor is usually straightforward.

However, soft tissue (gingival mucosa, granulation tissue, or debris) is often observed to obliterate the tooth socket. A final diagnosis of oroantral fistula might be difficult. The puffed cheek technique separates the buccal and gingival mucosa (39,42) and, in our experience, makes it easier to detect an air passageway between the maxillary sinus and oral cavity (Fig 24). A swish of water-soluble iodinated contrast medium before acquisition of CT images can also be useful. Diagnosis of oroantral fistula is made when contrast medium is identified inside the maxillary sinus (43).

Presurgical imaging is useful to evaluate the relationship between the tooth and maxillary

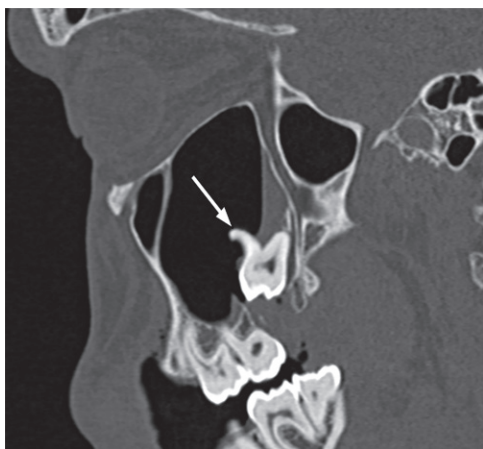


Figure 21. Traumatic tooth displacement. Sagittal nonenhanced CT image (bone window) shows a third molar (arrow) displaced into the maxillary sinus.

sinus floor, as well as the thickness of the alveolar process, which may indicate a higher risk of fistula formation. When the connection is less than 2 mm wide, it usually heals spontaneously. Larger interruptions may require surgical intervention (3,44).

Complications of Dental Implants

Dental implants are the best long-term substitute for missing teeth and have become very popular over the past few decades because they restore nearly normal function in partially or completely edentulous patients (45). Most implants are composed of a metallic hollow supporting screw that receives a supraprosthetic device after a healing period for osseointegration (46). Dental implants are readily observed at CT using a bone window, as well as at radiography (45).

Patients must have sufficient bone volume in the jaw to anchor implants and to avoid damaging surrounding structures, in particular the mandibular canal and maxillary sinus. Bone graft materials can be used to increase the height and thickness of the alveolar bone.

Maxillary sinus augmentation (also known as sinus floor elevation) procedures have become increasingly popular before placement of dental implants. They are used when the alveolar bone of the maxilla is thin owing to alveolar bone atrophy, sinus pneumatization, or trauma (47).

On CT images, the bone graft material used to augment the alveolar process appears as irregular masses of high attenuation similar to bone in the inferior half of the maxillary sinus, which may lead to misdiagnosis as bone lesions such as fibrous dysplasia and osteoma. Failure of these procedures may result from infection and lack of integration of the graft material into the alveolar bone, usually accompanied by graft fragmentation (45). Bone graft fragments inside the maxil-



Figure 22. Bone fracture. Axial nonenhanced CT image (bone window) after third molar extraction shows fracture of the right maxillary sinus floor (arrowheads).



Figure 23. Hematoma with active bleeding. Axial contrast-enhanced CT image (soft-tissue window) after third molar extraction shows a large hematoma containing serpentine foci with enhancement (arrowhead).

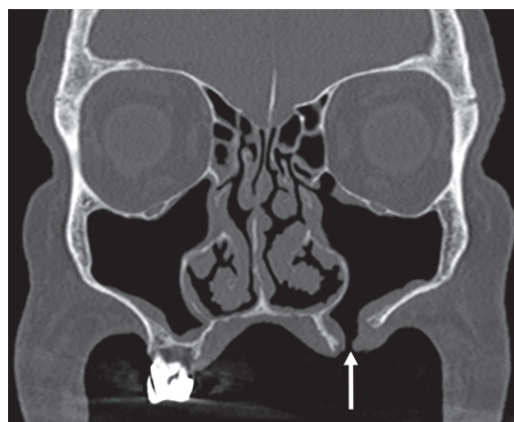


Figure 24. Oroantral fistula. Coronal nonenhanced CT image (bone window) demonstrates a bony defect connecting the left maxillary sinus floor with the oral cavity. The puffed cheek technique made diagnosis possible by separating the adjacent soft tissues and filling the fistulous tract with air (arrow).

lary sinus may mimic fungal sinusitis, in which case the clinical history is essential to distinguish between these two conditions (Fig 25).

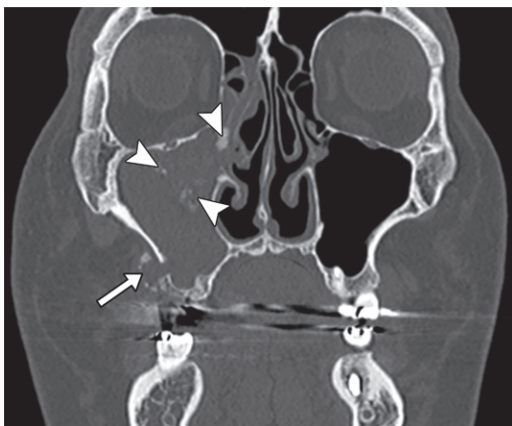


Figure 25. Bone graft fragmentation. Coronal nonenhanced CT image (bone window) shows complete opacification of the right maxillary sinus. The bone graft material is diffusely dispersed inside the sinus (arrowheads) and adjacent to a bony discontinuity at the maxillary sinus floor (arrow).

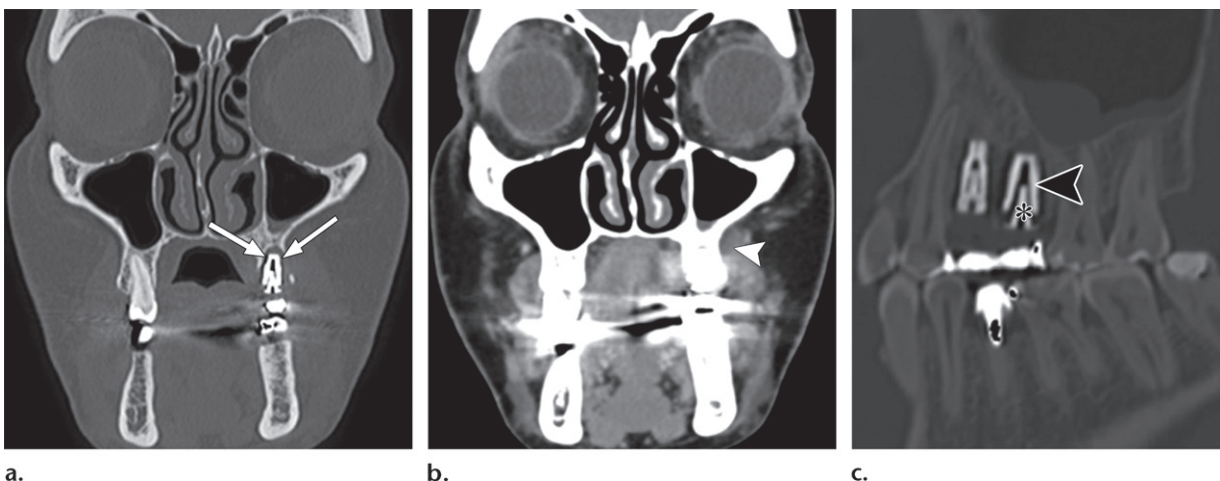


Figure 26. Peri-implantitis. (a) Coronal nonenhanced CT image (bone window) demonstrates peri-implant bone resorption (arrows). (b) Coronal image (soft-tissue window) shows inflammatory changes of the adjacent soft tissues (arrowhead). (c) Sagittal image (bone window) shows loosening between the implant fixture (arrowhead) and abutment (*).



Figure 27. Dental implant dislodgement. Sagittal nonenhanced CT image (bone window) demonstrates a dental implant (*) dislodged into the maxillary sinus. There is also a large bone discontinuity of the maxillary sinus floor (arrow).

Poor osseointegration of dental implants can be detected on radiographs and CT images as radiolucent peri-implant areas. It can be a result of a foreign-body inflammatory reaction or infection, although the underlying cause is often not deter-

mined (48). Infection related to a dental implant may lead to “peri-implantitis,” a condition in which peri-implant osteolysis can threaten the hold of a dental implant, often associated with inflammation of adjacent soft tissues (Fig 26) (49,50).

Dislodgement of an implant into the maxillary sinus can occur several days or even years after implantation or abutment connection surgery (Fig 27). This may occur because of positioning of an implant in an unnecessary apical position, excessive pressure during placement, or widening of the ridge due to overdrilling (47).

In addition to the maxillary sinus and mandibular canal (Fig 28), dental implants can damage other adjacent structures, such as the nasal cavity floor, mental foramen, incisive foramen, and nasopalatine canal (48).

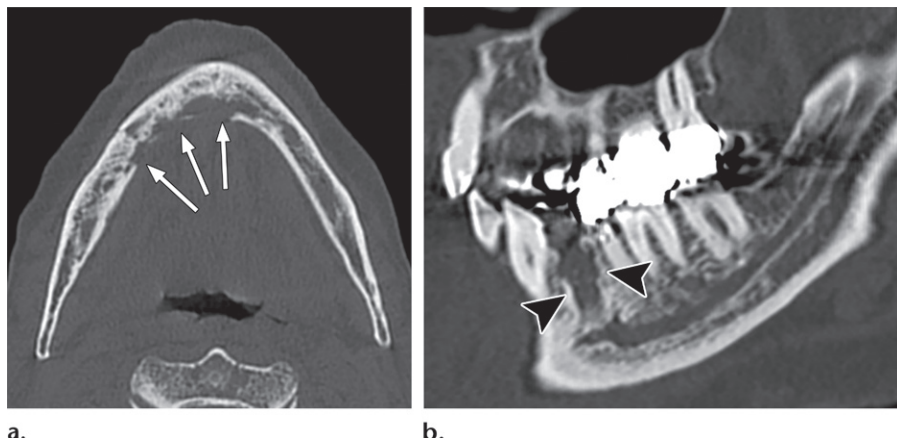
Medication-related Osteonecrosis of the Mandible

Medication-related osteonecrosis of the mandible is related to use of bisphosphonates or other medications administered to inhibit bone turnover



Figure 28. Dental implant dislodgement. Sagittal nonenhanced CT image (bone window) demonstrates a dental implant (*) dislodged into the mandibular canal.

Figure 29. Medication-related osteonecrosis of the mandible. (a) Axial CT image (bone window) demonstrates sclerotic and lytic areas in the mandible with discontinuities of the cortical bone (arrows). (b) Sagittal CT image (bone window) reveals the nonhealing socket of an extracted tooth (arrowheads).



a.

b.

(51,52). It is characterized as a nonhealing area of exposed bone at trauma sites in patients who did not undergo craniofacial radiation therapy, more frequently in dental extractions. The risk of developing the disease is associated with the dose, duration, and potency of the drug used (51). It is usually painful but can be asymptomatic. Only a minority of cases affect the maxilla (22). Clinical findings define the diagnosis, but imaging is relevant to determine the extent of disease, exclude other diagnoses, and help evaluate complications, such as fracture (51).

Panoramic radiography, CT, and MRI are imaging modalities that can be used. The disease is characterized by bone sclerosis permeated by osteolytic areas, irregularity and destruction of cortical margins, and periosteal thickening (Fig 29). Examinations can also show the persistent alveolar tooth socket, bone sequestrum, pathologic fracture, fistula, or soft-tissue extension. In the early phases of the disease, CT usually shows a sclerotic bone area without corticomedullary differentiation around the extracted tooth socket or at the site of bone trauma. At MRI, signal intensity abnormalities can be variable depending on the stage of the disease, and it can better demonstrate the extent of disease compared with CT (51).

Conclusion

The high prevalence of craniofacial trauma, sinus infection disease, and maxillomandibular procedures, among other conditions, frequently requires interpretation of dental images in daily emergency practice. Teeth can be the source or the extension of a pathologic process and therefore must not be overlooked by radiologists when performing emergency imaging. Radiologists can use their knowledge of the main dental imaging findings in emergency radiology to add great value to image interpretation.

Acknowledgment.—The authors thank Leticia Antunes Naves for the tooth illustrations.

References

- Brecher EA, Keels MA, Quiñonez RB, Roberts MW, Bordley WC. A policy review of after-hours emergency dental care responsibilities. *J Public Health Dent* 2016;76(4):263–268.
- Hammel JM, Fischel J. Dental Emergencies. *Emerg Med Clin North Am* 2019;37(1):81–93.
- Scheinfeld MH, Shifteh K, Avery LL, Dym H, Dym RJ. Teeth: what radiologists should know. *RadioGraphics* 2012;32(7):1927–1944.
- Gonzalez-Beicos A, Nunez D. Imaging of acute head and neck infections. *Radiol Clin North Am* 2012;50(1):73–83.
- Hayeri MR, Ziai P, Shehata ML, Teytelboym OM, Huang BK. Soft-Tissue Infections and Their Imaging Mimics:

- From Cellulitis to Necrotizing Fasciitis. *RadioGraphics* 2016;36(6):1888–1910.
6. Chapman MN, Nadgir RN, Akman AS, et al. Periapical lucency around the tooth: radiologic evaluation and differential diagnosis. *RadioGraphics* 2013;33(1):E15–E32.
 7. Capps EF, Kinsella JJ, Gupta M, Bhatki AM, Opatowsky MJ. Emergency imaging assessment of acute, nontraumatic conditions of the head and neck. *RadioGraphics* 2010;30(5):1335–1352.
 8. Henrot P, Blum A, Toussaint B, Troufleau P, Stines J, Roland J. Dynamic maneuvers in local staging of head and neck malignancies with current imaging techniques: principles and clinical applications. *RadioGraphics* 2003;23(5):1201–1213.
 9. Steinklein J, Nguyen V. Dental anatomy and pathology encountered on routine CT of the head and neck. *AJR Am J Roentgenol* 2013;201(6):W843–W853.
 10. Zohrabian VM, Poon CS, Abrahams JJ. Embryology and Anatomy of the Jaw and Dentition. *Semin Ultrasound CT MR* 2015;36(5):397–406.
 11. Husain MA. Dental Anatomy and Nomenclature for the Radiologist. *Radiol Clin North Am* 2018;56(1):1–11.
 12. Mardini S, Gohel A. Imaging of Odontogenic Infections. *Radiol Clin North Am* 2018;56(1):31–44.
 13. Lechien JR, Filleul O, Costa de Araujo P, Hsieh JW, Chantrain G, Saussez S. Chronic maxillary rhinosinusitis of dental origin: a systematic review of 674 patient cases. *Int J Otolaryngol* 2014;2014:465173.
 14. Matsumoto Y, Ikeda T, Yokoi H, Kohno N. Association between odontogenic infections and unilateral sinus opacification. *Auris Nasus Larynx* 2015;42(4):288–293.
 15. Bomeli SR, Branstetter BF 4th, Ferguson BJ. Frequency of a dental source for acute maxillary sinusitis. *Laryngoscope* 2009;119(3):580–584.
 16. Saibene AM, Vassena C, Pipolo C, et al. Odontogenic and rhinogenic chronic sinusitis: a modern microbiological comparison. *Int Forum Allergy Rhinol* 2016;6(1):41–45.
 17. Kuan EC, Suh JD. Systemic and Odontogenic Etiologies in Chronic Rhinosinusitis. *Otolaryngol Clin North Am* 2017;50(1):95–111.
 18. Mattos JL, Ferguson BJ, Lee S. Predictive factors in patients undergoing endoscopic sinus surgery for odontogenic sinusitis. *Int Forum Allergy Rhinol* 2016;6(7):697–700.
 19. Hegde AN, Mohan S, Pandya A, Shah GV. Imaging in infections of the head and neck. *Neuroimaging Clin N Am* 2012;22(4):727–754.
 20. Li RM, Kiemeny M. Infections of the Neck. *Emerg Med Clin North Am* 2019;37(1):95–107.
 21. Pak S, Cha D, Meyer C, Dee C, Fershko A. Ludwig's Angina. *Cureus* 2017;9(8):e1588.
 22. Curé JK, Vattoth S, Shah R. Radiopaque jaw lesions: an approach to the differential diagnosis. *RadioGraphics* 2012;32(7):1909–1925.
 23. Habib A, Sivaji N, Ashraf T. Maxillary Osteomyelitis: A Rare Entity. *Case Rep Otolaryngol* 2016;2016:9723806.
 24. Gupta D. Role of Maxillofacial Radiology and Imaging in the Diagnosis and Treatment of Osteomyelitis of the Jaws. *J Dent Oral Disord Ther* 2015;3(2):1–2.
 25. Desimpel J, Posadzy M, Vanhoenacker F. The Many Faces of Osteomyelitis: A Pictorial Review. *J Belg Soc Radiol* 2017;101(1):24.
 26. Lee YJ, Sadigh S, Mankad K, Kapse N, Rajeswaran G. The imaging of osteomyelitis. *Quant Imaging Med Surg* 2016;6(2):184–198.
 27. Thayil N, Chapman MN, Saito N, Fujita A, Sakai O. Magnetic Resonance Imaging of Acute Head and Neck Infections. *Magn Reson Imaging Clin N Am* 2016;24(2):345–367.
 28. Glendor U. Epidemiology of traumatic dental injuries: a 12 year review of the literature. *Dent Traumatol* 2008;24(6):603–611.
 29. Diangelis AJ, Andreasen JO, Ebeleseder KA, et al. International Association of Dental Traumatology guidelines for the management of traumatic dental injuries. I. Fractures and luxations of permanent teeth. *Dent Traumatol* 2012;28(1):2–12.
 30. Andersson L, Andreasen JO, Day P, et al. International Association of Dental Traumatology guidelines for the management of traumatic dental injuries. II. Avulsion of permanent teeth. *Dent Traumatol* 2012;28(2):88–96.
 31. Nalliah RP, Rampa S, Lee MK, Allareddy V, Allareddy V. Epidemiology and Outcomes of Hospital-based Emergency Department Visits with Tooth Fractures. *Pediatr Dent* 2015;37(4):348–354.
 32. Piccininni P, Clough A, Padilla R, Piccininni G. Dental and Orofacial Injuries. *Clin Sports Med* 2017;36(2):369–405.
 33. Andreasen FM, Kahler B. Diagnosis of acute dental trauma: the importance of standardized documentation—a review. *Dent Traumatol* 2015;31(5):340–349.
 34. American Academy on Pediatric Dentistry Council on Clinical Affairs. Guideline on management of acute dental trauma. *Pediatr Dent* 2008–2009;30(7 suppl):175–183.
 35. Mortazavi H, Baharvand M. Review of common conditions associated with periodontal ligament widening. *Imaging Sci Dent* 2016;46(4):229–237.
 36. Alimohammadi R. Imaging of Dentoalveolar and Jaw Trauma. *Radiol Clin North Am* 2018;56(1):105–124.
 37. Lodi G, Fugini L, Sardella A, Carrassi A, Del Fabbro M, Furness S. Antibiotics to prevent complications following tooth extractions. *Cochrane Database Syst Rev* 2012;11:CD003811.
 38. Baqain ZH, Karaky AA, Sawair F, Khraisat A, Duaibis R, Rajab LD. Frequency estimates and risk factors for postoperative morbidity after third molar removal: a prospective cohort study. *J Oral Maxillofac Surg* 2008;66(11):2276–2283.
 39. Weissman JL, Carrau RL. “Puffed-cheek” CT improves evaluation of the oral cavity. *AJNR Am J Neuroradiol* 2001;22(4):741–744.
 40. Miclotte I, Agbaje JO, Spaey Y, Legrand P, Politis C. Incidence and treatment of complications in patients who had third molars or other teeth extracted. *Br J Oral Maxillofac Surg* 2018;56(5):388–393.
 41. Dym H, Wolf JC. Oroantral communication. *Oral Maxillofac Surg Clin North Am* 2012;24(2):239–247, viii–ix.
 42. Bredesen K, Aaløkken TM, Kolbenstvedt A. CT of the oral vestibule with distended cheeks. *Acta Radiol* 2001;42(1):84–87.
 43. Petty B, Bezerra R, Berkowitz F, Mikula SK. Novel diagnostic method for oroantral fistulas. *Otolaryngol Head Neck Surg* 2013;149(5):791–792.
 44. Kretzschmar DP, Kretzschmar JL. Rhinosinusitis: review from a dental perspective. *Oral Surg Oral Med Oral Pathol Oral Radiol Endod* 2003;96(2):128–135.
 45. Zohrabian VM, Sonick M, Hwang D, Abrahams JJ. Dental Implants. *Semin Ultrasound CT MR* 2015;36(5):415–426.
 46. Guillaume B. Dental implants: a review. *Morphologie* 2016;100(331):189–198.
 47. Bathla SC, Fry RR, Majumdar K. Maxillary sinus augmentation. *J Indian Soc Periodontol* 2018;22(6):468–473.
 48. Liaw K, Delfini RH, Abrahams JJ. Dental Implant Complications. *Semin Ultrasound CT MR* 2015;36(5):427–433.
 49. Klinge B, Hultin M, Berglundh T. Peri-implantitis. *Dent Clin North Am* 2005;49(3):661–676, vii–viii.
 50. Sakka S, Baroudi K, Nassani MZ. Factors associated with early and late failure of dental implants. *J Investig Clin Dent* 2012;3(4):258–261.
 51. Morag Y, Morag-Hezroni M, Jamadar DA, et al. Bisphosphonate-related osteonecrosis of the jaw: a pictorial review. *RadioGraphics* 2009;29(7):1971–1984.
 52. Mücke T, Krestan CR, Mitchell DA, Kirschke JS, Wutzl A. Bisphosphonate and Medication-Related Osteonecrosis of the Jaw: A Review. *Semin Musculoskelet Radiol* 2016;20(3):305–314.

Traumatic Neck and Skull Base Injuries

John L. Go, MD

Jay Acharya, MD

Jasmine C. Branchcomb, MD

Anandh G. Rajamohan, MD

Abbreviations: BCVI = blunt cervicovascular injury; CSF = cerebrospinal fluid

RadioGraphics 2019; 39:1796–1807

<https://doi.org/10.1148/rg.2019190177>

Content Codes: **CT** **ER** **HN** **NR** **VA**

From the Division of Neuroradiology, Department of Radiology, Keck School of Medicine, University of Southern California, Los Angeles, Calif, and LAC+USC Medical Center, 1983 Marengo Street, D and T Tower, Room 3D321, Los Angeles, CA 90033. Received June 8, 2019; revision requested July 15 and received July 29; accepted July 30. For this journal-based SA-CME activity, the authors, editor, and reviewers have disclosed no relevant relationships.

Address correspondence to J.L.G. (e-mail: jlg@usc.edu).

©RSNA, 2019

SA-CME LEARNING OBJECTIVES

After completing this journal-based SA-CME activity, participants will be able to:

- Recognize traumatic neck and skull base injuries that warrant immediate surgical or endovascular treatment.
- Identify the anatomy of the neck and skull base relevant to traumatic injury.
- Describe typical imaging findings in the setting of cervicovascular, pharyngoesophageal, laryngotracheal, temporal bone, and skull base injuries.

See rsna.org/learning-center-rg.

Patients with blunt and penetrating traumatic injuries to the skull base and soft tissues of the neck present to the emergency department every day. Fortunately, truly life-threatening injuries to these regions are relatively uncommon. However, when encountered and not correctly diagnosed, these entities may result in severe morbidity or mortality. The radiologist plays a critical role recognizing these injuries, in which findings may often be subtle and the anatomy potentially challenging to identify. Multisection CT and CT angiography are commonly performed to assess these injuries in the emergency department. Vascular injury to the neck may result in dissection, occlusion, pseudoaneurysm formation, or frank extravasation resulting in stroke or death. Airway compromise may result from laryngotracheal injury. Injuries to the pharynx and esophagus may result in perforation. Injuries to the temporal bone may result in vascular injury to the internal carotid artery or facial nerve injury, which would require immediate surgery or intervention to prevent paralysis.

©RSNA, 2019 • radiographics.rsna.org

Introduction

In the emergency department, injuries to the neck and skull base may be readily apparent or inferred on the basis of the mechanism of injury. Blunt injury to the neck may result in bruising, ecchymosis, or hematoma at the site of injury. Dysphonia, dysphagia, or apparent deviation of the airway may be the result of extrinsic compression of the airway or direct injury to the larynx or pharynx. Palpable crepitus suggests the presence of a perforated viscus or laryngotracheal injury.

Acute neurologic symptoms associated with neck injury, such as acute stroke, cranial neuropathy, or Horner syndrome, may be the result of blunt cervicovascular injury (BCVI). The incidence of BCVI in the setting of blunt trauma ranges from 0.86% to 1.03%, with 53%–79% of patients asymptomatic at presentation (1,2).

Facial fractures may result in fractures of the anterior skull base, resulting in cerebrospinal fluid (CSF) rhinorrhea. The presence of a Battle sign, an ecchymosis postauricular in location, suggests a central skull base or temporal bone fracture. Other signs of temporal bone fracture include sudden onset of hearing loss, vertigo, or facial paralysis.

Penetrating trauma accounts for less than 1% of admissions to the emergency department (3). These types of injuries are evident at the time of patient presentation. The exact nature and course of the penetrating object may be difficult to ascertain clinically, and imaging is required. The decision of whether these patients should undergo immediate surgical exploration in the setting of life-threatening vascular or airway injury or undergo imaging is determined by the patient's stability at presentation and findings at initial clinical assessment.

TEACHING POINTS

- If there is a cervical fracture, care should be taken to determine if the fracture plane enters the transverse foramen or is close to the vertebral arteries. Fractures of the C1 ring or the C2 vertebral body may apply abnormal stretching to the vertebral artery, which may also result in injury.
- A number of different scales are used to characterize cerebrovascular injury, with the most common being the Biffi scale.
- The cricoid cartilage, the only complete cartilaginous ring within the larynx, maintains patency of the larynx. Fracture of the cricoid cartilage typically occurs in more than one place, and the lumen of the larynx may subsequently collapse.
- The type of injury to the larynx with the worst outcome is laryngotracheal separation. This typically occurs at the cricothyroid membrane and may be partial or complete. Significant subcutaneous emphysema is located around the larynx and visceral space on images, and it is usually fatal at the time of occurrence unless an artificial airway is established at the time of injury.
- If there is a bone fragment extending into the intratemporal facial canal in the setting of temporal bone fracture, facial nerve exploration at the site of fracture is required to prevent permanent disability. A complete and immediate facial paralysis also warrants immediate exploration of the intratemporal facial nerve at the site of injury.

Imaging of Neck and Skull Base Injuries

Imaging is vital for the modern evaluation of trauma, not only for diagnosing injury but also for providing anatomic assessment and other pertinent information needed for planning appropriate therapy or surgery. This is especially true in the neck, where external manifestations of trauma and physical examination findings may not completely reveal the extent of injury. Multidetector CT has revolutionized the diagnosis of injury to the neck and skull base region owing to the speed of acquisition and availability. Plain film radiography may be used sometimes in the initial diagnosis of bone or soft-tissue injury to the neck, showing findings of fracture, emphysema, soft-tissue swelling, and potential foreign bodies. However, the absence or presence of these findings on radiographs alone is simply not enough for key decision making.

On the other hand, multidetector CT of the head and neck can accurately help diagnose bone, soft-tissue, and vascular injuries with a high degree of diagnostic sensitivity and specificity. After initial volumetric acquisition in the axial plane using the thinnest sections possible, images are reconstructed in the three orthogonal planes for review at 1-mm intervals. Additional reformatted images are also obtained if needed by using a postprocessing workstation or readout workstation, if possible. Reformatted CT images also allow for optimal visualization of the aerodigestive tract and airway.

The decision to perform CT angiography of the head and neck after initial imaging of the

Table 1: Modified Denver Criteria

Risk factors

High-energy transfer mechanism with any of the following:

LeFort II or III fracture

Basilar skull fracture involving the carotid canal

Cervical vertebral body or transverse foramen fracture, subluxation, or ligamentous injury at any level; any fracture at C1–C3

Closed head injury consistent with DAI and GCS score <6

Near-hanging with anoxia

Clothesline-type injury or seat belt abrasion with significant swelling, pain, or altered mental status

Signs and symptoms

Arterial hemorrhage from neck, nose, or mouth

Cervical bruit (in patients <50 years of age)

Expanding cervical hematoma

Focal neurologic deficit: TIA, Horner syndrome, vertebrobasilar symptoms, hemiparesis

Stroke findings at CT or MRI

Neurologic deficit inconsistent with head CT findings

Sources.—References 1 and 4.

Note.—DAI = diffuse axonal injury, GCS = Glasgow Coma Scale, TIA = transient ischemic attacks.

brain, neck, and face is based on the findings at the patient's initial presentation to the emergency department, results of the initial assessment, and clinical suspicion of vascular injury. A number of clinical criteria have been used to determine the necessity for CT angiography of the head and neck, including the Denver criteria (Table 1) and the modified Memphis criteria (5).

MRI may also be used as an adjunct imaging modality, but it is not the primary modality of choice in the initial diagnosis of traumatic neck or skull base injuries given its potential lack of immediate availability for emergent workup, relatively long image acquisition times compared with those of CT, and inherent technical limitations in assessing the airway and aerodigestive tract owing to breathing artifact and susceptibility artifact related to the presence of air. T1-weighted images with fat saturation have been described as a potential tool to diagnose cervical vascular dissection and show high signal intensity of the intramural thrombus and/or diminished flow within the lumen (6), although detection of arterial injury can often be made more promptly at initial CT angiography. For these reasons, we focus on CT as the primary modality for traumatic neck and skull base injuries in this article.

Mechanism of Injury

Traumatic injury to the neck and skull base may be subdivided into nonpenetrating or penetrating trauma. Nonpenetrating trauma may result from a direct blow to the face and neck, resulting in fracture of the face, skull base, or cervical spine. A direct blow to the central aspect of the anterior neck may result in fracture of the laryngeal osteocartilaginous structures or injury to the laryngeal soft tissues or pharynx. Injury to the vascular structures may result in direct arterial injury, venous injury, or hematoma formation, which may impinge on the airway.

Penetrating trauma to the neck accounts for less than 1% of admissions to the emergency department (3). Penetrating trauma to the head and neck does not respect the normal fat planes, and ascertaining the path of the instrument or projectile necessitates evaluating all structures along its path. In the setting of a high-velocity projectile injury, vascular injury remote to the site of injury may occur owing to the resultant shock wave (7–10).

Relevant Anatomy and Injury Classification

In this article, the head and neck region includes the face and anterior and central skull base, with the inclusion of the temporal bones and neck. The orbit, cervical spine, and brachial plexus are reserved for a separate discussion. The neck is defined as the region extending from the skull base superiorly to the sternal notch (the superior margin of the first rib) and inferiorly to the T1 vertebral body. There are a number of classification systems for the anatomic categorization of the neck, including separation of the infrathyroid neck from the hyoid bone down to the clavicles and the suprathyroid neck from the hyoid bone up to the skull base.

In the suprathyroid neck, additional compartmental anatomy is often used for localizing injuries or other pathologic conditions. There are two primary fasciae in the neck with which to be familiar: the superficial cervical fascia and the deep cervical fascia.

The superficial cervical fascia is a thin connective tissue layer, lying between the dermis and the deep cervical fascia, and contains the platysma, subcutaneous blood vessels, and fat. The deep cervical fascia is comprised of three layers: superficial, middle, and deep layers. The superficial or investing layer of the deep cervical fascia encloses the sternocleidomastoid muscles, trapezius muscles, and masticatory muscles. The middle or pretracheal layer of the deep cervical fascia surrounds the pharynx and thyroid gland. The deep or prevertebral layer of the

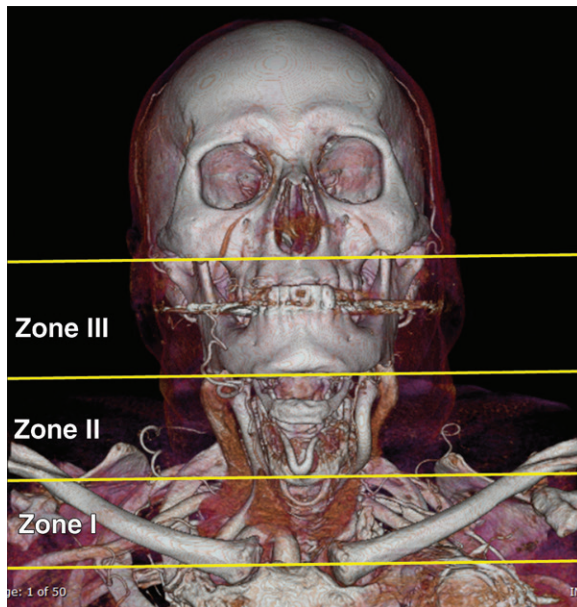


Figure 1. Zonal anatomy of the neck. Three-dimensional reconstructed CT image of the head and neck shows the three zones of the neck.

deep cervical fascia surrounds the perivertebral muscles and defines the posterior margin of the retropharyngeal space and the anterior margin of the prevertebral space. The deep cervical fascia layers subdivide and compartmentalize the neck into a series of spaces that, taken together, contain the main vital structures of the neck, including the major neurovascular bundles, cervical spine, and surrounding paravertebral musculature (11,12).

Wounds that penetrate into the deep cervical fascia of the neck put these vital structures at risk. Having a working knowledge of these spaces and how to describe them and the fascial anatomy may help the radiologist better characterize lacerations and penetrating wounds, patterns of subcutaneous emphysema, and areas of hematoma or contrast material extravasation.

Historically, zonal anatomy was used to describe the entry point of penetrating trauma to the neck based on physical examination findings (13,14) (Fig 1, Table 2). These zones were used to further classify neck trauma without clear indications for surgical exploration. A working knowledge of this zonal anatomy is necessary, as this may still be used by emergency and trauma physicians when describing neck injuries. Zone II is more accessible, and injuries within this zone are evaluated through surgical exploration (15). Zones I and III are more difficult to access through surgery; thus injuries in these zones are further evaluated more commonly at cross-sectional imaging. The task to diagnose clinically significant injuries and limit unnecessary surgi-

Table 2: Zonal Anatomy of the Neck

| Zone | Description |
|------|---------------------------------------------------------|
| I | From the sternal notch to the cricoid cartilage |
| II | From the cricoid cartilage to the angle of the mandible |
| III | From the angle of the mandible to the skull base |

cal neck exploration improved with the advent and implementation of CT (13,16).

For the radiologist, emergent injuries to the neck that extend beyond the deep cervical fascia can generally be subdivided as involving the central neck, resulting in laryngotracheal and/or pharyngoesophageal injury, and the lateral neck, with potential for cervicovascular injury. At the skull base and temporal bones, there may be emergent implications when fractures involve the carotid canal or extend to the cavernous sinuses. Fractures involving the facial canal may also potentially require urgent facial canal exploration and decompression. Paying careful attention to and reporting fractures that involve the skull base foramina can help prompt appropriate secondary imaging or potential treatment.

Cervicovascular Injury

Vascular injury to the vessels in the neck and skull base may range from minor injury requiring no intervention to catastrophic vascular rupture requiring emergent surgical or endovascular intervention. Important clinical information to note includes knowledge of a rapidly expanding hematoma in the neck; new onset of Horner syndrome; and other new neurologic deficits including cranial neuropathies or symptoms of acute stroke, which may manifest with acute vascular injury (17,18).

For many emergency department providers, penetrating trauma to the neck automatically warrants CT angiography (if the patient is hemodynamically stable) to further determine the extent and tract of the offending object to assess for vascular injury or active hemorrhage. Follow-up CT angiography is also vital for patients with established cervicovascular injuries or those who were initially too unstable for imaging and underwent open surgical exploration.

Fracture of the cervical spine may result in injury to the vertebral artery, as it travels within the transverse foramen within the lateral mass of the cervical vertebral bodies. The right and left vertebral arteries enter the transverse foramen as they ascend in the neck at the C5 or C6 level, respectively, and travel over the C1 level over the

superior arch of C1 to enter the foramen magnum. If there is a cervical fracture, care should be taken to determine if the fracture plane enters the transverse foramen or is close to the vertebral arteries. Fractures of the C1 ring or the C2 vertebral body may apply abnormal stretching to the vertebral artery, which may also result in injury (19–21).

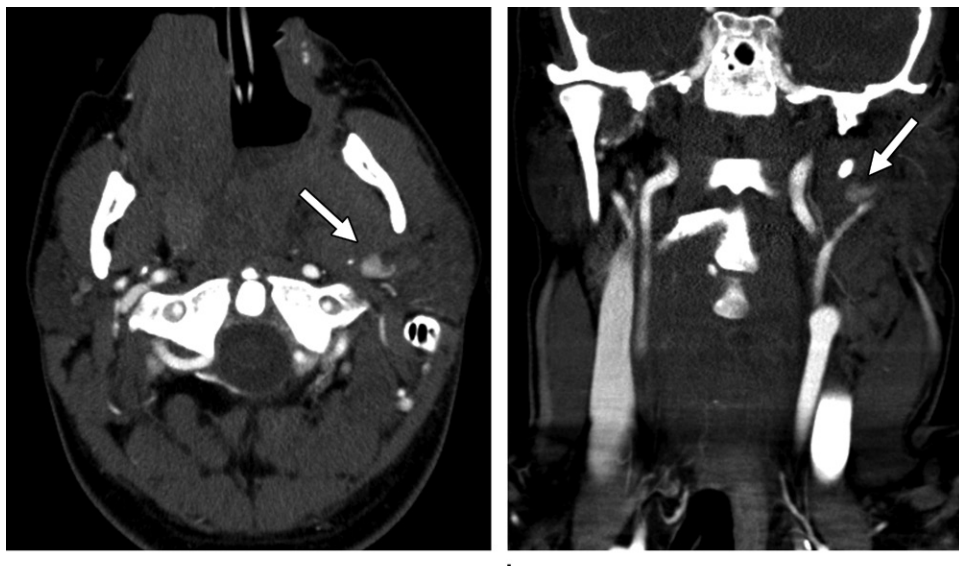
The aortic arch and great vessels should be individually inspected and should demonstrate a fat plane encircling the vessel. The vessel should be smooth and round in appearance and proximally to distally narrow from the parent vessel. Abrupt changes in vessel caliber, contour, wall thickening and/or irregularity, or loss of the fat plane around the vessels may represent underlying vascular injury. The vessels of the external carotid artery should also be inspected, as pseudoaneurysm formation or frank extravasation of contrast material may be present (Figs 2,3). Vascular occlusion, without active extravasation, of an external carotid artery branch does not typically necessitate treatment owing to the rich collateral circulation present.

The types of vascular injury include

(a) luminal narrowing owing to intimal or subintimal injury, (b) vascular dissection with the presence of a flap with a true and a false lumen or intramural thrombosis, and (c) frank vessel rupture. With traumatic dissection, thrombosis of the false lumen may cause tapering of the true lumen and occlusion. Rupture of the vessel may result in formation of a pseudoaneurysm, contained by the adventitia along the outer aspect of the vessel. Transection of the vessel may result in frank extravasation of contrast material, which may or may not be contained by surrounding hematoma. In penetrating ballistic injury, the kinetic energy released into the soft tissues may result in vascular injury away from the course of the projectile (9) (Fig 4). Venous injury may result in thrombosis or the formation of a hematoma and stranding of the surrounding fat but is generally not a life-threatening situation (22).

Biffl Scale for BCVI

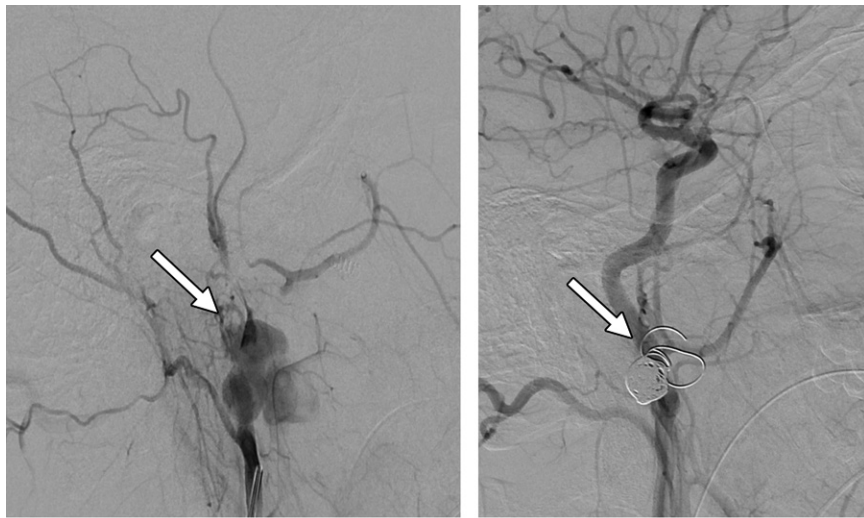
A number of different scales are used to characterize cerebrovascular injury, with the most common being the Biffl scale (Table 3) (23). The higher the grade, the worse the prognosis and the higher the risk for stroke. Grade I injuries heal over time and require no direct intervention. Grade II injuries are treated with heparin and potential endoluminal stent placement. Grade III injuries are treated nonsurgically with vascular stent placement in the parent vessel. Injection of thrombin into the pseudoaneurysm sac can also facilitate thrombosis (Fig 5). Grade IV injuries are difficult to manage, as the injured vessel often thromboses and cannot be



a.

b.

Figure 2. Left internal maxillary artery pseudoaneurysm in the neck. Axial (a) and coronal (b) CT angiograms show an area of contained contrast material opacification (arrow) arising from the left internal maxillary artery, a finding compatible with pseudoaneurysm formation (Biffl grade III BCVI). The contrast material is entirely contained, with no evidence of active extravasation outside the expanded pseudoaneurysm sac. Note that the attenuation of the contrast material in the pseudoaneurysm is slightly lower than that of the adjacent arterial structures, a finding that indicates slow filling owing to edema and hemorrhage.



a.

b.

Figure 3. Left internal maxillary artery pseudoaneurysm. (a) Lateral external carotid artery catheter angiogram shows a large multilobulated pseudoaneurysm (arrow). (b) Lateral common carotid artery catheter angiogram shows the coil (arrow) after coil embolization.

recanalized. Grade V injuries are typically lethal if left untreated and require immediate endovascular intervention or surgical repair (1).

Laryngotracheal Injury

Laryngotracheal injury results from blunt or penetrating trauma to the central neck. Blunt laryngotracheal injury is found most commonly in patients involved in motor vehicle collisions, but it can also manifest from hanging, strangulation, or a direct blow to the central neck (24).

Laryngotracheal injury owing to penetrating neck trauma accounts for 1%–7% of cases of penetrating trauma to the neck (15).

Evaluation for laryngeal patency is the most important initial step in cases of suspected or known laryngeal injury. Laryngeal compromise may be secondary to edema or extrinsic compression owing to hematoma or intramural hematoma (Fig 6). In the setting of supraglottic edema, CT is especially useful and may be the only method with which to evaluate the airway, as the passage

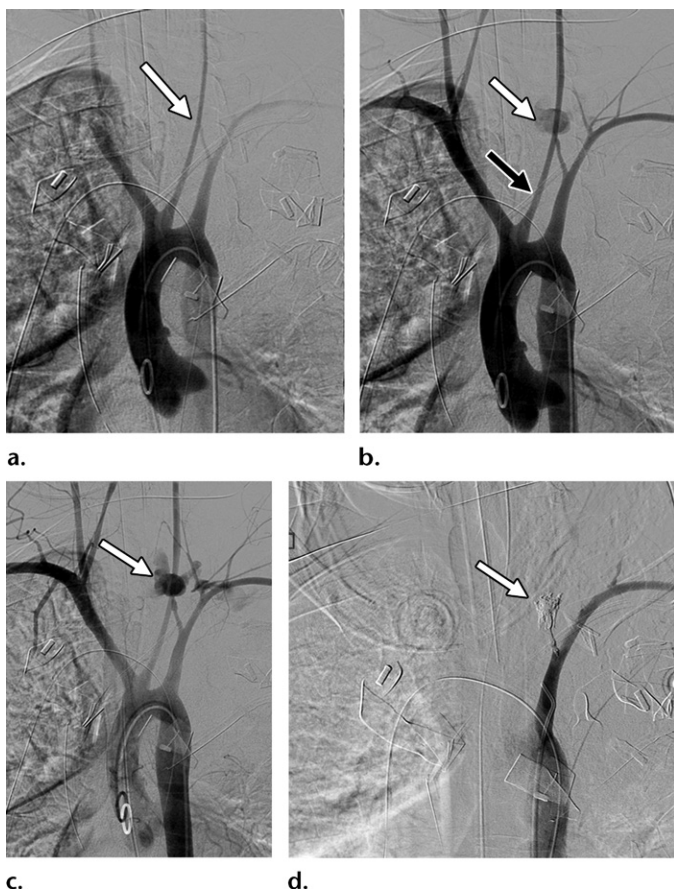


Figure 4. Left vertebral artery transection. Consecutive catheter aortograms obtained during coil embolization show lack of opacification of the left vertebral artery shortly beyond its origin, with extensive active extravasation of contrast material (white arrow) in this area. These findings are compatible with artery transection (Biffl grade V cerebrovascular injury). Coil embolization of the artery was performed, and the active hemorrhage was resolved. Fortunately, the left vertebral artery is nondominant. Note the smooth luminal narrowing (black arrow in **b**) of the proximal left common carotid artery, which may also reflect low-grade vascular injury (Biffl grade I) or a component of vasospasm.

Table 3: Biffl Scale for Blunt Cerebrovascular Injury

| Grade | Description |
|-------|----------------------------------------------------------------------------|
| I | Intimal injury or irregular intima |
| II | Dissection with an intimal flap causing luminal narrowing of less than 25% |
| III | Pseudoaneurysm formation |
| IV | Vessel occlusion or thrombosis |
| V | Vessel transection |

Source.—Reference 23.

of a laryngoscope for direct visualization may be limited (25). Asymmetric mucosal thickening and/or edema in the absence of extrinsic compression of the larynx should prompt close evaluation for mucosal tears and/or lacerations. CT may also effectively show suspicious patterns of emphysema associated with the larynx.

A direct blow to the larynx and supporting structures may result in fracture to the hyoid bone or cartilaginous injury, in addition to laryngeal compromise (Fig 7). The cartilaginous structures of the larynx include the epiglottis, thyroid cartilage, paired arytenoid cartilage, and cricoid cartilage. The epiglottis is a spoon-

shaped cartilaginous structure held in place by the hyoepiglottic ligament to the hyoid bone and the petiole to the larynx. Mucosal tear, rupture of the ligament, or cartilaginous fracture may occur (26,27). Mucosal tears of the aryepiglottic folds can also result in detachment of the epiglottis. The hyaline cartilage begins to demonstrate ossification in the 2nd decade of life, and determining if there is a fracture within the thyroid cartilage may be difficult.

A complete imaging evaluation should include inspection with both bone and soft-tissue window settings in all three planes. Fractures of the thyroid cartilage are most commonly vertical fractures of the thyroid laminae or through its midline aspect. Coronal reformatted images in conjunction with axial images can aid in determining the extent of the fracture, especially those with an oblique orientation. Fracture and/or dislocation of the greater or lesser cornu of the thyroid cartilage may also occur.

Injury at the level of the cricoarytenoid joint, located along the superior-posterior aspect of the cricoid cartilage, may result in subluxation or dislocation of the arytenoid cartilage. The most common type of injury of the arytenoid cartilage is anterior subluxation, and it is best depicted on parasagittal images. Because of malposition of the

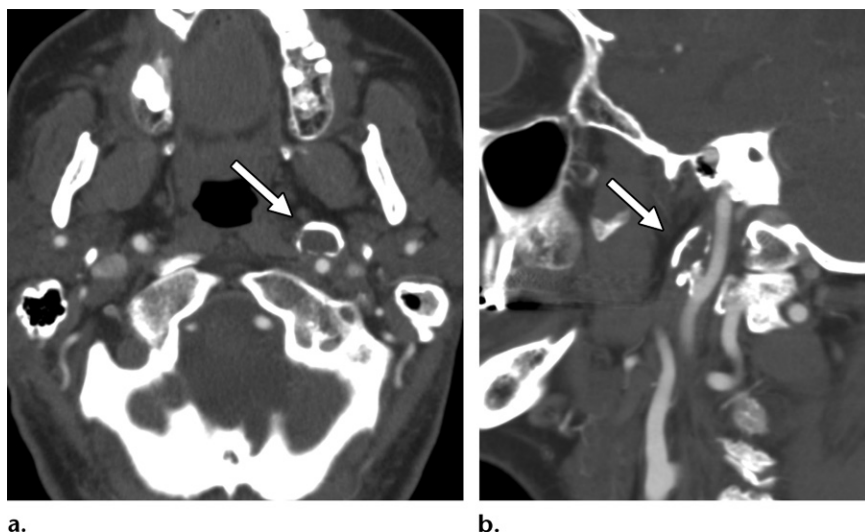


Figure 5. Thrombosed cervical internal carotid artery pseudoaneurysm in the neck. (a) Axial CT angiogram shows a thrombosed pseudoaneurysm (arrow) arising from the cervical segment of the left internal carotid artery. (b) Sagittal CT angiogram shows the thrombosed pseudoaneurysm (arrow) arising from the cervical segment of the left internal carotid artery. A narrow neck pseudoaneurysm may spontaneously thrombose over time. Thrombin injection into the pseudoaneurysm sac can also promote thrombosis of the pseudoaneurysm, but paying careful attention to avoid thrombus and embolism formation in the internal carotid artery is paramount.

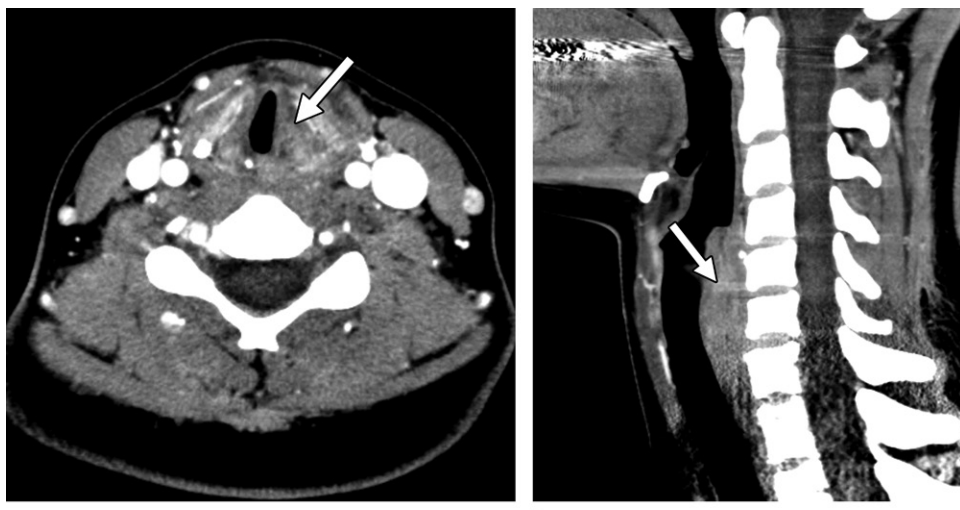


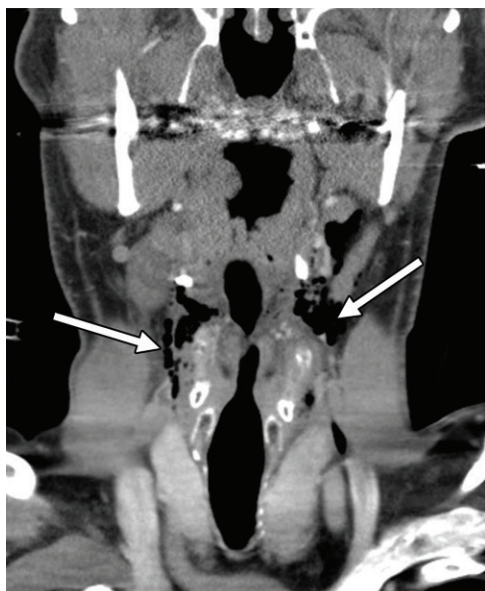
Figure 6. Laryngeal hematoma. (a) Axial contrast-enhanced CT image of the neck shows edema with hemorrhage in the left paralaryngeal space. Note the loss of the fat planes in the left paraglottic region and adjacent to the strap musculature. The airway at this level is mildly narrowed. The left true vocal fold (arrow) is medialized. (b) Sagittal contrast-enhanced CT image shows hematoma and edema in the posterior hypopharynx, without significant luminal compromise. Nonetheless, hemorrhage and edema can rapidly result in airway compromise, so continued monitoring and expeditious treatment are important.

arytenoid cartilage, findings on axial images may show loss of isomerism of the bilateral cricoarytenoid joints, with asymmetric appearance of the true vocal folds. The affected side may be in a more medial position, with laxity of the ipsilateral aryepiglottic fold. The determination of arytenoid cartilage subluxation is best visualized on sagittal images, as it can be missed on axial images.

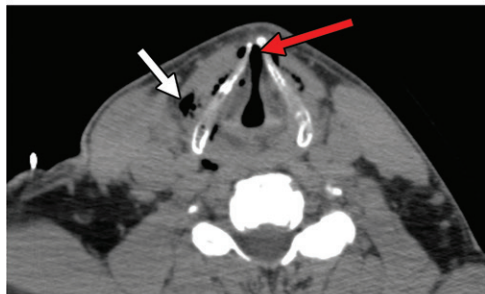
The cricoid cartilage, the only complete cartilaginous ring within the larynx, maintains

patency of the larynx. Fracture of the cricoid cartilage typically occurs in more than one place, and the lumen of the larynx may subsequently collapse (26–29) (Fig 8). On CT and MR images, the mucosal surface is thin and cannot be well visualized. Any soft-tissue thickening at the level of the cricoid cartilage within the subglottic larynx should therefore be considered abnormal.

The type of injury to the larynx with the worst outcome is laryngotracheal separation.



a.



b.

Figure 7. Laryngeal wall injury from attempted hanging. (a, b) Coronal (a) and axial (b) CT images of neck show significant subcutaneous gas (white arrows) adjacent to the thyroid cartilage and laryngeal soft tissues. Note the widening of the ventral soft tissues at the level of the false vocal folds (red arrow in b). (c) Sagittal CT image shows widening (arrow) of the ventral soft tissues at the level of the false vocal folds. Endoscopic examination results confirmed a laryngeal tear.



c.



a.



b.

Figure 8. Cricoid cartilage fracture in a patient with breathing difficulty. (a) Axial nonenhanced CT image of the cervical spine shows a displaced fracture (arrow) of the right cricoid arch. (b) Coronal nonenhanced CT image of the cervical spine shows luminal narrowing (arrow) of the right side of the laryngeal airway.

This typically occurs at the cricothyroid membrane and may be partial or complete. Significant subcutaneous emphysema is located around the larynx and visceral space on images, and it is usually fatal at the time of occurrence

unless an artificial airway is established at the time of injury. On rare occasions, patients can survive to present to the emergency department.

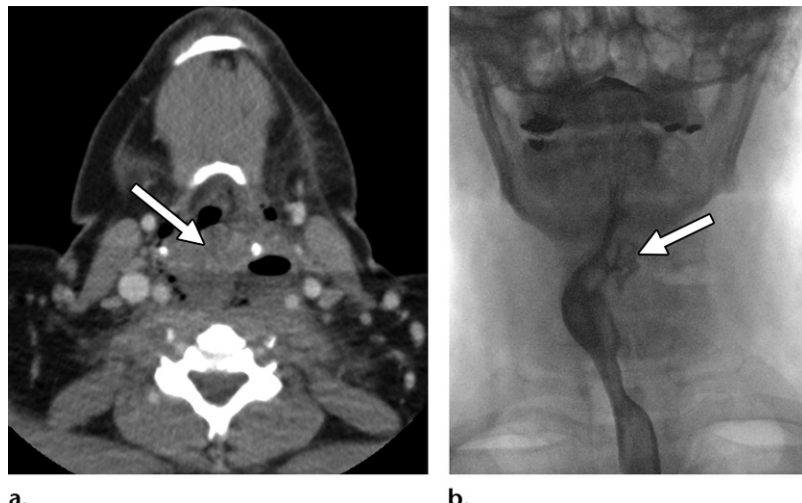
Laryngotracheal separation typically does not occur as an isolated event and may be associated

Table 4: Schaefer-Fuhrman Classification of Laryngeal Injury

| Grade | Injury Description |
|-------|-----------------------------------------------------------------------------------------------------------------------------------------------------------------|
| I | Minor endolaryngeal hematoma or laceration without detectable fracture; no airway compromise |
| II | Moderately severe edema, hematoma, or laceration without exposed cartilage or nondisplaced fracture; partial airway compromise with varying degrees of severity |
| III | Massive laryngeal edema, large mucosal lacerations, exposed cartilage, displaced fracture, or vocal cord immobility, with associated airway compromise |
| IV | Grade III findings with more severe anterior laryngeal disruption, unstable fracture, two or more fracture lines, or severe mucosal injuries |
| V | Complete laryngotracheal separation |

Source.—Reference 32.

Figure 9. Cervical esophageal injury. **(a)** Axial contrast-enhanced CT image of the neck shows gas and hemorrhage (arrow) in the region of the hypopharynx. Note the anterior displacement of the hypopharyngeal soft tissues owing to hematoma and edema from the injury. **(b)** Frontal esophagram shows an area of contrast material leakage (arrow) and rightward displacement of the hypopharyngeal soft tissues and cervical esophagus owing to the hematoma and edema from the injury.



with other injuries, including cartilaginous injury and associated carotid injury (7,30,31). If there is a complete laryngotracheal separation, there is inferior displacement of the trachea relative to the larynx at the site of the complete tear. There is also superior migration of the hyoid bone relative to the lower margin of the mandible. The Schaefer-Fuhrman classification system is used to classify laryngotracheal injury (32) (Table 4).

Pharyngoesophageal Injury

The vast majority of pharyngoesophageal injuries occur due to penetrating trauma and are diagnosed in approximately 1%–7% of traumatic head and neck injuries (15). The presence of subcutaneous air within the deep spaces of the neck should raise the possibility of pharyngoesophageal injury in addition to laryngeal injury. The trajectory of the offending instrument should be determined in an attempt to project the site of perforation.

The presence of mural or extrinsic hematoma and loss of fat planes surrounding the pharynx may also guide the determination of the site of perfora-

tion. As oral contrast material is typically not administered at contrast-enhanced CT or CT angiography of the neck, the presence of subcutaneous air within the deep spaces should trigger a swallow study with oral contrast material if endoscopy has not been performed (Fig 9). Not all perforations of the pharyngoesophageal region may demonstrate the presence of subcutaneous emphysema, although there may be irregularity of the mucosa or wall at imaging at the site of the tear. Endoscopy is complementary to CT in depicting the perforation and demonstrates sensitivity of 50%–60% and specificity of 100% (15, 33–35) (Fig 10).

Temporal Bone and Skull Base Fractures

Most fractures of the petrous temporal bone are the result of blunt trauma and are not treated in the emergency setting. However, facial nerve injury in the setting of temporal bone fracture may result in facial nerve paralysis and should prompt further evaluation with temporal bone CT. Additional indications for temporal bone CT include sudden

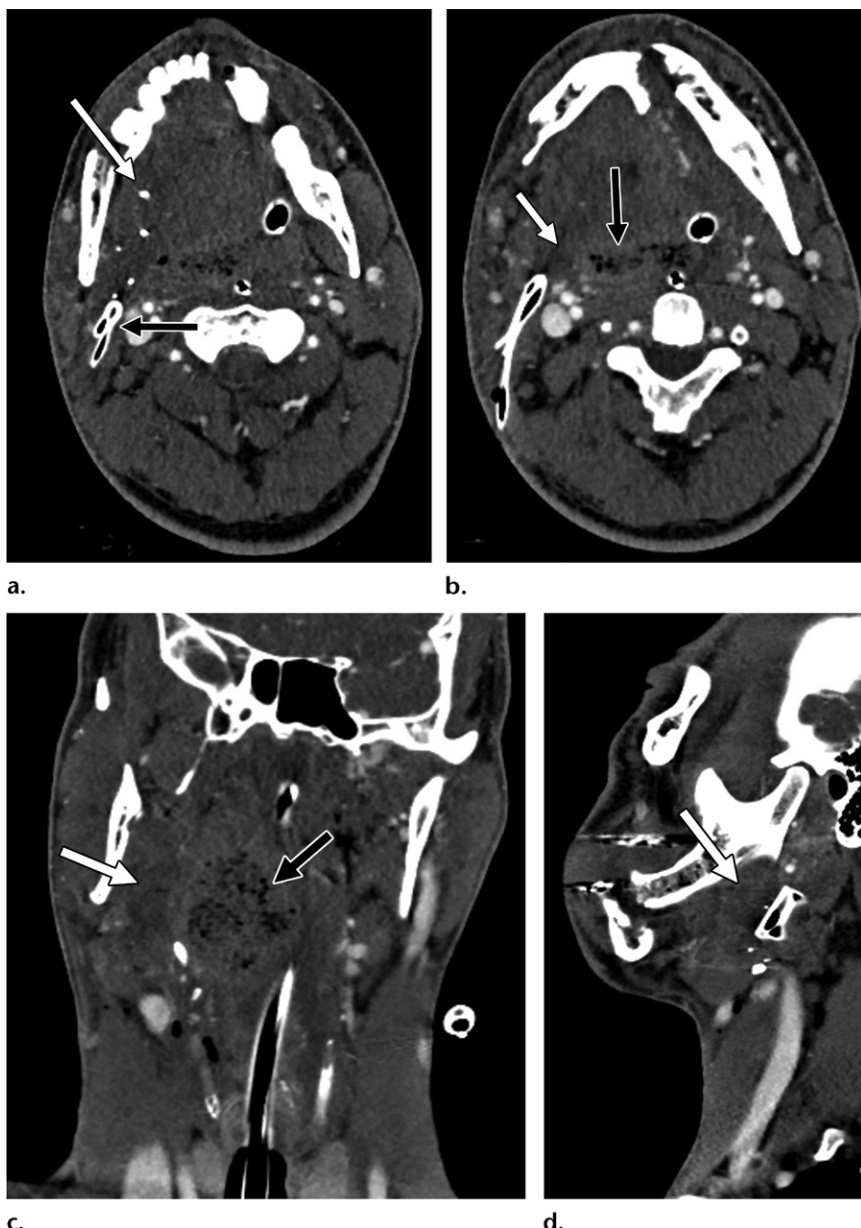


Figure 10. Lateral pharyngeal wall injury in a patient after surgery for primary repair of the pharynx. (a) Axial CT angiogram of the neck shows metallic ballistic material coursing along the right side of the oropharynx (white arrow) and a surgical drainage catheter (black arrow). (b) Axial CT angiogram obtained at a different level shows significant edema (white arrow) in the right oropharyngeal area. Surgical packing material (black arrow) is also depicted. (c) Coronal CT angiogram shows the edema in the right oropharynx (white arrow) and the surgical packing material in the neck (black arrow). (d) Sagittal CT angiogram shows edema (arrow) along the medial aspect of the mandible, along the course of the ballistic material.

conductive or sensorineural hearing loss, CSF leak, suspicion of an acute vascular injury, or preparation for immediate or potential surgical intervention (5).

Fractures of the temporal bone were historically classified based on the orientation of the fracture plane along the petrous ridge. Longitudinal fractures are oriented parallel to the long axis of the petrous ridge, from the external auditory canal toward the foramen ovale, anterior to the otic capsule. Transverse fractures are oriented perpendicular to the long axis of the petrous

ridge, from the foramen magnum toward the foramen spinosum, and often involve the internal auditory canal (1). A more recent classification system categorizes injuries as otic capsule violating or otic capsule sparing, which provides a description of both the fracture location and risk of functional complications (2).

Both otic capsule–sparing (longitudinal) and otic capsule–violating (transverse) fractures of the temporal bone may result in facial nerve injury, as the fracture plane may extend to the

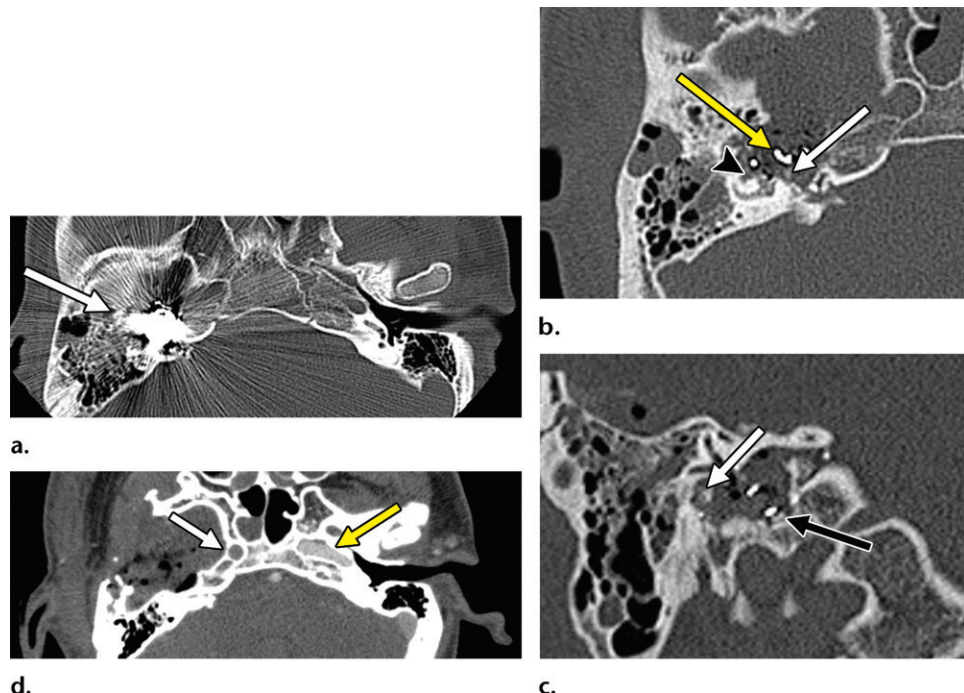


Figure 11. Facial nerve and internal carotid artery injury in a patient with immediate right facial nerve paralysis after a facial gunshot injury who immediately underwent surgery owing to high suspicion for petrous internal carotid artery injury. **(a)** Preoperative axial CT image of the temporal bones shows a bullet (arrow) lodged in the right petrous apex. **(b)** Postoperative axial CT image shows hyperattenuating curvilinear surgical ligation material (yellow arrow) in the internal carotid artery. There is also disruption of the labyrinthine and geniculate segments of the facial nerve canal (white arrow). Note the osseous fragments (arrowhead) in the vestibule, with associated injury to the anterior limb of the lateral semicircular canal. **(c)** Coronal CT image shows injury to the tympanic segment (white arrow) of the facial nerve canal, which courses inferior to the lateral semicircular canal. Surgical ligation material (black arrow) is also depicted. **(d)** Axial CT angiogram at the level of the skull base shows lack of enhancement of the right internal carotid artery (white arrow) owing to the emergent surgical ligation of the artery. The enhanced normal left internal carotid artery (yellow arrow) is also depicted.

intratemporal facial canal. Otic capsule–sparing fractures, involving the proximal tympanic segment of the facial canal, occur in 10%–20% of cases. Otic capsule–violating fractures typically involve the distal tympanic or mastoid segment of the facial canal, occurring in 50%–60% of cases. If there is a bone fragment extending into the intratemporal facial canal in the setting of temporal bone fracture, facial nerve exploration at the site of fracture is required to prevent permanent disability. A complete and immediate facial paralysis also warrants immediate exploration of the intratemporal facial nerve at the site of injury (14).

Morbidity is higher with otic capsule–violating fractures. Although the fracture plane may extend to the facial canal, secondary edema may result in facial paralysis and is treated with systemic steroid therapy. Fractures of the central skull base may extend to the foramen lacerum or carotid canals, resulting in carotid vascular injury (Fig 11). Fractures extending to the cavernous sinus may also result in carotid injury with carotid–cavernous sinus fistula or cavernous sinus thrombosis.

Properly identifying and reporting fractures involving the anterior skull base is also critical, as these fractures may result in CSF leak causing intracranial hypotension and may become a route for the spread of infection. Such injuries may be repaired in the acute setting. In addition, notifying the clinical team of an anterior skull base fracture involving the cribriform plate and/or fovea ethmoidalis may help prevent inadvertent intracranial penetration by support tubes (eg, a nasogastric tube). This is a key area where the radiologist can provide value.

Conclusion

Neck and skull base traumatic emergencies require that the radiologist have a familiarity with key anatomy and knowledge of imaging findings to properly describe, diagnose, and classify injuries. CT and CT angiography are the imaging modalities of choice for both blunt and penetrating trauma to this region, as they allow the radiologist to identify and properly characterize cervico-vascular, laryngotracheal, pharyngoesophageal, temporal bone, and skull base injuries. Detailed

assessment and reporting of critical findings allows the radiologist to convey the information necessary to determine appropriate time-sensitive surgery, endovascular care, and follow-up.

References

- Biffl WL, Moore EE, Ryu RK, et al. The unrecognized epidemic of blunt carotid arterial injuries: early diagnosis improves neurologic outcome. *Ann Surg* 1998;228(4):462–470.
- Miller PR, Fabian TC, Croce MA, et al. Prospective screening for blunt cerebrovascular injuries: analysis of diagnostic modalities and outcomes. *Ann Surg* 2002;236(3):386–393; discussion 393–395.
- Evans C, Chaplin T, Zelt D. Management of Major Vascular Injuries: Neck, Extremities, and Other Things that Bleed. *Emerg Med Clin North Am* 2018;36(1):181–202.
- Geddes AE, Burlew CC, Wagenaar AE, et al. Expanded screening criteria for blunt cerebrovascular injury: a bigger impact than anticipated. *Am J Surg* 2016;212(6):1167–1174.
- Malhotra A, Wu X, Seifert K. Blunt Cerebrovascular Injuries: Advances in Screening, Imaging, and Management Trends. *AJNR Am J Neuroradiol* 2018;39(9):E103.
- Snow RB, Zimmerman RD, Gandy SE, Deck MD. Comparison of magnetic resonance imaging and computed tomography in the evaluation of head injury. *Neurosurgery* 1986;18(1):45–52.
- Becker M, Leuchter I, Platon A, Becker CD, Dulguerov P, Varoquaux A. Imaging of laryngeal trauma. *Eur J Radiol* 2014;83(1):142–154.
- Bodanapally UK, Sliker CW. Imaging of Blunt and Penetrating Craniocervical Arterial Injuries. *Semin Roentgenol* 2016;51(3):152–164.
- Holt GR, Kostohryz G Jr. Wound ballistics of gunshot injuries to the head and neck. *Arch Otolaryngol* 1983;109(5):313–318.
- Nowicki JL, Stew B, Ooi E. Penetrating neck injuries: a guide to evaluation and management. *Ann R Coll Surg Engl* 2018;100(1):6–11.
- Harmsberger HR, Glastonbury CM, Michel MA, Koch BL. Diagnostic Imaging: Head and Neck. Philadelphia, Pa: Lippincott Williams & Wilkins, 2010.
- Mukherji SK, Castillo M. A simplified approach to the spaces of the suprathyroid neck. *Radiol Clin North Am* 1998;36(5):761–780, v.
- Roon AJ, Christensen N. Evaluation and treatment of penetrating cervical injuries. *J Trauma* 1979;19(6):391–397.
- Monson DO, Saletta JD, Freeark RJ. Carotid vertebral trauma. *J Trauma* 1969;9(12):987–999.
- Steenburg SD, Sliker CW, Shanmuganathan K, Siegel EL. Imaging evaluation of penetrating neck injuries. *RadioGraphics* 2010;30(4):869–886.
- Bell RB, Osborn T, Dierks EJ, Potter BE, Long WB. Management of penetrating neck injuries: a new paradigm for civilian trauma. *J Oral Maxillofac Surg* 2007;65(4):691–705.
- Anson J, Crowell RM. Cervicocranial arterial dissection. *Neurosurgery* 1991;29(1):89–96.
- Hart RG, Easton JD. Dissections of cervical and cerebral arteries. *Neurol Clin* 1983;1(1):155–182.
- Hart RG. Vertebral artery dissection. *Neurology* 1988;38(6):987–989.
- Schellhas KP, Latchaw RE, Wendling LR, Gold LH. Vertebralbasilar injuries following cervical manipulation. *JAMA* 1980;244(13):1450–1453.
- Sheth RD, Jaynes M, Gingold M, Ortiz O, Bodensteiner JB. Stroke due to a traumatic vertebral artery dissection in a girl. *Clin Pediatr (Phila)* 1994;33(8):503–506.
- Stallmeyer MJ, Morales RE, Flanders AE. Imaging of traumatic neurovascular injury. *Radiol Clin North Am* 2006;44(1):13–39, vii.
- Biffl WL, Moore EE, Offner PJ, Brega KE, Franciose RJ, Burch JM. Blunt carotid arterial injuries: implications of a new grading scale. *J Trauma* 1999;47(5):845–853.
- Al-Khalifa M, Buali F, Alshehabi M. Common Findings in Blunt Thyroid Fracture. *Saudi J Med Med Sci* 2017;5(3):267–270.
- Shi J, Uyeda JW, Duran-Mendicuti A, Potter CA, Nunez DB. Multidetector CT of Laryngeal Injuries: Principles of Injury Recognition. *RadioGraphics* 2019;39(3):879–892.
- Jalisi S, Zoccoli M. Management of laryngeal fractures: a 10-year experience. *J Voice* 2011;25(4):473–479.
- Robinson S, Juutilainen M, Suomalainen A, Mäkitie AA. Multidetector row computed tomography of the injured larynx after trauma. *Semin Ultrasound CT MR* 2009;30(3):188–194.
- Alexander AE Jr, Lyons GD, Fazekas-May MA, et al. Utility of helical computed tomography in the study of arytenoid dislocation and arytenoid subluxation. *Ann Otol Rhinol Laryngol* 1997;106(12):1020–1023.
- Bernat RA, Zimmerman JM, Keane WM, Pribitkin EA. Combined laryngotracheal separation and esophageal injury following blunt neck trauma. *Facial Plast Surg* 2005;21(3):187–190.
- Reynolds JK, Dart BW 4th, Maxwell RA, Barnes DR. Tracheal transection with associated bilateral carotid and esophageal injuries after blunt neck trauma. *Am Surg* 2014;80(8):E232–E233.
- Tobias ME, Sack AD, Carter G, McIntosh WA. Cricotracheal separation in blunt neck injury: the sign of hyoid bone elevation—A case report. *S Afr J Surg* 1989;27(5):189–191.
- Schaefer SD. The acute management of external laryngeal trauma: A 27-year experience. *Arch Otolaryngol Head Neck Surg* 1992;118(6):598–604.
- Català J, Puig J, Muñoz JM, Vivancos J, Llopard JR. Perforation of the pharynx caused by blunt external neck trauma. *Eur Radiol* 1998;8(1):137–140.
- Demetriades D, Velmahos GG, Asensio JA. Cervical pharyngoesophageal and laryngotracheal injuries. *World J Surg* 2001;25(8):1044–1048.
- Soliman AM, Ahmad SM, Roy D. The role of aerodigestive tract endoscopy in penetrating neck trauma. *Laryngoscope* 2014;124(Suppl 7):S1–S9.

Nontraumatic Head and Neck Emergencies

Shervin Kamalian, MD, MSc

Laura Avery, MD

Michael H. Lev, MD

Pamela W. Schaefer, MD

Hugh D. Curtin, MD

Shahmir Kamalian, MD

Abbreviation: ACE = angiotensin-converting enzyme

RadioGraphics 2019; 39:1808–1823

<https://doi.org/10.1148/rg.2019190159>

Content Codes: **CT** **ER** **HN** **MR** **NR**

From the Department of Radiology, Division of Emergency Radiology, Massachusetts General Hospital, 55 Fruit St, Blake SB Rm 0029A, Boston, MA 02114 (Shervin Kamalian, L.A., M.H.L., P.W.S., Shahmir Kamalian); and Department of Radiology, Massachusetts Eye and Ear Infirmary, Boston, Mass (H.D.C.). Presented as an education exhibit at the 2018 RSNA Annual Meeting. Received May 20, 2019; revision requested July 10 and received July 24; accepted July 29. For this journal-based SA-CME activity, the authors, editor, and reviewers have disclosed no relevant relationships. **Address correspondence to** Shahmir Kamalian (e-mail: skamalian@mgh.harvard.edu).

©RSNA, 2019

SA-CME LEARNING OBJECTIVES

After completing this journal-based SA-CME activity, participants will be able to:

- Describe fascial planes and spaces of the neck and other relevant head and neck anatomic landmarks.
- Identify a wide variety of acute infectious and inflammatory diseases of the head and neck and their acute complications.
- Recognize acute complications of head and neck neoplasms that bring patients to the emergency department.

See rsna.org/learning-center-rg.

Head and neck imaging is an intimidating subject for many radiologists because of the complex anatomy and potentially serious consequences of delayed or improper diagnosis of the diverse abnormalities involving this region. The purpose of this article is to help radiologists to understand the intricate anatomy of the head and neck and to review the imaging appearances of a variety of nontraumatic head and neck conditions that bring patients to the emergency department, including acute infectious and inflammatory diseases and acute complications of head and neck neoplasms. These conditions are presented in five sections on the basis of their primary location of involvement: the oral cavity and pharynx, neck, sinusal tract, orbits, and ears. Important anatomic landmarks are reviewed briefly in each related section.

Online supplemental material is available for this article.

©RSNA, 2019 • radiographics.rsna.org

Introduction

Patients present to the emergency department with symptoms of a variety of infectious and inflammatory diseases and with acute complications of neoplasms of the head and neck. Infections are more common than the other types of diseases, and they usually are treated by primary care providers in the absence of serious complications (1). Although complications can occur in otherwise healthy individuals, older patients and those with diabetes or a compromised immune system are at increased risk for complications (1,2). Delayed or improper diagnosis can lead to substantial morbidity or mortality (3–7); therefore, radiologists should be familiar with these conditions and scrutinize all patients for related clinical and imaging findings. Specifically, radiologists should pay attention to airway patency; vascular complications such as thrombosis, pseudoaneurysm formation, and hemorrhage; and spread of diseases to the mediastinum, spine, or intracranial compartments.

In this article, we review the fascial planes and spaces of the neck. The fascial planes are important barriers to the spread of abnormalities. However, once a disease is established in the spaces of the neck, the fascial planes provide specific routes of dissemination of the disease. Although the fascial layers are not seen at imaging, radiologists should be aware of them for proper interpretation of images and detection of potential complications.

We review a variety of acute infectious and inflammatory diseases of the head and neck and potentially life-threatening acute complications of head and neck cancers. The diseases are organized into five sections according to their primary location of involvement: the oral cavity and pharynx, the neck, the sinusal tract, the orbits, and the ears. Abnormalities of the neck are arranged according to location involved when possible, but they overlap, and sometimes multiple spaces are involved.

TEACHING POINTS

- Above the hyoid bone, the posterior aspect of the middle layer of the deep cervical fascia (or buccopharyngeal fascia) continues to the skull base and covers the pharyngeal constrictor muscles. However, above the carotid bifurcation, the contribution of the middle layer to the carotid sheath is inconsistent; it does not form a well-defined sheath around the internal and external carotid arteries and the internal jugular vein.
- The retropharyngeal space extends from the skull base to the thoracocervical junction as the alar fascia attaches to the buccopharyngeal fascia somewhere between the C6 and T4 vertebral levels.
- If the masticator space is involved, the infection has the potential to extend intracranially through the foramen ovale, along the course of the mandibular nerve (V3 branch of the trigeminal nerve).
- CT allows the radiologist to localize the infection accurately and distinguish a true abscess from retropharyngeal edema. Accurate diagnosis is important to avoid unnecessary and potentially harmful surgery for drainage of a reactive noninfected effusion. A true abscess appears as a rim-enhancing hypoattenuating collection that expands the retropharyngeal space and may contain foci of air.
- The degree of sinonasal mucosal thickening and opacification may be minimal and is not sensitive or specific for diagnosis of invasive fungal sinusitis in at-risk patients. Subtle stranding of the periantral fat can be the first imaging finding of vascular invasion and spread of infection beyond the sinuses.

Neck Anatomy

The neck is enclosed by the superficial and deep cervical fasciae. The superficial cervical fascia is not a true fascial sheath and is composed of fatty connective tissue between the skin and the superficial layer of the deep cervical fascia. It contains fat, the platysma muscle, nerve endings, lymph vessels, and portions of the anterior and external jugular veins (Fig 1a, 1b) (8). The deep cervical fascia is composed of three layers: the superficial, middle, and deep layers of the deep cervical fascia. These layers divide the neck into multiple spaces. The neck spaces are further divided into the suprathyroid and infrathyroid spaces, because the deep cervical fascial anatomy is slightly different above and below the level of the hyoid bone. However, some of these spaces cross the hyoid bone level and run throughout the entire neck (Table) (8).

Superficial Layer of the Deep Cervical Fascia

The superficial layer of the deep cervical fascia encases the entire neck deeper than the platysma. It splits and encloses the sternocleidomastoid and trapezius muscles in both the infrathyroid and suprathyroid neck and attaches posteriorly to the ligamentum nuchae and vertebral spinous processes (Fig 1a). In the suprathyroid neck, the superficial layer of the deep cervical fascia also splits, forming the masticator space and the submandibular and parotid gland

capsules (Fig 1b). The masticator space contains the temporalis, masseter, and pterygoid muscles, the ramus of the mandible, the mandibular nerve (V3 branch of the trigeminal nerve), the pterygoid venous plexus, and the trigeminal fat pad (8).

Middle Layer of the Deep Cervical Fascia

The middle layer of the deep cervical fascia encases all of the visceral organs and forms the visceral space in the infrathyroid neck. It contains the cervical esophagus, larynx, trachea, thyroid gland, parathyroid glands, visceral lymph nodes, and recurrent laryngeal nerves. In the infrathyroid neck, all three layers of the deep cervical fascia join to form the carotid sheath (Fig 1a). Above the hyoid bone, the posterior aspect of the middle layer of the deep cervical fascia (or buccopharyngeal fascia) continues to the skull base and covers the pharyngeal constrictor muscles. However, above the carotid bifurcation, the contribution of the middle layer to the carotid sheath is inconsistent; it does not form a well-defined sheath around the internal and external carotid arteries and the internal jugular vein (Fig 1b). Therefore, many experts recommend the use of the term *poststyloid* (or *retrostyloid*) *parapharyngeal space* instead of the terms *carotid sheath* and *carotid space* in the suprathyroid neck. The parapharyngeal space is divided into the prestyloid and poststyloid spaces by the tensor-vascular-styloid fascia, which runs approximately along a straight line from the styloid process to the medial pterygoid plate on each side (8).

Deep Layer of the Deep Cervical Fascia

The deep layer of the deep cervical fascia encases the paravertebral muscles and forms the perivertebral space. The deep layer attaches to the ligamentum nuchae and vertebral spinous processes posteriorly, similar to the superficial layer (Fig 1a, 1b). On each side, a flap extends to the cervical transverse processes posterior to the scalene muscles and divides the perivertebral space into the prevertebral component (anterior) and the paraspinal compartment (posterior) (8).

Anterior and medial to the scalene muscles, the deep layer splits into two leaves (Fig 1). The dorsal leaf is the *prevertebral fascia*, which is against the prevertebral muscles and the anterior longitudinal ligament. The ventral leaf is called the *alar fascia*. The space between the prevertebral fascia and the alar fascia is called the *danger space*. The space between the alar fascia and the posterior aspect of the middle layer of the deep cervical fascia (or the *buccopharyngeal fascia*) is called the *retropharyngeal space*. Finally, the space between the prevertebral fascia and the spine is called the *prevertebral space* (8).

The retropharyngeal space extends from the skull base to the thoracocervical junction as the

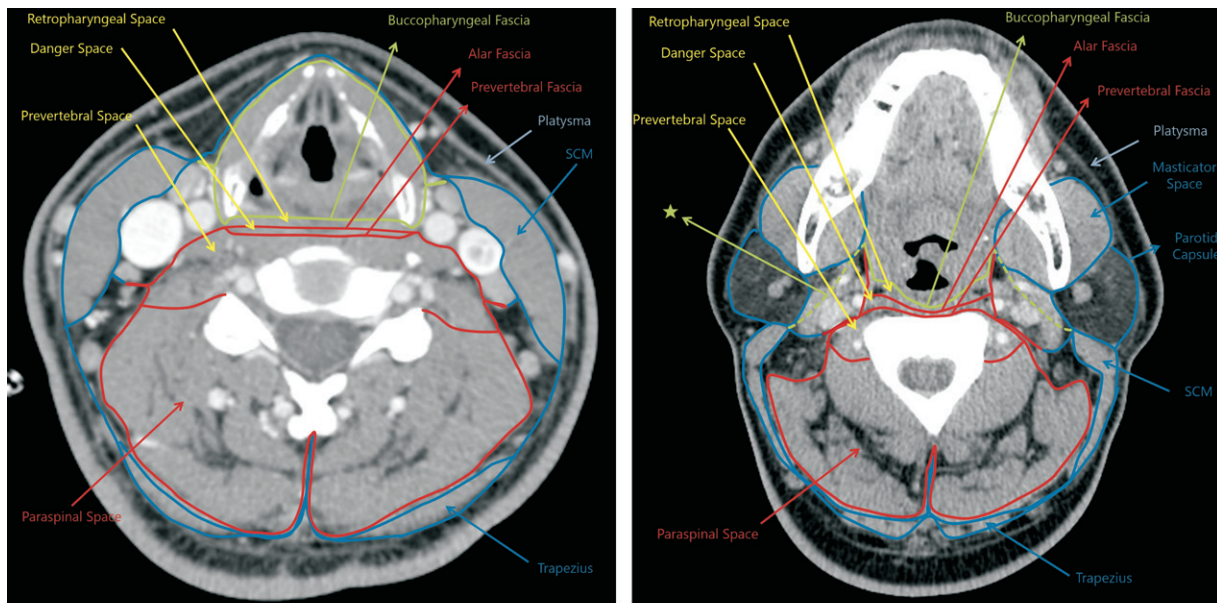
**a.**

Figure 1. Fascial sheaths and spaces. (a, b) Axial CT images show the fascial sheaths in the infrahyoid (a) and suprathyroid (b) neck and the superficial (blue lines), middle (green lines), and deep (red lines) layers of the deep cervical fascia. The contribution of the middle layer of the deep cervical fascia to the carotid sheath is inconsistent and incomplete in the suprathyroid neck (★ in b). SCM = sternocleidomastoid muscle. (c) Illustration shows the extent of the retropharyngeal and danger spaces.

alar fascia attaches to the buccopharyngeal fascia somewhere between the C6 and T4 vertebral levels (Fig 1c). The retropharyngeal space contains fat and deep cervical lymph nodes, including the lateral and medial retropharyngeal lymph nodes. A retropharyngeal abscess can form from an infected lymph node or direct spread (eg, penetrating trauma violating the buccopharyngeal fascia) (8).

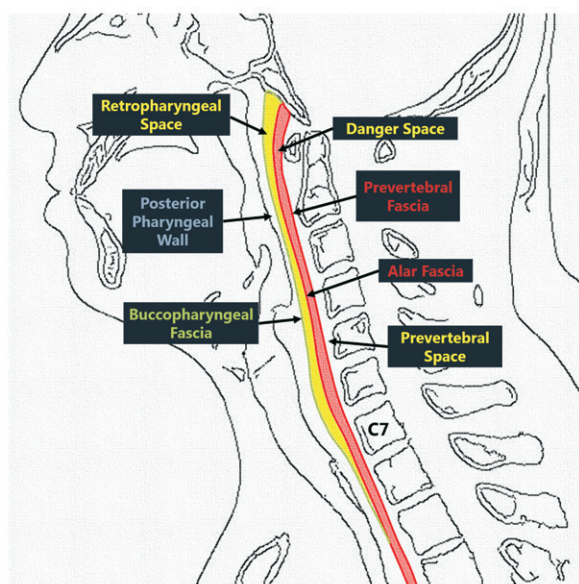
The danger space contains a small amount of loose fatty connective tissue and extends from the skull base to the mediastinum. The alar fascia is a well-defined structure in the midline at the level of C1, but it does not reach the skull base laterally and provides a potential point of entry into the danger space (9). If infection spreads to this space (eg, by direct spread or through the gap between C1 and the skull base), it can extend inferiorly to the chest and cause mediastinitis (Fig 1c) (8).

The prevertebral space contains muscles, vertebral arteries, and parts of the brachial plexus. The prevertebral fascia and space extend from the skull base along the entire spine. If infection involves this space, it has the potential to extend all the way to the coccyx (8).

Oral Cavity and Pharynx

Odontogenic Infection

Odontogenic infection is the most common cause of deep neck infection in adults (5). Poor

b.**c.**

dental care causes inflammation of the gingiva, or *gingivitis*. Further spread of inflammation between the tooth and the alveolar bone causes periodontal disease, or *periodontitis*, and results in widening of the lucency along the side of the tooth (10). Periodontal disease is less likely to cause a soft-tissue abscess than an apical or periapical abscess (10). An apical or periapical abscess (Fig 2a) is located near the tip of the root of the tooth and often is associated with caries and infection of the pulp (10). A periapical abscess causes more complications than does periodontal disease (Fig 2) (10).

Infection of the mandibular molars can involve the masticator and submandibular spaces, because the roots of these teeth extend below the insertion of the mylohyoid muscle, which

Spaces of the Neck Relative to the Hyoid Bone

Suprahyoid neck

- Masticator space
- Parotid space
- Sublingual space
- Submandibular space
- Parapharyngeal space
- Prestyloid space
- Poststyloid space
- Pharyngeal mucosal space

Infrahyoid neck

- Visceral space
- Carotid sheath

Suprahyoid and infrahyoid neck

- Superficial compartment and fascia
- Retropharyngeal space
- Danger space
- Perivertebral space
- Prevertebral space
- Paraspinal space
- Posterior cervical space

separates the submandibular space from the sublingual space. Infection of the other mandibular teeth typically involves the overlying facial soft tissues and sublingual space, because the roots of these teeth extend above the insertion of the mylohyoid muscle (11). Infection of the maxillary molars can involve the masticator space in addition to the maxillary sinuses, palate, and overlying soft tissues, as can infection of the other maxillary teeth. If the masticator space is involved (Fig 2b, Fig E1), the infection has the potential to extend intracranially through the foramen ovale along the course of the mandibular nerve (V3 branch of the trigeminal nerve) (Fig E1).

Ludwig Angina

Ludwig angina is a rapidly progressive and potentially life-threatening cellulitis of the floor of the mouth that involves the sublingual and submandibular spaces (12). Sublingual edema from infection can displace the tongue posteriorly and cause airway compromise. The usual cause is mandibular tooth infection and pericoronitis (13). Pericoronitis is an acute localized soft-tissue infection caused by food particles and microorganisms trapped between the gum flaps and teeth that usually is seen in association with the wisdom teeth in adults or during the eruption of the permanent teeth in children (10). Imaging is performed to assess airway patency and to check for an underlying dental infection or abscess (Fig 3).

Tonsillitis and Peritonsillar Abscess

Tonsillitis is the most common deep neck infection among children and adolescents (5,14,15). If untreated, the infection can extend to the peritonsillar space (a potential space between the tonsillar capsule and the superior pharyngeal constrictor muscle) and cause a peritonsillar abscess (14,15). A true tonsillar abscess is rare. Patients with tonsillitis, peritonsillar abscess, and true tonsillar abscess may present with a sore throat, odynophagia, and otalgia. Trismus is a common feature of a peritonsillar abscess and can be present in one-third of patients with true tonsillar abscess. Peritonsillar abscess usually is treated with incision and drainage. However, tonsillar abscess usually is treated with antibiotics and supportive measures, and most patients do not require surgical intervention (16). Infection can spread directly to the adjacent parapharyngeal, masticator, or submandibular spaces (Fig 4). Imaging is not always necessary for diagnosis but often is performed, because physical examination is limited and a drainage procedure is under consideration.

Angioedema

Angioedema manifests with transient subcutaneous or submucosal swelling. It can involve any portion of the body with loose connective tissue but primarily affects the face, tongue, lips, and larynx. It is a potentially life-threatening process because it can quickly cause airway compromise. The causes of angioedema include the use of angiotensin-converting enzyme (ACE) inhibitors or receptor blockers, allergic reaction, and in rare cases, hereditary disorders such as C1 esterase-inhibitor deficiency. In addition, thrombolysis with intravenous tissue plasminogen activator, which is commonly used in treatment of acute ischemic stroke, is associated with increased risk of angioedema, especially with concurrent use of an ACE inhibitor in approximately 2%–5% of patients (17,18). ACE inhibitor-mediated angioedema is not an anaphylactic reaction, and it has a subacute course, usually developing over 24–36 hours and resolving in 2–4 days. The treatment of anaphylactic angioedema is administration of epinephrine, fluids, and oxygen. The treatment of acute allergic angioedema (less severe than anaphylaxis) is administration of antihistamines and steroids. The treatment of ACE inhibitor-mediated angioedema is airway monitoring and discontinuation of the medication (19–21).

The typical imaging findings are diffuse infiltrative transpatial edema with circumferential mucosal thickening and varying degrees of airway narrowing (Fig 5). However, unilateral, focal, and masslike areas of involvement sometimes are seen (Fig E2).

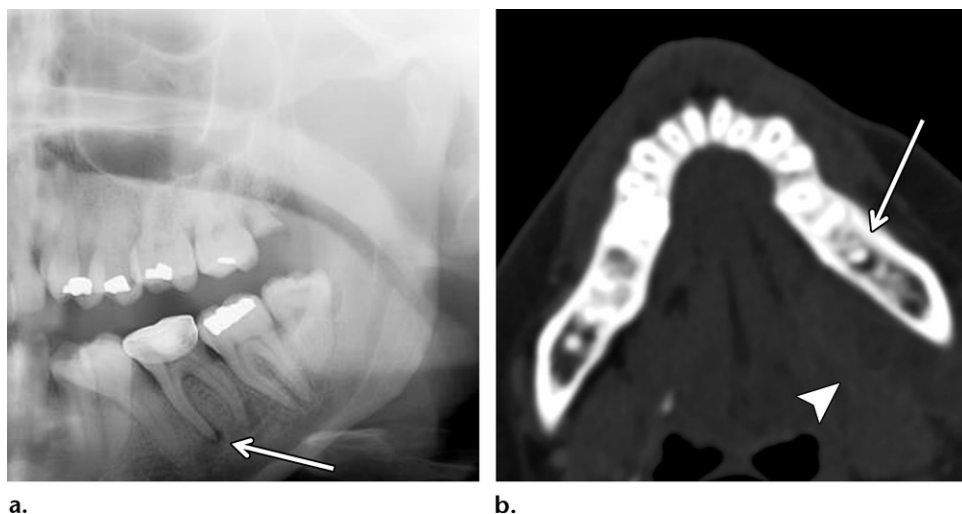


Figure 2. Periapical abscess of a mandibular molar in a 46-year-old woman who presented with left temporomandibular joint pain, difficulty opening her mouth, and altered mental status. (a) Radiograph shows a periapical lucency involving the mesial root of the left first mandibular molar (arrow). (b) Axial CT image (bone window) shows the periapical lucency (arrow), with soft-tissue stranding medial to the mandibular alveolar bone (arrowhead).

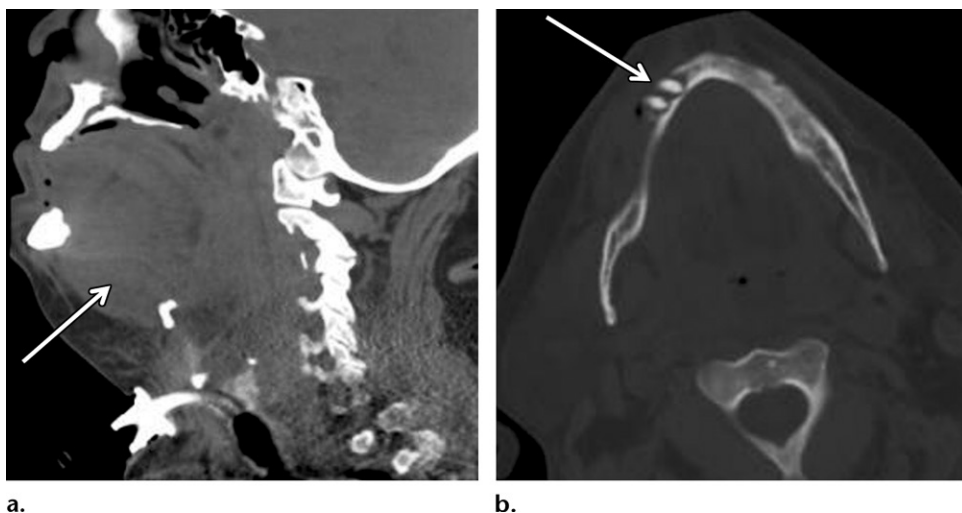


Figure 3. Ludwig angina in a 58-year-old man who presented with a sore throat, fever, chills, muffled voice, difficulty breathing, and drooling. (a) Sagittal CT image shows extensive soft-tissue swelling and stranding involving the floor of the mouth and tongue (arrow). (b) Axial CT image (bone window) shows an anterior mandibular tooth infection (arrow) as the underlying cause. The extensive soft-tissue swelling caused posterior displacement of the tongue and complete obstruction of the pharyngeal airway, resulting in the placement of an emergency tracheostomy tube, which can be seen in a.

Neck

Acute Sialadenitis

Acute sialadenitis usually manifests with pain and swelling of the affected gland that worsens with eating or anticipation of eating, which is also known as *salivary colic*. The most common cause of acute sialadenitis is a bacterial infection with *Staphylococcus aureus*. The infection is most commonly caused by salivary duct obstruction by stones (sialoliths). Other common causes are salivary stasis due to dehydration or viral infection (most commonly, mumps parotiditis in children). In addition, bilat-

eral parotid swelling is seen in patients with HIV-associated sialadenitis or immune reconstitution inflammatory syndrome. In rare cases, salivary duct carcinoma is the underlying cause of ductal obstruction and sialadenitis. The submandibular gland is involved most commonly (Fig 6); 85% of stones are seen in the submandibular duct because of the higher viscosity of the submandibular saliva and the upward course of the submandibular duct (22). The treatment usually is endoscopic or surgical stone removal. Less commonly, the duct and gland may be removed when stone removal is unsuccessful or symptoms do not resolve (23).

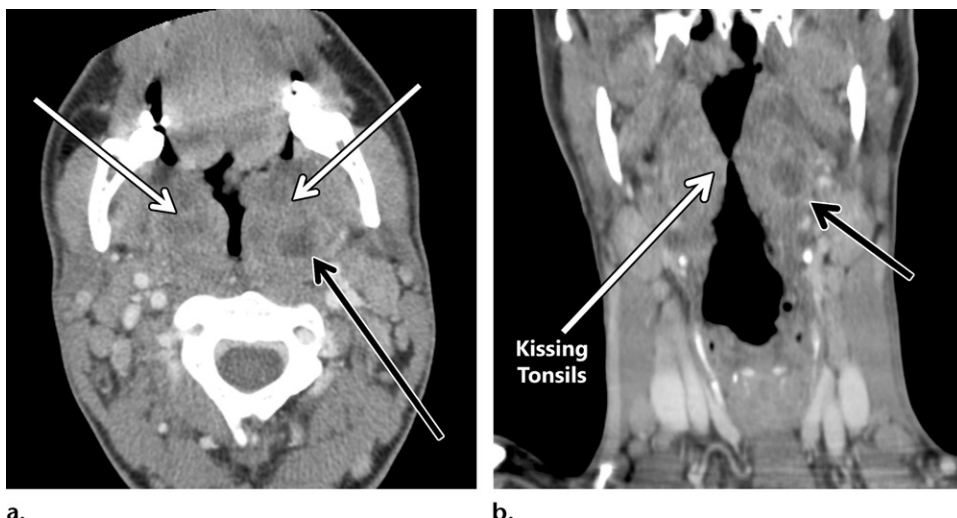


Figure 4. Tonsillitis with a peritonsillar abscess in a 21-year-old man who presented with a sore throat for 1 week, a fever, and worsening throat pain. Axial (**a**) and coronal (**b**) contrast-enhanced CT images show bilateral tonsillar enlargement (white arrows in **a**). The near-midline opposition is often called *kissing tonsils* (white arrow in **b**). A rim-enhancing cystic fluid collection posterolateral to the left tonsil represents a peritonsillar abscess (black arrow).

Acute Epiglottitis

Acute epiglottitis (also known as *supraglottitis*) is inflammation of the epiglottis and adjacent supraglottic structures (Fig 7). In children, it is rapidly progressive and life-threatening, with high risk of airway obstruction. The adult form is more indolent and has a lower risk of airway compromise. Adults better tolerate supraglottic edema because of the larger size of their airway (24,25).

Since the introduction of the *Haemophilus influenzae* type B vaccine, epiglottitis has become less prevalent overall and is more common in adults than in children. An increasing number of cases are caused by other bacteria such as *Streptococcus*, but *H influenzae* type B is still the most common cause due to incomplete community immunity and vaccine failure (26). Epiglottitis can be caused by direct extension of infection from other regions in the head and neck, such as skin cellulitis (Fig E3), dental infection, tonsillitis, and laryngopyocele (1,2,7,27–31).

Epiglottitis also can be caused by noninfectious inflammatory processes (Fig E4) such as sarcoidosis. Up to 8% of patients with sarcoidosis have laryngeal involvement, and it usually is limited to the supraglottic larynx (32). Because the true vocal cords have a sparse lymphatic system, they are usually spared (32). Patients may be asymptomatic or may present with hoarseness, dysphonia, dyspnea, and stridor, with reported cases requiring tracheostomy (33). The differential diagnosis for laryngeal supraglottic sarcoidosis includes types of infectious epiglottitis such as tuberculosis, primary laryngeal cancer (especially if it manifests as a focal polypoid mass), lymphoma, amyloidosis, granulomatosis with polyangiitis (formerly called

Wegener granulomatosis), and laryngeal pseudotumor (34). Biopsy is required even in patients with a known diagnosis of sarcoidosis because cases of concurrent sarcoidosis and laryngeal carcinoma have been reported.

Superinfected Laryngocele (Pyolaryngocoele)

Laryngoceles are air-filled or fluid-filled dilatations of the laryngeal saccule. They are classified as internal or combined laryngoceles. Internal laryngoceles are contained medial to the thyrohyoid membrane in the paraglottic space (35). Combined laryngoceles extend through the thyrohyoid membrane into the superficial neck. The average age at presentation is 50 years, with male predominance (36). Laryngoceles are usually seen in wind instrumentalists, glassblowers, and chronic coughers or are due to mechanical obstruction from an underlying neoplasm (15%–20% of cases). In 8% of cases, laryngoceles become severely infected (Fig 8) (37).

Infected Branchial Cleft Cysts

Branchial cleft cysts are due to persistence of the branchial clefts or pouches. Patients are usually young (10–40 years of age) and often present because of a superimposed infection (Fig E5). Branchial cleft cysts are located along the anterior border of the sternocleidomastoid muscle from the tragus to the clavicle (38). First branchial cleft cysts are seen above the level of the mandible angle near the external auditory canal within or close to the parotid gland. Second branchial cleft cysts are located between the level of the mandible angle and the carotid bifurcation deeper than

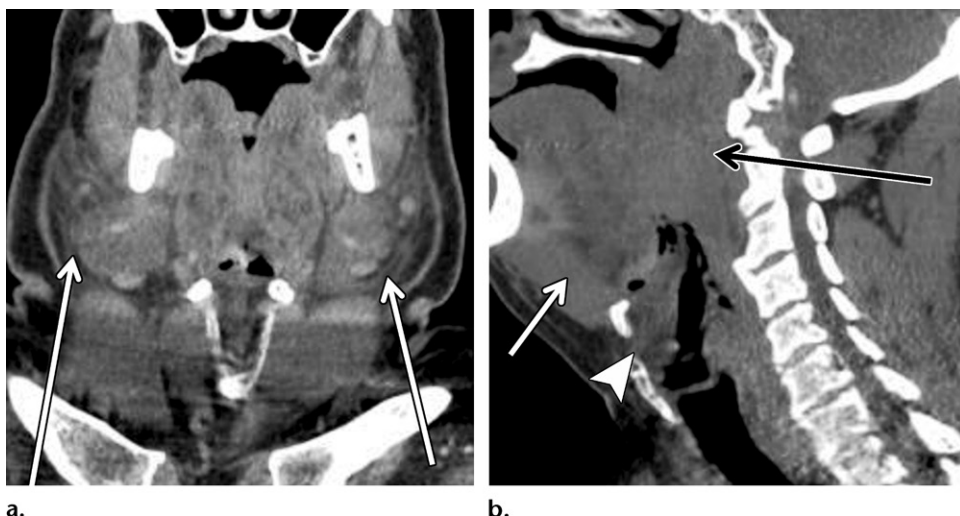


Figure 5. ACE inhibitor-mediated angioedema in a 59-year-old man with hypertension who presented with 4 days of hoarseness, oral edema, difficulty swallowing, and drooling. Coronal (a) and sagittal (b) CT images show diffuse transpatial edema involving the bilateral submandibular spaces (white arrows in a), tongue, floor of the mouth (white arrow in b), pre-epiglottic space (arrowhead in b), and pharynx (black arrow in b), causing marked pharyngeal airway narrowing.



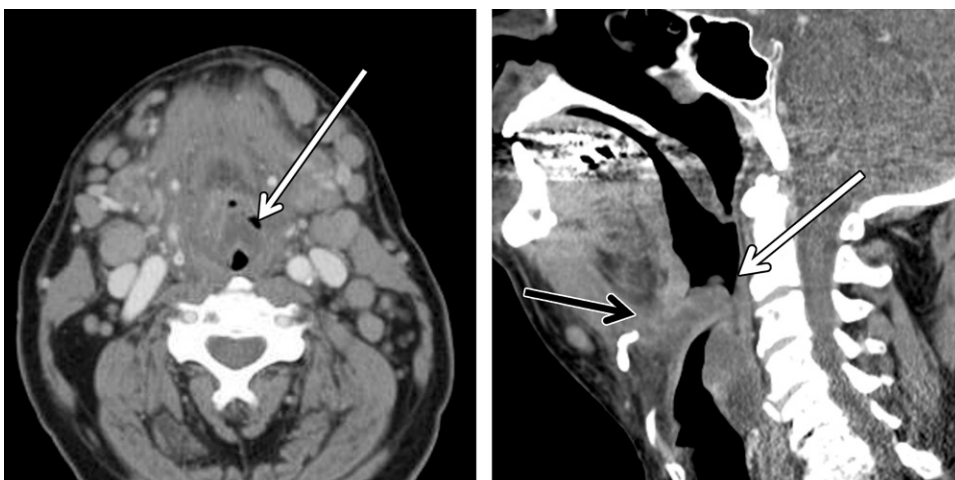
Figure 6. Sialadenitis in a 50-year-old woman with left neck swelling and severe pain after eating lunch. (a) Coronal CT image shows enlargement and enhancement of the left submandibular gland, with mild surrounding edema (arrow). (b) Axial CT image shows a stone at the submandibular duct orifice (arrow) in the floor of the mouth.

the platysma and the superficial layer of the deep cervical fascia (38). Third and fourth branchial cleft cysts are seen in the infrahyoid neck (38). Fourth branchial cleft cysts are usually adjacent to the thyroid gland (38). However, differentiation between third and fourth branchial cleft cysts is often difficult. The second branchial cleft cyst is the most common type (90%–95% of patients with branchial cleft cysts) (38). First branchial cleft cysts are seen in less than 10% of patients (39), and third and fourth branchial cleft cysts are rare. The differential diagnosis for these lesions includes a broad range of conditions such as paramedian thyroglossal duct cysts, thyroid nodules and cysts,

necrotic lymph node metastases (usually from squamous cell and papillary thyroid carcinomas), infectious adenitis (eg, tuberculosis), vascular lesions on nonenhanced CT images (eg, mycotic aneurysms of the neck), lymphatic malformations, neurogenic tumors with cystic degeneration (eg, schwannomas), and cervical dermoid cysts.

Neck Hemorrhage

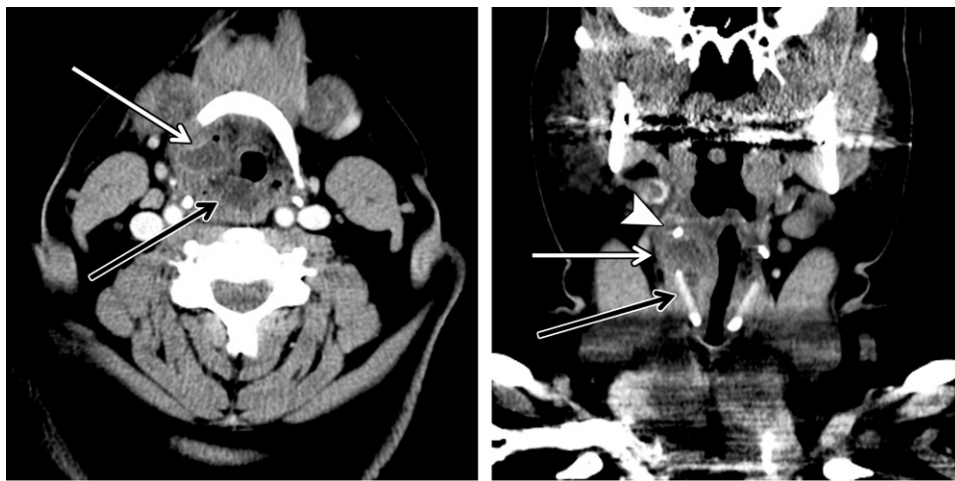
Neck hemorrhage is rare, and it usually results from carotid blowout syndrome or extraglandular bleeding due to an underlying thyroid or parathyroid lesion. The mass effect from a soft-tissue hematoma may lead to dysphasia and airway



a.

b.

Figure 7. Acute epiglottitis in a 70-year-old man with a sore throat for 3 days and progressive odynophagia. Axial (a) and sagittal (b) CT images show an enlarged and edematous epiglottis (white arrow) with mucosal enhancement and some stranding of the adjacent supraglottic larynx and tongue base (black arrow in b). Substantial airway narrowing is present.



a.

b.

Figure 8. Pyolaryngocoele in a 47-year-old woman with a severe sore throat, muffled voice, odynophagia, and stridor. Axial (a) and coronal (b) CT images show a rim-enhancing collection of fluid centered in the right paraglottic space (white arrow) in the expected region of the laryngeal saccule near the thyrohyoid membrane between the hyoid bone (arrowhead in b) and the thyroid cartilage (black arrow in b), with adjacent soft-tissue stranding and inflammation extending to the right aryepiglottic fold and arytenoids (black arrow in a).

compromise. Severe hemorrhage can happen, especially with carotid blowout syndrome (40,41).

Carotid blowout syndrome refers to the rupture of the carotid artery and its branches. The typical cause is pseudoaneurysm rupture as a complication of radiation treatment for head and neck cancer. The other causes of pseudoaneurysm rupture include infection (mycotic pseudoaneurysm), inflammatory diseases, or direct neoplastic invasion (Fig 9) (41).

Extral glandular thyroid hemorrhage can be seen with thyroid cancers, cysts, nodular goiter, or subacute thyroiditis, and extraglandular parathyroid hemorrhage can be seen with gland enlarge-

ment due to hyperplasia, adenoma, or cancer (42–44). Patients may present with swelling and ecchymosis centered in the lateral neck, dysphagia, and dyspnea. A primary parathyroid lesion should be suspected in a patient with hypercalcemia and high parathyroid hormone levels (44) (Fig E6).

Lemierre Syndrome

Lemierre syndrome is a potentially life-threatening condition characterized by suppurative thrombo-phlebitis in the neck, usually involving the jugular veins. Most commonly, it is a complication of acute pharyngitis or tonsillitis in otherwise healthy young adults (mean age, 20 years) (45). Other

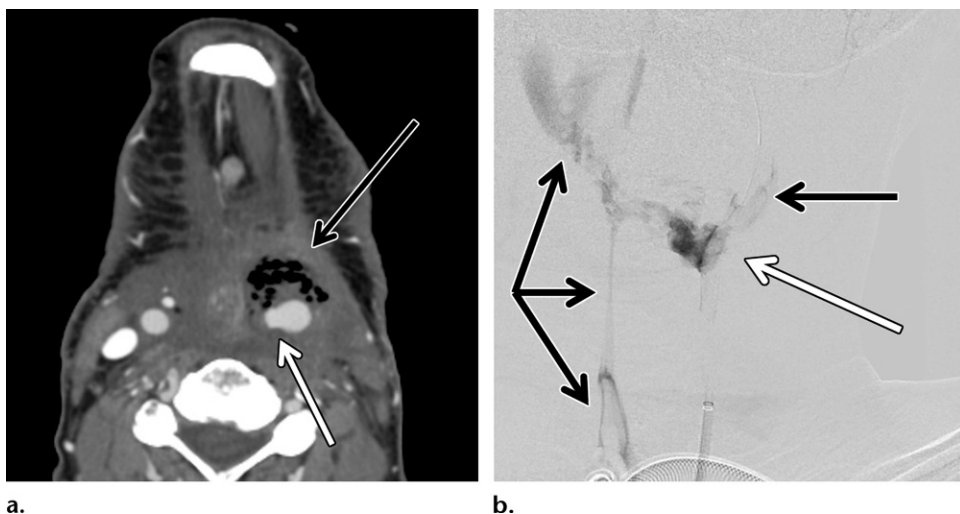
**a.****b.**

Figure 9. Carotid artery blowout syndrome in a 51-year-old woman with recurrent laryngeal cancer who was treated with total laryngectomy and radiation and who presented with intermittent hematemesis. (a) Axial contrast-enhanced CT image shows a peripherally enhancing necrotic mass with internal foci of air that is suggestive of ulceration and connection to the pharynx (black arrow). Involvement of the distal common carotid artery with formation of a pseudoaneurysm (white arrow) raises concern for an impending rupture with intermittent hematemesis. (b) Oblique angiogram from left common carotid artery injection shows the pseudoaneurysm in the distal left common carotid artery (white arrow), with extravasation of arterial contrast material into the pharynx (black arrows).

head and neck infections (eg, dental, ear, paranasal sinus, and orbit infections, and superficial cellulites from lip piercing), gastrointestinal infections, and trauma may precede Lemierre syndrome (45–47). Patients may develop disseminated abscesses and septic pulmonary emboli (Fig 10; Fig E7). Lemierre syndrome most often is caused by anaerobic gram-negative organisms and most frequently the *Fusobacterium necrophorum*, which is a part of normal oropharyngeal flora. Treatment is with anticoagulation therapy (in the absence of contraindications), intravenous antibiotics, and surgical drainage of nonresolving abscesses (48).

Carotidynia

Carotidynia, also known as transient perivascular inflammation of the carotid artery, is an inflammatory pseudotumor-like disease (49). Patients present with pain and tenderness in the region of the carotid bifurcation. The symptoms are treated with antiinflammatory medications and resolve on their own in days or weeks. Imaging shows circumferential thickening of the distal common carotid, bifurcation, and proximal internal carotid artery walls (49) (Fig E8). Carotidynia is a diagnosis of exclusion, and imaging should be repeated after treatment to confirm resolution and exclude other abnormalities. The differential diagnosis for the imaging findings includes vasculitis and dissection.

Retropharyngeal Abscess

Retropharyngeal abscesses are caused by the spread of infection from a site with drainage to



Figure 10. Lemierre syndrome in a 20-year-old woman with left-sided neck pain after a few days of sore throat and fulilike symptoms. Axial contrast-enhanced CT image shows intraluminal thrombosis and enlargement of the left internal jugular vein, with rimlike enhancement of the venous wall and adjacent inflammation (arrow) and a normal patent right internal jugular vein (arrowhead).

the retropharyngeal lymph nodes such as tonsillitis, pharyngitis, otitis, and oral cavity infections; direct spread from adjacent discitis-osteomyelitis; and inoculation from penetrating trauma. Patients usually present with a fever, sore throat, neck pain, and a limited range of motion. CT allows the radiologist to localize the infection accurately and to distinguish a true abscess from retropharyngeal edema (Fig 11; Fig E9). Accurate diagnosis is important to avoid unnecessary and potentially



Figure 11. Retropharyngeal abscess complicated by descending mediastinitis in a 22-year-old woman with worsening dyspnea and neck pain after 5 days of pharyngitis. Sagittal contrast-enhanced CT image shows fluid and air (white arrow) in the retropharyngeal space, which is consistent with a retropharyngeal abscess. A more posterior fluid collection (black arrow) extends inferiorly into the mediastinum, indicating extension of the infection into the danger space.

harmful surgery for drainage of a reactive noninfected effusion. A true abscess appears as a rim-enhancing hypoattenuating collection that expands the retropharyngeal space and may contain foci of air (24,50). Imaging is also useful for assessment of the potential complications, such as extension of the abscess into the mediastinum through the danger space; airway compromise; direct extension to the spine and epidural space; and involvement of the major cervical vessels, which can cause internal jugular vein thrombosis, carotid pseudoaneurysm, or carotid artery stenosis. Descending mediastinitis is a rare but serious complication of oral cavity and neck infections and has a high mortality rate because its nonspecific subtle symptoms and clinical findings often lead to delayed diagnosis. The abscess most commonly spreads through the danger space to the mediastinum (24,50), but it also may spread through the carotid sheaths and visceral space (Fig E9).

Longus Colli Calcific Tendinitis

Longus colli calcific tendinitis is a self-limited disease that is caused by deposition of hydroxyapatite crystals and responds to nonsteroidal anti-inflammatory drugs. The clinical manifestation is similar to that of retropharyngeal abscess, and CT is performed to differentiate between these conditions (Fig 12). Patients usually present with acute onset of neck pain and stiffness. Patients may have a fever or odynophagia, and a blood test result may show mild leukocytosis and an elevated C-reactive protein level similar to that

of retropharyngeal abscess (51). Accurate diagnosis is important to avoid unnecessary and potentially harmful surgery. The CT findings include effusion in the prevertebral space. The absence of substantial rim enhancement and detection of a small amount of calcification or ossification at the insertion of the longus colli muscles to the anterior arch of C1 are characteristic findings (51). The longus colli muscles also may appear hypoattenuating because of inflammation and edema.

Discitis-Osteomyelitis

The most common cause of discitis-osteomyelitis is hematogenous seeding from a distant focus, and it is more common in the thoracic and lumbar spine than in the cervical spine (52). Other less common causes are recent spinal procedures and spreading from adjacent soft tissue infections (52). CT findings are initially subtle and include loss of disk height and endplate irregularities, vertebral body collapse, and perivertebral soft-tissue inflammation and abscess (24). MRI is more sensitive than CT for early detection of the disease and epidural or paravertebral abscesses (Fig 13) (53). Risk factors for discitis-osteomyelitis include intravenous drug use, infective endocarditis, prior spinal surgery, diabetes, steroid therapy or other immunocompromised states, and degenerative disease (53).

Septic Facet Arthritis

Septic facet arthritis is an uncommon but serious cause of acute neck pain that typically involves a single level of the spine (54). CT findings are usually subtle, especially early in the course of the disease, and include mixed lytic and sclerotic changes in the facet and edema in the adjacent soft tissues. MRI is more sensitive than CT for early diagnosis and detection of the potential complications. Typical MRI findings are bone marrow edema and enhancement, expansion of the facet joint capsule with effusion and rim-like enhancement, and edema in the adjacent prevertebral and paraspinal spaces (Fig 14). The infection can extend into the adjacent spinal canal, causing an epidural abscess, with potential to cause spinal cord injury or meningitis (55). The causes of spinal cord injury are mass effect and direct compression by the abscess, thrombophlebitis of the adjacent veins, occlusion of the arterial supply, and direct extension of the infection and inflammation to the spinal cord.

Sinonasal Cavities

Acute Rhinosinusitis

The term *rhinosinusitis* is preferred over the term *sinusitis* because the nasal cavity is involved in almost all cases. Acute rhinosinusitis is a clinical

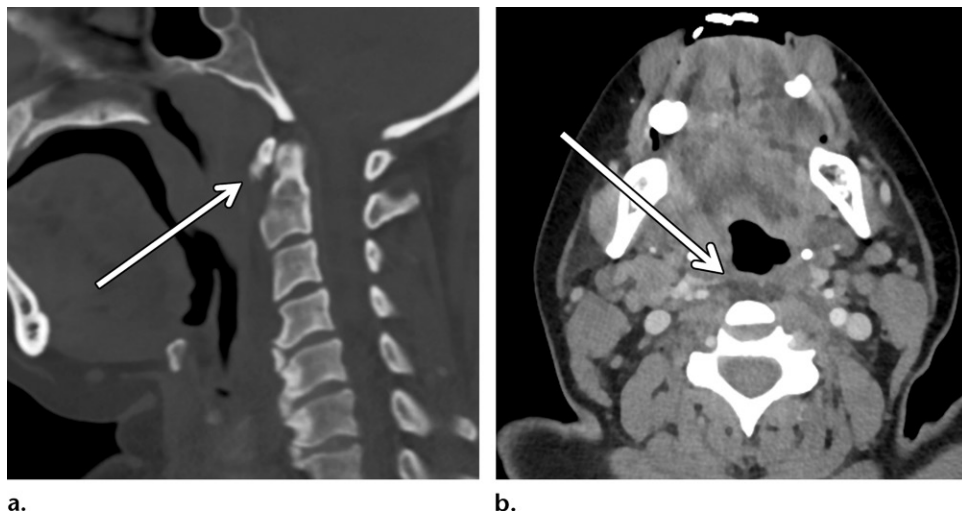


Figure 12. Longus colli calcific tendinitis in a 47-year-old man with transient pain and tenderness over the right middle neck. (a) Sagittal CT image (bone window) shows amorphous calcification (arrow) at the insertion of the longus colli tendon near the anterior arch of the C1 vertebra. (b) Axial contrast-enhanced CT image shows hypoattenuating effusion (arrow) in the prevertebral space without surrounding enhancement.

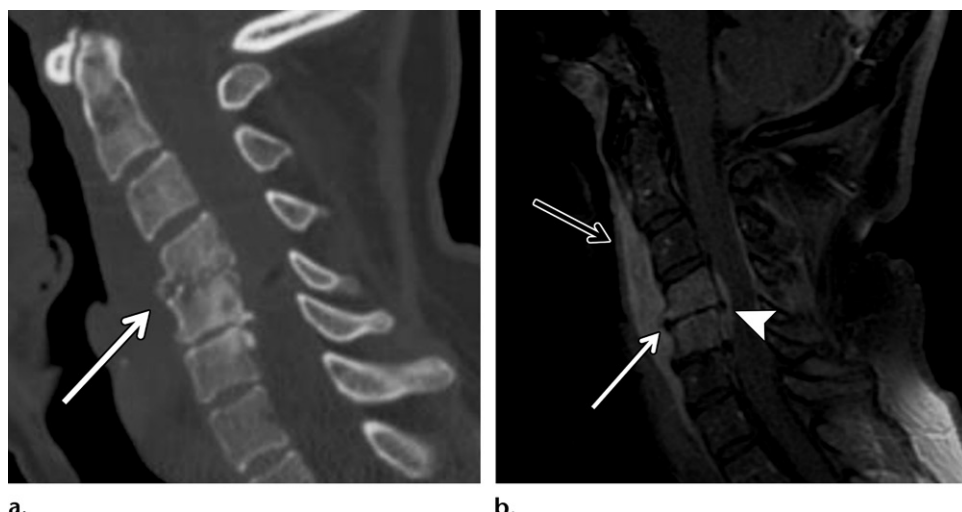


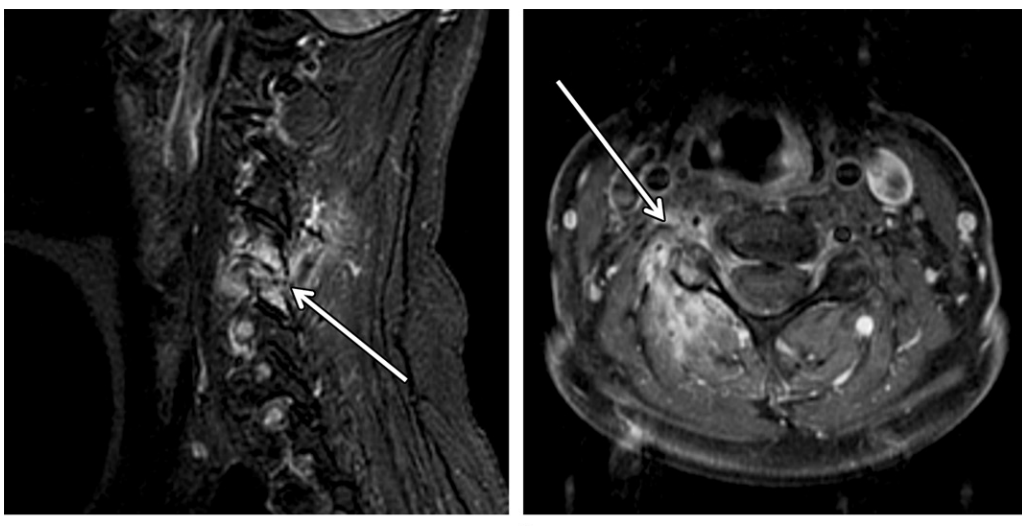
Figure 13. Discitis-osteomyelitis in a 55-year-old woman with a history of splenectomy who presented with 3 weeks of neck pain and tenderness in the right middle neck. Sagittal CT (a) and sagittal contrast-enhanced fat-suppressed T1-weighted MR (b) images show loss of disk height and endplate irregularities that involve two adjacent vertebral bodies (white arrow) with prevertebral (black arrow in b) and epidural (arrowhead in b) soft-tissue inflammation and abscess.

diagnosis defined by symptom duration of less than 4 weeks. Imaging findings are nonspecific and can be seen in up to 40% of asymptomatic adults and more than 80% of patients with minor upper respiratory tract infections. Therefore, the imaging findings should be interpreted with attention to clinical and endoscopic findings. The imaging findings are mucosal thickening, air-fluid level in the paranasal sinuses, aerated fluid or secretions, and obstruction of the osteomeatal complexes. CT can be performed if complications such as orbital cellulitis, venous sinus thrombosis, or intracranial extension are suspected. The maxillary teeth also should be

assessed carefully because up to 20% of maxillary sinus infections are odontogenic (56).

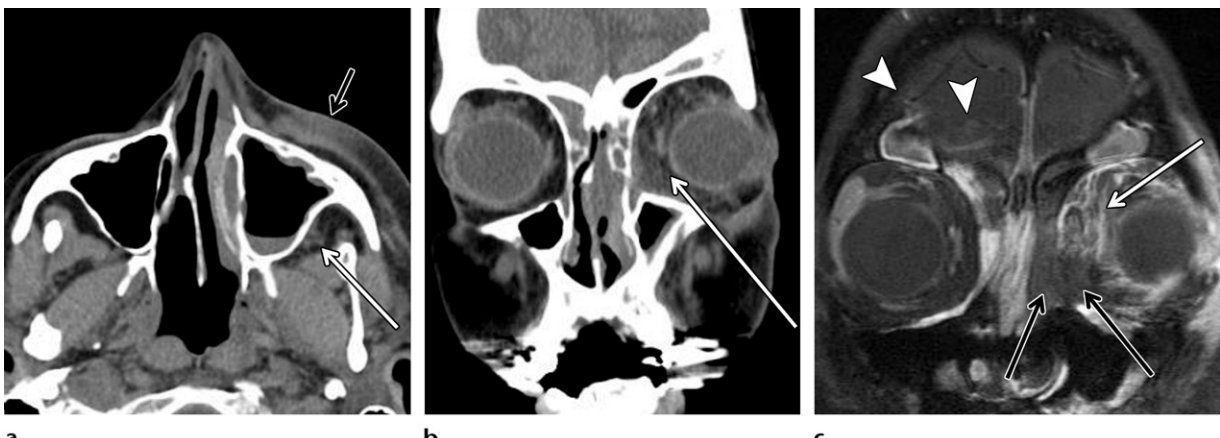
Invasive Fungal Sinusitis

Invasive fungal sinusitis is seen almost exclusively in immunocompromised patients with neutropenia or neutrophil dysfunction, usually in those with hematologic malignancies or poorly controlled diabetes and those undergoing immunosuppressive therapy for organ transplant or chemotherapy. It is most commonly caused by *Aspergillus* or *Mucor* fungi. Patients usually present with fever, facial pain, nasal congestion, and sensation loss in the malar areas. Patients



a. **b.**

Figure 14. Septic facet arthritis in a 58-year-old woman with fever, neck pain, and stiffness. Sagittal fat-suppressed T2-weighted (a) and contrast-enhanced T1-weighted (b) MR images show edema at one of the cervical facet joints, with adjacent soft-tissue inflammation (arrow) that extends into the prevertebral and paraspinal spaces and the adjacent neural foramen.



a.

b.

c.

Figure 15. Invasive fungal sinusitis in a 62-year-old man with neutropenia after bone marrow transplant who presented with sinus disease, eye pain, and periorbital swelling and ecchymosis. (a, b) Initial axial (a) and coronal (b) CT images show a small air-fluid level in the left maxillary sinus and opacification of the ethmoid air cells and frontal sinuses with mild premaxillary (black arrow in a), retromaxillary (white arrow in a), and orbital (arrow in b) fat stranding. (c) Contrast-enhanced fat-suppressed T1-weighted MR image from follow-up examination performed 24 hours after initial CT shows marked worsening of the orbital soft-tissue inflammation (white arrow), intracranial extension with meningeal enhancement (arrowheads), and extensive necrosis (black arrows), indicated by lack of contrast enhancement along the medial orbit and lateral wall of the left nasal cavity.

also may have a change in vision or mental status. The nasal and oral cavities should be examined carefully for necrotic ulceration. The infection rapidly spreads from the sinuses by means of vascular invasion, causing bony erosions, with extension to the orbit, brain, cavernous sinus, or carotid artery. Immediate treatment with systemic antifungal medications and aggressive surgical débridement is required. However, despite early treatment, the mortality rate is very high at approximately 50%–60% (57,58). CT findings include sinonasal mucosal thickening and opacification; stranding in the periantral fat, pterygopalatine fossa, nasolacrimal duct, lacrimal

sac, and orbit; bone erosion and dehiscence; and nasal septal ulceration. The imaging findings may be mild, especially early in the course of disease. The degree of sinonasal mucosal thickening and opacification may be minimal and is not sensitive or specific for diagnosis of invasive fungal sinusitis in at-risk patients. Subtle stranding of the periantral fat can be the first imaging finding of vascular invasion and spread of infection beyond the sinuses (Fig 15). A retrospective matched case-control analysis (59) of 42 patients with histopathologically proven invasive fungal sinusitis showed that the presence of only one of the CT findings has sensitivity of 95% and specificity of

86% for diagnosis of invasive fungal sinusitis in at-risk patients. The same study showed sensitivity of 88% and specificity of 100%, with two or more CT findings in at-risk patients. Leptomeningeal enhancement, cavernous sinus thrombosis, carotid pseudoaneurysm, cerebritis, and brain abscess can be seen with intracranial invasion (60).

Juvenile Nasopharyngeal Angiofibroma

Juvenile nasopharyngeal angiofibroma is a tumor that arises from the sphenopalatine foramen, posterior nasal cavity, or nasopharynx (61) (Fig 16). It is seen almost exclusively in young male patients (aged 8–25 years). It usually manifests with epistaxis, which can be life-threatening, or chronic otomastoiditis from obstruction of the eustachian tube. Imaging is crucial for diagnosis because the tumor is highly vascular, and biopsy should be avoided because of the risk of severe hemorrhage. CT findings include a lobulated soft-tissue mass with prominent enhancement near the sphenopalatine foramen, with extension to the nasopharynx and pterygopalatine fossa (62). The tumor typically causes remodeling of the adjacent bones and widening of the sphenopalatine foramen. The lesion has intermediate signal intensity at T1-weighted MRI. At T2-weighted MRI, the lesion is heterogeneous and usually contains flow void (62). Similar to its appearance at CT, the lesion shows prominent enhancement at MRI (62). The treatment is endovascular embolization to avoid life-threatening hemorrhage, followed by resection.

Orbits

Preseptal Cellulitis

Preseptal or periorbital cellulitis is an infection limited to the skin and soft tissues anterior to the orbital septum. The orbital septum is a thin sheet of fibrous tissue that extends from the orbital rim periosteum to the tarsal plates in the eyelids and separates superficial soft tissues from the orbit. Preseptal cellulitis often is caused by contiguous spread of an infection from the teeth, sinuses, or ocular adnexa; insect bites; or trauma (63) (Fig E10). It is treated with oral antibiotic therapy.

Orbital Cellulitis

Orbital cellulitis is an infection of the orbit posterior to the orbital septum, typically due to rhinosinusitis (64) (Fig 17). Orbital cellulitis is an emergency, and complications include loss of vision, superior ophthalmic vein thrombosis, and intracranial extension that leads to cavernous sinus thrombosis, meningitis, and intracranial abscess. Treatment is administration of intravenous antibiotics; however, surgical drainage



Figure 16. Juvenile nasopharyngeal angiofibroma in an 11-year-old boy who presented with severe epistaxis. Axial CT image shows a lobulated and intensely enhancing mass involving the right sphenopalatine foramen, posterior nasal cavity, right sphenoid sinus, and adjacent nasopharynx (white arrow), causing remodeling and widening of the sphenopalatine foramen and pterygopalatine fossa, and the normal contralateral sphenopalatine foramen (arrowhead) and pterygopalatine fossa (black arrow).



Figure 17. Orbital cellulitis in a 19-year-old man with right eye swelling and pain after sinusitis, which worsened with eye movement. Axial contrast-enhanced CT image shows opacification of the right ethmoidal air cells, with a small adjacent subperiosteal abscess (white arrow) and orbital fat stranding (black arrows).

may be necessary if there is a large subperiosteal abscess, poor response to antibiotics, or if vision is threatened (65). Orbital cellulitis must be differentiated from an orbital pseudotumor, or nonspecific orbital inflammation, which usually responds quickly to treatment with steroids. The muscles, lacrimal gland, or other orbital soft tissues may be involved. Immunoglobulin G4-related disease accounts for 25%–50% of cases of

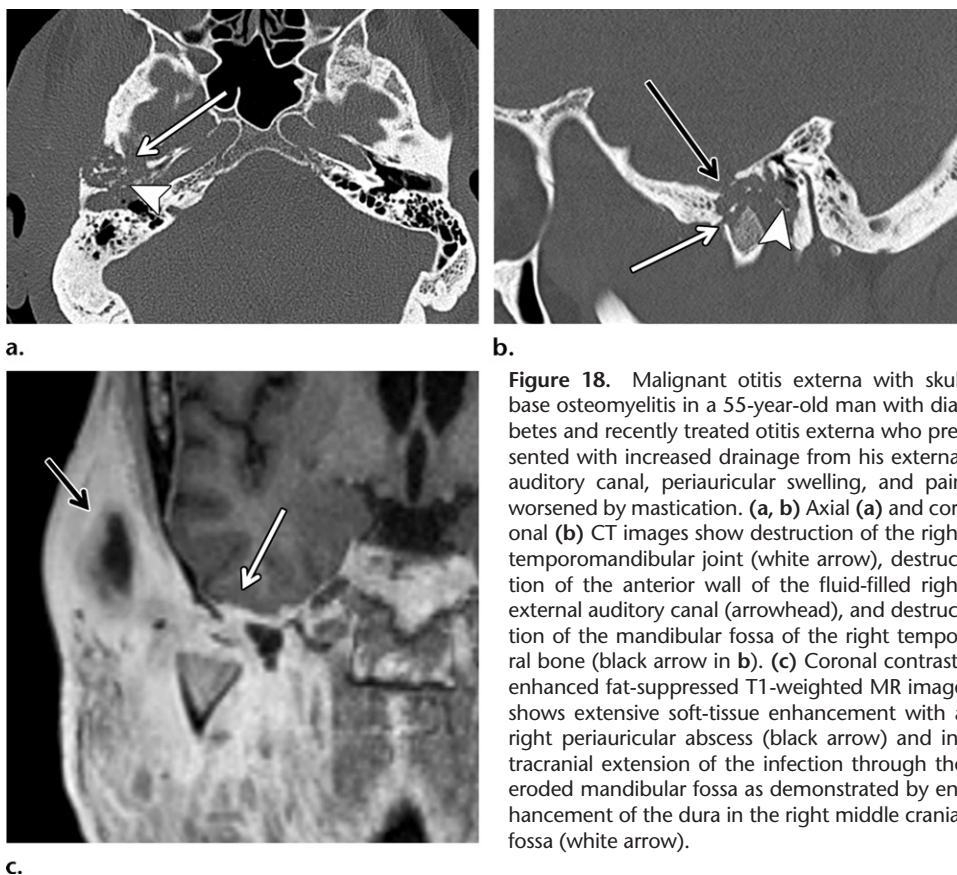


Figure 18. Malignant otitis externa with skull base osteomyelitis in a 55-year-old man with diabetes and recently treated otitis externa who presented with increased drainage from his external auditory canal, periauricular swelling, and pain worsened by mastication. (a, b) Axial (a) and coronal (b) CT images show destruction of the right temporomandibular joint (white arrow), destruction of the anterior wall of the fluid-filled right external auditory canal (arrowhead), and destruction of the mandibular fossa of the right temporal bone (black arrow in b). (c) Coronal contrast-enhanced fat-suppressed T1-weighted MR image shows extensive soft-tissue enhancement with a right periauricular abscess (black arrow) and intracranial extension of the infection through the eroded mandibular fossa as demonstrated by enhancement of the dura in the right middle cranial fossa (white arrow).

orbital pseudotumor (66). Acute progression of thyroid eye disease (also known as *thyroid orbitopathy*) also should be considered in the differential diagnosis of orbital cellulitis and orbital pseudotumor. The structures chiefly affected during the acute inflammatory phase are the orbital extraocular muscles and orbital adipose tissue. Unlike orbital pseudotumors, thyroid eye disease typically is characterized at imaging by bilateral and symmetrical enlargement of the extraocular muscle bellies, with sparing of the tendinous insertions (67).

Dacryocystitis

Dacryocystitis is an acute infection of the nasolacrimal system. The predisposing factor is stasis of lacrimal fluid due to stenosis or obstruction of the lacrimal duct, which can be congenital or acquired in patients who have experienced trauma, prior surgery, or systemic diseases such as sarcoidosis and Wegener granulomatosis (68). Patients usually present with acute onset of pain, erythema, warmth, and tenderness over the lacrimal sac, with purulent discharge. Complications are preseptal or orbital cellulitis, conjunctivitis, sepsis, and meningitis (68). The diagnosis typically is made clinically, but imaging may be performed for assessment of possible complications. CT findings include a cystic fluid

collection with rim enhancement along the inner canthus, with adjacent inflammation and soft-tissue thickening (Fig E11). Treatment is administration of either oral or intravenous antibiotics, depending on the severity of the infection and its complications.

Ears

Malignant External Otitis

Malignant external otitis, or necrotizing external otitis, is an invasive infection of the external auditory canal, skull base, and adjacent soft tissues that usually is seen in elderly patients with diabetes (Fig 18) or immunocompromised patients who are infected with HIV (69). The cause is almost always infection with *Pseudomonas aeruginosa*. The imaging findings include soft-tissue attenuation or cortical bone erosion of the external auditory canal and extension into the periauricular soft tissues and deep neck spaces such as the masticator space, nasopharynx, and parapharyngeal space; opacification of the mastoid air cells and the middle ear from direct extension of the infection, and skull base bone erosion with intracranial extension. The imaging appearance can be misinterpreted as a malignancy if one relies on imaging findings only without attention to the patient's clinical symptoms at presentation (70,71).

Complications include temporomandibular joint involvement, cranial nerve palsy due to skull base involvement, meningitis, brain abscess, and dural venous sinus thrombophlebitis.

Acute Middle Ear and Mastoid Infection (Otomastoiditis)

These common ear infections may be complicated by extension into the contiguous soft tissues or intracranial extension resulting in epidural abscess, sigmoid sinus thrombosis, meningitis, and intracranial abscess, particularly in children. Imaging is not necessary unless complications are suspected. The CT findings include fluid and soft-tissue attenuation in the middle ear cavity and mastoid, thickening and outward bulging of the tympanic membrane, or tympanic membrane perforation. When the mastoid trabeculae are destroyed, it is called coalescent mastoiditis, which may cause further erosion of the outer and inner cortex of the mastoid, resulting in periauricular cellulitis with or without an abscess and intracranial extension, respectively (72).

Conclusion

CT is an accurate tool for diagnosis of most of the nontraumatic head and neck emergencies and their complications, but MRI provides higher accuracy in diagnosis of abnormalities such as discitis-osteomyelitis, septic facet arthritis, and intracranial complications. Familiarity with the anatomic landmarks and the imaging appearance of head and neck diseases and their complications makes head and neck imaging a less intimidating subject for radiologists.

Disclosures of Conflicts of Interest.—**M.H.L.** Activities related to the present article: disclosed no relevant relationships. Activities not related to the present article: board membership for Takeda Pharma and GE Healthcare, consultancy for Siemens Healthineers. Other activities: disclosed no relevant relationships.

References

- Russell MD, Russell MS. Urgent Infections of the Head and Neck. *Med Clin North Am* 2018;102(6):1109–1120.
- Rana RS, Moonis G. Head and neck infection and inflammation. *Radiol Clin North Am* 2011;49(1):165–182.
- Cramer JD, Purkey MR, Smith SS, Schroeder JW Jr. The impact of delayed surgical drainage of deep neck abscesses in adult and pediatric populations. *Laryngoscope* 2016;126(8):1753–1760.
- McDowell RH, Hyser MJ. Neck Abscess. Treasure Island, Fla: StatPearls, 2019.
- Bakir S, Tanrıverdi MH, Gün R, et al. Deep neck space infections: a retrospective review of 173 cases. *Am J Otolaryngol* 2012;33(1):56–63.
- Boscolo-Rizzo P, Stellin M, Muzzi E, et al. Deep neck infections: a study of 365 cases highlighting recommendations for management and treatment. *Eur Arch Otorhinolaryngol* 2012;269(4):1241–1249.
- Reynolds SC, Chow AW. Life-threatening infections of the peripharyngeal and deep fascial spaces of the head and neck. *Infect Dis Clin North Am* 2007;21(2):557–576, viii.
- Som PM, Curtin HD. Fascia and Spaces of the Neck. In: Som PM, Curtin HD, eds. *Head and Neck Imaging*. 5th ed. St Louis, Mo: Mosby, 2011; 2203–2234.
- Scali F, Nash LG, Pontell ME. Defining the Morphology and Distribution of the Alar Fascia: A Sheet Plastination Investigation. *Ann Otol Rhinol Laryngol* 2015;124(10):814–819.
- Scheinfeld MH, Shifteh K, Avery LL, Dym H, Dym RJ. Teeth: what radiologists should know. *RadioGraphics* 2012;32(7):1927–1944.
- Smoker WRK, Som PM. Anatomy and Imaging of the Oral Cavity and Pharynx. In: Som PM, Curtin HD, eds. *Head and Neck Imaging*. 5th ed. St Louis, Mo: Mosby, 2011; 1617–1642.
- La'porte SJ, Jutla JK, Lingam RK. Imaging the floor of the mouth and the sublingual space. *RadioGraphics* 2011;31(5):1215–1230.
- Pak S, Cha D, Meyer C, Dee C, Fershko A. Ludwig's Angina. *Cureus* 2017;9(8):e1588.
- Schraff S, McGinn JD, Derkay CS. Peritonsillar abscess in children: a 10-year review of diagnosis and management. *Int J Pediatr Otorhinolaryngol* 2001;57(3):213–218.
- Ungkanont K, Yellon RF, Weissman JL, Casselbrant ML, González-Valdepeña H, Bluestone CD. Head and neck space infections in infants and children. *Otolaryngol Head Neck Surg* 1995;112(3):375–382.
- Giurintano JP, Kortbein S, Sebelik M, Thompson J, McLevy-Bazzanella J. Intratonsillar abscess: A not-so-rare clinical entity. *Int J Pediatr Otorhinolaryngol* 2019; 119:38–40.
- Hill MD, Lye T, Moss H, et al. Hemi-orolingual angioedema and ACE inhibition after alteplase treatment of stroke. *Neurology* 2003;60(9):1525–1527.
- Engelter ST, Fluri F, Buitrago-Téllez C, et al. Life-threatening orolingual angioedema during thrombolysis in acute ischemic stroke. *J Neurol* 2005;252(10):1167–1170.
- Caballero T, Baeza ML, Cabañas R, et al. Consensus statement on the diagnosis, management, and treatment of angioedema mediated by bradykinin. Part I. Classification, epidemiology, pathophysiology, genetics, clinical symptoms, and diagnosis. *J Investig Allergol Clin Immunol* 2011;21(5):333–347; quiz 347.
- Caballero T, Baeza ML, Cabañas R, et al. Consensus statement on the diagnosis, management, and treatment of angioedema mediated by bradykinin. Part II. Treatment, follow-up, and special situations. *J Investig Allergol Clin Immunol* 2011;21(6):422–441; quiz 442–443.
- Ishigami K, Averill SL, Pollard JH, McDonald JM, Sato Y. Radiologic manifestations of angioedema. *Insights Imaging* 2014;5(3):365–374.
- Abdel Razek AAK, Mukherji S. Imaging of sialadenitis. *Neuroradiol J* 2017;30(3):205–215.
- Holden AM, Man CB, Samani M, Hills AJ, McGurk M. Audit of minimally-invasive surgery for submandibular sialolithiasis. *Br J Oral Maxillofac Surg* 2019;57(6):582–586.
- Capps EF, Kinsella JJ, Gupta M, Bhatki AM, Opatowsky MJ. Emergency imaging assessment of acute, nontraumatic conditions of the head and neck. *RadioGraphics* 2010;30(5):1335–1352.
- Shah RK, Stocks C. Epiglottitis in the United States: national trends, variances, prognosis, and management. *Laryngoscope* 2010;120(6):1256–1262.
- Guardiani E, Bliss M, Harley E. Supraglottitis in the era following widespread immunization against *Haemophilus influenzae* type B: evolving principles in diagnosis and management. *Laryngoscope* 2010;120(11):2183–2188.
- Ito K, Chitose H, Koganemaru M. Four cases of acute epiglottitis with a peritonsillar abscess. *Auris Nasus Larynx* 2011;38(2):284–288.
- Orhan İ, Aydin S, Karlidağ T. Infectious and Noninfectious Causes of Epiglottitis in Adults, Review of 24 Patients. *Turk Arch Otorhinolaryngol* 2015;53(1):10–14.
- Pattini V, Porter G, Omakobia E. An unusual presentation of an infected vallecular cyst presenting as supraglottitis. *BMJ Case Rep* 2013;2013:bcr2013009180.
- Fröhlich S, O'Sullivan E. Repeated episodes of airway obstruction caused by a pyolaryngocoele. *Eur J Emerg Med* 2011;18(3):179–180.

31. Hafidh MA, Sheahan P, Keogh I, Walsh RM. Acute epiglottitis in adults: a recent experience with 10 cases. *J Laryngol Otol* 2006;120(4):310–313.
32. Chapman MN, Fujita A, Sung EK, et al. Sarcoidosis in the Head and Neck: An Illustrative Review of Clinical Presentations and Imaging Findings. *AJR Am J Roentgenol* 2017;208(1):66–75.
33. Ryu C, Herzog EL, Pan H, Homer R, Gulati M. Upper Airway Obstruction Requiring Emergent Tracheostomy Secondary to Laryngeal Sarcoidosis: A Case Report. *Am J Case Rep* 2017;18:157–159.
34. Nwawka OK, Nadgir R, Fujita A, Sakai O. Granulomatous disease in the head and neck: developing a differential diagnosis. *RadioGraphics* 2014;34(5):1240–1256.
35. Thomé R, Thomé DC, De La Cortina RA. Lateral thyrotomy approach on the paraglottic space for laryngocele resection. *Laryngoscope* 2000;110(3 Pt 1):447–450.
36. Zelenik K, Stanikova L, Smatanova K, Cerny M, Kominek P. Treatment of Laryngoceles: what is the progress over the last two decades? *BioMed Res Int* 2014;2014:819453.
37. Stell PM, Maran AG. Laryngocoele. *J Laryngol Otol* 1975;89(9):915–924.
38. Adams A, Mankad K, Offiah C, Childs L. Branchial cleft anomalies: a pictorial review of embryological development and spectrum of imaging findings. *Insights Imaging* 2016;7(1):69–76.
39. Fastenberg J, Nassar M. First Branchial Cleft Cyst. *N Engl J Med* 2016;375(16):e33.
40. Powitzky R, Vasan N, Krempel G, Medina J. Carotid blowout in patients with head and neck cancer. *Ann Otol Rhinol Laryngol* 2010;119(7):476–484.
41. Suárez C, Fernández-Alvarez V, Hamoir M, et al. Carotid blowout syndrome: modern trends in management. *Cancer Manag Res* 2018;10:5617–5628.
42. Giotakis EI, Hildenbrand T, Dodenhöft J. Sudden massive neck swelling due to hemorrhage of a thyroid adenoma: a case report. *J Med Case Reports* 2011;5(1):391.
43. Ulrich L, Knee G, Todd C. Spontaneous cervical haemorrhage of a parathyroid adenoma. *Endocrinol Diabetes Metab Case Rep* 2015;2015:150034.
44. Merante-Boschin I, Fassan M, Pelizzo MR, Ide EC, Rugge M. Neck emergency due to parathyroid adenoma bleeding: a case report. *J Med Case Reports* 2009;3(1):7404.
45. Karkos PD, Asrani S, Karkos CD, et al. Lemierre's syndrome: A systematic review. *Laryngoscope* 2009;119(8):1552–1559.
46. Sinave CP, Hardy GJ, Fardy PW. The Lemierre syndrome: suppurative thrombophlebitis of the internal jugular vein secondary to oropharyngeal infection. *Medicine (Baltimore)* 1989;68(2):85–94.
47. Bukari SM, Roxas R, Kamat D. Variant of Lemierre's Syndrome Secondary to Trauma. *Int J Pediatr* 2010;2010:123943.
48. Campo F, Fusconi M, Ciotti M, et al. Antibiotic and Anticoagulation Therapy in Lemierre's Syndrome: Case Report and Review. *J Chemother* 2019;31(1):42–48.
49. Lecler A, Obadia M, Savatovsky J, et al. TIPIC Syndrome: Beyond the Myth of Carotidynia, a New Distinct Unclassified Entity. *AJR Am J Neuroradiol* 2017;38(7):1391–1398.
50. Gonzalez-Beicos A, Nunez D. Imaging of acute head and neck infections. *Radiol Clin North Am* 2012;50(1):73–83.
51. Alamoudi U, Al-Sayed AA, AlSallumi Y, et al. Acute calcific tendinitis of the longus colli muscle masquerading as a retropharyngeal abscess: A case report and review of the literature. *Int J Surg Case Rep* 2017;41:343–346.
52. Berbari EF, Kanj SS, Kowalski TJ, et al. 2015 Infectious Diseases Society of America (IDSA) Clinical Practice Guide-
- lines for the Diagnosis and Treatment of Native Vertebral Osteomyelitis in Adults. *Clin Infect Dis* 2015;61(6):e26–e46.
53. Johnson SM, Shah LM. Imaging of Acute Low Back Pain. *Radiol Clin North Am* 2019;57(2):397–413.
54. Sethi S, Vithayathil MK. Cervical facet joint septic arthritis: a real pain in the neck. *BMJ Case Rep* 2017;2017:bcr-2016-218510.
55. Jones JL, Ernst AA. Unusual cause of neck pain: septic arthritis of a cervical facet. *Am J Emerg Med* 2012;30(9):2094. e1–2094.e4.
56. Expert Panel on Neurologic Imaging, Kirsch CFE, Bykowski J, et al. ACR Appropriateness Criteria® Sinonasal Disease. *J Am Coll Radiol* 2017;14(11S):S550–S559.
57. Cho HJ, Jang MS, Hong SD, Chung SK, Kim HY, Dhong HJ. Prognostic factors for survival in patients with acute invasive fungal rhinosinusitis. *Am J Rhinol Allergy* 2015;29(1):48–53.
58. Ergun O, Tahir E, Kuscu O, Ozgen B, Yilmaz T. Acute Invasive Fungal Rhinosinusitis: Presentation of 19 Cases, Review of the Literature, and a New Classification System. *J Oral Maxillofac Surg* 2017;75(4):767.e1–767.e9.
59. Middlebrooks EH, Frost CJ, De Jesus RO, Massini TC, Schmalfuss IM, Mancuso AA. Acute Invasive Fungal Rhinosinusitis: A Comprehensive Update of CT Findings and Design of an Effective Diagnostic Imaging Model. *AJR Am J Neuroradiol* 2015;36(8):1529–1535.
60. Aribandi M, McCoy VA, Bazan C 3rd. Imaging features of invasive and noninvasive fungal sinusitis: a review. *RadioGraphics* 2007;27(5):1283–1296.
61. McKnight CD, Parmar HA, Watcharotone K, Mukherji SK. Reassessing the Anatomic Origin of the Juvenile Nasopharyngeal Angiofibroma. *J Comput Assist Tomogr* 2017;41(4):559–564.
62. López F, Triantafyllou A, Snyderman CH, et al. Nasal juvenile angiomyxoma: Current perspectives with emphasis on management. *Head Neck* 2017;39(5):1033–1045.
63. Santos JC, Pinto S, Ferreira S, Maia C, Alves S, da Silva V. Pediatric preseptal and orbital cellulitis: A 10-year experience. *Int J Pediatr Otorhinolaryngol* 2019;120:82–88.
64. Danishyar A, Sergent SR. Orbital Cellulitis. Treasure Island, Fla: StatPearls, 2019.
65. Tsirouki T, Dastiridou AI, Ibáñez Flores N, et al. Orbital cellulitis. *Surv Ophthalmol* 2018;63(4):534–553.
66. Andrew NH, Sladden N, Kearney DJ, Selva D. An analysis of IgG4-related disease (IgG4-RD) among idiopathic orbital inflammations and benign lymphoid hyperplasias using two consensus-based diagnostic criteria for IgG4-RD. *Br J Ophthalmol* 2015;99(3):376–381.
67. Verity DH, Rose GE. Acute thyroid eye disease (TED): principles of medical and surgical management. *Eye (Lond)* 2013;27(3):308–319.
68. Taylor RS, Ashurst JV. Dacryocystitis. Treasure Island, Fla: StatPearls, 2019.
69. Thio D, Reece P, Herdman R. Necrotizing otitis externa: a painless reminder. *Eur Arch Otorhinolaryngol* 2008;265(8):907–910.
70. Subburaman N, Chaurasia MK. Skull base osteomyelitis interpreted as malignancy. *J Laryngol Otol* 1999;113(8):775–778.
71. Adams A, Offiah C. Central skull base osteomyelitis as a complication of necrotizing otitis externa: Imaging findings, complications, and challenges of diagnosis. *Clin Radiol* 2012;67(10):e7–e16.
72. Juliano AF, Ginat DT, Moonis G. Imaging review of the temporal bone: part I. Anatomy and inflammatory and neoplastic processes. *Radiology* 2013;269(1):17–33.

Diagnostic Approach to Intrinsic Abnormality of Spinal Cord Signal Intensity

Michael J. Lee, MD

Ryan Aronberg, MD, MS

Matthew S. Manganaro, MD

Mohannad Ibrahim, MD

Hemant A. Parmar, MD

Abbreviations: ADEM = acute disseminated encephalomyelitis, ALS = amyotrophic lateral sclerosis, CSF = cerebrospinal fluid, dAVF = dural arteriovenous fistula, FLAIR = fluid-attenuated inversion recovery, HIV = human immunodeficiency virus, MS = multiple sclerosis, NMOSD = neuromyelitis optica spectrum disorder, SACD = subacute combined degeneration, SI = signal intensity, STIR = short inversion time inversion-recovery, TM = transverse myelitis

RadioGraphics 2019; 39:1824–1839

<https://doi.org/10.1148/rg.2019190021>

Content Codes:   

From the Department of Radiology, Division of Neuroradiology, University of Michigan Health System, 1500 E Medical Center Dr, UH B1-D502, Ann Arbor, MI 48109. Presented as an education exhibit at the 2018 RSNA Annual Meeting. Received February 15, 2019; revision requested May 13 and received June 27; accepted July 2. For this journal-based SA-CME activity, the author M.J.L. has provided disclosures (see end of article); all other authors, the editor, and the reviewers have disclosed no relevant relationships. **Address correspondence to** M.J.L. (e-mail: mjlnlee@med.umich.edu).

©RSNA, 2019

SA-CME LEARNING OBJECTIVES

After completing this journal-based SA-CME activity, participants will be able to:

- Develop a systematic algorithmic approach to evaluating intramedullary SI abnormality at T2-weighted spinal MRI.
- Describe the clinical and imaging features of different causes of intrinsic spinal cord T2 SI abnormality with a focus on demyelinating disorders.
- Recognize pitfalls and mimics in evaluation of intrinsic spinal cord SI abnormalities, including those related to artifacts or extrinsic compression.

See rsna.org/learning-center-rg.

Intramedullary cord hyperintensity at T2-weighted MRI is a common imaging feature of disease in the spinal cord, but it is non-specific. Radiologists play a valuable role in helping narrow the differential diagnosis by integrating patient history and laboratory test results with key imaging characteristics. The authors present an algorithmic approach to evaluating intrinsic abnormality of spinal cord signal intensity (SI), which incorporates clinical evaluation results, time of onset (acute vs nonacute), cord expansion, and pattern of T2 SI abnormality. This diagnostic approach provides a practical framework to aid both trainees and practicing radiologists in workup of myelopathy.

©RSNA, 2019 • radiographics.rsna.org

Introduction

Myelopathy is a broad term that references the clinical symptoms related to spinal cord dysfunction such as motor and sensory changes and bowel and bladder dysfunction. MRI plays a key role in evaluation of suspected myelopathy because it can help identify a cause and delineate the extent of the abnormality.

Hyperintense intramedullary signal at T2-weighted imaging is a common and important indicator of myelopathy at MRI (1). T2 hyperintensity can reflect many processes at the microscopic level, including edema, blood-spinal cord barrier breakdown, ischemia, myelomalacia, or cavitation (2). The differential diagnosis includes a large number of diseases that affect the spinal cord. As such, abnormality of intramedullary signal intensity (SI) is somewhat nonspecific and can present a diagnostic dilemma.

Clinical evaluation (including patient history, physical examination, and laboratory tests) is the cornerstone of workup of suspected spinal cord disease. As such, the radiologist should be aware of the patient's clinical evaluation results, which greatly influence the differential diagnosis. When appropriate, this information is integrated into the diagnostic algorithm.

Extrinsic compression is a common cause of intramedullary T2 SI abnormality, and excluding this cause is critical during imaging evaluation. In cases of extrinsic compression, the cause of abnormality is known and does not pose a diagnostic dilemma. Therefore, this review focuses on intrinsic spinal cord SI abnormality that occurs in the absence of an extrinsic compressive lesion. We present a practical approach to diagnosis when an intrinsic cord SI abnormality is found. Rather than presenting an exhaustive list of spinal cord diseases, we focus on the common intrinsic disorders of the spinal cord with special attention to demyelinating conditions.

Algorithmic Approach

The algorithmic approach shown in Figure 1 first focuses on excluding artifact or extrinsic compression as a cause of cord SI abnormality. Next, a combination of clinical evaluation results,

TEACHING POINTS

- The algorithmic approach shown in Figure 1 first focuses on excluding artifact or extrinsic compression as a cause of cord SI abnormality. Next, a combination of clinical evaluation results, time of onset (acute vs nonacute), cord expansion, and pattern of T2 SI abnormality helps the radiologist arrive at a more specific diagnosis or at least narrow the differential diagnosis.
- Once a true (nonartifactual) spinal cord SI abnormality is identified, it is important to evaluate for the presence of an extrinsic compressive cause. Common extrinsic compressive causes include discogenic myelopathy, ligamentous thickening or redundancy from spondylotic change, vertebral body compression fracture with retropulsion, traumatic facet dislocation, and malignancy or infection of the surrounding spinal column.
- Demyelinating diseases are a common cause of intrinsic spinal cord SI change.
- Acute infectious myelopathy can be caused by viral, bacterial, and fungal pathogens. MRI demonstrates diffuse, typically nonexpansile T2 hyperintensity, with or without SI alterations at dedicated brain imaging. These findings make it essentially indistinguishable from demyelinating conditions, and differentiation is more likely to be made after CSF sampling and laboratory tests.
- In the nonacute setting, intrinsic SI alteration with associated focal expansion of the cord suggests a neoplastic process.

time of onset (acute vs nonacute), cord expansion, and pattern of T2 SI abnormality helps the radiologist arrive at a more specific diagnosis or at least narrow the differential diagnosis. Ancillary findings such as additional clinical workup results, extraspinal manifestations, and features on other MR images are appropriate for inclusion. This algorithmic approach may be a useful tool for practicing radiologists as well as trainees.

Artifacts

Quality control is the first step in image interpretation. Although quality control and artifact are not the focus of this article, the radiologist should be mindful of the causes of artifact at spinal imaging. These include Gibbs (aka truncation) artifacts seen at high-contrast interfaces, respiratory motion, vascular pulsation, cerebrospinal fluid (CSF) pulsation, and magnetic field inhomogeneity or susceptibility artifact related to surgical implants (3). Of particular note, Gibbs artifact can appear as alternating lines of low and high SI extending along the long axis of the spinal cord, which can mimic a cord SI abnormality or a syrinx (3) (Fig 2). This pattern is caused by the high-contrast interface of CSF with the spinal cord and can be minimized by increasing the number of phase-encoding steps, switching the frequency- or phase-encoding directions, or decreasing the field of view (3).

Extrinsic Compression

Once a true (nonartifactual) spinal cord SI abnormality is identified, it is important to evaluate for the presence of an extrinsic compressive cause. Common extrinsic compressive causes include discogenic myelopathy, ligamentous thickening or redundancy from spondylotic change, vertebral body compression fracture with retropulsion, traumatic facet dislocation, and malignancy or infection of the surrounding spinal column. Usually, cord SI alteration is seen focally at or adjacent to the causative feature. However, long-segment cord SI abnormality has also been associated with spondylotic change and may mimic inflammatory or neoplastic causes (4,5) (Fig 3). While some of these causes may manifest in a nonacute setting, localized cord SI alteration in a patient with acute myelopathic symptoms should be considered to be acute edema until proved otherwise and may necessitate emergent surgical intervention.

Acute versus Nonacute Symptom Onset

Once artifacts and extrinsic compression are excluded as possible causes of cord SI abnormality, the remaining cord SI alterations can be considered intrinsic to the spinal cord. At this point, it is essential to know whether the symptom onset is acute or nonacute, as this will strongly influence the differential diagnosis.

Acute Onset

If the symptom onset is acute, categories of causes to be considered are demyelination, ischemia, and infection. Among these, demyelination is the most common.

Demyelinating Disease

Demyelinating diseases are a common cause of intrinsic spinal cord SI change. Demyelinating diseases represent a heterogeneous group of diseases with variable clinical manifestation and imaging features. These include multiple sclerosis (MS), acute disseminated encephalomyelitis (ADEM), neuromyelitis optica spectrum disorder (NMOSD), and idiopathic transverse myelitis (TM). Notably, MS is at least 10 times as common as the others in this category (Table).

Multiple Sclerosis.—MS is a demyelinating disease of the central nervous system that is mediated by T cells and macrophages and is characterized by focal symptomatic lesions in the brain and spinal cord (1,6). With an incidence of about 3.6 per 100 000 person-years, MS is the most common demyelinating disease, with a higher incidence in females and in populations farther from the equator (7) (Table). The clinical course and severity of

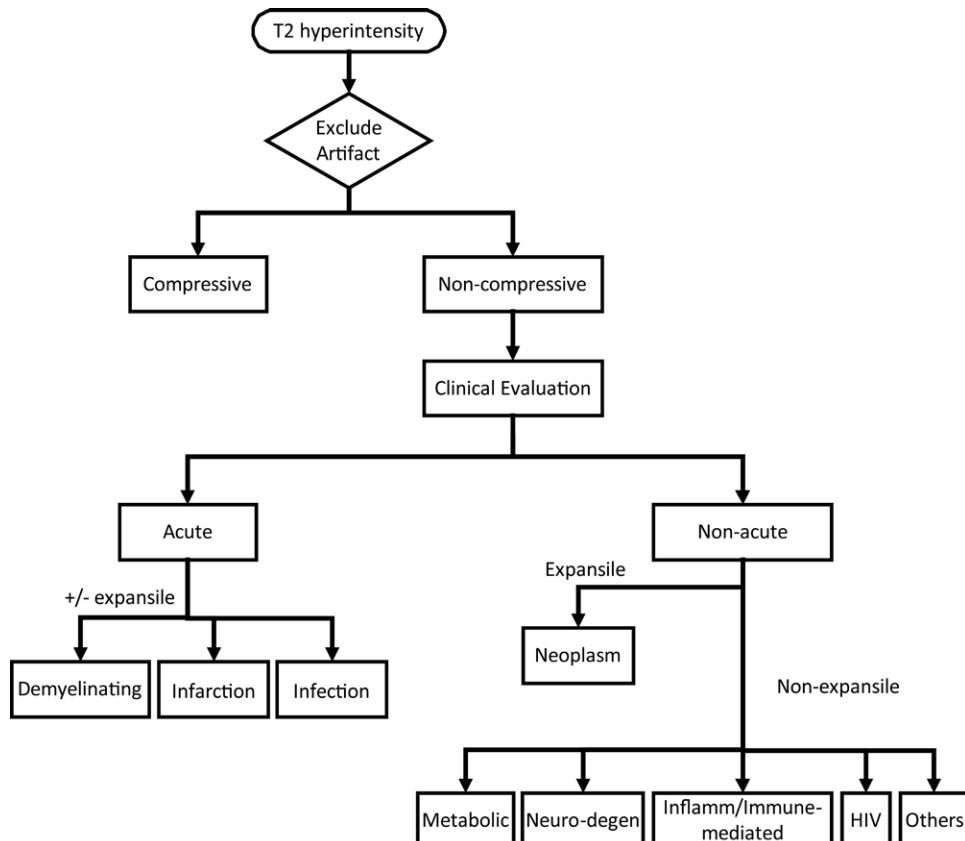
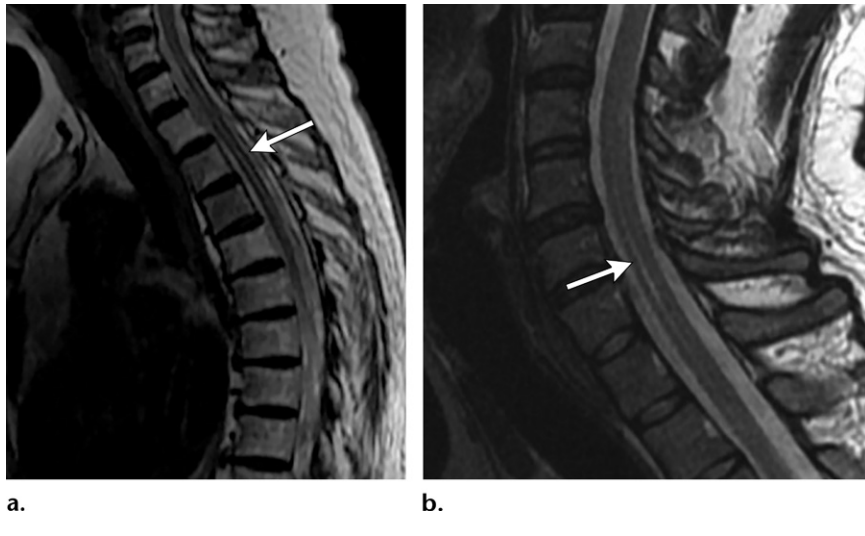


Figure 1. Algorithmic approach to evaluating T2 spinal cord hyperintensity at MRI. HIV = human immunodeficiency virus, Inflamm/Immune-mediated = inflammatory or immune-mediated, Neuro-degen = neurodegenerative.

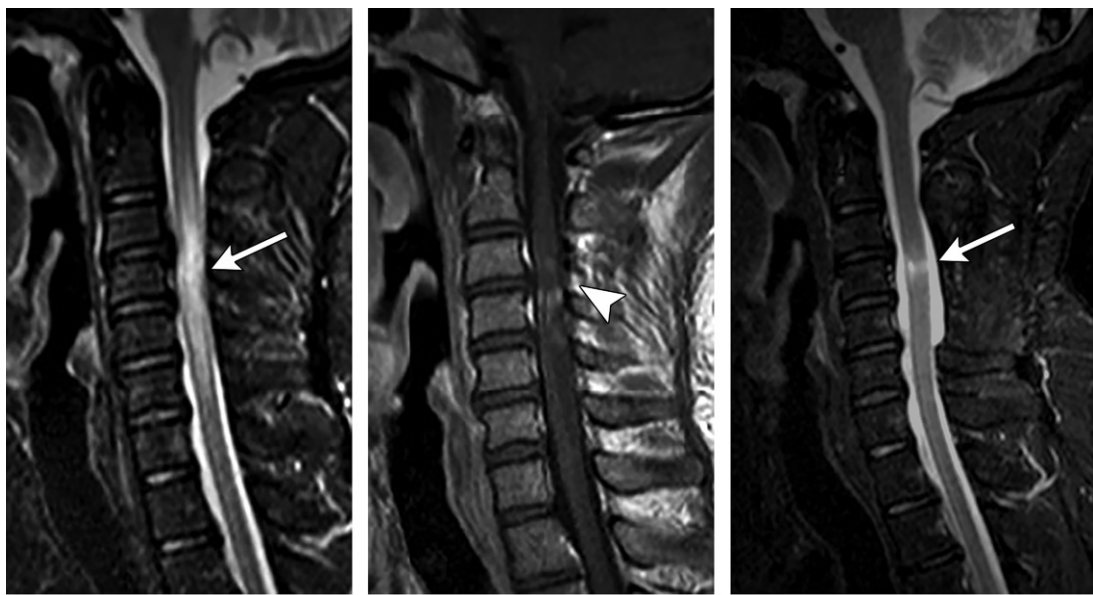
Figure 2. Gibbs (aka truncation) artifact in two patients. Sagittal MR images show multiple alternating light and dark parallel lines (arrow) at high-contrast interfaces, mimicking intrinsic cord SI abnormality or a syrinx.



the disease can vary greatly, with several clinical variants identified (8). The McDonald criteria are used to diagnose MS by incorporating clinical and radiologic evidence of multiple attacks disseminated in space and time (6,9). The criteria include the presence of oligoclonal bands in the CSF, which is both sensitive and specific for MS (10).

The spinal cord is affected in more than 90% of patients with clinically definite MS, and up to

20% of patients will have only spinal cord manifestations (11). MS in the spinal cord commonly affects the cervical region (1). Lesions are typically short (ie, <1.5 vertebral body segments) in craniocaudal extent, peripheral, and wedge-shaped or round and affect less than half of the cross-sectional area of the cord (1,12) (Figs 4, 5). There is involvement of both the gray and white matter in the brain and spinal cord; however, gray matter



a.

b.

c.

Figure 3. Spondylotic myelopathy in a 40-year-old man with leg weakness. (a, b) Sagittal short inversion time inversion-recovery (STIR) MR image (a) and MR image obtained after administration of contrast material (b) demonstrate T2 cord hyperintensity (arrow in a) and irregular patchy enhancement (arrowhead in b) secondary to extrinsic compression from surrounding disk bulge and degenerative change at the level of the most severe narrowing. (c) Follow-up MR image 14 months after posterior decompression surgery demonstrates significant improvement of the cord edema with residual focal myelomalacia (arrow).

Clinical Features of Demyelinating Diseases

| Parameter | MS | ADEM | NMOSD | TM |
|--------------------------------------|-----------------------------------------------------------------------------------------------|-----------------------------------------------------------------------------------------------------------------------------------------------|--------------------------------------------------------------------|------------------------|
| Incidence (per 100 000 person-years) | 3.6 | 0.4 | 0.05–0.40 | 0.001–0.008 |
| Clinical history | Multiple episodes | Abrupt single episode Signs of encephalopathy Occurs after viral illness or infection | Visual symptoms | Abrupt single episode |
| Laboratory test results | Oligoclonal bands | CSF analysis shows pleocytosis and no oligoclonal bands | Positive serum or CSF aquaporin-4 antibody No oligoclonal bands | NA* |
| Other neurologic sequelae | Dissemination in time and space Brain lesions in periventricular and juxtacortical regions | Symmetric bilateral brain lesions or large brain lesions involving deep gray matter or cortex with relative sparing of periventricular region | Optic nerves affected | May be precursor to MS |

*NA = not applicable.

involvement is more evident in the spinal cord than in the brain at routine imaging (1,12,13).

In acute or active disease, the lesions can demonstrate contrast enhancement (from transient blood-spinal cord barrier breakdown) or cord swelling (1,12). In chronic and long-standing or progressive disease, there can be spinal cord atrophy, which is thought to represent axonal loss (1,11). Many patients with MS have intracranial manifestations, so it is essential to evaluate for

concomitant juxtacortical, periventricular, or infratentorial brain lesions (8) (Fig 5).

Acute Disseminated Encephalomyelitis.—

ADEM typically manifests as an acute monophasic illness after viral infection or vaccination, predominantly occurring in the pediatric population (1,14). The proposed mechanism is development of an autoimmune antibody against myelin basic protein (1). It is much less

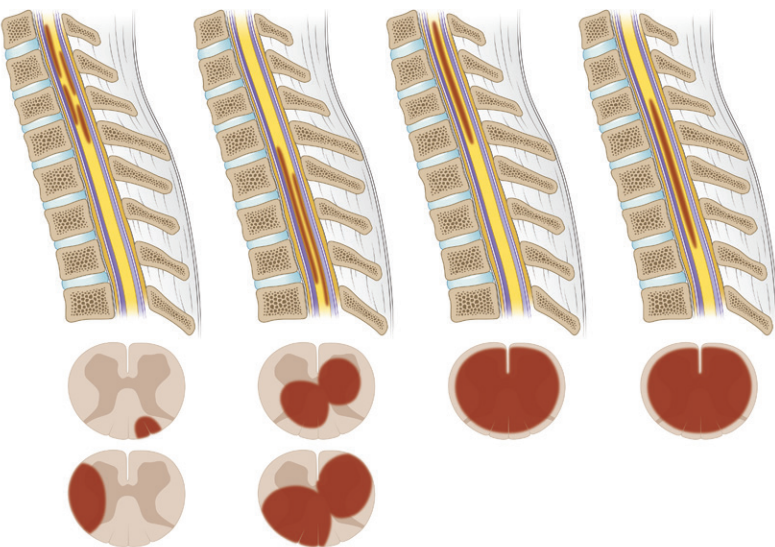


Figure 4. Distinguishing imaging features of demyelinating diseases. A short lesion is defined as less than 1.5 vertebral bodies in length, compared to a long lesion, which is greater than 1.5 vertebral bodies in length.

| | MS | ADEM | NMOSD | TM |
|-----------------------------|--------------------------------------------------|--------------------------------------|------------------------------------------|-------------------------------------|
| Cord cross-section affected | Asymmetric, small peripheral, wedge-shaped/round | Variable, can be confluent and large | 2/3 or more of diameter, central cord | 2/3 or more of diameter |
| Length | Short | Long | Long | Long |
| Location /number of lesions | Cervical/multiple | Thoracic/variable | Cervical with brainstem extension/single | Cervicothoracic and thoracic/single |

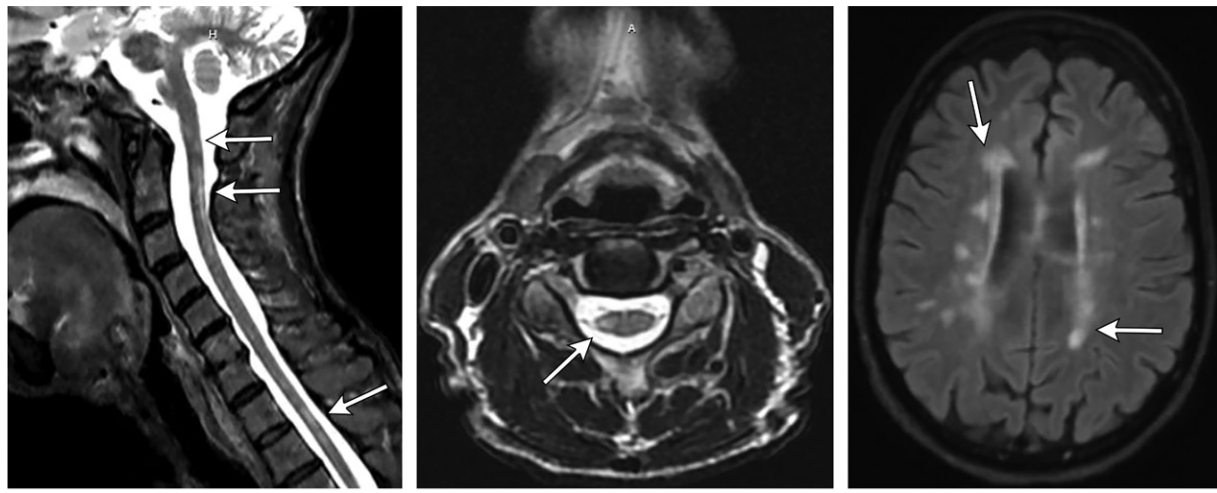


Figure 5. Spinal cord and intracranial involvement in a 62-year-old woman with long-standing MS. (a, b) Sagittal STIR (a) and axial T2-weighted (b) MR images of the cervical and upper thoracic spine show areas of patchy and short-segment (<1.5 vertebral body length) hyperintensity with a peripheral wedge-shaped appearance (arrows). (c) Axial fluid-attenuated inversion-recovery (FLAIR) MR image of the brain demonstrates areas of bilateral patchy T2 or FLAIR high SI in a pericallosal and periventricular distribution (arrows). The combined imaging features are typical of a demyelinating disease such as MS.

common than MS, with a reported incidence of 0.4 per 100 000 person-years (15). ADEM can be differentiated clinically from MS by its monophasic course, signs of encephalopathy, and CSF analysis showing pleocytosis without oligoclonal bands (16) (Table).

At spinal imaging, lesions of ADEM may be indistinguishable from those of MS, with some potential differences. ADEM lesions are found more commonly in the thoracic cord, are usually poorly marginated (owing to adjacent edema), and are larger in cross-sectional area and longer

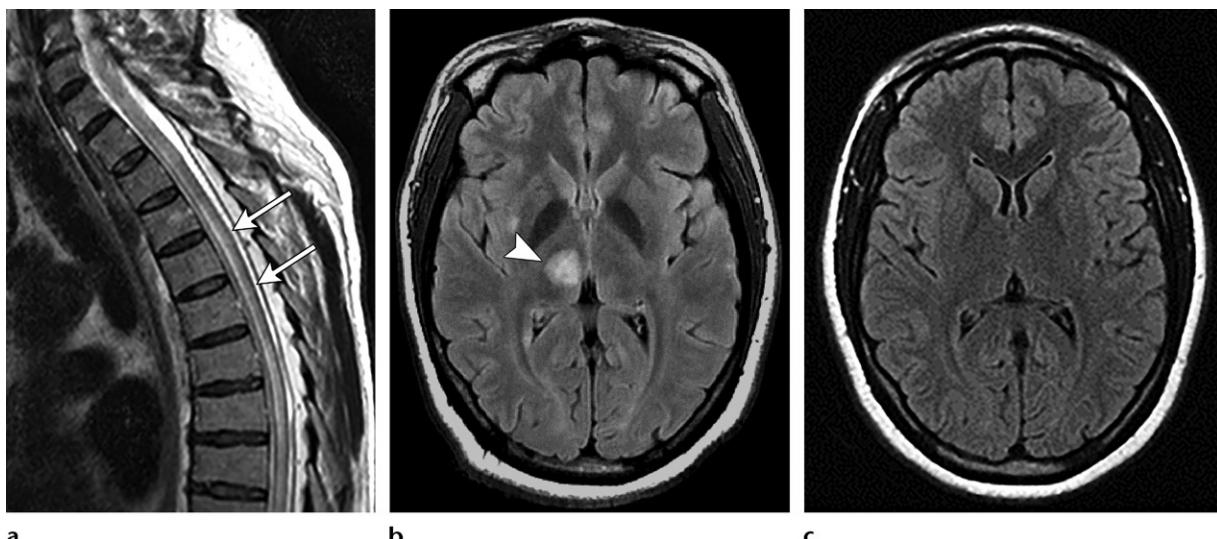


Figure 6. ADEM in a 10-year-old boy with acute onset of weakness. (a) Sagittal T2-weighted MR image demonstrates long-segment hyperintensity (arrows) extending from the upper to mid thoracic cord without expansion. (b) Axial FLAIR image of the brain demonstrates additional T2 or FLAIR hyperintensity in the right thalamus (arrowhead). (c) Follow-up axial MR image 6 months later demonstrates complete resolution of the previously seen hyperintense lesion in the right thalamus.

in craniocaudal extent (although variable in size) (1,17,18) (Figs 4, 6). On images obtained during the acute phase, the cord may show mild expansion and lesions may demonstrate a variable enhancement pattern (1).

MRI of the brain as well as the spinal cord is essential and may further help distinguish ADEM from MS. Intracranial findings may mimic MS, but certain features help confirm the diagnosis of ADEM, such as the presence of larger lesions in the subcortical white matter, involvement of the deep gray matter structure (basal ganglia and thalamus) and brainstem, and relative sparing of the periventricular region (14,16) (Fig 6). Notably, given the monophasic nature of many cases, follow-up imaging may show resolution (Fig 6c).

Neuromyelitis Optica Spectrum Disorder.

NMOSD is a demyelinating disease that predominantly affects the optic nerves and spinal cord, although brain lesions appear to be more common than previously recognized (1,12,19). The overall incidence is about 0.05–0.40 per 100 000 person-years, predominantly affecting females (1,20).

Laboratory tests in patients with NMOSD are likely to show the presence of the NMO-IgG antibody, a serum autoantibody that reacts to the water channel protein aquaporin-4. The presence of the NMO-IgG antibody is approximately 70% sensitive and 90% specific for NMOSD (14,21,22). CSF oligoclonal IgG bands are usually absent (14,23) (Table).

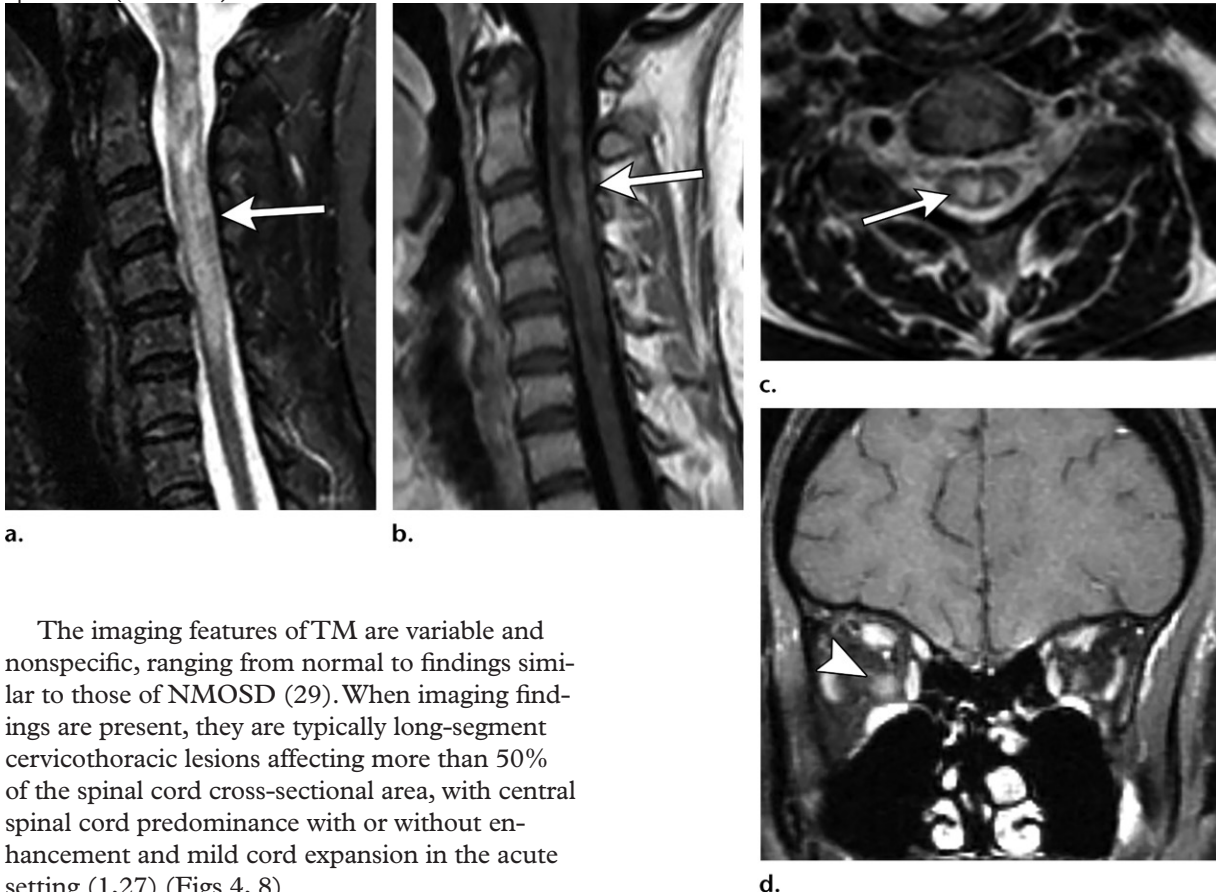
The overall prognosis is worse and the physical manifestations are more severe in patients with NMOSD than in patients with MS (1,6). The mainstay therapies for MS (eg, interferon- β and

natalizumab) have been reported to be ineffective against or even exacerbate the underlying disease in patients with NMOSD (24). Because of the differing disease course and divergent therapeutic approach, it has become critical to differentiate NMOSD from MS when possible.

At imaging, NMOSD lesions in the spinal cord are usually longer in craniocaudal extent than those in MS (>1.5 vertebral body) and involve the central gray matter of the cord, sometimes seen as longitudinally extensive spinal cord lesions (25) (Figs 4, 7). They frequently extend upward into the medulla (26). These “bright spotty lesions”—focal internal areas of T2 hyperintensity that are at least as bright as CSF with corresponding low SI at T1-weighted imaging—have recently been shown to be highly specific to NMOSD and are seen in about one-half of patients (25,26). Contrast enhancement and cord expansion can be seen in an acute setting (1).

Idiopathic Acute Transverse Myelitis.—Idiopathic acute TM is not a single disease entity but a diagnosis of exclusion when there are clinical signs of acute myelitis without a clear identifiable cause (27). Reported incidence rates ranging from 0.001 to 0.008 per 100 000 person-years, with the variation likely owing to differences in the definition and advances in diagnostic techniques over time (28) (Table). Because this entity is rare and is diagnosed from the clinical standpoint, the radiologist should use this term sparingly or not at all, as a large number of other causes must be excluded before considering TM in the differential diagnosis.

Figure 7. NMOSD in a 36-year-old woman. (a, b) Sagittal T2-weighted (a) and contrast-enhanced T1-weighted (b) MR images demonstrate cord T2 hyperintensity extending from the lower medulla to the C6 level associated with mild cord expansion (arrow in a) and heterogeneous enhancement (arrow in b). (c) Axial T2-weighted MR image shows hyperintensity (arrow) affecting more than two-thirds of the cross-sectional area of the cord. (d) MR image shows mild expansion and patchy enhancement of the right optic nerve (arrowhead).



The imaging features of TM are variable and nonspecific, ranging from normal to findings similar to those of NMOSD (29). When imaging findings are present, they are typically long-segment cervicothoracic lesions affecting more than 50% of the spinal cord cross-sectional area, with central spinal cord predominance with or without enhancement and mild cord expansion in the acute setting (1,27) (Figs 4, 8).

Ischemic Myelopathy

Spinal cord infarction is a rare cause of acute myelopathy, accounting for about 6% of cases of myelopathy (30). As in infarction involving the brain, the onset of symptoms is abrupt and the neurologic deficits depend on the vascular territory and the level of cord affected (30). In addition to neurologic symptoms, back pain is also common and is seen in about 70% of patients (30).

Spinal cord ischemia can be arterial or venous. The arterial supply to the spinal cord arises from multiple radiculomedullary arteries, which ultimately form the anterior and posterior spinal arteries. The anterior spinal artery perfuses the anterior two-thirds of the spinal cord, and the posterior spinal arteries supply the posterior one-third of the spinal cord.

Compromise of the anterior or posterior circulation causes different neurologic sequelae (30). Anterior spinal artery syndrome causes bilateral loss of motor and spinothalamic function with sparing of the dorsal columns, while posterior spinal artery syndrome results in loss of proprioception and perception of vibration below the level of the dorsal cord (30,31).

Acute arterial compromise is often associated with plaque-related thrombosis or emboli. Other causes include occlusion related to aortic or cardiac interventions, trauma, systemic arteriopathy, or rarely fibrocartilaginous embolization (30,32,33). Classically, anterior spinal artery infarct produces T2 hyperintensity in the anterior horns and surrounding white matter, forming the “owl’s eye” sign (Fig 9). Posterior spinal artery infarct produces T2 hyperintensity that is limited to the dorsal columns and posterior horns (31,34). Restricted diffusion at diffusion-weighted imaging can improve diagnostic certainty when cord infarct is suspected (Fig 9) (35,36).

In the subacute setting, there may be enhancement and hemorrhagic conversion (30). Another helpful imaging feature is the presence of concomitant vertebral body infarction due to common vasculature shared by the spinal cord and vertebral body (30).

Frank venous spinal cord infarction is uncommon, although edema from venous congestion is common, and resultant ischemia can lead to

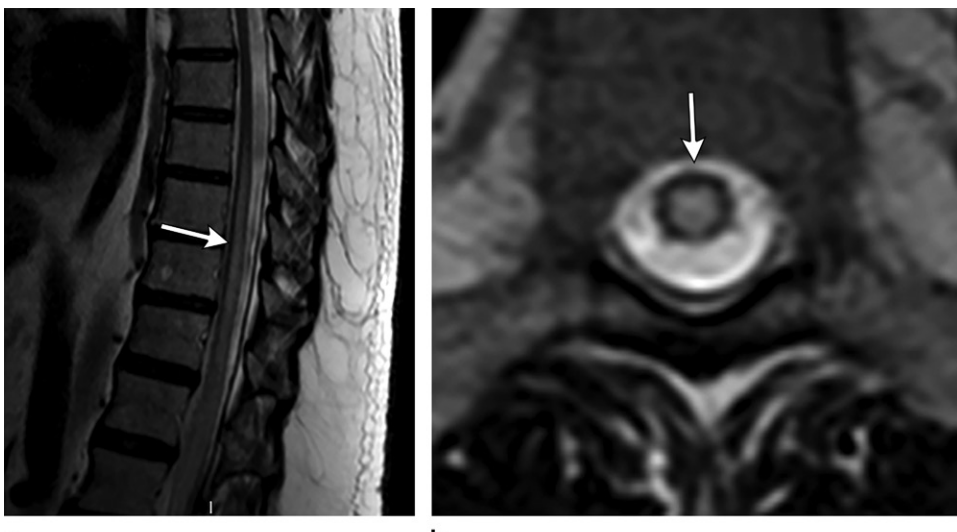
**a.****b.**

Figure 8. Recurrent idiopathic TM in a 60-year-old man with several weeks of worsening bilateral lower extremity weakness, pain, and numbness that progressed to an inability to walk. He was diagnosed with recurrent idiopathic TM after an extensive workup was negative for an alternate cause. (a) Sagittal T2-weighted MR image shows a longitudinally extensive cord hyperintensity extending from the T9 level to the tip of the conus (arrow). (b) On an axial T2-weighted MR image, the lesion is seen to affect nearly the entire cross-sectional volume of the spinal cord without associated expansion (arrow).

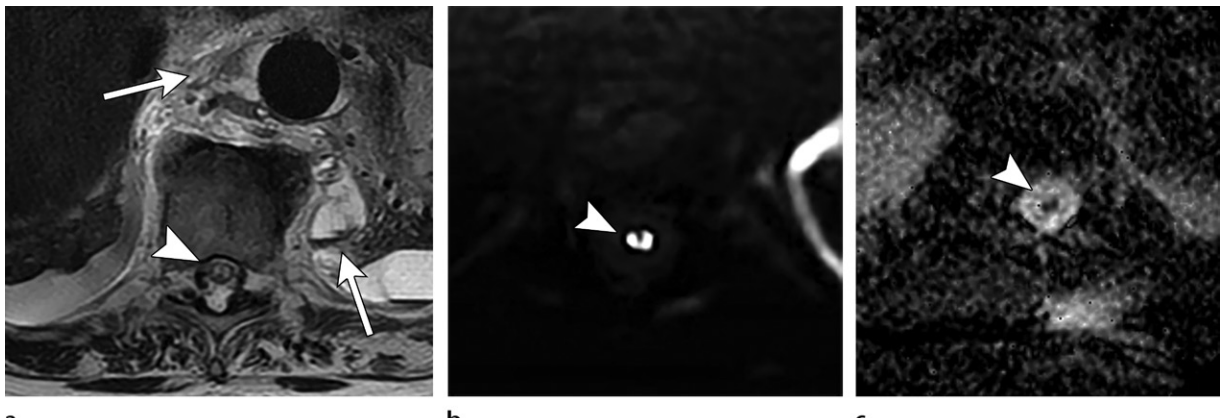
**a.****b.****c.**

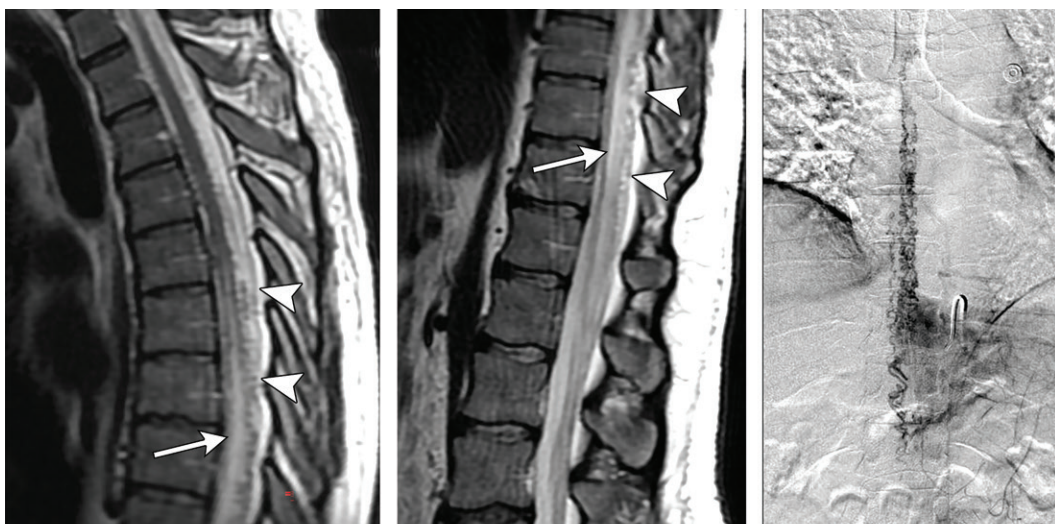
Figure 9. Acute cord infarct in a 60-year-old woman after thoracoabdominal aortic aneurysm repair. Axial T2-weighted MR image (a), diffusion-weighted MR image (b), and apparent diffusion coefficient (ADC) map (c) show postoperative changes in the paraspinal soft tissues (arrows in a). There is abnormal T2 hyperintensity involving the anterior horns of the central gray matter, demonstrating the owl's eye sign (arrowhead in a), with a corresponding area of low SI on the ADC map (arrowhead in b and c), suggesting impeded diffusion from acute spinal cord infarction.

progressive insidious onset of myelopathic symptoms (30,37). Spinal dural arteriovenous fistula (dAVF) can cause increased venous pressure and has a subtle but characteristic appearance at MRI. dAVF usually manifests with poorly defined T2 hyperintensity and cord enlargement, which represent spinal cord edema. The location of SI abnormality depends on the site of the dAVF, and it is often seen in the thoracic cord extending to the conus medullaris. The dilated perimedullary vessels manifest as multiple serpentine flow voids along the surface of the spinal cord (1,37) (Fig 10). Advanced imaging techniques such as contrast-enhanced MR angiography or

thin-section FIESTA (fast imaging employing steady-state acquisition) may serve as useful tools in indeterminate cases or for further characterization (38).

Infectious Myelopathy

Acute infectious myelopathy can be caused by viral, bacterial, and fungal pathogens (39). MRI demonstrates diffuse, typically nonexpansile T2 hyperintensity, with or without SI alterations at dedicated brain imaging. These findings make it essentially indistinguishable from demyelinating conditions, and differentiation is more likely to be achieved after CSF sampling and laboratory tests.

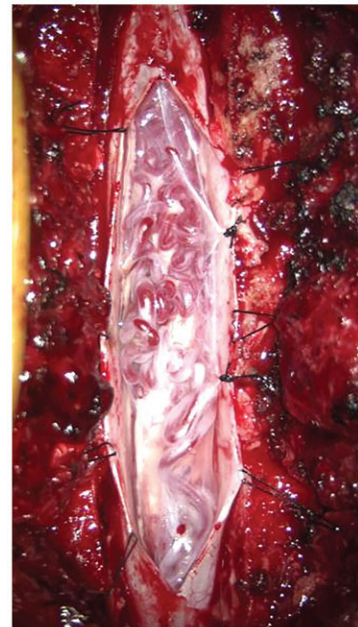


a.

b.

c.

Figure 10. dAVF in a 37-year-old man with a 4-month history of progressive lower extremity dysesthesias, gait unsteadiness, and weakness. (a, b) Sagittal T2-weighted MR images demonstrate longitudinally extensive abnormal T2 hyperintensity extending from the lower thoracic cord to the conus medullaris (arrow) with prominent surrounding flow voids (arrowheads). (c) Image from digital subtraction angiography (DSA) helps confirm a type 1 spinal dAVF supplied by the left T9 segmental artery with drainage into the dilated and tortuous posterior coronal venous plexus. (d) Intraoperative image obtained during T8-T10 laminectomies demonstrates findings seen on the MR images and DSA image.



d.

Intramedullary spinal cord abscess is a more serious although rare diagnosis, which has also been reported as being caused by several pathogens. Abscess is characterized by ring enhancement at MRI, which develops approximately 1 week after an acute infection (40). Diffusion restriction can be a useful ancillary imaging feature, similar to in intracranial abscesses (41).

Nonacute Onset

The diseases associated with nonacute myelopathy are distinct from those that manifest acutely. They include neoplastic, metabolic, neurodegenerative, and inflammatory or immune-mediated disease and human immunodeficiency virus (HIV) infection.

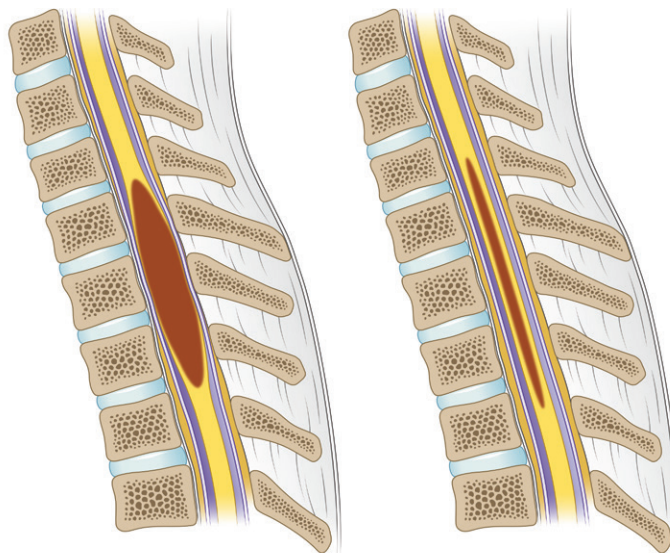
Nonacute Expansile Neoplastic Myelopathy

If the onset of symptoms is subacute or chronic, the next task is to examine the contour of the spinal cord to determine if the cord is focally expanded. In the nonacute setting, intrinsic SI alteration with associated focal expansion of the cord suggests a neoplastic process. Typically, spinal cord expansion is an imaging feature that helps distinguish neoplastic from nonneoplastic conditions (42) (Fig 11).

In addition to cord expansion, ancillary characteristics often seen in intramedullary neoplasm include enhancement (especially focal or nodu-

lar), hemorrhage, and associated cystic changes. Clinical manifestation of intramedullary neoplasms typically involves insidious and progressive neurologic symptoms, with back or neck pain depending on the tumor location (43). This pain is typically exacerbated by a recumbent position and may be related to secondary irritation or distention of the dura (43). It is important to be aware that nonneoplastic causes, such as ADEM or NMOSD, can demonstrate cord expansion, especially on images obtained during the acute phase. However, the acuity of symptoms helps determine the cause, which underscores the importance of the clinical evaluation.

If the diagnosis is still uncertain after spinal imaging and clinical workup, additional imaging of the brain may be helpful. The presence of



| | Neoplastic | Nonneoplastic |
|-------------------|------------|---------------|
| Cord expansion | Common | Not common |
| Number of lesions | Single | Variable |

Figure 11. Neoplastic versus nonneoplastic causes of intrinsic spinal cord SI abnormality. The presence of cord expansion is used to differentiate between neoplastic and nonneoplastic causes.

intracranial lesions may indicate an inflammatory cause. If uncertainty persists, short-term follow-up spinal imaging may be helpful, as persistence or enlargement of the spinal lesion indicates a neoplastic process.

Neoplastic lesions of the spinal cord and spinal column are commonly categorized as intramedullary or extramedullary. This discussion focuses on imaging features of intramedullary lesions, which can manifest as focal T2 hyperintensity within the cord. Frequently encountered intramedullary neoplasms include astrocytoma, ependymoma, and hemangioblastoma. Although far less common, lymphoma and metastases can manifest as intramedullary lesions and could also be considered in patients with a history of malignancy.

Astrocytoma, the most common glial tumor in the pediatric population, is an infiltrative glial tumor often involving multiple vertebral body levels of the cervical, thoracic, and sometimes the entire spinal cord (42,43). Owing to their infiltrative pattern of growth, they are typically poorly defined lesions with patchy enhancement and a large amount of peritumoral edema (42). Spinal astrocytoma occurs most frequently in young males (mean age of presentation, 29 years) and is associated with neurofibromatosis type 1 (42).

Ependymoma is the most common glial tumor in adults and is often seen in the cervical spinal cord (42). Unlike astrocytoma, it is a sharply defined encapsulated tumor and is associated with neurofibromatosis type 2 (42,43). Ependymoma is usually centrally located, enhances avidly, and commonly demonstrates peritumoral cystic

change and hemorrhage (42). About 20%–30% of cases demonstrate the hemosiderin “cap” sign, characterized by a rim of T2 hypointensity at one or both poles of the tumor (42) (Fig 12).

Hemangioblastoma is a well-demarcated highly vascular nonglial tumor (42). It can appear similar to cerebellar hemangioblastoma, with an avidly enhancing mural nodule with or without an associated tumor cyst or syrinx formation (42). Classically, internal flow voids and presence of a large draining vein are seen; however, despite its high vascularity, associated hemorrhage is rare (42). When there are multiple lesions or additional lesions in the cerebellum, the diagnosis of von Hippel–Lindau disease should be considered (42,43).

Nonacute Nonexpansile Myelopathy

Metabolic Disease.—Several metabolic derangements can lead to spinal cord SI alteration, including various vitamin and mineral deficiencies, mitochondrial diseases, leukodystrophies, and genetic syndromes. For example, subacute combined degeneration (SACD) can be seen in the setting of vitamin B₁₂ deficiency and is usually related to malabsorption or inadequate intake (44). This entity tends to affect the dorsal columns and lateral corticospinal tracts, hence patients present with paresthesia of the hands and feet with loss of proprioception, which may progress to gait ataxia and even ataxic paraparesis in severe cases (44).

Sagittal MRI demonstrates nonexpansile T2 hyperintensity predominantly involving long

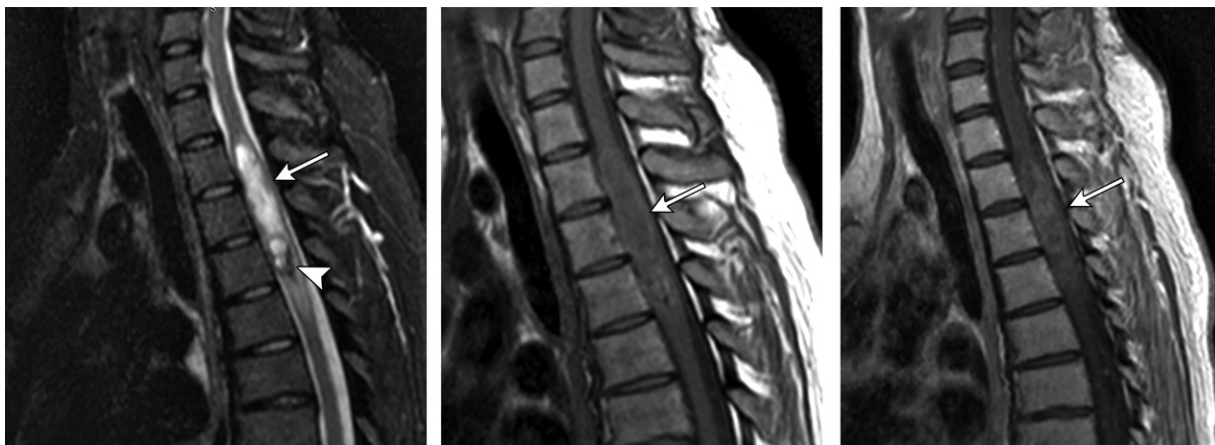
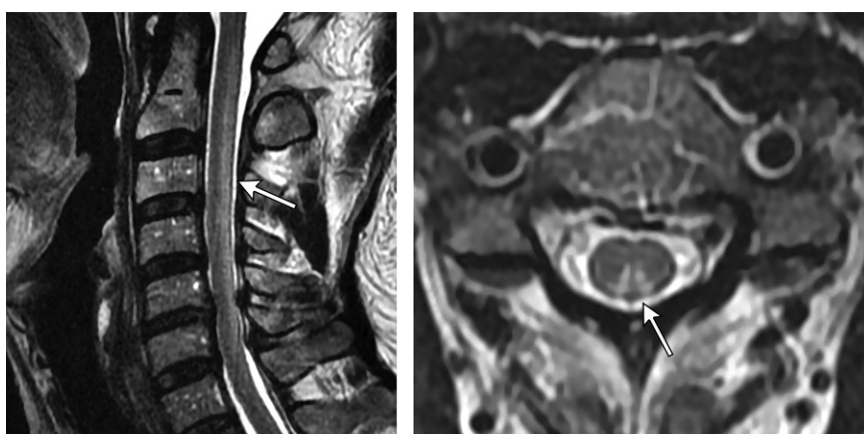
**a.****b.****c.**

Figure 12. Cord ependymoma in a 25-year-old woman with a history of neurofibromatosis type 2 who presented with progressive back pain and leg numbness. Sagittal STIR (a), T1-weighted (b), and contrast-enhanced T1-weighted (c) MR images demonstrate a heterogeneous mildly enhancing intramedullary lesion in the upper thoracic cord, causing cord expansion (arrow). The mass shows hemorrhagic products along the inferior aspect (arrowhead in a), demonstrating the hemosiderin cap sign.

Figure 13. SACD in a 54-year-old man with progressive sensory and gait disturbance with mild cognitive slowing who was found to have a low serum vitamin B_{12} level. (a) On a sagittal STIR image, hyperintensity involving the dorsal aspect of the cord extends from C1 to C6 (arrow). (b) Axial T2-weighted MR image demonstrates nonexpansile hyperintensity in the dorsal columns in the inverted V pattern (arrow). The patient's neurologic symptoms markedly improved after supplemental vitamin B_{12} injections.

**a.****b.**

segments in the posterior cervical and thoracic spinal cord without associated enhancement (1). Axial T2-weighted MR images of SACD demonstrate hyperintensity involving bilateral dorsal columns, classically in an “inverted V” configuration (45) (Fig 13). Such typical imaging findings in a patient with normal serum vitamin B_{12} levels should raise suspicion for alternate causes of SACD, such as nitrous oxide toxic effects, zinc toxic effects, or copper deficiency (46–48).

Neurodegenerative Disease.—Motor neuron diseases of the spinal cord represent a rare group of fatal progressive neurodegenerative diseases, including primary lateral sclerosis, spinocerebellar ataxia, iron neurodegeneration, Friedreich ataxia, and amyotrophic lateral sclerosis (ALS) (39). ALS is the most common type of motor neuron disease (49).

ALS has an incidence of about two in 100 000 person-years, with a short median survival time (50,51). Atrophy of the anterior horn cells affect-

ing both upper and lower motor neurons results in muscle weakness, cramps, fasciculations, and eventual progression to respiratory failure. The diagnosis of ALS is rarely made by using imaging alone, and other causes such as acute flaccid paraparesis can have a similar imaging appearance (52). Nonetheless, imaging of the cord in suspected ALS can help confirm the diagnosis, exclude other causes, and monitor progression (50,51).

MRI demonstrates T2 hyperintensity involving the anterolateral columns with or without associated spinal cord atrophy. The SI abnormality may be seen to extend cephalad along the cortico-spinal tracts into the intracranial compartment (50) (Fig 14). The degree of spinal cord atrophy, especially gray matter, correlates with the degree of disability at both baseline and follow-up examinations (51).

Inflammatory and Immune-mediated Disease.—The three common multisystem inflammatory and

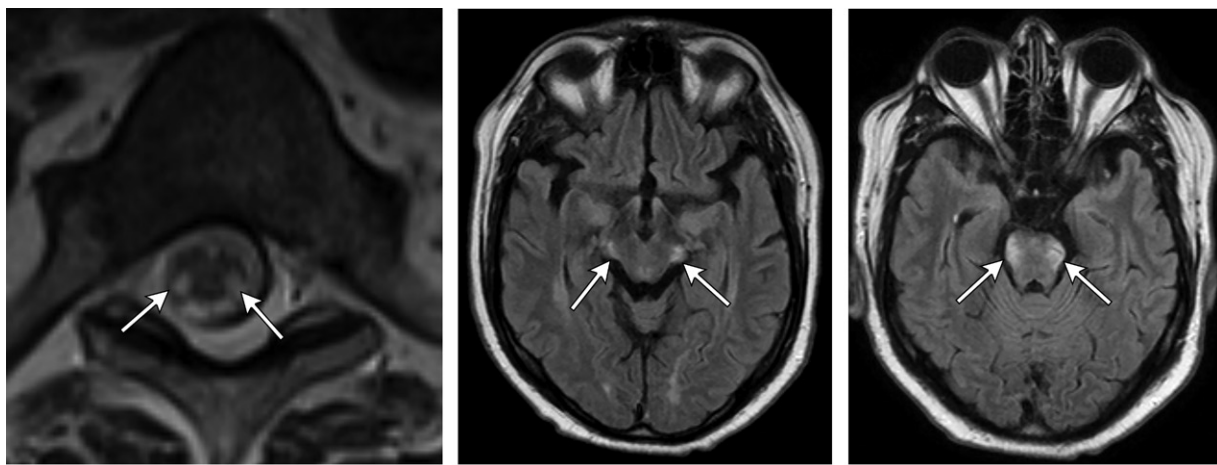
**a.****b.****c.**

Figure 14. ALS in a 52-year-old man with progressive spastic quadriplegia. (a) Axial T2-weighted MR image shows hyperintensity in the lateral aspects of the cervical spinal cord (arrows) without enhancement or cord expansion. (b, c) Additional axial MR images demonstrate T2 or FLAIR hyperintensity in the corticospinal tracts within the cerebral peduncles and lateral aspects of the midbrain and pons (arrows).

immune-mediated disorders affecting the spinal cord are systemic lupus erythematosus, Sjögren disease, and neurosarcoidosis. Manifestations of these diseases are variable, and often the diagnosis will be made by considering the clinical history or any prior nonneurologic manifestations. In general, central nervous system involvement in these entities is uncommon, and spinal cord involvement in particular is rare. If the spinal cord is affected, patients can present with typical myelopathic symptoms such as numbness or sphincter dysfunction (53). If there is concurrent involvement of the brain, patients may present with cranial neuropathy and aseptic meningitis (14).

At MRI, there is usually long-segment nonexpansile T2 hyperintensity, which can be seen in all three entities. Variable intramedullary enhancement can be seen in any of these conditions; however, neurosarcoidosis may have distinguishing features including dorsal spinal cord predominance, leptomeningeal enhancement, and the trident sign—crescentic posterior subpial enhancement with subtle additional central canal enhancement (53,54) (Fig 15). All corners of the available images should be evaluated for extraspinal manifestations of these multisystem disorders, such as cystic changes in the salivary glands associated with Sjögren disease or hilar lymphadenopathy associated with neurosarcoidosis (Fig 15). When there is persistent diagnostic uncertainty, CSF sampling can help distinguish these causes because each condition manifests with specific disease markers.

In addition to multisystem disorders, post-treatment change after spinal irradiation can produce myelitis within the irradiated field (55). Radiation myelitis has a widely variable latent period and manifests as slowly progres-

sive myelopathy including leg paresthesia, motor weakness, and back pain (56). At MRI, there is typically extensive long-segment T2 hyperintensity. In the initial phase, there may be a variable degree of enhancement. In later stages, there may be chronic atrophy or even cystic necrosis (55,56) (Fig 16). The ancillary finding of fatty bone marrow replacement in the corresponding vertebral bodies supports the diagnosis (56).

HIV Myelopathy.—Despite widespread use of antiretroviral therapy, the incidence of neurologic sequelae in patients with HIV infection remains high at around 70% (57). HIV and associated opportunistic infections can affect both the central and peripheral nervous systems (57,58). In primary HIV-associated myelopathy, patients typically present with progressive spastic paraparesis, ataxia, and loss of sensation.

The vacuolization within the white matter of the cord seen at histologic analysis can be seen at MRI as an area of symmetric nonenhancing high SI in the posterior columns. This appearance mimics that of SACD and is possibly related to an altered vitamin B₁₂ metabolic pathway (59,60) (Fig 17). However, findings at MRI are often nonspecific and can vary significantly in patients with a clinical diagnosis of HIV myelopathy, likely owing to the heterogeneous nature of this disease entity. Imaging features can range from normal to diffuse T2 hyperintensity in the central spinal cord with associated cord atrophy (58) (Fig 17).

Other Abnormalities.—Rare anatomic abnormalities such as spinal cord herniation and arachnoid webs can be seen at imaging as intramedullary T2 hyperintensity and may progress to syrinx

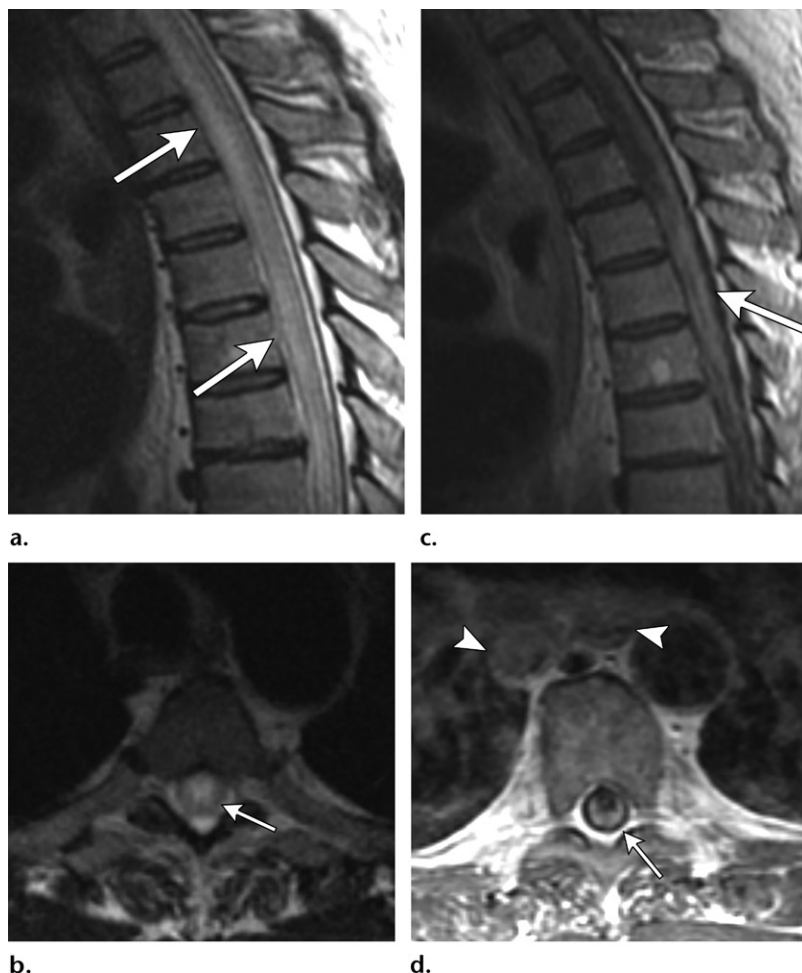


Figure 15. Neurosarcoidosis in a 52-year-old man with lower extremity weakness and fecal and urinary retention. (a, b) Sagittal (a) and axial (b) T2-weighted MR images show extensive central T2 hyperintensity (arrows) without expansion extending from the cervicomедullary junction to the conus medullaris. (c, d) Sagittal (c) and axial (d) contrast-enhanced MR images show associated dorsal pial enhancement (arrow) and enlarged mediastinal lymph nodes (arrowheads in d). This combination of findings is typical for neurosarcoidosis.

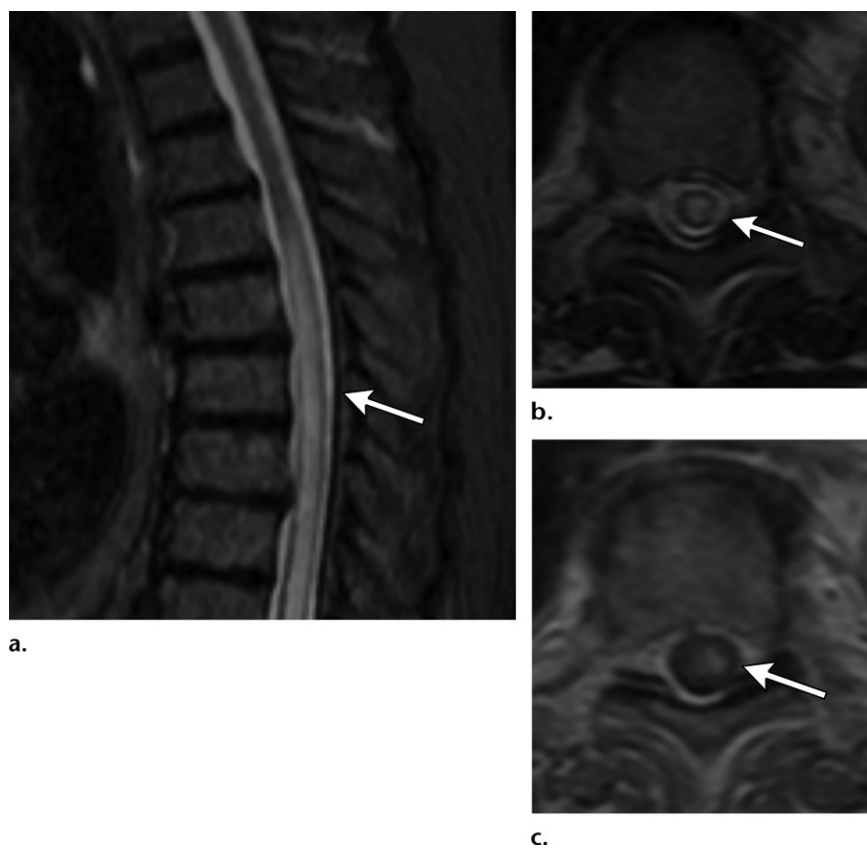
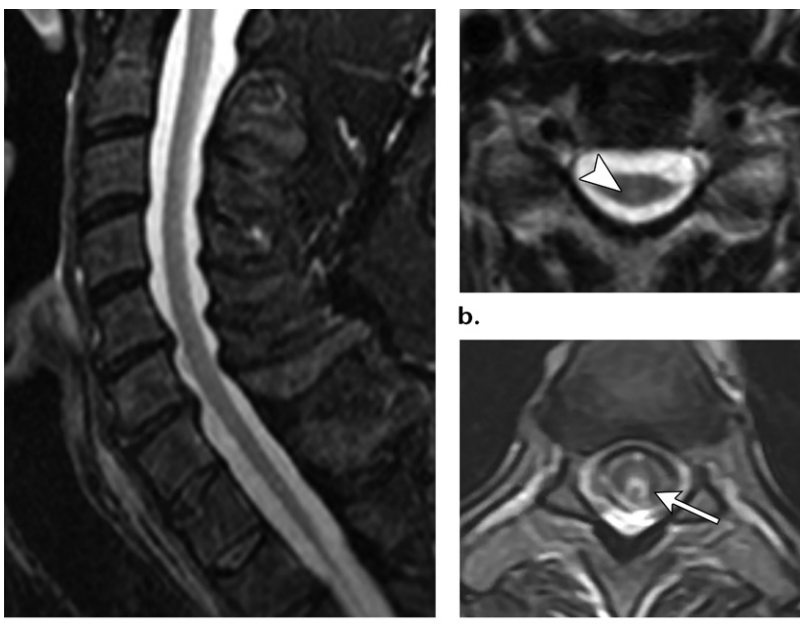


Figure 16. Radiation myelopathy in a 63-year-old man with multiple myeloma who presented with progressive weakness and urinary retention approximately 6 months after targeted spinal radiation therapy. (a, b) Sagittal STIR image (a) and axial T2-weighted MR image (b) show extensive central T2 hyperintensity (arrow) without thoracic cord expansion in the prior radiation field. (c) Axial contrast-enhanced T1-weighted MR image demonstrates mild patchy enhancement within the left hemicord (arrow). The combination of clinical history and imaging findings is typical of radiation myelopathy.



a.

b.

c.

Figure 17. HIV myelopathy. (a, b) Images in a 50-year-old man with progressive spastic quadriplegia show diffuse cord atrophy through visualized segments of the cervical and upper thoracic spinal cord (a) with subtle T2 SI involving the central portion of the spinal cord (arrowhead in b). (c) Axial T2-weighted MR image in a different patient with suspected HIV myelopathy demonstrates hyperintensity in the dorsal columns (arrow), mimicking SACD.



a.

b.

c.

d.

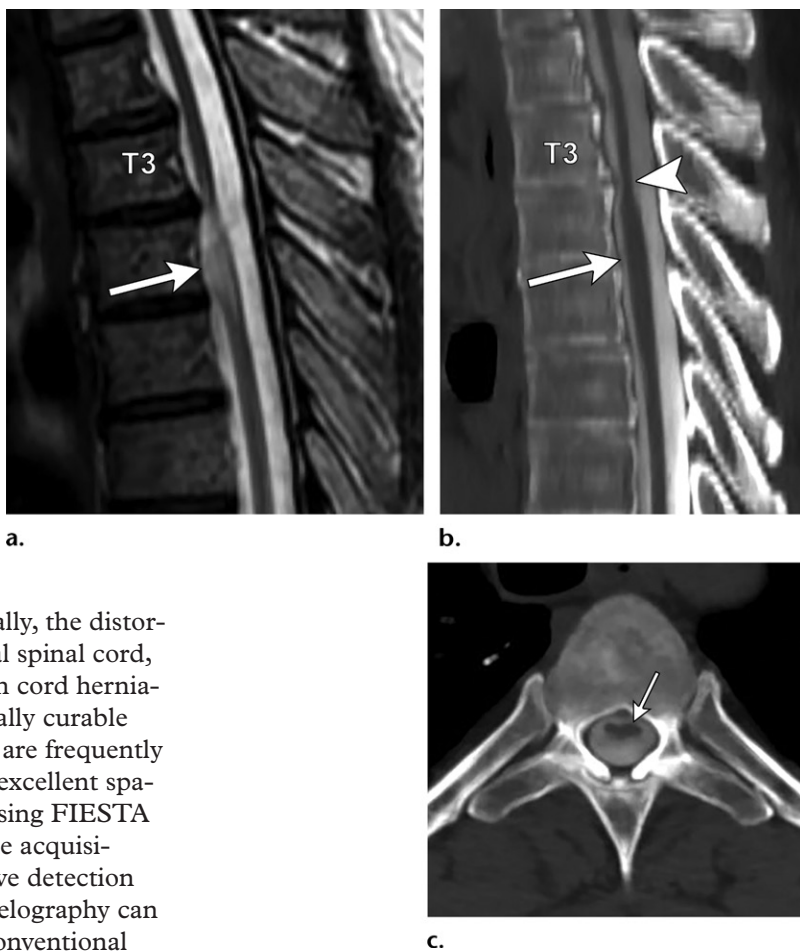
Figure 18. Spinal cord herniation in a 66-year-old man with a history of chronic back pain and acute onset of thoracic intrascapular pain. (a) Sagittal T2-weighted MR image demonstrates a syrinx extending from C7 to the level of the T2-T3 disk space (arrow) with adjacent cord SI abnormality. (b) Axial T2-weighted MR image shows that the cord appears to be apposed to the ventral aspect of the dura with no visible CSF ventral to the spinal cord (arrow). (c) Sagittal CT myelogram shows a ventrally displaced spinal cord that is closely apposed to the dorsal aspect of the vertebral bodies throughout the thoracic spine (arrowheads), with focal distortion of the posterior cord contour at the T3-T4 level with a transition in the cord caliber (arrow). (d) Axial CT myelogram at the T3-T4 level demonstrates the center of the cord possibly extending through the anterior surface of the dural sac (arrow). Intraoperatively, this was confirmed to be a ventral thoracic dural defect causing spinal cord herniation.

formation secondary to a disruption of CSF flow dynamics (61). These abnormalities appear as characteristic cord contour distortion at imaging. Spinal cord herniation occurs when the spinal cord herniates through a postsurgical or idiopathic dural defect. Imaging shows characteristic anterior kink-

ing of the spinal cord with enlargement of the subarachnoid space dorsal to the cord (62) (Fig 18).

Arachnoid webs are intradural extramedullary arachnoid tissue that crosses over the dorsal surface of the spinal cord (61). These result in a cord contour distortion that appears similar to

Figure 19. Arachnoid web in a 47-year-old man with a history of progressive paraparesis and lower extremity numbness. (a) Sagittal T2-weighted MR image demonstrates focal intramedullary abnormal SI with cord distortion at the T3-T4 level adjacent to slight cord expansion (arrow). (b) Sagittal CT myelogram demonstrates relative expansion of the cord at the T4 level (arrow) with focal cord thinning at the T3-T4 level (arrowhead), corresponding to the cord abnormality seen on the MR image. (c) Axial CT myelogram shows marked thinning with anterior displacement of the cord at the T3-T4 level (arrow). Intraoperatively, this was confirmed to be related to arachnoiditis with webs without evidence of cord herniation.



cord herniation (Fig 19). Occasionally, the distortion causes indentation of the dorsal spinal cord, known as the scalpel sign (61). Both cord herniation and arachnoid web are potentially curable with surgical intervention, but they are frequently overlooked diagnoses (61,62). The excellent spatial resolution of images acquired using FIELA (fast imaging employing steady-state acquisition) sequences at MRI may improve detection (63,64). In equivocal cases, CT myelography can help localize the dural defect and conventional myelography shows real-time movement of CSF, so that other causes of intradural filling defect such as arachnoid cyst can be excluded (62).

Conclusion

Spinal cord SI abnormality at MRI is a commonly encountered finding in spinal cord disease and poses diagnostic challenges owing to the broad differential diagnosis and variable appearances at imaging. Our algorithmic approach that combines clinical evaluation, acute versus nonacute time of onset, cord expansion, and pattern of T2 SI abnormality provides a framework for radiologists to help narrow their differential diagnosis in imaging evaluation of myelopathy.

Acknowledgments.—The authors would like to thank Danielle Dobbs and Vanessa Allen for the illustrations.

Disclosures of Conflicts of Interest.—M.J.L. Activities related to the present article: disclosed no relevant relationships. Activities not related to the present article: honorarium from *Contemporary Diagnostic Radiology* for writing an article. Other activities: disclosed no relevant relationships.

References

- Grayev AM, Kissane J, Kanekar S. Imaging approach to the cord T2 hyperintensity (myelopathy). *Radiol Clin North Am* 2014;52(2):427–446.
- Nouri A, Martin AR, Mikulis D, Fehlings MG. Magnetic resonance imaging assessment of degenerative cervical my-
- elopathy: a review of structural changes and measurement techniques. *Neurosurg Focus* 2016;40(6):E5.
- Taber KH, Herrick RC, Weathers SW, Kumar AJ, Schomer DF, Hayman LA. Pitfalls and artifacts encountered in clinical MR imaging of the spine. *RadioGraphics* 1998;18(6):1499–1521.
- Bae YJ, Lee JW, Park KS, et al. Compressive myelopathy: magnetic resonance imaging findings simulating idiopathic acute transverse myelopathy. *Skeletal Radiol* 2013;42(6):793–802.
- Kelley BJ, Erickson BJ, Weinshenker BG. Compressive myelopathy mimicking transverse myelitis. *Neurologist* 2010;16(2):120–122.
- Kearney H, Miller DH, Ciccarelli O. Spinal cord MRI in multiple sclerosis: diagnostic, prognostic and clinical value. *Nat Rev Neurol* 2015;11(6):327–338.
- Alonso A, Hernán MA. Temporal trends in the incidence of multiple sclerosis: a systematic review. *Neurology* 2008;71(2):129–135.
- Filippi M, Rocca MA. MR imaging of multiple sclerosis. *Radiology* 2011;259(3):659–681.
- Thompson AJ, Banwell BL, Barkhof F, et al. Diagnosis of multiple sclerosis: 2017 revisions of the McDonald criteria. *Lancet Neurol* 2018;17(2):162–173.
- Bernitsas E, Khan O, Razmjou S, et al. Cerebrospinal fluid humoral immunity in the differential diagnosis of multiple sclerosis. *PLoS One* 2017;12(7):e0181431.
- Lycklama G, Thompson A, Filippi M, et al. Spinal-cord MRI in multiple sclerosis. *Lancet Neurol* 2003;2(9):555–562.
- Bou-Haidar P, Peduto AJ, Karunaratne N. Differential diagnosis of T2 hyperintense spinal cord lesions: part B. *J Med Imaging Radiat Oncol* 2009;53(2):152–159.
- Geurts JJ, Barkhof F. Grey matter pathology in multiple sclerosis. *Lancet Neurol* 2008;7(9):841–851.
- Cho TA, Bhattacharyya S. Approach to Myelopathy. *Continuum (Minneapolis Minn)* 2018;24(2, Spinal Cord Disorders):386–406.

15. Leake JA, Albani S, Kao AS, et al. Acute disseminated encephalomyelitis in childhood: epidemiologic, clinical and laboratory features. *Pediatr Infect Dis J* 2004;23(8):756–764.
16. Young NP, Weinshenker BG, Lucchinetti CF. Acute disseminated encephalomyelitis: current understanding and controversies. *Semin Neurol* 2008;28(1):84–94.
17. Lee YJ. Acute disseminated encephalomyelitis in children: differential diagnosis from multiple sclerosis on the basis of clinical course. *Korean J Pediatr* 2011;54(6):234–240.
18. Rossi A. Imaging of acute disseminated encephalomyelitis. *Neuroimaging Clin N Am* 2008;18(1):149–161, ix.
19. Wang KY, Chetta J, Bains P, et al. Spectrum of MRI brain lesion patterns in neuromyelitis optica spectrum disorder: a pictorial review. *Br J Radiol* 2018;91(1086):20170690.
20. Marrie RA, Gryba C. The incidence and prevalence of neuromyelitis optica: a systematic review. *Int J MS Care* 2013;15(3):113–118.
21. Wang Y, Wu A, Chen X, et al. Comparison of clinical characteristics between neuromyelitis optica spectrum disorders with and without spinal cord atrophy. *BMC Neurol* 2014;14(1):246.
22. Lennon VA, Wingerchuk DM, Kryzer TJ, et al. A serum autoantibody marker of neuromyelitis optica: distinction from multiple sclerosis. *Lancet* 2004;364(9451):2106–2112.
23. Jarius S, Paul F, Franciotta D, et al. Cerebrospinal fluid findings in aquaporin-4 antibody positive neuromyelitis optica: results from 211 lumbar punctures. *J Neurol Sci* 2011;306(1–2):82–90.
24. Jarius S, Wildemann B, Paul F. Neuromyelitis optica: clinical features, immunopathogenesis and treatment. *Clin Exp Immunol* 2014;176(2):149–164.
25. Yonezu T, Ito S, Mori M, et al. “Bright spotty lesions” on spinal magnetic resonance imaging differentiate neuromyelitis optica from multiple sclerosis. *Mult Scler* 2014;20(3):331–337.
26. Pekcevik Y, Mitchell CH, Mealy MA, et al. Differentiating neuromyelitis optica from other causes of longitudinally extensive transverse myelitis on spinal magnetic resonance imaging. *Mult Scler* 2016;22(3):302–311.
27. Jacob A, Weinshenker BG. An approach to the diagnosis of acute transverse myelitis. *Semin Neurol* 2008;28(1):105–120.
28. Berman M, Feldman S, Alter M, Zilber N, Kahana E. Acute transverse myelitis: incidence and etiologic considerations. *Neurology* 1981;31(8):966–971.
29. Scotti G, Gerevini S. Diagnosis and differential diagnosis of acute transverse myelopathy: the role of neuroradiological investigations and review of the literature. *Neurol Sci* 2001;22(8 suppl 2):S69–S73.
30. Vargas MI, Gariani J, Sztajzel R, et al. Spinal cord ischemia: practical imaging tips, pearls, and pitfalls. *AJR Am J Neuroradiol* 2015;36(5):825–830.
31. Novy J, Carruzzo A, Maeder P, Bogousslavsky J. Spinal cord ischemia: clinical and imaging patterns, pathogenesis, and outcomes in 27 patients. *Arch Neurol* 2006;63(8):1113–1120.
32. Bansal S, Brown W, Dayal A, Carpenter JL. Posterior spinal cord infarction due to fibrocartilaginous embolization in a 16-year-old athlete. *Pediatrics* 2014;134(1):e289–e292.
33. Mascalchi M, Cosottini M, Ferrito G, Salvi F, Nencini P, Quilici N. Posterior spinal artery infarct. *AJR Am J Neuroradiol* 1998;19(2):361–363.
34. Masson C, Pruvot JP, Meder JF, et al. Spinal cord infarction: clinical and magnetic resonance imaging findings and short term outcome. *J Neurol Neurosurg Psychiatry* 2004;75(10):1431–1435.
35. Kranz PG, Amrhein TJ. Imaging Approach to Myelopathy: Acute, Subacute, and Chronic. *Radiol Clin North Am* 2019;57(2):257–279.
36. Goh C, Phal PM, Desmond PM. Neuroimaging in acute transverse myelitis. *Neuroimaging Clin N Am* 2011;21(4):951–973, x.
37. Krings T, Lasjaunias PL, Hans FJ, et al. Imaging in spinal vascular disease. *Neuroimaging Clin N Am* 2007;17(1):57–72.
38. Krings T, Geibprasert S. Spinal dural arteriovenous fistulas. *AJR Am J Neuroradiol* 2009;30(4):639–648.
39. Granados Sánchez A, García Posada L, Ortega Toscano C, López López A. Diagnostic Approach to Myelopathies. *Rev Colomb Radiol* 2011;22(3):1–21. http://www.webcir.org/revistavirtual/articulos/diciembre11/colombia/col_ingles_a.pdf.
40. Murphy KJ, Brunberg JA, Quint DJ, Kazanjian PH. Spinal cord infection: myelitis and abscess formation. *AJR Am J Neuroradiol* 1998;19(2):341–348.
41. Dörflinger-Hejlek E, Kirsch EC, Reiter H, Opravil M, Kaim AH. Diffusion-weighted MR imaging of intramedullary spinal cord abscess. *AJR Am J Neuroradiol* 2010;31(9):1651–1652.
42. Koeller KK, Rosenblum RS, Morrison AL. Neoplasms of the spinal cord and filum terminale: radiologic-pathologic correlation. *RadioGraphics* 2000;20(6):1721–1749.
43. Samartzis D, Gillis CC, Shih P, O’Toole JE, Fessler RG. Intramedullary Spinal Cord Tumors. I. Epidemiology, Pathophysiology, and Diagnosis. *Global Spine J* 2015;5(5):425–435.
44. Ravina B, Loevner LA, Bank W. MR findings in subacute combined degeneration of the spinal cord: a case of reversible cervical myelopathy. *AJR Am J Roentgenol* 2000;174(3):863–865.
45. Kumar A, Singh AK. Teaching NeuroImage: inverted V sign in subacute combined degeneration of spinal cord. *Neurology* 2009;72(1):e4.
46. Baer AH, McKnight CD, Ibrahim M, Parmar HA. Imaging of the Spinal Cord: Classic Syndromes and Non-neoplastic Lesions. *Neurographics* 2015;5(6):238–253.
47. Kumar N. Copper deficiency myelopathy (human swayback). *Mayo Clin Proc* 2006;81(10):1371–1384.
48. Winston GP, Jaisser SR. Copper deficiency myelopathy and subacute combined degeneration of the cord: why is the phenotype so similar? *Med Hypotheses* 2008;71(2):229–236.
49. Reznak K, Roos RP. Spinal cord: motor neuron diseases. *Neurol Clin* 2013;31(1):219–239.
50. Agosta F, Chiò A, Cosottini M, et al. The present and the future of neuroimaging in amyotrophic lateral sclerosis. *AJR Am J Neuroradiol* 2010;31(10):1769–1777.
51. Paquin ME, El Mendili MM, Gros C, Dupont SM, Cohen-Adad J, Pradat PF. Spinal Cord Gray Matter Atrophy in Amyotrophic Lateral Sclerosis. *AJR Am J Neuroradiol* 2018;39(1):184–192.
52. Maloney JA, Mirsky DM, Messacar K, Dominguez SR, Schreiner T, Stence NV. MRI findings in children with acute flaccid paralysis and cranial nerve dysfunction occurring during the 2014 enterovirus D68 outbreak. *AJR Am J Neuroradiol* 2015;36(2):245–250.
53. Soni N, Bathla G, Pillenahalli Maheshwarappa R. Imaging findings in spinal sarcoidosis: a report of 18 cases and review of the current literature. *Neuroradiol J* 2019;32(1):17–28.
54. Zalewski NL, Krecke KN, Weinshenker BG, et al. Central canal enhancement and the trident sign in spinal cord sarcoidosis. *Neurology* 2016;87(7):743–744.
55. Bou-Haidar P, Peduto AJ, Karunaratne N. Differential diagnosis of T2 hyperintense spinal cord lesions: part A. *J Med Imaging Radiat Oncol* 2008;52(6):535–543.
56. Khan M, Ambady P, Kimbrough D, et al. Radiation-Induced Myelitis: Initial and Follow-Up MRI and Clinical Features in Patients at a Single Tertiary Care Institution during 20 Years. *AJR Am J Neuroradiol* 2018;39(8):1576–1581.
57. Bilgrami M, O’Keefe P. Neurologic diseases in HIV-infected patients. *Handb Clin Neurol* 2014;121:1321–1344.
58. Chong J, Di Rocco A, Tagliati M, Danisi F, Simpson DM, Atlas SW. MR findings in AIDS-associated myelopathy. *AJR Am J Neuroradiol* 1999;20(8):1412–1416.
59. Sartoretti-Schefer S, Blättler T, Wichmann W. Spinal MRI in vacuolar myelopathy, and correlation with histopathological findings. *Neuroradiology* 1997;39(12):865–869.
60. Thurnher MM, Post MJ, Jinkins JR. MRI of infections and neoplasms of the spine and spinal cord in 55 patients with AIDS. *Neuroradiology* 2000;42(8):551–563.
61. Reardon MA, Raghavan P, Carpenter-Bailey K, et al. Dorsal thoracic arachnoid web and the “scalpel sign”: a distinct clinical-radiologic entity. *AJR Am J Neuroradiol* 2013;34(5):1104–1110.
62. Parmar H, Park P, Brahma B, Gandhi D. Imaging of idiopathic spinal cord herniation. *RadioGraphics* 2008;28(2):511–518.
63. Ferré JC, Carsin-Nicol B, Hamlat A, Carsin M, Morandi X. MR imaging features of idiopathic thoracic spinal cord herniations using combined 3D-fiesta and 2D-PC Cine techniques. *J Neuroradiol* 2005;32(2):125–130.
64. Goetti R, Wille D, Kretschmar U, Klein A, Scheer I. Idiopathic spinal cord herniation: first reported case in a child. *JAMA Neurol* 2013;70(1):125–126.

Postoperative Spinal CT: What the Radiologist Needs to Know

Nevil Ghodasara, MD

Paul H. Yi, MD

Karen Clark, MD

Elliot K. Fishman, MD

Mazda Farshad, MD, MPH

Jan Fritz, MD

Abbreviations: ACDF = anterior cervical discectomy and fusion; BMP = bone morphogenic protein

RadioGraphics 2019; 39:1840–1861

<https://doi.org/10.1148/rg.2019190050>

Content Codes: **CT** **ER** **HN** **NR**

From the Russell H. Morgan Department of Radiology and Radiologic Science (N.G., P.H.Y., K.C.), Sections of Body CT (E.K.F.) and Musculoskeletal Radiology (J.F.), Johns Hopkins Hospital, 601 N Caroline St, Room 3014, Baltimore, MD 21287; and Spine Division, Department of Orthopedics, Balgrist University Hospital Zurich, Zurich, Switzerland (M.F.). Presented as an education exhibit at the 2018 RSNA Annual Meeting. Received March 8, 2019; revision requested May 8 and received June 21; accepted June 26. For this journal-based SA-CME activity, the authors E.K.F., M.F., and J.F. have provided disclosures (see end of article); all other authors, the editor, and the reviewers have disclosed no relevant relationships. **Address correspondence to** J.F. (e-mail: jfritz9@jhmi.edu).

©RSNA, 2019

SA-CME LEARNING OBJECTIVES

After completing this journal-based SA-CME activity, participants will be able to:

- Describe the technical challenges, and related solutions, of performing postoperative spinal CT in patients with metal implants.
- List the different categories of spinal surgery and the various instrumentations and implants used in spinal procedures.
- Identify normal and abnormal findings at postoperative spinal CT.

See rsna.org/learning-center-rg.

During the past 2 decades, the number of spinal surgeries performed annually has been steadily increasing, and these procedures are being accompanied by a growing number of postoperative imaging studies to interpret. CT is accurate for identifying the location and integrity of implants, assessing the success of decompression and intervertebral arthrodesis procedures, and detecting and characterizing related complications. Although postoperative spinal CT is often limited owing to artifacts caused by metallic implants, parameter optimization and advanced metal artifact reduction techniques, including iterative reconstruction and monoenergetic extrapolation methods, can be used to reduce metal artifact severity and improve image quality substantially. Commonly used and recently available spinal implants and prostheses include screws and wires, static and extendable rods, bone grafts and biologic materials, interbody cages, and intervertebral disk prostheses. CT assessment and the spectrum of complications that can occur after spinal surgery and intervertebral arthroplasty include those related to the position and integrity of implants and prostheses, adjacent segment degeneration, collections, fistulas, pseudomeningocele, cerebrospinal fluid leaks, and surgical site infections. Knowledge of the numerous spinal surgery techniques and devices aids in differentiating expected postoperative findings from complications. The various types of spinal surgery instrumentation and commonly used spinal implants are reviewed. The authors also describe and illustrate normal postoperative spine findings, signs of successful surgery, and the broad spectrum of postoperative complications that can aid radiologists in generating reports that address issues that the surgeon needs to know for optimal patient management.

©RSNA, 2019 • radiographics.rsna.org

Introduction

Owing to innovations in surgical techniques and devices, the frequencies of spinal surgery procedures have been increasing steadily during the past decades. Between the years 2004 and 2015, the number of elective spinal surgeries performed to achieve lumbar fusion reportedly increased from 122 679 to 199 140 (1). This amounted to a 177% increase in total hospital costs, with more than \$10 billion in hospital costs in 2015 (1). Similarly, the total number of cervical spine surgeries performed reportedly increased from 27 061 to 34 582 between the years 2001 and 2013, with a 64% increase in costs (2). The highest rate of increase in the volume of spinal surgery procedures occurred among individuals aged 65 years or older (1). With a prevalence of 23% (3), neck pain and lower back pain are the two main indications for spinal surgery, and the prevalence is likely to increase owing to the growing population of elderly persons.

TEACHING POINTS

- An interbody graft is accurately positioned when the distance between the radiopaque marker of the posterior graft margin and the posterior vertebral body margin is 2 mm or greater. When the interbody graft is placed closer than 2 mm to the posterior margin of the endplate, there is an increased risk of posterior migration into the spinal canal, with mass effect on the ventral thecal sac.
- The clinical importance of variant implant positioning is usually unknown. Screws may breach the osseous cortex and even come in contact with the thecal sac, neural elements, or paraspinal structures, causing symptoms or adverse clinical outcomes. Although pedicle screw breaches have been reported in up to 5.1% of cases, neurologic symptoms occur with a frequency of less than 0.2%.
- Circumferential peri-implant osteolysis around spinal implants larger than 2 mm suggests implant loosening. However, to diagnose implant loosening with certainty, a change in the position of the implant must be demonstrated at serial imaging.
- The pattern of peri-implant osteolysis can help differentiate an infectious cause from a mechanical loosening-related cause. With mechanical loosening of a screw, the osteolysis may be more prominent along the distal tip owing to a pivot point around which the screw moves, whereas infectious osteolysis is often more diffuse.
- Adjacent segment disease is the development or progression of motion segment degeneration directly above and below a spinal instrumentation construct. In adjacent segment disease, the degeneration is accelerated secondarily to the summation of forces and resultant increased transmission of the biomechanical load from the instrumentation-managed and immobilized spinal segments. These segments act as a lever arm and exert torque forces at the levels of the adjacent native motion segments above and below the instrumentation construct.

The increasing numbers of spinal surgeries are resulting in increasing numbers of postoperative imaging studies for radiologists to interpret. Knowledge of the initial clinical manifestations and imaging characteristics of the preoperative spinal abnormality (or abnormalities), type of surgery performed, and length of time since surgery is helpful for accurately interpreting a postoperative spinal imaging study. This knowledge is also helpful for subsequent patient management. In addition, having an understanding of spinal surgery techniques, approaches, and devices aids in differentiating expected postoperative findings from abnormalities and complications.

CT is accurate for identifying the location and integrity of implants, assessing the success of decompression and intervertebral arthrodesis, and detecting and characterizing complications. Used in conjunction with radiography, CT is a powerful problem-solving tool for detecting radiographically occult abnormalities and characterizing suspected abnormalities.

In this article, we review various types of spinal surgery procedures and describe commonly used

spinal implants. We further describe and illustrate normal postoperative findings, signs of successful surgery, and a wide spectrum of common and less common postoperative complications, which can aid radiologists in generating reports that address issues that the surgeon needs to know for optimal patient management.

Imaging Modalities

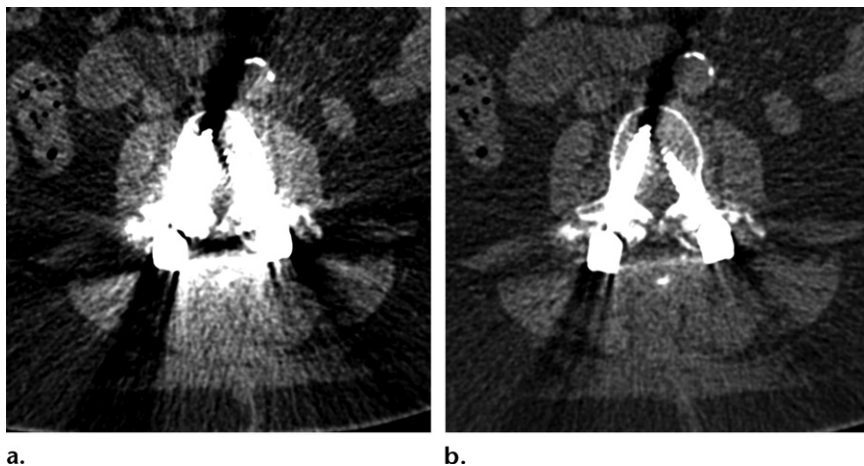
Radiography is the primary modality used for immediate postoperative assessment and long-term follow-up after spinal instrumentation surgery. Although radiography has limitations, it often can be used to determine the position of the implant and progression of osseous fusion, and to diagnose with certainty complications such as fractures and adjacent segment degeneration (4). A comparison of follow-up radiographic findings to baseline postoperative radiographic findings is important for detecting changes in device position and loss of implant fixation. US can be used to detect and characterize superficially located collections; however, accurate characterization of the depth of involvement is often difficult or not possible with this modality.

Radionuclide imaging, including technetium 99m medronate bone scintigraphy, can be used to diagnose osteomyelitis. However, the high sensitivity of this modality often interferes with identification of the specific underlying abnormality. Gallium 67 scintigraphy has higher specificity than does triple-phase bone scanning. Thus, these two examinations are often combined (5). Labeled leukocyte scintigraphy and fluorine 18 fluorodeoxyglucose PET/CT may be used to successfully diagnose spinal infection.

In the postoperative setting, MRI is used primarily to visualize spinal canal patency and nerve root compression, and, importantly, to detect and characterize collections and infections (6). However, artifacts from metallic implants may limit the usefulness of MRI in their immediate vicinity.

After spinal instrumentation surgery, common indications for CT include characterization of the integrity and position of the implant, visualization of the presence and progression of osseous fusion, and diagnosis of complications such as peri-implant osteolysis, radiographically occult fractures, and soft-tissue collections (4). CT depicts osseous structures with high detail, and high-spatial-resolution isotropic datasets enable capability for multiplanar reformations, which can improve the evaluation of implant position and alignment, and osseous fusion. Ultimately, multiplanar reformation capability facilitates improved assessment of the success of the surgery. CT myelography is an invasive examination that serves as an alternative to MRI in evaluations of

Figure 1. Metal artifact reduction at CT of a 62-year-old woman who underwent posterior spinal instrumentation surgery at the L3–S1 vertebral body level with pedicle screws, vertical rods, midline decompression, and posterolateral bone graft placement. Axial CT images at the level of the L3 vertebral body at 100 keV (a) and 140 keV (b) show increased metal artifact severity and contrast resolution at 100 keV, with decreased metal artifact severity and contrast resolution at 140 keV.



the spinal canal and nerve roots when infection, fibrosis, or impingement is suspected. Furthermore, it can be used to determine the location of postoperative cerebrospinal fluid leaks (4).

CT Techniques and Protocols

In the presence of metallic implants, CT evaluation of the spine is limited by implant-related artifacts. When the x-ray beam traverses high-attenuation implants, photon starvation, beam hardening, and beam scattering occur and manifest as dark and bright bandlike or streaklike artifacts on CT images. These artifacts limit the visibility of the implant and surrounding structures (7). The severity of artifacts depends on fixed and modifiable variables. Fixed variables are based on the inherent properties of the implant, including the composition and geometric features of the metal. The higher the density of the metal, the more artifacts will be produced (8). Hence, titanium, which is less dense than stainless steel, causes less x-ray attenuation and fewer artifacts (9). Polyetheretherketone is a material commonly used for interbody grafts and has many useful properties, including the feature that it causes minimal artifacts on CT images (4). The thicker the implant, the higher the attenuation and the greater the artifact severity.

Improvement of the image quality and diagnostic accuracy of postoperative spinal CT is mainly dependent on the modifiable variables, which are related to the CT techniques, parameters, and protocols used. Several modifiable variables can be optimized to improve CT image quality in the presence of spinal implants. Performing imaging perpendicular to the implant, with the x-ray beam traversing the smallest cross section, reduces the severity of artifacts (10).

Image acquisition factors that reduce artifact severity include high peak voltage, high tube current, narrow collimation, and thin sections (11). The peak voltage (Fig 1) affects the ability of an

x-ray beam to penetrate a structure, and the tube current corresponds to the number of photons that reach the detectors to produce the CT image. Use of a higher peak voltage and higher tube current results in fewer artifacts (10). However, the quadratic relationship between increasing peak voltage and increasing radiation dose should be carefully considered. In addition, the use of higher peak voltages leads to decreased contrast resolution on CT images, which can interfere with the detectability of soft-tissue processes.

Patient motion during image acquisition causes additional artifacts but is minimized owing to the high speed of data acquisition achieved with current multidetector CT scanners (9). Acquiring CT data with use of a low pitch can decrease the severity of implant-related artifacts, whereas the use of smooth reconstruction kernels facilitates a decrease in noise. High-spatial-resolution datasets with an isotropic voxel size equal to or less than $0.75 \times 0.75 \times 0.75 \text{ mm}^3$ yield high image detail and enable three-dimensional postprocessing (12,13).

Metal implant-induced CT artifacts can be further minimized by using advanced techniques, including metal artifact reduction reconstruction algorithms and dual-energy data acquisition with virtual monoenergetic extrapolation postprocessing (14). Although many vendors have their own proprietary reconstruction algorithms and metal artifact reduction software, many use projection completion. With projection completion, inaccurate or missing x-ray projections are replaced by interpolations from adjacent projections (14). Dual-energy CT images can be acquired by using several different methods, most of which involve the use of specialized CT scanner systems (Fig 2) (14,15).

On the basis of the CT datasets acquired with different tube energies, several calculations can be performed to determine the differential mass densities of the base materials. When the differ-

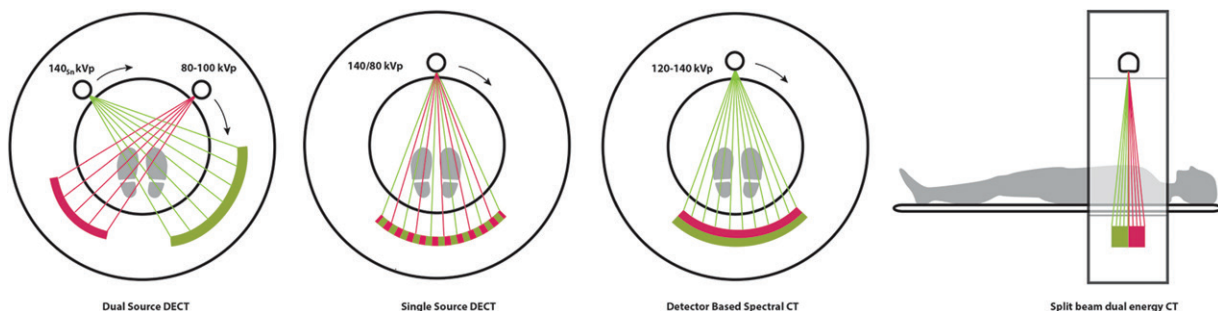


Figure 2. Drawings illustrate dual-energy CT (DECT) acquisition techniques, including dual-source dual-energy CT with two x-ray tubes and two detectors (far left), single-source dual-energy CT with fast tube energy switching (second from left), single-source detector-based spectral CT (third from left), and single-source dual-energy CT with split x-ray beam technology (far right).

ential mass densities are combined with the mass attenuation coefficients, virtual monoenergetic images can be created (14). The acquisition of virtual monoenergetic images at higher energies reduces the severity of high-attenuation beam-hardening artifacts (Fig 1), but it does not account for other causes of artifacts such as scattering (16).

Iterative and monoenergetic CT techniques can be used to substantially reduce spine implant- and prosthesis-induced metal artifacts and improve the visibility of bone, soft tissues, and pathologic processes (17–19). The use of three-dimensional postprocessing with multiplanar and curved reformations, as well as volume and cinematic rendering techniques, can further decrease the severity of streak artifacts by averaging the axial data in reformation planes in which true signal and random artifacts are balanced (14,20).

Spinal Instrumentation Techniques

Familiarity with the indications for a given spinal surgery, types of procedures performed, and goals of the surgical intervention aids in the accurate interpretation of postoperative CT findings. The main types of spinal surgery include decompression, fixation, stabilization and fusion, deformity correction, and lesion excision and débridement (10,15,21–23).

Decompression is mainly performed to minimize mass effects by means of herniated disk material removal or to relieve spinal or neuroforaminal stenosis. Decompression can be achieved by performing a laminotomy, sequestrectomy, or (optional) nucleotomy if the annulus defect is surgically accessible. Unilateral laminotomy involves the removal of a portion of the lamina to gain access for stepwise removal of disk fragments in the setting of a herniated disk (23). Midline laminotomy, which includes the removal of the caudal part of the upper lamina and the cranial part of the lower lamina, is the standard procedure for surgical treatment of spinal stenosis.

Laminectomy involves the complete removal of the lamina, and it can be unilateral, with removal

of one lamina, or bilateral, with removal of both laminae and the spinous process. Rarely, this procedure is used in extensive midline decompression procedures to relieve spinal canal stenosis.

A partial facetectomy is indicated when an exiting nerve root is compressed. The goal is to remove only enough of the facet joint to decompress the nerve root without causing segmental instability, which may result in anterior subluxation (23). Laminectomy and facetectomy are usually accompanied by instrumentation for fixation.

Stabilization is performed to achieve osseous spinal fusion when there is suspected or proven instability as a result of degenerative disk disease, spondylolysis with spondylolisthesis, trauma, infection, and/or malignancy. In this setting, the goals of spinal implants are to (a) immobilize the motion segment to allow osseous fusion, (b) maintain or restore alignment, and (c) enable the ability to adequately address biomechanical forces after the removal of a portion of the spine.

Many published and nonpublished surgical approaches and spinal instrumentation systems are based on the clinical scenario, local expertise, practice preferences, and current abnormalities. In this review, we describe the concepts that are most pertinent for the interpretation of postoperative CT findings.

There are multiple anterior and posterior surgical approaches to the cervical spine, depending on the underlying abnormality and level of involvement (24). The classic approach for the cervical spine is the Smith-Robinson anterior approach, which is used for anterior access to the C2–T1 cervical spine level in several procedures, including anterior cervical discectomy and fusion (ACDF), anterior cervical corpectomy and fusion, and cervical disk replacement. A transoral approach is needed to access the clivus and the C1 and C2 vertebral bodies (25). The posterior approach, which is less preferred, may be performed for laminoplasty, laminectomy, and posterior instrumentation. Posterior cervical spinal instrumentation involves placing lateral

Figure 3. ACDF in a 62-year-old woman who underwent cervical spinal instrumentation extending from the C3 to C5 motion segments, including C3–C4 and C4–C5 discectomies with interbody graft placements, and anterior plate and screw fixation. Sagittal CT image shows the vertebral anatomy after successful intervertebral arthrodesis, as indicated by solid osseous bridging through (*) and around (arrows) the interbody grafts.

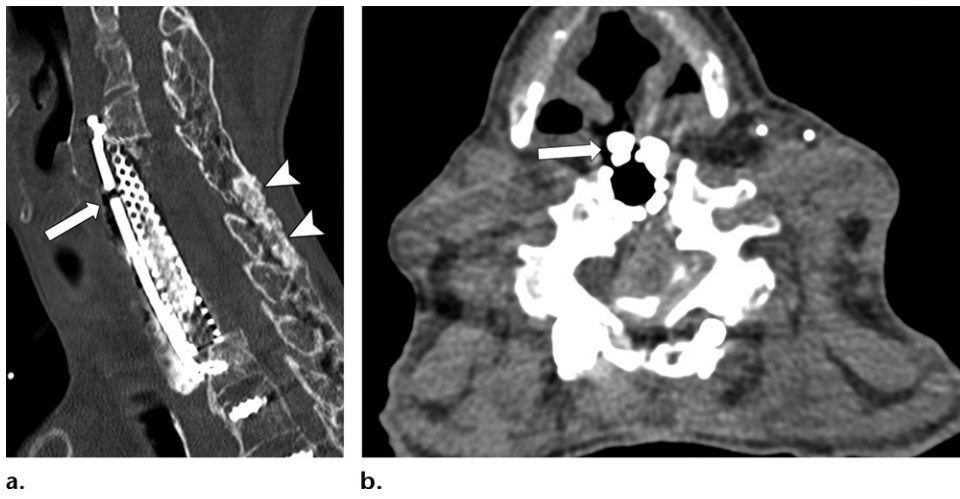
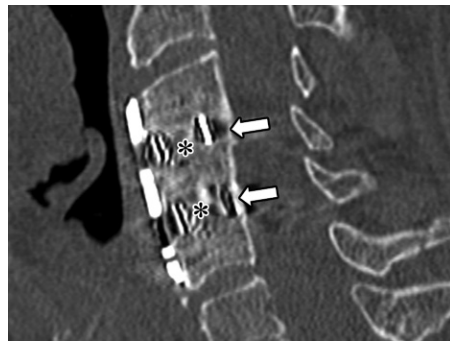


Figure 4. Fistula in a 66-year-old woman who underwent posterior cervicothoracic instrumentation including C5–T1 corpectomies with interbody graft placement, C4–T2 anterior plate and screw fixation, and posterior C2–T5 pedicle screw and rod fixation. Sagittal CT image of the cervical spine enhanced with oral iodine-based contrast material (a) and axial CT myelography image of the cervical spine (b) show a fistula (arrow) between the esophagus and interbody graft. There is mature osseous bridging across the posterolateral bone graft site (arrowheads in a).

mass screws in the C3–C7 vertebral bodies and transpedicular screws in the C2 vertebral body with vertical rods bilaterally (24,25). In certain clinical scenarios, a combined anterior and posterior approach may be performed. Advancements in patient-specific instrumentation and navigation techniques enable the placement of pedicle screws in the C3–C6 vertebral bodies (26).

ACDF is the most commonly used technique for the surgical treatment of central and foraminal stenoses (27) (Fig 3). It involves removal of the intervertebral disk (discectomy) and placement of an interbody cage or tricortical bone graft to restore neural foraminal height, maintain the cervical lordosis, and promote intervertebral arthrodesis (4). An anterior plate with unicortical or bicortical screws can be added at multilevel ACDF, in cases of traumatic lesions, and when only a tricortical bone graft, rather than a titanium, polyetheretherketone, or carbon cage, is placed to improve the promotion of osseous fusion. In anterior cervical corpectomy and fusion, one or more vertebral bodies are resected (Fig 4) (10). An interbody

cage with bone graft material is most commonly used to replace the resected vertebral bodies (28). Resection of more than two vertebral bodies often requires additional posterior stabilization.

Disk replacement is performed to maintain physiologic segmental motion in younger patients who do not have degenerative facet or uncovertebral arthrosis (Figs 5, 6) (4). Most implants have a ball-and-socket design, with the superior and inferior base plates of the prosthesis secured to the vertebral body above and below by keels, spikes, or screws. However, the number of different designs is increasing.

There are various basic approaches and techniques for lumbar spinal surgery (Fig 7). However, many variations and individual techniques and approaches exist (9,29). Recognition of the surgical approach used enables the radiologist to predict the sites of surgical dissection changes in both the body wall and the surgical bed. Evaluation of paraspinal anatomic structures such as the psoas muscle and abdominal vasculature is helpful for determining the surgical approach (23,29).



Figure 5. Lumbar intervertebral disk replacement in a 48-year-old man who underwent the procedure because of back pain related to disk degeneration of the L4-L5 motion segment. Sagittal CT image shows accurate placement and anchoring of the disk prosthesis within the endplates and successful osseous integration, as indicated by the extension of cancellous bone to the implant surfaces (arrows) without sclerosis or osteolysis. The anatomic alignment of the lumbar spine is preserved. Dark (white *) and bright (black *) metal artifacts are seen.

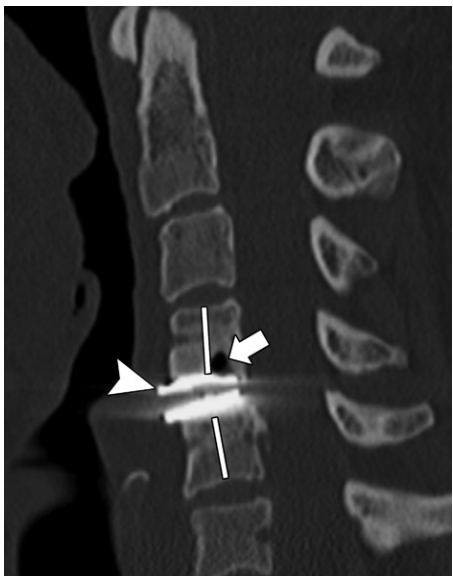


Figure 6. Cervical intervertebral disk replacement in a 51-year-old man who underwent the procedure because of back pain related to disk degeneration of the C4-C5 motion segment. Sagittal CT image shows variant placement of the disk prosthesis, with the implant margins (arrowhead) anteriorly positioned approximately 3 mm from the endplates. Consequently, there is nonanatomic alignment with mild posterior angulation of the superoinferior implant axes, a disproportional anterior opening, and mild segmental lordosis (lines). A small area of subcortical osteolysis (arrow) also is seen.

A posterior approach is most common and enables access to the posterior elements, spinal canal, and disk (23). Laminotomy, laminectomy, facetectomy, and discectomy, along with pedicle screw and rod fixation, may be performed according to the indication for and intent of the surgery (23). Anterior approaches are used primarily to access the lumbosacral junction. Indications for lateral approaches include discectomy with interbody graft placement when there is no need for posterior decompression and when indirect posterior decompression is intended through the following distraction of the posterior elements (29).

Spinal Instrumentation and Implant Nomenclature

Spinal fixation can be accomplished by using a variety of implants (21,22,30,31). There are many different instrumentation systems, devices, implants, and individualized constructs. We provide an overview of the most commonly used spinal implants and devices that are most relevant in the interpretation of postoperative spinal CT findings.

Screws and Wires

Screws are used for various purposes in spinal surgery, from fracture fixation to surgery for osseous spinal fusion (Fig 3). Single screws can provide stability and compression for the healing of fractures, such as unilateral pars fracture; however, they are rarely indicated. Pairs of transpedicular, translaminar, and transarticular screws serve as anchors for posterior connecting rods in posterior spinal fixation constructs to achieve osseous spinal fusion and intervertebral arthrodesis (25). Screws are used to fix plates to vertebral osseous elements to provide stability for osseous spinal fusion, such as that in ACDF procedures (21). Although wires placed in the sublaminar position are now used less commonly than screws, they can provide stability for fracture fixation (32) and deformity correction (33).

Plates

When used together with screws, plates provide stability and induce compression in spinal constructs that are used in the setting of neural decompressions, traumatic injuries, osseous defects, and oncologic reconstructions (Figs 3, 4). Plates are typically placed in an anterior, anterolateral, or lateral position and span two or more vertebral levels. They usually have a low-profile design to be as flush as possible with the vertebral body cortex and to minimize injury or irritation to adjacent structures and organs.

Rods

Rods are used in conjunction with anchoring pedicle screws to stabilize a fixation construct,

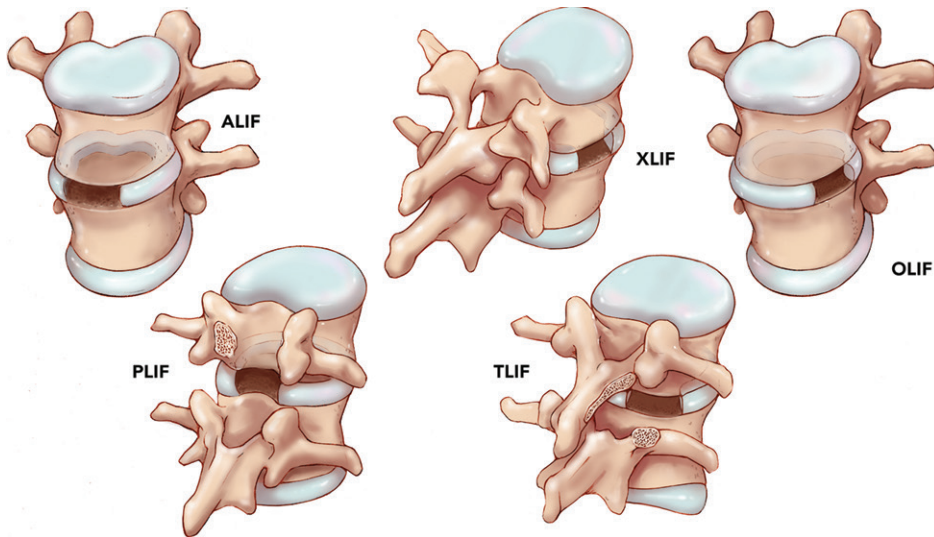


Figure 7. Drawings depict several surgical approaches for interbody graft placement in the lumbar spine. Anterior (ALIF), oblique (OLIF), lateral (XLIF), transforaminal (TLIF), and posterior (PLIF) lumbar interbody fusion access techniques, with different discectomy access sites, are illustrated. Anatomic structures, including the psoas muscle and abdominal vasculature, guide the surgical approach at various lumbar levels. Posterior lumbar interbody fusion involves bilateral laminotomies, with removal of the posterior element. Transforaminal lumbar interbody fusion involves unilateral laminectomy and inferior facetectomy.

correct deformity, and maintain alignment of the spine through distraction, such as that used in scoliosis correction surgery (Fig 8). Although the eponym *Harrington rod* is frequently used to describe posterior spinal fixation rods, it describes a specific rod that was designed in the early 1960s (34) and used for scoliosis correction surgery until the late 1990s. Similarly, the Luque rod was introduced in the early 1980s (35) as an alternative tool for posterior fixation and distraction involving the use of sublaminar wires to fix rods. However, neither the Harrington rod nor the Luque rod is used in modern spinal surgeries. Given the wide variability of rod designs in modern spinal fixation constructs, the use of simple descriptors such as “rod” can often prevent inaccuracies.

Growing rods (36) are used for adjustable fixation constructs in scoliosis correction surgery (Figs 9, 10). In a growing rod construct, one or two rods are fixed to the screws or hooks above and below the scoliotic curve. The rods include mechanisms that enable incremental lengthening either by means of minimally invasive surgical access or noninvasively by means of transcutaneous application of magnetic forces (eg, with an external remote controller) (37).

The core component of a growing rod construct is the actuator, which is wider than the proximal and distal rod components. The actuator houses the internal magnet and distraction mechanism of the rod. Actuators come in different sizes, which facilitate the capacity for different postoperative distractions. For example, 70- and 90-mm

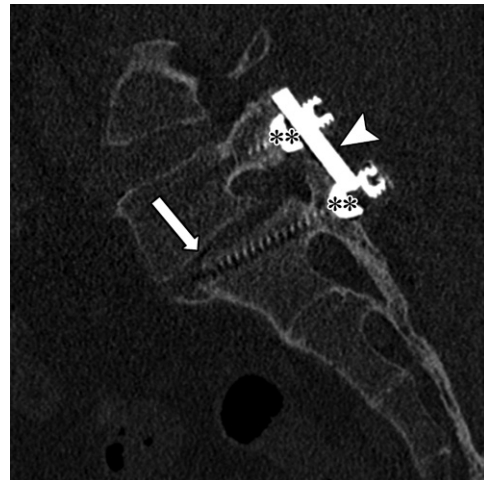
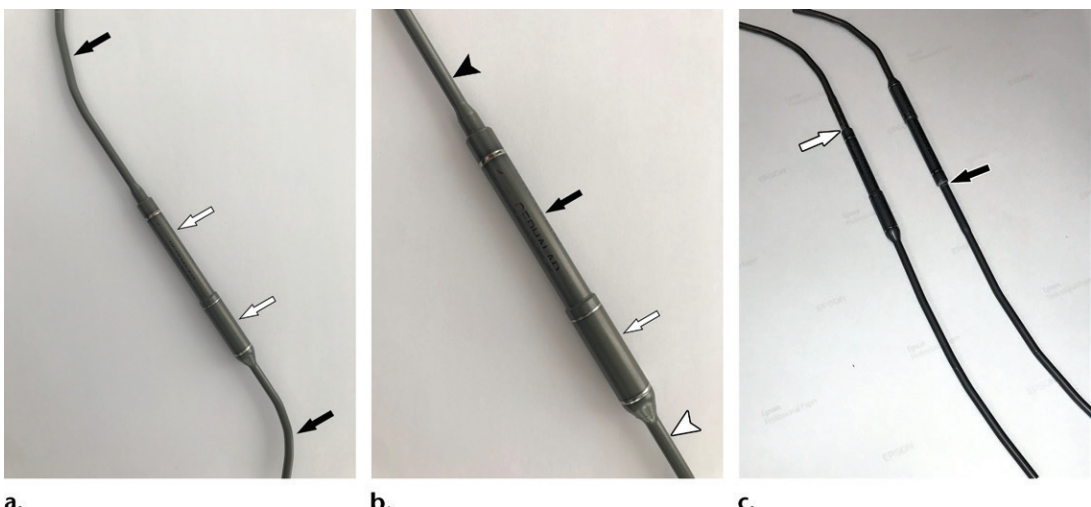


Figure 8. Rod disengagement in a 62-year-old man who underwent posterior lumbar spinal instrumentation extending from the L5 to S1 vertebral bodies to address Meyerding grade 1 anterolisthesis. Sagittal CT image shows mechanical rod disengagement characterized by angular malalignment and superior migration of the rod (arrowhead) relative to the connector (**). A small vacuum cleft phenomenon (arrow) in the disk space and the lack of osseous bridging indicate micromotion and construct instability.

actuators can provide a maximum of 28 and 48 mm of postoperative distraction, respectively.

There are two rod polarities: standard rods and offset rods. In the standard rod, the magnet is housed within the distal or inferior portion of the actuator and lengthening occurs in a cephalic direction. In contrast, in the offset rod, the mag-

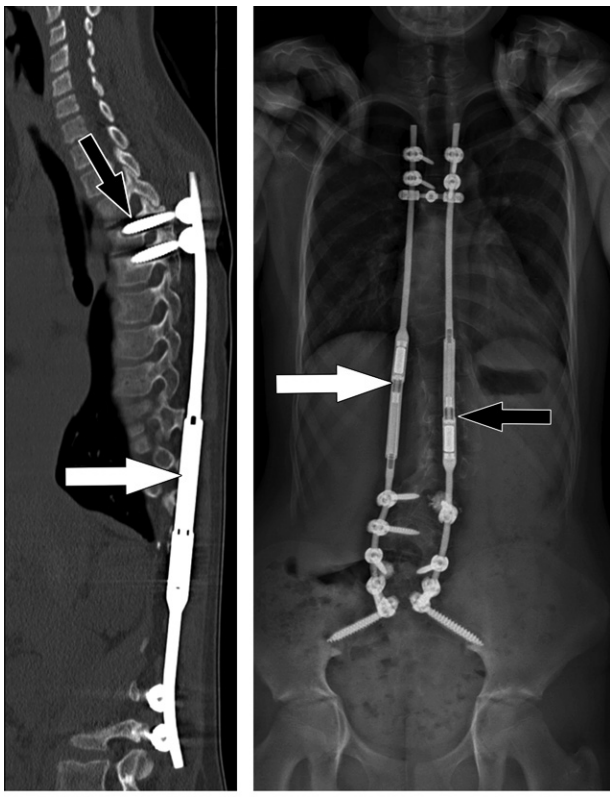


a.

b.

c.

Figure 9. Photographs show magnetically controlled growing rods. (a) Each rod consists of an actuator component (white arrows), which houses the magnet and lengthening mechanism, and rods (black arrows), which the surgeon adapts to the kyphotic and lordotic spinal curvature. (b) In a standard rod, lengthening in the actuator occurs in cephalic directions. The actuator consists of a more narrowed sleeve component (black arrow) and a wider magnet component (white arrow). The rods can be differentiated as the extendable telescopic rod (black arrowhead) and the static rod (white arrowhead). (c) A standard rod (white arrow) and offset rod (black arrow) construct allows independent lengthening with use of an external remote controller (not shown).



a.

b.

Figure 10. Scoliosis correction with magnetically controlled growing rods in a 7-year-old girl with Marfan syndrome. (a) Sagittal CT image of a unilateral standard growing rod shows the actuator with a lengthening mechanism (white arrow) in the cephalic direction, and the rods. The osteolysis (black arrow) around the proximal anchoring screws indicates nonsuccessful osseous fixation. (b) Frontal radiograph of the spine after revision surgery shows a construct consisting of a standard rod (black arrow) and offset rod (white arrow). This construct allows independent lengthening in caudal (offset rod) and cephalic (standard rod) directions with use of an external remote controller (not shown).

net is housed in the proximal or superior portion of the actuator and lengthening occurs in a caudal direction (Figs 9, 10). In a construct with two standard rods, the rods can be lengthened simultaneously, whereas a construct with standard and offset rods enables independent lengthening when an external remote controller is used.

Bone Grafts and Other Biologic Materials

Bone grafts are often used posterolaterally in fixation constructs as biologic adjuncts to promote osseous fusion. Bone grafts are autologous when they are harvested from the patient and allogenic when they are harvested from cadaveric bone. Other biologic materials used to promote osseous fusion include demineralized bone matrix and bone morphogenetic protein (BMP) (38). On CT images, these materials often have the appearance of osseous elements at the instrumentation sites.

Interbody Cages

Interbody grafts and cages, which may also be referred to as intervertebral spacers, have varying designs and are commonly used to restore disk height after discectomy and promote immobilizing osseous bridging across the disk space (Fig 3). Solid interbody cages usually are hollow and thus can be packed with other biologic materials (7,25). Interbody grafts may be composed of metallic alloys such as titanium; plastics such as polyetheretherketone; carbon fibers; and ceramics. Some cages are designed to not only restore disk height but also replace an entire vertebral body or segment of vertebral

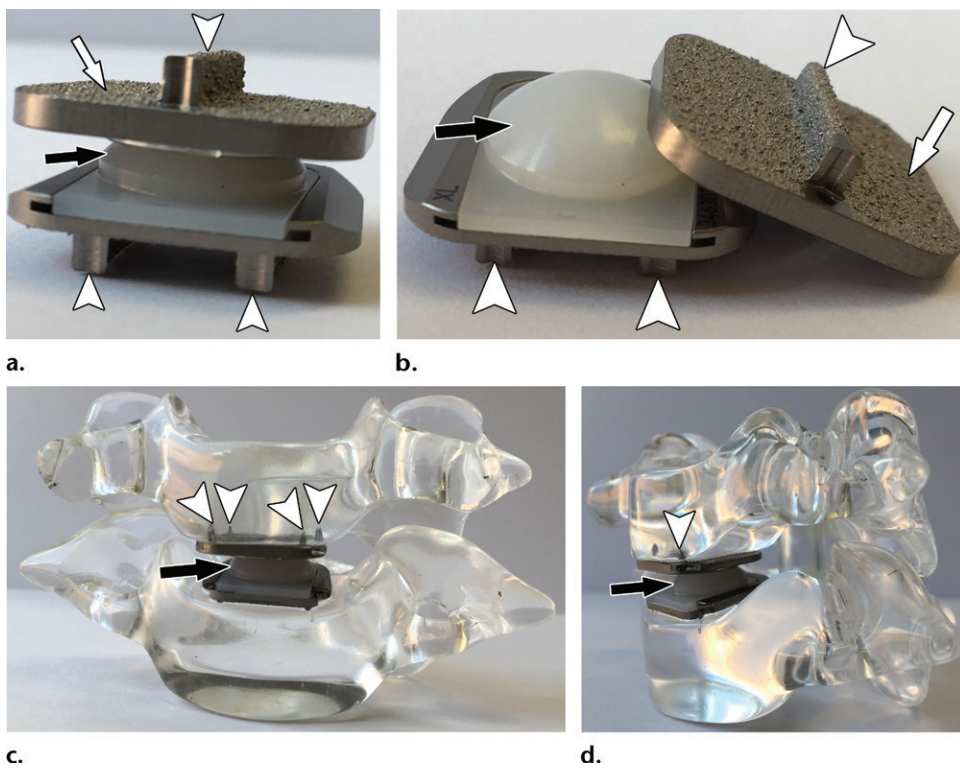


Figure 11. Two cervical disk prosthesis designs. (a, b) Photographs show an unconstrained design consisting of a ball-and-socket articulation (black arrow) and a bone-to-prosthesis interface featuring keels (arrowheads) and flat high-porosity surfaces (white arrow). (c, d) Photographs show an unconstrained design consisting of a ball-and-socket articulation (arrow) and a bone-to-prosthesis interface featuring spikes (arrowheads) and curved high-porosity surfaces. The curved high-porosity surfaces are hidden by the semitransparent spine model.

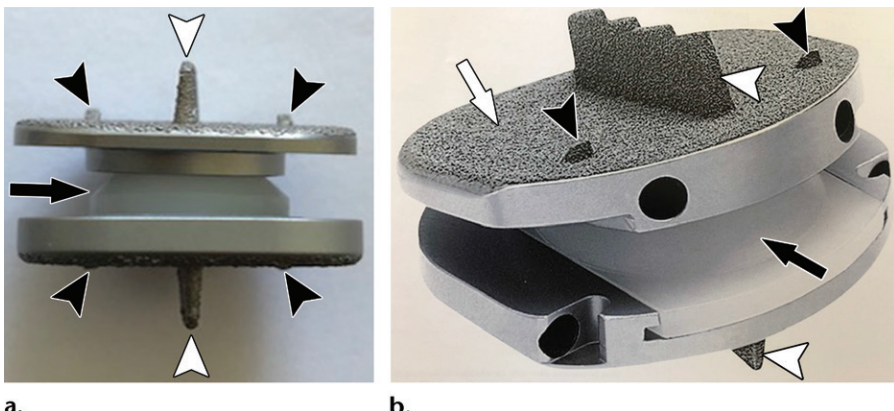


Figure 12. Lumbar disk prosthesis. Photographs show an unconstrained lumbar disk prosthesis design that consists of a ball-and-socket articulation (black arrow) and a bone-to-prosthesis interface featuring keels (white arrowheads), spikes (black arrowheads), and flat high-porosity surfaces (white arrow in b).

bodies in the setting of corpectomy for severe traumatic or tumor surgery (Fig 4) (39).

Intervertebral Disk Replacements

Motion-preserving total intervertebral disk prostheses are an alternative to immobilizing osseous fusion-promoting intervertebral and spinal instrumentations (Figs 5, 6). Intervertebral disk replacement has the advantage that spinal seg-

mental motion is maintained after the procedure, whereas osseous fusion results in loss of segmental motion and increasing transmission of force to the adjacent segments.

Disk replacement prostheses typically consist of articulating polyethylene-bearing surfaces and two metallic endplate components, with keels and porous surfaces used to anchor into the superior and inferior host vertebral bodies (40) (Figs 5, 6).

Intervertebral disk prosthesis systems vary moderately in design, materials, bone-to-prosthesis interfaces, and articulation type (Figs 11, 12). A constrained-design intervertebral disk prosthesis consists of a bearing that contains a stopping mechanism within the normal physiologic range of motion, whereas an unconstrained-design prosthesis does not contain motion-restricting mechanisms. Most prostheses are made of alloys that contain cobalt and titanium, and polyethylene components.

A variety of bone-to-prosthesis interface structures are available to promote osseous integration into the host bone. These structures include keels, spikes, wire mesh, high-porosity surfaces, fixation screws, and surface coatings made of plasma-sprayed titanium, aluminum oxide, hydroxyapatite, and calcium phosphate. Articulation types can be differentiated into ball-and-socket articulation, which allows rotation around one individual point, and saddle articulation, which allows more than one center of rotation. Intervertebral disk replacements have been performed primarily in the cervical and lumbar spine and have not had widespread use (41,42).

Indications for Postoperative CT

Indications for CT following spinal surgery include assessment of the type, integrity, and position of spinal implants. Other indications include delineation of the relationship of the implant(s) to the underlying spinal anatomy and abnormalities. Postoperative CT can also be used to assess the spinal alignment and effects of decompression surgery on the spinal canal and neural foramina, determine the success of intervertebral arthrodesis, and detect and characterize postoperative abnormalities (29).

Normal Postoperative CT Findings

In the immediate postoperative period after spinal surgery, expected CT findings include soft-tissue edema and small amounts of gas and fluid along the surgical access site and around implants and instrumentation-treated spine segments. Seromas, another normal postoperative finding, are commonly observed simple collections in the surgical bed. When these collections are superficially located, they often are self-limiting and resorb over time (43).

Recombinant human BMP-2 at bone graft and interbody graft sites often incites an initial acute inflammatory response, which may result in focal osteolysis, limited endplate resorption at the graft site, and surrounding soft-tissue swelling (43,44).

Transpedicular screws should traverse the central portion of the pedicle and enter the vertebral body parallel to the endplate without breaching

the vertebral body cortex or having contact with neural elements and vascular structures. As an exception, sacral fixation screws may penetrate the anterior cortex for a short distance (15).

In cervical spinal instrumentation constructs, transpedicular C2 and C7 screws should have a horizontal orientation, extending anteriorly and slightly medially without breaching the pedicle cortex (4). Lateral mass screws in the C3–C7 vertebral bodies should have a superior and slightly lateral orientation (31). After ACDF, the anterior cervical plate should have a lordotic contour and be flush against the vertebral bodies. There should be a distance of at least 5 mm between the superior and inferior margins of the plate and the adjacent endplates to prevent periplate ossification (45). The screws should be fastened such that their heads are level with the plate.

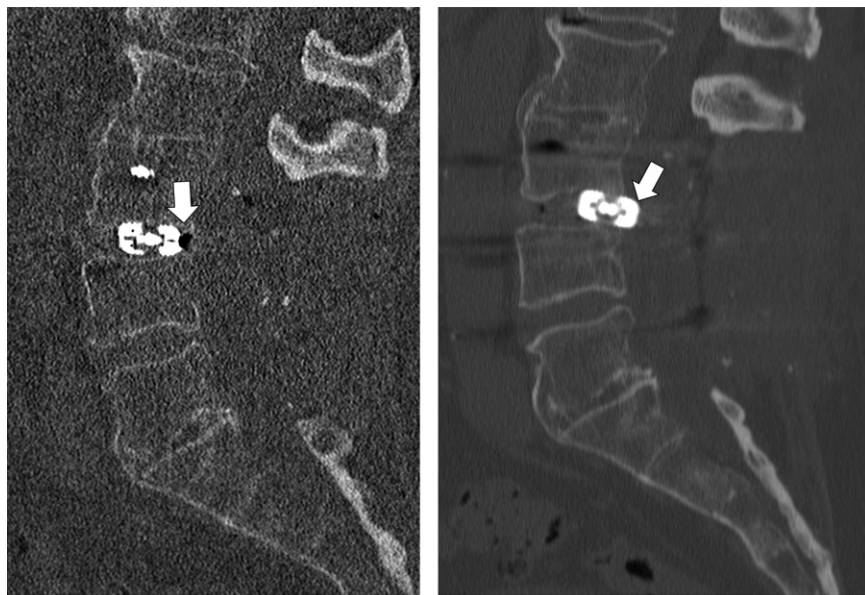
In the setting of posterior spinal instrumentation constructs with screws and rods, the junction of the screw and rod should be carefully evaluated to ensure that the connector cap is completely fastened to the connector socket and the rod is engaged and aligned correctly. Angular malalignment of the rod in the connector can be a sign of construct instability (Fig 8).

An interbody graft is accurately positioned when the distance between the radiopaque marker of the posterior graft margin and the posterior vertebral body margin is 2 mm or greater (9,10,15) (Fig 13). When the interbody graft is placed closer than 2 mm to the posterior margin of the endplate, there is an increased risk of posterior migration into the spinal canal, with mass effect on the ventral thecal sac. Interbody grafts, especially stand-alone cages, may subside into the adjacent vertebral body for 3 mm or less before osseous fusion occurs (10).

Depending on the length of time since surgery, various degrees of osseous bridging across bone graft placement sites occur. At 6 months following discectomy with interbody graft placement, trabecular osseous bridging should be visible on CT images, either around or through the interbody graft (43) (Fig 3). Similarly, after posterolateral bone graft placement with pedicle screw and rod fixation, bridging bone should be visible between the transverse processes and facet joints (15,29). One year after surgery, mature trabeculation and solid cortical bridging should be present across the disk spaces (Fig 14) and posterolateral bone graft placement sites (Fig 4) (29,46).

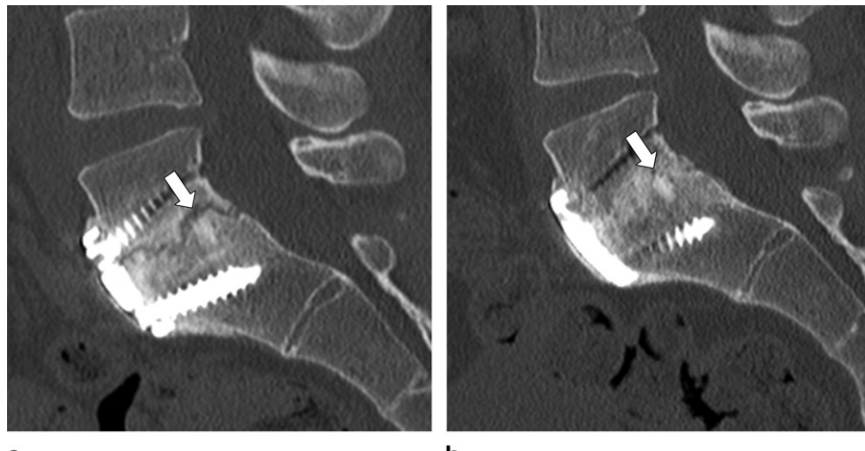
On follow-up CT scans, asymptomatic granulation or scar tissue along the surgical tract and peridural spaces is part of the normal healing process (30,46). Epidural fibrosis typically has attenuation values that range from 50 to 75 HU and may partially resolve over time (46). Paraspinal muscle

Figure 13. Posterior interbody graft migration in a 69-year-old man who underwent posterior lumbar spinal instrumentation extending from the L3 to L5 vertebral bodies and including L3-L4 disectomy and interbody graft placement, posterior midline decompression, and pedicle screw and rod fixation (not shown). (a) Sagittal CT image obtained immediately following surgery shows successful placement of the L3-L4 interbody graft between the endplates, with a 2-mm distance between the posterior graft margin and posterior vertebral body margin (arrow). (b) Sagittal CT image obtained 6 weeks after surgery shows posterior migration of the interbody graft (arrow) into the central spinal canal, with mass effect on the ventral thecal sac.



a.

b.



a.

b.

Figure 14. CT findings in a 29-year-old man with a history of L5-S1 spondylolysis and Meyering grade I spondylolisthesis, who underwent lumbar spinal instrumentation of the L5-S1 motion segments, including disectomy with interbody graft placement and anterior plate and screw fixation. (a) Sagittal CT image obtained 39 weeks after surgery shows an irregular area of lucency (arrow) along the superior endplate-graft junction space, representing incomplete osseous integration and incomplete arthrodesis. (b) Sagittal CT image obtained 2 years after surgery shows complete osseous integration (arrow) along the endplate-graft interface and successful arthrodesis.

atrophy with fat replacement is a common finding following posterior surgical procedures (43).

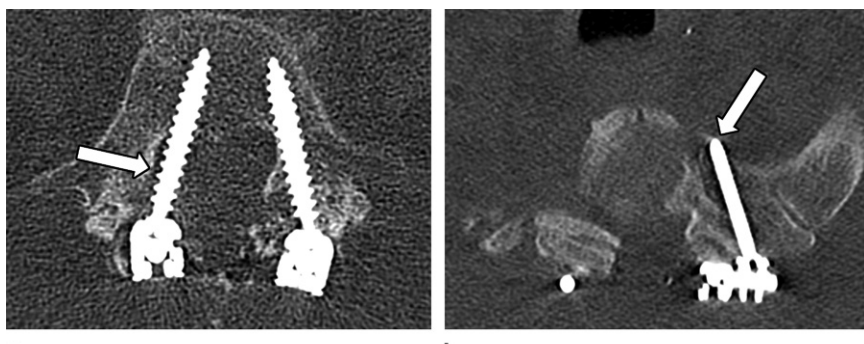
CT Appearances of Postoperative Spinal Complications

Implant Placement

The position of the implant is important information gleaned from postoperative spinal CT. Any deviation from the expected position should be described (Fig 15). However, the clinical importance of variant implant positioning is usually unknown. Screws may breach the osseous cortex

and even come in contact with the thecal sac, neural elements, or paraspinal structures, causing symptoms or adverse clinical outcomes. Although pedicle screw breaches have been reported in up to 5.1% of cases, neurologic symptoms occur with a frequency of less than 0.2% (42). The most common cases of variant implant positioning are those involving misplaced pedicle screws.

Therefore, in the absence of visible injury to an adjacent structure or organ, we recommend using neutral descriptors to characterize implant positioning. This includes avoiding the use of words that denote blame or assign fault, such as *bad*,



a. **b.**

Figure 15. Variant screw placement. (a) Axial CT image at the L5 vertebral body level in a 71-year-old man who underwent lumbar spinal instrumentation of the L3–S1 motion segments, including midline decompression and posterior instrumentation with pedicle screws and vertical rods, shows a right pedicle screw (arrow) traversing the right lateral recess of the spinal canal. (b) Axial CT image at the T1 vertebral body level in a 60-year-old woman who underwent thoracic spinal instrumentation of the T1–T6 motion segments, including midline decompression and posterior instrumentation with pedicle screws and vertical rods, shows a left pedicle screw traversing the left articular process (arrow) lateral to the left pedicle.

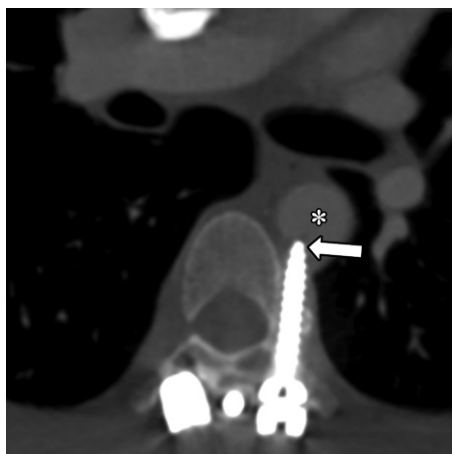


Figure 16. Variant placement of a thoracic pedicle screw in a 52-year-old man who underwent posterior spinal instrumentation extending from the occiput to the T8 vertebral body after resection of a cervical mass. Axial CT image shows the left T7 pedicle screw tip (arrow) reaching beyond the anterolateral vertebral body cortex to indent into the descending thoracic aorta (*). Subsequently, a covered endovascular mesh stent graft was placed to minimize the risk of aortic injury.

malpositioned, and misdirected. For example, a description of a variant implant position could read as follows: “The left L1 pedicle screw tip abuts the posterior margin of the inferior vena cava, with preservation of adjacent fat planes.” This example accurately describes the hardware position, effect of the screw tip on the vena cava, and relevant additional findings such as preservation of adjacent fat planes, which implies that there is no radiologic evidence of injury. On this same token, findings of direct (eg, organ or vessel laceration) or indirect (fat stranding) injury to adjacent structures must be described and relayed in an emergent radiologist-to-surgeon communication.

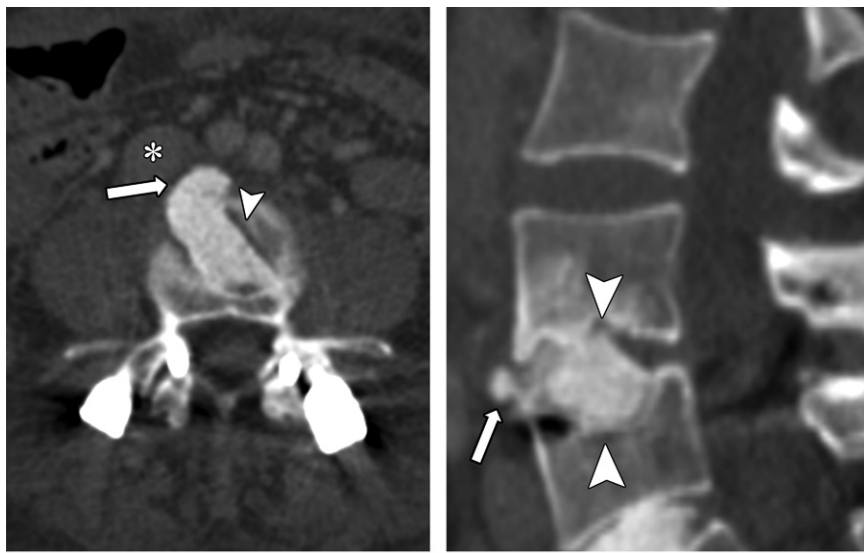
Medial angulation of pedicle screws, with breach of the medial cortex, may result in nerve root contact and irritation, the most common pedicle screw-related complication (6,15). In posterior cervical spine instrumentation, lateral angulation of the screw may breach the foramen transversarium and damage the vertebral artery (15). In posterior instrumentation of the thoracic and lumbar spine, the screw can traverse the anterior cortex and come in contact with retroperitoneal structures, leading to an immediate or delayed injury (Fig 16). Similarly, interbody cement grafts may extend beyond the vertebral body margin to adjacent structures (Fig 17).

The position of the interbody grafts and vertebral body plates may predict the development of future complications. Interbody grafts that are placed too close to the endplate margin may result in subsequent migration (15) (Figs 13, 18). A lateralized position of an interbody graft results in abnormal axial loading and abnormal spinal alignment (15). Placing an anterior plate within 5 mm of the adjacent endplate predisposes the patient to osteophyte formation (45).

Peri-implant Osteolysis

Evaluation for possible spinal implant loosening is performed according to principles that are similar to those for evaluating structures in other parts of the skeleton, such as the hip and knee following arthroplasty (47,48). Peri-implant osteolysis of the spine may be secondary to micromotion, infection, or a foreign body reaction to polyethylene and metal products (4,49) (Figs 19–21). In addition, the breakdown products of the BMP-2 that is used in conjunction with interbody grafts can cause temporary endplate osteolysis (50). Circumferential peri-implant osteolysis around spinal

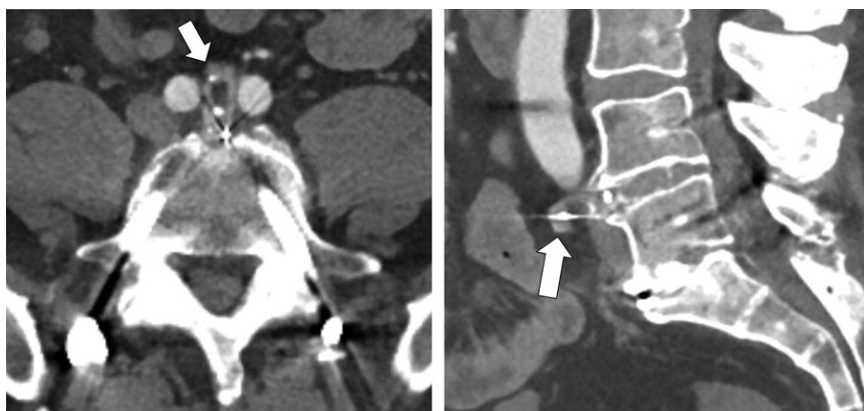
Figure 17. Periprosthetic osteolysis and graft migration in a 47-year-old man who underwent posterior lumbar spinal instrumentation extending from the L4 to S1 vertebral bodies, with interbody cement graft placement, posterior midline decompression, and pedicle screw and rod fixation. Axial (a) and sagittal (b) CT images show anterior extension of the interbody cement graft (arrow), which is in contact with the right common iliac vein (* in a), as well as osteolysis along the graft-endplate interfaces (arrowheads), with subsidence.



a.

b.

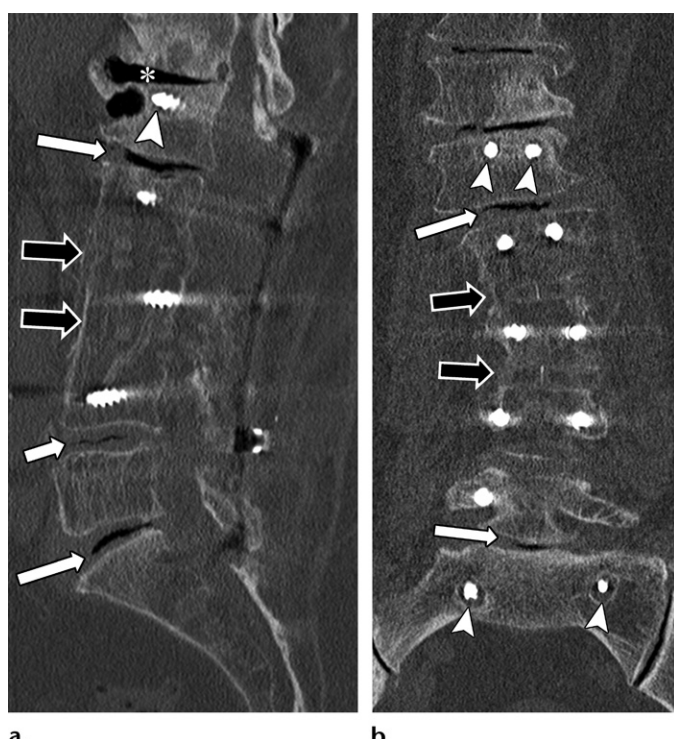
Figure 18. Interbody graft migration in a 52-year-old man who underwent posterior lumbar spinal instrumentation from the L4 to S1 vertebral bodies, including disectomy and interbody graft placement. Axial (a) and sagittal (b) CT images show anterior displacement of the L4-L5 interbody graft (arrow), which lies immediately inferior to the aortic bifurcation and comes in contact with the proximal right and left common iliac arteries.



a.

b.

Figure 19. CT findings in a 70-year-old man who continued to have back pain after lumbar spinal instrumentation extending from the L1 to S1 motion segments, including posterior midline decompression, L2-L3 and L3-L4 discectomies with interbody graft placements, and pedicle screw and rod fixation 8 years earlier. Sagittal (a) and coronal (b) CT images show osteolysis around the L1 and S1 pedicle screws (arrowheads) and L1-L2, L4-L5, and L5-S1 vacuum cleft phenomena (white arrows), suggesting micromotion as an explanation for unsuccessful arthrodesis. The L2-L3 and L3-L4 arthrodeses (black arrows) were successful, as indicated by the solid osseous bridging across the disk spaces. Adjacent segment disease with severe disk degeneration (*) in a) also is seen.



a.

b.

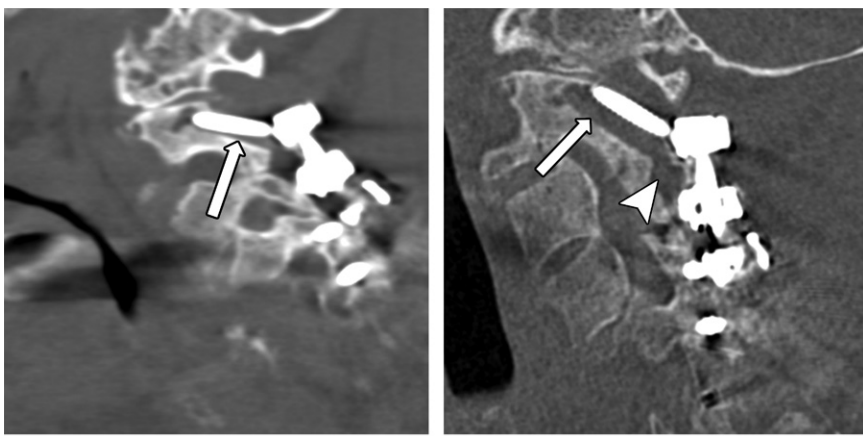
**a.****b.**

Figure 20. Periprosthetic osteolysis and implant migration in a 66-year-old man who underwent posterior spinal instrumentation extending from the C2 to T2 vertebral bodies, with midline decompression and rod and pedicle screw fixation. (a) Sagittal CT image shows osteolysis (arrow) around the right C2 screw, which suggests impaired osseous fixation. (b) Sagittal CT image obtained at 16-month follow-up shows progressive osteolysis (arrow) and angular migration of the right C2 screw, with extension into the right C1-C2 facet joint (arrowhead).



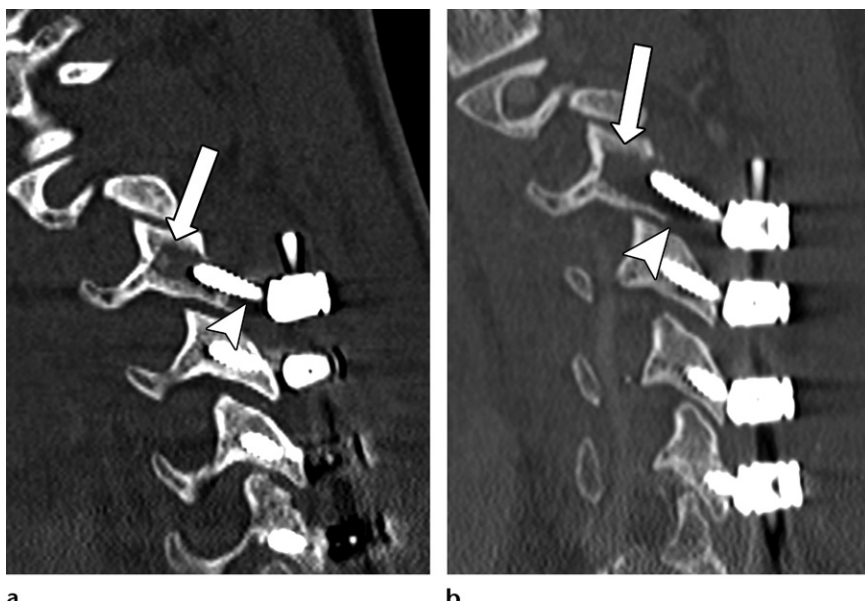
Figure 21. Variant screw placement in a 71-year-old man who underwent posterior cervicothoracic spinal instrumentation starting at the C3 vertebral body. Sagittal CT image shows a lack of osseous purchase (arrow) of the right C3 lateral mass screw, with the tip reaching the right C2-C3 facet joint, and retraction of the instrumentation construct (arrowhead).

implants larger than 2 mm suggests implant loosening (51). However, to diagnose implant loosening with certainty, a change in the position of the implant must be demonstrated at serial imaging. Sclerosis around a screw is highly suggestive of an adaptive response to prior hardware loosening. Implant migration may result in a change in spinal alignment, such as increasing anterolisthesis in the setting of a loose pedicle screw (Fig 22).

Because infection can manifest with peri-implant osteolysis, it is important to distinguish infection from mechanical loosening; however, this can be challenging. The pattern of peri-implant osteolysis can help differentiate an infectious cause

from a mechanical loosening-related cause. With mechanical loosening of a screw, the osteolysis may be more prominent along the distal tip owing to a pivot point around which the screw moves, whereas infectious osteolysis is often more diffuse (Fig 23). However, because the CT appearances of mechanical loosening-related osteolyses and those of infection-related osteolyses overlap, correlation of the CT appearance with the clinical presentation, laboratory values, prior imaging study findings, and/or radionuclide imaging findings is often part of the workup (29,45). The inflammatory effects of using recombinant human BMP-2 can result in inflammatory stranding of soft tissues and abnormal enhancement and thus mimic infection on CT images of the postoperative spine (29).

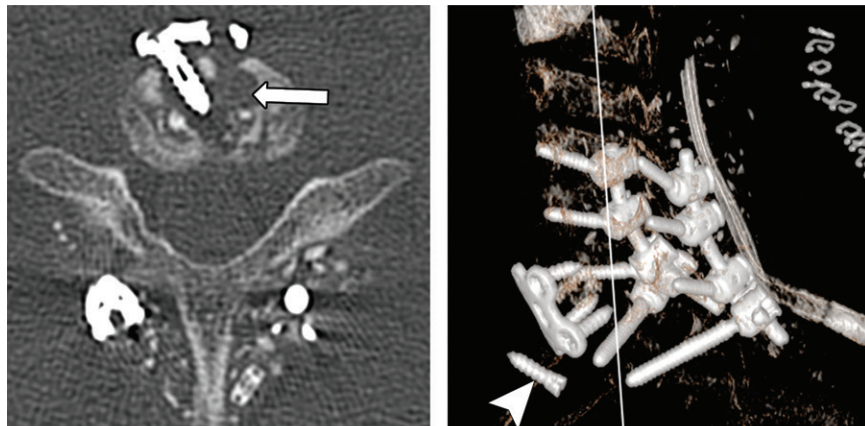
Loosening and motion of spinal implants are important contributors to unsuccessful intervertebral arthrodesis, pseudoarthrosis, and nonunion, which are visible on CT images owing to the lack of mature osseous bridging 1 year after surgery. Pseudoarthrosis may cause pain and increased implant stress that ultimately leads to implant failure (52). Radiographically, a greater than 2-mm change in the interspinous distance and a 2° or greater change in Cobb angle measurements are functionally diagnostic of pseudoarthrosis (52). At CT, pseudoarthrosis manifests as a lucent line through the intervertebral bone graft material or along the graft postpone interface, with or without adjacent sclerosis (Figs 14, 24, 25). Following interbody graft placement, subcortical cysts, vacuum cleft phenomena (Figs 14, 24), and lack of mature trabeculations across the disk space 24 months following surgery are additional signs that suggest micromotion and



a.

b.

Figure 23. Periprosthetic osteolysis and implant displacement in a 31-year-old man who underwent anterior cervical spinal instrumentation, including C6-C7 discectomy with anterior plate and screw fixation, C5-T1 midline decompression, and posterior screw and rod fixation. (a) Axial CT image shows geographic osteolysis around the anterior right C6 vertebral screw (arrow) due to infection. (b) Oblique volume-rendered image shows displacement of the left C6 screw (arrowhead) into the prevertebral soft tissue.



a.

b.



Figure 24. Intervertebral pseudoarthrosis. Sagittal CT image shows so-called "locked" pseudoarthrosis, which is characterized by attempted but incomplete osseous bridging through the interbody graft (arrowheads), where a nonossified layer remains between the opposing ossified columns (*). The presence of a vacuum cleft phenomenon (arrow) at the nonossified layer and graft-endplate interface suggests motion and segmental microinstability.

Figure 25. Intervertebral pseudoarthrosis. Sagittal CT image shows locked pseudoarthrosis, which is characterized by attempted but incomplete osseous bridging through the interbody graft (arrowheads), where a nonossified layer (arrow) remains between the opposing ossified columns (*). The absence of a vacuum cleft phenomenon at the nonossified layer and graft-endplate interface suggests segmental stability.

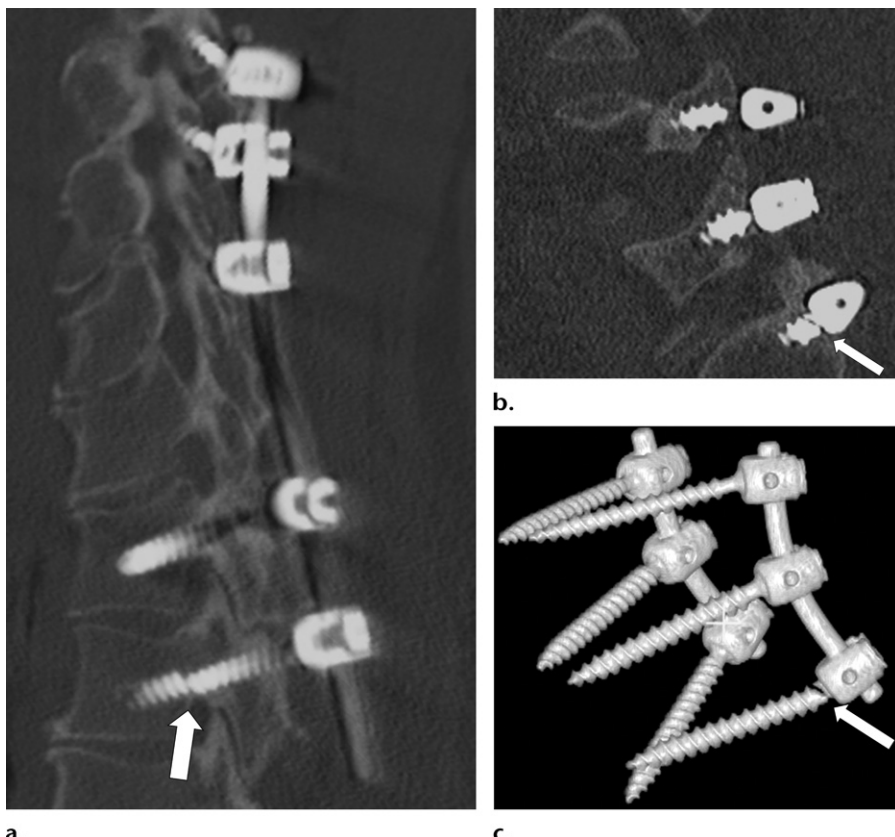


Figure 26. Screw fractures in two patients. (a) Sagittal CT image in a 66-year-old woman shows a fracture (arrow) of a left T2 screw shaft in the pedicle, with minimal displacement. (b, c) Sagittal (b) and oblique volume-rendered (c) CT images in a 78-year-old man show a neck fracture (arrow) of a left S1 screw. Screw fractures may be better depicted on volume-rendered CT images.

pseudoarthrosis. Interbody graft migration, subsidence, resorption, and fracture after interbody graft placement also may suggest micromotion and pseudoarthrosis (Figs 24, 25) (29,51). In addition, failed coalition of osseous fragments and absence of bridging bone at posterolateral bone graft placement sites and in posterior elements 24 months after spinal instrumentation suggest nonunion (29).

Implant Failure

Implants can fail owing to a number of mechanisms. The implant itself can become fractured as a result of fatigue caused by repetitive stress (Fig 26) (10). Three-dimensional postprocessing can help to detect minimally displaced implant fractures. Fractured implants may result in micromotion and segmental microinstability, which interfere with the progression of osseous fusion (Fig 27). Although the implant may be intact, there can be mechanical disengagement of screws, bolts, and/or rods, such as those used in posterior fixations (Fig 8). In extreme cases, there can be loosening of a cap with a completely unsecured rod (Fig 28). In plate and screw fixation constructs, screws should engage with the plate to ensure compression. However, when there are multiple screws, a single failing screw may not interfere with the stability of the construct, and osseous fusion still may occur (Fig 29).

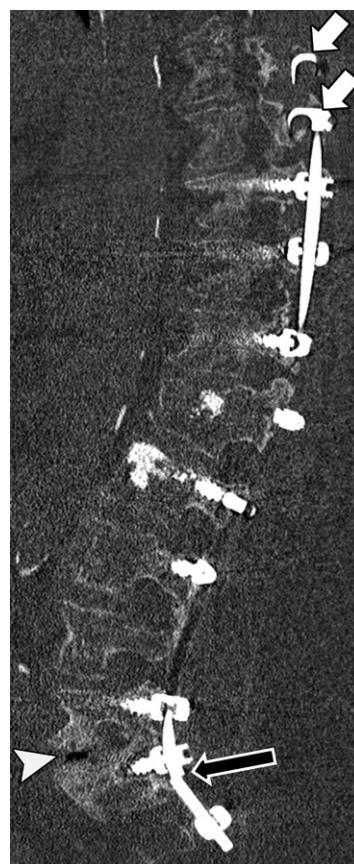


Figure 27. Rod fracture in a 69-year-old woman who underwent posterior lumbar spinal instrumentation extending from the T8 to S2 motion segments, with disengaged hooks at the T8-T9 level (white arrows), a fractured rod at the S1 level (black arrow), osteolysis around the S1 screw, and a vacuum cleft phenomenon (arrowhead) of the L5-S1 disk space, indicating micromotion and segmental instability.

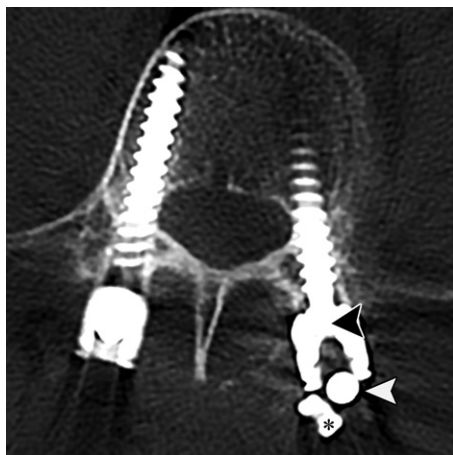


Figure 28. Rod disengagement in a 77-year-old woman who underwent posterior lumbar spinal instrumentation extending from the L3 to S1 vertebral bodies. Axial CT image shows rod disengagement of the left S1 pedicle screw (white arrowhead) due to displacement of the locking head screw (*) from the connector socket (black arrowhead).

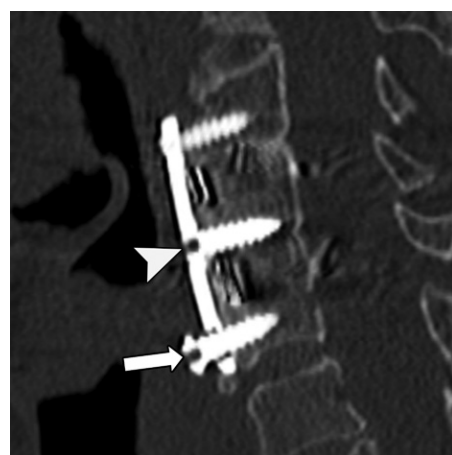


Figure 29. Sagittal CT image obtained after cervical discectomy with interbody graft placement and anterior plate and screw fixation of the C3–C5 motion segments shows an incompletely engaged screw (arrow) at the C5 level and a successfully engaged screw (arrowhead) superiorly. There is successful intervertebral arthrodesis, as indicated by the complete osseous bridging across the disk spaces.

Migration and subsidence of failing implants can cause spinal canal and neuroforaminal narrowing, pseudoarthrosis, instability, and adjacent segment degeneration. A small degree of subsidence of interbody grafts and cages into the adjacent endplate is expected. However, subsidence exceeding 3 mm in depth can narrow the disk space and neural foramen enough to cause radicular pain (Fig 30) (15,52). Given the current use of titanium and polyetheretherketone implants, streak artifacts no longer significantly limit the detection of subsidence (29).

Fractures around Implants and Prostheses

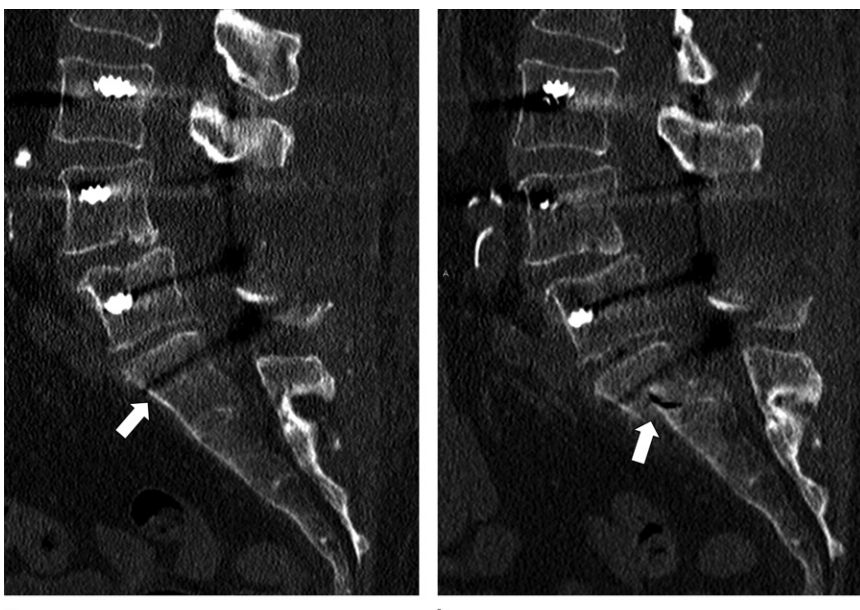
Owing to weakened bone strength secondary to osteolysis, prior bone resection, and/or increased biomechanical loading through a fixation construct, osseous fractures can occur around any spinal implant or prosthesis that is embedded in bone (Figs 31, 32). Fracture descriptors that are helpful to the surgeon include orientation of the fracture line, degree of comminution, extension of the fracture line to articular surfaces and foramina, abnormal alignment, and additional abnormalities in the spine.

Adjacent Segment Disease

Adjacent segment disease is the development or progression of motion segment degeneration directly above and below a spinal instrumentation construct (10). In adjacent segment disease, the degeneration is accelerated secondarily to the summation of forces and resultant increased transmission of the biomechanical load from the instrumentation-managed and immobilized spinal



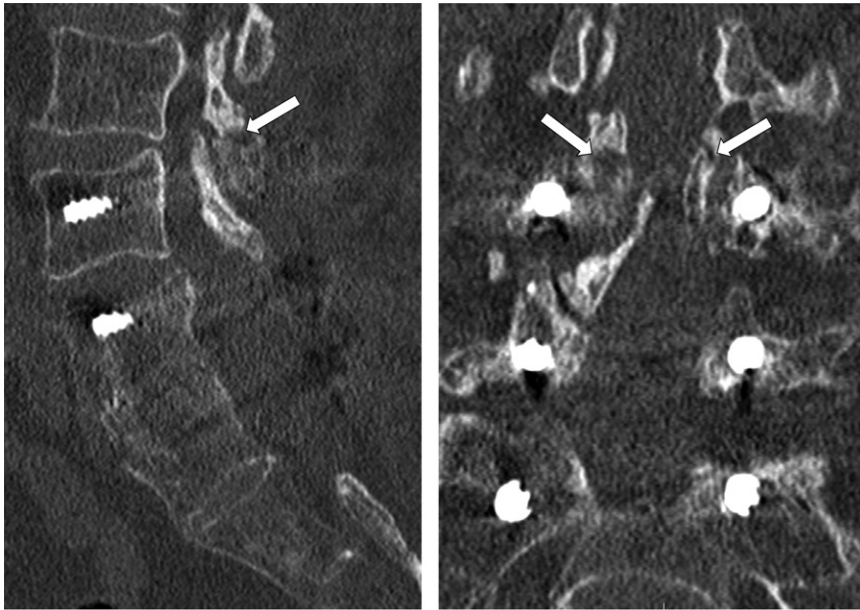
Figure 30. CT findings in a 71-year-old man who presented with persistent low back pain after undergoing lumbar spinal instrumentation of the L4-L5 motion segment, including disectomy with interbody graft placement and posterior plate and screw fixation, approximately 6 months ago. Coronal CT image shows a vacuum cleft phenomenon (arrow) of the L4-L5 interspace, as well as greater than 3-mm abnormal graft migration into the endplate with surrounding osteolysis (arrowheads), indicating micromotion and a lack of osseous integration.



a.

b.

Figure 31. Periprosthetic bone fracture in a 77-year-old woman who underwent posterior lumbar spinal instrumentation extending from the L3 to S1 vertebral bodies. (a) Sagittal CT image obtained 1 day after the instrumentation surgery shows baseline alignment, with an intact S1 vertebral body (arrow). (b) Sagittal CT image obtained 1 month after the surgery shows a new fracture (arrow) of the adjacent S1 segment, with anterior displacement.



a.

b.

Figure 32. Periprosthetic fracture in a 73-year-old woman who underwent posterior lumbar spinal instrumentation from the L4 to S1 vertebral bodies, including midline decompression and pedicle screw and rod fixation. Sagittal (a) and coronal (b) CT images show fractures (arrows) of the right and left articular processes of the adjacent L3 vertebral body.

segments. These segments act as a lever arm and exert torque forces at the levels of the adjacent native motion segments above and below the instrumentation construct. CT findings include disk degeneration and facet joint arthrosis, which may progress to spinal stenosis. Adjacent segment disease is more common in the lumbar spine and at the levels above the instrumentation-managed segment (Fig 19) (10,15).

Collections and Fistulas

After spinal surgery, postoperative collections are common and include seroma, hematoma, abscess, and pseudomeningocele, which may be

symptomatic or incidental findings (25). Accurate differentiation of the various collection types is important for implementing the most appropriate management.

A postoperative hematoma is a focal collection of blood products, which may be located within or around the spinal canal or implant, and/or along the surgical access. Hematomas commonly develop in the subcutaneous tissue, and typically no intervention is required in such cases. The majority of postoperative hematomas develop within hours to days after surgery. The symptoms that result from postoperative hemorrhage are based on the location of the collection.

Figure 33. Postoperative collections in a 68-year-old woman who underwent posterior spinal instrumentation from the T4 to S1 vertebral bodies, including midline decompression of the L2–L4 vertebral bodies. Sagittal (a) and axial (b) CT images of the lumbar spine at the L3–L4 level show a low-attenuation collection (arrows), representing a postsurgical seroma, in the posterior decompression bed.

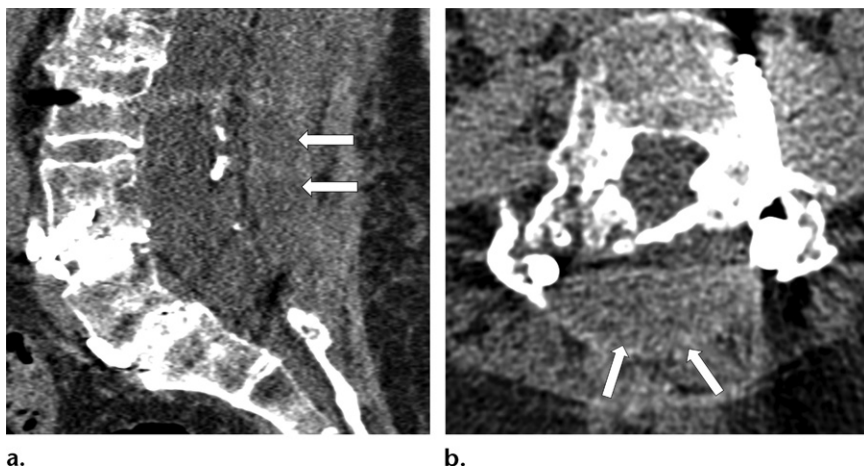
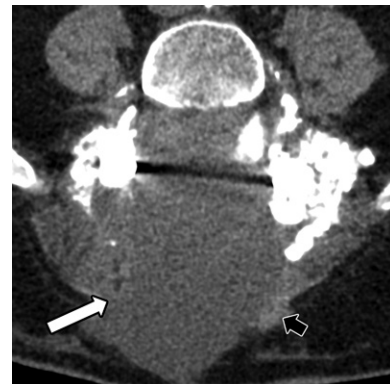


Figure 34. Postoperative collection in a 70-year-old man who underwent posterior lumbar spinal instrumentation extending from the L4 to S1 vertebral bodies, including midline decompression, interbody graft placements, and posterior pedicle screw and rod fixation. Axial CT image obtained at the L4–L5 level shows a large hypoattenuating collection (white arrow) in the area of the midline decompression and surgical access, without separation from the thecal sac. The border of the collection consists of reactive fibrous tissue (black arrow), which is suggestive of a pseudomeningocele. Head MRI (not shown) demonstrated signs of intracranial hypotension, and lumbar spine MRI (not shown) depicted a small dural defect with cerebrospinal fluid leakage at the L4–L5 level, confirming a pseudomeningocele.



Epidural and subdural spinal hematomas can exert mass effect on neural elements and may cause pain and neurologic deficits. However, the incidence of symptomatic epidural hematomas is commonly overestimated, with the actual incidence ranging between 0.1% and 1.0% (53). Non-contrast material-enhanced CT depicts a clotted hematoma as a high-attenuation extradural collection with a biconvex shape (54). The high-attenuation collection is distinct from the adjacent low-attenuation epidural fat and spinal cord (54). Epidural hematomas often occur dorsolateral to the spinal cord. Subdural hemorrhages are uncommon, with only a few cases reported.

A postoperative seroma (Fig 33) is a collection of clear serous fluid that contains blood plasma or inflammatory fluid from severed small blood vessels or soft tissues, respectively (55). The collection can be located in the subcutaneous or paraspinal tissues. The use of BMP has been associated with an increased risk of postoperative seroma (56). Treatments include the use of a compression bandage for smaller seromas and percutaneous or surgical drainage for large, symptomatic, and infected seromas (25). CT attenuation measurements may be used to differentiate seromas from hematomas. However, MRI is more accurate in areas without impeding metal artifacts (51).

Pseudomeningoceles and Dural Leakage

A pseudomeningocele (Fig 34) is an abnormal collection of cerebrospinal fluid in paraspinal regions that communicate with the cerebrospinal fluid space around the spinal cord through a meningeal defect. Pseudomeningoceles occur in fewer than 2% of patients following laminectomy or discectomy (57). Pseudomeningoceles can be symptomatic owing to mass effect and accompanied by intracranial hypotension and meningitis related to cerebrospinal fluid hypovolemia. The border of a pseudomeningocele, unlike that of a true meningocele, consists of reactive fibrous tissue (Fig 34) (25). Pseudomeningoceles can extend from the spinal canal through a posterior defect at the site of resected posterior elements. On CT images, a pseudomeningocele typically appears as a hypoattenuating collection that extends to the dura, with minimal peripheral enhancement. At laminotomy and laminectomy sites, the dural sac may protrude posteriorly and should not be mistaken for a pseudomeningocele (15). CT myelography can be helpful for differentiating a communicating pseudomeningocele from a seroma and visualizing dural leaks (58). The CT-guided injection of iodine-based contrast material into the subarachnoid space can be helpful for visualizing a defect, as indicated by

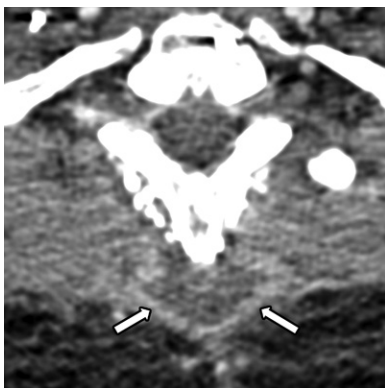
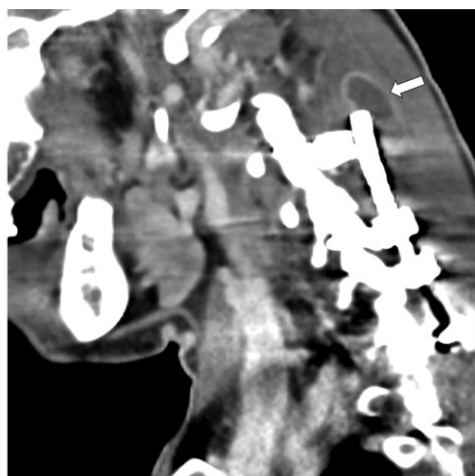


Figure 35. Paraspinal abscesses in a 31-year-old man who underwent posterior cervicothoracic instrumentation extending from the C5 to T1 vertebral bodies. Axial CT image obtained after the intravenous administration of iodine-based contrast material shows a rim-enhancing collection (arrows), representing a soft-tissue abscess, posterior to the spinous processes, with adjacent fat stranding.



a.



b.

Figure 36. CT findings in a 33-year-old man who underwent posterior cervical instrumentation extending from the C4 to C7 vertebral bodies. Axial (a) and coronal (b) CT images obtained after the intravenous administration of iodine-based contrast material, with iterative metal artifact reduction postprocessing, show a rim-enhancing collection (arrow) cranial to the right rod, representing a soft-tissue abscess.

iodine-based contrast material traversing into a pseudomeningocele.

Surgical Site Infection and Abscess

Surgical site infection is an important complication that occurs most commonly during the 1st month following spinal surgery. Causes of these infections include direct contamination during surgery, hematogenous seeding, and implant-associated infection (59). Patient-related risk factors include diabetes mellitus, smoking, renal failure, malnutrition, immunosuppression, obesity, and older age (60). Surgery-related risk factors include lengthy surgery, prolonged retraction, implant placement, and bone graft placement (59). The most common infecting organisms are *Staphylococcus aureus* and gram-negative bacteria (59).

Although MRI is more accurate than CT for evaluation of postoperative fluid collections, contrast-enhanced CT can be used to detect rim-enhancing abscesses within the surgical bed and paraspinal musculature (Figs 35, 36). Additional findings include paraspinal edema and phlegmon,

muscular enhancement, vertebral body destruction, and gas formation in the soft tissue and bone (25).

Conclusion

CT is an important modality for evaluating the success of spinal instrumentation surgery and detecting postoperative complications. The use of optimized CT protocols and advanced metal artifact reduction techniques can facilitate substantially reduced artifacts and improved image quality.

CT is accurate for determining the location and integrity of implants and identifying peri-implant osteolysis, fractures, and adjacent segment disease. CT can depict collections and often can be used to diagnose abscesses. However, myelography and MRI are often needed to fully characterize and diagnose fistulas, pseudomeningoceles, and surgical site infections. Familiarity with spinal implants, spinal surgical techniques, normal postoperative spine appearances, and various related complications will aid in accurately interpreting postoperative CT findings and guiding medical, surgical, and interventional management.

Acknowledgment.—The authors thank Hannah Ahn for creating the drawings in Figures 2 and 7.

Disclosures of Conflicts of Interest.—**E.K.F.** Activities related to the present article: disclosed no relevant relationships. Activities not related to the present article: research support from Siemens and GE Healthcare, co-founder and stockholder in Hip-Graphics. Other activities: disclosed no relevant relationships. **M.F.** Activities related to the present article: disclosed no relevant relationships. Activities not related to the present article: board member of and shareholder in Incemed and Prognostic. Other activities: disclosed no relevant relationships. **J.F.** Activities related to the present article: disclosed no relevant relationships. Activities not related to the present article: grants or grants pending, payment for lectures (including service on speakers bureaus), and payment for travel and meeting expenses from Siemens; grants or grants pending from BTG International. Other activities: patent(s) or copyright(s) pending, and patent(s) or copyright(s) issued from Siemens.

References

- Martin BI, Mirza SK, Spina N, Spiker WR, Lawrence B, Brodke DS. Trends in Lumbar Fusion Procedure Rates and Associated Hospital Costs for Degenerative Spinal Diseases in the United States, 2004 to 2015. *Spine* 2019;44(5):369–376.
- Liu CY, Zygourakis CC, Yoon S, et al. Trends in Utilization and Cost of Cervical Spine Surgery Using the National Inpatient Sample Database, 2001 to 2013. *Spine* 2017;42(15):E906–E913.
- Hoy D, Bain C, Williams G, et al. A systematic review of the global prevalence of low back pain. *Arthritis Rheum* 2012;64(6):2028–2037.
- Petcavage-Thomas JM, Ha AS. Imaging current spine hardware. I. Cervical spine and fracture fixation. *AJR Am J Roentgenol* 2014;203(2):394–405.
- Krumme JW, Lauer MF, Stowell JT, Beteselassie NM, Kotwal SY. Bone Scintigraphy: A Review of Technical Aspects and Applications in Orthopedic Surgery. *Orthopedics* 2019;42(1):e14–e24.
- Berquist TH. Imaging of the postoperative spine. *Radiol Clin North Am* 2006;44(3):407–418.
- McLellan AM, Daniel S, Corcuera-Solano I, Joshi V, Tanenbaum LN. Optimized imaging of the postoperative spine. *Neuroimaging Clin N Am* 2014;24(2):349–364.
- Katsura M, Sato J, Akahane M, Kunimatsu A, Abe O. Current and Novel Techniques for Metal Artifact Reduction at CT: Practical Guide for Radiologists. *RadioGraphics* 2018;38(2):450–461.
- Rutherford EE, Tarplett LJ, Davies EM, Harley JM, King LJ. Lumbar spine fusion and stabilization: hardware, techniques, and imaging appearances. *RadioGraphics* 2007;27(6):1737–1749.
- Thakkar RS, Malloy JP 4th, Thakkar SC, Carrino JA, Khanna AJ. Imaging the postoperative spine. *Radiol Clin North Am* 2012;50(4):731–747.
- Splendiani A, D’Orazio F, Patriarca L, et al. Imaging of post-operative spine in intervertebral disc pathology. *Musculoskelet Surg* 2017;101(Suppl 1):75–84.
- Fritz J, Fishman EK, Small KM, et al. MDCT arthrography of the shoulder with datasets of isotropic resolution: indications, technique, and applications. *AJR Am J Roentgenol* 2012;198(3):635–646.
- Calhoun PS, Kuszyk BS, Heath DG, Carley JC, Fishman EK. Three-dimensional volume rendering of spiral CT data: theory and method. *RadioGraphics* 1999;19(3):745–764.
- Khodarahmi I, Fishman EK, Fritz J. Dedicated CT and MRI Techniques for the Evaluation of the Postoperative Knee. *Semin Musculoskelet Radiol* 2018;22(4):444–456.
- Bittane RM, de Moura AB, Lien RJ. The postoperative spine: what the spine surgeon needs to know. *Neuroimaging Clin N Am* 2014;24(2):295–303.
- Khodarahmi I, Haroun RR, Lee M, et al. Metal Artifact Reduction Computed Tomography of Arthroplasty Implants: Effects of Combined Modeled Iterative Reconstruction and Dual-Energy Virtual Monoenergetic Extrapolation at Higher Photon Energies. *Invest Radiol* 2018;53(12):728–735.
- Dangelmaier J, Schwaiger BJ, Gersing AS, et al. Dual layer computed tomography: Reduction of metal artefacts from posterior spinal fusion using virtual monoenergetic imaging. *Eur J Radiol* 2018;105:195–203.
- Guggenberger R, Winklhofer S, Osterhoff G, et al. Metallic artefact reduction with monoenergetic dual-energy CT: systematic ex vivo evaluation of posterior spinal fusion implants from various vendors and different spine levels. *Eur Radiol* 2012;22(11):2357–2364.
- Kotsenas AL, Michalak GJ, DeLone DR, et al. CT Metal Artifact Reduction in the Spine: Can an Iterative Reconstruction Technique Improve Visualization? *AJNR Am J Neuroradiol* 2015;36(11):2184–2190.
- Rowe SP, Fritz J, Fishman EK. CT evaluation of musculoskeletal trauma: initial experience with cinematic rendering. *Emerg Radiol* 2018;25(1):93–101.
- Slonc RM, MacMillan M, Montgomery WJ. Spinal fixation. I. Principles, basic hardware, and fixation techniques for the cervical spine. *RadioGraphics* 1993;13(2):341–356.
- Slonc RM, MacMillan M, Montgomery WJ, Heare M. Spinal fixation. II. Fixation techniques and hardware for the thoracic and lumbosacral spine. *RadioGraphics* 1993;13(3):521–543.
- Mobbs RJ, Phan K, Malham G, Seex K, Rao PJ. Lumbar interbody fusion: techniques, indications and comparison of interbody fusion options including PLIF, TLIF, MI-TLIF, OLIF/ATP, LLIF and ALIF. *J Spine Surg* 2015;1(1):2–18.
- Kani KK, Chew FS. Anterior cervical discectomy and fusion: review and update for radiologists. *Skeletal Radiol* 2018;47(1):7–17.
- Bellini M, Ferrara M, Grazzini I, Cerase A. Neuroimaging of the Postoperative Spine. *Magn Reson Imaging Clin N Am* 2016;24(3):601–620.
- Moser M, Farshad M, Farshad-Amacker NA, Betz M, Spirig JM. Accuracy of Patient-Specific Template-Guided Versus Freehand Cervical Pedicle Screw Placement from C2 to C7: A Randomized Cadaveric Study. *World Neurosurg* 2019;S1878–S8750(19)30575–3. doi: 10.1016/j.wneu.2019.02.152. Accessed August 18, 2019.
- Geer CP, Papadopoulos SM. The argument for single-level anterior cervical discectomy and fusion with anterior plate fixation. *Clin Neurosurg* 1999;45:25–29; discussion 21.
- Young PM, Berquist TH, Bancroft LW, Peterson JJ. Complications of spinal instrumentation. *RadioGraphics* 2007;27(3):775–789.
- Zampolin R, Erdfarb A, Miller T. Imaging of lumbar spine fusion. *Neuroimaging Clin N Am* 2014;24(2):269–286.
- Ha AS, Petcavage-Thomas JM. Imaging of current spinal hardware: lumbar spine. *AJR Am J Roentgenol* 2014;203(3):573–581.
- Murtagh RD, Quencer RM, Castellvi AE, Yue JJ. New techniques in lumbar spinal instrumentation: what the radiologist needs to know. *Radiology* 2011;260(2):317–330.
- Quinn JC, Patel NV, Tyagi R. Hybrid lateral mass screw sublaminar wire construct: A salvage technique for posterior cervical fixation in pediatric spine surgery. *J Clin Neurosci* 2016;25:118–121.
- Pizones J, Sánchez-Mariscal F, Zúñiga L, Izquierdo E. The effect of sublaminar wires on the rib hump deformity during scoliosis correction manoeuvres. *Eur J Orthop Surg Traumatol* 2016;26(7):771–777.
- Harrington PR. Treatment of scoliosis: correction and internal fixation by spine instrumentation. *J Bone Joint Surg Am* 1962;44-A(4):591–610.
- Luque ER. Segmental spinal instrumentation for correction of scoliosis. *Clin Orthop Relat Res* 1982;(163):192–198.
- Yazici M, Olgun ZD. Growing rod concepts: state of the art. *Eur Spine J* 2013;22(suppl 2):S118–S130.
- Akbarnia BA, Pawelek JB, Cheung KM, et al. Traditional Growing Rods Versus Magnetically Controlled Growing Rods for the Surgical Treatment of Early-Onset Scoliosis: A Case-Matched 2-Year Study. *Spine Deform* 2014;2(6):493–497.
- Kadam A, Millhouse PW, Kepler CK, et al. Bone substitutes and expanders in Spine Surgery: A review of their fusion efficacies. *Int J Spine Surg* 2016;10:33.
- Sasani M, Ozer AF. Single-stage posterior corpectomy and expandable cage placement for treatment of thoracic or lumbar burst fractures. *Spine* 2009;34(1):E33–E40.

40. Koreckij TD, Gandhi SD, Park DK. Cervical Disk Arthroplasty. *J Am Acad Orthop Surg* 2019;27(3):e96–e104.
41. Leven D, Meaik J, Radcliff K, Qureshi S. Cervical disc replacement surgery: indications, technique, and technical pearls. *Curr Rev Musculoskelet Med* 2017;10(2):160–169.
42. Salzmann SN, Plais N, Shue J, Girardi FP. Lumbar disc replacement surgery: successes and obstacles to widespread adoption. *Curr Rev Musculoskelet Med* 2017;10(2):153–159.
43. Ortiz AO, de Moura A, Johnson BA. Postsurgical Spine: Techniques, Expected Imaging Findings, and Complications. *Semin Ultrasound CT MR* 2018;39(6):630–650.
44. Weisbrod LJ, Arnold PM, Leever JD. Radiographic and CT Evaluation of Recombinant Human Bone Morphogenetic Protein-2-assisted Cervical Spinal Interbody Fusion. *Clin Spine Surg* 2019;32(2):71–79.
45. Park JB, Cho YS, Riew KD. Development of adjacent-level ossification in patients with an anterior cervical plate. *J Bone Joint Surg Am* 2005;87(3):558–563.
46. Herrera Herrera I, Moreno de la Presa R, González Gutiérrez R, Bárcena Ruiz E, García Benassi JM. Evaluation of the postoperative lumbar spine. *Radiología (Madr)* 2013;55(1):12–23.
47. Fritz J, Lurie B, Miller TT, Potter HG. MR imaging of hip arthroplasty implants. *RadioGraphics* 2014;34(4):E106–E132.
48. Fritz J, Lurie B, Potter HG. MR Imaging of Knee Arthroplasty Implants. *RadioGraphics* 2015;35(5):1483–1501.
49. Pace N, Marinelli M, Spurio S. Technical and histologic analysis of a retrieved carbon fiber-reinforced poly-ether-ether-ketone composite alumina-bearing liner 28 months after implantation. *J Arthroplasty* 2008;23(1):151–155.
50. Lewandrowski KU, Nanson C, Calderon R. Vertebral osteolysis after posterior interbody lumbar fusion with recombinant human bone morphogenetic protein 2: a report of five cases. *Spine J* 2007;7(5):609–614.
51. Malhotra A, Kalra VB, Wu X, Grant R, Bronen RA, Abbed KM. Imaging of lumbar spinal surgery complications. *Insights Imaging* 2015;6(6):579–590.
52. Cannada LK, Scherping SC, Yoo JU, Jones PK, Emery SE. Pseudoarthrosis of the cervical spine: a comparison of radiographic diagnostic measures. *Spine* 2003;28(1):46–51.
53. Amiri AR, Fouyas IP, Cro S, Casey AT. Postoperative spinal epidural hematoma (SEH): incidence, risk factors, onset, and management. *Spine J* 2013;13(2):134–140.
54. Post MJ, Becerra JL, Madsen PW, et al. Acute spinal subdural hematoma: MR and CT findings with pathologic correlates. *AJNR Am J Neuroradiol* 1994;15(10):1895–1905.
55. Capen DA, Calderone RR, Green A. Perioperative risk factors for wound infections after lower back fusions. *Orthop Clin North Am* 1996;27(1):83–86.
56. Garrett MP, Kakarla UK, Porter RW, Sonntag VK. Formation of painful seroma and edema after the use of recombinant human bone morphogenetic protein-2 in posterolateral lumbar spine fusions. *Neurosurgery* 2010;66(6):1044–1049; discussion 1049.
57. Hawk MW, Kim KD. Review of spinal pseudomeningocele and cerebrospinal fluid fistulas. *Neurosurg Focus* 2000;9(1):5.
58. Luetmer PH, Schwartz KM, Eckel LJ, Hunt CH, Carter RE, Diehn FE. When should I do dynamic CT myelography? Predicting fast spinal CSF leaks in patients with spontaneous intracranial hypotension. *AJNR Am J Neuroradiol* 2012;33(4):690–694.
59. Quaile A. Infections associated with spinal implants. *Int Orthop* 2012;36(2):451–456.
60. Pull ter Gunne AF, Hosman AJ, Cohen DB, et al. A methodological systematic review on surgical site infections following spinal surgery. I. Risk factors. *Spine* 2012;37(24):2017–2033.

Nontraumatic Spinal Cord Compression: MRI Primer for Emergency Department Radiologists

Olga Laur, MD, MHS

Hari Nandu, MD¹

David S. Titelbaum, MD

Diego B. Nunez, MD, MPH

Bharti Khurana, MD

Abbreviations: ADEM = acute disseminated encephalomyelitis, AQP4-IgG = aquaporin-4 immunoglobulin G, CSF = cerebrospinal fluid, DAVF = dural arteriovenous fistula, MS = multiple sclerosis, NMO = neuromyelitis optica, STIR = short τ inversion-recovery

RadioGraphics 2019; 39:1862–1880

<https://doi.org/10.1148/rg.2019190024>

Content Codes: ER MR NR OI

From the Departments of Radiology (O.L., D.B.N.), Neuroradiology (H.N., D.B.N.), and Emergency Radiology (B.K.), Brigham and Women's Hospital, 75 Francis St, Boston, MA 02115; and Department of Radiology, Shields Health Care, Brockton, Mass (D.S.T.). Recipient of a Certificate of Merit award for an education exhibit at the 2018 RSNA Annual Meeting. Received February 15, 2019; revision requested April 29 and received June 28; accepted July 25. For this journal-based SA-CME activity, the author B.K. has provided disclosures (see end of article); all other authors, the editor, and the reviewers have disclosed no relevant relationships. Address correspondence to O.L. (e-mail: olga.laur@bwh.harvard.edu).

¹Current address: CP Advanced Imaging, New York, NY.

©RSNA, 2019

SA-CME LEARNING OBJECTIVES

After completing this journal-based SA-CME activity, participants will be able to:

- Describe the anatomy of the spinal canal compartment and localize compressive lesions to an epidural, intradural extramedullary, or intramedullary space.
- Differentiate common compressive causes of acute myelopathy according to compartment location and characteristic imaging findings.
- List common causes of noncompressive myelopathy and refine the differential diagnosis according to the location and longitudinal extension of abnormal signal intensity within the spinal cord, neural tracts involved, and ancillary clinical history and laboratory data.

See rsna.org/learning-center-rg.

The occurrence of acute myelopathy in a nontrauma setting constitutes a medical emergency for which spinal MRI is frequently ordered as the first step in the patient's workup. The emergency department radiologist should be familiar with the common differential diagnoses of acute myelopathy and be able to differentiate compressive from noncompressive causes. The degree of spinal cord compression and presence of an intramedullary T2-hyperintense signal suggestive of an acute cord edema are critical findings for subsequent urgent care such as surgical decompression. Importantly, a delay in diagnosis may lead to permanent disability. In the spinal canal, compressive myelopathy can be localized to the epidural, intradural extramedullary, or intramedullary anatomic spaces. Effacement of the epidural fat and the lesion's relation to the thecal sac help to distinguish an epidural lesion from an intradural lesion. Noncompressive myelopathy manifests as an intramedullary T2-hyperintense signal without an underlying mass and has a wide range of vascular, metabolic, inflammatory, infectious, and demyelinating causes with seemingly overlapping imaging appearances. The differential diagnosis can be refined by considering the location of the abnormal signal intensity within the cord, the longitudinal extent of the disease, and the clinical history and laboratory findings. Use of a compartmental spinal MRI approach in patients with suspected nontraumatic spinal cord injury helps to localize the abnormality to an epidural, intradural extramedullary, or intramedullary space, and when combined with clinical and laboratory findings, aids in refining the diagnosis and determining the appropriate surgical or nonsurgical management.

Online supplemental material is available for this article.

©RSNA, 2019 • radiographics.rsna.org

Introduction

Acute compressive myelopathy in the setting of minimal to no trauma is a medical emergency for which timely intervention is essential to minimize irreversible loss of neurologic function. Decompression of the spinal cord within the first 24 hours after the onset of myelopathy has been shown to improve neurologic outcomes (1–3). As a result, MRI of the spine is frequently performed on an emergent basis, including after hours, to assess suspected cord compression. Thus, it is imperative that emergency department radiologists have a good understanding of the common differential diagnoses of acute myelopathy and be able to differentiate the compressive versus noncompressive causes. The anomalies commonly included in the differential diagnosis of acute myelopathy and the compressive and noncompressive causes of this disease are described in this review.

TEACHING POINTS

- An intramedullary T2-hyperintense signal of the spinal cord by itself is a nonspecific finding and cannot be used to reliably predict surgical outcomes. However, a high T2 signal intensity change when comparing a compressed segment to a noncompressed segment, or a low T1 signal intensity change with high T2 signal intensity of the compressed segment, has been associated with worse outcomes, as these differences may indicate advanced histologic damage.
- MRI reveals a T1-hypointense, T2-hyperintense epidural collection that may enhance diffusely in a phlegmon state or show peripheral enhancement, with central nonenhancement, in cases of a mature abscess. The collection is rarely an isolated finding and almost always is associated with spondylodiscitis and paravertebral muscle involvement.
- Neurofibromas, and to a lesser degree schwannomas, tend to have a characteristic “target sign” appearance, with central T2 hypointensity and peripheral T2 hyperintensity.
- It is important to note that in cases of slow flow during early DAVF, these venous plexi may not be well seen at T2-weighted MRI. In such cases, contrast-enhanced MRI is the most reliable modality for visualizing dilated serpentine enhancing perimedullary vessels, which are suggestive of DAVF.
- The classic triad of NMO consists of optic neuritis, longitudinally extensive transverse myelitis involving more than three vertebral segments, and serologic analysis findings positive for AQP4-IgG antibody.

“Red Flags” for Myelopathy and Importance of Spinal MRI in the Clinical Workup

Myelopathy is defined as a neurologic deficit secondary to a spinal cord abnormality. Classic “red flags” for myelopathy include rapidly developing muscle weakness, sensory deficit, and loss of bowel and bladder sphincter control (4). Cauda equina syndrome is a myelopathy characterized by saddle anesthesia, loss of bowel and bladder control, sexual dysfunction, and frequently lower extremity weakness (5). The clinical history and laboratory values indicative of infection or malignancy can further influence the decision to pursue MRI.

According to the American College of Radiology Appropriateness Criteria, patients who present with symptoms of nontraumatic painful or sudden-onset progressive myelopathy should undergo MRI of the spine without contrast material. In cases of suspected infection, concern for malignancy, or a suspected inflammatory or vascular cause, contrast material–enhanced spinal MRI is preferable. If vascular disease is suspected, spinal MR angiography can be performed as an adjunctive examination.

MRI can be used to directly determine compressive versus noncompressive causes of myelopathy, assess for intramedullary disease, and determine the specific spinal level of involvement. Sagittal and axial T1- and T2-weighted and short

τ inversion-recovery (STIR) MRI sequences typically are used and may be supplemented by fat-suppressed, gradient-echo, diffusion-weighted, and contrast-enhanced sequences (Table).

Anatomic Compartment-based Approach to Myelopathy

Knowledge of the spinal canal anatomy is critical for localizing myelopathies, and acquiring an understanding of this anatomy should be the first step in the spinal MRI evaluation. Myelopathies can be broadly attributed to compressive or noncompressive causes. Compressive myelopathy results from a lesion’s external compression on the spinal cord and can be further localized to an extradural, intradural extramedullary, or intramedullary space. It is important to understand that an intramedullary T2-hyperintense signal in the setting of symptoms of acute cord compression is an urgent finding and probably indicates acute cord edema and ischemia. Lesions associated with cord atrophy and chronic blood products probably represent irreversible changes such as necrosis and cavitation and may not respond to treatment.

Noncompressive myelopathy is confined to the intramedullary space and is not associated with an underlying space-occupying lesion. Whereas compressive myelopathy is commonly managed with neurosurgical decompression, treatment of noncompressive myelopathy depends on the specific cause of the disease.

Localization of Compressive Myelopathy

Epidural space is defined as the space between the bony spinal canal and the dura mater. It contains epidural fat, spinal nerves, small arterioles, venous plexi, and lymphatics and communicates directly with the paravertebral space by way of the intervertebral foramina. *Intradural space* is defined as the space between the arachnoid mater and pia mater. It contains cerebrospinal fluid (CSF), nerve fibers, vascular elements, and glial tissue. The potential subdural space lies between the arachnoid mater and dura mater, which are closely opposed to each other secondary to bridging thin strands of collagen (6). Finally, the intramedullary compartment is the space within the substance of the spinal cord.

On MR images, the dura mater and arachnoid mater are difficult to differentiate owing to their close proximity. They appear as a T1- and T2-hypointense membrane defining the thecal sac (Fig 1), with epidural space external to the thecal sac and intradural space internal to it. At MRI, a compressive lesion in the epidural space causes effacement of the epidural fat, inward displacement of the dura mater, and compression of the spinal cord (Fig 2, Table E1). T2-weighted MRI

Sequences That Can Be Added to the Spinal MRI Protocol for Myelopathy

| MRI Sequence | Assessed Pathologic Entity |
|---------------------------------------------|---------------------------------------------------------------------|
| Contrast-enhanced T1 weighted | Metastatic, infectious, inflammatory, or autoimmune disease |
| Contrast-enhanced fat-saturated T1 weighted | Lipomatous epidural lesions vs nonlipomatous phlegmon or metastasis |
| Gradient echo | Epidural hematoma, intramedullary cavernous malformation |
| Diffusion weighted | Spinal cord infarction, abscess |

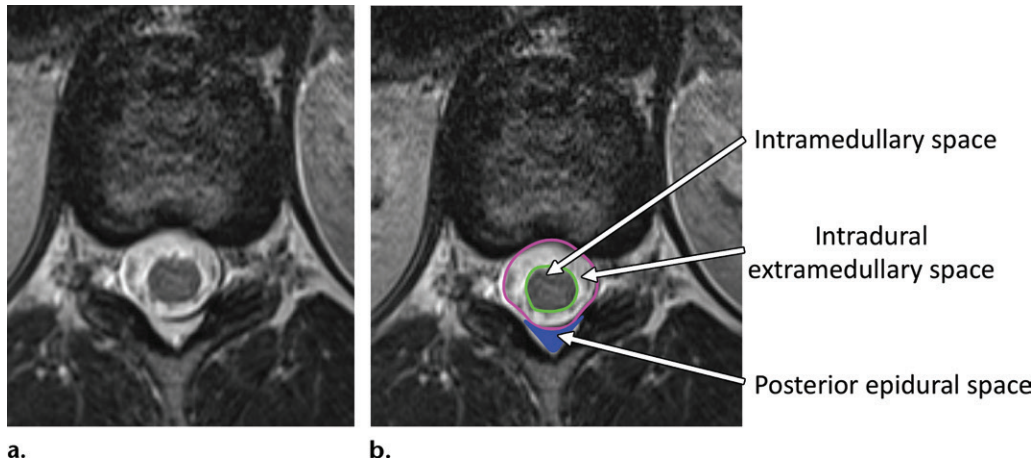


Figure 1. MRI findings in a healthy 23-year-old woman. Axial nonlabeled (a) and labeled (b) T2-weighted MR images of the thoracic spine at the T11-T12 spinal level show the thecal sac (pink outline in b) and pia mater (green outline in b), which compartmentalize the spinal canal into the epidural, intradural extramedullary, and intramedullary spaces. In b, the posterior epidural space (blue) is filled with fat.

has been shown to have the highest inter- and intrareader reliability for grading the degree of compression, with *high-grade compression* defined as deformation of the spinal cord with partial or complete obliteration of the CSF space (7).

In contrast, an intradural lesion is located deep to the thecal sac, with preservation of the epidural fat, on MR images (Table E2). Because lesions in the intradural space lie within the CSF, there is usually ipsilateral enlargement of the CSF space to accommodate the space-occupying lesion. A cleft of CSF may be seen separating the lesion from the spinal cord. Finally, an intramedullary lesion results in expansion of the spinal cord.

Noncompressive Myelopathy

At MRI, noncompressive myelopathy manifests as an abnormal T2-hyperintense signal within the spinal cord. It has a wide range of vascular, metabolic, inflammatory, infectious, and demyelinating causes with seemingly overlapping imaging appearances (Table E3). The differential diagnosis can be refined by considering the lesion's location within the cord, its longitudinal

extent, and the pertinent clinical history and laboratory findings.

Epidural Causes of Compressive Myelopathy

Degenerative Disease

Disk Herniation.—Spondylotic myelopathy secondary to acute disk herniation is the most common cause of cauda equina syndrome and the most common cause of spinal cord dysfunction in adults worldwide (5,8). Disk extension into the anterior epidural space varies from a broad disk bulge to a focal herniation. The herniation can be further categorized as disk protrusion, extrusion, or sequestration (9). Acute neurologic deficit due to acute disk extrusion is a potential neurosurgical emergency. More chronic forms of disk extrusion can be addressed with cord adaptation and may be asymptomatic. In many cases, the degree of disk herniation can regress with time (10).

At MRI, the epidural component of the herniated disk has the same signal intensity characteristics as the donor disk (Fig 3). In cases of seque-

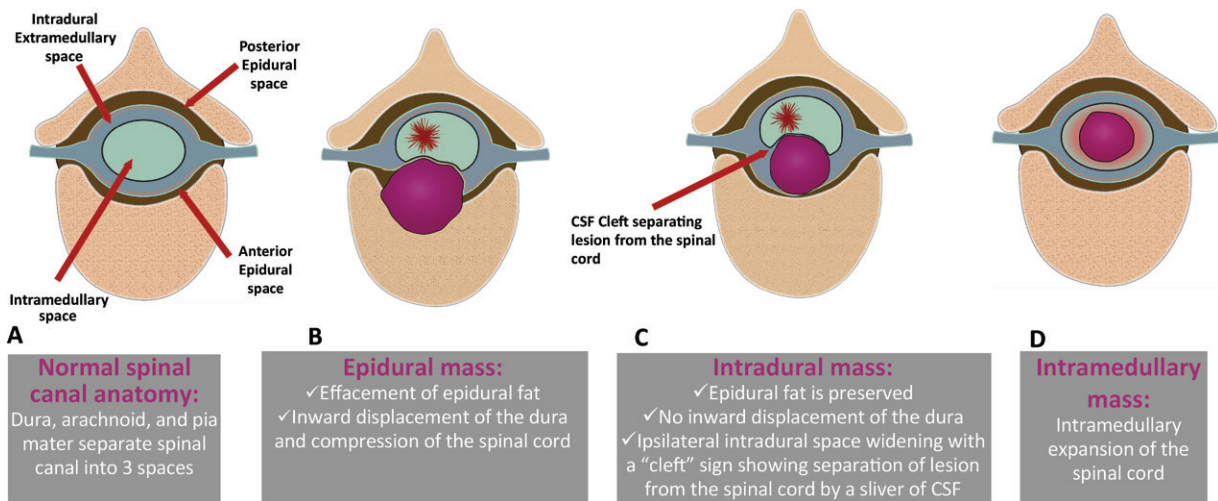
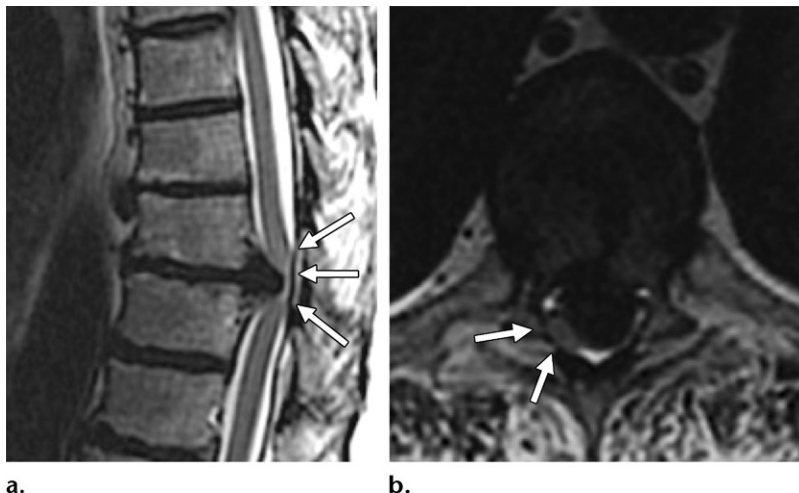


Figure 2. Drawings illustrate the anatomic compartments of the spinal canal and their typical imaging appearances in the presence of a space-occupying lesion. The normal axial anatomy of the spinal cord (*A*) and the axial appearances of the spinal cord when a mass is localized to the epidural (*B*), intradural extramedullary (*C*), and intramedullary (*D*) spaces are depicted.



a.

b.

Figure 3. Acute disk herniation in a 50-year-old man who presented with leg numbness and weakness. Sagittal (*a*) and axial (*b*) T2-weighted MR images of the thoracic spine show intervertebral disk extrusion at the T11-T12 spinal level, with posterolateral displacement and significant compression on the spinal cord (arrows in *b*). Note the continuity of the extruded disk with the donor disk. The focal increase in spinal cord signal intensity (arrows in *a*) probably indicates acute cord edema.

tration, owing to its increased fluid component, the fragment may appear to have higher signal intensity than the donor disk at T2-weighted MR imaging. Frequently, a layer of granulation tissue surrounds the avascular sequestered material, causing it to have peripheral enhancement (11).

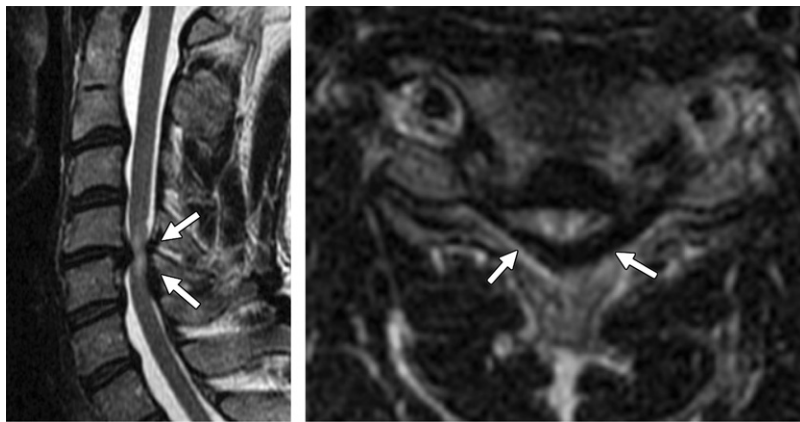
Spinal Canal Stenosis.—Acquired spinal canal stenosis represents multifactorial degenerative changes characterized by facet joint hypertrophy, disk bulging or herniation, multilevel endplate osteophytes, buckling of the ligamentum flavum, and ligamentous ossification. In addition, nerve root and spinal cord compression can be aggravated by dynamic mechanisms, particularly in the cervical spine. MR images show an hourglass appearance of the spinal canal, with effacement of the CSF space (Fig 4). If the lumbar region is affected, the cauda equina nerve roots may have a crowded, serpiginous appearance (12,13).

An intramedullary T2-hyperintense signal of the spinal cord by itself is a nonspecific finding and cannot be used to reliably predict surgical outcomes. However, a high T2 signal intensity change when comparing a compressed segment to a noncompressed segment, or a low T1 signal intensity change with high T2 signal intensity of the compressed segment has been associated with worse outcomes, as these differences may indicate advanced histologic damage (8). Chronic mechanical compression of the spinal cord can lead to cord flattening and enhancement, with destruction of the blood-spinal cord barrier.

Infectious Disease

Epidural abscess is usually secondary to spondylodiscitis and less commonly secondary to septic arthritis. The abscess typically extends into the anterior or posterior epidural space and may

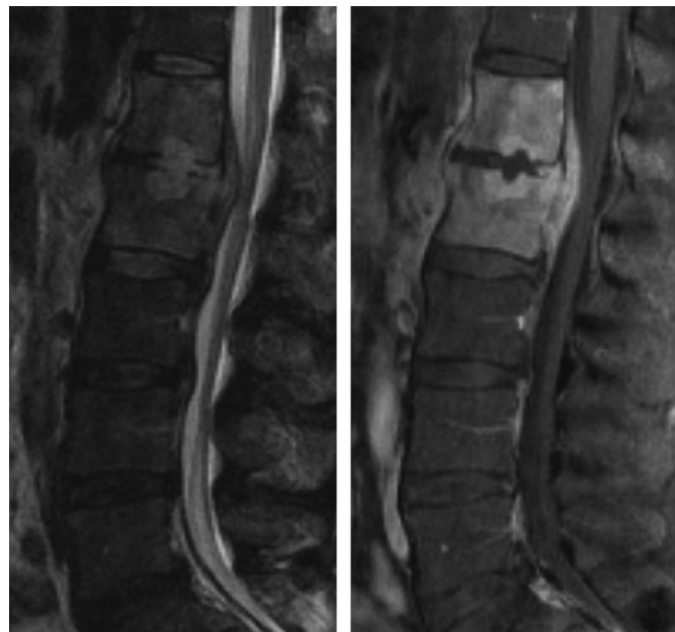
Figure 4. Spinal stenosis and cord compression in a 48-year-old man who had progressive gait disturbance of several months duration and bowel and bladder dysfunction for 2 days. Sagittal (a) and axial (b) T2-weighted MR images of the cervical spine show severe cervical stenosis at the C4-C5 spinal level secondary to a herniated disk-osteophyte complex extending into the anterior epidural space, and buckling of the ligamentum flavum in the posterior epidural space (arrows). These findings result in complete focal CSF effacement and ventral and dorsal cord compression with intramedullary T2 hyperintensity.



a.

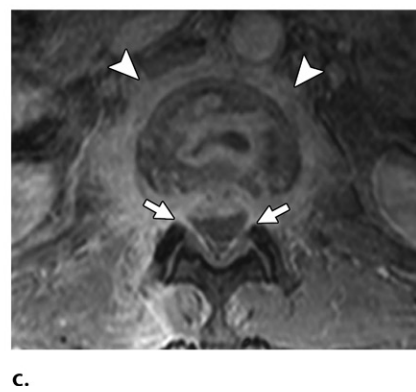
b.

Figure 5. L1-L2 spondylodiscitis with an epidural phlegmon in a 50-year-old man who presented with bilateral lower extremity weakness. (a, b) Sagittal T2-weighted (a) and contrast-enhanced T1-weighted (b) MR images of the lumbar spine show T2-hyperintense, abnormally enhancing L1-L2 vertebral bodies, with intervertebral disk destruction and an anterior epidural homogeneously enhancing phlegmon spanning the L1-L2 vertebra. (c) Axial contrast-enhanced T1-weighted MR image of the lumbar spine at the L1-L2 level shows posterior displacement of the thecal sac by the phlegmon (arrows). There is also diffuse prevertebral and paraspinal enhancement (arrowheads), indicating an intramuscular phlegmon.



a.

b.



c.

result in myelopathy secondary to either mass effect on the thecal sac or septic thrombo-phlebitis. Symptoms can progress from pain and radiculopathy to weakness and eventual paralysis. An epidural abscess is a surgical emergency for which appropriate management is critical to preventing paralysis.

Neurologic deficit is the most important factor in the treatment decision of surgical débridement versus medical therapy only (14). Spinal instability in the setting of spondylodiscitis with bone destruction, severe deformity, and/or kyphosis also contributes to the cord compression and symptoms of myelopathy and is a frequent indication for surgical management (15). *Staphylococcus aureus* is the most common pathogen. Intravenous drug use and immunosuppression are predisposing factors for spinal epidural abscess formation.

MRI reveals a T1-hypointense, T2-hyperintense epidural collection that may enhance diffusely in a phlegmon state or show peripheral enhancement, with central nonenhancement, in cases of a mature abscess (Figs 5, 6). The collection is rarely an isolated finding and almost

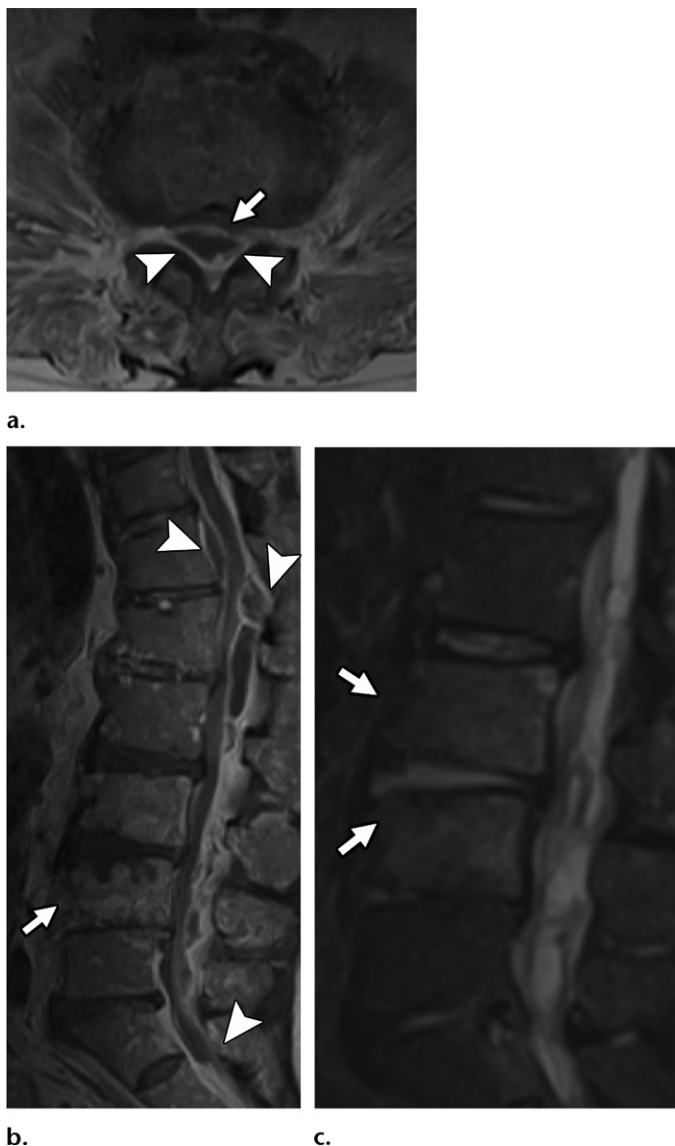


Figure 6. L3-L4 spondylodiscitis and a large epidural abscess, with blood cultures yielding methicillin-sensitive *S aureus*, in a 65-year-old man. Axial contrast-enhanced T1-weighted MR image at the L1-L2 level (a) and sagittal contrast-enhanced T1-weighted (b) and STIR (c) MR images of the lumbar spine show an elongated T2-hyperintense peripherally enhancing collection with an anterior epidural component at the T12 level, extensive posterior epidural extension to the S1 level (arrowheads in a and b), and anterior thecal sac displacement and compression at the L1-L2 level (arrow in a). L3-L4 spondylodiscitis is also depicted; it is seen as abnormal hyperintensity of the intervertebral disk and adjacent bone at STIR imaging and as abnormal bone enhancement at contrast-enhanced imaging (arrows in b and c).

always is associated with spondylodiscitis and paravertebral muscle involvement (16).

Vascular Disease

Atraumatic development of an epidural hematoma can be seen in the setting of anticoagulation therapy or coagulopathy, vascular malformations, Paget disease, and/or iatrogenic causes. In the setting of rapidly progressive symptoms, an epidural hematoma is considered a surgical emergency, as a delay in decompression may result in permanent deficits. Epidural hematomas occur most commonly in the cervical or thoracic spine, typically in the dorsal epidural space. The classic appearance is characterized by a biconvex morphology (Fig 7). An epidural hematoma has variable signal intensity at T1- and T2-weighted MRI, depending on the age of the blood products, which has been described in the literature (17).

It should be noted that a hyperacute hematoma that has existed for less than 24 hours is expected to appear T1 isointense and T2 hyperintense and thus is difficult to distinguish from CSF. Displacement of the thecal sac and effacement of the epidural fat are subtle clues to the underlying space-occupying lesion. Epidural hematoma typically has peripheral enhancement on contrast-enhanced images. The presence of enhancing foci may indicate active extravasation.

Metastatic Disease

The spine is the most common site of skeletal metastases, with an annual prevalence of malignant spinal cord compression of approximately 3%–5%. Metastatic spinal disease represents the initial manifestation of malignancy in approximately 20% of patients (18,19). Involvement of the spinal column with epidural cord compression is significantly more common than intradural and

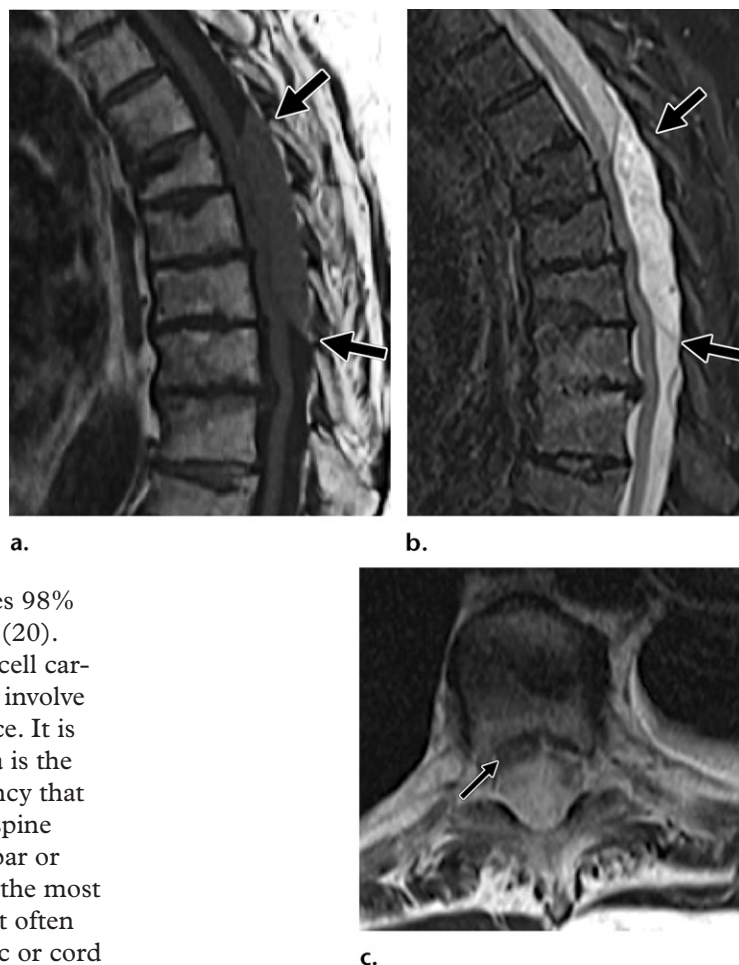


Figure 7. Epidural hematoma in an 84-year-old woman after a fall and epidural catheter placement for pain, with rapid development of lower extremity weakness. (a, b) Sagittal T1-weighted (a) and STIR (b) MR images of the thoracic spine show a large biconvex heterogeneous collection (arrows) in the posterior epidural space, extending from the T6 to T9 vertebral level. The collection is T1 isointense and has high signal intensity at STIR MRI. (c) Axial T2-weighted image at the T8 level shows effacement of the posterior epidural fat and ventral displacement of the spinal cord, with severe compression (arrow).

intramedullary metastases and constitutes 98% of cases of spinal cord metastatic lesions (20). Prostate, lung, and breast cancers; renal cell carcinoma; and lymphoma most commonly involve the spine and extend to the epidural space. It is important to note that multiple myeloma is the most common primary osseous malignancy that can lead to cord compression. Thoracic spine compression is more common than lumbar or cervical spine compression. Back pain is the most common symptom at presentation, and it often worsens at night. The degree of thecal sac or cord compression correlates with the degree of neurologic impairment and the functional outcome.

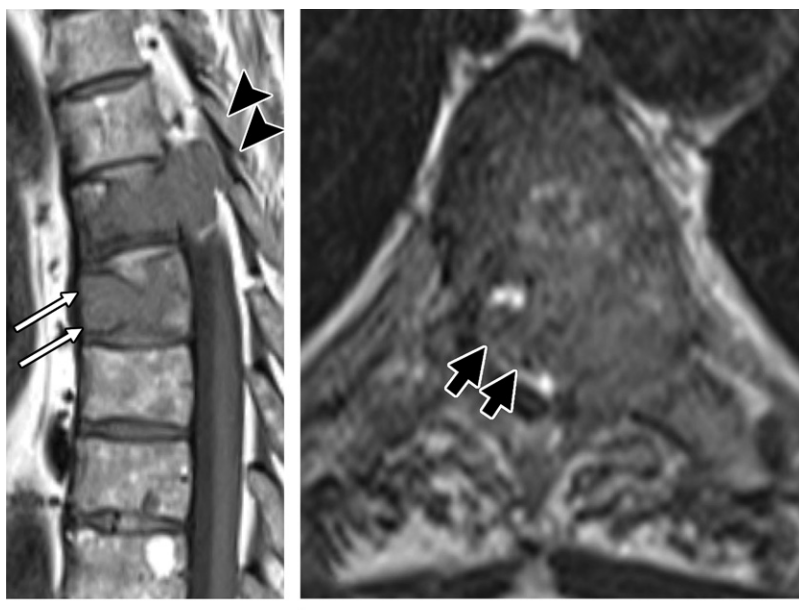
Hematogenous spread is most common, with vertebral body involvement being more common than posterior element involvement, presumably because of the high vascularity and larger volume of the vertebral body. Cord compression results from the spread of metastasis from the vertebral body to the dura, direct infiltration of the dura, and transforaminal extension. Even in the absence of significant mass effect, a hyperintense signal may be seen in the spinal cord at T2-weighted MRI. This high signal intensity is suggestive of edema that may be caused by a vascular phenomenon such as venous hypertension secondary to impingement of the epidural venous plexi by the tumor.

MRI aids in assessing the presence and extent of osseous involvement, paravertebral and epidural extension, and thecal sac impingement. Since metastatic disease commonly occurs at multiple levels and recurrent disease is common, contrast-enhanced MRI of the entire spine is performed (21). An epidural tumor typically is hypointense at T1-weighted MRI, has variable signal intensity at T2-weighted MRI, and has variable enhancement depending on the degree of necrosis and/or sclerosis (Figs 8, 9).

The degree of epidural cord compression can be graded—for example, by using the Epidural Spinal Cord Compression Scale—to help determine whether the patient may benefit from radiation treatment or surgical decompression. In addition, various models, such as the Spinal Instability Neoplastic Score (SINS) model, have been developed to aid in interpreting images and triaging cases of spine instability in patients with oncologic conditions. In such models, a high score indicates the need for urgent surgical intervention. Factors such as location of the metastatic lesion, alignment of the spine, degree of vertebral body involvement, lesion appearance, and degree of pain are considered in the SINS model (22).

Metabolic Disease

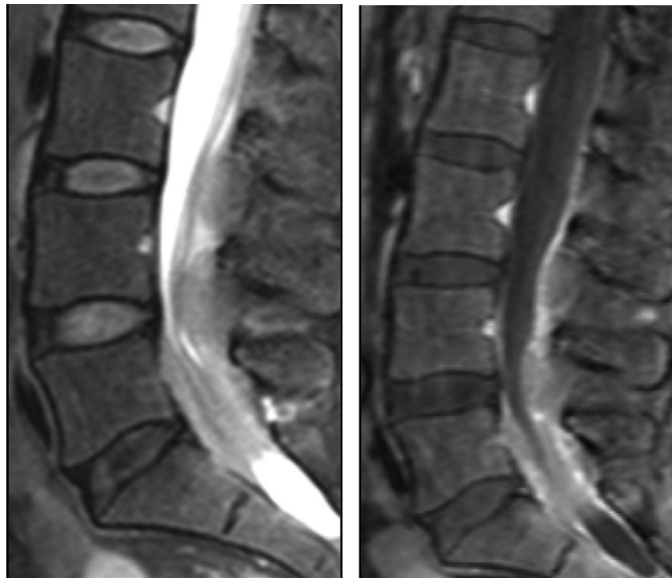
Extramedullary hematopoiesis expansion outside the bone marrow occurs in the setting of ineffective erythropoiesis. It is associated with myelofibrosis, sickle cell anemia, β thalassemia, lymphoma and leukemia, Gaucher disease, Paget disease, and pernicious anemia. Epidural extramedullary hematopoiesis is believed to result from hematopoietic rest cells in the spinal canal



a.

b.

Figure 8. Metastatic prostate cancer in a 72-year-old man. Sagittal T1-weighted image of the thoracic spine (**a**) and axial T2-weighted image at the T7 vertebral level (**b**) show a destructive soft-tissue mass involving the T7 vertebral body and left posterior elements, with extension into the anterior epidural space (arrowheads in **a**) and lateral displacement and compression of the spinal cord (arrows in **b**). An additional T1-hypointense lesion (arrows in **a**) in the T8 vertebra is noted.



a.

b.

Figure 9. Lymphoma in a 55-year-old man. Sagittal T2-weighted (**a**) and contrast-enhanced T1-weighted (**b**) MR images of the lumbar spine show multiple enhancing masses in the anterior and posterior epidural space. (**c**) Axial T2-weighted image at the L4 vertebral level shows effacement of the posterior epidural space, with anterior displacement of the thecal sac (arrows).



c.

or direct extension of the paravertebral hematopoietic tissue into the spinal canal (23). It occurs most commonly in the middle to lower thoracic spine.

At MRI, well-defined multilevel epidural lobulated masses that are T1 hypointense and mildly T2 hyperintense are seen, often in association with extrapleural paravertebral masses. In extramedullary hematopoiesis, a T2-hypointense signal also may be seen and is secondary to the increased iron content in the hematopoietic tissue (Fig 10). Because active lesions are vascular, they enhance at contrast-enhanced imaging. Inactive older lesions often have more fat tissue and iron deposits.

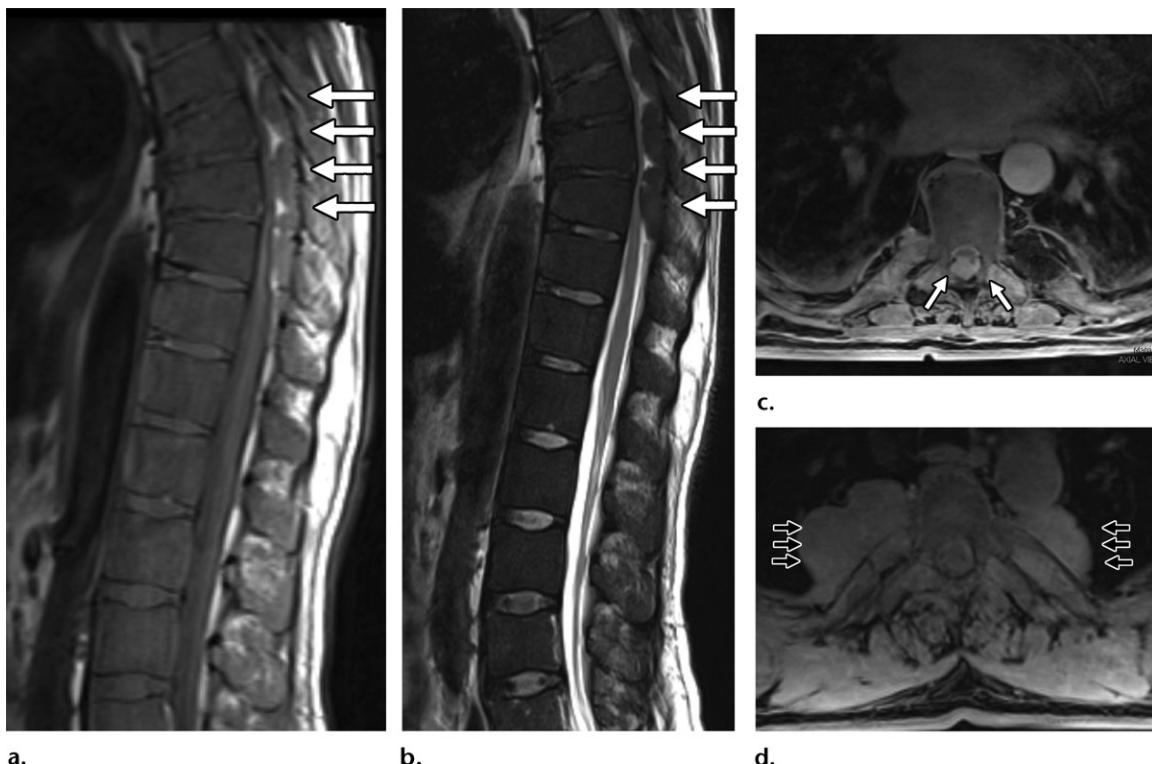


Figure 10. Extramedullary hematopoiesis in a 53-year-old man with a history of β thalassemia, who presented with lower-extremity weakness. Sagittal T1-weighted (a) and T2-weighted (b) MR images of the thoracolumbar spine, and axial contrast-enhanced T1-weighted MR images at the level of the abnormality (c, d) show multilevel lobulated T1-isointense and T2-hypointense avidly enhancing soft-tissue masses (arrows in a and b) in the posterior epidural space and associated large bilateral paravertebral extrapleural masses (arrows in d). These findings are typical of extramedullary hematopoiesis. There is also posterior epidural fat effacement and anterior displacement and deformation of the spinal cord (arrows in c). The diffuse decrease in T1 and T2 bone marrow signal intensity indicates red marrow conversion.

Other Epidural Causes of Compressive Myelopathy

Spontaneous cord herniation involves the thoracic spinal cord. The cord gradually herniates through the anterior or lateral defect in the dura to result in slowly progressive myelopathy. It affects patients in their 5th decade of life, has a female predominance, and is hypothesized to have a congenital cause (24). MR images show an abnormal contour of the spinal cord, with anterior kinking and an increase in dorsal CSF space. Cord deformation and narrowing may be present, with increased intramedullary T2 signal intensity. CSF turbulence artifact at the level of the herniation can help to differentiate a cord herniation from an intradural arachnoid cyst (Fig 11).

Intradural Causes of Compressive Myelopathy

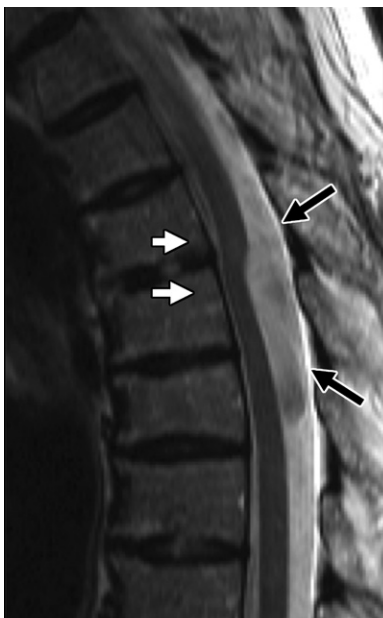
Arachnoid Cyst

Arachnoid cyst represents a splitting of the arachnoid layer, which creates a potential space where CSF can accumulate. Patients commonly present with symptoms that indicate a slowly progressive myelopathy, which typically arises in

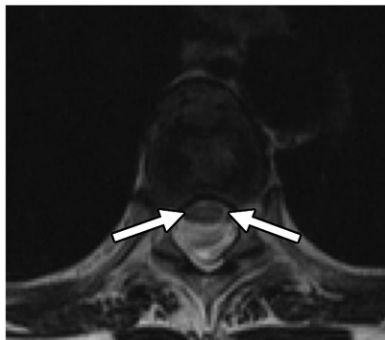
the thoracic spine dorsal to the spinal cord. An arachnoid cyst has the signal intensity of CSF, with its walls often invisible on images and spinal cord displacement often being the only clue (25). The appearance of an arachnoid cyst often mimics that of thoracic cord herniation. Contrary to the thoracic cord herniation, space-occupying arachnoid cyst will displace the cord anteriorly, and, thus, CSF pulsation artifact will be absent. (Fig 12). Primary arachnoid cysts are congenital, while acquired arachnoid cysts can be caused by prior spinal surgery or lumbar puncture, trauma, or arachnoiditis.

Infection

An intradural extramedullary abscess is extremely rare and portends a poor prognosis (26). Few cases have been reported in the literature, and most of them have involved *S aureus* or *Mycobacterium tuberculosis* infections (27). Similar to the population at risk for epidural abscess, the population at risk for intradural extramedullary abscess includes immunocompromised patients, intravenous drug users, and patients who have recently undergone surgery. On MR images, an intradural abscess appears as an elongated T2-hyperintense,



a.



b.

Figure 11. Thoracic cord herniation in a 65-year-old man. (a) Sagittal T2-weighted MR image of the thoracic spine shows a dorsal contour abnormality of the mid-thoracic spinal cord, with anterior cord deviation (white arrows) and expansion of the posterior CSF containing a prominent pulsation artifact (black arrows). (b) Axial T2-weighted MR image at the level of the abnormality shows focal anterior herniation of the spinal cord (arrows).



a.



b.

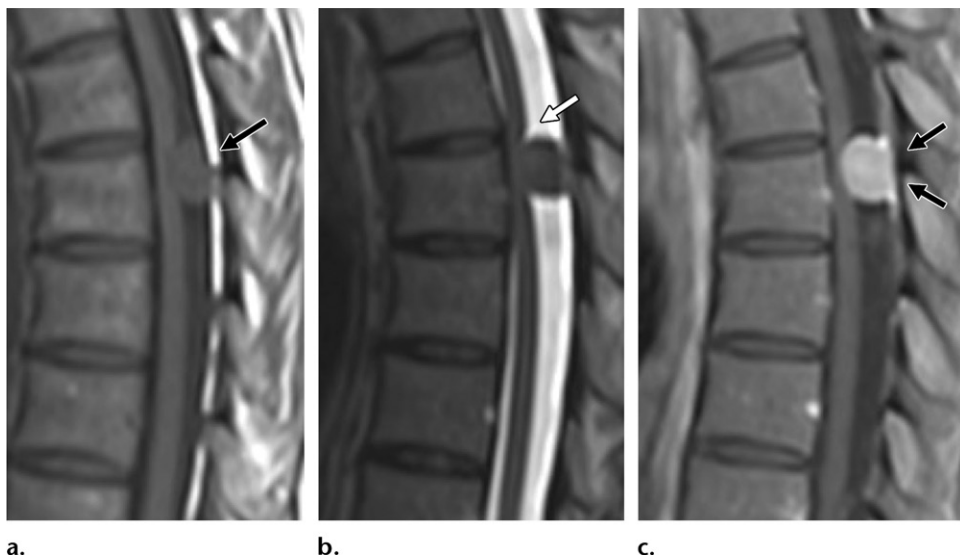
Figure 12. Thoracic arachnoid cyst (Ac) in a 55-year-old woman. Sagittal T1-weighted (a) and STIR (b) MR images of the thoracic spine show a well-circumscribed ovoid cystic structure (arrows) in the posterior intradural space. The cyst has CSF signal intensity with all MRI sequences and exerts anterior mass effect on the spinal cord. The absence of CSF pulsation artifact posterior to the spinal cord abnormality should raise suspicion for an arachnoid cyst, even when the walls of the abnormality are not well seen.

T1-hypointense collection with peripheral enhancement. When the abscess is small, a phlegmon may mimic an intradural primary tumor such as schwannoma or meningioma.

Primary Tumors and Metastases

Meningioma.—The majority of intradural extramedullary tumors are meningiomas, schwannomas, or neurofibromas. A meningioma is usually a solitary mass, with the peak incidence occurring in individuals who are in their 5th–6th

decade of life. Meningiomas typically are located anterior to the spinal cord in the cervical spine and posterior to the cord in the thoracic spine. A unique feature of meningioma is its broad dural base, with thickening and enhancement at contrast-enhanced MRI (28). This tumor may have intratumoral calcifications and prominent flow voids and rarely has a cystic appearance. On MR images, it appears as a T1- and T2-isointense avidly enhancing oval or round lesion (Fig 13). Multiple meningiomas are associated with neurofibromatosis type 2.



a. b. c.

Figure 13. Meningioma in a 46-year-old woman who presented with back pain, leg paresthesia, and difficulty urinating. Sagittal T1-weighted (a), T2-weighted (b), and contrast-enhanced fat-suppressed T1-weighted (c) MR images of the thoracic spine show a well-circumscribed oval posterior intradural T1- and T2-isointense mass with avid enhancement, broad dural attachment (arrows in c), and dorsal spinal cord compression. A cleft of CSF (arrow in b) is present between the mass and spinal cord, and the posterior epidural fat (arrow in a) is preserved, indicating an intradural location of the meningioma.

Schwannoma and Neurofibroma.—Schwannoma and neurofibroma are benign nerve sheath tumors that can be difficult to differentiate on MR images. The majority of these tumors are intradural, and approximately 15% of them have both intradural and extradural components. In those cases, a characteristic dumbbell-shaped lesion extends into and causes enlargement of the neural foramen (Fig 14). A schwannoma is an encapsulated neoplasm that can be removed during surgery when it is freed from the capsule, whereas a neurofibroma is intrinsically intertwined with the nerve and needs to be resected. Solitary schwannomas and neurofibromas tend to occur in individuals before their 6th decade of life. Multiple neurofibromas are common in patients with neurofibromatosis type 1 and have an earlier manifestation, while multiple schwannomas are common in patients with neurofibromatosis type 2 (29). Both of these lesions usually are T1 hypointense, with variable enhancement.

Neurofibromas, and to a lesser degree schwannomas, tend to have a characteristic “target sign” appearance, with central T2 hypointensity and peripheral T2 hyperintensity. Schwannomas tend to appear more heterogeneous on T2-weighted and contrast-enhanced MR images, secondary to cyst formation and vascular changes. Transformation to a malignant peripheral nerve sheath tumor should be suspected in cases of rapid growth, which is metabolically active at PET.

Intradural Metastases.—Intradural extramedullary spinal “drop” metastases represent hematogenous spread and frequently occur at the site of the conus medullaris. Lung, breast, and hematologic malignancies are common. The lumbar spine is the most frequently involved, and multifocal disease is common, with at least 50% of patients having brain metastases. Common symptoms include localized or radicular back pain, weakness, bladder dysfunction, and bowel dysfunction. On MR images, intradural metastases are deep to the dura, are typically T1 hypointense and T2 hyperintense, and enhance on contrast-enhanced images (Fig 15).

Vascular Disease

Intradural hematomas occur less frequently than do epidural hematomas and are more likely to be associated with coagulopathy and recent surgery than with trauma. Symptoms of acute myelopathy associated with intradural hematoma can occur more rapidly than those associated with epidural hematoma. On MR images, intradural hematomas are deep to the dura, with preservation of the epidural fat, and have T1 and T2 signal intensity that varies according to the age of blood products.

The morphology of an intradural hematoma may resemble an inverted Mercedes Benz sign, whereby the intradural collection is separated into two posterolateral components and one anterior component owing to the presence of intradural bilateral dentate ligaments and a dorsal midsagittal septum (17).

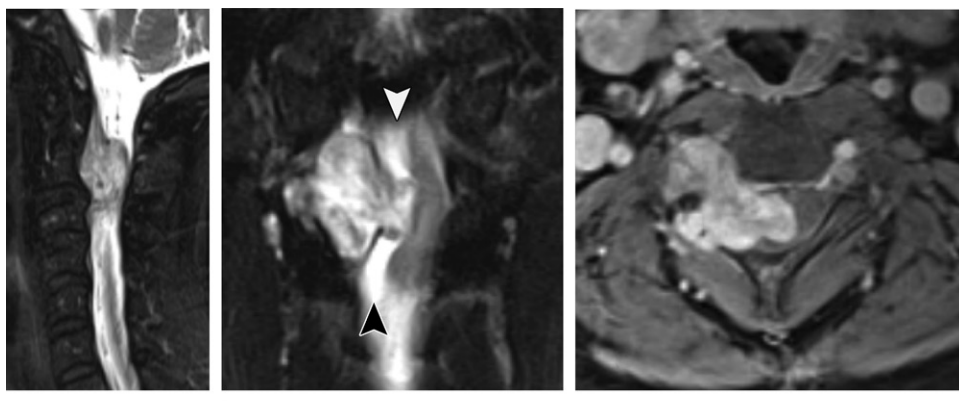


Figure 14. Schwannoma with intradural and epidural components in a 65-year-old woman who presented with upper extremity weakness. Sagittal (a) and coronal (b) T2-weighted MR images of the cervical spine and axial contrast-enhanced T1-weighted MR image at the C2 spinal level (c) show a dumbbell-shaped T2-heterogeneous lesion with avid enhancement causing lateral displacement and compression of the spinal cord. The CSF cleft between the lesion and spinal cord is indicative of the intradural component (arrowheads in b) of the tumor.

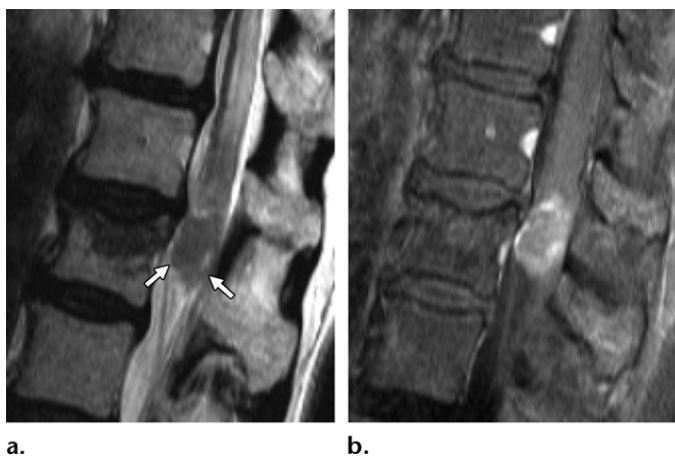


Figure 15. Metastatic breast cancer in a 51-year-old woman who presented with new-onset bilateral leg weakness. Sagittal T2-weighted (a) and contrast-enhanced T1-weighted (b) MR images of the thoracolumbar spine show a large T2-hypointense enhancing intradural drop metastasis (arrows in a) at the level of the conus medullaris-cauda equina junction, with displacement of the cauda equina nerve roots and preservation of the posterior epidural fat. These findings are indicative of the intradural location of the metastasis. Leptomeningeal metastatic disease was identified at brain MRI (not shown).

Intramedullary Causes of Compressive Myelopathy

Intramedullary masses result in spinal cord expansion, and although different types of masses may be similar in appearance to each other, a few characteristic signs can help to narrow the differential diagnosis.

Intramedullary metastases represent a small percentage of the intramedullary tumor types and usually have edema that is out of proportion to the size of the lesion (Fig 16). Primary tumors include ependymoma, which is the most frequent adult intramedullary tumor; astrocytoma; and hemangioblastoma.

Ependymoma arises from glial cells that line the central canal and typically has an expansile well-circumscribed appearance, usually in the cervical cord (Fig 17). This tumor is slow growing, well defined, T2 hyperintense, and T1 hypointense, and it demonstrates avid enhancement (Fig 18). Polar cysts are commonly seen, and intratumoral cysts are less commonly seen (13). A T1-hyperintense

signal may indicate intratumoral hemorrhage. The “tumor cap” sign is characteristic of ependymoma and appears as a T2-hypointense signal at the margin of the lesion secondary to the hemorrhage.

Astrocytoma is the second most common intramedullary tumor in adults and typically manifests within the cervical or thoracic spinal cord. Unlike ependymoma, astrocytoma is characterized by diffuse fusiform expansion of the cord, with the lesion not as sharply delineated. It is usually T2 hyperintense and T1 iso- to hypointense and has variable enhancement. An astrocytoma may have an eccentric growth pattern. Blood products are not as common with astrocytomas as they are with ependymomas.

Noncompressive Causes of Acute Myelopathy

Metabolic Cause

Subacute combined degeneration is a metabolic condition caused by vitamin B₁₂ deficiency. It



a.

b.

Figure 16. Intramedullary lung metastasis in a 46-year-old man. Sagittal STIR (a) and contrast-enhanced T1-weighted (b) MR images of the cervical spine show an enhancing intramedullary mass with peritumoral edema that is extensive and out of proportion to the size of the lesion.

results in a dorsal cord syndrome that is secondary to demyelination of the posterior columns. In severe cases, it also involves the corticospinal tracts. Subacute combined degeneration usually is secondary to B_{12} malabsorption and can be seen in patients who have pernicious anemia, have undergone bariatric surgery, or are on a strictly vegan diet. The onset of symptoms usually is insidious. Patients often present with sensory ataxia, paresthesia, and/or a history of frequent falls. They may also have spasticity and hyperreflexia with corticospinal tract involvement. Symptoms of dementia may be present in severe cases.

The abnormal signal intensity is usually contiguous in length, spanning several vertebral segments. At MRI, increased symmetric signal intensity on T2-weighted images, with corresponding hypointensity on T1-weighted images, is seen in the posterior columns, often with an inverted "V" configuration (Fig 19) (13). Mild enhancement caused by the breakdown of the blood–spinal cord barrier secondary to demyelination may be present. Treatment with parenteral B_{12} usually resolves symptoms, with the success of the treatment being dependent on the duration of the deficiency. Imaging abnormalities may not be completely resolved after treatment.



a.

b.

Figure 17. Cervical spine ependymoma in a 51-year-old woman. Sagittal T2-weighted (a) and contrast-enhanced T1-weighted (b) MR images of the cervical spine show a well-defined expansile T2-heterogeneous intramedullary mass with avid contrast enhancement and large cranial and caudal polar cysts (arrows in a).



a.

b.

Figure 18. Ependymoma in a 40-year-old woman. Sagittal STIR (a) and contrast-enhanced T1-weighted (b) MR images of the cervical spine show a central expansile intramedullary T2-hyperintense mass with a small amount of peritumoral edema and avid enhancement.

Vascular Causes

Spinal Cord Infarction.—Anterior spinal artery ischemia and spinal cord infarction cause ventral cord syndrome with involvement of the anterior

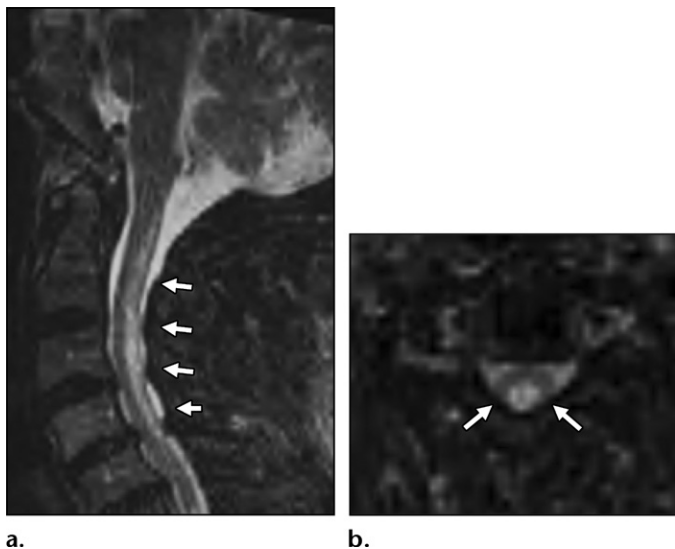


Figure 19. Subacute combined degeneration in a 67-year-old man who presented with distal paresthesia, loss of proprioception, and a history of frequent falls. Sagittal STIR (a) and axial T2-weighted (b) MR images of the cervical spine show a multisegmental intramedullary T2-hyperintense signal abnormality (arrows) that is localized to the posterior columns and has an inverted "V" morphology.

two-thirds of the spinal cord. Patients present with acute and often painful symptoms of motor deficiency at the level below the level of infarction. These symptoms are often accompanied by bladder and/or bowel incontinence and spinothalamic tract involvement characterized by loss of temperature and pain sensation (13,30). Infarction of the posterior one-third of the spinal cord is rare secondary to the presence of bilateral posterior spinal arteries, as well as collateral vessels from the vascular pial plexus. In approximately half of patients, the cause of the infarction is unknown. Known causes include systemic hypotension secondary to shock, aortic or vertebral artery dissection, fibrocartilaginous emboli, a vascular complication after aortic surgery or coronary artery bypass graft placement, sickle cell disease, and/or cocaine abuse. Cord ischemia with venous hypertension also may occur in the setting of spinal arteriovenous malformation or epidural venous plexus thrombosis caused by an epidural phlegmon or tumor.

If cord ischemia is suspected, axial and sagittal diffusion-weighted imaging should be included in the MRI examination, as restricted diffusion is indicative of acute infarction. The transition from a normal appearance of the spinal cord to an abnormal appearance is typically well defined and indicative of an abnormality in the vascular territory. T2-weighted MRI reveals a linear pencil-like hyperintense signal within the spinal cord, corresponding to the ischemic vascular territory. Involvement of the anterior gray matter may cause an "owl's eye" appearance with corresponding high signal intensity at T2-weighted imaging (31). Of note, the intramedullary T2 signal intensity can appear normal during the first few hours after the onset of ischemia because the abnormal T2 signal intensity is proportional to the net inflow of edema (32).

T1-weighted MRI reveals spinal cord expansion in the acute phase. In rare cases of hemorrhagic conversion, the spinal cord will appear T1 hyperintense. Diffusion-weighted images show corresponding restricted diffusion secondary to cytotoxic edema (Fig 20). The restricted diffusion should resolve within a week, but the T2-hyperintense signal abnormality will persist. There may be an associated signal intensity abnormality of the adjacent vertebral bodies corresponding to bone marrow infarction.

Dural Arteriovenous Fistula.—Dural arteriovenous fistula (DAVF) of the spinal cord most commonly affects elderly men with symptoms of progressive myelopathy. These symptoms include gait disturbance, paresthesia, sensory loss, and radicular pain, which can be aggravated by exercise and eventually progress to bowel and bladder dysfunction. DAVF is one of the most common vascular lesions of the spine. It is considered to be an acquired disease and affects the thoracolumbar spine. DAVF results from an abnormal anastomosis between a spinal radiculomeningeal artery and radicular vein. This anastomosis leads to venous perimedullary arterialization and venous congestion, reduced cord perfusion, and subsequent chronic cord ischemia. Spinal cord edema may occur distant to the site of DAVF and often progresses in the caudocranial orientation.

DAVF can be frequently confused with degenerative cervical or lumbar stenosis, diabetic neuropathy, and other disorders with similar symptoms that affect this age group. Imaging is paramount to quickly determine the correct diagnosis, which is important because affected patients with longer delays to diagnosis have been shown to improve the least following treatment (33).

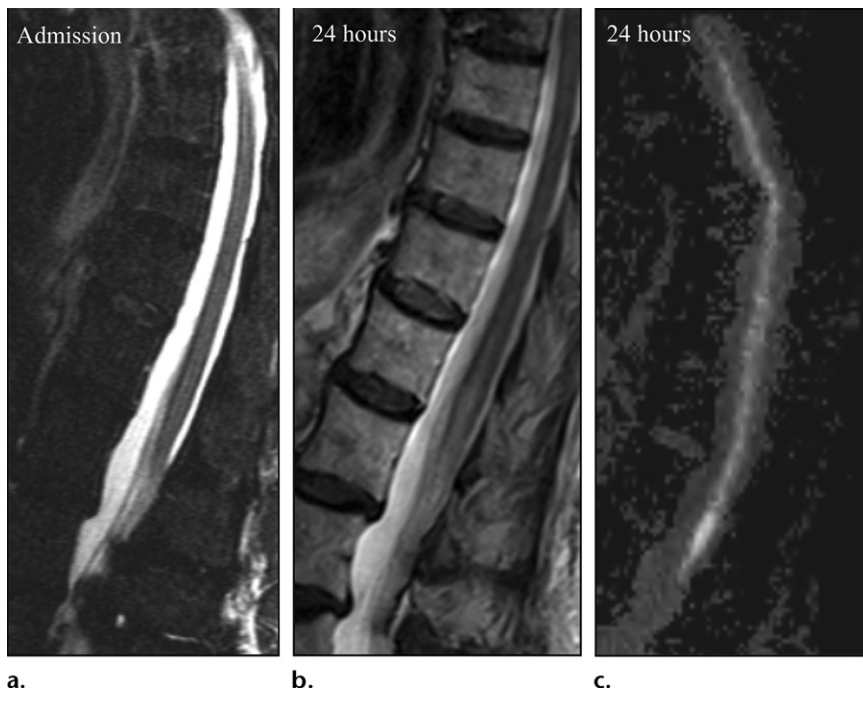


Figure 20. Spinal cord infarction in a 72-year-old man with a sudden onset of paraplegia and numbness. (a) Sagittal STIR image of the thoracic spine obtained at hospital admission shows normal spinal cord signal intensity. (b) Repeat sagittal STIR image obtained 24 hours later shows that a central abnormal T2-hyperintense intramedullary signal has developed. (c) Concurrent sagittal diffusion-weighted image shows diffuse intramedullary signal intensity, consistent with acute spinal cord infarction.

On MR images, the spinal cord typically is enlarged over multiple spinal levels and has central T2 hyperintensity with flame-shaped margins. A T2-hypointense rim may be seen and probably represents deoxygenated blood within the surrounding dilated capillary vessels. Of note, edema may not be present in cases of early DAVF detection. Multiple serpentine perimedullary flow voids from the arterialized and distended venous plexi often are seen and are key findings for a correct and prompt diagnosis. It is important to note that in cases of slow flow during early DAVF, these venous plexi may not be well seen at T2-weighted MRI. In such cases, contrast-enhanced MRI is the most reliable modality for visualizing dilated serpentine enhancing perimedullary vessels, which are suggestive of DAVF (Fig 21) (33). Ill-defined diffuse enhancement of the affected cord caused by the chronic breakdown of the blood–spinal cord barrier is often present. MR angiography and selective spinal digital subtraction angiography are useful for DAVF detection and catheter angiography guidance. DAVFs are treated with endovascular embolization, open surgical ligation, or a multimodality approach.

Inflammatory Causes

Multiple Sclerosis.—Multiple sclerosis (MS) is an autoimmune cell-mediated demyelinating disease that affects the brain and spinal cord, with lesions separated over time and space. It preferentially involves women, particularly those between the ages of 20 and 40 years. MS may

be asymptomatic or manifest with paresthesias, muscle weakness, gait disturbance, bowel dysfunction, and/or bladder dysfunction. The CSF typically shows oligoclonal bands. MRI reveals focal discrete or ill-defined T2-hyperintense spinal cord lesions, with isolated spinal lesions seen in 10%–20% of cases. The cervical spine is most commonly affected. The lesions are often peripheral, with a preference for dorsal and lateral white matter tracts; oval or wedge shaped; and asymmetric (34).

Unlike with intramedullary tumors, with MS, there is no perilesional cord edema or marked cord expansion. Enhancing lesions represent acute to subacute demyelination, and the enhancement pattern changes with the evolution of inflammation, often from focal to ill-defined enhancement. It has been suggested that an incomplete ring enhancement pattern is specific for the diagnosis of MS (35). Cord atrophy may be seen during later stages of MS and correlates with clinical disability. MRI of the brain helps in determining the correct diagnosis, as abnormal white matter signal intensity in a periventricular, pericallosal, cerebellar, or brainstem distribution at T2-weighted imaging strongly suggests a diagnosis of MS (Fig 22).

Neuromyelitis Optica Spectrum Disorder.—Neuromyelitis optica (NMO) is an inflammatory disease of the central nervous system that typically reveals seropositivity for the astrocytic aquaporin-4 immunoglobulin G (AQP4-IgG) water channel receptor. The classic triad of NMO consists of optic neuritis, longitudinally extensive transverse myeli-

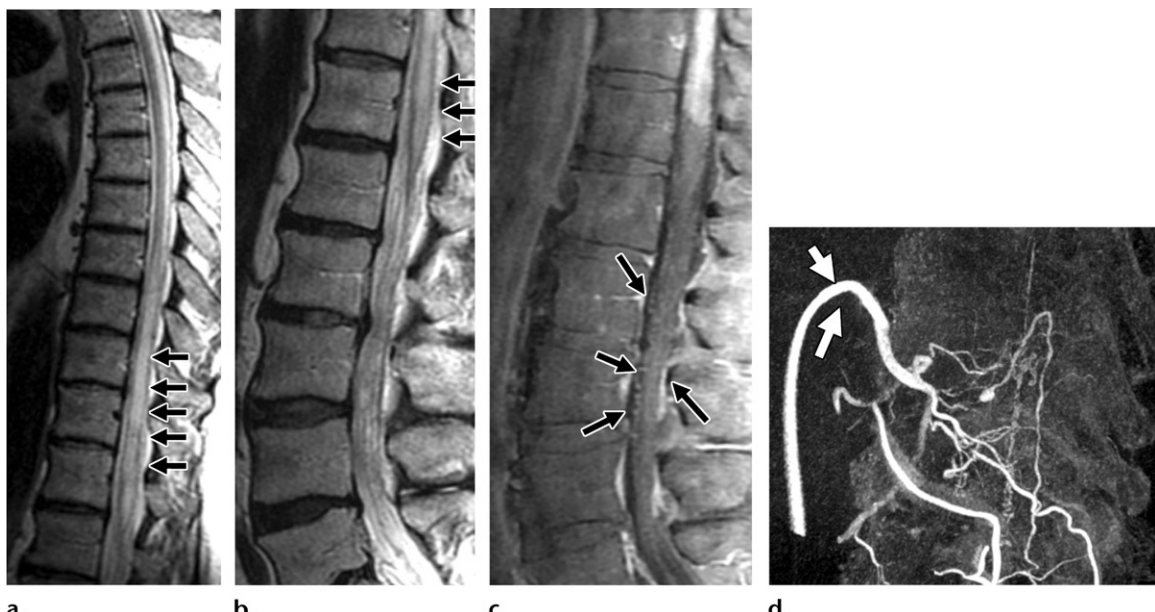


Figure 21. DAVF in a 63-year-old man who presented with bilateral leg numbness. (a–c) Sagittal T2-weighted (a, b) and contrast-enhanced T1-weighted (c) MR images of the thoracic and lumbar spine show an expanded and enhancing spinal cord from the T8 vertebral level to the conus medullaris, with central T2 hyperintensity, flame-shaped margins, and a T2-hypointense peripheral rim (arrows in a and b). There are multiple dilated intradural veins (arrows in c), which are best seen on contrast-enhanced images and appear as subtle flow voids on T2-weighted images. (d) MR angiogram of the thoracic spine shows dilated early-filling right T10 vertebral level perimedullary veins with a right T10 radiculomedullary feeding artery (arrows), consistent with DAVF. The incidental focal vascular dilatation medial to the fistula probably represents an aneurysm of the proximal aspect of the artery of Adamkiewicz. Although a fistula is present at the T10 level, the spinal cord involvement occurs in the caudocranial direction.

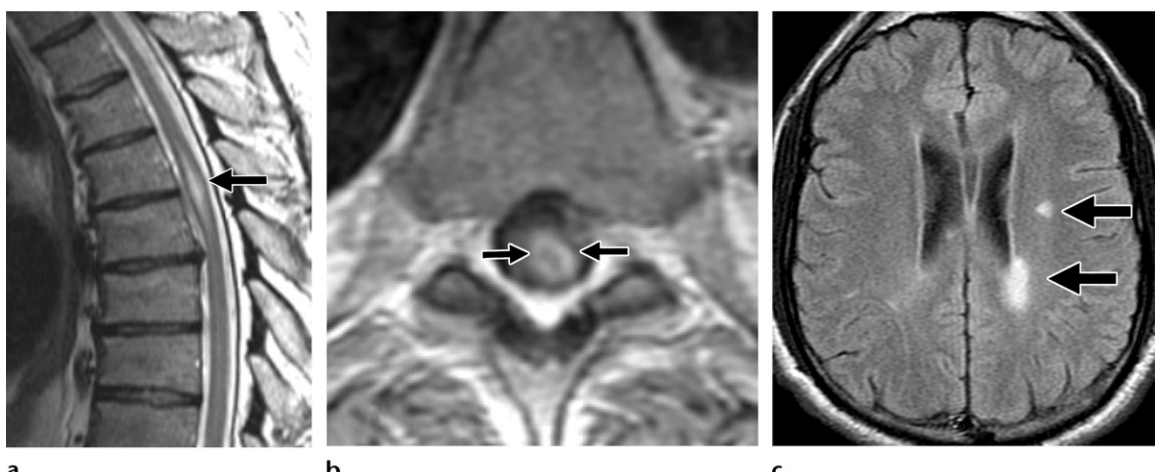


Figure 22. MRI findings in a 37-year-old man with a history of MS who presented with new-onset chest wall numbness. (a, b) Sagittal T2-weighted (a) and axial contrast-enhanced T1-weighted (b) MR images at the T5 vertebral level show a focal eccentric intramedullary T2-hyperintense lesion (arrows), with mild cord expansion and ring enhancement. (c) Axial fluid-attenuated inversion-recovery brain MR image shows T2-hyperintense periventricular foci (arrows), which are typical of demyelinating lesions.

tis involving more than three vertebral segments, and serologic analysis findings positive for AQP4-IgG antibody. The spectrum of NMO disorders includes AQP4-IgG-positive and AQP4-IgG-negative forms of NMO, as well as NMO disorders coexisting with other autoimmune diseases.

Similar to patients with MS, patients with NMO may have relapses. However, unlike with MS, with NMO there is no gradual decline in

functional status between the relapses (36,37). Importantly, many medications used for the treatment of MS may cause NMO to worsen. A minority of patients with clinical characteristics of NMO and seronegativity for AQP4-IgG have a detectable serum myelin oligodendrocyte glycoprotein (MOG) antibody. Fewer than 20% of patients with NMO have oligoclonal bands at CSF analysis.



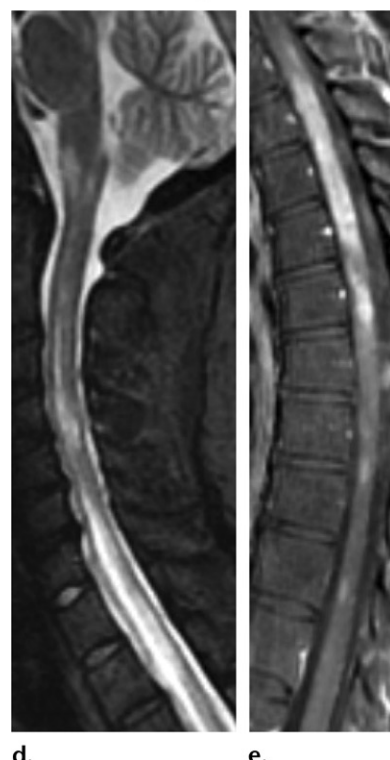
Figure 23. AQP4-IgG-seropositive NMO in a 53-year-old woman who presented with acute paraparesis and left-sided vision loss. (a, b) Coronal STIR (a) and contrast-enhanced T1-weighted fat-suppressed (b) MR images of the orbits show an edematous T2-hyperintense enhancing left optic nerve (arrows), indicating acute optic neuritis. (c) Coronal contrast-enhanced T1-weighted brain MR image shows enhancement of the septum pellucidum (arrows). (d, e) Sagittal STIR (d) and contrast-enhanced T1-weighted (e) MR images of the cervicothoracic spine show a longitudinally extensive T2-hyperintense central intramedullary signal with spinal cord expansion and enhancement, and extension to the brainstem.

In the acute setting, the spinal cord is expanded and shows central abnormal T2-hyperintense signal and enhancement longitudinally involving three or more segments, potentially extending into the brainstem (Fig 23). Brain MRI typically shows, in addition to optic neuritis, T2-hyperintense lesions in areas with the highest aquaporin-4 receptors, including the periependymal surfaces of the third and fourth ventricles and at the area postrema. There is often involvement of the dorsal medulla, hypothalamus, and thalamus, with long confluent corpus callosum lesions. Bright spotty lesions, described as T2-hyperintense foci with signal intensity similar to that of CSF within a T2-hyperintense spinal cord lesion, are suggestive of NMO (38).

Acute Disseminated Encephalomyelitis.—Acute disseminated encephalomyelitis (ADEM) is considered to represent a postinfectious or postvaccination sequela that involves widespread demyelination affecting the brain and spinal cord. Multiple viral and bacterial diseases have been implicated in the development of ADEM and include varicella, rubella, measles, Epstein-Barr virus, and mycoplasma infection. Although the exact mechanism of this condition is not well understood, it is suspected to be secondary to an autoimmune response to a myelin antigen (39).

ADEM typically affects children and young adults. The onset usually is rapid, with systemic symptoms including myalgia, headache, nausea, vomiting, drowsiness following a multifocal neurologic disorder with encephalopathy, cranial nerve palsy, ataxia, and paresis.

Spinal MRI reveals mild cord expansion with multifocal T2-hyperintense flame-shaped enhanc-

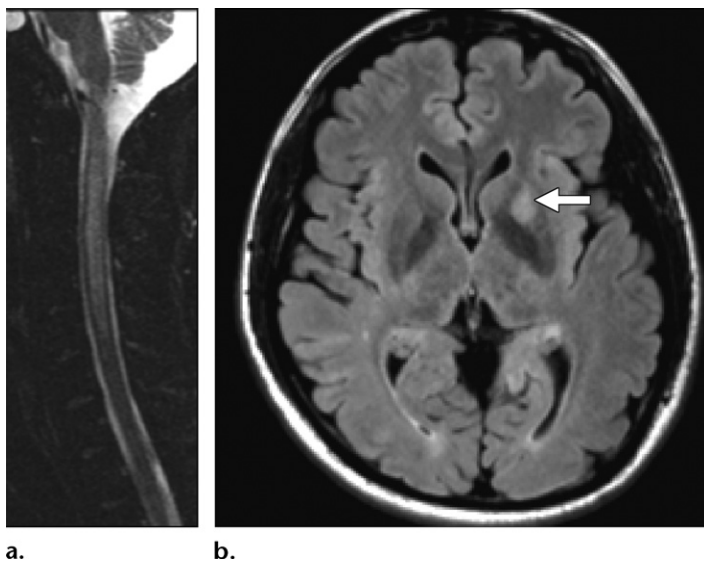


d. e.

ing white matter lesions, which may be similar in appearance to MS lesions (31). The spinal involvement can be focal or segmental (Fig 24). Unlike polyphasic MS lesions, ADEM lesions are of the same age, indicating a monophasic disorder. Brain involvement is common and consists of patchy asymmetric T2-hyperintense regions involving the gray matter–white matter junction. The cranial nerves and gray matter, the basal ganglia and thalamus in particular, can be involved; this is atypical with MS. Corpus callosum involvement is infrequent.

The CSF usually demonstrates lymphocytic pleocytosis, increased protein levels, and increased pressure. Oligoclonal bands are rare. ADEM responds to steroids, and recovery most frequently occurs within weeks or months, with complete recovery in 50% of cases (39).

Postviral Acute Transverse Myelitis.—Postviral acute transverse myelitis represents an acute inflammatory condition of the spinal cord. This disease occurs either secondary to a direct viral



a. b.

infection or as a postviral immune response. Enteroviruses are the most common pathogens, with signs of acute myelopathy developing after a febrile illness (40). On MR images, the spinal cord has an edematous appearance, with a segmental contiguous T2-hyperintense signal in the affected regions and variable patchy enhancement. At T1-weighted MRI, the spinal cord can have central low signal intensity, simulating syrinx, that is higher than the signal intensity of the CSF. The CSF demonstrates elevated mononuclear cells and protein levels. Brain involvement is not common.

Idiopathic Acute Transverse Myelitis.—Idiopathic acute transverse myelitis is the diagnosis of exclusion in the setting of bilateral rapid development of myelopathy. With this disease, there is a well-defined sensory level, evidence of inflammation at CSF analysis, and clinical symptom progression to nadir within 4 hours to 21 days (41). Radiologically, *idiopathic acute transverse myelitis* is defined as longitudinally extensive central intramedullary T2 hyperintensity involving gray and white matter, with expansion of the spinal cord, involvement of two or more vertebral levels, and variable contrast enhancement. Thus, in the absence of other definitive clues, acute transverse myelitis can be added to the differential diagnosis of most noncompressive myelopathies. For this reason, an initial diagnosis of idiopathic transverse myelitis is frequently discounted at additional workup. In prior studies (42), a more specific diagnosis, most commonly MS or spinal cord infarction, has been established in approximately 70% of cases initially diagnosed as idiopathic acute transverse myelitis.

Conclusion

The occurrence of acute myelopathy in a non-traumatic setting constitutes a medical emer-

Figure 24. ADEM in a 20-year-old man who initially presented with a decreased level of consciousness and lower extremity weakness. (a) Sagittal STIR MR image of the cervical spine shows mild cord expansion at the C2–C7 spinal level, with central longitudinally extensive intramedullary T2 hyperintensity. (b) Axial fluid-attenuated inversion-recovery MR image of the brain shows abnormal high T2 signal intensity in the left putamen (arrow), which is typical of the gray matter involvement in ADEM. These signal intensity abnormalities were resolved on MR images obtained 2 months later.

gency in which spinal MRI is frequently ordered as the first step in the patient's workup. Symptoms of myelopathy may have a compressive cause that can be further localized to the extradural, intradural extramedullary, or intramedullary compartments of the spinal canal. Use of a compartmental approach in combination with clinical and laboratory findings aids in refining the diagnosis and determining the appropriate surgical or nonsurgical management.

Noncompressive myelopathy represents abnormal intramedullary signal intensity without an underlying space-occupying lesion. It has a wide range of vascular, metabolic, inflammatory, infectious, and demyelinating causes with seemingly overlapping imaging appearances. The differential diagnosis may be refined by considering the location and longitudinal extent of the abnormal signal intensity within the cord, pertinent clinical history, and laboratory findings.

Acknowledgment.—The authors thank Dr. Zlatko Minev for creating the drawing in Figure 2.

Disclosures of Conflicts of Interest.—B.K. Activities related to the present article: disclosed no relevant relationships. Activities not related to the present article: received book royalties from Cambridge University Press. Other activities: disclosed no relevant relationships.

References

- Parizel PM, van der Zijden T, Gaudino S, et al. Trauma of the spine and spinal cord: imaging strategies. Eur Spine J 2010;19(Suppl 1):S8–S17.
- New PW, Cripps RA, Bonne Lee B. Global maps of non-traumatic spinal cord injury epidemiology: towards a living data repository. Spinal Cord 2014;52(2):97–109 [Published correction appears in Spinal Cord 2014;52(5):417.]
- Fehlings MG, Vaccaro A, Wilson JR, et al. Early versus delayed decompression for traumatic cervical spinal cord injury: results of the Surgical Timing in Acute Spinal Cord Injury Study (STASCIS). PLoS One 2012;7(2):e32037.
- Arce D, Sass P, Abul-Khoudoud H. Recognizing spinal cord emergencies. Am Fam Physician 2001;64(4):631–638.

5. Fraser S, Roberts L, Murphy E. Cauda equina syndrome: a literature review of its definition and clinical presentation. *Arch Phys Med Rehabil* 2009;90(11):1964–1968.
6. Sakka L, Gabrillargues J, Coll G. Anatomy of the Spinal Meninges. *Oper Neurosurg (Hagerstown)* 2016;12(2):168–188.
7. Bilsky MH, Laufer I, Fourney DR, et al. Reliability analysis of the epidural spinal cord compression scale. *J Neurosurg Spine* 2010;13(3):324–328.
8. Tetreault L, Goldstein CL, Arnold P, et al. Degenerative cervical myelopathy: A spectrum of related disorders affecting the aging spine. *Neurosurgery* 2015;77(Suppl 4):S51–S67.
9. Williams AL, Murtagh FR, Rothman SLG, Sze GK. Lumbar disc nomenclature: version 2.0. *AJNR Am J Neuroradiol* 2014;35(11):2029.
10. Mochida K, Komori H, Okawa A, Muneta T, Haro H, Shinomiya K. Regression of cervical disc herniation observed on magnetic resonance images. *Spine* 1998;23(9):990–995; discussion 996–997.
11. Song KJ, Kim KB, Lee KB. Sequestered thoracic disc herniation mimicking a tumoral lesion in the spinal canal: a case report. *Clin Imaging* 2012;36(4):416–419.
12. McNamee J, Flynn P, O'Leary S, Love M, Kelly B. Imaging in cauda equina syndrome: a pictorial review. *Ulster Med J* 2013;82(2):100–108.
13. Kunam VK, Velayudhan V, Chaudhry ZA, Bobinski M, Smoker WRK, Reede DL. Incomplete Cord Syndromes: Clinical and Imaging Review. *RadioGraphics* 2018;38(4):1201–1222.
14. Shweikeh F, Saeed K, Bukavina L, Zyck S, Drazin D, Steinmetz MP. An institutional series and contemporary review of bacterial spinal epidural abscess: current status and future directions. *Neurosurg Focus* 2014;37(2):E9.
15. Guerado E, Cerván AM. Surgical treatment of spondylodiscitis: An update. *Int Orthop* 2012;36(2):413–420.
16. Yeom JA, Lee IS, Suh HB, Song YS, Song JW. Magnetic resonance imaging findings of early spondylodiscitis: Interpretive challenges and atypical findings. *Korean J Radiol* 2016;17(5):565–580.
17. Pierce JL, Donahue JH, Nacey NC, et al. Spinal Hematomas: What a Radiologist Needs to Know. *RadioGraphics* 2018;38(5):1516–1535.
18. Mak KS, Lee LK, Mak RH, et al. Incidence and treatment patterns in hospitalizations for malignant spinal cord compression in the United States, 1998–2006. *Int J Radiat Oncol Biol Phys* 2011;80(3):824–831.
19. Savage P, Sharkey R, Kua T, et al. Malignant spinal cord compression: NICE guidance, improvements and challenges. *QJM* 2014;107(4):277–282.
20. Cavaliere R, Schiff D. Epidural spinal cord compression. *Curr Treat Options Neurol* 2004;6(4):285–295.
21. Rizvi T, Wintermark M, Schiff D. Imaging of Epidural Spinal Cord Compression. In: Newton HB, ed. *Handbook of Neuro-Oncology Neuroimaging*. 2nd ed. London, England: Academic Press/Elsevier, 2016.
22. Gibbs WN, Nael K, Doshi AH, Tanenbaum LN. Spine Oncology: Imaging and Intervention. *Radiol Clin North Am* 2019;57(2):377–395.
23. Sohawon D, Lau KK, Lau T, Bowden DK. Extra-medullary haematopoiesis: a pictorial review of its typical and atypical locations. *J Med Imaging Radiat Oncol* 2012;56(5):538–544.
24. Bartels RHMA, Brunner H, Hosman A, van Alfen N, Grotenhuis JA. The Pathogenesis of Ventral Idiopathic Herniation of the Spinal Cord: A Hypothesis Based on the Review of the Literature. *Front Neurol* 2017;8:476.
25. French H, Somasundaram A, Biggs M, et al. Idiopathic intradural dorsal thoracic arachnoid cysts: A case series and review of the literature. *J Clin Neurosci* 2017;40:147–152.
26. Agarwal N, Shah J, Hansberry DR, Mammis A, Sharer LR, Goldstein IM. Presentation of cauda equina syndrome due to an intradural extramedullary abscess: a case report. *Spine J* 2014;14(2):e1–e6.
27. Shim DM, Oh SK, Kim TK, Chae SU. Intradural extra-medullary tuberculoma mimicking en plaque meningioma. *Clin Orthop Surg* 2010;2(4):260–263.
28. Ledbetter LN, Leever JD. Imaging of Intraspinal Tumors. *Radiol Clin North Am* 2019;57(2):341–357.
29. Jeon JH, Hwang HS, Jeong JH, Park SH, Moon JG, Kim CH. Spinal schwannoma: analysis of 40 cases. *J Korean Neurosurg Soc* 2008;43(3):135–138.
30. Küker W, Weller M, Klose U, Krapf H, Dichgans J, Nägle T. Diffusion-weighted MRI of spinal cord infarction: high resolution imaging and time course of diffusion abnormality. *J Neurol* 2004;251(7):818–824.
31. Sheerin F, Collison K, Quaghebeur G. Magnetic resonance imaging of acute intramedullary myelopathy: radiological differential diagnosis for the on-call radiologist. *Clin Radiol* 2009;64(1):84–94.
32. Weidauer S, Nichtweiss M, Lanfermann H, Zanella FE. Spinal cord infarction: MR imaging and clinical features in 16 cases. *Neuroradiology* 2002;44(10):851–857.
33. Fox S, Hnenny L, Ahmed U, Meguro K, Kelly ME. Spinal dural arteriovenous fistula: a case series and review of imaging findings. *Spinal Cord Ser Cases* 2017;3(1):17024.
34. Muccilli A, Seyman E, Oh J. Spinal Cord MRI in Multiple Sclerosis. *Neurol Clin* 2018;36(1):35–57.
35. Klawiter EC, Benzinger T, Roy A, Naismith RT, Parks BJ, Cross AH. Spinal cord ring enhancement in multiple sclerosis. *Arch Neurol* 2010;67(11):1395–1398.
36. Ciccarelli O, Cohen JA, Reingold SC, Weinshenker BG; International Conference on Spinal Cord Involvement and Imaging in Multiple Sclerosis and Neuromyelitis Optica Spectrum Disorders. Spinal cord involvement in multiple sclerosis and neuromyelitis optica spectrum disorders. *Lancet Neurol* 2019;18(2):185–197.
37. Tackley G, O'Brien F, Rocha J, et al. Neuromyelitis optica relapses: Race and rate, immunosuppression and impairment. *Mult Scler Relat Disord* 2016;7:21–25.
38. Hyun JW, Kim SH, Jeong IH, Lee SH, Kim HJ. Bright spotty lesions on the spinal cord: an additional MRI indicator of neuromyelitis optica spectrum disorder? *J Neurol Neurosurg Psychiatry* 2015;86(11):1280–1282.
39. Garg RK. Acute disseminated encephalomyelitis. *Postgrad Med J* 2003;79(927):11–17.
40. Cassidy H, Poelman R, Knoester M, Van Leer-Buter CC, Niesters HGM. Enterovirus D68: The New Polio? *Front Microbiol* 2018;9:2677.
41. Transverse Myelitis Consortium Working Group. Proposed diagnostic criteria and nosology of acute transverse myelitis. *Neurology* 2002;59(4):499–505.
42. Zalewski NL, Flanagan EP, Keegan BM. Evaluation of idiopathic transverse myelitis revealing specific myelopathy diagnoses. *Neurology* 2018;90(2):e96–e102.